EGS Exploration Methodology Project using the Dixie Valley Geothermal System, Nevada as a Calibration Site

Part II—Final Scientific Report Enhanced Conceptual Model

2 January 2014

DOE Award: DE-EE0002778

ALTAROCK ENERGY INC

TABLE OF CONTENTS

LIST OF FIGURES[1,3]

---

[1] Only partial figure and table captions are presented given their occasional extensive description and the total number of figures and tables.

[2] A duplication in numbering for Figure 77 exists in Part I and Part II of the Final Scientific Report. However, each Figure 77 reference in the respective "part" is unique to that "part" of the report.

[3] There is no figure 135

[4] There is no Figure 150

LIST OF TABLES[1,5]

LIST OF APPENDICES[5]

[5] Figures and tables are numbered consecutively from Part I of the Final Scientific Report. Appendices in Part 1 of the report are number consecutively from 1 to x and in Part II, they are numbered as indicated.

LIST OF PLATES

LIST OF ACRONYMS

Acronym	Description
AltaRock	AltaRock Energy Inc.
ARRA	American Recovery and Reinvestment Act
asl	Above sea level
B&R	Basin and Range
BHT	Bottom hole temperature
BHTV	Borehole Televiewer
BLM	U.S. Bureau of Land Management
CBA	Complete Bouguer Anomaly
CNSB	Central Nevada Seismic Belt
COCORP	Consortium for Crustal Reflection Profiling
CSC	Coulomb Stress Change
DOE	U.S. Department of Energy
DVF	Dixie Valley Fault
DVFZ	Dixie Valley Fault Zone
DVGD	Dixie Valley Geothermal District
DVGS	Dixie Valley Geothermal System

LIST OF ACRONYMS

Acronym	Description
DVGW	Dixie Valley Geothermal Wellfield
DVPF	Dixie Valley Producing Field
DVPP	Dixie Valley Power Partners
DVESA	Dixie Valley Extended Study Area
DVSA	Dixie Valley Study Area
EGS	Engineered Geothermal System
EM	Electromagnetic
GDB	ESRI ArcGIS geodatabase
GIS	Geographic Information System
HS	Hot Spring
HTGF	High Temperature Geothermal Fluids
Jg	Jurassic rocks
Jgnm	Jurassic rock, non-magnetic
MT	Magnetotelluric
NGDR	National Geothermal Data Repository
NV	Nevada
NBMG	Nevada Bureau of Mines and Geology
PASSCAL	Program for Array Seismic Studies of the Continental Lithosphere
QFFDB	Quaternary Fault and Fold Database
Qp	Attenuation of the P-wave
Qs	Attenuation of the S-wave
QTbf	Quaternary-Tertiary basin fill
RF	Receiver Fault
rho	Seismic inferred density
SF	Source Fault
SF	Stillwater Fault
SFZ	Stillwater Fault Zone
S_{hmin}	Horizontal minimum stress direction
SME	Subject Matter Expert/Expertise/Experience
Terra-Gen	Terra-Gen Power, LLC
TGH	Temperature Gradient Hole
USGS	United States Geological Survey
Vp	P-wave velocity in km/sec
Vs	S-wave velocity in km/sec

9. NEW DATA COLLECTION AND INDIVIDUAL DISCIPLINE INTERPRETATION

The baseline data review (Sections 1 through 6) indicated that there were significant data gaps in key geological and geophysical data sets. Additional detailed geologic work is beyond the scope and budget of this project. However, additional geophysical data collection was recognized early in the proposal preparation process and planned in the project. The additional geophysical data collected throughout the Project Area (Figure 77) are:

1. 278 new gravity stations;
2. 42 new seismic stations with data obtained in two separate field deployment campaigns of up to 3 months each; and
3. 70 new MT stations.

In addition to the geophysical data collection, we conducted a focused, 308 station soil CO_2 gas survey. Each of these new surveys is discussed below.

In addition to the data presented within, Dr. Daniel Stockli at the University of Texas at Austin and his students are conducting structural, geological, geochemical, and thermochronometric analyses, Dr. J. D. Walker at the University of Kansas conducting collaborative structural work, and Drs. B. M. Kennedy and J. Lewicki conducting soil gas and noble gas work as a following-on to the Baseline Geothermal Conceptual Model presented in Section 7; see http://www1.eere.energy.gov/geothermal/pdfs/stockli_thermochronometric_peer2013.pdf. Also researchers at the Lawrence Berkeley National Laboratory Earth Science Division in collaboration with AltaRock, as a result of the Baseline Conceptual Geothermal Model work have published several geochemistry papers on Dixie Valley geothermal area (Wanner, 2012, 2013; Peiffer, 2012, 2013).

9.1 GRAVITY AND MAGNETICS

9.1.1. Gravity Survey

The Gravity and Magnetics Task Leader, Dr. Robert Karlin (Section 1.4), used the compilation of existing gravity and magnetic data to forward model a series of cross-sections in the wellfield that inferred lithology and structure at depth (e.g., Plate 1). These were used in the construction of the baseline model and the qualitative correlations that were found. This work is reported in Sections 3 and 7 (of the Baseline EGS Conceptual Model Report submitted to the NGDR and this Final Report) and in Iovenitti et al. (2011; 2012). To fill in data gaps and expand the modeling efforts outside of the wellfield, a total of 278 new gravity stations (Figure 78) were acquired to better characterize the subsurface and target EGS drilling sites. Joint 2 ¾-D forward modeling[6] of the enhanced (baseline + new) gravity and (baseline) magnetic data has been done on selected profiles to determine subsurface structure and faulting.

The new gravity stations were acquired in August 2011 using a *LaCoste and Romberg Model G* gravimeter and were reduced to complete Bouguer anomaly (CBA) values in September 2012 after first processing the GPS elevation data. The new stations were selected to fill in data gaps, particularly in the Stillwater and Clan Alpine ranges. A series of short transects were obtained

[6]Refers to modeling objects on a x-z plane with y components that have finite extents.

perpendicular to the Stillwater range front and into the basin to better define the zone of piedmont faulting on which lie all of the current geothermal production wells. Rigorous quality checking of the new gravity data revealed several data transcription errors and problems with a GPS base station for one day's observations which necessitated reducing and reprocessing all of the new gravity data provided in an earlier (i.e., November 2011) update report.

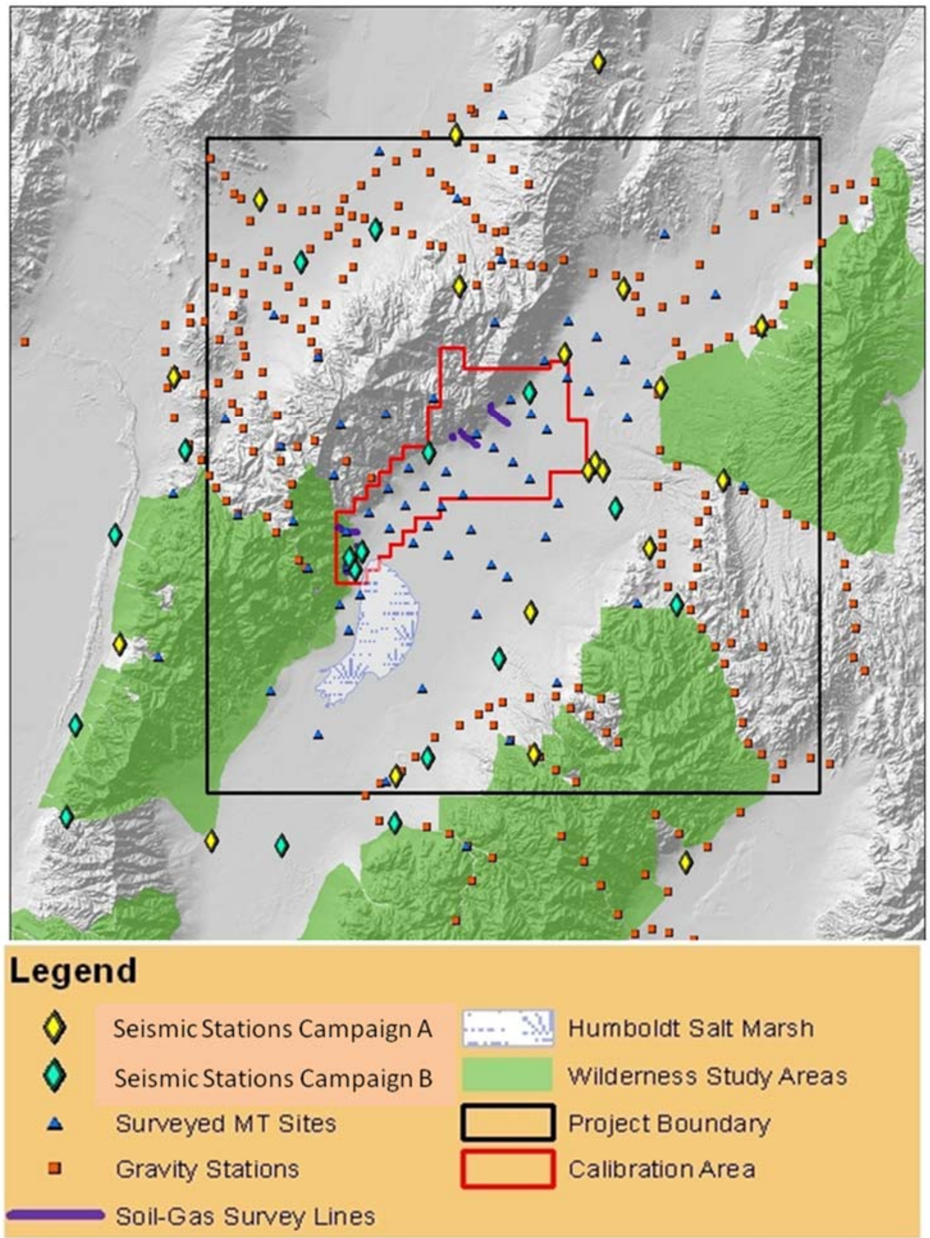

Figure 77. Project Area Map showing the locations of new data collected. The Project Area is shown by the black box, while the wellfield calibration area is shown in red. Diamonds indicated the location of seismic stations used for the passive seismic 3-month deployment campaigns A (yellow) and B (blue). The new magnetotelluric stations are shown by blue triangles. New gravity stations are shown by orange boxes. The location of the CO2 soil-gas survey lines are shown in purple. All of the data was collected from the summer of 2011 through the early winter of 2012.

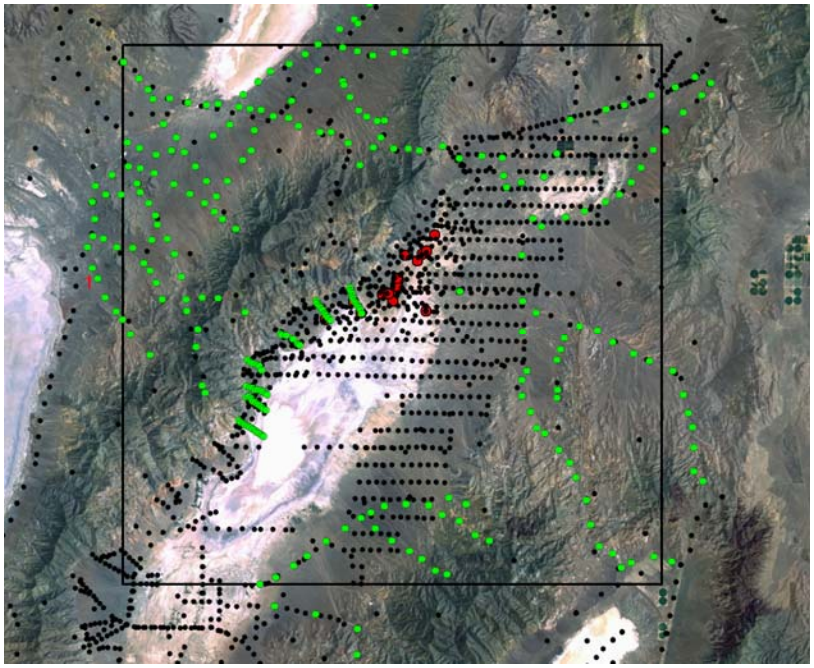

Figure 78. New 2011 gravity stations (green circles) complement the coverage of baseline gravity stations (black circles) from Smith et al. (2001) and Blackwell et al. (2005) overlain on a satellite image. The EGS Exploration Methodology Project Area is outlined in black. Geothermal wells are shown as red circles.

New CBA, RGA, and Gradient Maps

The new CBA map (Figure 79) and its derivative horizontal gravity gradient map (Figure 80a) are similar in gross aspects to the baseline conceptual model versions except that they show better definition in the ranges and a more accurate depiction of the horizontal gradients from which major faults can be delineated in the piedmont area. A linear regional gravity trend surface was computed and removed from the CBA values to produce a residual gravity anomaly (RGA) map (Figure 81). The regional trend decreases ~0.5 mgal/km in a NW/SE direction. The RGA map to some extent minimizes the high gravity values in the northern part of the Carson Sink and enhances features in the southeastern part of the study area, particularly an area of high gravity in the southwestern Clan Alpines. The CBA and RGA horizontal gradient maps (Figures 80a and 80b, respectively) show many of the same features, except for the removal of a high gradient area in the Clan Alpines in the SE portion of the map.

9.1.2 Composite Total Magnetic Field Anomaly Map

The total magnetic field map in Figure 82 is a compilation of the high resolution HELIMAG data (Graugh, 2002, see http://irpsrvgis08.utep.edu/viewers/flex/GravityMagnetic/) in Dixie Valley proper and the lower resolution PACES data (http://irpsrvgis00.utep.edu/repositorywebsite) which offers wider coverage. Several discrete magnetic highs are observed throughout the area and appear to have a NW/SE trend. These have been identified to be part of the Jurassic volcanic complex referred to as either an upper thrust ophiolite suite or a lopolith torn apart by Basin and Range extension (Blackwell et al., 1999, 2002, 2005).

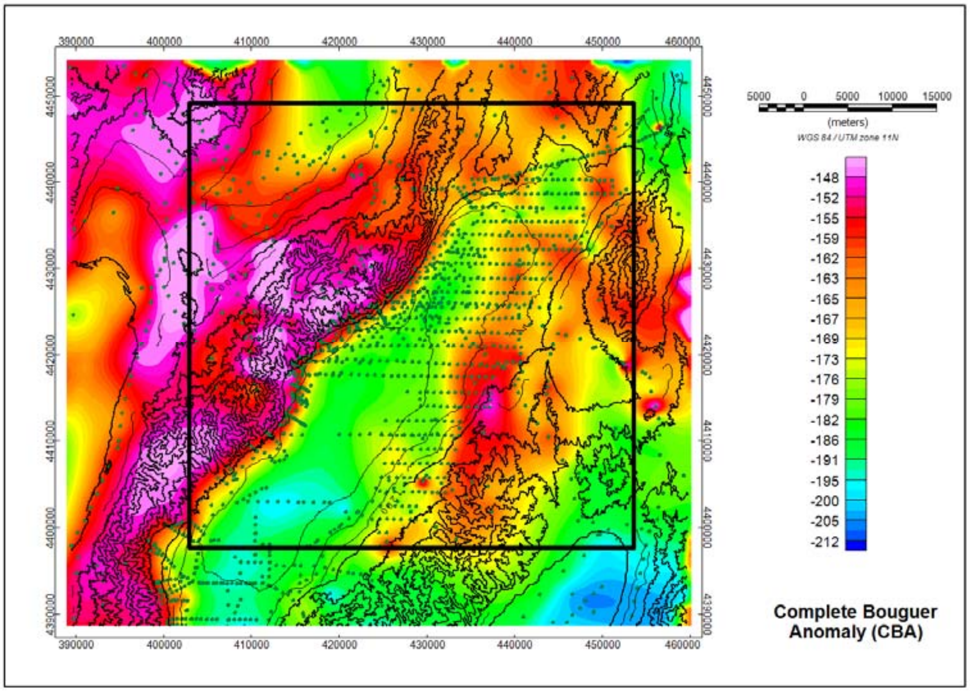

Figure 79. Complete Bouguer Anomaly (CBA) gravity map of the Dixie Valley area with all gravity stations (new and baseline, see Figure 2). Warm values are gravity highs associated with the Virginia, Stillwater, and Clan Alpine Mountain Ranges. The EGS Exploration Methodology Project Area is outlined in black. Topographic contours are in 100 m intervals. Gravity stations are based on Smith et al. (2001), the USGS gravity database (see http://irpsrvgis08.utep.edu/viewers/flex/GravityMagnetic/), and this study.

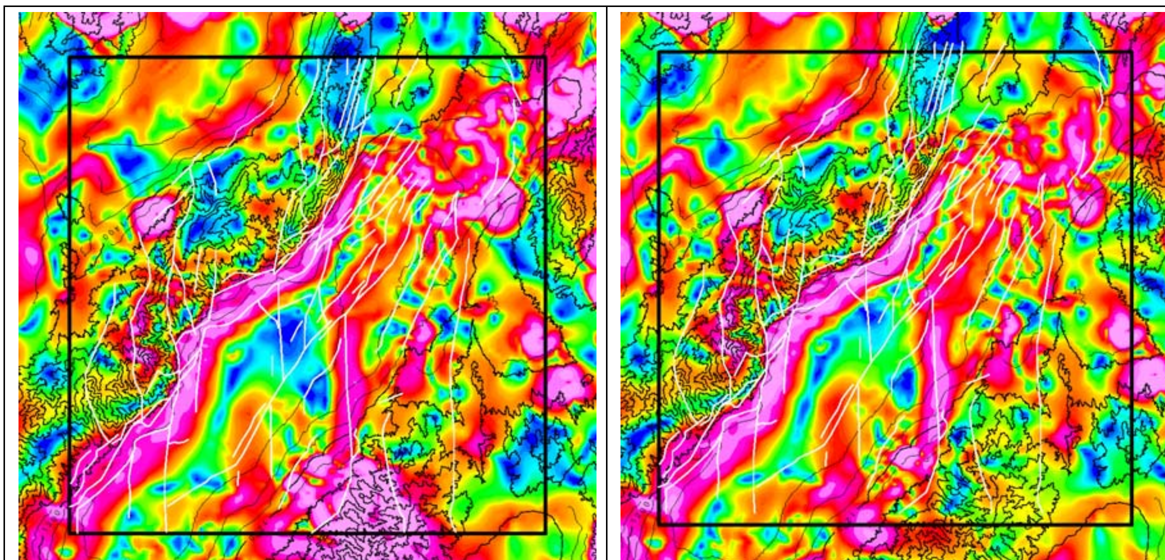

(a) (b)

Figure 80. Complete Bouguer Anomaly (a) and Residual Gravity Anomaly (b) horizontal gravity gradient maps of the project area (bolded black outline) with 100m contours (faint black lines). Known and inferred faults are shown as white lines. High values (warm colors) indicate either fault zones or regions of major lithologic (i.e., density) change.

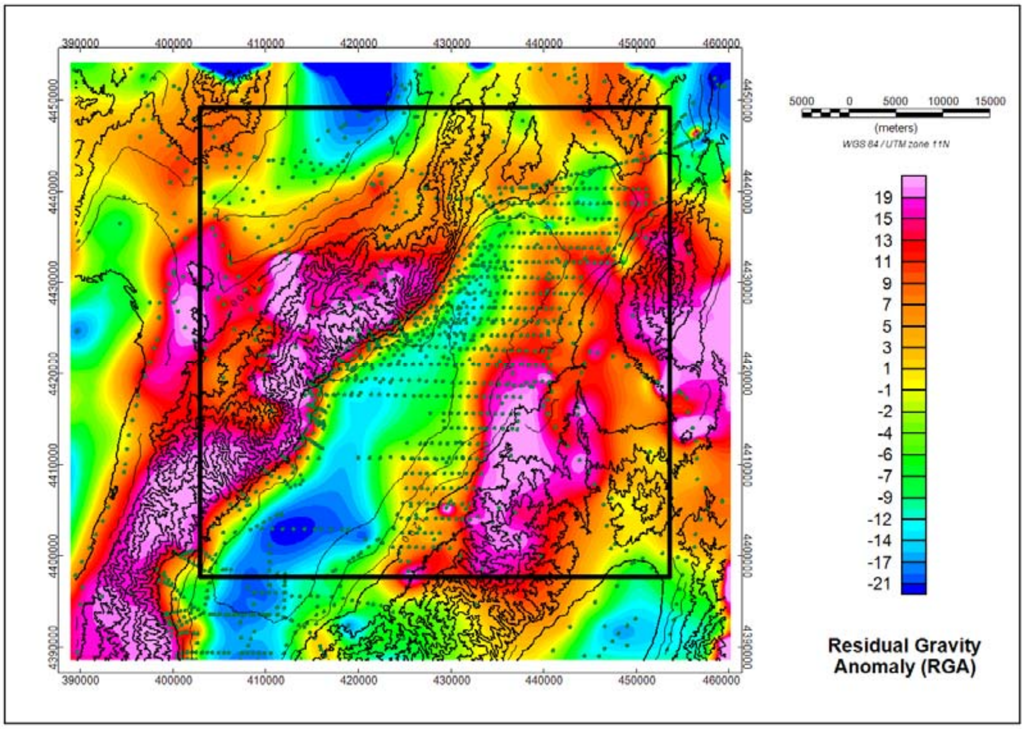

Figure 81. Residual gravity anomaly (RGA) map (in mgal) after removing a regionally decreasing gravity trend of 0.5mgal/km in a NNW/SSE direction. The EGS Exploration Methodology Project Area is outlined in black. Topographic contours are in 100 m intervals. All gravity stations in the project region are described in Figure 78.

9.1.3 Forward Joint Gravity/ Magnetic Modeling Procedures

Four sets of modeling profiles were created using the magnetics and enhanced (new + baseline) gravity data (1) Lines C through J, the updated baseline area profiles, see Sections 3 and 7, (2) shortline profiles (A1 to A6) along Stillwater range front, (3) Longlines (LL1 to LL4), and (4) an along-axis Stillwater Range profile (AX) (Figures 82 and 83). With the exception of AX, the profiles were oriented perpendicular to the Stillwater range front and chosen to pass through locations of maximum gravity station coverage. In most cases, the actual station CBA data were used for modeling instead of the interpolated grid to minimize artifacts due to sparse coverage. Hybrid models consisting of the baseline HELIMAG aeromagnetic data of Grauch (2002) and Smith et al. (2002) flown at 120 m (304 ft) and the PACES data flown at 305 m (1000 ft) elevation were combined. The PACES data shows only relatively long wavelength features compared to the HELIMAG data, which makes Dr. Karlin, the Gravity-Magnetics Task Leader, suspect that either the PACES data were filtered or that the original aeromagnetic data was flown at a much higher elevation (+8000ft) prior to downward continuation. Each profile presented different challenges to model.

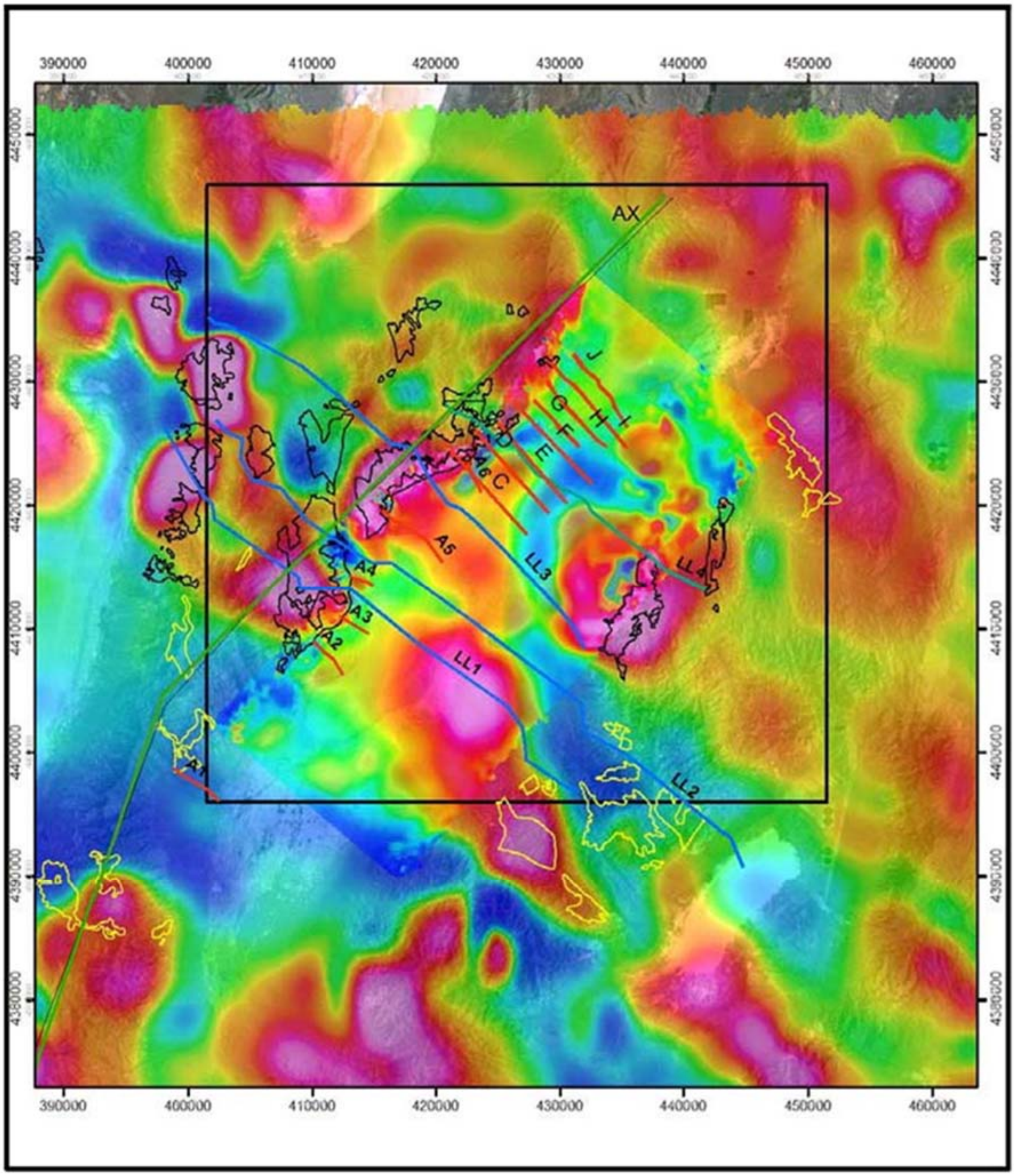

Figure 82. Total aeromagnetic intensity map (in nanotesla) using HELIMAG and PACES data (see text for reference) superimposed on a satellite image along with section lines described herein. Four long-lines are oriented NW-SE and are labeled LL1 to LL44 in blue. The along-axis line (AX) is green, while the short-lines are labeled A1 to A6 (in red). The EGS Exploration Methodology Project Area is outlined in black. Intensities vary from 669nT to 70 nT. Outlines areas are Jurassic igneous rocks (Jgb and Jvb) in black and Tertiary andesites and basalts (Ta1) in yellow.

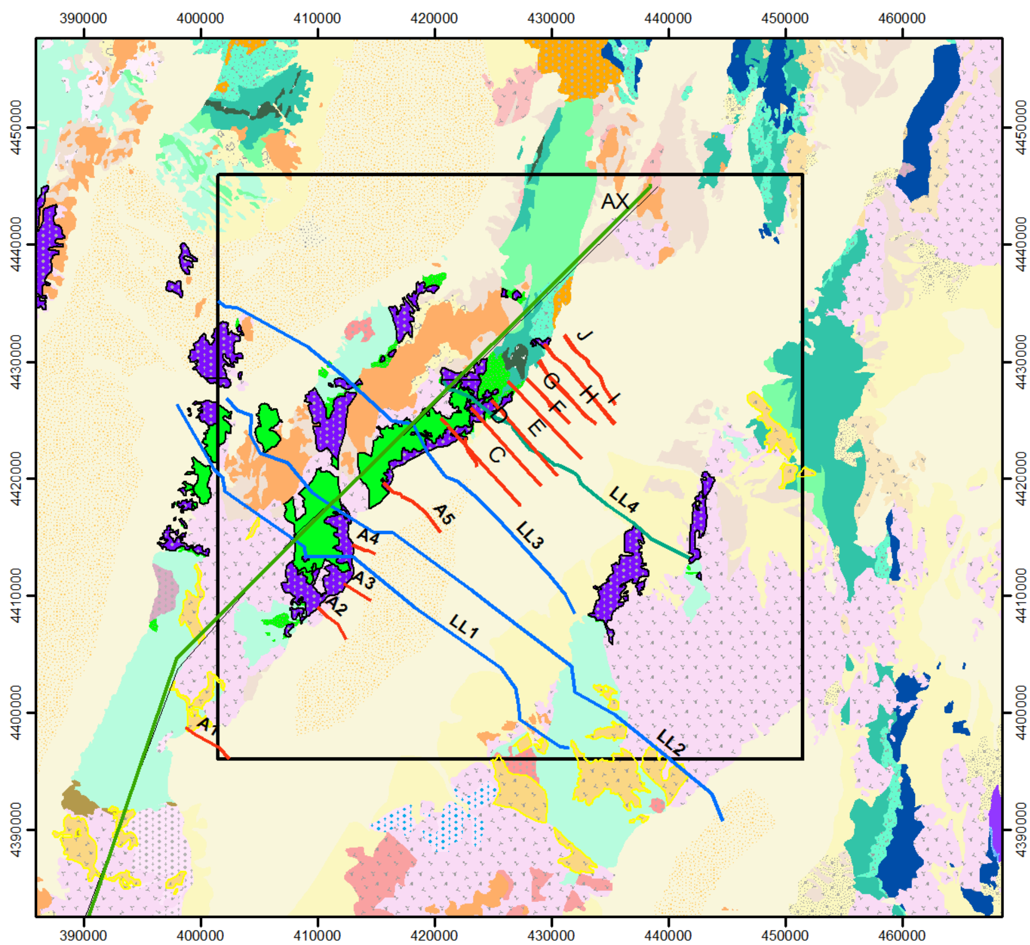

Figure 83. Locations of labeled forward modeling profiles superimposed on a geologic map after Crafford (2007). The EGS Exploration Methodology Project Area is outlined in black. Units are: Triassic sedimentary rocks (TRs) (light green and teal); Jurassic gabbroic rocks (Jg) (purple); Jurassic mafic volcanic rocks (Jv) (green); Tertiary rhyolites (Tr) (pink), Tertiary basalt (Tba) (orange), and valley alluvium Qya (pale yellow).

In general, fits of 1-2% precision were achievable for the short line and updated baseline area models, but the precision of long line models was 1-3%. In some cases it was necessary to model off-axis magnetic features. Each line showed minor scatter of up to 2-3 mgal off a smoothed curve. We think that much of the lack of fit in the gravity data was due to elevation uncertainties, base station differences (NAD 27 spheroid versus NAD83 and WGS84 geocentric framework) and perhaps different methods of processing and survey errors accumulated over 50 years of data collection. Magnetics offsets were observed between the PACES and HELIMAG data although the major magnetic anomalies in map view agree very well between the two data sets. This is probably due to the difference in flight elevations (120m vs. 305m [304ft vs. 1000ft]). We also suspect that the PACES data were originally downward continued from a much higher flight path because the anomalies are much smoother and of longer wavelength than one would expect from the nominal 305m (1000ft) flight path.

The bedrock and basins could be modeled with a density contrast of ~0.4 gm/cc. We modeled the profiles in two ways (1) using basement D= 2.876 gm/cc and fill D= 2.445 gm/cc and (2) using bedrock D= 2.67 gm/cc and basin-fill inverted for best fit. Both methods yielded similar results, again verifying that the density contrast was the most important factor. In magnetics modeling we used a susceptibility of S = 0.007 (cgs) for Jg and Jv (herein called Jz) rocks and S=0.0 for all other units. This is equivalent to a magnetization of M= ~0.0035 emu/gm. The field was calculated from the International Geomagnetic Reference Field (2011) yielding 50200 nT, inclination I = 64° and declination D =13° based on the latitude (40°) and longitude (-118°). Modeling was done with D= 0° which is the secular variation averaged geocentric axial dipole value.

Model fits for each of the CBA models and station locations are given in Appendices 22-24. Care should be exercised in placing much significance to the gravity models in the areas with little or no station coverage. In the ensuing interpretations, these areas have been blanked out.

9.1.4 Stratigraphic setting of the profiles

Updated Baseline Area Models

The updated baseline area eight profiles in the calibration area (i.e., production area) labeled C through J (Figure 83) were taken perpendicular to the range front in areas that had the highest gravity station density. Lines C, D, E, and H started in the Jurassic volcanics (Jg and Jv) units and extended into the alluvium. Lines F and G were anchored in Triassic sediments in the range, while J was completely in the alluvium.

Shortline Models

A total of six short-line profiles (A1 to A6) were extracted in areas where new gravity station profiles were specifically targeted to allow tracing the active portions of the piedmont fault system and determining which faults are dominant. Determining the geometry is considered important because all of the producing wells and some of the hot springs lie on or near the piedmont fault and we seek to find methods to define new targets for geothermal exploration. Line A1, furthest to the south, started in the Tertiary rhyolites, while the rest of the lines began in Jurassic volcanic units exposed in the range front.

Longline Models

The locations of the longlines are presented in Figures 82 and 83.

Line LL1

The furthest south line starts at the edge of the Carson Sink, passes through the Stillwater Range over Jurassic volcanics (Jv), Tertiary rhyolites (Tt2), next to Tertiary basalts (Tba), again over Jv and Jurassic gabbros (Jg) then into Dixie Valley alluvial sediments. Figure 83 presents a generalized lithologic map of the area investigated with the new gravity lines constructed during this analysis. As Line LL1 encounters the Clan Alpine Range, it first passes over Tba, near the granite (Kg) and stops in Triassic sediments. The magnetics signature consists of two highs in the Stillwater Range and a buried high just west of the Clan Alpines, ending in a pronounced low.

Line LL2

The next line north starts in alluvium north of the Carson sink, passes through Jv, then along a boundary between Tertiary rhyolite (Tr) and Tertiary basalt (Tba), then into Jv, and Jg on the eastern margin of the Stillwater range. The line passes through Dixie Valley and into the Clan Alpines where it encounters Triassic meta-sediments (Trs) and more Tertiary rhyolites and basalts. It then goes across the Edwards Creek Valley and into the Tertiary rhyolites and Paleozoic sedimentary rocks of the Desatoya Mountains.

Line LL3
This line is about 3km south of line C. This profiles starts in playa and alluvium of the Carson Sink then in the Stillwater complex encounters Trs, Tba, Tt2, Jv and Jg. It then passes through the alluvium of Dixie Valley and ends in the Clan Alpines next to a Jg/Trs contact.

Line LL4
The profile partially overlaps and extends line E. It starts in the complex Jg and Jv of the Stillwater Range and goes though Dixie Valley and ends in Jg of the Clan Alpines.

Line AX (along-axis)
Examination of the magnetics map (Figure 82) shows that the Stillwater Range proper contains relative highs and lows. The highs are associated with surface exposures of the Jurassic volcanic complex. To determine if the observed lows in the magnetic anomalies were due to reversed blocks or the result of interactions between separated normally magnetized block, an along-axis was created to run roughly across the peak axis of the Stillwater Range. The stratigraphy varies from Triassic sediments in the north, to Jurassic volcanics to Tertiary rhyolites to Triassic sediments at the bend of the line then back into rhyolites, then near Tertiary basalts at the end.

9.1.5 Results

Production area lines
Lines C to J were run in the vicinity of the available wells to calibrate the models and compare our results with other geological and geophysical studies in the project. These models use a basement density of 2.67 gm/cc and basin fill varies between 2.1-2.2 gm/cc. Individual models with station locations and residual errors for each line are given in Part II-Appendix 1. In Figure 84, faults were assigned based on sharp slopes between basin fill and bedrock and/or offsets and gaps in the Jurassic magnetic units. The basin shape is defined by the gravity data. On lines C, E and H, it is necessary to introduce a lower density surficial layer in the basin fill to account for short wavelength variations in the gravity data. On line C, the rhyolites are exposed at the surface and the model requires a low density (D=2.3 gm/cc) unit in the range. The fit of lines D to F requires a non-magnetic high density (D=2.8-2.9 gm/cc) block near the surface. The upper and lateral boundaries of the magnetic units are strongly constrained by the fit of the magnetic data; however the magnetic lower boundaries have some flexibility. On line G, it is necessary to introduce a reversely magnetized block on the eastern side of the basin. On line H, the small Jz unit at depth on the eastern side of the valley could also be modeled as a small normally magnetized unit (lava flow?) within the basin fill. On lines H, I and J, the nonmagnetic bedrock between the basin fill and the Jz (Jv+Jg) units area may be inferred to represent Tertiary rhyolites derived from the Clan Alpine range. On all of the lines, the nonmagnetic bedrock between the non-continuous Jz (Jg+Jv) units could be interpreted either as non-magnetized Jz rocks, hydrothermally altered Jz rocks, originally non-existent Jz rocks, or a combination of the above. With the exception of well 65-18 on line D, the modeled basin fill depths for all of the lines are in very good agreement with the well data.

On every line, the piedmont faults rather than the range front faults of the Stillwater Range are the dominant structures controlling the western part of Dixie Valley. More than one piedmont fault appears to be present in lines C-G and possibly H. Most of the piedmont faults appear to be steeply dipping to near vertical. Jurassic magnetic units appear as discontinuous down-dropped blocks which underlie the bedrock/basin fill contact. The complexity of the piedmont fault system appears to become simpler to the north and there are fewer Jurassic blocks. The depth of the basin appears relatively constant among the profiles, although the basin shoals to the north. Where imaged, the eastern margin of the basin appears to be controlled by steep westward dipping faulting.

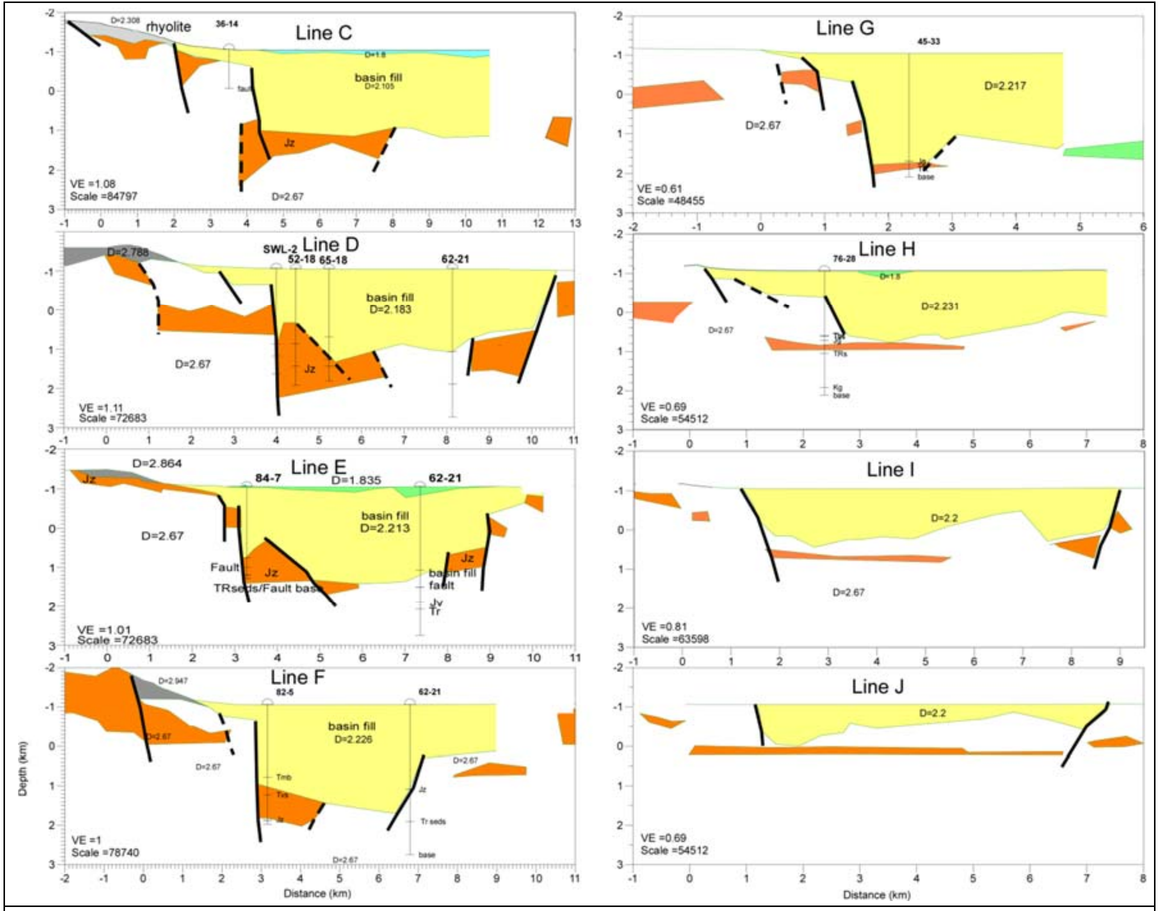

Figure 84. Updated baseline models of lines C-J in the northwest portion of the calibration area are plotted with available well data. Yellow represents basin fill, and orange denotes magnetized Jz units. Light blue is low density basin fill. Light grey in line C is low density rhyolite. Dark grey is a dense nonmagnetic unit and green in line G is a reversely magnetized unit.

Shortlines A1 to A6

The 'geological' models for the six short-line profiles (A1 to A6) are shown in Figure 85. In the modeling the basement rock density along these lines was set at 2.67 gm/cc and the basin fill density was allowed to vary to obtain a best fit. In every case, the best fit of modeled basin fill density was 2.15 to 2.2 gm/cc. Modeling was accomplished successfully with errors less than 1%. The model fits of the A1 to A6 lines are given in Appendix 1.

In all of the profiles, the major displacement occurs on the piedmont faults. Surprisingly the present range front faults show relatively little offset. The geometry of the piedmont fault system is suggestive of several down-dropped blocks. The faults are for the most part steeply dipping although there is a trend for the fault dips to shallow to the north approaching the reentrant in center of the study area, (cf. lines A1 to A3) then again steepen further north (cf. lines A5 and A6). In lines A1 to A4 the major offset occurs on NS faults suggesting that the majority of basin formation mostly likely occurred when the stress regime was oriented NS rather than in the present NE/SW orientation. In lines A5 and A6 the major offset is on NE/SW structures.

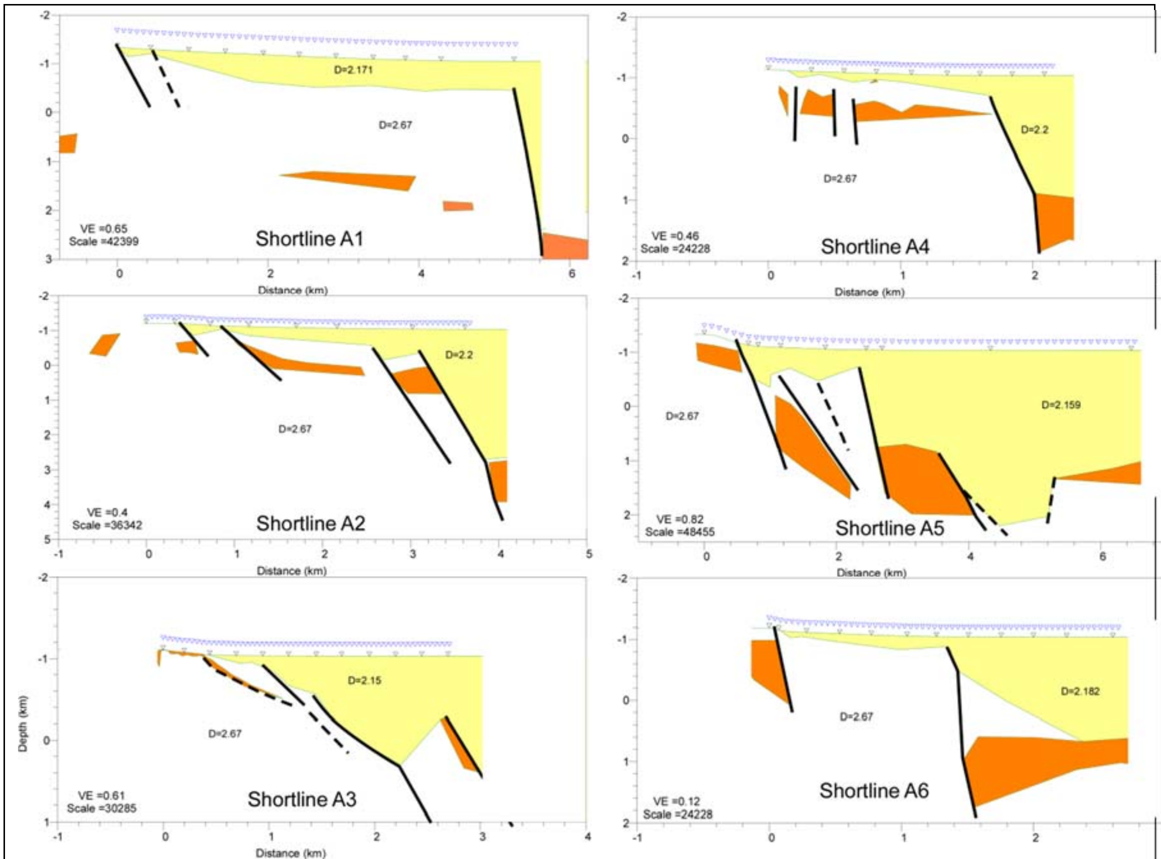

Figure 85. CBA models of shortlines A1-A6. Color coding as in Figure 83.

Longlines LL1 to LL4 and the Along-Axis Line AX

The model fits of the longline LL1 to LL4 and line AX (Figures 82 and 83) are presented in Part II-Appendix 1. Jointly modeled fits of the long-line gravity and aeromagnetic data are shown in Figure 86 and the resultant models and interpretations are summarized in Figure 79. Triangles denote station location for gravity stations (height =0 m), HELIMAG stations (height= 120 m) and PACES gridded data (nominal height = 305m). Basin fill is in yellow, Jurassic magnetized units are in orange, and rhyolitic units are in grey. The green unit in line LL2 represents Paleozoic sediments. More than 800 nT of magnetic change and 60 mgal of gravity variation are seen in the profiles.

Long-line 1

With a few exceptions the magnetic anomalies are of long wavelength implying deeply seated sources. A few kinks in the magnetics data suggest near surface contributions. Generally, the basin fill is a faulted graben with east steeply dipping faults to the west and more gently west-dipping faults to the east. The east side of the valley may contain antithetic faults compensating for the master fault system next to the Stillwater range. Basin fill is in excess of 4km.

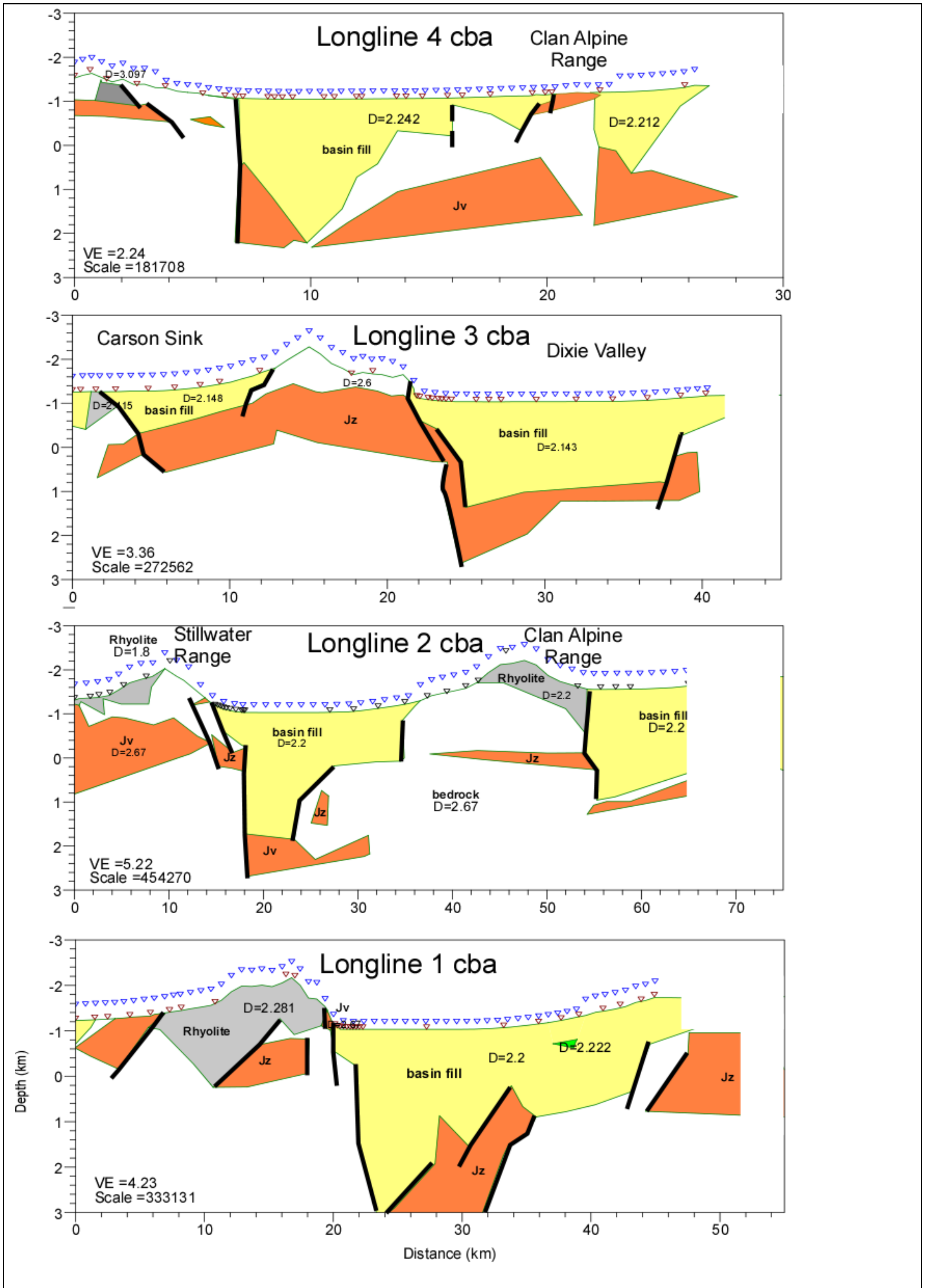

Figure 86. Models of longlines LL1 to LL4. Color coding the same as in Figure 84, except that Paleozoic sedimentary rocks in LL3 are in green.

Long-line 2

This section spans the Stillwater and Clan Alpine ranges and Dixie and Edwards Creek valleys. Short wavelength spiky magnetic anomalies suggest near surface sources in the Stillwater Mountains while more subdues anomalies to the east imply deep-seated sources. Most notable is a large ramp of decreasing gravity across the Clan Alpines and to the east. Indeed, this low is observed throughout the southeastern part of the study area and extends all the way past Eureka, NV (Thompson et al., 1989).

Thompson et al. (1989) modeled a COCORP deep seismic reflection line and gravity from Fallon to Eureka, NV along Highway 50 which is slightly to the south of the study area. They showed a bimodal distribution of gravity with the major discontinuities occurring on the Stillwater/Dixie and the Clan Alpine/Edwards Creek fault system (Figure 87). The sharp drop in gravity just east of the Clan Alpines is slightly misleading, because Highway 50 jogs north for several kilometers just east of the Clan Alpine fault. They argued that the gravity and seismic velocity changes were due to an increase in thickness of the crust and/or lithosphere to the east, or alternatively, thinning and extension to the west. This is a major regional structural feature. To fit the low gravity values in long-line LL2, it was necessary to introduce 4-5km of crustal compensation into the model at 27-32km depth. With no well control or physical property data for the Paleozoic sedimentary rocks in the Desatoya Mountains and uncertainty in the crustal thicknesses, the modeling is not well constrained east of the Clan Alpine fault.

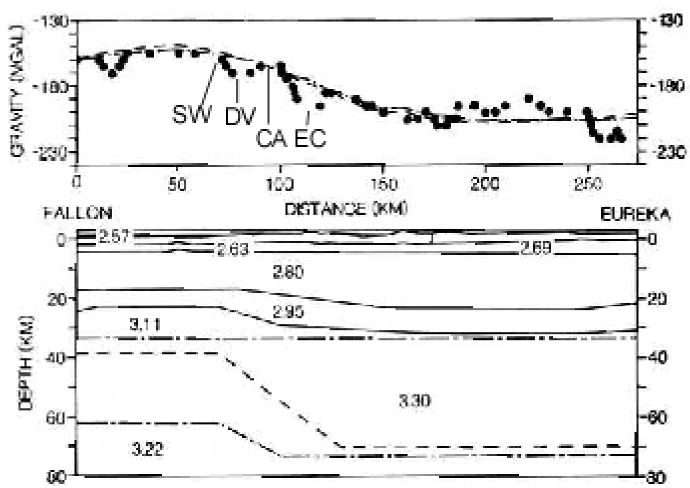

Figure 87. Crustal model of Thompson et al. (1989) for the Fallon to Eureka COCORP transect along Highway 50 showing thickening of the crust and/or lithosphere in eastern Nevada. Note the abrupt gravity discontinuities at the Stillwater (SW)/ Dixie Valley (DV) and Clan Alpine (CA)/ Edwards Creek Valley (EC) range front faults.

Long-line 3

This line contains several irregular short-wavelength magnetic anomalies suggest near surface sources. The model suggests that the Jurassic units are relatively continuous under the Stillwater range but broken up into down-dropped blocks on the range front and piedmont faults. The basin is ~2km thick and is immediately underlain by Jz units.

Long-line 4

This line shows discontinuous Jurassic rocks under the basin. The interval between the basin fill and the Jz units is dense but non-magnetic and may represent massive rhyolitic units, such as exposures found in the Clan Alpines. Jurassic units appear to thin out under the Stillwater Range. Unlike the other lines, the main fault appears to be a single zone, perhaps bifurcated at depth.

Along Axis line AX

Modeling of the along axis line clearly showed that the lows can be readily explained as due to interaction between separated normally magnetized Jurassic volcanic (Jz) blocks (Figure 88). This is important because if the units were originally contiguous, their separation may be caused by faulting and perhaps amplified by demagnetization due to hot fluid flow in the fractures, or breakup of the unit during its initial emplacement. Indeed in most cases, shallow thermal areas such as Senator fumaroles, Section 10 hot springs, Dixie Meadows, and Hyder hot springs lie in magnetic lows or near the boundaries of relative magnetic lows and highs (Figure 89).

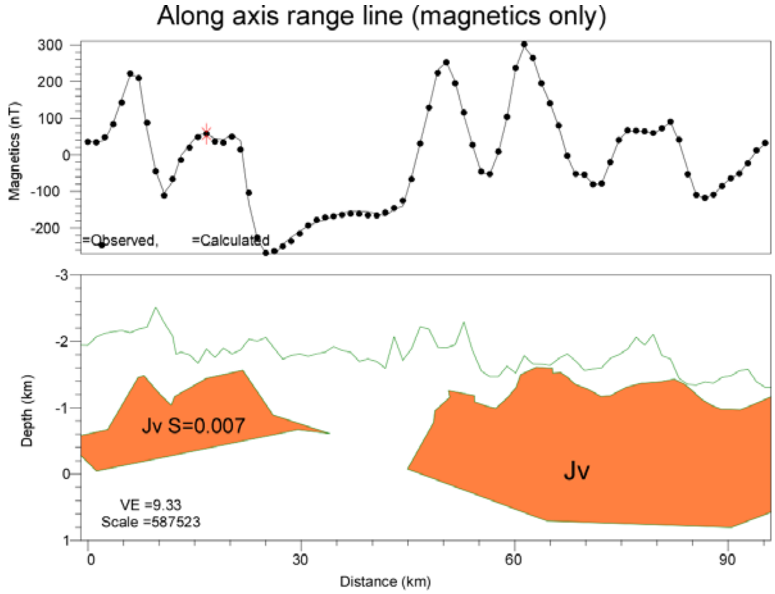

Figure 88. Along Axis range line AX. Relative highs and lows in aeromagnetic data in the Stillwater Range (top) can be modeled by separate blocks of normally magnetized Jurassic volcanics (below). Reversely magnetized units are not needed.

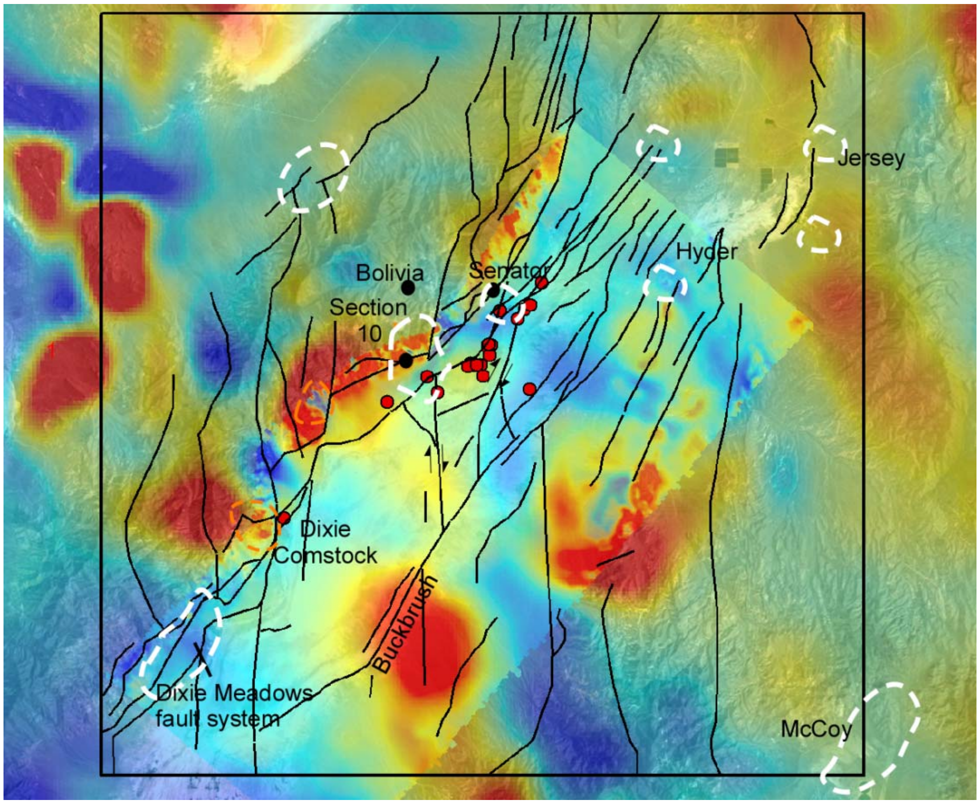

Figure 89. Relation between shallow geothermal anomalies (white and red dashed areas, Blackwell et al., 2005) and aeromagnetic anomalies. Most shallow hot spots (white dashed area) occur near the boundaries between relative magnetic lows and highs which probably areas where the Jurassic volcanics have been rifted apart by N/S faulting. The EGS Exploration Methodology Project Area is outlined in black.

9.1.6 Residual Gravity Models

The large region of relatively low gravity observed in the SE quadrant of Figure 79 might suggest the need to remove a regional gravity gradient. The rationale for creating a residual gravity map is that the study area lies in a transitional region between stable crust to the east and Basin and Range extension to the west, as suggested by Thompson et al. (1989). This idea is supported by our difficulties in obtaining an adequate joint model for longline LL2 without introducing a change in crustal thickness or asthenospheric density. How to best accomplish a regional trend removal is a problem faced by many gravity analysts, particularly if well or deep seismic data are not readily available in the particular area of interest (i.e., the Clan Alpine Range). Factors to consider are how large an area to include and what type of trend to remove (e.g., linear, higher order, transitional, abrupt, isostatic, etc.). An isostatic model was not considered because the Basin and Range is probably not in isostatic equilibrium, although this may be a question for future research. For simplicity, we decided to create a first order linear regional trend from the CBA data in the entire Project Area of Figure 79. One arguably could have just worked with the data in the project area; however, we considered this choice to be arbitrary and encompassing only a small part of the regional trend. As mentioned earlier, the trend surface showed a decreasing NW to SE gradient of 0.5 mgal/km.

New joint 2 ¾ D models of gravity residuals and a hybrid of HELIMAG and PACES magnetics data were created for all twenty lines. The RGA model fits are given in Part II-Appendix 2 and the resultant 'geological' models are summarized for the updated baseline area (Figure 90), shortlines (Figure 91) and longlines (Figure 92). The location of these lines is presented in Figures 82 and 83.

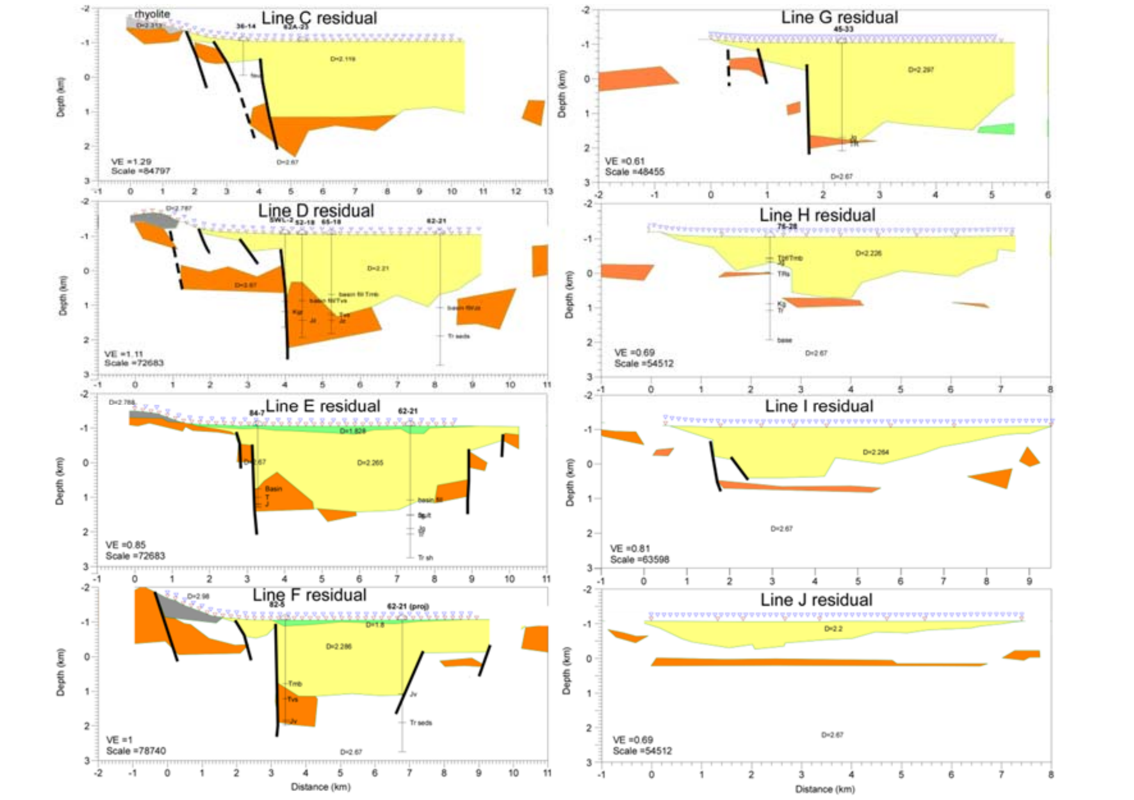

Figure90. RGA models of the lines C to J in the northwest portion of the calibration area. Color coding as in Figure 83.

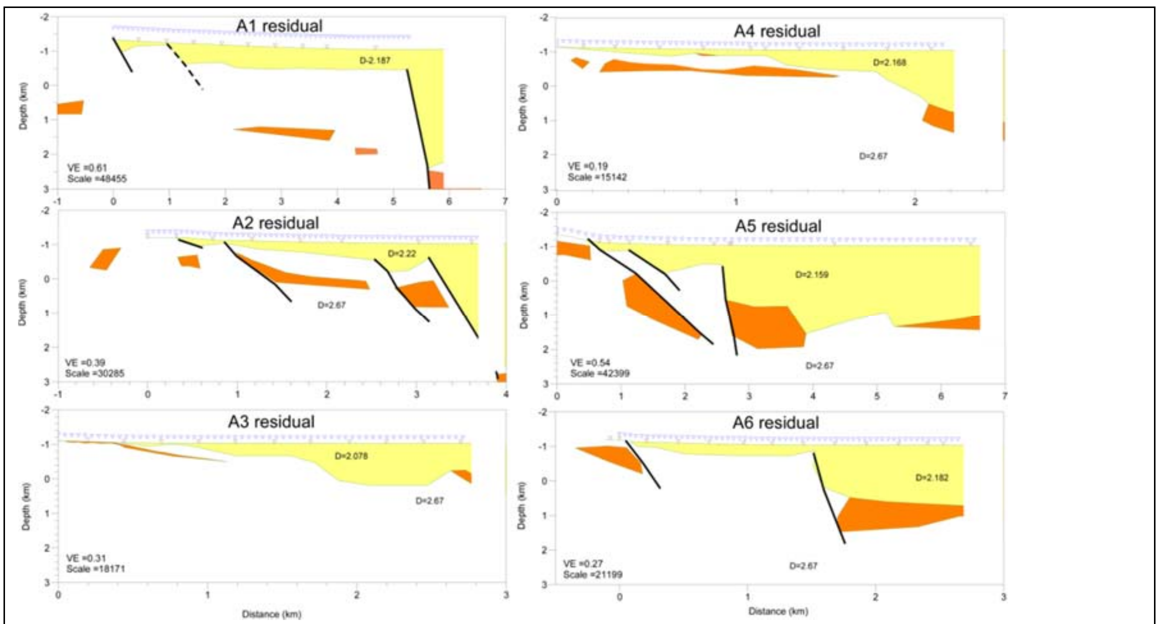

Figure 91. Residual Gravity Anomaly models of shortlines A1 to A6. Color coding as in Figure 83.

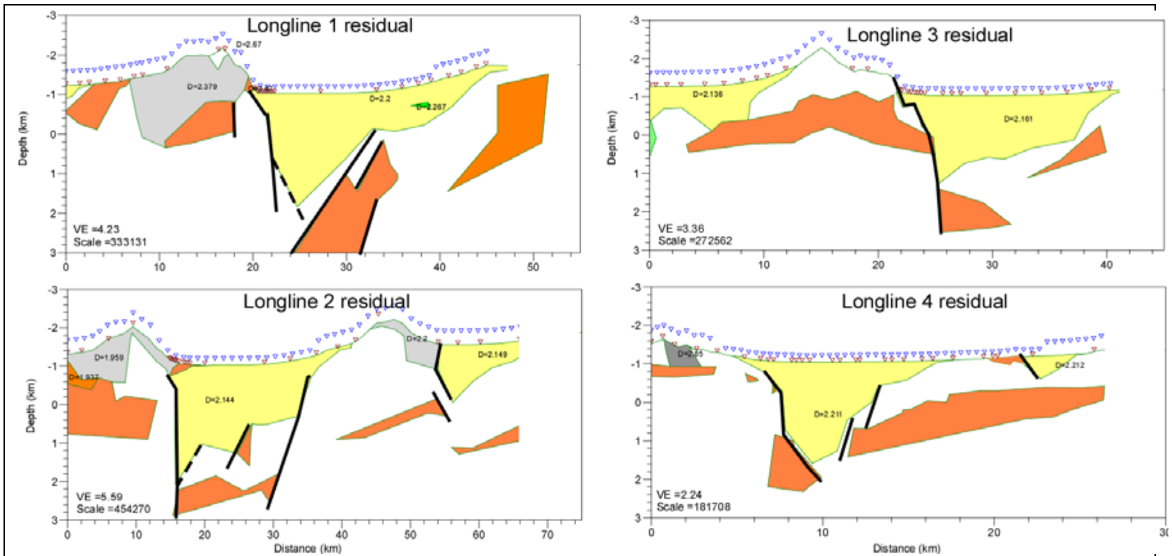

Figure 92. Residual Gravity Anomaly models of longlines LL1 to LL4. Color coding as in Figure 82.

9.1.7 Comparison of RGA and CBA Joint Models

RGA and CBA models are compared graphically in Figures 93-95 and Part II-Appendix 3 for the updated baseline area, shortlines, and longlines, respectively. The full models are shown rather than having non-station areas blanked out to facilitate actual comparison of the model; however, the basin edges are not well constrained by the gravity data where there is no data.

For Lines C to J (Figure 93), in general, the residuals can be modeled with a minor change in basin density and a shallowing of the basin to the east compared with the CBA models. In lines C, D, and E, the locations of the major piedmont fault structures and the basin configuration are very similar in both the CBA and residual models. The residual models for Lines G and H show significant basin shallowing and eastward shifting of the western piedmont fault(s). The basin fill/bedrock contact of the line F RGA model F shows good agreement with the contact found in well 82-5, but the modeled Jz units lie within the lithologies of Miocene basalt (Tmb) and Oligocene silicic volcanics (Tvs) identified in the well. The basin depths of Line H and the CBA model of Line G agree closely with those of wells 45-33 and 76-28, although the basin fill for the Line G residual model is too shallow. Both models for lines I and J show a very shallow basin but there is no well data to calibrate\validate the model.

For shortlines A1 to A6 (Figure 94), the RGA models of A1, A2, and A3 are almost identical to the CBA models, except for a slight shift in the location of the major piedmont fault in A2. Lines A4, A5 and A6 show some relative change in basin shape between the two models.

For the longlines (Figure 95), the eastern portion of the Dixie Valley basin and the Edwards Creek Valley are significantly shallower by as much as 0.5km to 1.5km in the residual models. The LL2 residual and CBA models differ significantly even though crustal compensation was applied to the CBA model. This illustrates the difficulty in applying regional corrections. Without well data control, it is difficult to decide which is the better model. While the locations of the Jz blocks in LL1 to LL3 are similar, the residual Jz units in LL4 are significantly shallower than in the CBA model. We should caution that the longline models were very difficult to fit and errors were much larger than for the other lines. The gravity data was also sparse in many areas.

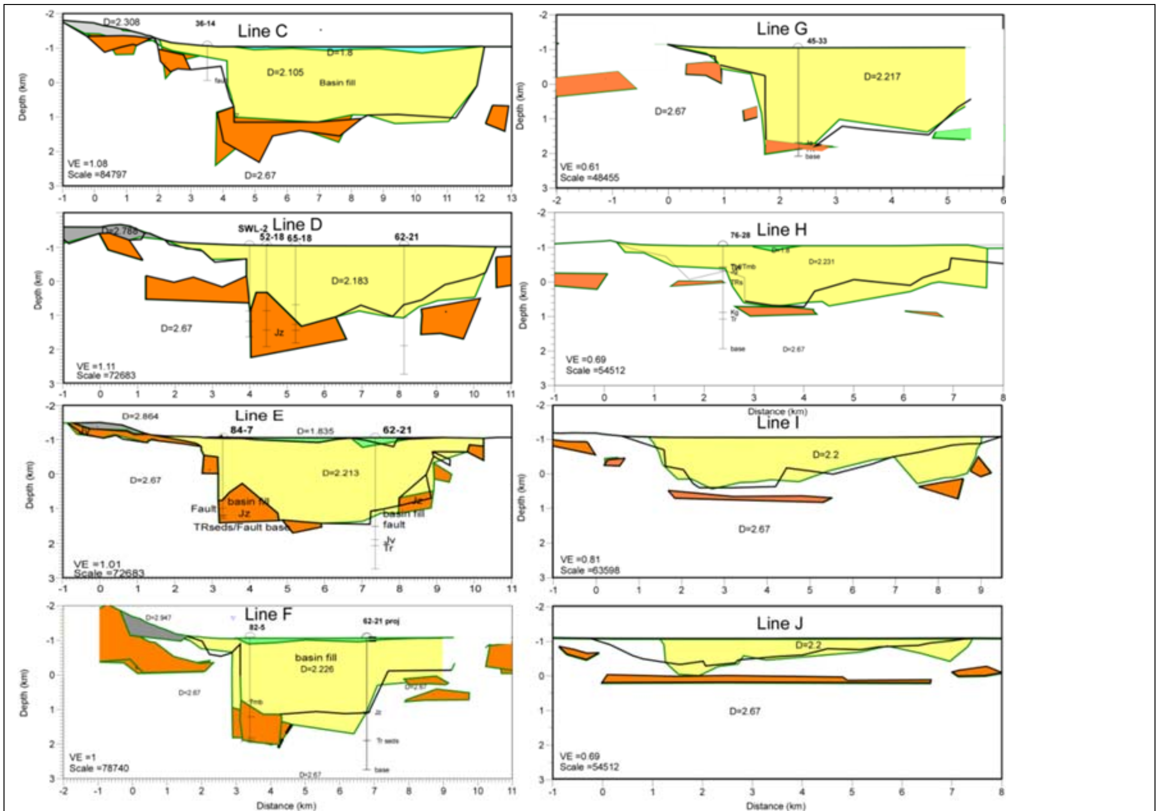

Figure 93. Complete Bouguer and Residual Gravity Anomalies (CBA and RGA, respectively) models of lines C to J in the calibration area. CBA models (filled solids with green outlines) and RGA models (black outlines) for Lines C to J in the northwest portion of the calibration area. Basin fill (D=2.1 to 2.2 gm/cc) is in yellow and light blue (D <2.0 gm/cc). Bedrock (white) density is assumed to be D=2.67 gm/cc. Positively magnetized Jurassic volcanic units (S=0.007 cgs, D=2.67) are shown as orange shaded blocks and reversely magnetized unit are shown in green. Dense nonmagnetic units are in dark grey (D>2.8 gm/cc) and presumed non-magnetic Tertiary rhyolitic units are in light grey (D=~2.3 gm/cc).

9.1.8 Comparison of Models with Seismic Lines

One way to test which model is correct is to compare the joint gravity/magnetics models to the available seismic data provided by Dr. David Blackwell (Figures 96 and 97) (Blackwell et al., 2005). In Figure 96, Line E is compared to seismic line 6 whose tracklines parallel and are close to each other. The basin fill shows considerable internal structure with broken southeastward dipping beds in the western part of the section and northwestward dipping beds in the central and eastward part. The boundaries of the basin from both the CBA and RGA models are permissible by the seismic data are the western piedmont faults. It is difficult, however, to decide whether the CBA or the RGA model is more correct as they are very similar to each other, except in the east where basin in the RGA model shoals. The seismic data also lacks resolution in this area. In the interpretation of Blackwell et al. (2005) in Figure 21, the layer marked basalt lies very close to the basin fill/bedrock contact and the inferred faults follow the edges of the magnetic Jz units. In Figure 22, Line F is compared to seismic line 102. The same observations as above apply to this comparison, although the RGA model would seem to provide a better fit in the center of the diagram.

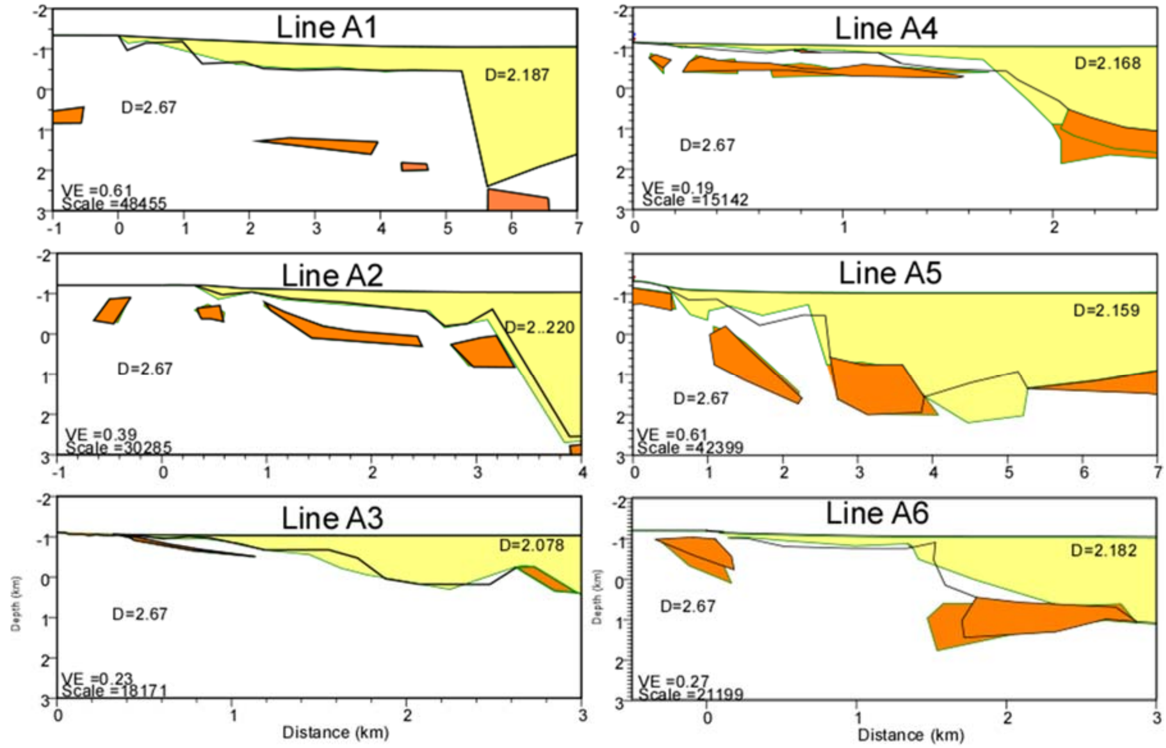

Figure 94. Comparison of the Complete Bouguer Anomaly model fit (filled solids with green outlines) with the Residual Gravity Anomaly model fit with the regional gravity gradient removed (black outlines) for Shortlines A1 to A6. Basin fill (D=2.1 to 2.2 gm/cc) is in yellow fill. Magnetic Jurassic units (S=0.007 cgs, D=2.67) are shown as orange shaded blocks.

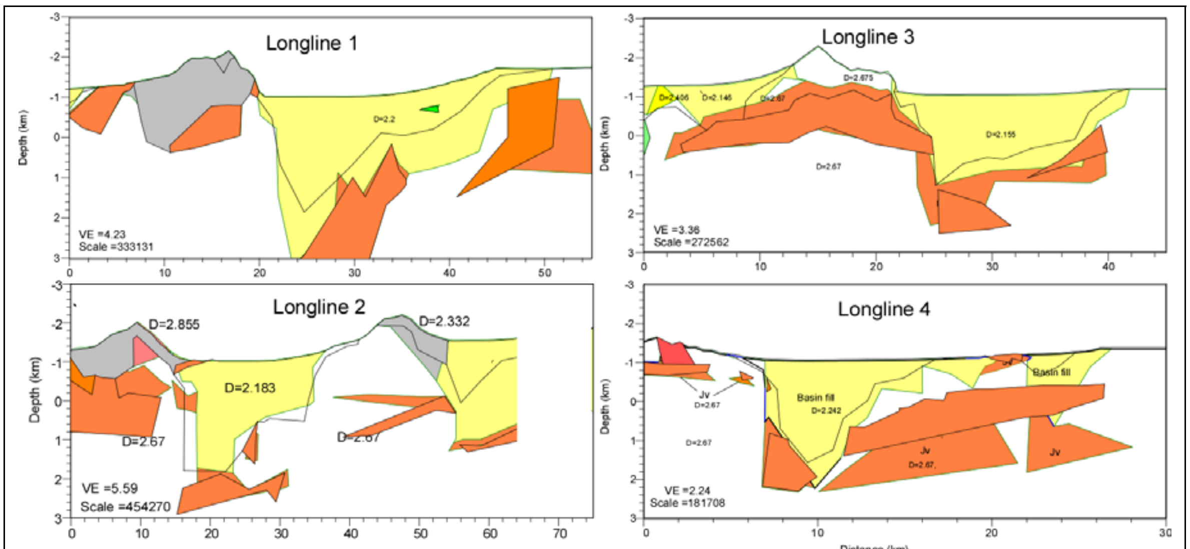

Figure 95. Comparison of Complete Bouguer Anomaly and Residual Gravity Anomaly models of Longlines LL1 to LL4. Color coding as in Figure 83.

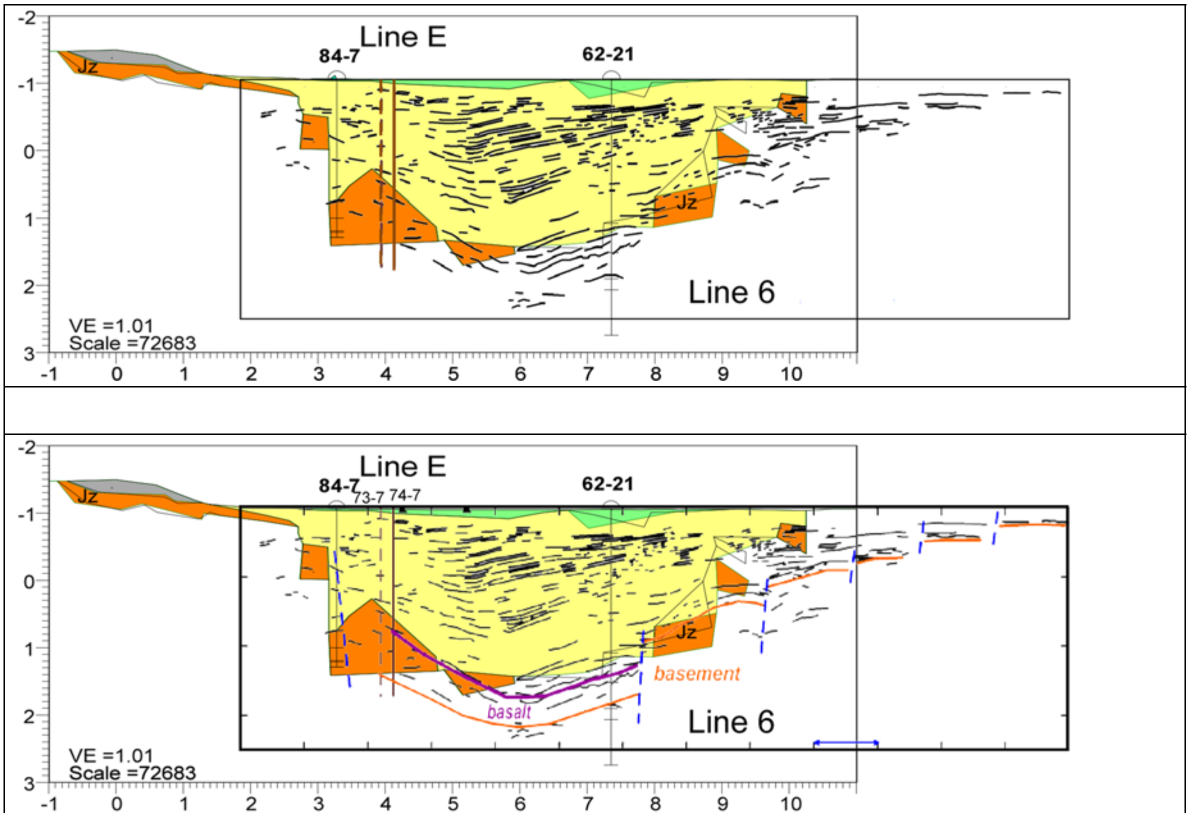

Figure 96. Comparison of the Line E joint gravity/magnetic CBA and RGA model fits with a) an uninterrupted line drawing; and b) an interpreted line drawing of seismic line 6 with features and faults (dashed) adapted from by Blackwell et al. (2005). The track of the seismic and model lines almost coincide. Horizontal axes on seismic box are spaced 1km apart.

9.1.9 Comparison of Modeled Faults with Mapped Faults

The locations of the modeled faults can be compared with those derived from surface geology and earlier geophysical work compiled in Section 7 (e.g., Figures 49B) from references such as Smith et al. (2001); Graugh (2002); Blackwell et al. (2005); and faults recognized by the State of Nevada and the USGS database of Quaternary faults in the US (Figure 97). The major piedmont fault with offset of >1km and the Buckbrush fault were previously identified by Smith et al. (2001) from the maximum gravity horizontal gradient and agree with our models. With the exception of three minor modeled faults in the western Stillwater Range, most of the modeled faults lie on previously recognized structures. The advantage of incorporating our section is to identify which faults are dominant and have the most offset.

9.1.10 Magnetic Susceptibility Sensitivity Analysis

A range of magnetic susceptibility (S) values were tested, S=0.007-0.21cgs to evaluate the effect of this parameter on the modeling results. The S values <0.007 gave volcanic units that were unrealistically large (>1km thick) compared to what is known from drilling and surface geology, while values of S>0.021 were difficult and, in some cases not possible, to model.

For each of the lines model (Section 9.1.10), the magnetic bodies location remains the same, although the bodies decrease in thickness particularly from the lower boundary. This implies that changing the

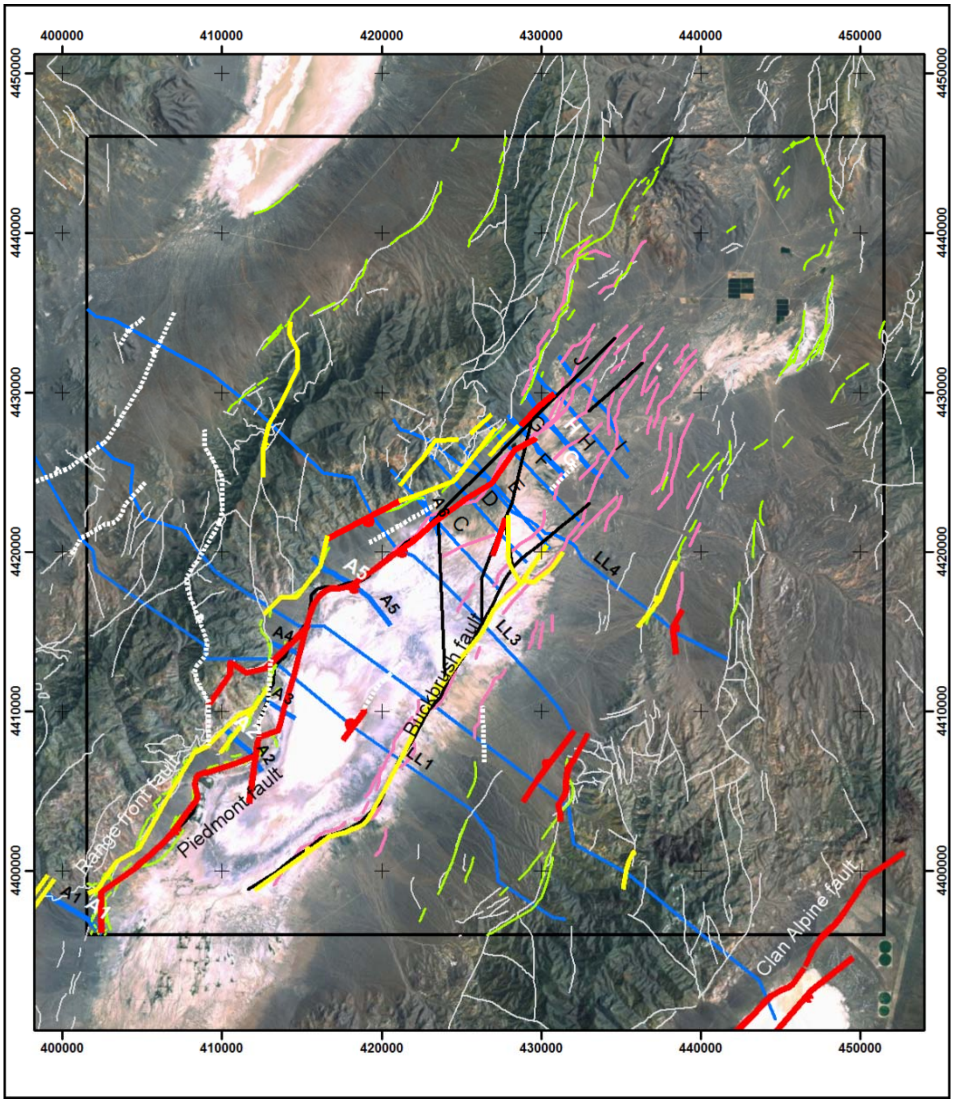

Figure 97. Comparison of faults from gravity/magnetics modeling (colored) with those mapped by other studies. Profile track are shown in blue. Red lines are modeled major faults having >1km displacement; yellow lines are modeled faults having 0.5km to 1km offset and white dashed lines are modeled faults with <0.5km displacement. Thin gray lines are from the State of Nevada/USGS fault catalog; green lines are from the Quaternary fault data base; magenta lines are derived HELIMAG derivative studies by Grauch (2002); and black lines are subsurface faults inferred by Smith et al. (2001) and Blackwell et al., (2005). The EGS Exploration Methodology Project Area is outlined in black.

magnetization does not significantly affect the positions of inferred faults reported, although the dips of the faults may not be as well constrained.

The results of the magnetic susceptibility sensitivity analysis for sections CC', DD', EE' and FF' are presented in Part II-Appendix 4.

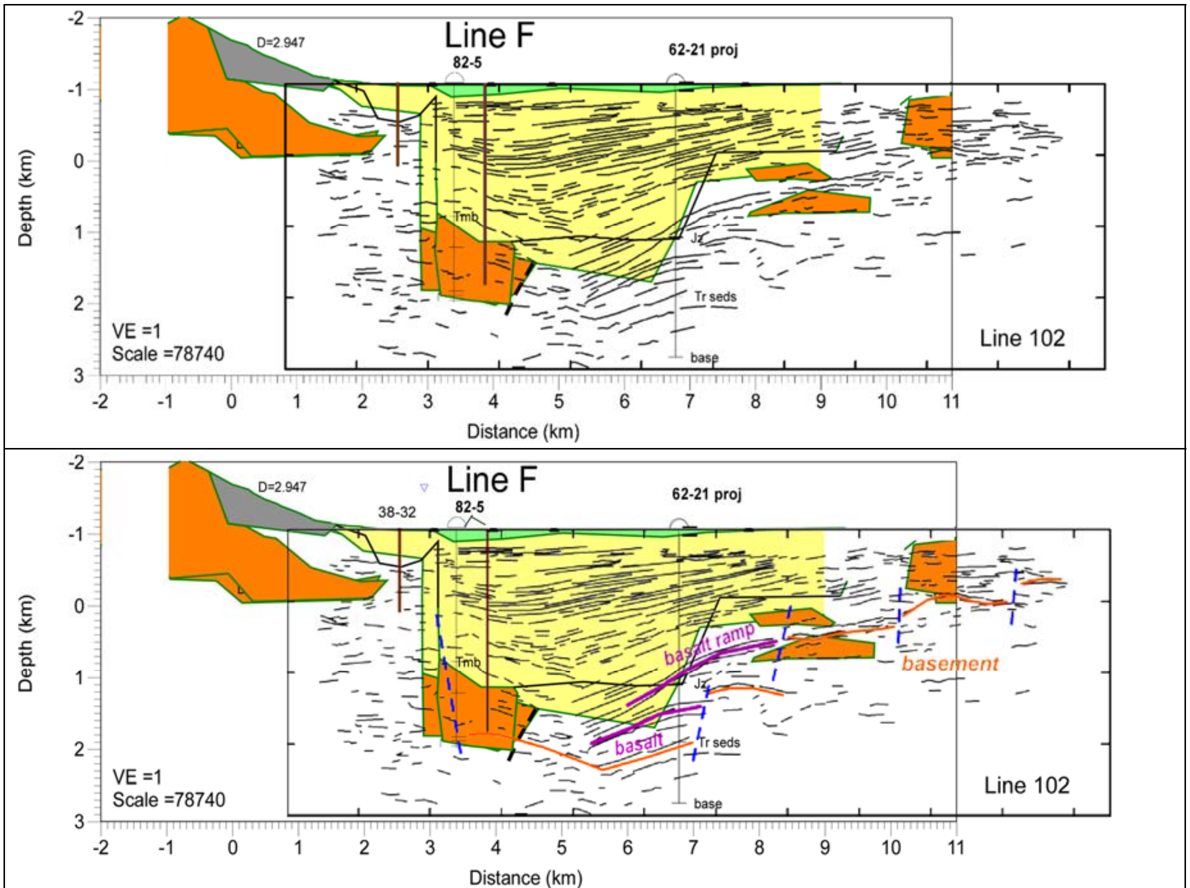

Figure 98. Comparison of the Line F joint gravity/magnetic CBA and RGA model fits with (a) an un-interpreted seismic line drawing and (b) an interpreted line drawing of seismic line 6 with features and faults (dashed) adapted from by Blackwell et al. (2005).

9.2 AMBIENT SEISMIC NOISE SURVEY

9.2.1 Introduction

The primary objective of this study was to develop and test the seismic component of a calibrated exploration method that integrated geological, geophysical, and geochemical data to identify potential drilling targets for Engineered Geothermal Systems (EGS). In exploring for EGS sites, the primary selection criteria identified by the AltaRock Energy, Inc. (AltaRock) Team were, in order of importance, (1) temperature greater than 200C at 1.5km depth, (2) rock type at the depth of interest (brittle rocks at 1-3km); and (3) stress regime (tensional environment).

The core exploration methodology developed by Dr. Ileana Tibuleac, the Seismic Task Leader and Dr David von Seggern (see Section 1.4), for this project was a new seismic technique which used complementary information derived from regional tomographic models of body (P and S) and surface waves statistically integrated with shear velocity models derived from ambient noise to predict temperature and rock type. Using the new estimated seismic models, we tested the supposition that the uncertainty and the degree of non-uniqueness in predictions of temperature and rock type from the seismic data could be reduced by integration with other geophysical and geochemical data into an EGS conceptual model that will form the basis of an exploration methodology. The new method has been applied to the EGS Exploration Methodology Project Area in Dixie Valley (DV), NV (referred to in this seismic section as the DVSA), one of the best characterized geothermal areas in the Basin and Range in the public domain, also known for low seismicity between large seismic events. DVSA is the hottest known Basin and Range system with measured temperatures of approximately 285°C at 3.05km total depth. Historical and recent deep-well measurements suggest the existence of large masses of conductively heated rock that may be commercially viable for EGS development in this area. DV includes a fault-controlled geothermal reservoir located in the Basin and Range Province of the western United States. DVV structurally asymmetric basin bounded by a complex zone of faulting on the northwest and by step faulting to the southeast (Okaya and Thompson, 1985; Blackwell et al, 2005; Section 9.1 of this report). Historical seismicity in DV (Blackwell et al, 2007) available from the United States Geological Survey (USGS) includes the July 6 (M_L 6.8) and August 23, 1954 (ML 6.8) Rainbow Mountain earthquakes to the west of DV, and the December 16, 1954 DV (M_L 7.1)-Fairview Peak (M_L 7.2) earthquakes in and to the south of DV.

The objective of the seismic investigation was to estimate a high resolution (~ 5km) *P/S* seismic velocity model in the DVSA, the EGS Exploration Methodology Project Area, using new, and baseline information, from independent sources. This inexpensive method, in combination with other geological and geophysical methods, was developed to help with the first-order identification of EGS favorable areas. Our studies focused on extracting maximum information in the Dixie Valley Project Area (PA), DVGW, also referred to as the Calibration Area (CA), the black square outline and the red enclosure in Figure 99a, respectively. Since our study was based on seismic tomography, to develop the required data for the DVSA without significant model edge effects, a larger region referred to as the Dixie Valley Extended Study Area (DVESA) needed to be assessed (Figure 99b).

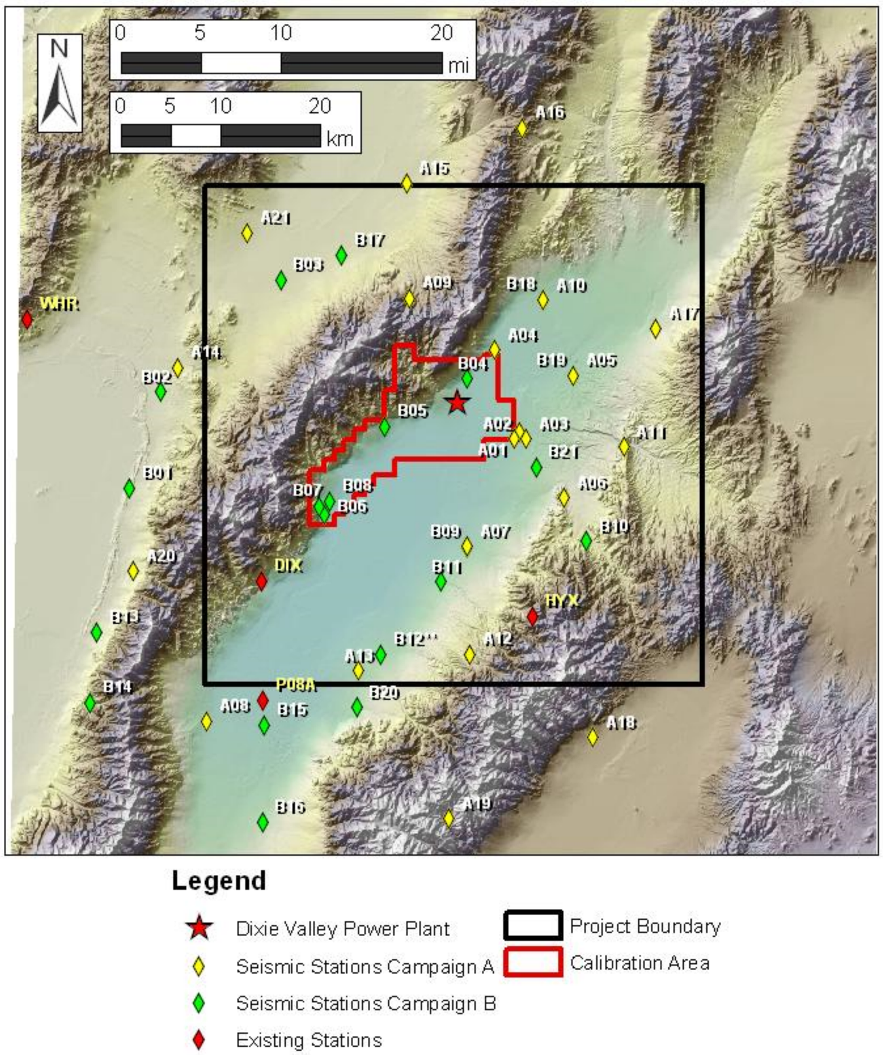

Figure 99a. Map of the seismic survey locations in the Dixie Valley Study Area (DVSA), also referred to, elsewhere in the text, as the EGS Exploration Methodology Project Area (PA, black outline). Co-located campaign stations are identified with their respective station IDs. The Dixie Valley Geothermal Wellfield (DVGW) or the Calibration Area (CA) is shown in red. Stations DIX, P08A and RYX (red diamonds) recorded continuously until several months prior to the DVSA seismic experiment. The Dixie Valley power plant is shown as a red star.

The initial publicly available information review concluded that not only seismic model spatial resolution must be improved in the study area, the uncertainty that resulted from the non-uniqueness of geophysical data also needed to be reduced. Because temperature and rock type were not directly measured by geophysical methods they had to be inferred. Seismic methods directly measured velocity, which is affected by temperature, however, velocity is also affected by numerous other factors including fluid conditions and fractures, lithostatic pressure and rock type. Comparison of velocity anomalies with mapped and suspected rock types from other geophysical techniques may identify regions where velocity anomalies are not explained by petrology, and thus are more likely to be due to anomalous temperatures. The seismic results will be integrated with other geoscience data to infer temperature and rock type.

To improve spatial resolution, a dense seismic array (21 three-component, broadband sensors, with an overall array aperture of 45km) was installed in two deployments, each having a three-month duration (Figure 99a, Appendix 5-Table 5-1). Ambient seismic noise and signal rather than active sources were used to retrieve inter-station and same-station Green's Functions (GFs), to be used for subsurface imaging. We used ambient seismic noise interferometry to extract GFs from crosscorrelation of continuous records. Another innovative aspect of the seismic work was to determine if estimating the receiver functions

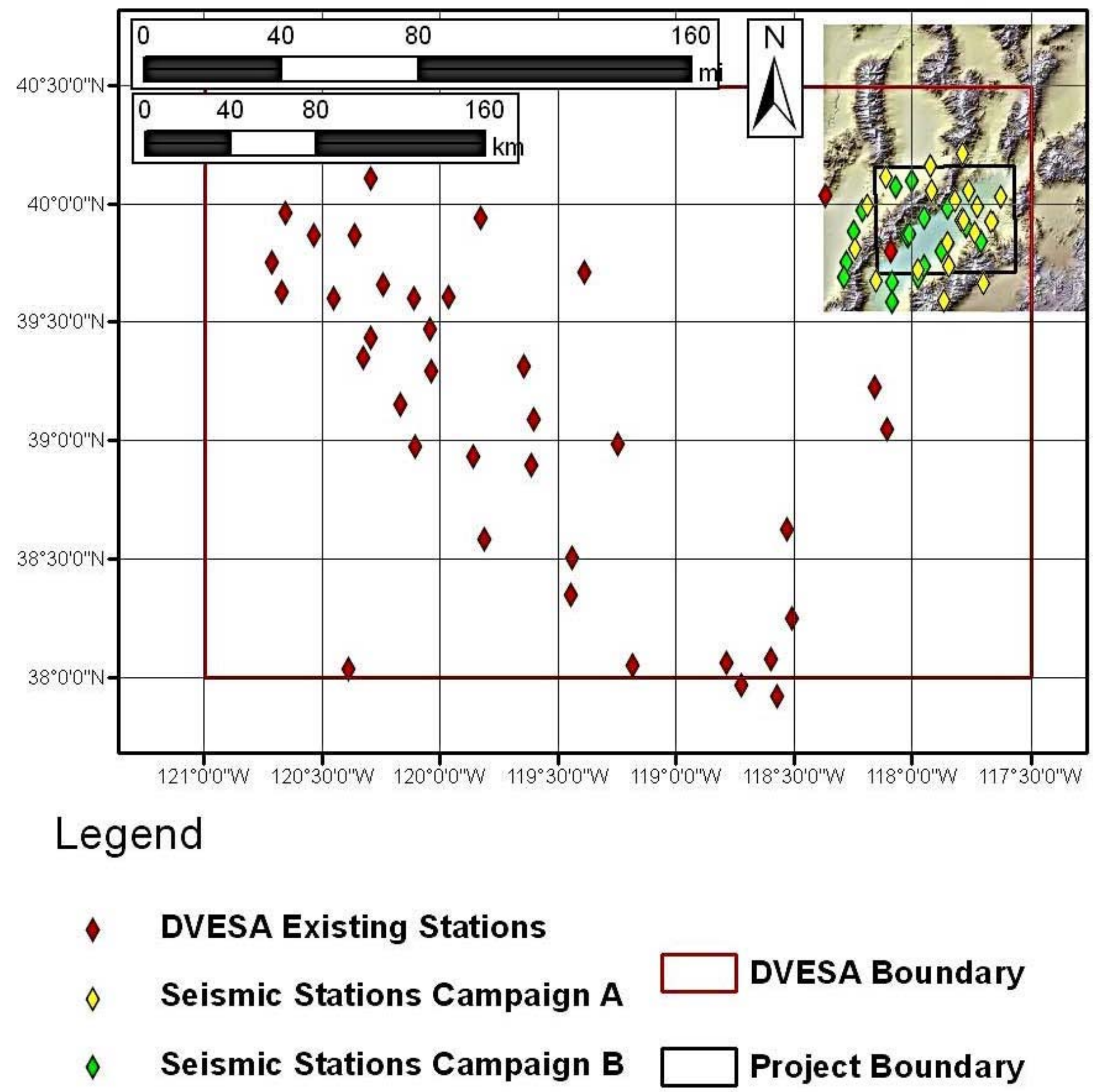

Figure 99b. Dixie Valley Extended Study Area (DVESA) and the seismic stations operating during this investigation.

beneath the stations using noise auto-correlation could be used to image the substructure. We report results of applying the technique to estimate a *P/S* velocity model from the GF surface wave components and from the GF body-wave reflection component, retrieved from ambient noise and signal cross-correlation and auto-correlation beams. Using seismic velocity models to infer temperature is statistically assessed, in combination with other geophysical technique results.

In summary, to investigate crustal structure in the upper 20km, we measured fundamental mode Rayleigh group velocity from GFs extracted from all available station pairs in the Reno Basin and vicinity. The GFs were extracted from crosscorrelated and autocorrelated continuous waveform beams. We estimated fundamental Rayleigh phase group velocity maps and then inverted the model in each grid cell for crustal structure (see discussion in *High Resolution Seismic Velocity Model Estimation in the DVSA* section of a definition of a grid cell). Finally, we discuss implications of the new models for EGS favorability.

9.2.2 The Method

Figure 100 shows an outline of the major tasks in our seismic study and of the analysis method, which was first tested in the Reno, NV area (Tibuleac, in prep. for *Seismological Research Letters*). To prepare for the inversion of the final DVSA model we created an input P/S model (DVSA_INITIAL_MOD) as a superposition of (1) the baseline *P/S* velocity seismic model (DVESA_BL_MOD), (2) the low resolution *P/S*-velocity model (DVESA_LR_MOD) estimated from ambient noise and signal, (3) a *P/S* velocity-tomography model (DVESA_LOTOS_MOD) estimated using earthquakes and explosions, (4) a *P*-velocity model (DVSA_ACOR_MOD) estimated from *P*-autocorrelation beam forward modeling, and (5) a *P/S*-velocity model inverted from phase velocity measurements at ad-hoc arrays in the study area (DVSA_PHVEL_MOD). All the estimated *P/S* velocity models were integrated using a set of algorithms named MAT_MOD, which is described below. The resulting model, DVSA_INITIAL_MOD, was the input model in the inversion to complete the final high resolution DVSA P/S seismic model. The resulting model was a P/S model named the DVSA_FINAL_MOD.

We used seismic interferometry, which is a relatively new technique (Campillo and Paul, 2003; Lobkis and Weaver, 2001; Larosse et al., 2005; Weaver and Lobkis, 2004). Seismic noise can be processed at all frequencies, starting with the high range (tens of Hz) down to 30-40 second(s) period Rayleigh or Love waves, for inter-station distance respectively from meters to hundreds of km. The technique is based on the theoretical result which states that, if A and B are two passive sensors (seismic stations), the GFs, or the signal that B would receive when A is given an impulsive excitation, can be recovered from the temporal cross-correlation of incoherent ambient noise received at A and B. Over the past decade, ambient seismic noise tomography has provided important constraints on 3D crustal structure in many regions in the world, including the western United States (Sabra et al., 2005; Shapiro et al., 2005; Bensen et al., 2007 Yang and Ritzwoller, 2008; Lin et al., 2008). The lateral extent of most of these studies ranged from several hundred to several thousand kilometers, with inter-station distances more than 60km and period range 5s to 30s, thus sampling deeper than 5km. A study of an area in the Taipei Basin, China, with similar dimensions to the Dixie Valley Project Area (PA) has been published by Huang et al. (2010). We used algorithms for extracting ambient noise-derived GFs developed at the Nevada Seismological Laboratory (NSL) (Tibuleac et al., 2011; von Seggern et al, 2009) to derive velocity models, for inter-station distance less 60km, and for different sensor types. The algorithms were closely following the Bensen et al. (2007) method. We have included, however, modifications to account for different-instrument pairs and smaller inter-station distance analysis. Modifications included distance-dependent filtering and data processing after conversion into records of the same instrument type, i.e. broadband with 0.1 Hz corner frequency.

9.2.3 Results

Green's Functions (GFs) Extraction and Analysis

Tomographic models have edge effects, due to limited information availability close to the model edge. This is why we considered the extended areal DVESA study, including a network of 120 broadband and short-period stations (Figure 99b), of which 42 three-component broadband station locations in the 2011-2012 ambient seismic noise survey deployment conducted in this study (Figure 99a). For the entire study, GFs were extracted on more than 1200 inter-station paths, including but not limited to the raypaths shown in Figure 101. In particular, the stations in Figure 101 were used for fundamental Rayleigh phase velocity estimation, as discussed in the section *Lines and ad-hoc sub-arrays of stations* (below)**.** Data was processed using ambient seismic noise and signal autocorrelation and crosscorrelation algorithms in a package of optimized analysis codes (Tibuleac et al, 2011; Tibuleac and von Seggern, 2012; see also directory "matlab_scripts" in the supplementary material directory, further referred to as Part II-Appendix 10).

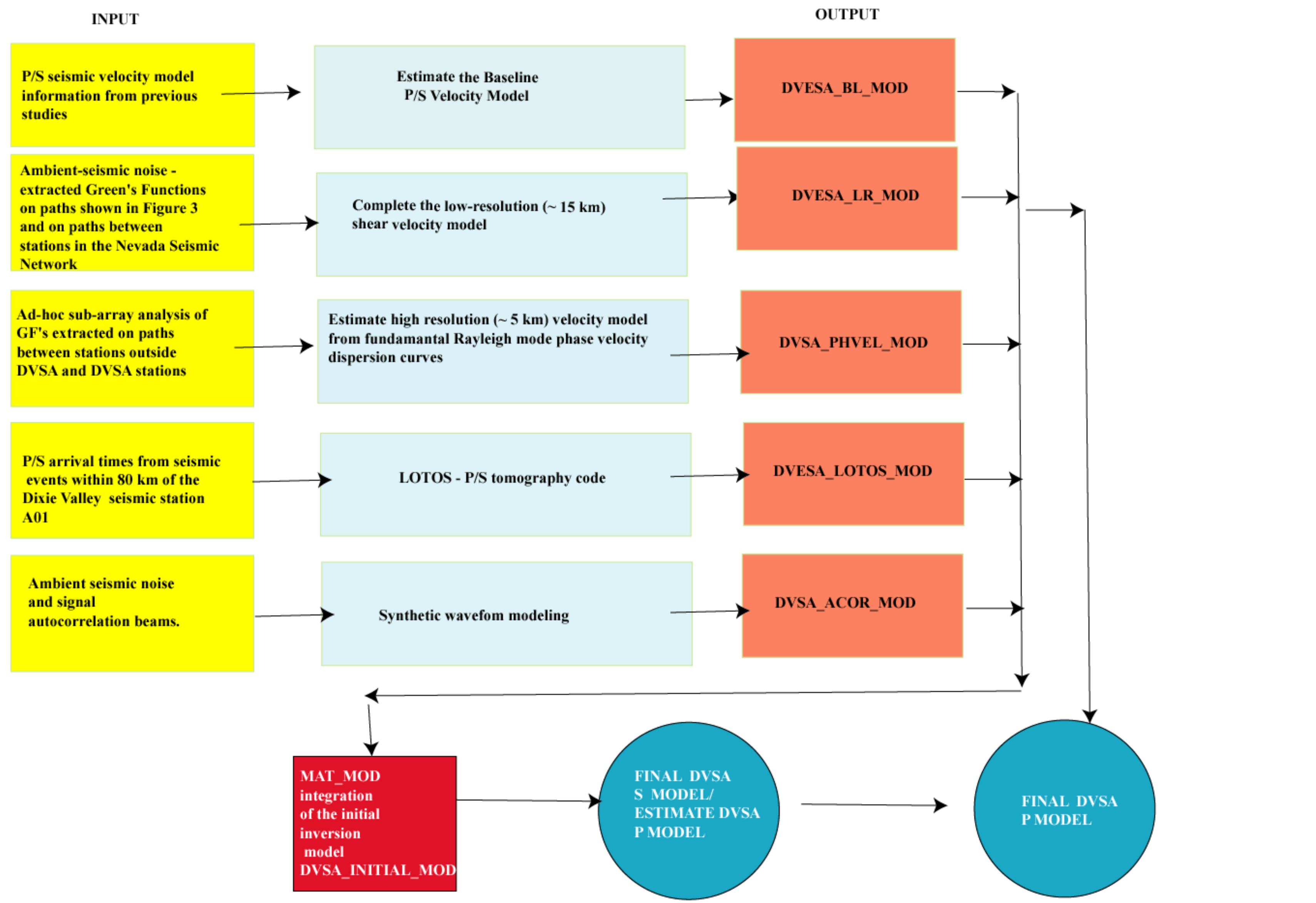

Figure 100. The analytical method to generate a final seismic model.

The autocorrelations were estimated at all stations for a sample rate of 100 samples per second (sps), in an effort to obtain better resolution of the layers below each station. A sample rate of 20sps was considered high enough for crosscorrelations, for station spacing which ranges from 1-75km in the DVSA, since the observed Rayleigh waves have periods lower than 0.2s.

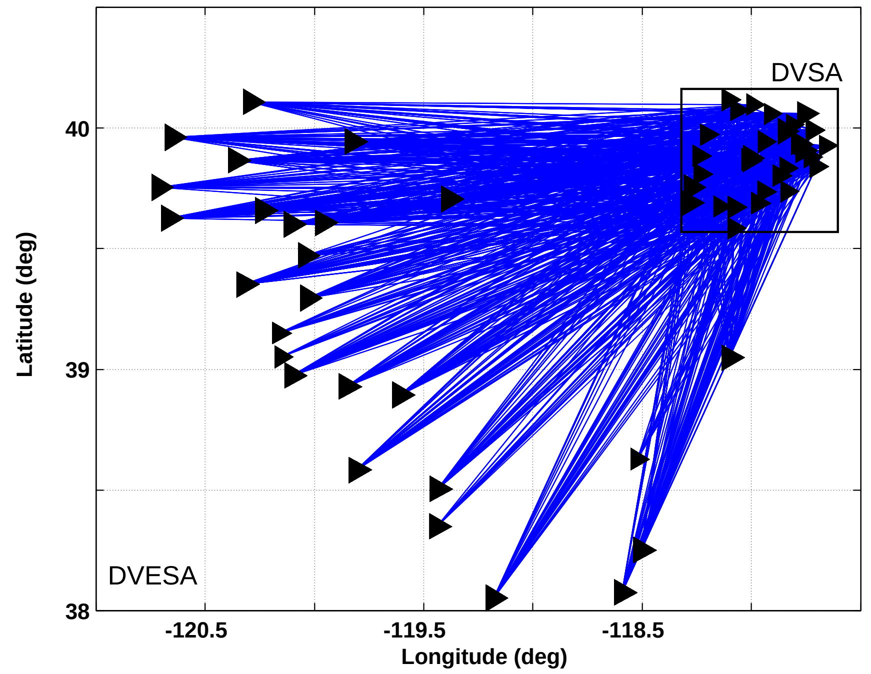

Figure 101. Inter-station raypaths for ambient seismic survey station locations in the Dixie Valley Study Area (DVSA) and University of Nevada Reno Seismological Laboratory seismic stations in the extended Dixie Valley Study Area (DVESA).

High Resolution Seismic Velocity Model Estimation in the DVSA

The GFs extracted between pairs of stations in DVSA are shown in Figure 102. An approximate 5km resolution P/S velocity model has been estimated using 396 highest signal-to-noise ratio (SNR) inter-station GFs extracted in the DVSA (the PA). Fundamental Rayleigh group velocity dispersion curves were estimated and inverted for shear wave velocity models using CPS3.3, a set of analysis codes made available to the project by Dr. Robert Herrmann of the Saint Louis University (personal communication with Dr. Ileana Tibuleac, Seismic Task Leader). The dispersion of fundamental mode Rayleigh was estimated and inverted using the CPS3.3 algorithms *do_mft* and *surf96* (Herrmann and Ammon, 2002). To estimate a group velocity tomographic model and to perform grid-dispersion inversion we used the code *gridsp*, written by Dr. Hafidh Ghalib (personal communication with Dr. Tibuleac). The propagations paths were assumed to be straight rays. A stochastic inversion code was used, following a method by Feng and Teng (1983). The fundamental mode Rayleigh group velocity tomography results are shown in Figure 103. A "rule" of thumb" is that the numeric value of the period of the fundamental mode Rayleigh corresponds to the depth best sampled by a waveform (at 1/2 of the wavelength from the surface), assuming the group velocity ~3km/s. Dispersion curves have been analyzed at periods from 2s to 10s. The surface of the DVSA was partitioned into a grid with elements 0.05˚ on one side. A dispersion curve has been estimated for each of the 140 total grid elements in the DVSA. To invert for the DVSA model, a starting P/S velocity model named DVSA_INITIAL_MODEL (Figure 100) was needed. This model was extracted from the compilation of all available current velocity models in the area, as described below.

Estimation of the DVSA_INPUT_MODEL

Generating a higher resolution DVSA input model (DVSA_INPUT_MODEL) was the focus of our efforts, as a necessary step before estimation of the final DVSA model. Such a detailed seismic shear velocity model was not available in the area. High resolution (hundreds of meters) P-velocity models were available only from reflection lines, as concluded after the EGS Baseline Geothermal Conceptual Model (submitted to the NGDR with a 15 May 2013 publication date) P/S velocity model estimation (DVESA_BL_MOD in Figure 24). New, higher resolution, independent P/S velocity model estimates were integrated into the DVSA_INPUT_MODEL using a new set of Matlab algorithms named MAT_MOD (provided in the directory matlab_scripts in Part II-Appendix 10).

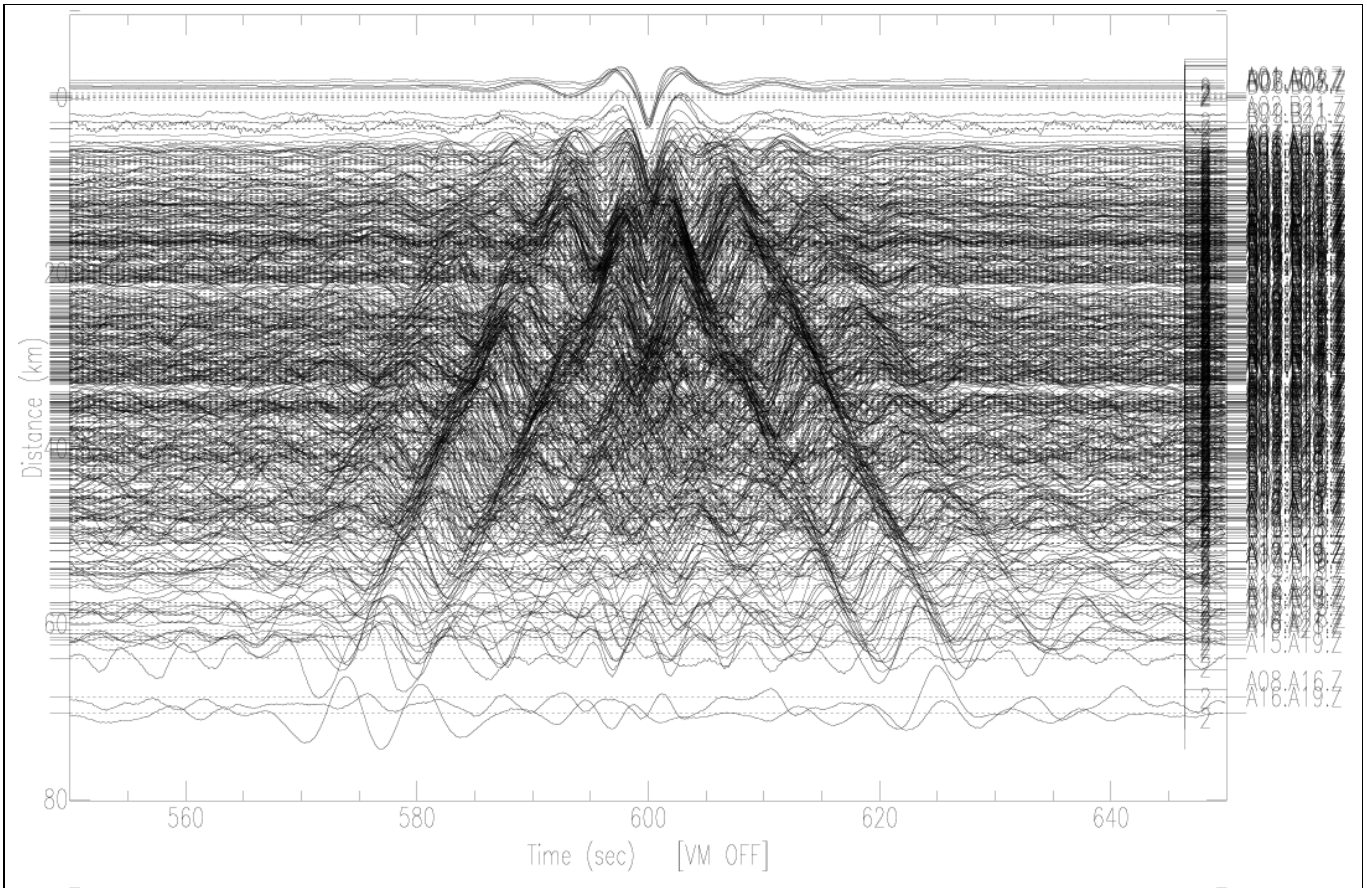

Figure 102. Record section of raw GF waveforms extracted in the DVSA area. The vertical axis shows inter-station distance. Fundamental mode Rayleigh traveling with a group velocity of ~ 3km/s are the largest arrivals at all distances.

MAT_MOD

Each model we collected or estimated was stored into a Matlab structure. A "structure" is a named collection of data representing a single idea or "object". For anything in a computer more complicated than a list of numbers, structures can be used. The structure contains a list of fields, each being a variable name for some sub-piece of data. Structures are similar to arrays in that they contain multiple data, but the main difference is, instead of an Index to each piece of data, we have a "name"; and instead of every piece of data being the same type, we can have a different type for each "field". The fields of a MAT_MOD structure were: the reference to the model; the model area (which is a square oriented North-South, East-West; and the model matrix. The model matrix had eleven columns: depth, P velocity in km/s, S velocity in km/s, density (g/cm3), P and S attenuation factors Qp and Qs and five trust factors, one for *P, S*, density, Qp and Qs. For "no information" the matrix element value was set to -99. The "trust" factor (a value from 0 to 1) was, for example, set by the analyst up to 0.9 for reflection/refraction lines and is set to 0.01 for general (non-local) models. Using the "trust" parameter, seismic lines and local data were given higher weights than the global model weights. A "slack" number (in this case 0.04˚) for each model represents the area where the model is considered valid. When, for example, the P/S-velocity model at a point characterized by (latitude, longitude) is requested by the user, MAT_MOD finds all the models including a square centered on the respective point, i.e., within 0.04˚ from the respective point. A side of the square is twice the slack number value. For example, the resulting P-velocity at the respective point is a "trust" - parameter weighted mean, after the "-99" estimates are discarded. The choice of the "slack" factor can "sharpen" or "smooth" the P/S extracted velocity models.

The MAT_MOD algorithms were particularly suitable for this study, because they allowed integration of independent information from multiple sources.

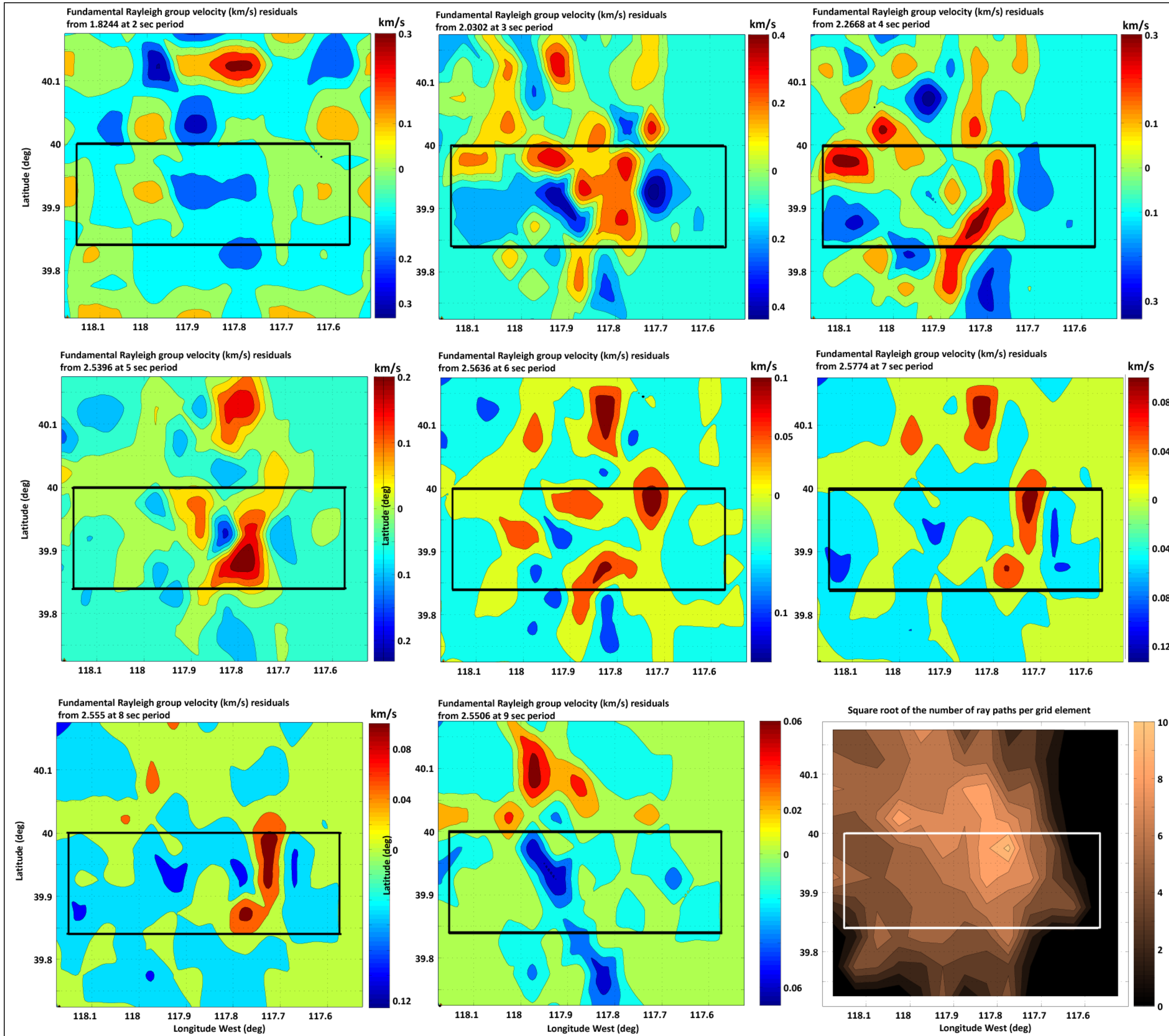

Figure 103. All plan-view plots, except for the lower right plot, show fundamental mode Rayleigh group velocity maps in the DVSA at periods of 2-10s. For waveforms with group velocity ~ 3km/s the rule of thumb is that the best sampled depth has a numerical value similar to the period. The generalized boundaries of the Calibration Area (CA) is included in the black rectangle in each plot. The lower right plot shows log10 of the ray density in the area. The best resolved regions (light color) are intersected by the largest number of ray paths.

DVESA_BL_MOD

An initial, low-resolution (~ 40km) *P/S* seismic velocity model of the area (DVESA_BL_MOD, Figure 100,), presented in the EGS Baseline Geothermal Conceptual Model was estimated using all the existing literature and all the experimental information. Publicly available velocity models were used to build this model, with crust-mantle boundary (Moho) discontinuity constraints and with seismic attenuation information. Two improved resolution (~ 30km), University of Nevada Reno (UNR)-estimated, velocity models in Nevada were added to the DVESA_BL_MOD: (1) a low resolution (30-50km), Nevada *P/S* seismic velocity model by Preston and von Seggern (2008) and (2) a *P/S* model estimated by Biasi *et al.* (2010).

DVESA_LR_MOD

A new, improved resolution (~ 0.15˚ or ~15x15km^2 grid size) seismic velocity model in the DVESA (DVESA_LR_MOD, Figure 100) was extracted from 1285 inter-station GF dispersion curves estimated from ambient seismic noise and signal. Broadband, as well as at short period sensor pairs were used. Vertical component GFs extracted on paths in DVESA are shown in Figure 104, with fundamental mode Rayleigh waves as the largest arrivals. With the same method as for DVSA, fundamental mode Rayleigh wave group velocity maps were estimated at periods from 5s to 20s and maps for selected periods are illustrated in Figure 105. The DVESA surface was partitioned into a grid with elements 0.15˚ on one side. A dispersion curve was interpolated for each of the 572 grid elements. The mean dispersion curve for the DVESA area is shown in Figure 106 in satisfactory comparison to a dispersion curve theoretically derived using the Priestley and Brune (1978) Basin and Range seismic velocity model. Shear-wave velocity models are estimated by inversion of the velocity maps in Figure 105 at 5km, 7km, 10km, 15km and 20km depth from the surface are shown in Figure 107. One model, from Priestley and Brune (1978) and Tibuleac et al. (2012) has been used as the initial model for DVESA_LR_Mod (Table 15).

Table 15. Mean shear velocity models extracted from the dispersion curves in DVESA and DVSA (see text for an explanation), the model used to generate a synthetic reflection waveform (Figure 113) and the starting model for DVESA shear velocity inversion.

Layer thickness	**DVESA**	**DVSA**	**Synthetic waveform empirical model: DVSA_ACOR_MOD**		**Initial model for DVESA_LR_MOD *P/S* seismic velocity model inversion**
(km)	Vs (km/s)	Vs (km/s)	Vp (km/s)	Vs (km/s)	Vs (km/s)
1	1.4	1.4	2.1	1.0	2.2
1	1.5	1.6	3	2	2.2
2	2.0	1.9	5.2	3.1	2.5
2	2.5	2.5	5.6	3.4	2.9
2	3.3	3.5	5.6	3.4	3.6
12	---	---	5.5	3.3	---
8	---	---	7.4	4.0	---

The studies described below provided independent constraints to the DVSA velocity models.

DVESA_LOTOS_MOD

Precise location of the events used for tomographic inversion is one of the most important conditions for accurate velocity model estimates. Local events, earthquakes and explosions, which occurred during the 2011-2012 ambient seismic noise (passive) survey deployment in DVSA (Figure 108), have been detected and located, from distances up to 80km from DVSA station A05, in an area from 39.25N to 40.65N and from 117.15W to 118.55W (Appendix 6,-Table 6.4). As expected, the incorporation of the DVSA array data provided a significant improvement over the Nevada Seismological Laboratory (NSL) locations. Because of poor permanent Nevada Network station coverage in the DVESA,

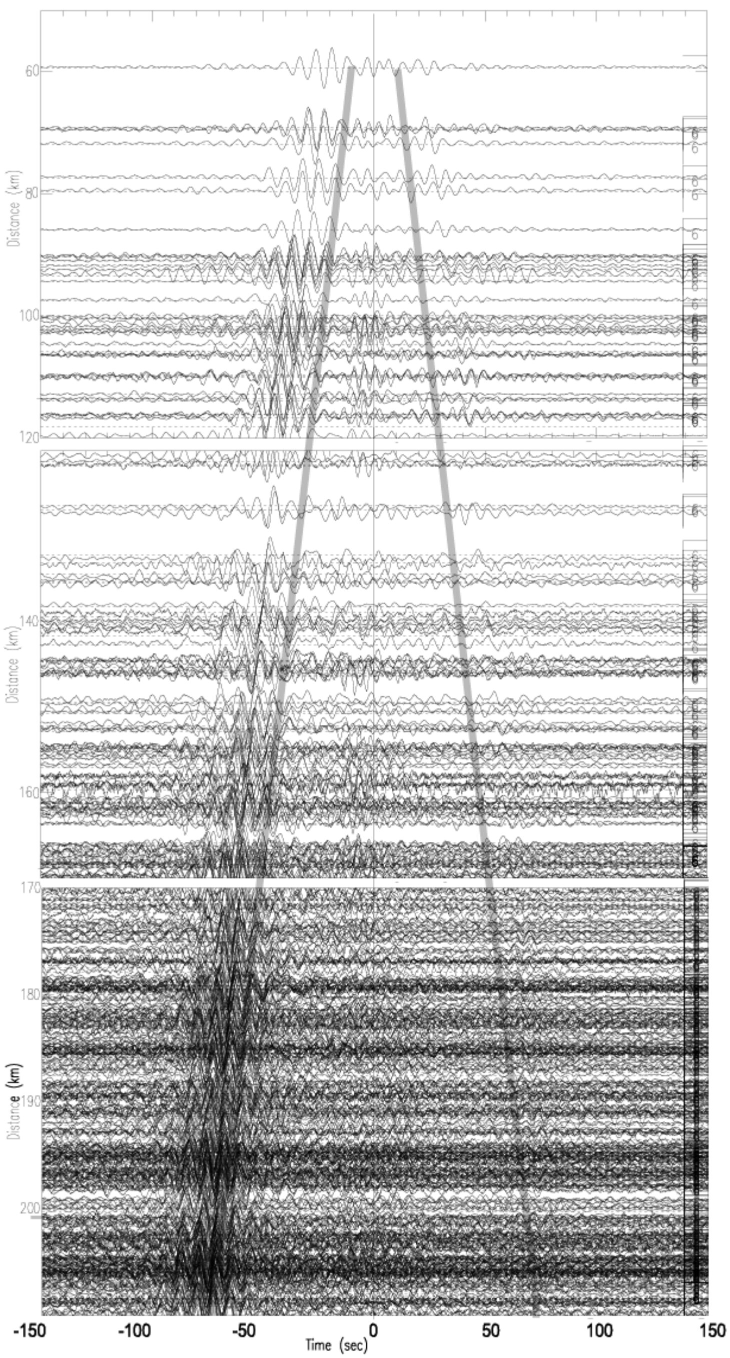

Figure 104. Record section of two-sided, raw vertical component GFs extracted in the DVESA area (see Figure 99b). The vertical axis shows the inter-station distance. Fundamental mode Rayleigh traveling with a group velocity of ~ 3km/s were the largest arrivals at all distances. The gray lines show the 3km/s arrival time. If the ambient seismic noise field and the seismic signals would be isotropic, the waveforms would be symmetrical on one side and the other of the zero time lag. The seismic noise and signal propagating towards DVSA is stronger, thus, the GFs are observed on the left side of the crosscorrelation time series.

larger DVESA earthquake epicenters were mis-located by NSL by up to 20km. DVESA mining and military explosions were also not analyzed at NSL, they were located and identified specifically for this project. Their locations were corrected to the locations shown in Figure 108. We also located small magnitude earthquakes which occurred in the DVSA. A total of 43 events had well-defined P- and S- arrivals.

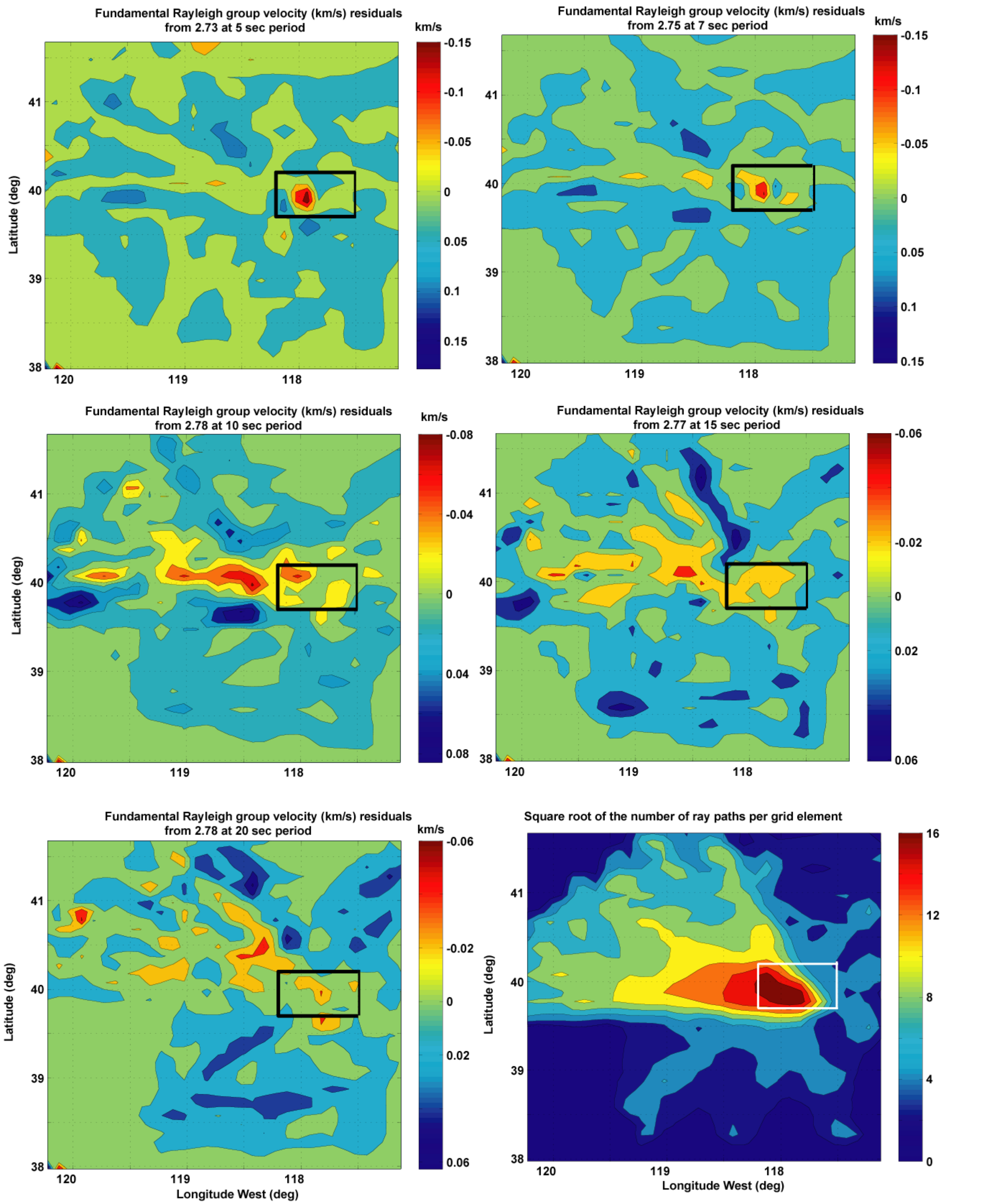

Figure 105. Fundamental Rayleigh group velocity maps at periods of 5s, 7s, 10s, 15s and 20s in the DVESA. The DVSA area is shown as a black rectangle in each plot. The lower right plot shows the square root of the number of paths per grid element used to estimate the velocity models, and DVSA in a white rectangle.

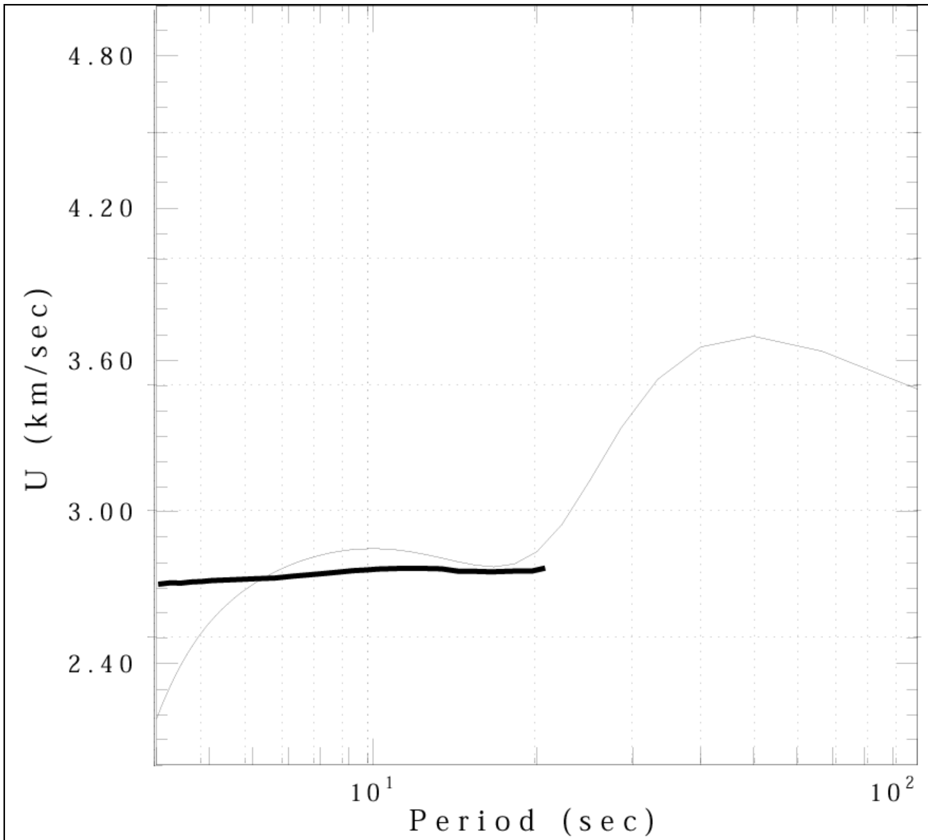

Figure 106. Note good correspondence between the mean DVESA fundamental mode Rayleigh group velocity (thick black curve) and the thin black curve, which was the fundamental model Rayleigh group velocity as a function of period derived from a model published by Priestley and Brune (1978) for Nevada.

A set of tomographic inversion algorithms, *LOTOS-10* for 3D tomographic inversion based on passive seismic data (Koulakov, 2009) has been used. One of the key features of the *LOTOS-10* code is a ray tracing algorithm based on the Fermat principle of travel time minimization called bending tracing (see Koulakov, 2009).

Following the procedure in Preston and von Seggern (2008), although we calculated *P*-arrival time static corrections (Part II-Appendix 7), the corrections have not been applied to the P and S-arrival times prior to running the LOTOS code. Only elevation corrections have been applied using an empirically chosen replacement velocity of 4km/s relative to the station A05 elevation (Figure 99a). Thus, the depth of the estimated P/S velocity model (DVESA_LOTOS_MOD) was from surface. The inversion for P/S velocity anomalies was performed by LOTOS in several steps, described in detail in Part II-Appendix 5, (1) simultaneous optimization for the best 1D velocity model and preliminary relocation of sources, (2) re-location of sources in the 3D velocity model, and (3) simultaneous inversion for the source parameters and velocity model using several parameterization grids. Steps 2 and 3 were repeated in several iterations. Figure 108 shows the re-located events (red dots) and the stations (blue triangles) used in the P/S tomographic inversion, after 5 iterations. The input (gray) and final (red) mean P/S wave seismic velocity model (estimated at step 1) in the LOTOS study area are shown in Figure 109.

A set of tomographic inversion algorithms, *LOTOS-10* for 3D tomographic inversion based on passive seismic data (Koulakov, 2009) has been used. One of the key features of the *LOTOS-10* code is a ray tracing algorithm based on the Fermat principle of travel time minimization called bending tracing (see Koulakov, 2009).

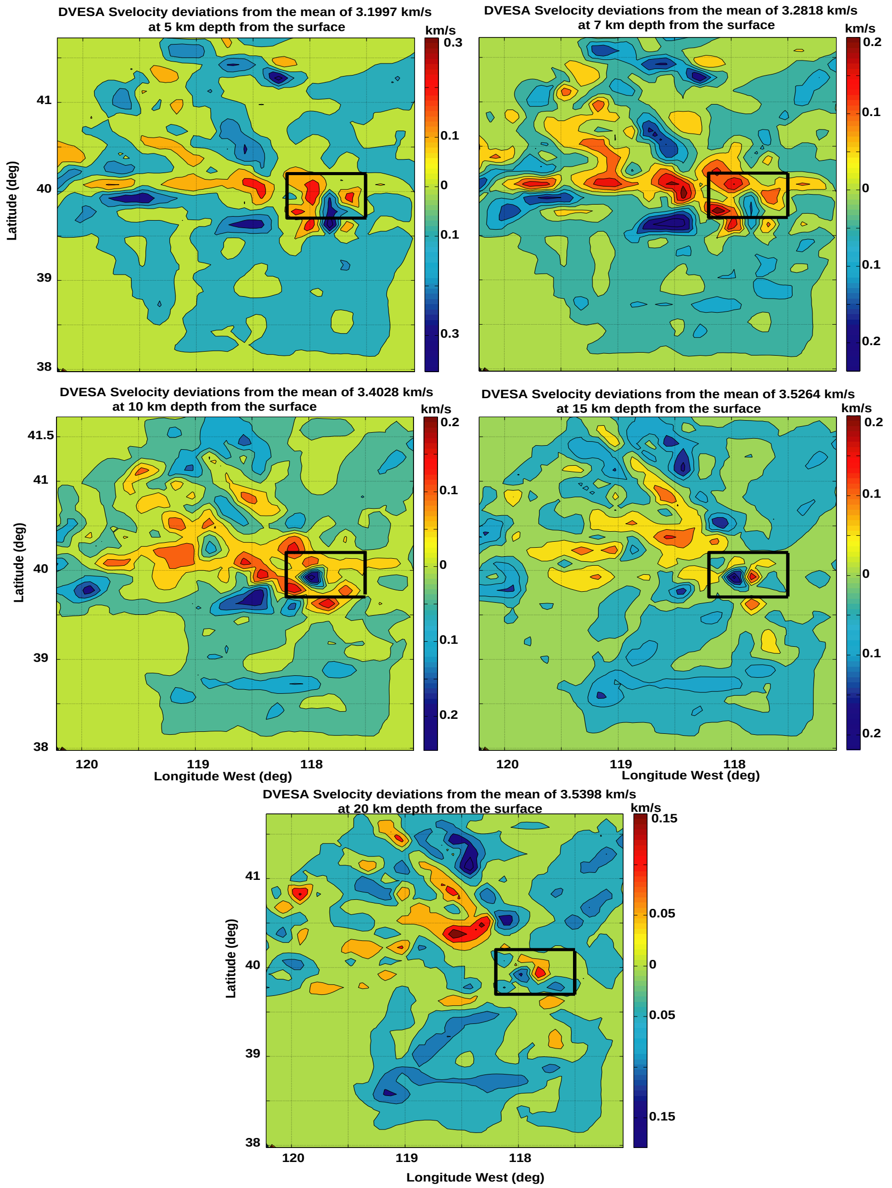

Figure 107. Shear velocity maps at depths of 5km, 7km, 10km, 15km and 20km. The DVSA area is shown as a black rectangle in each plot. These results provide important constraints for the DVSA_INITIAL_MODEL and can be used for comparison of the seismic experiment results with results of other geophysical studies.

Following the procedure in Preston and von Seggern (2008), although we calculated *P*-arrival time static corrections (Part II-Appendix 7), the corrections have not been applied to the P and S-arrival times prior to running the LOTOS code. Only elevation corrections have been applied using an empirically chosen replacement velocity of 4km/s relative to the station A05 elevation (Figure 99a). Thus, the depth of the estimated P/S velocity model (DVESA_LOTOS_MOD) was from surface.

The inversion for P/S velocity anomalies was performed by LOTOS in several steps, described in detail in Part II-Appendix 6, (1) simultaneous optimization for the best 1D velocity model and preliminary relocation of sources, (2) re-location of sources in the 3D velocity model, and (3) simultaneous inversion for the source parameters and velocity model using several parameterization grids. Steps 2 and 3 were repeated in several iterations. Figure 108 shows the re-located events (red dots) and the stations (blue triangles) used in the P/S tomographic inversion, after 5 iterations. The input (gray) and final (red) mean P/S wave seismic velocity model (estimated at step 1) in the LOTOS study area are shown in Figure 109. Examples of vertical sections were shown in Appendix 6-Table 6.2, Figures 6.7 -6.12) and plan view maps at

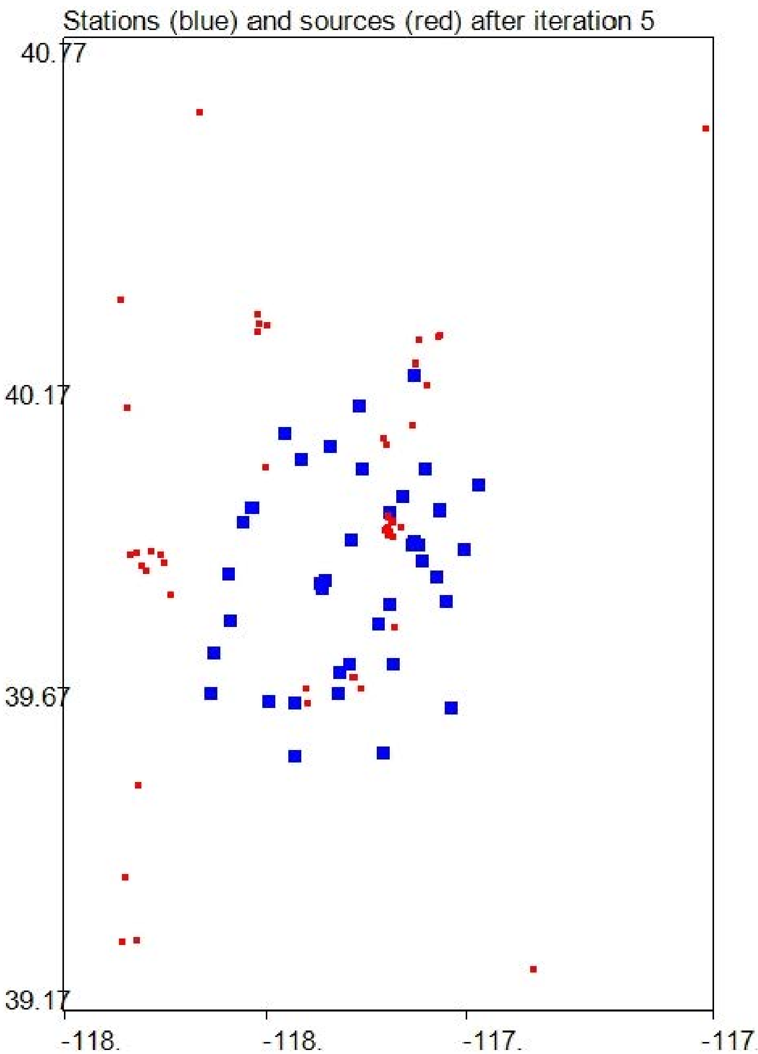

Figure 108. Shows the P/S tomography study area, the DVSA and a portion of the DVESA. Three-component, broadband seismic station locations (see Figure 99a were shown as blue squares and the events were represented by red dots. Each event has been relocated by the LOTOS code, however, with strong preference for the initial location. We estimated that the events were well- located, considering the visual identification of most of the mines. Once a mining event was identified, its location was replaced with the mine location (Appendix 5-Table 5-2).

3km depth are shown in Figure 110[7]. Anomalies in each plan view and vertical section are estimated as percentages of the final velocity model in Figure 109, at the respective depth. Additional vertical and plan view maps (at 1km, 2km, 4km, 5km, 7km, 9km, 12km and 15km) are shown in Appendix 6-Figure 6-3. More than 600 P- and over 200 S-arrival travel time measurements have been used as input to LOTOS. The DVESA_LOTOS_MOD is the P/S seismic velocity model estimated from LOTOS-inversion. It was observed that the location of the earthquakes in the study area was in the regions of relatively large slow Vp and at the boundary of opposite sign Vs anomalies. A disadvantage of using LOTOS in an area of low-seismicity like DVSA was that the best model resolution (with most uniform grid coverage) was obtained at 5-12km (which is actually the depth range of the earthquakes). At 1-3km depth, the grid nodes used in calculations were concentrated within 3km of each station. Thus, despite the fact the P/S velocity models were smoothed to show continuous velocity variation, the shallow (<3km deep) model was best described subsurface features in the vicinity of the station.

[7] Note in Figure 111A and in subsequent seismic plan view maps in this text, the surface faults are shown and the seismic anomalies at various depths resented are interpreted relative to the surface structure. This approach is not technically accurate. Ideally, the structure should be interpreted at the depth of the data being presented. However, such an analysis is beyond the scope and budget for this project.

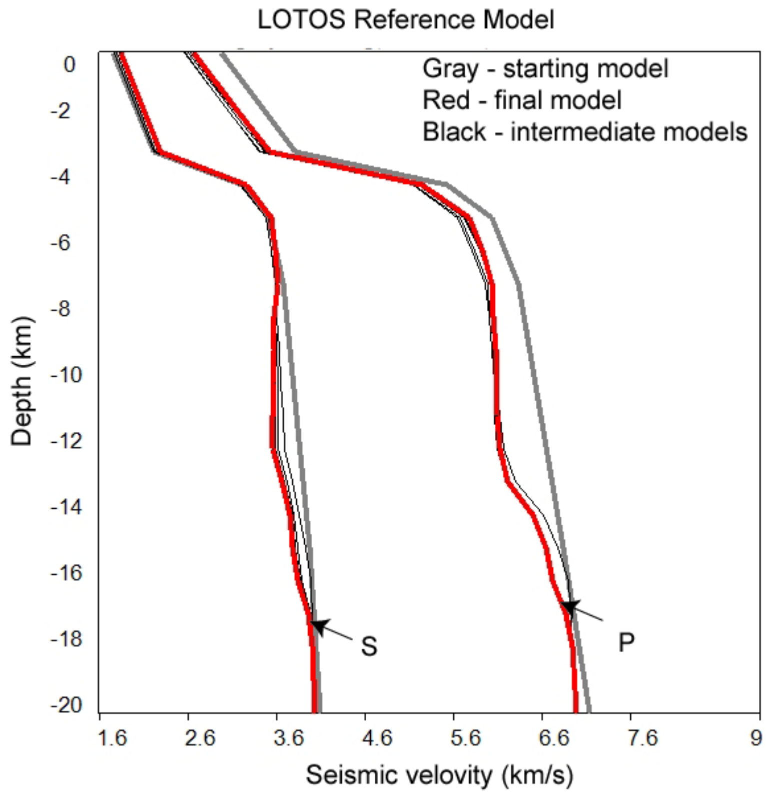

Figure 109. The mean P/S wave seismic velocity model in the DVESA area, estimated with LOTOS (see text for explanation). Gray shows the starting model, the intermediate models are shown as thin lines and red is the final model. Note low P-velocity in the mid-crust at ~12km, confirmed by autocorrelation and phase velocity results, as shown below (Appendix 6, Tables 6-2 and 6-3).

Vp/Vs ratios

Saturation conditions and possibly porosity could occasionally be inferred from the comparison of Vp and Vs data (Lees and Wu, 2000). Saturated, unconsolidated sediments typically have high *Vp /Vs* ratios (Nicholson and Simpson, 1985), however, the LOTOS events are not shallow enough to resolve structure at depths less than 5km. Using the LOTOS programs and only seismic events, *Vp/Vs* horizontal (Figure 111) maps were created. The seismic events are located close to regions of high gradient in the *Vp/Vs* ratios. Note that the earthquake location errors can be as high as 5km due to errors in the velocity model.

In a western Washington subduction zone tomographic study, Calkins et al. (2011) concluded that the low Vs, high Vp/Vs signature was likely due to a highly porous, fluid rich lower crust, and to potentially high pore fluid pressures. In the case shown in Figure 111, the hydrothermal production area is associated with low Vp/Vs values at 5-9km depth and it is located close to the transition to an area with high Vp/Vs values (i.e., on a fault). An intriguing feature is delineated at 9km depth, which is a relatively sharp discontinuity northeast of the power plant, perpendicular to the "Stillwater Seismic Gap" (Wallace and Whitney, 1984).

DVSA_ACOR_MOD

Ambient seismic noise survey and autocorrelation analysis were conducted to develop the DVSA_ACOR_MOD. An example of autocorrelation beams is shown in Figure 112. More autocorrelation results obtained in this study are shown in the figures of Part II-Appendix 7 and in Part II-Appendix 10. However, prior to analysis of nearly-vertically propagating waveforms, such as those extracted from autocorrelation beams, corrections were made for elevation and complex geology beneath each station to the *P*-travel times recorded at an array (Tibuleac et al., 2001).

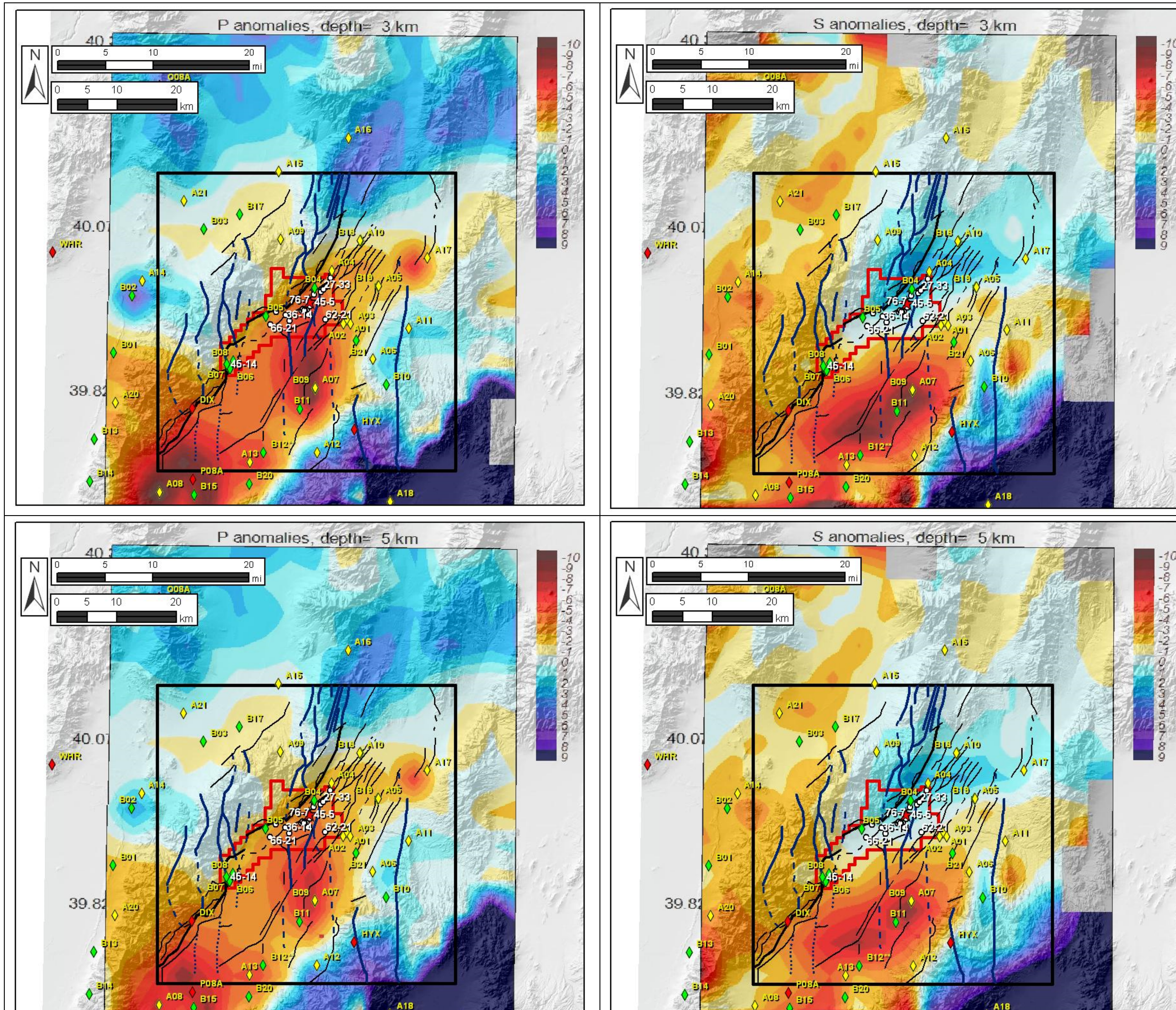

Figure 110. *Upper plots:* Example of LOTOS results at 3km and 5km depth. Superimposed on this figure are (1) the DEM for the area, (2) surface faults, (3) Project Area as black outline, (5) Calibration Area, and (6) the seismic stations with their IDs (Figure 99a). The left plot shows the estimated P-wave velocity (Vp) anomalies (%) and the right plot shows the estimated S-velocity (Vs) anomalies (%) when compared to the reference model at 3km depth (Figure 108). Note a NE-SW trending fault crossing the earthquake location, as shown by opposite sign P and S-velocity anomalies. A possible north-south trending fault is also observed, south of the power plant (red star located between wells 76-7 and 45-5) at a depth of 3km and 5km. *Lower plots:* Same as in the upper plots at 5km depth. Large Vs anomalies at the bottom of each figure are probably edge effects.

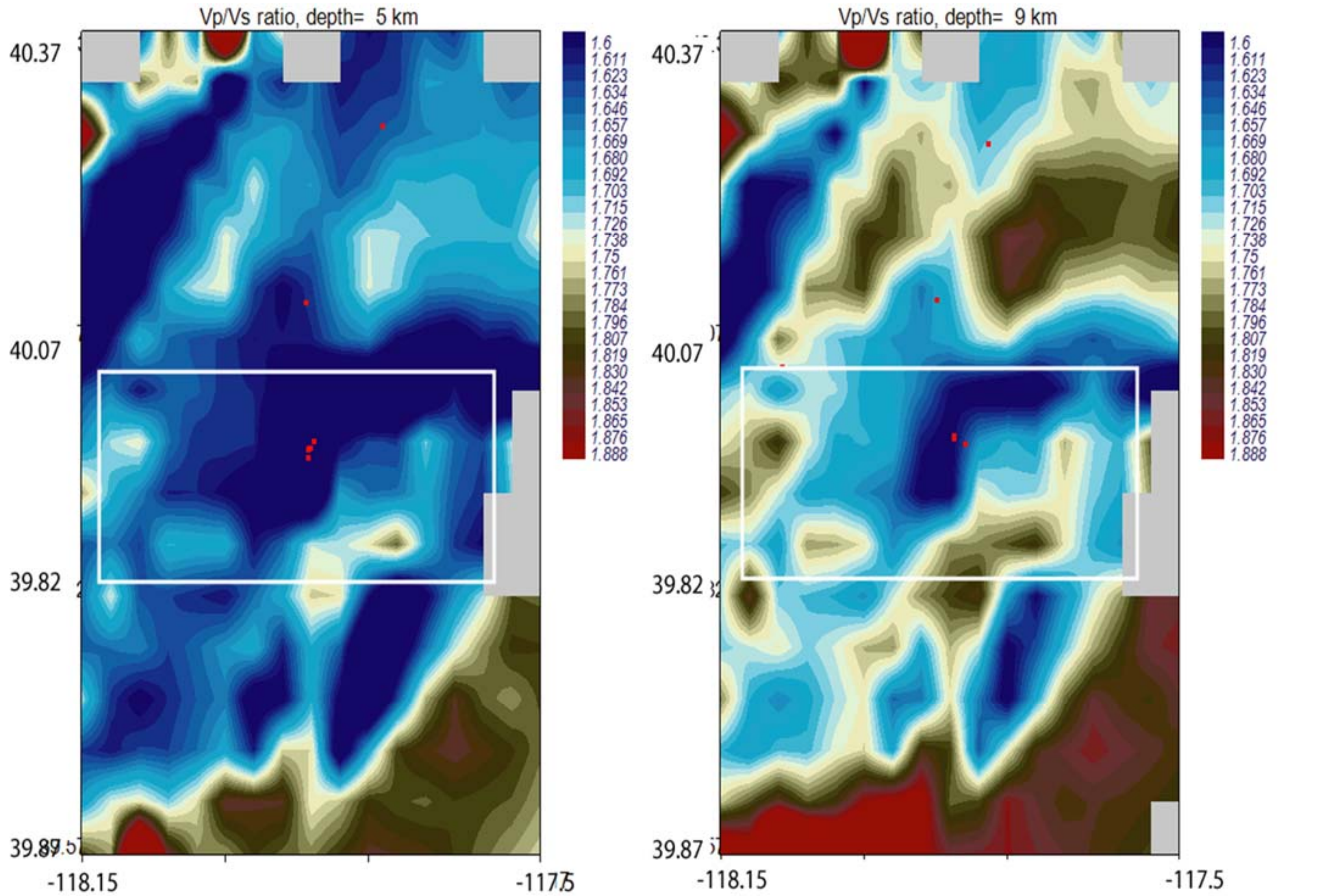

Figure 111. Plan view Vp/Vs maps in the DVSA estimated by the LOTOS programs. The center of the left plot (seismic events located within 2km are shown as red dots) is beneath the power plant, in a relatively low Vp/Vs region, however, in a region of high Vp/Vs gradient. Due to limited earthquake data availability, only the ratios deeper than 5km are shown here. The gray areas are regions where no data was available. The white rectangle shows the calibration area. Expected values for crustal rocks are of 1.75–1.82 (Brocher and Christensen, 2001).

Static Corrections for P-arrivals

The elevation difference between the DVSA ambient seismic noise survey stations was generally less than 200m, however, three stations were up to 1200m higher elevation than the majority of stations. Also, the geologic structure varies beneath each station. Simple P-phase travel time corrections using a replacement velocity (Lindquist et al, 2005) did not remove geology and elevation difference time delays. Thus, static corrections to P arrivals are estimated at all stations. Estimation of the static corrections (Figure 113) for P-wave arrivals was discussed in Part II-Appendix 8. Teleseismic earthquake waveform crosscorrelation, with reference the lowest elevation station A05 (Figure 99a), were used to estimate static corrections. The teleseisms were chosen such that the waveforms are arriving nearly vertically at the stations. After applying corrections for horizontal propagation using the United States Geological Survey estimated slowness (the inverse of the *P*-horizontal velocity), static corrections were estimated at every station. The static correction value varies from -0.55s at A09, to 0.48s at A15. Static corrections did not show a pattern either as a function of elevation, known geology, or known temperature distribution.

Autocorrelation

Autocorrelation beams (Part II-Appendix 7), representing the reflection response beneath each station, were processed for supplementary constraints on subsurface features. A synthetic waveform was estimated for a velocity model described in Part II-Appendix 7-Table 7-2. The model provides a good approximation of the geologic formations beneath each station, once the static corrections (Figure 113) have been applied. A possible explanation is that, except for variations within the first 2km, the reflectors in the DVSA may be at similar depth intervals. This affirmation, however, needs to be supported by supplementary synthetic modeling evidence, which is the object of further investigations. Figure 112 shows a comparison of a synthetic waveform (SYN) and the autocorrelations along a cross-section line to the west of the Clan Alpine Range, crossing the DVSA Calibration A to the east side of the valley. More examples are shown in Part II-Appendix 7 for groups of stations in Figure 99a.

Because of time limitations, we only used the P-reflections identified on the GF's extracted from autocorrelations to estimate a mean model for the DVSA. Several general observations resulted from the autocorrelation analysis. First, the lower the filter frequency band, the deeper was the first crustal reflection observed. Second, small (km - thick) variations were observed along every set of station locations. Third, a crustal reflection at 8s rather than at 10s (the standard for a 30km deep crust-mantle transition) was observed, which means that the crust-mantle boundary transition may start shallower in Dixie Valley than in regions with common crustal thickness. Fourth, when compared to stations in other areas, the stations in the vicinity of the production area did show differences in the reflection patterns. The last observations are currently analyzed in other projects.

Lines and Ad-hoc Sub-arrays of Stations

Because there are hundreds of possible combinations of stations, our challenge was to identify lines and ad-hoc sub-arrays of stations (Appendix 9-Figures 9-1 and 9-2) for GF investigation using array processing techniques (Tibuleac et al., 2011). A GF was extracted for each path between an available DVESA station and a station in an ad-hoc sub-array. The sub-arrays (Part II-Appendix 9-Table 9-1 and -Figure 9-1) were selected based on conductive heat flow modeling (Section 9.4.1), or to include wells of interest in the focus areas. The far DVESA station has been considered the virtual source of an "event" recorded at the ad-hoc DVSA sub-array. A fundamental mode Rayleigh phase velocity dispersion curve has been extracted, which depends on the subsurface structure at the respective sub-array. Figure 114 shows examples of the GFs estimated between the DVESA far-stations used in this study and ad-hoc arrays of stations in the DVSA. The individual station locations are shown in Appendix 5-Table 5-3. If the seismic "noise" would be isotropic, each GF would be symmetrical with respect to the zero lag. Noise directionality, i.e., more energy propagating from the Sierra Nevada to DVSA compared to the energy propagating in the opposite direction, results in asymmetrical GFs. GFs extracted on paths of similar length, using ambient seismic noise survey deployment A and B stations, are shown in the black rectangle in Figure 114 lower plot. As observed for other inter-station paths, note that the deployment “A” GF is noisier when compared to the deployment “B” GF, possibly because deployment B was during the winter, when less energy close to 1 Hz was recorded (Tibuleac and von Seggern, 2012).

GFs were analyzed from paths including a total of 22 far-stations in and in the vicinity of DVESA (Figure 99b, Appendix 5-Table 5-3), at 30 ad-hoc-arrays in the DVSA. Figure 115 shows examples of frequency-wavenumber (*fk*) analysis for stations virtual sources at stations WVA and SBT (Appendix 5-Table 5-3, Tibuleac et al., 2011) and virtual receivers in the DVSA. Fundamental mode Rayleigh phase velocity dispersion curves in DVSA (Figure 116) are inverted for shear-wave velocity models. The models are integrated into the DVSA_PHVEL_MOD (Figure 100).

THE FINAL MODEL

In this section we discuss the final velocity models obtained in each of the three regions of interest (1) the Calibration Area (CA), (2) the Project Area (PA) and (3) the DVESA. As shown in Figure 100, the Vs component of the DVSA_FINAL_MODEL was used for the CA and PA to 10km depth and a combination of all available seismic velocity models generated in this investigation were used to derive the final DVESA seismic velocity model. The DVSA P-velocity models derived from this study were all estimated from the S-velocity models by the *surf96* program, thus they had similar seismic velocity anomaly patterns to the Vs anomalies. The only areas in the PA with better Vp resolution were the regions containing reflection lines. Thus, the available high-resolution (0.5km) Vp models were spatially limited. The DVSA_LOTOS_MODEL provided useful information deeper than 3km. Layer depth information beneath each seismic station was estimated in the DVSA_ACOR_MODEL with good resolution, however, only DVSA mean models were derived from autocorrelations in this study, because of time and budget constraints. Thus, to estimate the Vp model, all the existing Vp information was used in each area.

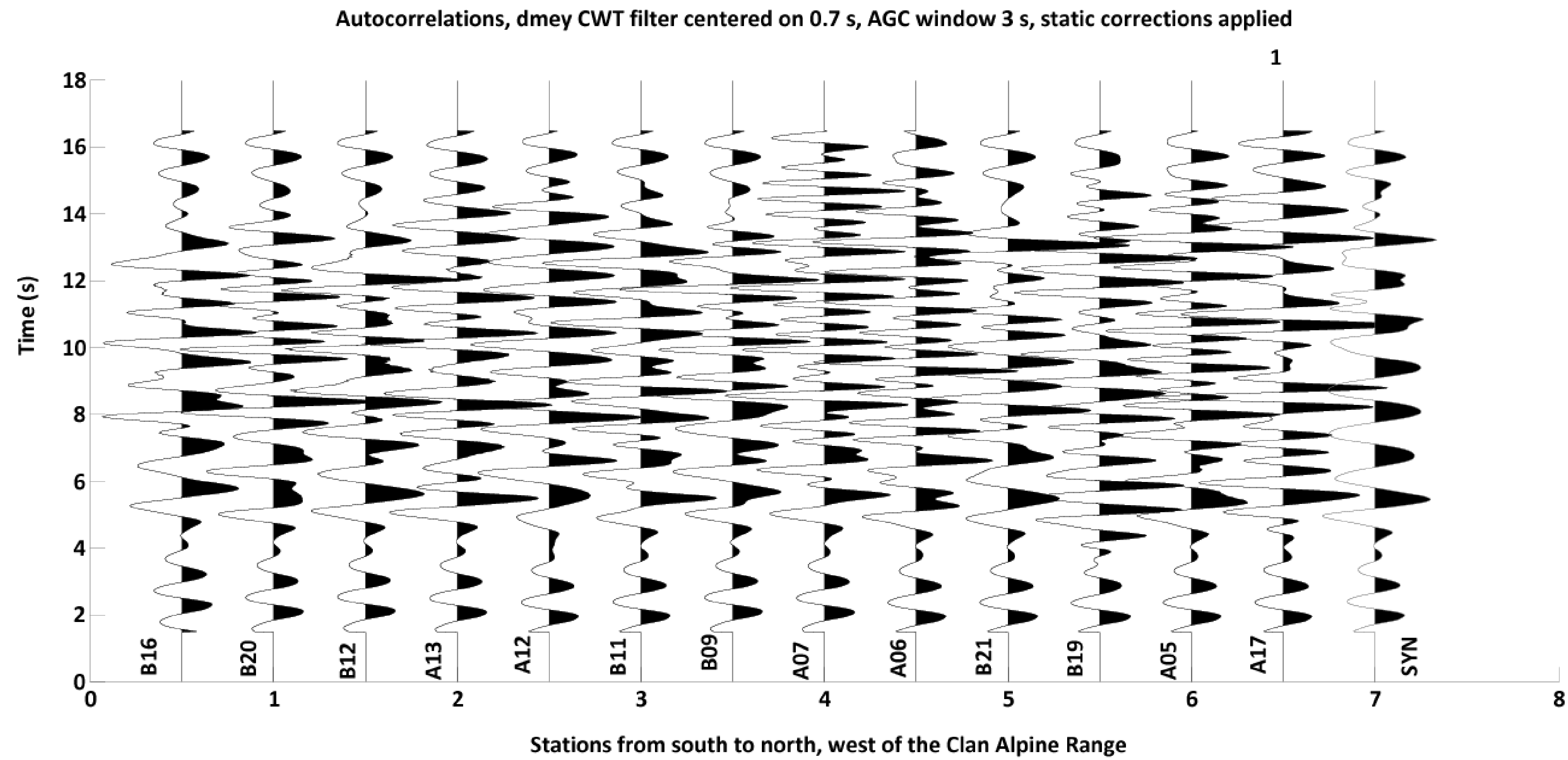

Figure 112. An example of autocorrelation beams on a profile west of the Clan Alpine Range, including stations B16,B20, B12, A13, A12 ,B11, B9, A7, A6, B21, B19, A5 and A17 (see Figure 99a for station locations and Appendix 5-Table 5-3). Automatic gain control (AGC) was applied in a window of 3s on each trace. The waveform to the right is synthetic. Note a clear arrival at ~6s, possibly a reflection from a layer ~10km deep. We observed that the lower the filtered frequency band, the deeper were the layers interpreted as being resolved by autocorrelations.

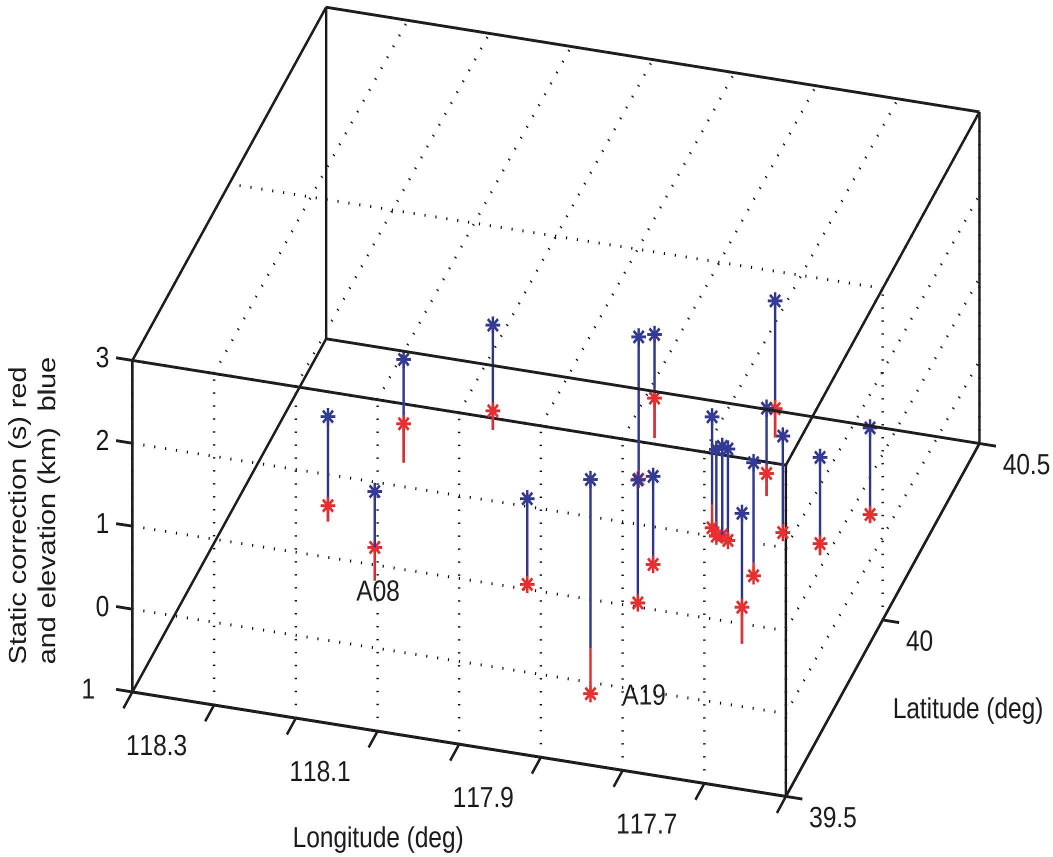

Figure 113. Static corrections for P arrivals

The DVSA velocity model

Using the DVSA_INITIAL_MODEL in each grid cell (see Section 8 for a discussion of grid cells), we inverted the waveforms for the DVSA final model. These results were the DVSA_FINAL_MODEL and were used for comparison of the Vp and Vs velocity models in DVSA to results of other geophysical studies.

P-velocity (Vp) Data

A number of Vp anomalies are observed at the depths of this investigation, -0.5km[8] to 5km below the ground surface (Figure 117). The ground surface is at ~1km elevation relative to the sea level. The color scale in Figure 119 shows Vp deviations (km/s) from the mean velocity at the respective depth. The general features of these anomalies are described below.

1. A large, NE-SW trending Vp gradient generally occurs in the eastern portion of the CA occurs along the piedmont fault component of the DVFZ starting at a depth of 0.5km, which disappears by 1km depth below the surface (Figure 117). All the depths below are relative to the surface. A major N-S structure in the valley (~center of the CA) which appears to be offset to the east relative to NNE trending structure in the Stillwater Range (which goes through Coyote Canyon [see Figure 1]). This N-S structure in the valley bounds a high Vp zone to the east starting at a depth of 1km which becomes very marked by a depth of 2km and persists to a depth of 4km. The high Vp anomaly expands in the east portion of the CA from a depth of 1.5km to 4km and is bounded on its western side by the aforementioned N-S and NNE trending faults. The high Vp zone grows to the west of the NNE trending fault underneath the Stillwater Range, along the range-front fault, and extending into the DVFZ to the east and by a depth of 4km, the high Vp zone is located west of the NNE-trending fault.

---

[8] The seismic data is presented in depth below the surface while other geophysical data in this report is presented in depth relative to above sea level (asl). For examples, a depth of -0.5km, 0km, 1km below the ground surface in this section corresponds to 0.5km below the ground surface, seal level, and 1km below the ground surface, respectively. Note that the valley floor in the Calibration Area is at +1km asl.

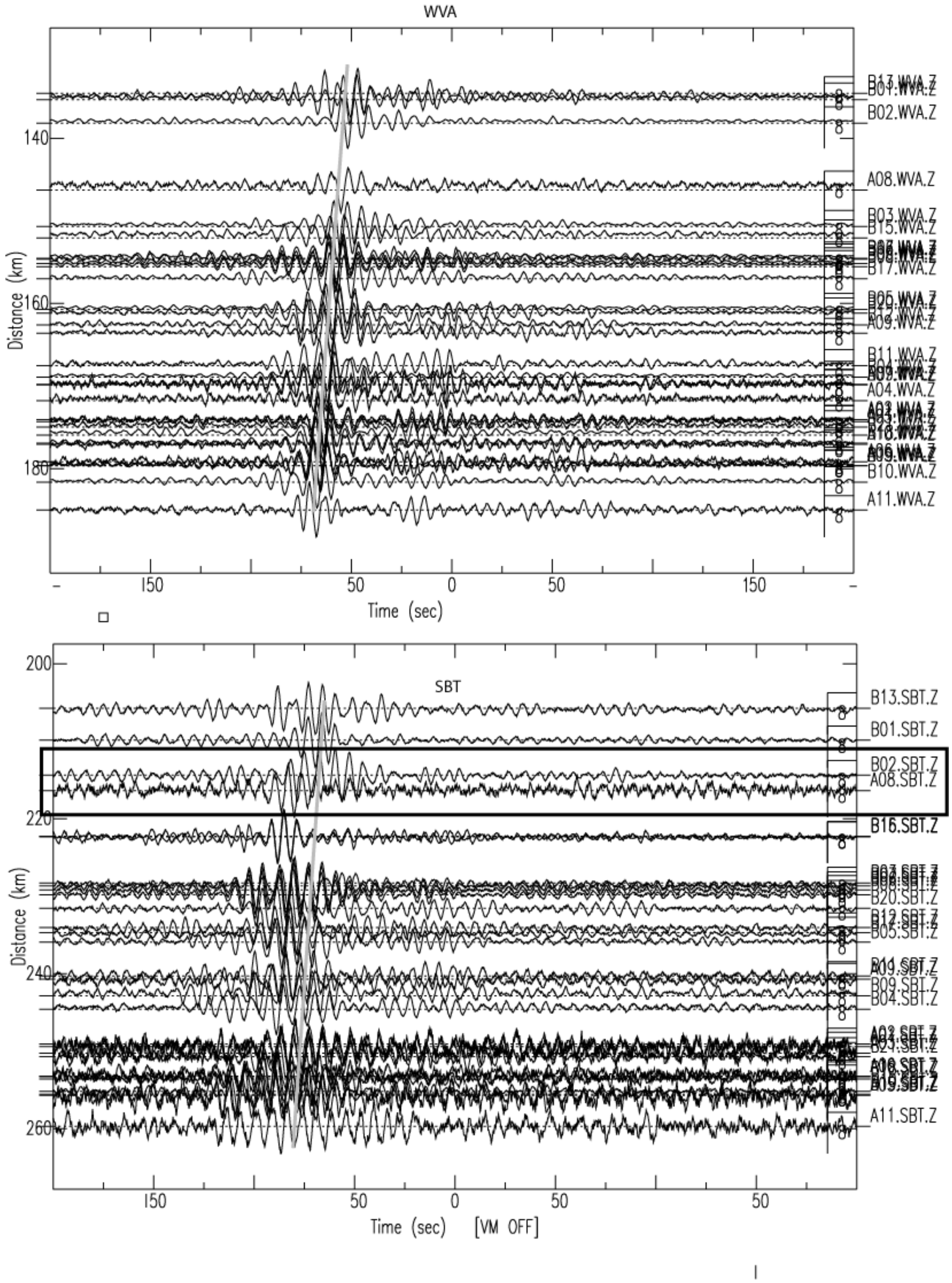

Figure 114. *Upper plot*: Two-sided GFs extracted between DVSA stations and the DVESA (Nevada Network or NN) station WVA (Appendix 5-Table 5-3). The left gray line shows the 3km/s time marks. *Lower plot:* Two-sided GFs extracted from crosscorrelation beams between DV stations and NN station SBT (Appendix 5-Table 5-3).

2. A Vp low is observed to develop on the western side of the NNE fault in the Stillwater Range, described above, from +0.5km to 1km. It evolves into a Vp high by a depth of 3km.
3. Isolated modest low Vp develops predominantly to the east of the N-S trending faults from a depth of 3.5km to 6km.
4. A major Vp low occurs along the northern boundary of the CA from a depth of 4km to 6km.
5. Well 62-21 (a dry hole with a total depth [TD= 2.97km]) was drilled in an area of moderate high Vp at a depth of 0.5Km which evolves to Vp with insignificant anomalies from 1 to 2.5km and then decreases to a moderate high Vp at a depth of 3-5km.

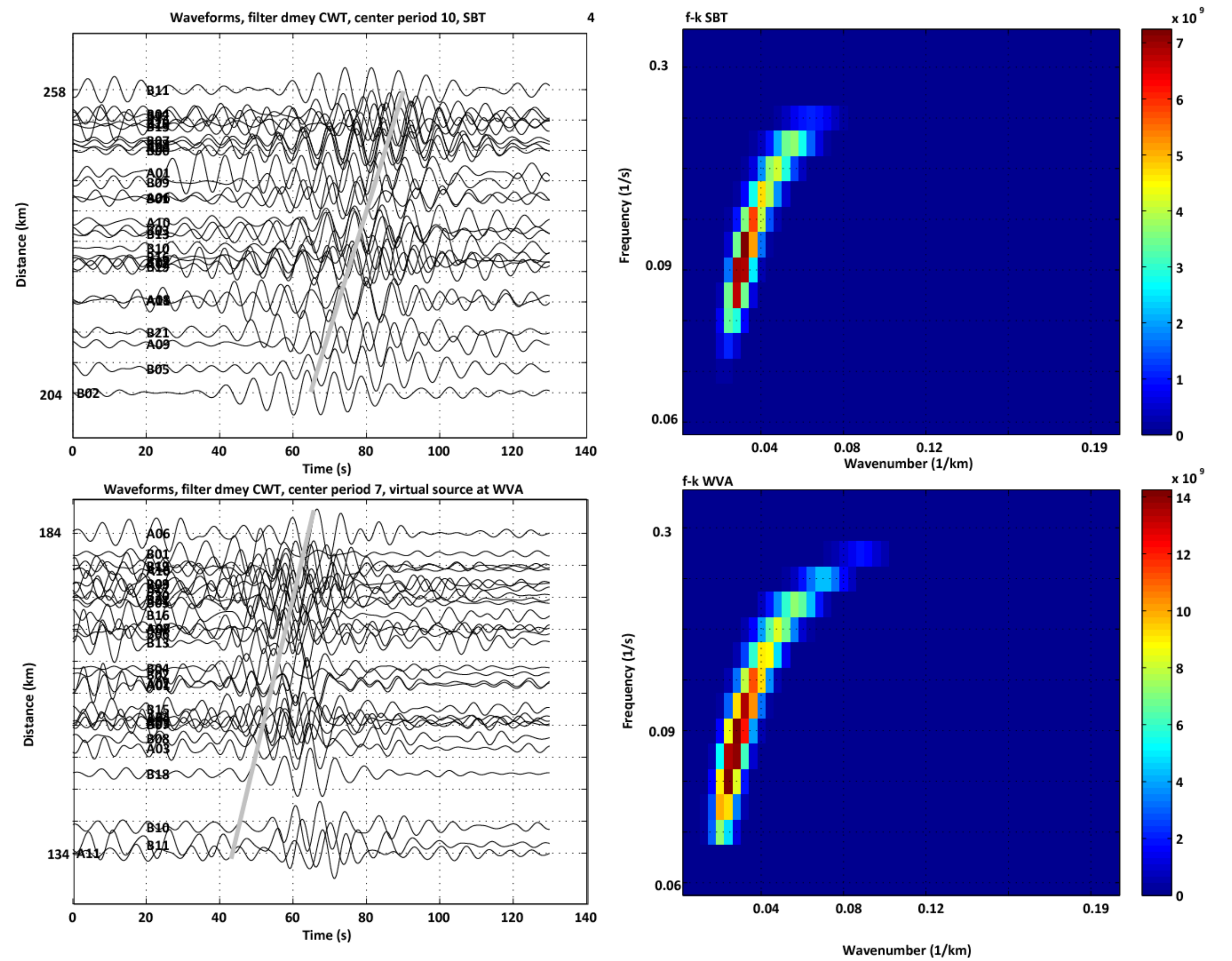

Figure 115. Example of frequency-wavenumber (fk) analysis for stations virtual sources at stations WVA and SBT (Appendix 5-Table 5-3) and virtual receivers in the DVSA. The gray line shows the 3km/s time marks in the left plots. Left plots in show the GFs estimated from ambient noise, scaled to the maximum value. The right plots show the phase velocity estimated at the DVSA array. Waveforms are filtered using a Continuous Wavelet Transform with a Meyer wavelet centered on 10s (upper right plot) or 7s (lower left plot) period as indicated on the plot. The "hot" (towards red) colors on the fk plots show the maximum fk value for each wave number.

6. Well 45-14 (a dry hole with a TD=2.75km) was drilled in an area of moderate low Vp at the surface which decreases to low VP region at a depth of 1km which persists to a 3km depth where it becomes a Vp high from a depth of 3.5-5km.
7. Well 76-28 (a dry hole with a TD=3.17km) generally occurs in the same Vp domain as the production and injection wells.

8. Wells 36-34 (a sub-commercial well which was directionally drilled to the range-front fault, TD=3.55km and also the hottest well in the B&R, 285°C at 3.05km TD), 66-21 (a dry hole with a TD=2.97km) and 62A-23 (a dry hole with a TD=3.47km) occur in the mid-field within the CA. These wells appear to have been drilled around but on the outside of a low Vp anomaly that is most pronounced at a depth of 1.5-4.5km and persists to 6km. This low Vp anomaly occurs principally within the DVFZ and lies in close and slightly N of an intersection of a NNW trending fault with the piedmont fault of the DVFZ.

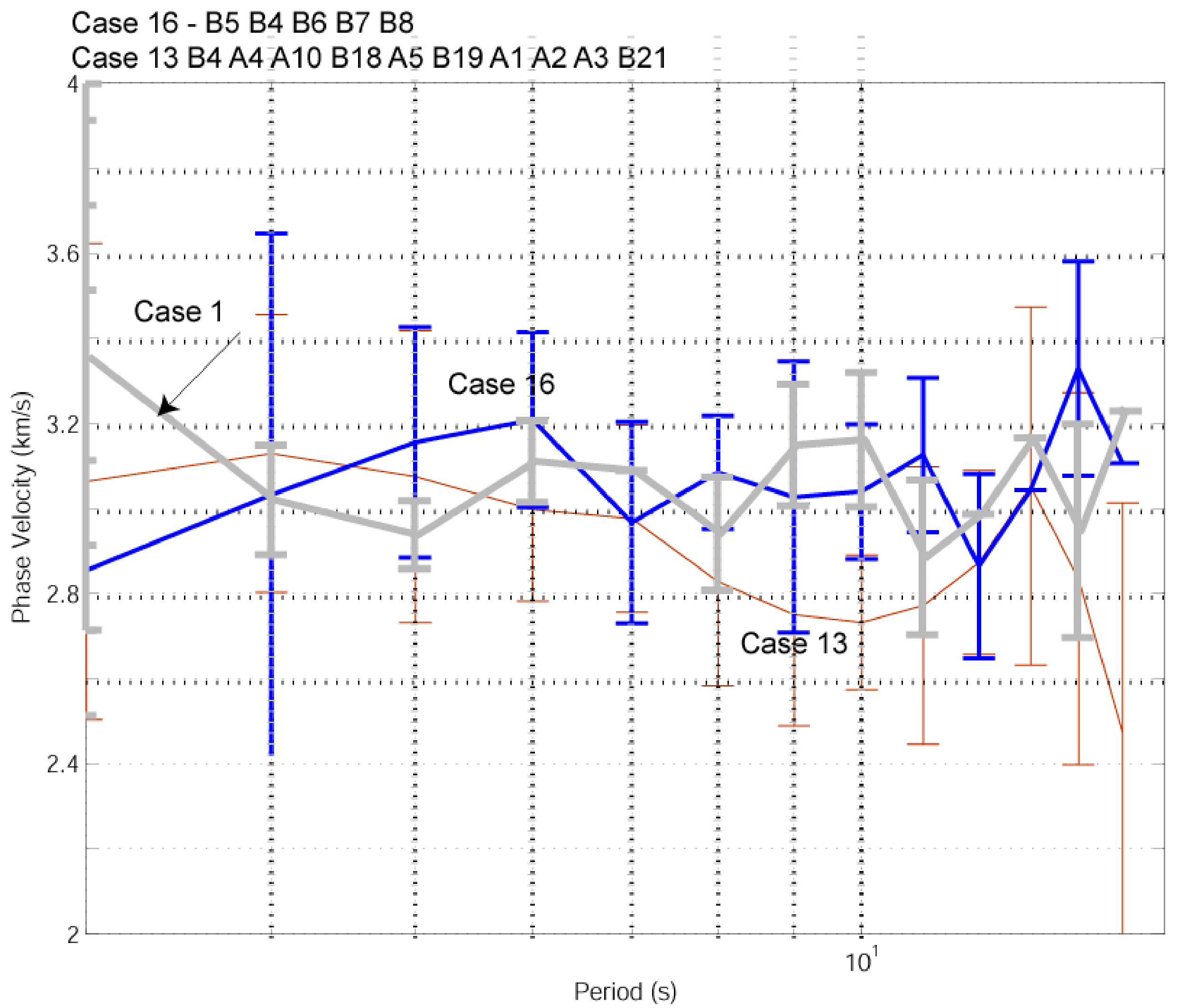

Figure 116. Fundamental mode Rayleigh phase velocity dispersion curves (FMRPHD) extracted using frequency-wavenumber (fk) analysis from ad-hoc sub-arrays of stations in DVSA; see Figure 23a for station locations. Each dispersion curve follows the mean of all the measured phase velocity values, represented for each period, and the standard deviation at each period is shown as vertical bars. Gray shows the FMRPHD when the sub-array includes all the DVSA stations. This is a mean FMRPHD for the Dixie Valley. Blue shows FMRPHD for a line of stations on the eastern flank of the Stillwater range, southwest of the Stillwater power plant location (including well 45-14, Appendix 5, Table 5-1), Figure 99a. Red shows the FMRPHD beneath a small sub-array NE of the Stillwater geothermal power plant (Figure 99a), including well 66-21 (Appendix 5, Table 5-1). This curve has larger errors, and represents results from a small number of stations. For this NE Stillwater Range sub-array, note lower velocities in the 8-12s period range, which are inverted into low S-velocity models in the upper crust at depths of approximately the same numerical value as the periods. The results are confirmed by the autocorrelation analysis (see Part II-Appendix 8). Next, we invert these dispersion curves to obtain shear velocity variation with depth and estimate DVSA_PHVEL_MOD, Part II-Appendix 9 and Figure 100.

9. The production and injection wells for which the project has data have TD in the range from 0-3km (Appendices 11 and 16b). In these depth ranges the wells lie on the boundary of a high Vp area.
10. Based on Table 16 we observe that the mean velocity in the CA increases with depth up to 4km and then decreases. We interpret this behavior as pressure and lithology effects on velocity being stronger than temperature and porosity effects down to 4km (as discussed below).

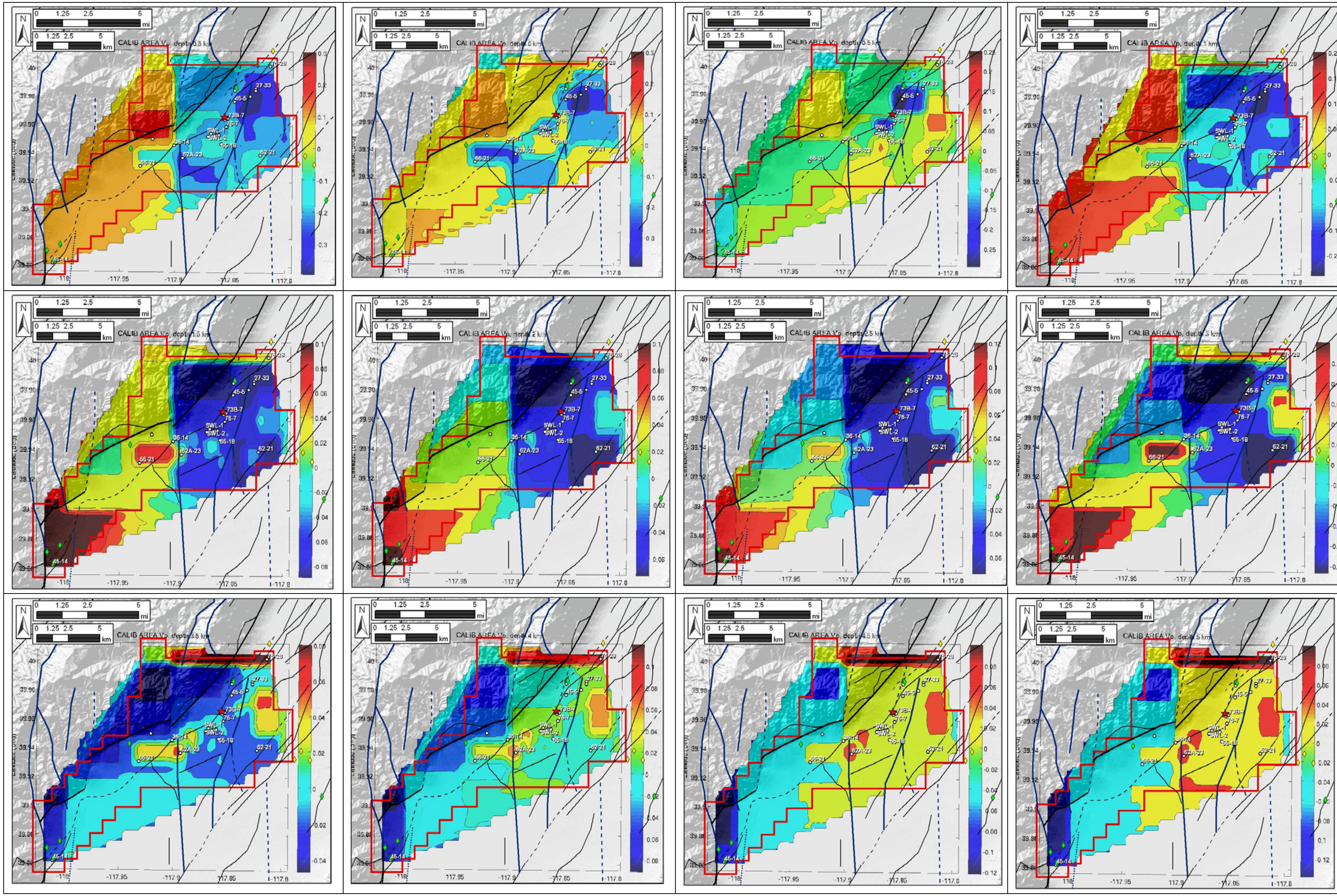

Figure 117. P-velocity (Vp) maps in the Calibration Area at depths of -0.5km, 0km, 0.5km, 1km, 1.5km, 2km, 2.5km, 3km, 3.5km, 4km, 4.5km, and 5km below ground surface (with a depth of 0km below ground surface being equivalent to sea level) from upper left to lower right. Superimposed on the Vp maps are the (1) DEM for the area, (2) Project Area, black outline, (3) Calibration Area, red outline, (4) seismic stations with their IDs, (5) well locations with their IDS, and (6) identified surface structure from this study. Note that the color code scale is different in each figure as a result of the velocity deviations from the mean values shown in Table 16.

Table 16. Mean Vp velocity values in Figure 117

Mean Vp velocity (km/s)	Depth (km)
3.15	-0.5
3.4	0
3.9	0.5
4.29	1
4.8	1.5
5.24	2
5.61	2.5
5.80	3
5.94	3.5
5.93	4
5.87	4.5
5.82	5

S-velocity (Vs) Data

The resolution of the S models (Figure 118) was the lowest at depths less than 2km. Within this depth range, improved resolution (for both P and S velocity models) was obtained in the CA immediately beneath the stations (see discussion below). Although the seismic experiment was designed to provide a 5km resolution velocity model in the PA, the resulting resolution is as good as 3km in selected regions in the CA. The largest density of seismic stations (and thus, of inter-station paths) was in the CA, where two micro-arrays with a 1-km aperture were deployed around wells 45-14 and 66-21. Despite all the above, and because the seismic experiment was designed for a 5km, as opposed to 0.5km (the resolution for the CA used in the geoscience correlations[9], see Sections and 10) the CA sampling by the tomographic grid was sparse, especially for Vs. In seismology the best resolution of a model is estimated as half the closest inter-station distance. The Vp, Vs and Vp/Vs models are shown respectively in Figures 117-119. The trust factor maps and velocity model maps are presented in Part II-Appendix 10 (which is a set of directories containing the files generated in this study).

A number of Vs anomalies are observed at the depths of this investigation, 0.5km to 5km (Figure 118). The general features of these anomalies are described below:

1. At a depth of 0.5km, two prominent Vs lows occur (a) W of the major NNE trending fault cutting through the middle of the CA in the Stillwater Range and (b) E of the major N-S trending fault in the valley in the middle of the CA, S and SW of the power plant. Both low Vs anomalies increase in velocity with depth. The low Vs in the Stillwater Range becomes a Vs high by the depth of 4-4.5km. The low Vs anomaly on the east side of the N-S trending fault progressively becomes a high Vs anomaly by 5km and then decreases slightly at 6km.
2. Well 62-21 occurs generally in a moderate Vs low at a depth of 0.5km to 2.0km, where it becomes a high Vs at 2.5km to ~5.5km, and a moderate high at 6km.
3. Well 45-14 occurs in a high Vs from a depth of 0.5km to 2km, where it decreases to a strong Vs low at 3.5km to 4.5km and persists to 5km.
4. Well 76-28 generally lies in the same Vs environment as production and injection wells in the NW portion of the field.

[9] The seismic array design was focused on the Project Area. The 0.5km by 0.5km geoscience correlation analysis (Sections and 10) was determined during the early stages of the project for the CA. The reason for this change resulted from the realization that the only area where the exploration tools used in this study could be calibrated was in the DVGW (or the CA). Given complexities with the U.S. Bureau of Land Management with respect to permitting and the project schedule at the time it was too late to change the seismic array deployment design.

5. Well 62A-23 occurs in a low Vs from 0.5km to 3-3.5km, where it increases to a high Vs at a depth of 5.5km.
6. Well 36-14 was directionally drilled into the structural offset to the west which occurs in a low Vs area from a depth of 0.5km to 2.5km where it becomes a moderate high Vs to a depth of 6km.
7. Well 66-21 occurs in a high Vs from 0.5km to 2.5km where the velocity transitions to a generally moderate Vs to 6km.
8. The area of the production and injection wells is, at all depths, a region of transition from very low anomaly to either slightly low Vs (shallower) or slightly high Vs (deeper), which we interpret as fault presence. Well 76-28 generally lies in the same Vs environment as production and injection wells in the NW portion of the field.

Discussion of Vp and Vs Observations

The conventional interpretation is that low P and S velocities are associated with unconsolidated rocks, and/or rocks having higher temperature (Wang et al., 1990) and/or with higher degree of rock fracturing. For the same rock type high velocity anomalies are usually observed in rocks which are colder, less fractured and/or have higher degrees of consolidation. According to Ramachandran (2011) "subsurface faults that are not clearly interpretable from velocity model plots can be identified by sharp contrasts in velocity gradient plots". Above we reported similar observations.

Vp/Vs ratio

A number of Vp/Vs anomalies are observed at the depths of this investigation, 0.5km to 6km (Figure 119). A high Vp/Vs ratio may be an indicator fluid-saturated rock (Wang et al, 1990). The average value of Vp/Vs ratio was estimated (in northeastern Japan) as 1.69 in the upper crust, 1.75 in the lower crust, and 1.77 in the uppermost mantle by Nakajima et al. (2001). As already mentioned in the LOTOS model discussion, Calkins et al. (2011) explained a relatively high Vp/Vs ratio (>1.9) in the middle to lower continental crust, directly above the portion of the slab expected to be undergoing dehydration reactions beneath the Olympic Peninsula, western Washington, as a fluid-rich lower crust property.

1. At a depth of 0.5km, two low Vp/Vs anomalies are observed. One low anomaly, Vp/Vs<1.7, occurs on the west side of the NNE-trending fault in the Stillwater Range in the same area as the low Vs anomaly (see Vs discussion above). This low Vp/Vs anomaly in the Stillwater Range increases with depth 5.5km and then decreases slightly at 6km. The other low anomaly west of the N-S trending fault in the valley persists to a depth of 3.5km, where it becomes a moderate to high Vp/Vs anomaly to depth.
2. At the depth of 0.5km two high to very high Vp/Vs anomalies exist. One lies east of the NNE-trending fault in the Stillwater Range and extends into the DVFZ near the power plant. This low becomes moderate by a depth 1.5km and generally persists to 6km. The other high occurs to the SW along the range front fault and the area of wells 45-15 and 66-21. The area of Vp/Vs high becomes a strong low by at depth of 6km.
3. Well 62-21 lies in a moderate Vp/Vs high at a depth of 0.5km which becomes a strong low by a depth of 3-5.5km.
4. Well 45-14 lies in a Vp/Vs low from a depth of 0.5km to 2km, where it decreases to a very strong low Vp/Vs at a depth of 4-6km.

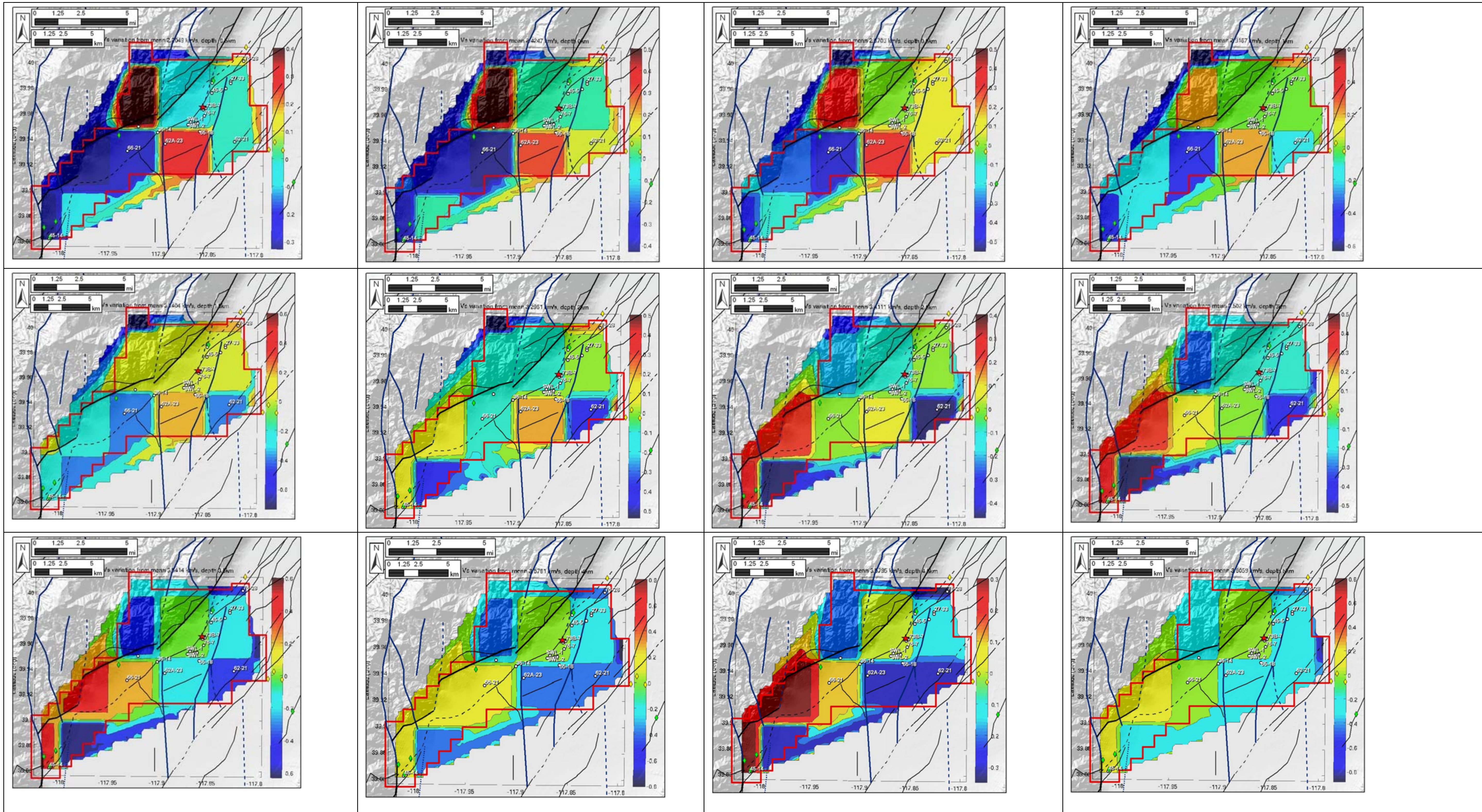

Figure 118. S-velocity (Vs) maps in the Calibration Area at depths of -0.5km, 0km, 0.5km, 1km, 1.5km, 2km, 2.5km, 3km, 3.5km, 4km, 4.5km, and 5km below ground surface (with a depth of 0km below ground surface being equivalent to sea level) from upper left to lower right. The mean elevation in the area is 1km above sea level. A depth of 1km and 2km corresponds to -2km above sea level (asl) and -3km asl, respectively. Superimposed on the Vs maps are the (1) DEM for the area, (2) Project Area, black outline, (3) Calibration Area, red outline, (4) well locations with their IDS, and (5) identified surface structure from this study (see Section 7). Note that the color code scale is different in each figure.

5. Well 36-14 total depth is in a low Vp/Vs at a depth of 0.5km to 2.5km where it becomes a moderate high by a depth of 5.5km.
6. Well 76-28 as in previous discussions above generally lies in the same type of domain as the production and injection wells in the NW portion of the field.
7. Well 66-21 lies in a Vp/Vs high from a depth of -0.5km to 1.5km where it decrease to a low at 4-5km.
8. Well 62A-23 lies in a Vp/Vs low from -0.5km to 2.5km where it increases to a high at 4.5km.
9. Production and injection wells generally occur in a moderate Vp/Vs area from -0.5km to 5km.
10. Note low Vp/Vs below the dry wells.

Project Area Results

Figures 120, 121A and 121B, and 122A and 122B show plan views of respectively Vp, Vs and Vp/Vs in the PA at selected depths. Major observed velocity anomalies are discussed below. Note lower resolution for the Vp when compared to the CA. This is due to the model extraction method and to the larger slack (5km for the PA as opposed to 1km for the CA). When lower resolution is required, all the models within the "slack" of the search point are extracted, weighted and mediated. Thus, the resulting model has lower resolution.

P-wave velocity (Vp)

1. A high Vp anomaly is observed at a depth of 1km beneath the power plant and the eastern portion of the CA and extending to the NW where it appears to have a N-S orientation (Figure 120, left upper left plot).
2. This shallow high Vp anomaly becomes a broad moderate high anomaly in roughly oriented NW-SE through the most of the project area from the Cal Alpine Range on the SE side of the PA to the Carson Sink on the NW side at a depth of 3km. At a depth of 6km, a moderate low develops oriented NE-SW through the valley and encompassing the northern Stillwater Range. This moderate low evolves into two N-S trending low anomalies by a depth of 11km, one on the SE side of the CA and one of the SW side of the CA. The latter is coincident with the Fairview Peak Fault and the former is bounded on the western side by the N-S trending valley fault. These lows become more intense with depth and develop an E-W connection by a depth of 11-14km.
3. In the depth range of 5-11km below the surface, the Vp decreases and two major N-S trending low Vp anomalies develop at a depth of 12km below the surface (Figure 120, lower plots), one in the eastern portion of the PA and one SSE of the southwestern corner of the PA.

   These two low Vp anomalies merge SE of the CA starting at a depth of 13km below the surface (Figure 120, lower right plot).

S-velocity (Vs) Data

A number of anomalies are identified in Figures 121A and 121B. From the southwest to northeast, these are:

1. A NW-trending low Vs anomaly S of the SW boundary of the CA from the range-front fault of the DVFZ to the hanging wall of the Buckbrush Fault a**t** a depth of 1km depth with disappears by 2km depth (Figure 121A), reappears fully and shifted to the NE at a depth of 9-10km depth (Figure 121B), and slowly dissipating at a 11-15km depth.

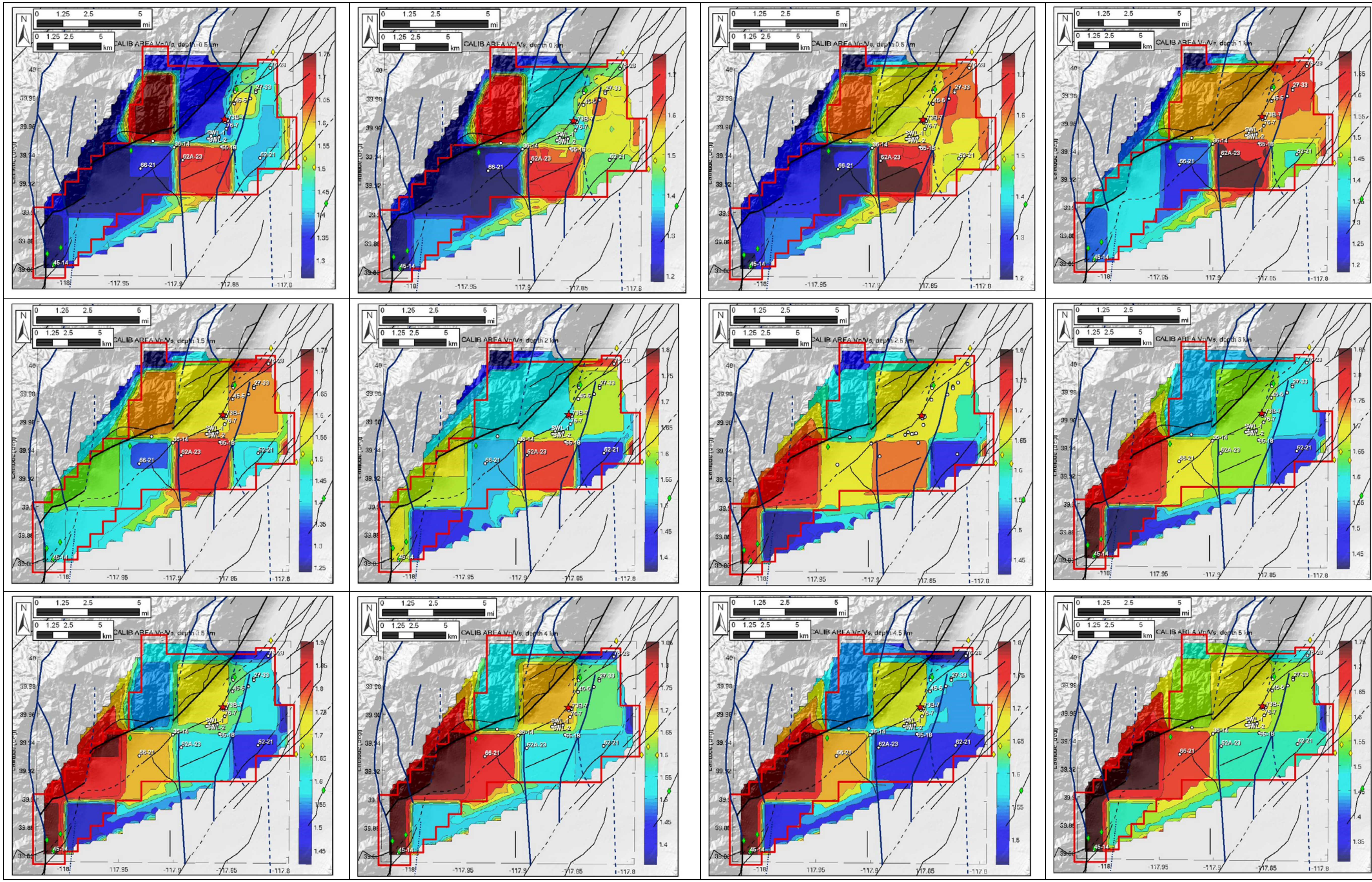

Figure 119. Vp/Vs-velocity maps in the Calibration Area at depths of -0.5km, 0km, 0.5km, 1km, 1.5km, 2km, 2.5km, 3km, 3.5km, 4km, 4.5km, and 5km below ground surface (with a depth of 0km below ground surface being equivalent to sea level) from upper left to lower right. The mean elevation in Dixie Valley area is +1km above sea level; a depth of 1km and 2km corresponds to -2km above sea level (asl) and -3km asl, respectively. Superimposed on the Vp maps are the (1) DEM for the area, (2) Project Area, black outline, (3) Calibration Area, red outline, (4) seismic stations, (5) well locations with their IDs, (6) the location of the geothermal power plant as a red star, and (7) identified surface structure from this study (see Section 7). Note that the color code scale is different in each figure.

2. An apparent NW-trending two-lobed Vs anomaly with a pronounced low in the footwall of the range-front fault north of station B05 (Figures 121A and 99A), west of the NNE-trending fault in the Stillwater Range and a second anomaly in the hanging wall of the piedmont fault portion of the DVFZ and straddle between the N-S trending fault and a NNE trending in the valley at a depth of 1-3km. This two-lobed anomaly disappears at 4km and eventually develops a modest high NW-trending at 13km.
3. A N-S trending anomaly on the eastern side and somewhat to the south of the CA at a depth of 1km which appears to trending NW through the Stillwater Range and into the Carson Sink. This anomaly decreases in intensity at 2-3km and by 4km exhibits a low intensity trending NE-SW. At 4-9km it becomes a relative high Vs area.
4. A low Vp anomaly in the area of Hyder Hot Springs occurs a depth of 1km and disappears by a depth of 4km.
5. A low Vs anomaly was observed in the Carson Sink to the NW of the PA, deepening to the N-NE from 2km to 14km depth (Figure 121A and B). Beneath the hot springs in the vicinity of A05 and A17 (Figure 99a), a low Vs persisted down to 9km. In this region, a strong Vs anomaly gradient with a NW-SW trend was observed from 5-9km depth. A low Vs anomaly was observed at less than 3km depth on the E-W system of faults between station B05A and stations A01-A03. Deeper than 9km, low Vs was estimated on the east side of a fault on which stations A11 and B10 were located. A significant low Vs region was resolved SW of the calibration area starting at 9km depth. This anomaly looks like a conduit deepening to the SW of the power plant. While in the upper 6km high Vs was observed SW of the calibration area, high Vs was observed below 6km depth in the same region, deepening to the east.
7. Starting at 4km depth, between stations A09 and A16, left of the Stillwater Gap, a high N-S trending low Vs region was bounded by a relatively low Vs region from 4-7km depth. The low Vs region was replaced by relatively high Vs deeper than 7km (Figure 121). A hypothesis was suggested by the DVESA models discussed below, i.e., that an E-W seismic velocity anomaly trend was observed in the upper ~10km of the crust (Figure 123A, which was replaced by a NW-SE anomaly trend from 10-15km (Figure 123B).

Vp/Vs ratio

Very high Vp/Vs >1.75 was observed within 1km of the surface in the vicinity of the power plant, beneath stations A1, A2 and A3 (Figure 122A. At 4km depth, high Vp/Vs values were observed to the SW of the CA and in the vicinity of the hot spring near station A05. From 5-12km depth the NE half of the CA has low (< 1.5) Vp/Vs values. Increasingly high Vp/Vs values appeared to deepen beneath the Clan-Alpine range from 9-14km from the surface. High Vp/Vs values were observed at depths greater than 12km beneath the whole CA, extending to the SW of the PA. As mentioned before, higher Vp/Vs ratio was interpreted by other researchers as an indication of fluid-rich crust.

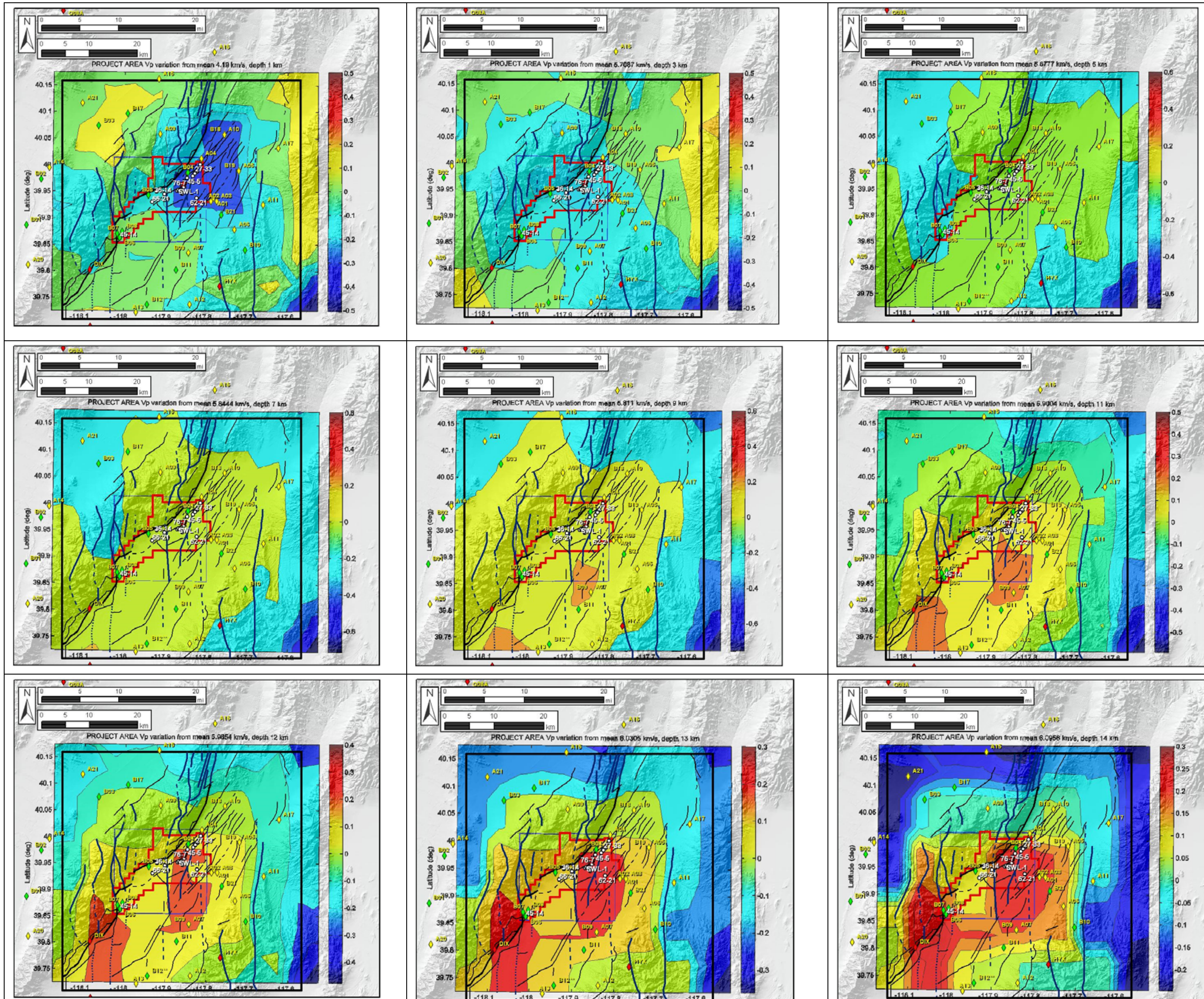

Figure 120. Project Area: Vp maps at depths below the surface of 1km, 3km, 5km, 7km, 9km, 11km,and 12km, 13km and 14km presented from upper left to lower right . The mean elevation in Dixie Valley is +1km above sea level. A depth below the surface in these Vp maps of 1km and 3km, for example, corresponds to -2km above sea level (asl) and -4km asl, respectively. Superimposed on the Vp maps are the (1) DEM for the area, (2) Project Area, black outline, (3) Calibration Area, red outline, (4) seismic stations with their IDs, (5) well locations with their IDS, and (6) identified surface structure from this study (see Section 7). Note that the color code scale is different in each figure.

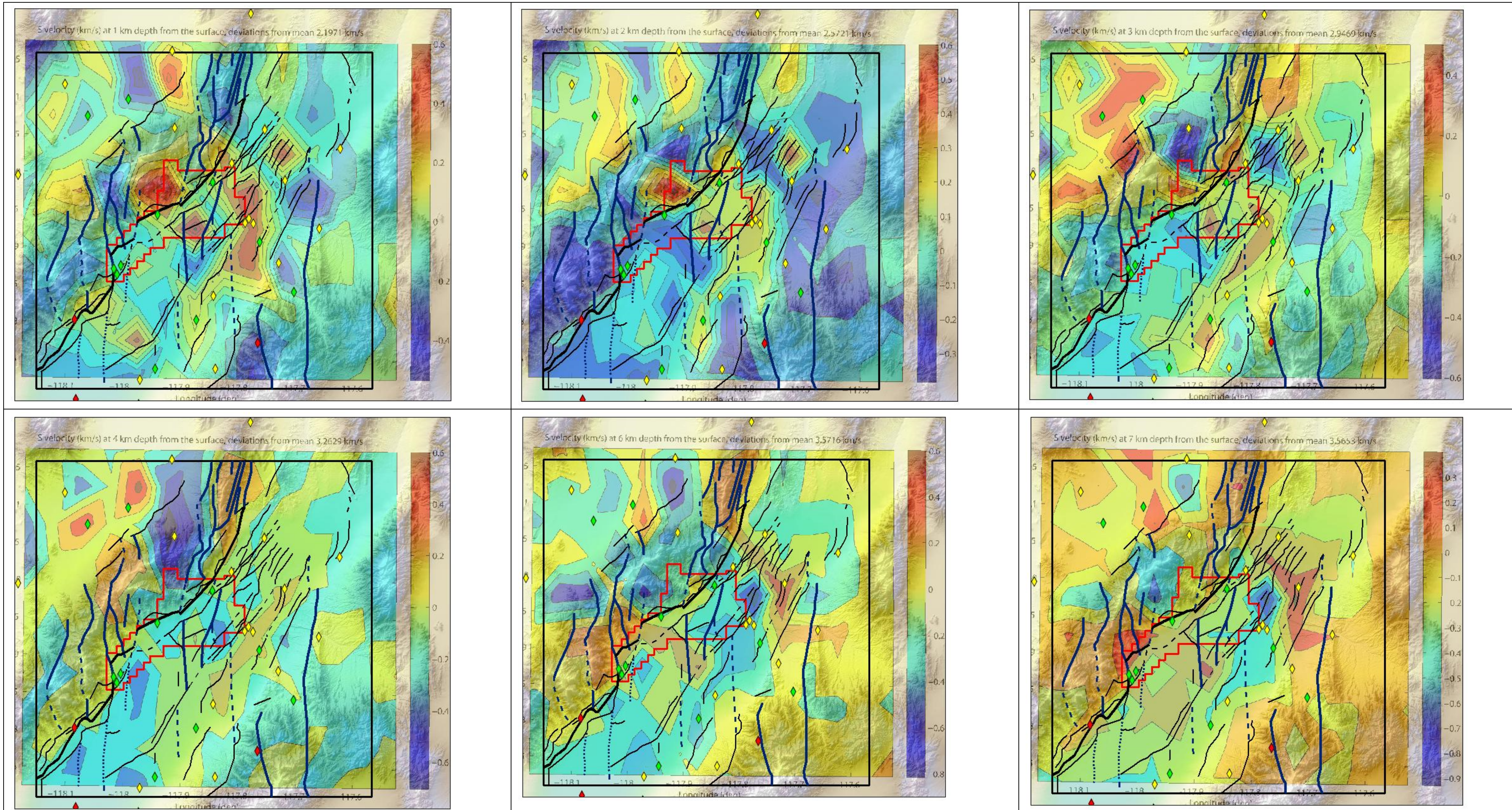

Figure 121A. Project Area S-wave velocity (Vs) maps from 1-7km below the ground surface at 1km depth intervals sequentially from the upper left to lower right. The mean elevation in Dixie Valley is +1km above sea level. A depth of 1km and 2km in these Vs maps corresponds to -2km above sea level (asl) and -3km asl, respectively. Superimposed on the Vs maps are the (1) DEM for the area, (2) Project Area, black outline, (3) Calibration Area, red outline, (4) seismic stations with their IDs, (5) well locations with their IDS, and (6) identified surface structure from this study (see Section 7). Note that the color code scale is different in each figure.

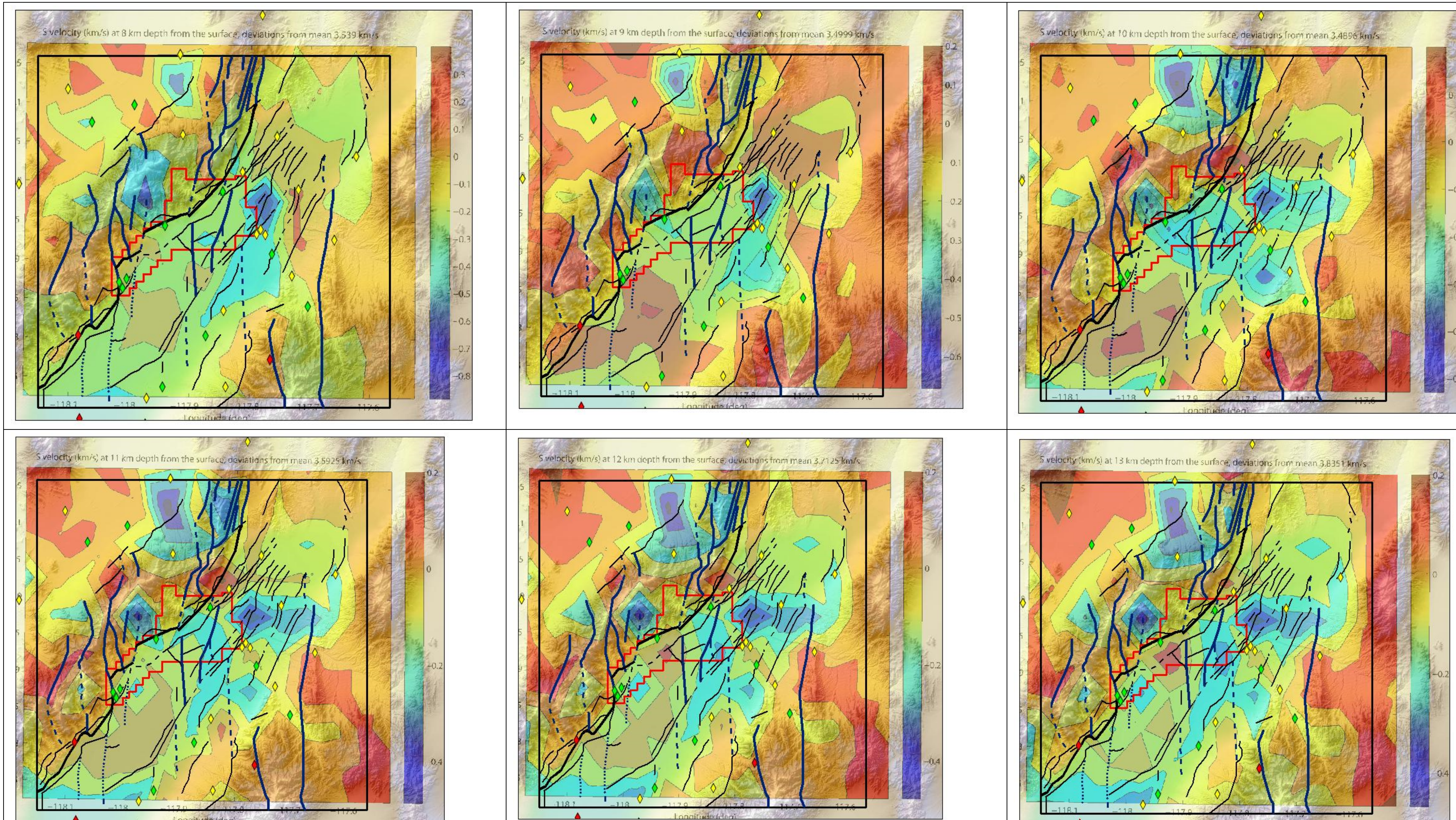

Figure 121B. Project Area S-wave velocity (Vs) maps from 8-13km below the ground surface at 1km depth intervals sequentially from the upper left to lower right. A depth of 9km and 13km in these Vs maps corresponds to -10km above sea level (asl) and -14km asl, respectively. Superimposed on the Vs maps are the (1) DEM for the area, (2) Project Area, black outline, (3) Calibration Area, red outline, (4) seismic stations with their IDs, (5) well locations with their IDS, and (6) identified surface structure from this study (see Section 7). Note that the color code scale is different in each figure.

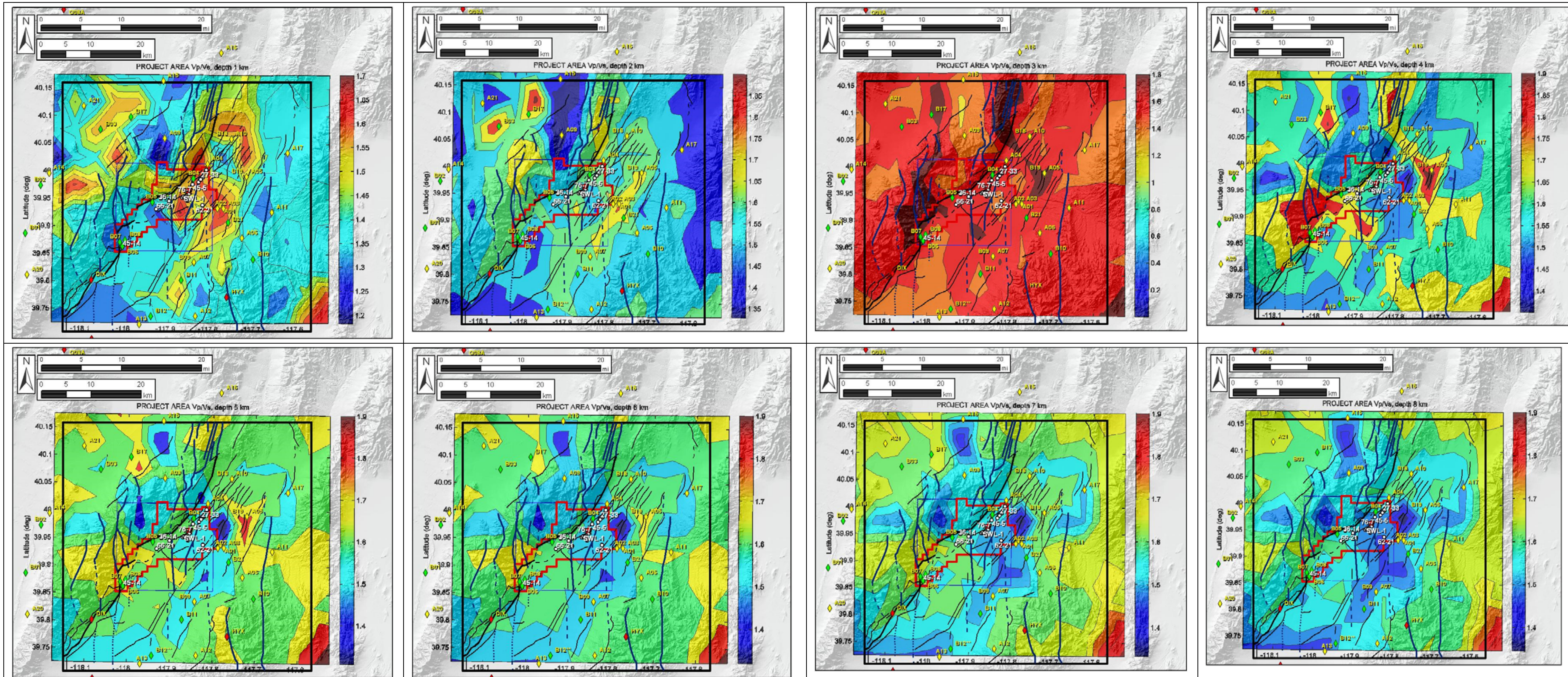

Figure 122A. Project Area: Same as in Figure 121A and 121B, for the Vp/Vs-velocity models. The shallowest (depth < 11km) S-velocity models were estimated using only data in this study. There was not enough resolution in our DVSA_FINAL_MODEL in the Project Area below 10km depth, thus the S-velocity models below 10km were estimated using all S-velocity models available. Vp/Vs maps from 1-8km below the ground surface at 1km depth intervals sequentially from the upper left to lower right. A depth of 1km and 2km in these Vp/Vs maps corresponds to -2km above sea level (asl) and -3km asl, respectively. Superimposed on the Vs maps are the (1) DEM for the area, (2) Project Area, black outline, (3) Calibration Area, red outline, (4) seismic stations with their IDs, (5) well locations with their IDS, and (6) identified surface structure from this study (see Section 7). Note that the color code scale is different in each figure.

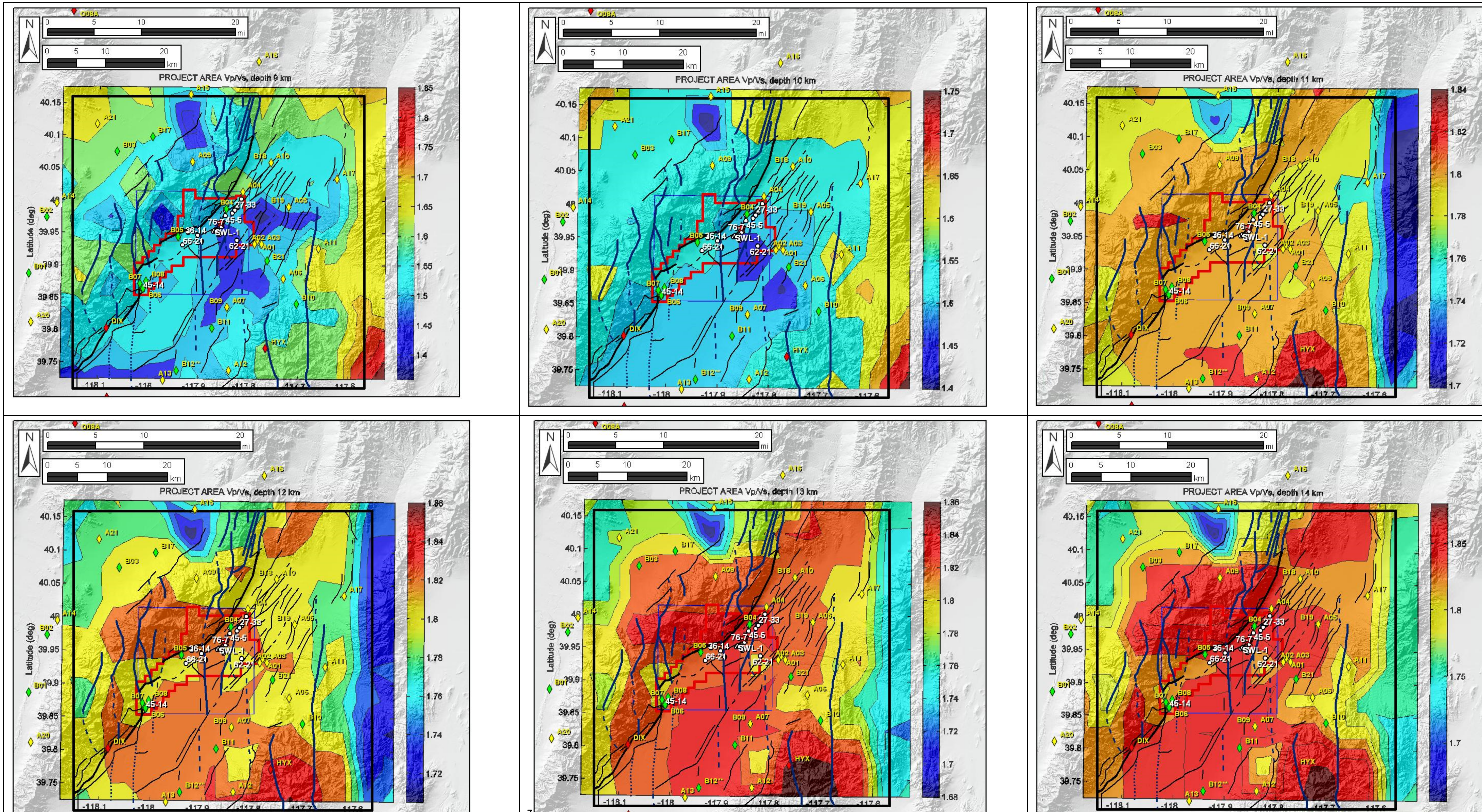

Figure 122B. Project Area: Same as in Figure 121A and B, for the Vp/Vs-velocity models. The shallowest (depth < 11km) S-velocity models were estimated using only data in this study. There was not enough resolution in our DVSA_FINAL_MODEL in the Project Area below 10km depth, thus the S-velocity models below 10km were estimated using all S-velocity models available. Vp/Vs maps from 9-14km depth below the ground surface sequentially from the upper left to lower right. A depth of 1km and 2km in these Vp/Vs maps corresponds to -2km above sea level (asl) and --3km asl, respectively. Superimposed on the Vs maps are the (1) DEM for the area, (2) Project Area, black outline, (3) Calibration Area, red outline, (4) seismic stations with their IDs, (5) well locations with their IDS, and (6) identified surface structure from this study (see Section 7). Note that the color code scale is different in each figure.

DVESA Final Velocity Model

A final model (different from the DVESA_INPUT_MODEL) including the DVSA results and all the other models available, was estimated in the DVESA, as shown in Figures 124A, 124B, and 125, for Vp and Vs, respectively. Pronounced low Vp and Vs velocity anomalies, implying high mid-crustal temperature, were observed in Dixie Valley. From 6-8km depth, these anomalies extend along an E-W corridor to the Reno Basin Area on the eastern side of Figures 124A and 124B. Between 10km and 15km depth the low velocity anomaly in the PA appears to migrate as a conduit to the NE, then it deepens towards SE, to 19km depth.

From 12-15km depth the DVESA low-Vs anomalies (Figure 124) show a clear NW-SE trend, and a pronounced low velocity anomaly in the Reno Basin area. At 17km depth, low Vs was observed in the southeastern corner of the PA, near Fairview Peak. Christensen and Mooney (1995) may have provided an explanation for the low-Vp anomalies observed SE of the DVSA in the mid-crust. For average granite/granodiorite and average mafic garnet granulite, to depths of 10-15km they observed an increase in velocity with depth until grain boundary cracks were closed. The increase of velocity with pressure appeared to be stronger than the velocity decrease with increasing temperature. Below 15km depth, a pronounced decrease in velocity (6-8%) was observed by these authors in regions with high heat flow. We believe that below 15km the effect of temperature is more important that the increase in velocity due to pressure and that the relatively low velocity is due to high temperatures. We are not aware, however, of such information being estimated for the upper 5km of the crust.

DVSA S-velocity Model Error Discussion

In this section, we describe the empirical estimation of the S-velocity model trust factors in each grid cell at each depth *i.*

The DVSA_FINAL_MODEL was the product of an inversion by CPSS3.3 program *surf96*. The inversion took place for each grid cell and required two estimates: an input model and the dispersion curve. The program *surf96* varied the initial input model and estimated an output model to minimize the difference between the observed and calculated dispersion curves, for a given set of input parameters. The *surf96* input parameters, such as smoothing and damping values, were constant in this study and were as recommended by the CPSS3.3 documentation. Variations of the smoothing and damping values may produce final model velocity variations on the order of tenths of km/s for shear wave velocity. For high smoothing the velocity discontinuities were less sharp between grid cells. The final output of the CPSS3.3 algorithms was a velocity model with estimated values in *each depth slice i*. The number of depth slices was chosen by the analyst and is given in the input model. In our case, *surf96* first was applied with constrained layer thickness looking for best layer velocity, and second, was applied with the previously estimated velocity fixed, however, looking for best layer thickness. The estimated layer thickness variations, however, were under 0.2km.

1) The input model, DVSA_INITIAL_MODEL

The *DVSA_INITIAL_MODEL* incorporates all the errors (of which most are unknown) of the component models (Figure 99a) and is estimated by extracting multiple models at one location in Dixie Valley. Empirically assessed errors for each component model are expressed as trust factors and are the assessment of the Subject Matter Expert, Dr. Ileana Tibuleac, the Seismic Task Leader, based on the model resolution which for the P and S-velocity models estimated in this study 0.1 - 0.5 units have been added to all the trust factors in DVSA so that the S-models prevail when they are extracted from the Dixie Valley Seismic Model Database (see Part II-Appendix 10 directory Integrated_model). Each grid cell input model has trust factors for *Vp, Vs, RHO* (density) and *Qp* and *Qs,* estimated at each depth *i* as the

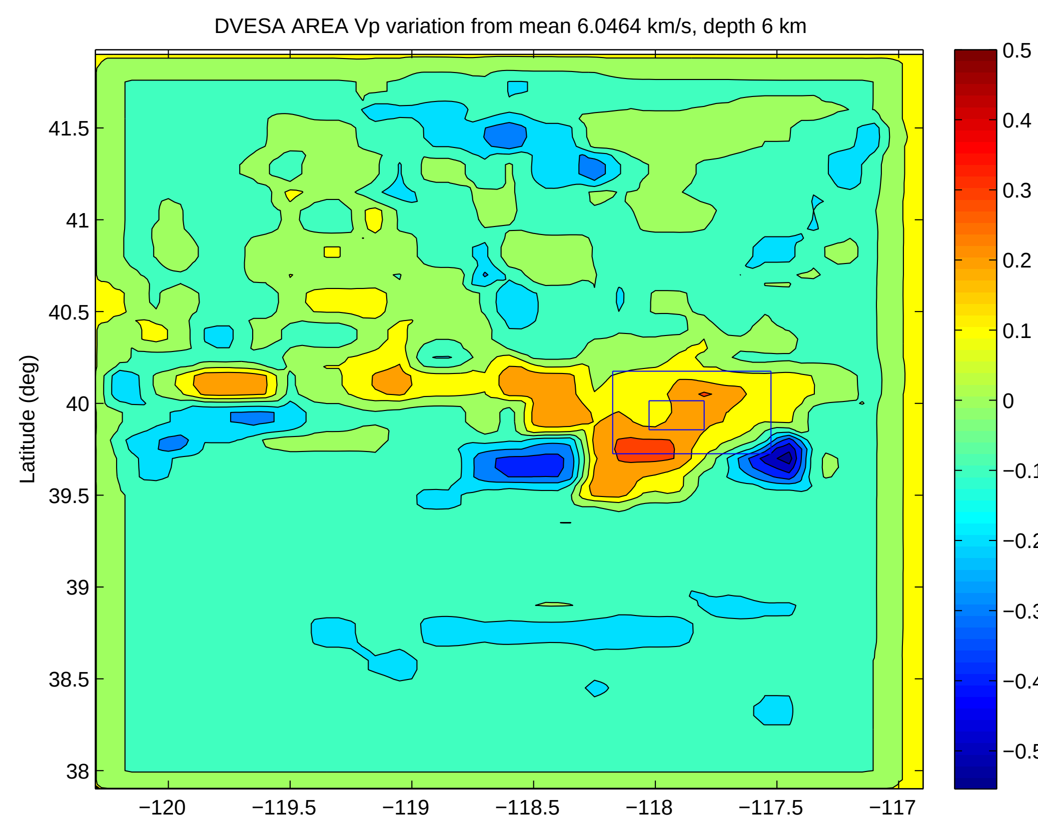

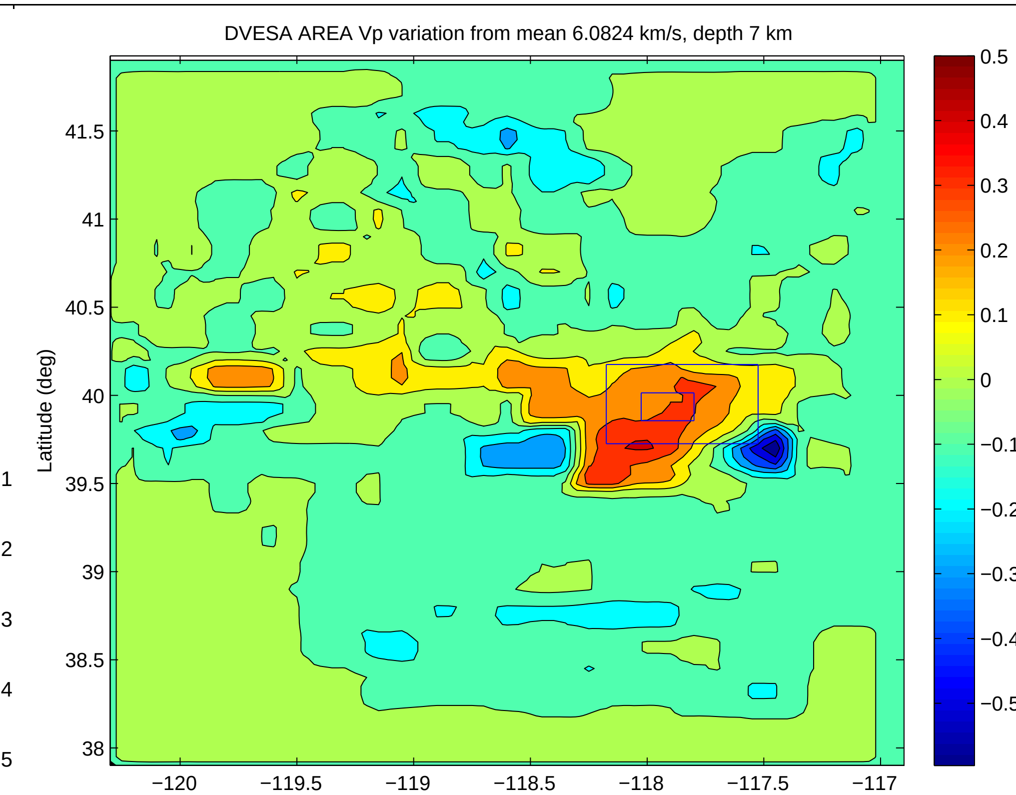

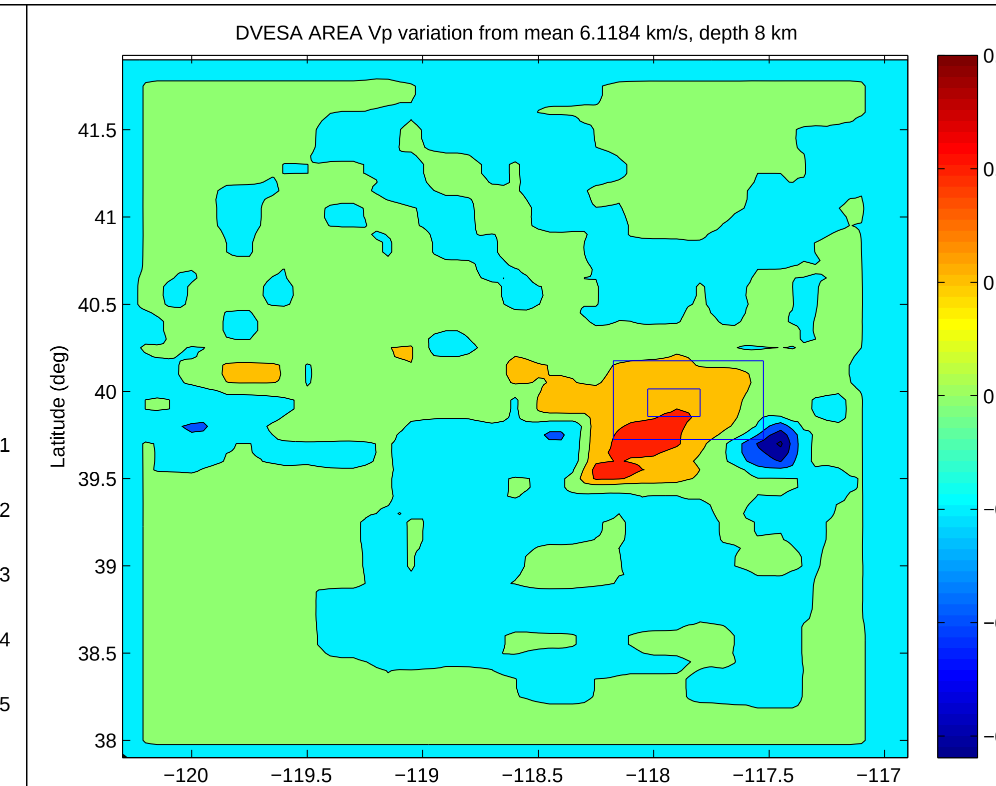

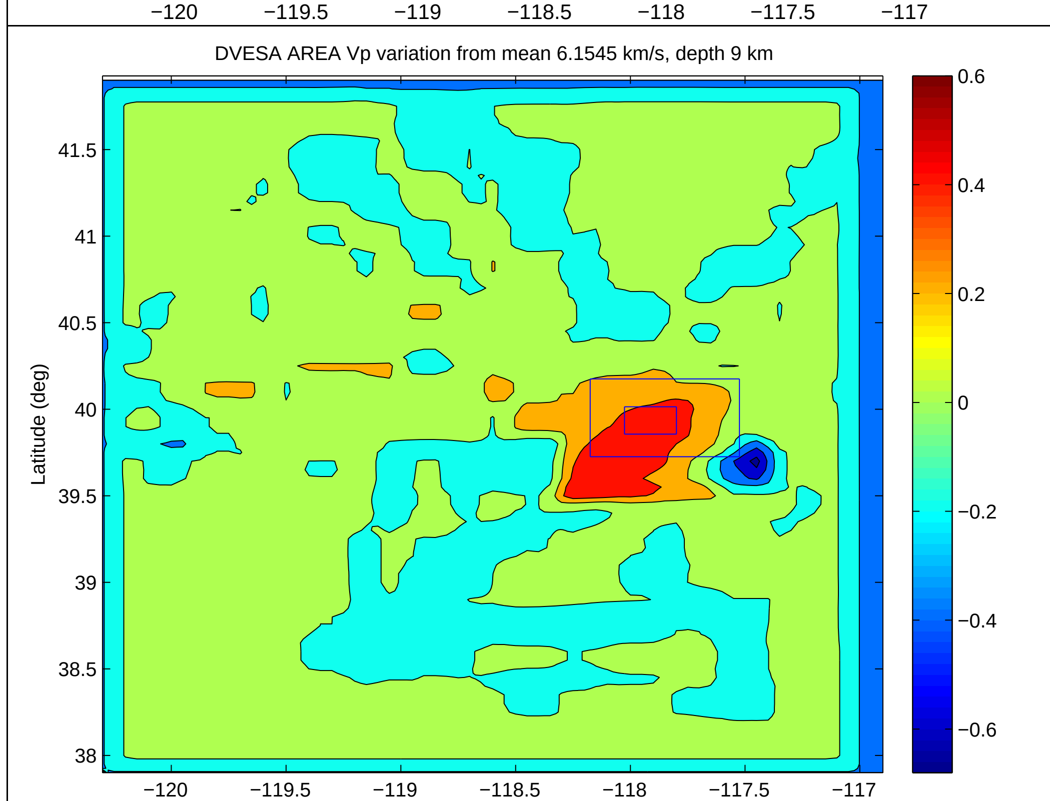

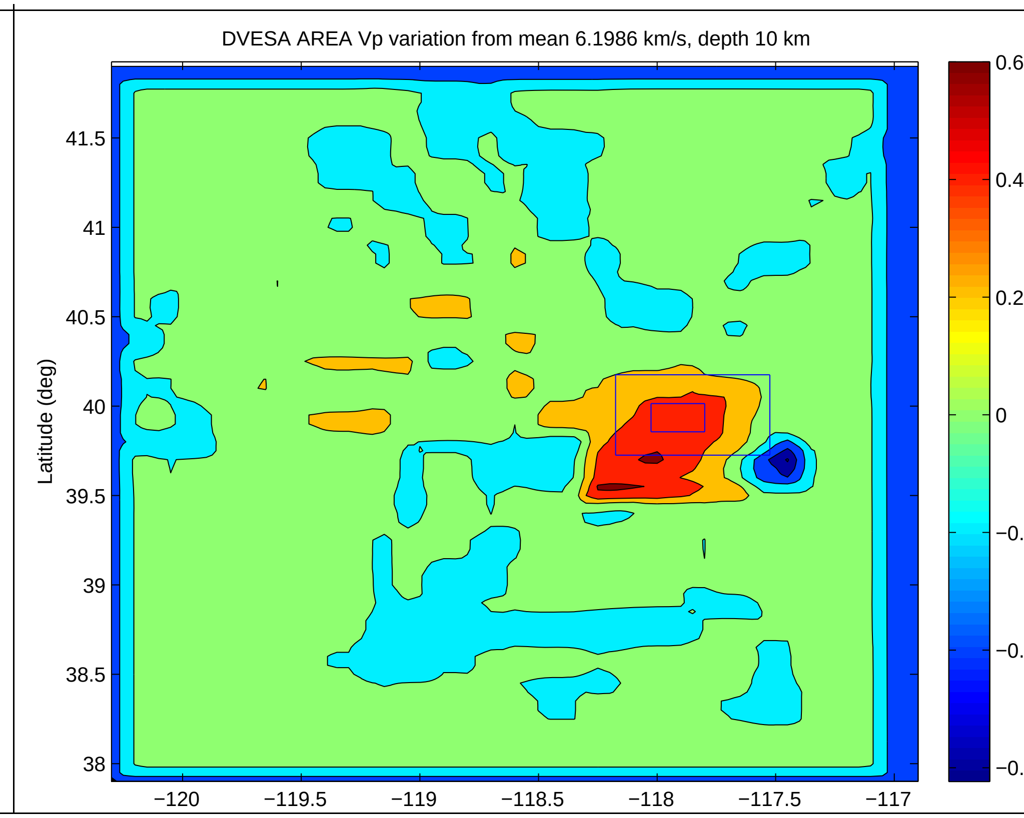

Figure 123A. P-wave velocity (Vp) maps for the DVESA from 6km to 10km below the surface at 1km depth intervals. The Project Area (larger blue outline) and Calibration Area (smaller blue outline).

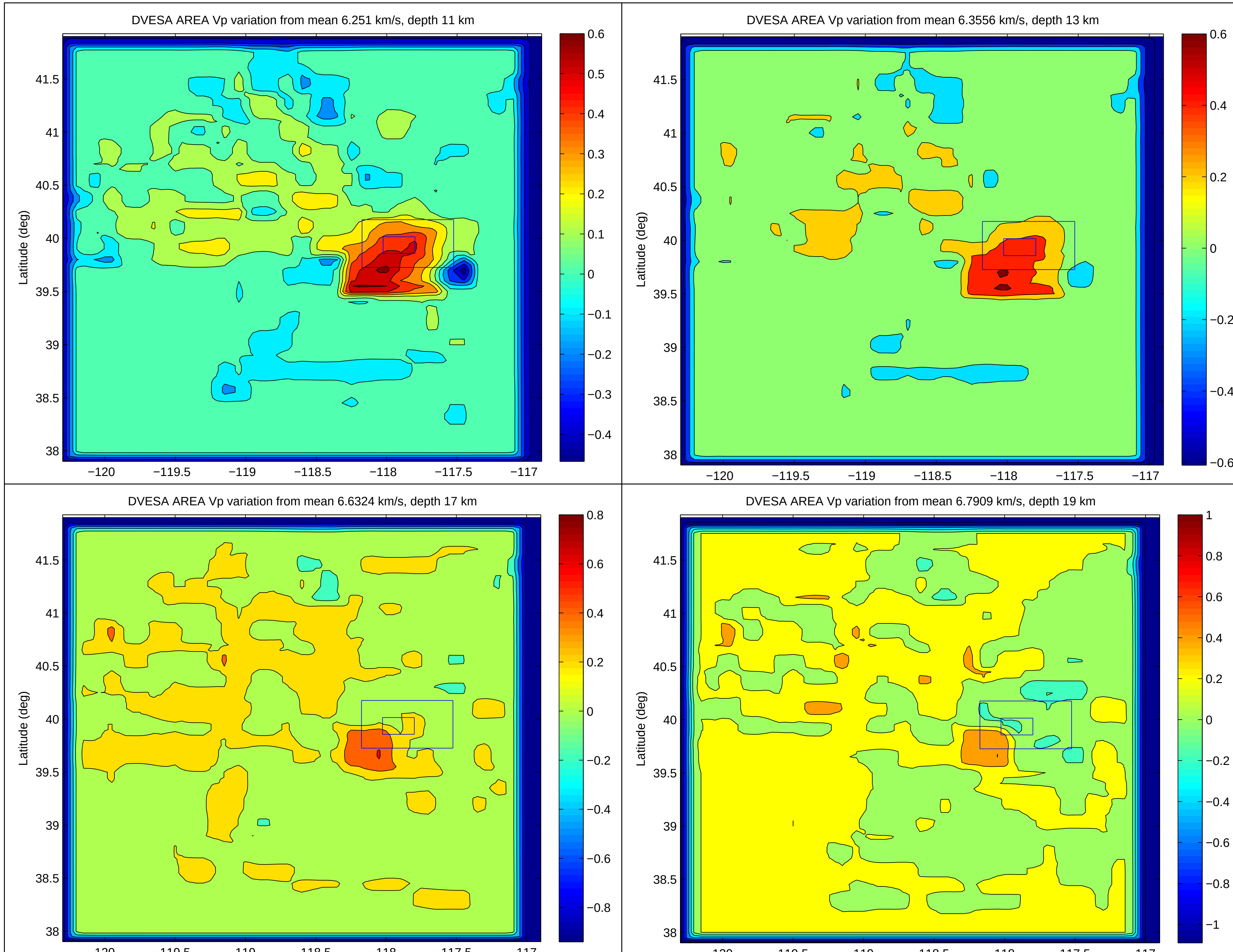

Figure 123B. S-wave velocity (Vs) maps obtained from Vs for the DVESA, from 11km below the surface to 19km below the surface at 2km depth intervals. The Project Area (larger blue outline) and Calibration Area (smaller blue outline).

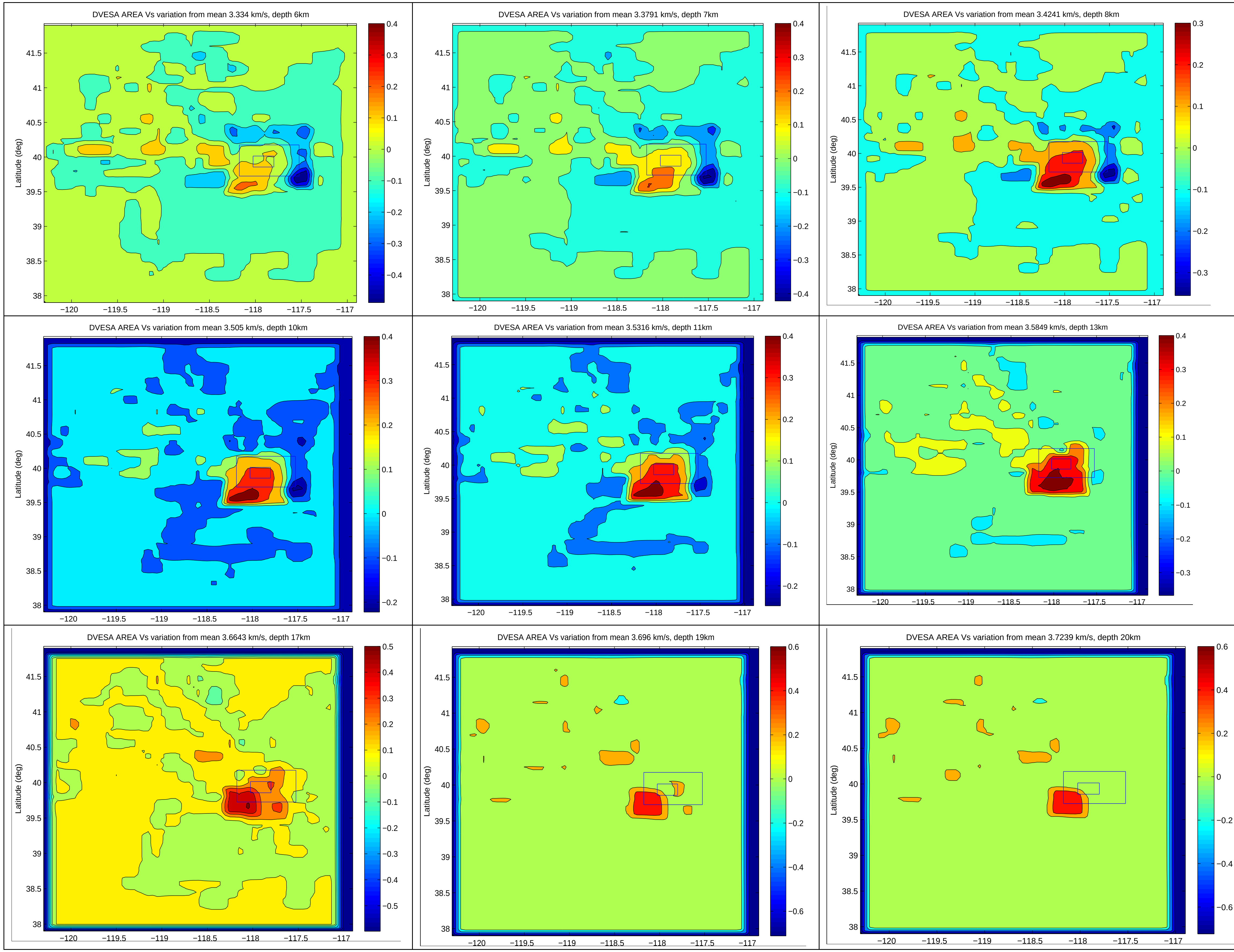

Figure 124. Same as in Figure 123A and 123B, for the S-velocity models in the DVESA at 10km to 20km depth. These models were estimated using all S-velocity models available. The Project Area (larger blue outline) and Calibration Area (smaller blue outline).

weighted mean of all the trust factors of all the models available at that depth. These trust factors are named T_{IDVSA} and are provided in Part II-Appendix 10.

2) The dispersion curve in each grid cell:

In a grid cell the DVSA dispersion curve, estimated using the CPSS3.3 program *do_mft,* had errors at each period. The main question was how these errors propagated into the inverted model. An analyst picked the fundamental mode Rayleigh dispersion curve which was usually the largest amplitude arrival. Errors could occur when several Rayleigh models were present in the time series and they were misidentified. Mode identification was easier at an array, and that was the advantage of the DVSA array (Figure 99a). Errors in velocity estimates could occur if the GFs have low Signal-to-Noise Ratio (SNR). The errors were inversely proportional to the amplitude of the arrival at each period. The maximum amplitudes at each period were recorded for each dispersion curve and are input in the inversion program (*surf96*), thus, were taken into consideration in the resolution matrix calculation (described below). A plot of all the estimated dispersion curves in DVSA is shown in Figure 125. In this figure, the mean of the standard deviations at all periods is 0.25km/s. These dispersion curves, however, are different most probably because of real crustal structure variations, thus their variation at each period should not be used as an estimate of errors.

An experiment has been conducted using these curves, however. Assuming that these curves were random realizations of the same measurement, we investigated how the variation of these curves was mapped into the estimated model. Using these 140 dispersion curves, with what we considered random realizations of the dispersion curve velocity variations of 0.25km/s around a mean velocity at each period, and the same input model, realizations of the output model shown in Figure 126 were obtained. The normalized inverse standard deviation at each depth *i* was calculated as a trust vector $T_{surf96,i}$/max($T_{surf96,i}$) used in all the grids at depths *i.* The results were that the input model variations mapped into the output model variations, with slightly larger variations at higher depths (i.e., deeper in the crust).

3) Ray-path-density.

A dispersion curve in each grid cell was best resolved by the tomography code, *gridsp*, when more paths intersected the grid cell. This was why the number of paths per grid cell (at all depths *i*) was an important indicator of how well resolved the model was in the respective cell. Thus, a normalized trust factor matrix T_{gc} (mn) = 1/(Nr Paths in cell *mn*)/max(T_{gc}) was assigned to each grid cell *mn* (m and n are the number of rows and columns in the grid matrix projection on the surface). We acknowledged the limitations of this trust factor estimate, which were due to ignoring the path density at different depths.

4) The choice of damping and smoothing parameters

If the damping and smoothing parameters changed, velocity variations of less than 0.2km/s in the estimated model were observed for an ideal dispersion curve and a given model (see CPS3.0 instructions). Although these parameters were constant for all the inversions, their choice usually only slightly modifies the resolution matrix (see below).

5) The surf96 inversion resulted in a resolution matrix estimate:

If the group velocity dispersion curves were perfect, a "true model" would have been the result of the inversion. However, because the dispersion curves were not perfect, the estimated model (a vector of parameters, for example velocities, one parameter for each depth layer) was the resolution matrix (which was a square matrix) multiplied with the "true model". The resolution matrix is not symmetrical in the presence of smoothing and damping. In the following formula

$V_{i\ estimated} = \sum_j RijV_{j\ true}$, *i* is the depth interval number.

The j'th column of the resolution matrix R_{ij} showed how a unit perturbation in $V_{j\ true}$ mapped into each of the elements of the $V_{j\ estimated.}$ That means the true model was blurred by the inversion and the resolution matrix shows how this happens. Figure 128 shows an example of the estimated model and the observed (dots) and calculated (solid line) fundamental Rayleigh dispersion as well as an example of a resolution matrix representation for the same grid cell as in Figure 127. For most of the layers, the resolution matrix is larger at the layer depth, however, for some of the layers, a perturbation in the layer maps into perturbations in other depth layers. Resolution matrices were calculated for each grid cell and a value was estimated for each depth layer. These are the trust factors T_R.

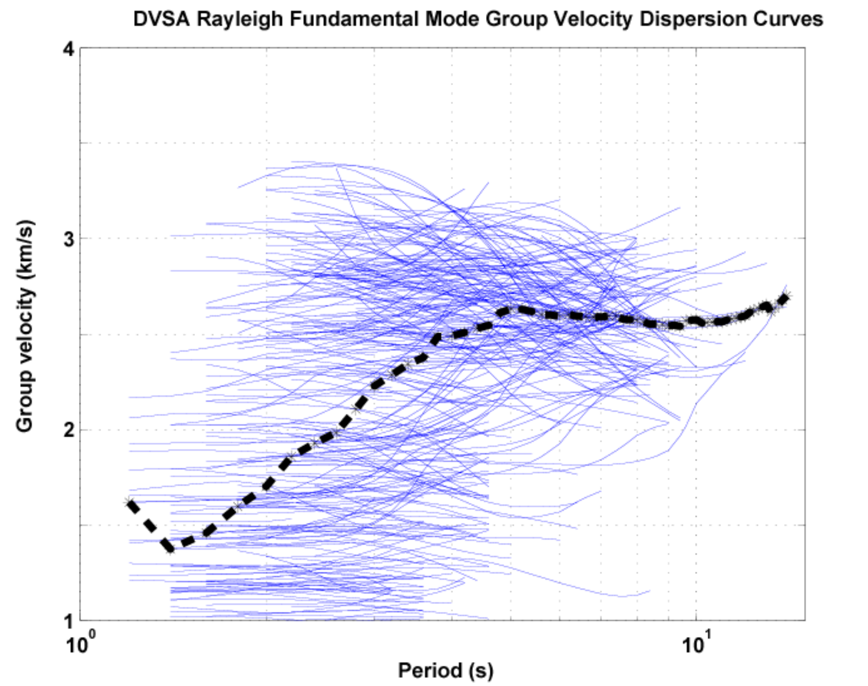

Figure 125. Estimated fundamental mode Rayleigh dispersion curves measured in DVSA (blue) and the median dispersion curve (black). In this figure, the mean of the standard deviations at all periods is 0.25km/s.

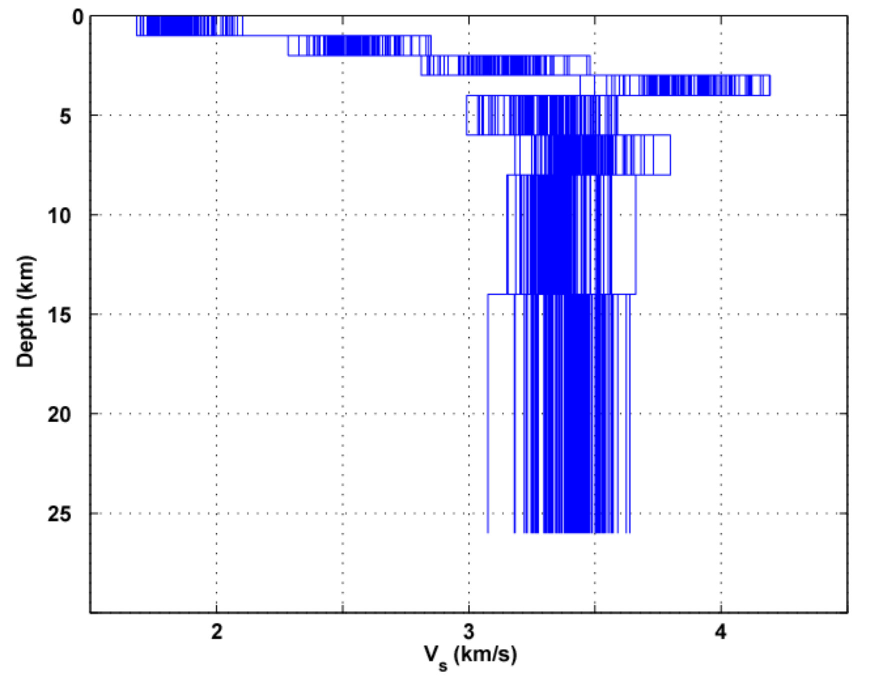

Figure 126. Realizations of the inverted shear-velocity models in DVSA when the input model randomly varies 0.25km/s around the mean velocity in Figure 127. The input model velocity variations produce similar output model variations relative to the mean.

Considering all the above errors, an empirical trust factor has been estimated for each layer *i* in a cell *mn* as:

$T_{i,\ mn}=(T_{R,i,\ mn}*\ T_{surf96,i}\ *T_{gc,mn}*T_{IDVSA,\ I,\ mn})^{1/4}$.

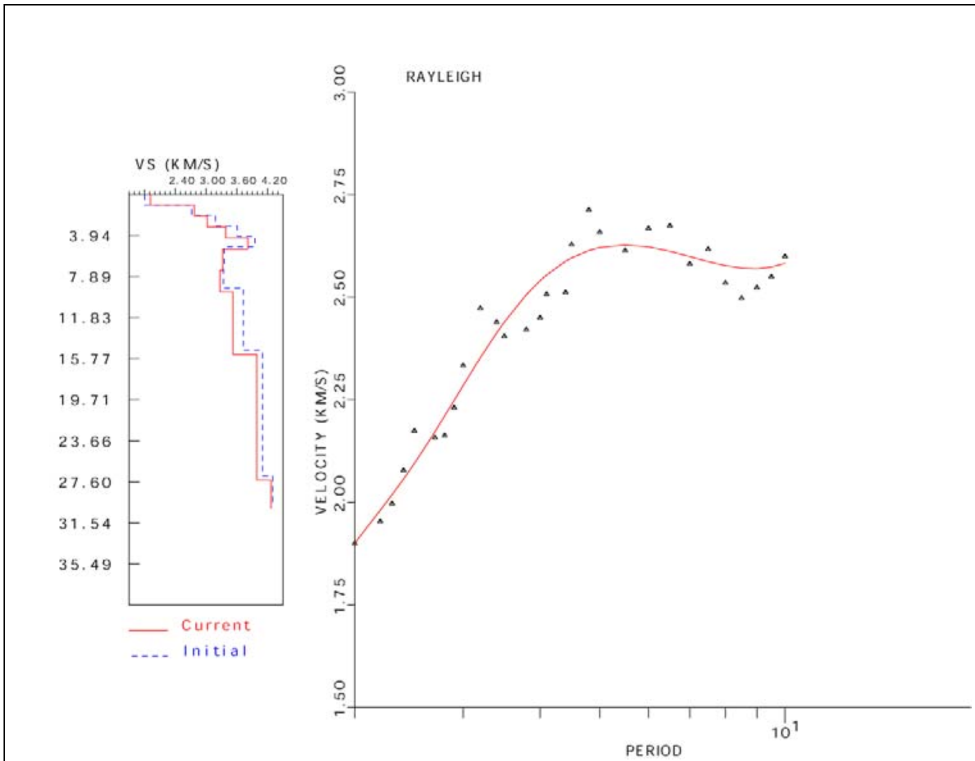

Figure 127. The right plot shows an example of observed fundamental-mode Rayleigh dispersion curve in DVSA (black triangles) inverted to obtain the "current" (final) model (red continuous line) in the left plot. DVSA_INPUT_MODE L for this grid cell is shown in the left plot as the blue dotted line. The dispersion curve calculated using the current model is shown in red in the right plot.

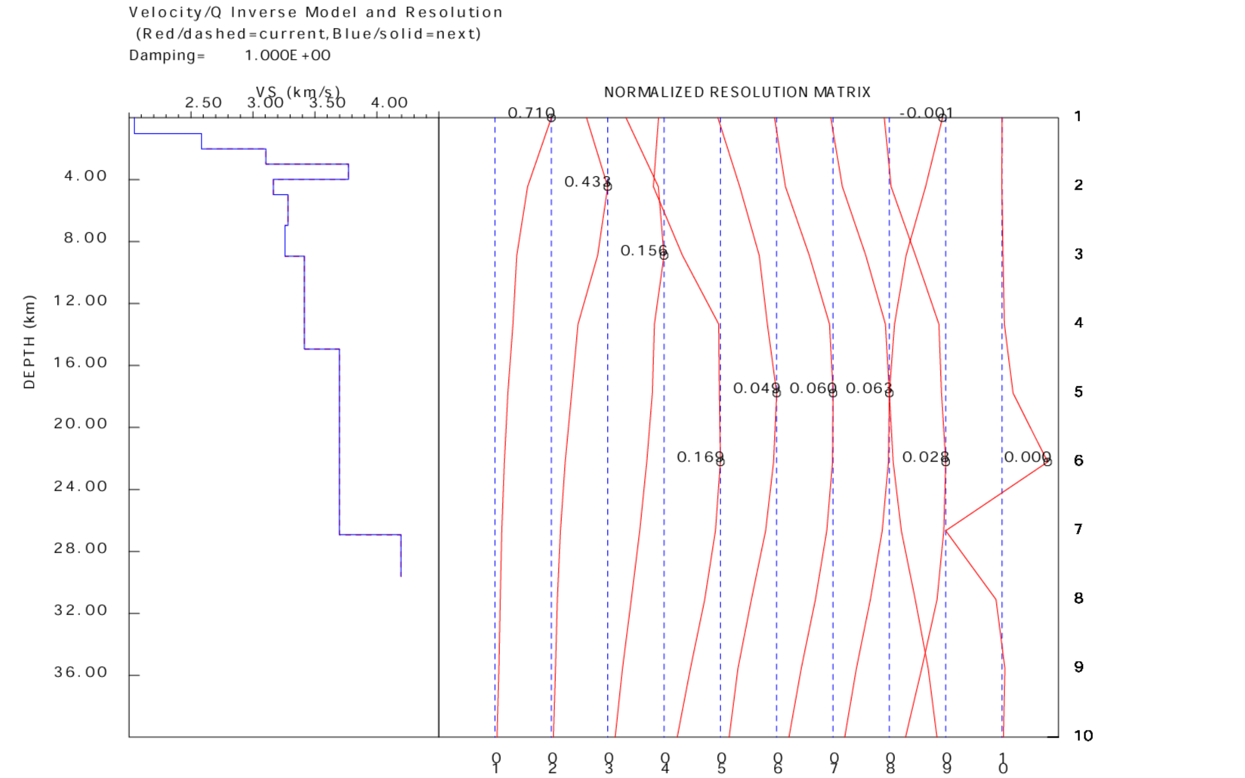

Figure 128. Final DVSA model in same grid cell as in Figure 127 (left plot) and its resolution matrix (right plot). In the right plot the model layers are numbered from 1 to 10. Each layer has a curve representing the resolution matrix component associated with the respective layer. In the ideal case, the curve would peak at 1 in the respective layer and would be zero in all the other layers.

Rock Type, Temperature and Seismic Velocity in the DVSA

Seismic velocity depends on multiple parameters the influence of which should be assessed in a specific region:

1. ***Phase state:*** The seismic velocity is known to decrease in the presence of partial melt.
2. ***Composition (lithology, mineralogy and chemistry):*** When pores and cracks are closed, velocities are primarily a function of mineralogy at the same pressure. For many suites of continental rocks, systematic changes in velocities with mineralogy have been observed in studies of the whole crust. Vp/Vs ratios are generally low in quartz-rich rocks and high in anorthosites and serpentinites (Christensen and Wepfer, 1989).
3. ***Density**:* The seismic velocity was expressed as a linear solution in the form $V = a + bp$ (Christensen and Mooney, 1995), although for some rock suites a nonlinear solution may be more appropriate. A single value dependence of velocity on density was valid only for limited compositions. At 100MPa Christensen and Salisbury,(1995) found for basalt a=-4.44 and b=3.64 for Vp and for Vs a=-2.79 and b=2.08.Possibly due to the large variations in the composition of the shallow crust, which made general studies difficult, most of the published studies estimated a and b for the mid to lower crust.
4. ***Temperature:*** Studies of the influence of rock temperature on seismic velocity show that both Vp and Vs are lower when the rock is heated at the same pressure. Table 17 presents the well temperatures used in this portion of the study. Christensen (1979) observed a velocity gradient with temperature in basalt of 0.00042km/s/^{o}C. These values are up to 10 times less than the values observed in the DVSA wells (Table 17). According to Christensen

and Wepfer (1989) for regions with normal geothermal gradients (25°-to 40°C/km), the change in compressional velocity with depth dVp/dz is close to zero (Christensen, 1979). However, in high heat-flow regions, crustal velocity reversals are expected if compositional changes with depth are minimal.

5. ***Rock porosity:*** The influence of pore pressure on velocity and attenuation has been widely studied for sedimentary rocks; however, only a limited amount of data were available for crystalline rocks. Raising the pore pressure has approximately the same effect on velocities as lowering the confining pressure by the same amount (Christensen, 1986). The dramatic lowering of velocities with increasing pore pressure appears to be a common feature for crystalline continental rocks and may be one possible explanation for crustal low velocity zones. Of significance, increases of pore pressure in crustal regions will be accompanied by marked increases in Poisson's ratios (Christensen, 1984). Although pore pressure attenuation data is sparse for crystalline rocks, the investigations on sedimentary rocks have found that fluid flow in microcracks is the mechanism responsible for the observed drop in Q with increasing saturation (Christensen and Wepfer (1989) and references herein). This effect should be seen in crystalline rocks as well.
6. ***Pressure:*** The velocity increase at higher pressure results from changes in intrinsic properties of the rock, such as finite compression of the minerals. All other parameters constant, the seismic velocity increases 5% in basalt when the pressure increases from 10 to 100 MPa (Christensen, 1968). Qp and Qs also increases with increasing pressure. The characteristic shape of the curve of velocity as a function of pressure is attributed to the closure of microcracks. According to Christensen and Wepfer (1989), much of the closure takes place over the first 100 MPa (equivalent to ~5km depth in DVSA).
7. ***Seismic anisotropy:*** Preferred orientation of minerals and alignment of cracks produce anisotropy. Common continental crustal rocks such as schists, gneisses, and amphibolites are anisotropic due to orientation of micas and amphiboles (Christensen, 1965). At confining pressures less than approximately 20MPa (depth <2km), laboratory anisotropy measurements are influenced by crack orientation as well as mineral orientation. Anisotropy is likely to originate from aligned stress-induced cracks in dilatancy zones in seismic regions (Crampin and McGonigle, 1981). Anisotropy studies were beyond the scope of work for this project, however, we are currently pursuing these investigations in another project, together with attenuation studies.

In this study, we estimated derived properties: velocity and attenuation of P- and S-waves, (Vp, Vs, Qp, Qs), Vp/Vs ratios and density (RHO). Only Vp, Vs and Vp/Vs were estimated with a higher degree of trust. Reducing multiple geological and physical processes to two simple seismic observations is non-unique. Converting Vp and Vs models to three-dimensional variations of rock states would be mostly speculation, because a comprehensive data base of field based seismic properties related to rock physics laboratory studies is currently not available. Furthermore, most laboratory studies are performed in conditions significantly different from real earth situations, usually at pressures characteristic to the mid and lower crust, and at frequencies substantially higher than typical seismic recordings (Kern, 1982).

Given these uncertainties, interpretation of tomographic images was done using more geophysical information (i.e., geology, well temperature, geochemistry, heat flow and gravity/magnetic investigations) than a simple velocity–density–temperature correlation. When coupled with experimental information on seismic properties of continental rocks at pertinent temperatures and pressures, the geological and geophysical data can be used to correlate measurements of seismic velocities with mineralogic composition at depth. No multiple assumptions of parameter values (pressure, temperature gradient etc.) were made, and instead the velocity variations were compared to the well data. A correlation index was established for the DVSA_BL_MODEL and the well data in the Baseline Conceptual Model (Section 7), Iovenitti et al. (2012).

The wells are represented in Figure 129 in the order in Table 17 (from Number 1 to 25), i.e., in the increasing order of their modeled temperature at 1.5km depth (Table 17 and Appendix 16b). In Figure 129 note a relatively larger variation of the seismic velocity values in each layer in the "colder" wells (T in Table 17 <200°C).

Table 17. Dixie Valley Geothermal Wellfield well temperature data used in this portion of the study from Appendix 16b. Wells not used but described in Appendix 16b are those that are shallow, had no lithology, or temperature data.

Well	Well ID Figure 129	Latitude (deg)	Longitude (deg)	T (°C)[1]
76-28	1	40.0020	-117.8140	150
62-21	2	39.9328	-117.8198	155
45-14	3	39.8659	-118.0049	196
37-33	4	39.9860	-117.8310	206
66-21	5	39.9311	-117.9280	210
SWL-2	6	39.9520	-117.8710	210
45-05	7	39.9770	-117.8490	212
45-33	8	39.9897	-117.8260	215
SWL-3	9	39.9530	-117.8640	215
65-18	10	39.9470	-117.8610	218
32-18	11	39.9530	-117.8620	218
38-32	12	39.9843	-117.8470	225
SWL-1	13	39.9540	-117.8690	225
28-33	14	39.9850	-117.8320	225
76-07	15	39.9590	-117.8570	225
82-05	16	39.9828	-117.8098	226
52-18	17	39.9534	-117.8629	230
62-23	18	39.9370	-117.8940	240
63-07	19	39.9650	-117.8550	240
74-07	20	39.9640	-117.8580	240
27-33	21	39.9870	-117.8310	245
84-07	22	39.9640	-117.8580	247
73-07	23	39.9660	-117.8580	250
36-14	24	39.9460	-117.9010	250
82-07	25	39.9680	-117.8550	250

[1]Measured/modeled temperature at 1.5km depth and well type are from Appendix 16b.

Figure 130 shows Vp, Vs and Vp/Vs estimated at each depth for all wells indicated in Table 17. *Wells with lower temperature have lowest values of Vp, Vs and Vp/Vs, except for depths from 4km to 8km*. Low Vp/Vs in the "cold" wells (T<200°C) suggest possible dry crust (Figure 130, lower plots). Deeper than 4km the Vs, however, increases in the "cold" wells more than it increases for all the other wells (Figure 130, middle right plot). Some of the higher temperature wells also have low Vp/Vs, and one explanation could be that pore pressure may be a significant factor in the velocity variations at the respective locations. No significant differences were observed between the injection and production wells. At 5km depth the Vp values suggest a basalt layer. Christensen (1968) estimated the Vp basalt velocity as 5.9km/s. The results of experiments in Berea Sandstone by Wang et al. (1990) showed that the Vp/Vs and Poisson's ratio increased with increasing differential pressure in gas-saturated rocks but decreased with increasing differential pressure in the low pressure range when the rocks were saturated with liquids. In a liquid-saturated rock, both Vp /Vs and Poisson ratio decreased with increasing pressure for pressure range less than 50MPa. When the rock was filled with air, the Poisson ratio increased with increasing pressure from 10MPa to 100 MPa, all at room temperature (T=22^{o}C). Although no wells reached 5km depth, the known stratigraphy in the CA (generally known to 4km depth) appears to not support the presence of basalt of 5km (Section 7).

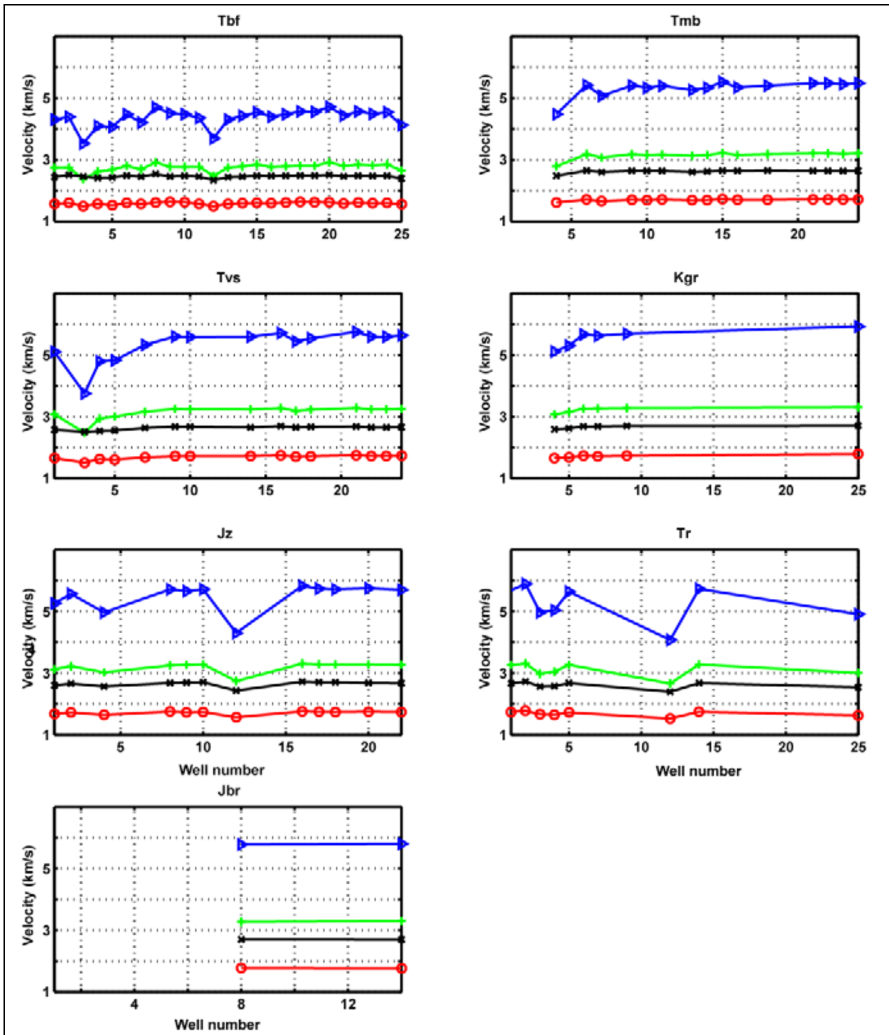

Figure 129. The Vp (blue), Vs (green), 10*Poisson coefficient (black) and Vp/Vs (red) for each geological formation in the Calibration Area (CA). The median value of the parameters in each layer is shown in Table 18.

Table 18. Seismic parameter median values estimated for each geological formation for all wells in the Calibration Area (CA). The formations are: Tbf - basin-fill sediments and lowermost tuffaceous sediments and tuffs; Tmb - Miocene basalt; Tvs - Oligocene silicic volcanics (tuffs, volcaniclastics, underlying sediments); Kgr - Cretaceous granodiorite; Jz - Jurassic Humboldt Igneous group; Tr - Triassic meta-sediments and Jbr were Jurassic Boyer Ranch quartzite. The "trust" factors (0 is low, 1 is high) were estimated from the seismic velocity models.

Geologic Form-ation	Vp (km/s)	Vs (km/s)	Dens-ity (g/cm^3)	Vp/ Vs	Qp *0.001	Qs *0.001	Trust Vp	Trust Vs	Trust Density	Trust Qp	Trust Qs
Tbf	4.43	2.76	2.46	1.59	0.382	0.184	0.50	0.46	0.0593	0.07	0.07
Tmb	5.40	3.17	2.63	1.70	0.779	0.334	0.56	0.63	0.0518	0.06	0.06
Tvs	5.58	3.23	2.65	1.72	0.901	0.381	0.56	0.63	0.0511	0.06	0.06
Kgr	5.64	3.26	2.68	1.72	0.954	0.401	0.56	0.63	0.0509	0.06	0.06
Jz	5.70	3.27	2.68	1.74	0.966	0.406	0.56	0.63	0.0502	0.06	0.06
Tr	5.34	3.15	2.62	1.69	0.784	0.336	0.56	0.63	0.0507	0.05	0.05
Jbr	5.78	3.28	2.69	1.76	0.920	0.388	0.56	0.63	0.0496	0.05	0.05

The values estimated in Table 18 are similar to values estimated by other researchers and thus, could be used for first-order identification of lithological units. As shown in Appendix 6 (Baseline Model) a velocity of 4.7km/s was estimated in Dixie Valley by Stauder and Ryal (1967) for "hard rock". Abbott et al. (2001) estimated the Tmb density as 2.3g/cm^3 and the Tvs density was estimated as 2.67g/cm^3. Georgsson et al. (2000) estimated 4.4 - 4.7km/s Vp in unaltered young basalts and sediments at a depth of 0.6-1.4km (density 2.7 g/cm^3) and Vp of 5.5km/s from 1km to 2.7km depth (density 2.7g/cm^3) in basaltic lavas. We did not estimate the density in this study and all the values are from previous studies.

Common temperature gradients with depth in the crust are 25-40^{o}C/km (Christensen and Wepfer, 1989). In the cases shown in Figure 131A, B, and C, the temperature gradient was independent of well type (i.e., production, injection or dry). Most of the wells have higher temperature gradient than what has been referred to by Christensen and Wepher (1989) as common. The amount of velocity change with pressure may indicate the amount of soft, crack-like pore space. While this change is similar at all wells at pressures higher than 100Mpa (14,404 psi or ~5km given the pressure gradient in Dixie Valley [Hickman et al. 1997; 1998; 2000]) at the surface large differences were observed, possibly due to well-specific microcrack closure mechanism (Christensen and Wepfer, 1989).

Vp, Vs, and Vp/Vs gradients with temperature at all the depths in each well were estimated respectively in Figures 132A and 132B, Figures 133A and 133B and Figures 134A and 134B. Although the Vp gradients were larger than common in the shallow crust (<3km) in the majority of the wells, again, no systematic difference has been observed between productive, injection and other wells. *Contrary to the laboratory experiment results, the velocity gradient with temperature in each well was positive (Figures 132A, 132B, 134A, and 134B), i.e., the velocity did not decrease when the temperature increased.* This may be explained by the velocity increase with pore pressure and lithostatic pressure being larger, overcoming the temperature effects in the upper 3km. Some of the "hottest" wells (**62-23, SWL-1, 65-18, 37-33, 66-21, SWL-3, 84-07, 73-07)**, however, showed very low DT/dVs (Figures 133A and 133B) when compared to the dT/dVp slopes, possibly because Vs was more sensitive to temperature changes than Vp.

In the Section 7.4.2, it was found that the vast majority of wells did show elevated temperatures and Vp values at comparable depths and lithologies (Figure 61A and Appendix 18). The only exception was 62-23A, where at a depth of 2.5km (8200ft), Vp is slightly lower than 62-21 within the same lithology, even though the reported temperature was much higher. Using the new data (Figure 136) we have found that, except for well 36-14, all the other wells have higher Vp and Vs than well 62-21. A low Vp/Vs in well 62-21 could be due to lower fluid content and that fact that well 62-21 is conductive through its entire depth supports this postulation. Note that deeper than 5km the velocity is the highest in wells 62-21 and 36-14, possibly due to less fracturing at depth.

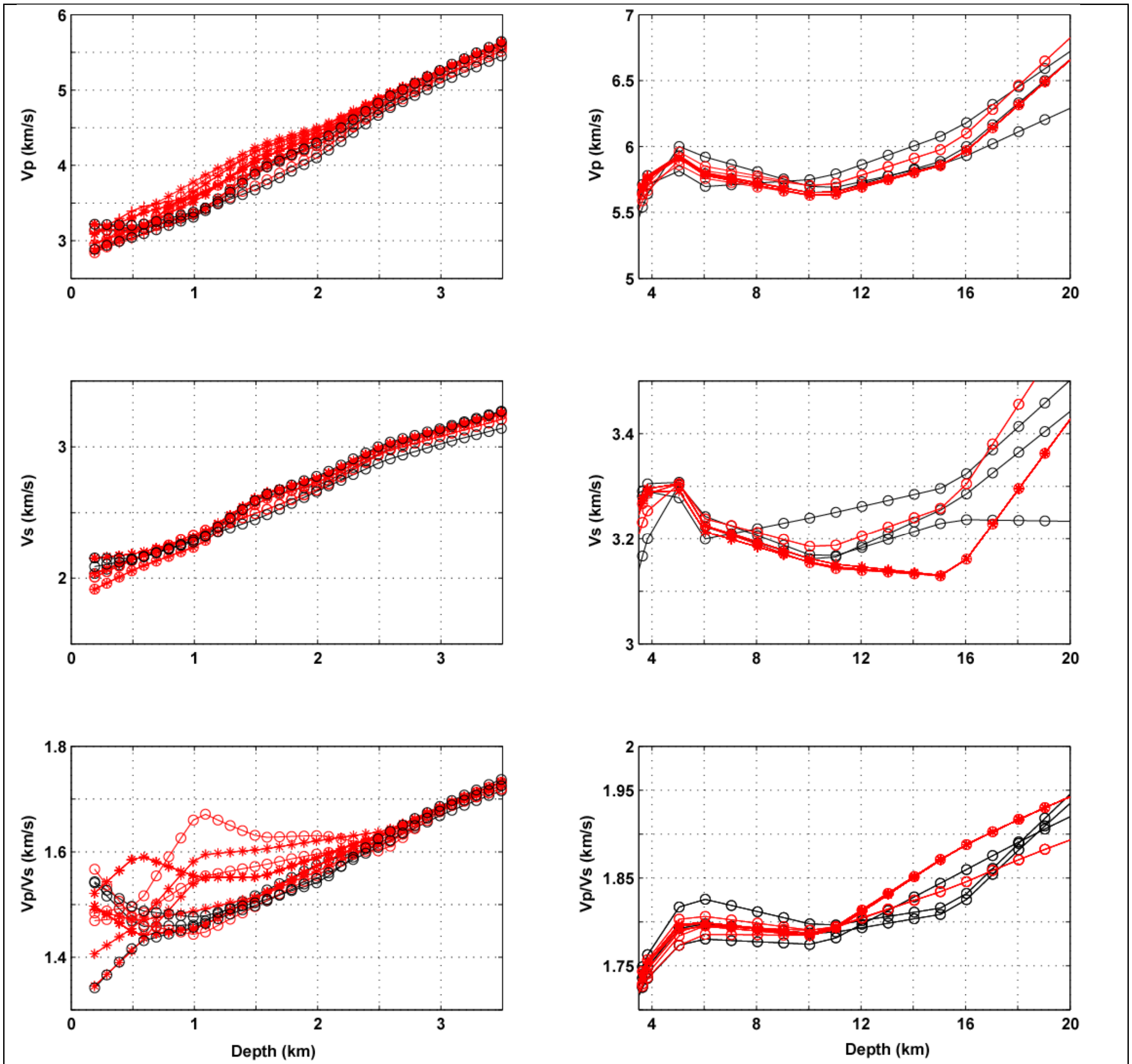

Figure 130. Parameter value for all wells presented in Table 17. The "cold" wells are shown in black. Open circles show wells classified as "other" in Appendix 16.b. Stars show producer wells and crosses show injector wells.

Some of the wells have negative Vp/Vs slopes with temperature, showing a different dependence of velocity with depth. All the wells with a negative Vp/Vs gradient with temperature, except for well 76-07 have Cretaceous granodiorite at 2km depth. As shown in Figure 137, unlike for Vp (upper right plot), slightly better correspondence was observed between dT/d(Vp/Vs) and dT/dD (upper left plot and lower right plot). Lower dT/dVs gradient is observed in the "hottest" wells (lower left plot).

The velocity gradient with temperature in each well was positive possibly because the velocity increase with pore pressure and lithostatic pressure were larger, overcoming the temperature effects in the upper 3km. In some of the "hottest" wells however, Vs was more sensitive to temperature changes than Vp. The closest variations to the dT/dD were observed for the temperature variations with Vp/Vs (dT/d(Vp/Vs)).

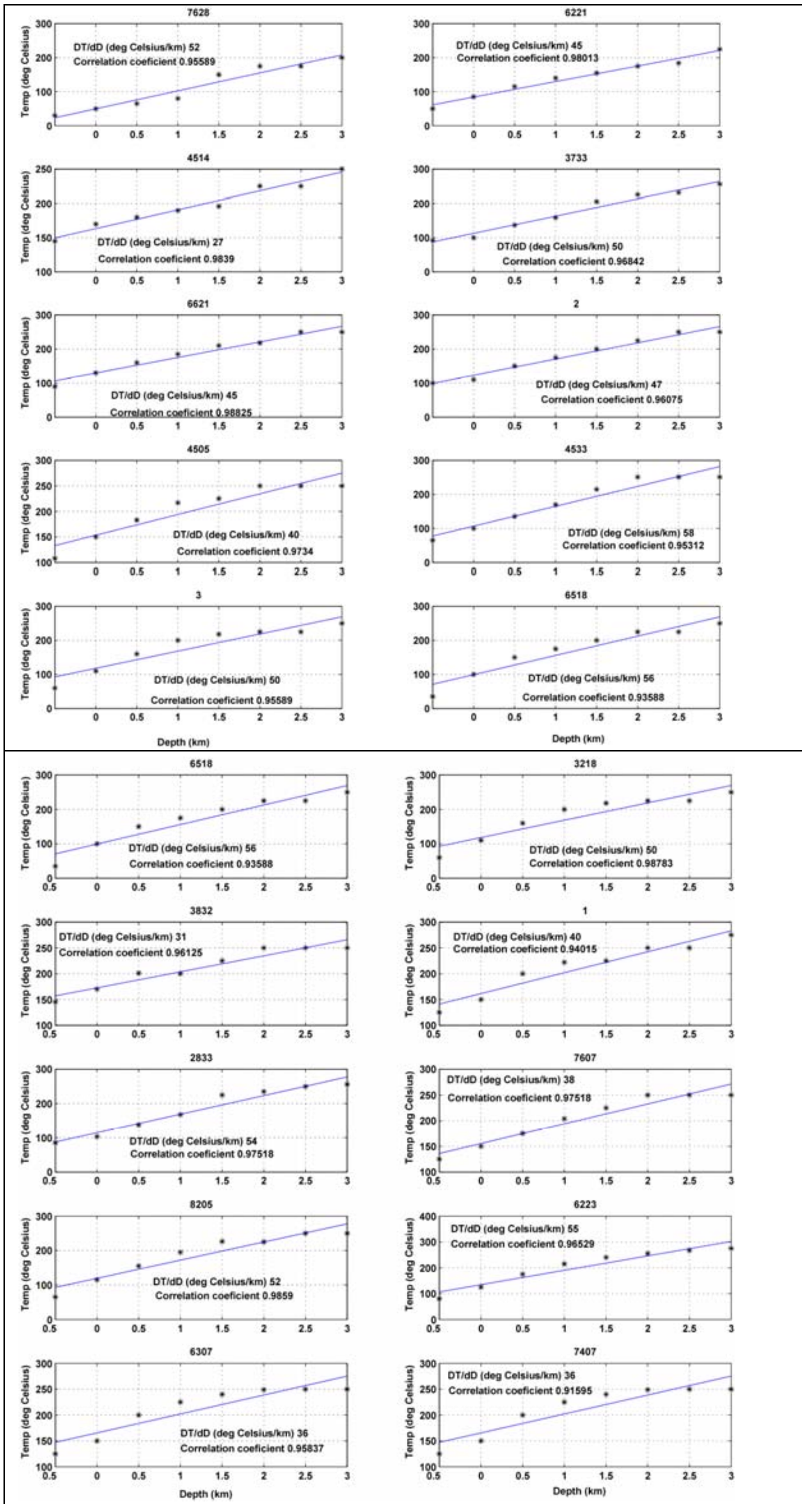

Figure 131A. The temperature gradient (TG) with depth varies in each well in Table 17; the well ID is given at the top of each plot. A linear TG was interpolated, to the first order. The TG (DT/dD) is given in each plot along with its correlation coefficient.

Seismic data alone (Vp, Vs and Vp/Vs) did not show a systematic difference between the production, injection, and dry wells. This may explained by insufficient resolution, and/or by insufficient measurement categories considered. This is why the seismic data was analyzed together with other geophysical parameters in the EGS analysis. Other potentially useful seismic parameters, such as anisotropy and attenuation are currently evaluated within a continuation project.

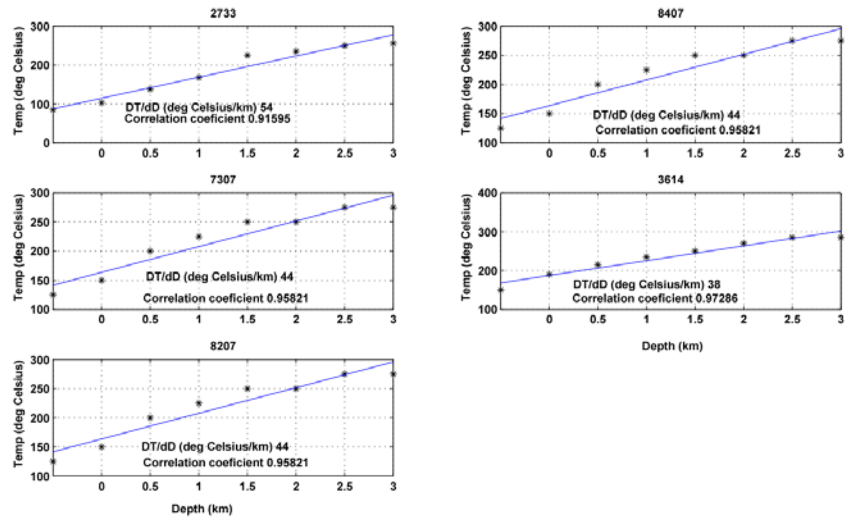

Figure 131B. The temperature gradient (TG) with depth varies in each well in Table 17; the well ID is given at the top of each plot. A linear TG was interpolated, to the first order. The TG (DT/dD) is given in each plot along with its correlation coefficient.

Summary

The goal of our seismic experiment was to assess the capability of ambient seismic noise based methods to indicate EGS favorability at a local (~ 5km) and regional scale. This project estimated new velocity models at three different scales ranging from hundreds of km to km, in the Dixie Valley region. At each scale, the new models had at least a factor of two improved resolution when compared to the baseline models. Our main conclusion is that the structure at different scales in Dixie Valley is closely related and several specific characteristics are listed below.

On a larger scale (DVESA), the PA is at the intersection of two different velocity model trends (1) an E-W low velocity corridor in the upper crust (less than 10km depth), and (2) a low-velocity corridor NW-SE at depths from 10km to 20km. We interpreted the E-W low-velocity trend in the upper crust as corresponding to the ~ 180km E-W extension along the 40'th parallel during the latter part of the Cenozoic (middle Miocene and Holocene) as reported by Bogen and Cshwieckert (1985). This extension was accompanied by volcanism manifested as younger (23-26Ma) calderas identified between Austin and Reno, NV (McKee and Moring, 1996). The NW-SE low-velocity trend corresponds to an earlier extension, in the late Eocene-Oligocene, accompanied by volcanism and calderas 30-36 Ma old (McKee and Moring, 1996). The intersection of the upper and lower crustal trends under the PA may explain the complex system of faults underlying the PA, which is interpreted as a region of elevated crustal temperature (as suggested by a pronounced low velocity in the SW of the PA). At this intersection, low velocity anomalies start in the lower crust beneath Fairview Peak, "raising" from SW to NW towards the mid-crust, and breaking up in narrower "conduits" at the surface.

At a local scale, in the PA, the highest velocity gradients appear to follow faults. Low-velocity areas correlated (at least at the shallowest depths) with heat flow anomalies and low velocity areas are observed in the vicinity of the power plant (see the DVSA_FINAL_MODEL description). Our interpretation of the PA velocity model is that there may be a close relationship between the high temperature (shown by low velocity) in the lower crust and the geothermal production area in the upper crust. The "hottest" lower crustal area is to the SW of the PA in the lower crust, and the low velocity appears to ascend on a SW-NE direction and to peak in the CA, where the highest temperature (285°C at ~3km depth) has been estimated in well 36-14. The existence of a highly fractured upper crust overlying a hot lower crust may be a possible cause of unusually high heat flow in the region. The production area in the PA is located on known faults which we delineate to the first order using high seismic velocity gradients.

We have estimated Vp and Vs models in the CA, PA and DVESA. Each of these new models had at least a factor of two improved resolution when compared to the baseline models. These velocity models are the expression of crustal structure and tectonic features at three different scales. Our main conclusion is that the structure at different scales in Dixie Valley is closely related. The large picture shows low velocity anomalies starting in the lower crust, "raising" from SW to NW towards the mid-crust, and breaking up in narrower "conduits" at the surface. The PA picture shows velocity gradients on faults, low-velocity areas correlated (at least at the shallowest depths) with heat flow anomalies and low velocity areas in the vicinity of the power plant (see the DVSA_FINAL_MODEL description).

Although the Vs model velocity resolution (~5km) was lower than the Vp velocity model resolution (~3km) in the CA, and much lower than the required CA resolution (~0.5km), first order seismic velocity, density and attenuation values were associated with lithologic layers in Dixie Valley, using well data. We calculated velocity gradients with temperature and velocity gradients with pressure in each well, and found them larger than the common crustal values. Positive variations of the seismic velocity with temperature, more pronounced for Vp than for Vs, were estimated from the well data (in the upper 3km). These variations were contrary to laboratory experiments which predicted negative velocity gradients with temperature increase, all other conditions being constant. We interpreted the results as evidence that lithology and pressure affect the velocity more than the temperature increase and or porosity in the upper 3km. This interpretation may change as better resolution velocity models will be estimated. Because Vs seems to be affected by temperature and porosity more than Vp, the Vp/Vs variations with temperature appeared to be best correlated to the temperature versus depth variations at the well location within the production area. We also calculated Vp/Vs and found a slight correlation of high Vp/Vs with high well temperature gradients. Median seismic velocity of lithologic layers previously resolved in wells was estimated as a possible indicator of similar lithology in future experiments. With limited resolution above 1km depth, it was found that the seismic velocity was approximately linearly correlated with temperature increasing in each well. We interpreted this behavior as dominant pressure (or porosity) effects within the upper 3km. Vp/Vs should increase with increasing temperature at the same pressure, however, some wells show decreases of the ratio with increasing temperature. Causes for this behavior would be as pore pressure and lithology variations. It was also found that, with one exception, Vp/Vs was lower in the "cold" wells ($T<200°C$) than at the same depth in the high-temperature wells. The low Vp/Vs was in all cases observed at mid crustal depths (12-15km) at the "cold" wells.

The seismic velocity alone is insufficient for estimation of EGS favorability, and the seismic results should be used in combination with other geological and geophysical information. Studies of seismic anisotropy and attenuation may improve the seismic interpretation.

Based on the observations in this study, another possibly favorable area for EGS exploration is between the seismic stations B02 and B03 and the system of faults to the south, on the Carson Sink and Stillwater Range boundary. There, a low Vs zone was observed, from 10km deep up to the upper crust, with a velocity low beneath these stations at 3-4km deep. Hot springs are also located close to B03.

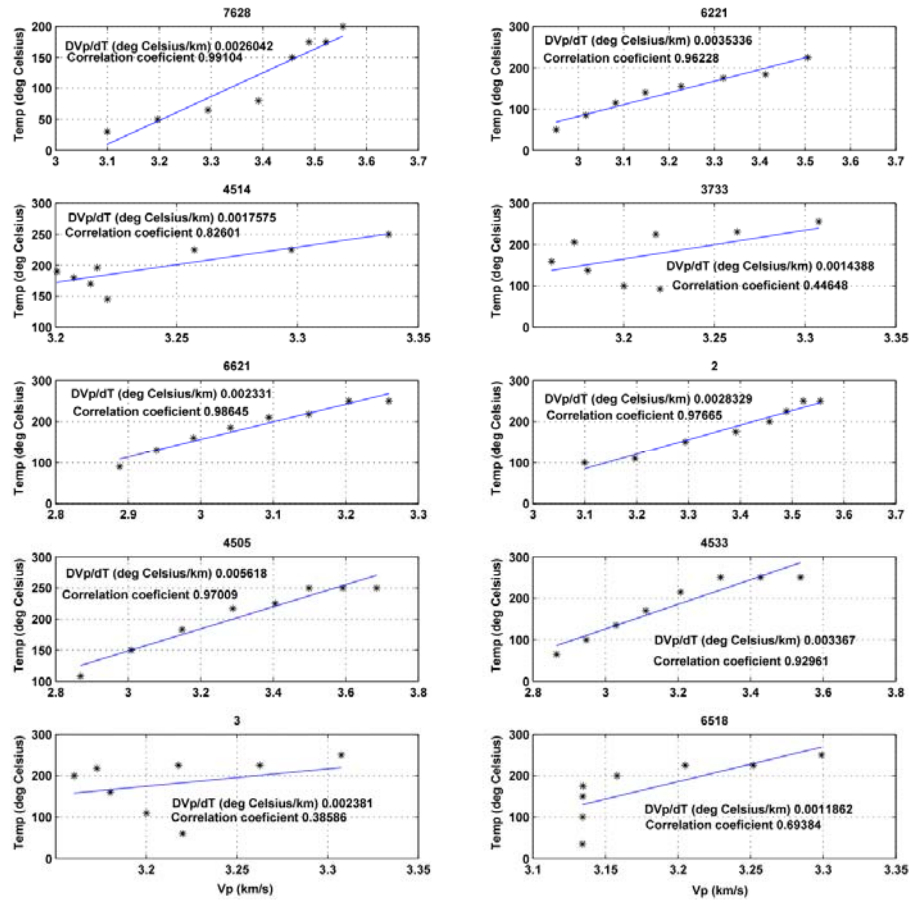

Figure 133A. The temperature (T) vs. Vp in each well presented in Table 17 (well ID at the top of each plot). These values were derived from an interpolation of these data at each depth in the well (see below). A linear temperature gradient trend was interpolated, to the first order and the gradient is shown in each plot. The correlation coefficient is for the two parameters plotted. The measured/modeled T data with depth in and the velocity variation with depth derived in the study with depth.

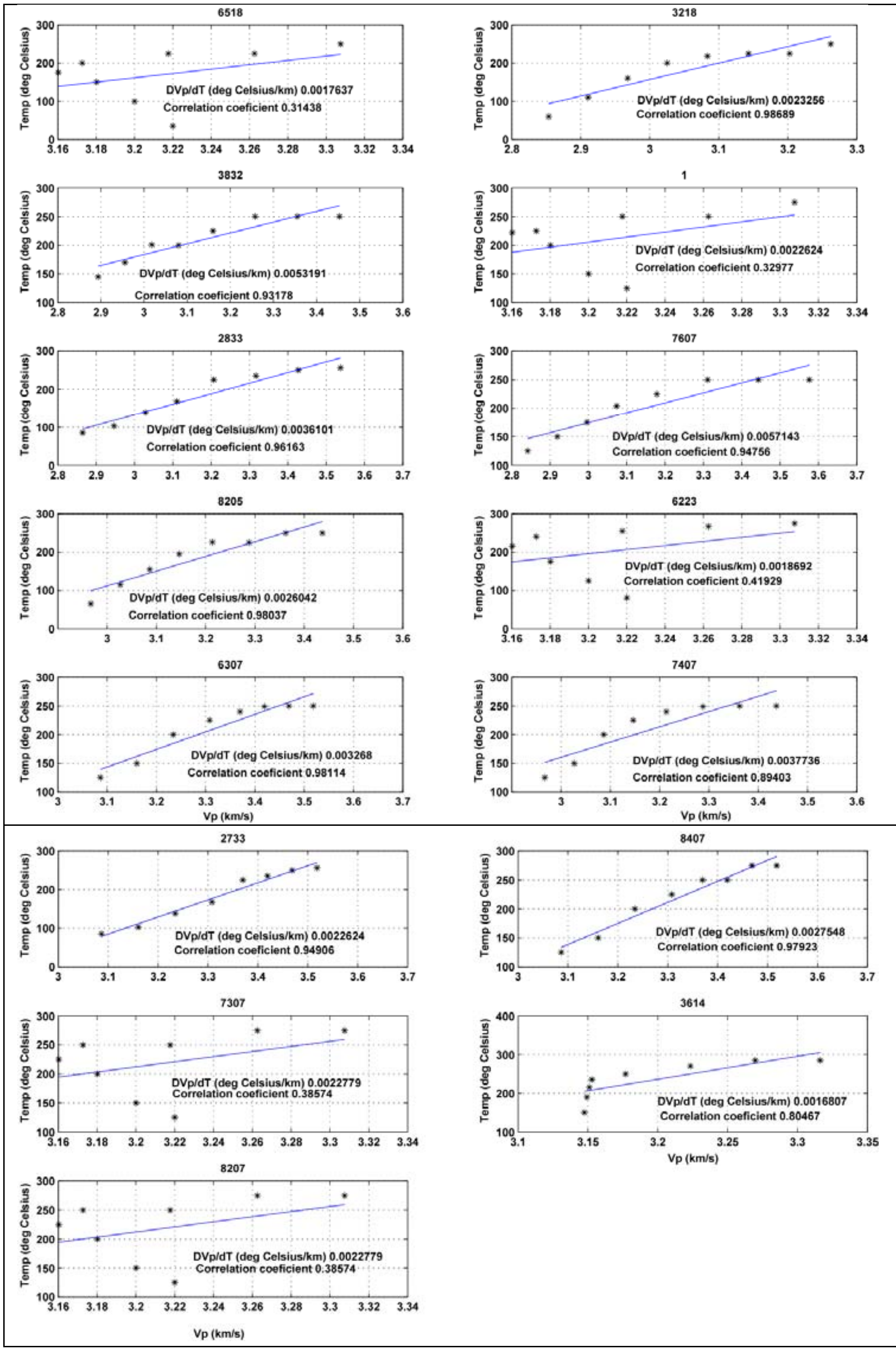

Figure 133B. The temperature (T) vs. Vp in each well presented in Table 17; well ID at the top of each plot. These values were derived from an interpolation of these data at each depth in the well (see below). A linear temperature gradient trend was interpolated, to the first order and the gradient is shown in each plot. The correlation coefficient is for the two parameters plotted. The measured / modeled T data with depth is presented in Appendix 16b and the velocity variation with depth derived in the study.

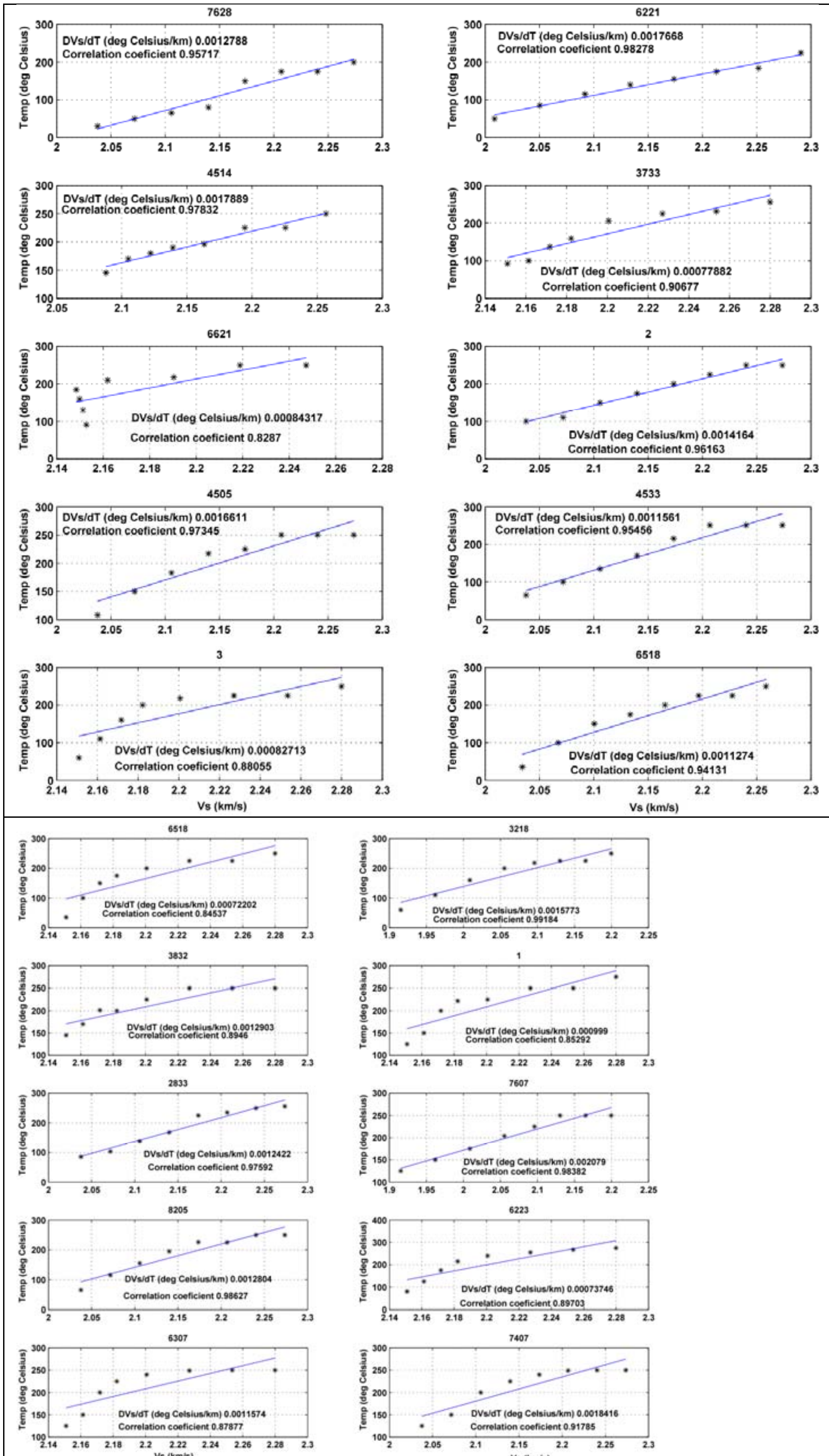

Figure 133A. The temperature (T) with Vs varies in each well in Table 17 as shown in each plot; well ID at the top of each figure. Note that wells labeled 1, 2, and 3 correspond to the wells SWL-1, -2, and -3, respectively. A linear trend for the temperature gradient was interpolated, to the first order and the gradient. The measured / modeled T data for each well (Appendix 16b) was used.

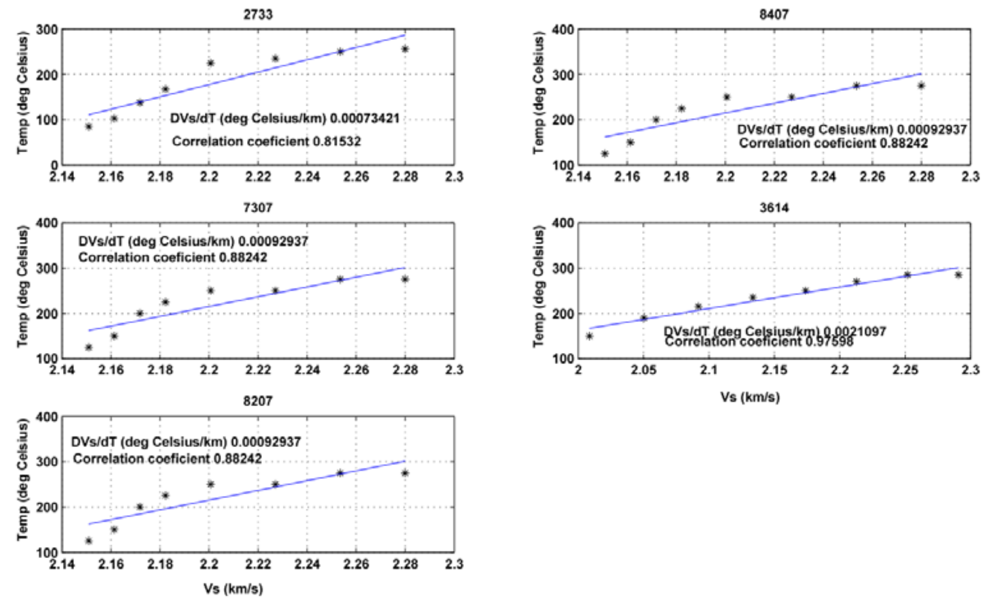

Figure 133B. The temperature (T) with Vs varies in each well in Table 17 as shown in each plot; well ID at the top of each figure. A linear trend for the TG was interpolated, to the first order and the gradient. The measured/modeled T data for each well (Appendix 16b) was used.

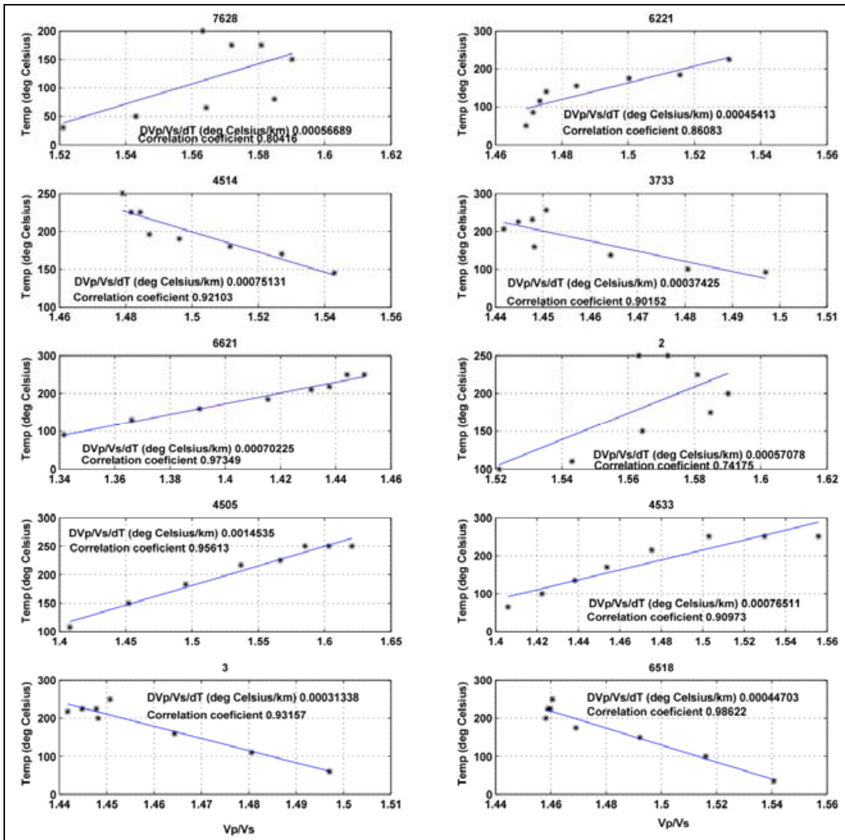

Figure 134A. The temperature (T) with Vp/Vs varies in each well in Table 17 as shown in each plot; well ID at top of each plot. Note that wells labeled 1, 2, and 3 correspond to the wells SWL-1, -2, and -3, respectively. A linear TG trend was interpolated, to the first order. The measured / modeled T data in Appendix 16b was used.

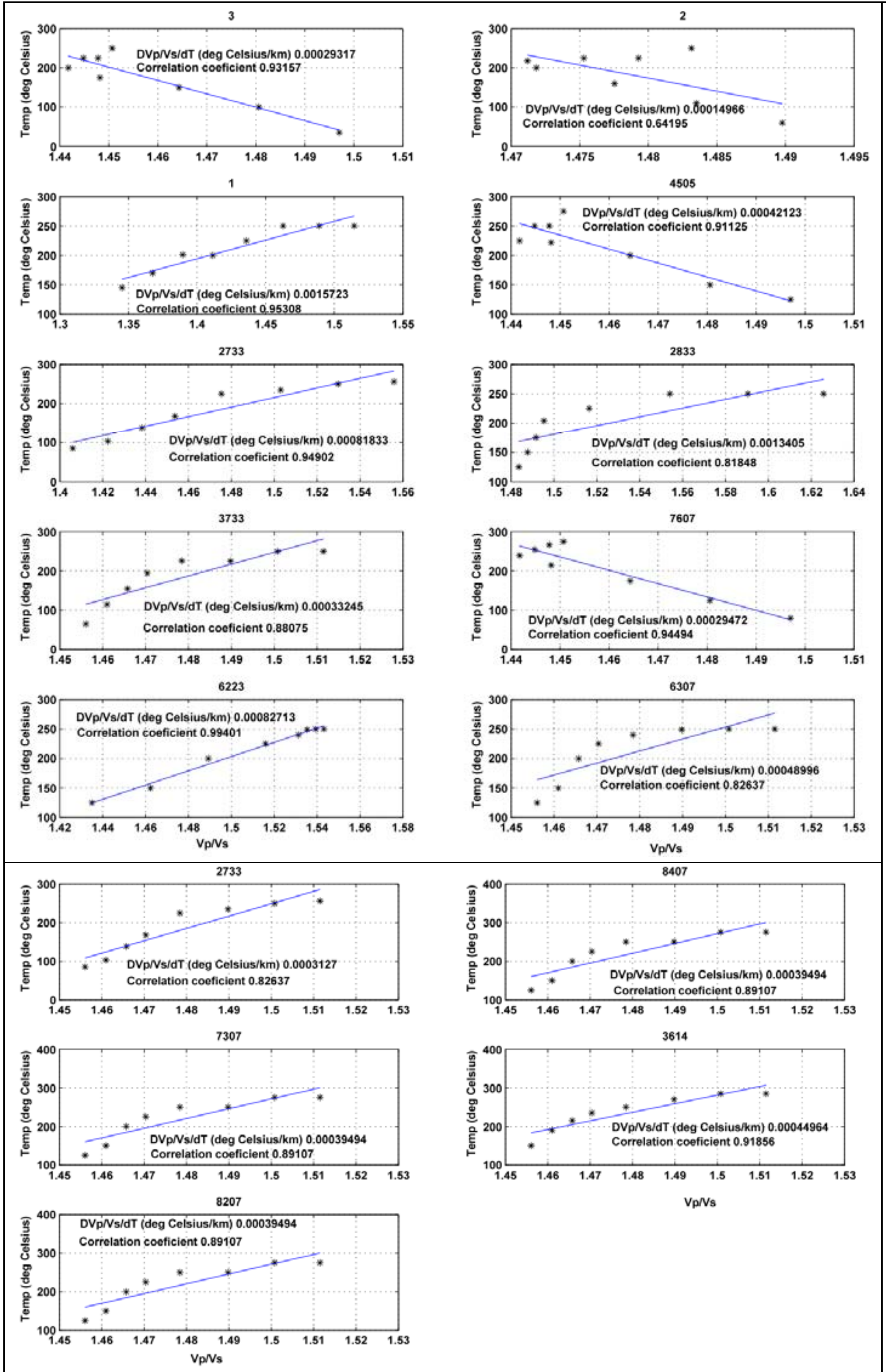

Figure 134B. The temperature (T) with Vp/Vs varies in each well in Table 17 as shown in each plot; well ID at top of each plot. Note that wells labeled 1, 2, and 3 correspond to the wells SWL-1, -2, and -3, respectively. A linear TG trend was interpolated, to the first order. The measured / modeled T data in Appendix 16b was used.

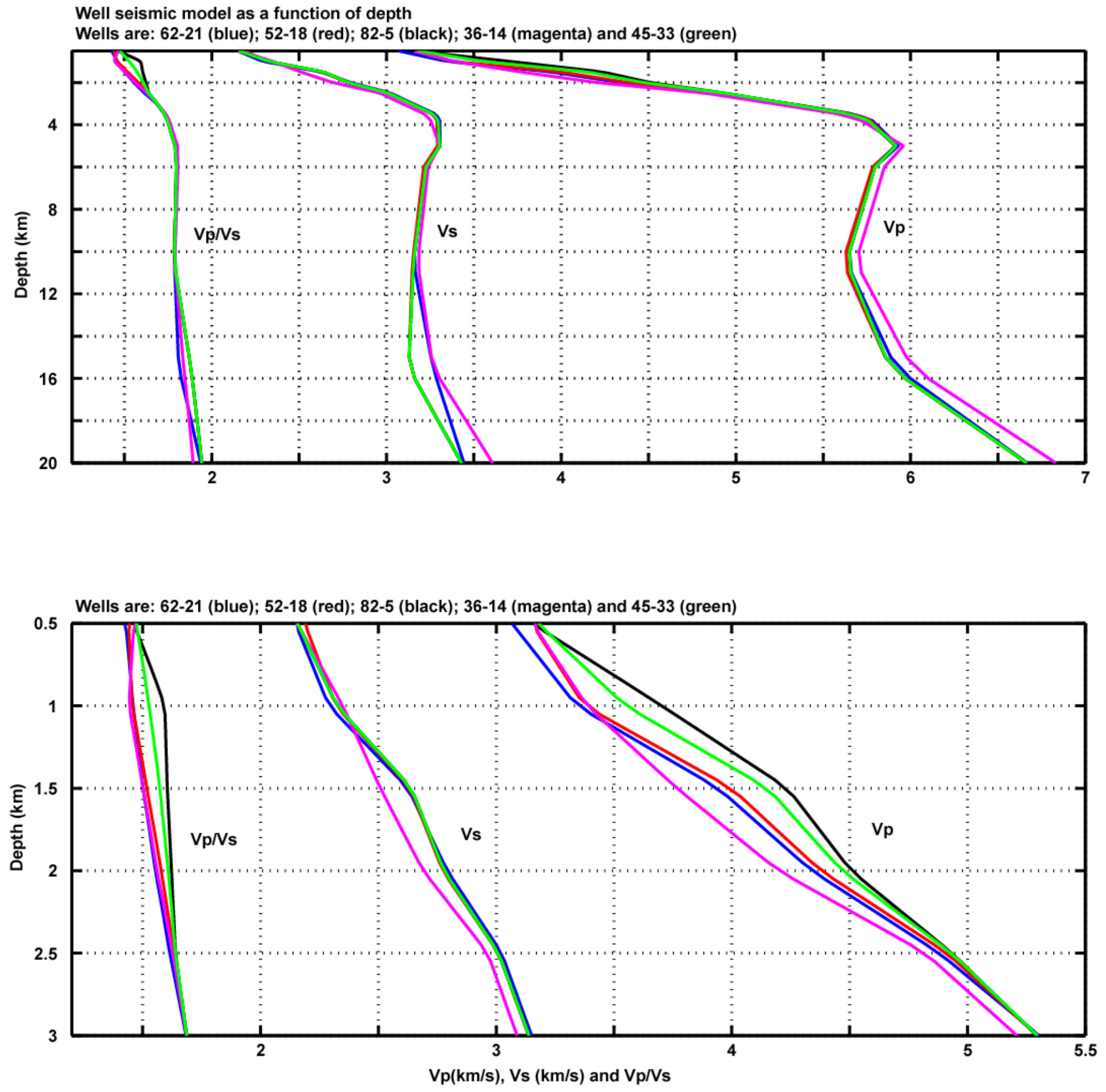

Figure 135.-Vp, Vs, and Vp/Vs as a function of temperature (°C). Wells directly compared to 62-21 (blue) are: 52-18 (red), 82-5 (black), 45-33 (green) and 36-14 (magenta). All wells show elevated Vp values over similar lithologies (basin-fill vs. basement) and depths. Well 62-21, unlike the other wells, is purely conductive.

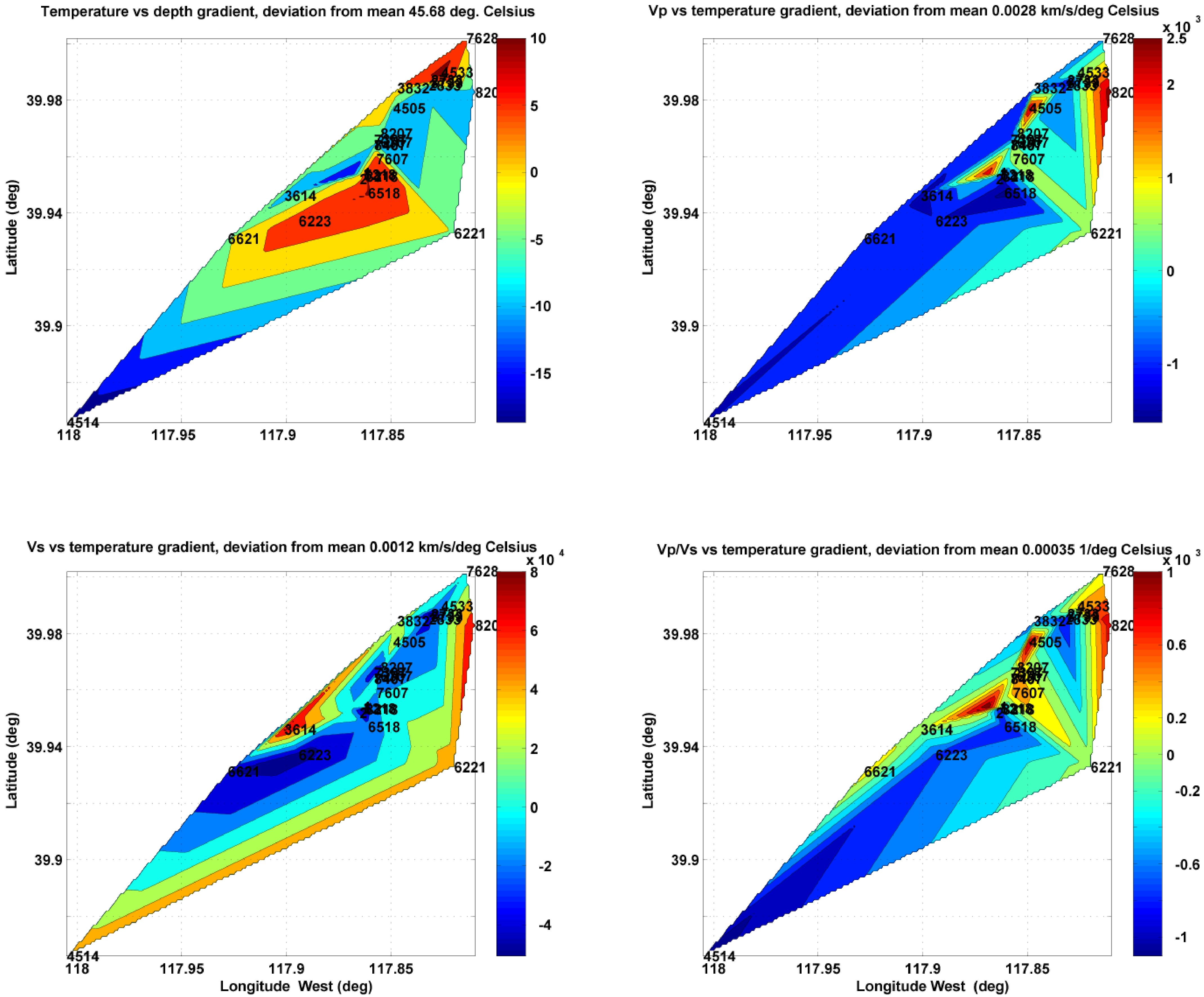

Figure 137. The dT/dD, dT/dVp, dT/dVs and dT/d(Vp/Vs) (assuming linear variations like in Figures 132, 134 and 135) for each well. The "dry" wells are 45-14 and 62-21, 76-28 (not analyzed here) and 62-23A. Unlike for Vp (upper right plot) note slightly better correspondence between dT/d(Vp/Vs) and dT/dD (upper left plot and lower right plot). Also, the lower dT/dVs gradient is observed in the "hottest" wells (lower left plot).

9.3 THREE-DIMENSIONAL MAGNETOTELLURIC (MT) SURVEY[10]

9.3.1 Introduction

The magnetotelluric (MT) method measures the scattering within the Earth of naturally occurring, vertically-incident, planar electromagnetic (EM) waves as a means of producing images of subsurface electrical resistivity (e.g., Vozoff, 1991; Chave et al., 2011). At typical geothermal conditions, electrical resistivity in turn is controlled primarily by (1) the quantity, salinity and efficiency of long-range interconnection of aqueous fluids in pores and fractures, and (2) the presence of hydrothermal alteration mineralogy with appreciable cation exchange capacity (Palacky, 1987; Ussher, 2000; Kulenkampff, 2005). Secondary controls on the resistivity of host rock lithologies include minor variations in porosity and clay content, most of which may predate geothermal activity of interest.

Research is being led by AltaRock Energy Inc. to establish a method to evaluate engineered geothermal systems (EGS) exploration methodology in the northern Basin and Range (Great Basin) region through an integrated geoscience analysis using the Dixie Valley Geothermal System (DVGS) as a calibration site, As a component of this research, 70 new tensor MT stations were taken and merged with 24 existing (baseline) soundings[11] for a total of 94 sites (Figure 138) over the DVGS for development of an enhanced MT interpretation for this project. The resultant 3D resistivity model is being analyzed together with physical property, structure and state models arising from potential fields, mapping, downhole stress and temperature in an attempt to provide a calibration of EGS favorability against observables. The new MT soundings were acquired by Quantec Geoscience Inc. (Quantec) using their standard L-array with steel plate electrodes and high-moment induction coils their Spartan survey system (Figure 139). Data quality was high given generally low noise conditions and use of a remote reference site near Austin, Nevada, as exemplified in Figure 140 and discussed in Section 4.2. High frequencies (e.g., 100Hz) penetrate to a depth on the order 100m, while frequencies of <0.01Hz penetrate to near the base of the crust, 20km.

The results of analyzing the 3D data set can be compared to models from the more localized baseline survey completed in 2002 that acquired three lines of MT stations oriented northwest-southeast across the field (Figure 141). These baseline survey lines consisted of dense MT array profiles using the Quantec Titan-24 multi-channel system[12] (Figure 142) located primarily up against the range-front, plus discrete five-channel sites with the predecessor of their Spartan system appended to one or both ends to increase aperture (Wannamaker et al., 2007). The Titan-24 system was designed for small-scale, prospect-oriented resistivity imaging and acquires MT sites typically every 100m with the electric bipoles being contiguous[13]. The central longest line ran through the main geothermal power producing area, while the northern and southern lines crossed the Senator fumaroles and Dixie Valley Power Partners (DVPP) section 14 areas, respectively. Although achieving finer lateral sampling along each profile (~100m) than the 3D survey discussed here, the analysis of these older profiles was restricted to being essentially 2D whereas Dixie Valley possesses substantial departures from that simple geometry. However, we did utilize selected soundings from the baseline arraying profiling to fill in the overall 3D coverage.

---

[10]Section provided by Dr. Philip E. Wannamaker, MT Task Leader, and his post-doctoral researcher, Dr. Virginia Maris.

[11]Baseline sites chosen to be included in the enhanced (3D) data analysis was based on matching the scale used in the new survey (90stations).

[12]Both Spartan and Titan systems record MT time series in basically similar ways with a few differences. Spartan is meant for traditional 5-channel MT sites that are well separated from each other. The Titan system is meant for concentrated targets and is designed to acquire MT soundings only 100 m apart typically by placing the bipoles end-on-end. It works best when a 2Dassumption is workable.

[13]The data quality for the baseline data is comparable to that collected by the Spartan system.

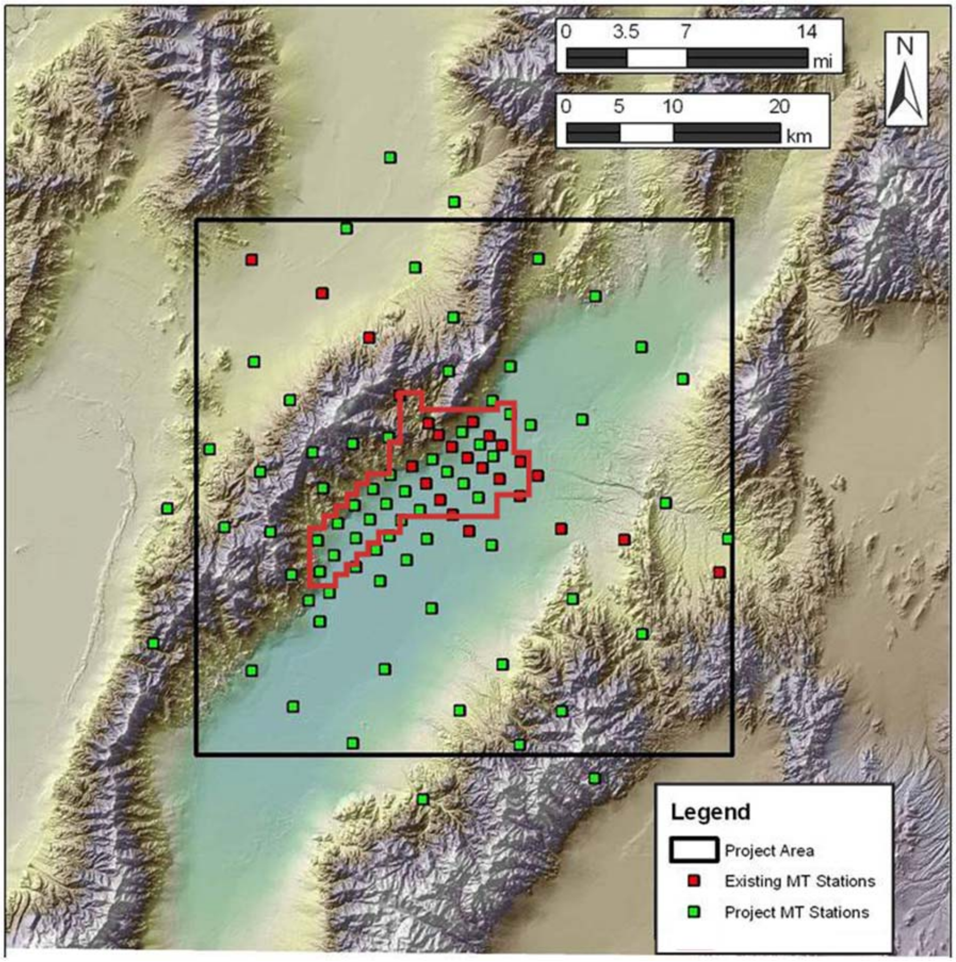

Figure 138. MT site distribution over the Dixie Valley thermal area for analysis through 3D inversion. The Dixie Valley Geothermal Wellfield or calibration area is outlined in red.

9.3.2 Analysis conducted

In Figure 139, the upward directed electric bipole is typically assigned to the x-axis of MT measurement while the right directed bipole is along the y-axis. In turn, x normally is geographic north and y is east. The coordinate conventions are somewhat arbitrary and usually meant to standardize field procedure; after the time series data are transformed to the frequency domain and the four tensor impedance quantities (Zxx, Zxy, Zyx, Zyy) formed, those quantities can be rotated to any other user-desired coordinate orientation through application of a simple 2x2 rotation matrix (e.g., Vozoff, 1991). Given the visual trend of the Stillwater range-front and Dixie Valley, and inferred Dixie Valley Fault Zone (DVFZ) (Johnson and Hulen, 2002; Blackwell et al., 2005; Iovenitti et al., 2011 and 2012), we selected a N040°E coordinate system for input to the inversion image algorithm discussed below. However, we are aware that other resistivity structural trends may emerge in the inversion model, such as N-S aligned features. In principle, apart from inescapable issues such as lateral sampling, the coordinate system chosen should be immaterial[14] as all calculations internal to the inversion code would be consistently rotated as well and we invert all four elements of the impedance tensor.

[14]Assumptions are (1) finite spatial sampling is adequate and (2) application of an error floor to the data that varies some with coordinate rotation.

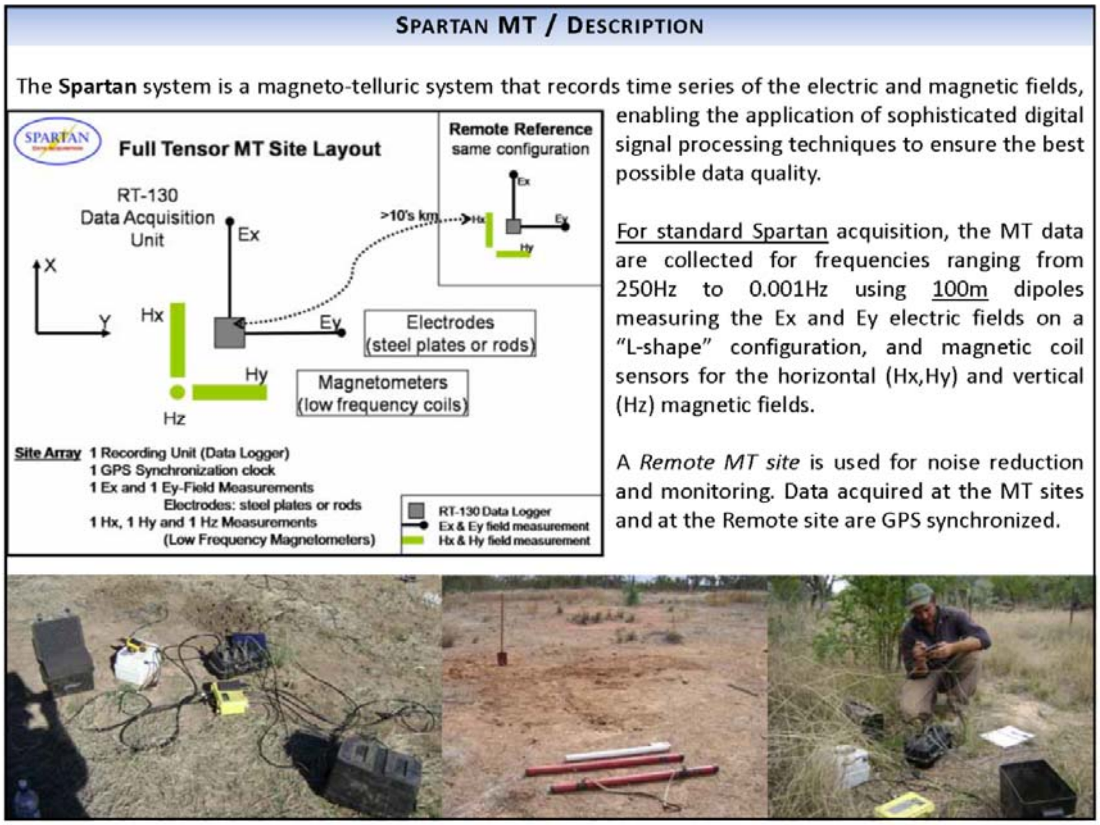

Figure 139. The Spartan MT data collection system used by Quantec Geoscience Inc. in the EGS Exploration Methodology Project

The soundings exemplified in Figure 140 have ~135 individual frequency data points over the range of data collected, and thus are highly oversampled in frequency, a consequence of a typically long time series acquired over ~16 hrs at 1000 samples per second[15]. For computational efficiency, we bin the sounding samples into a coarser set of four per decade in frequency using a Gaussian weighting procedure that causes no overall error inflation or deflation following general statistical principles such as in Bevington (1969). We thus selected soundings with 12 data points over the frequency range 10Hz to 0.02Hz to cover the depth range a few 100m to >20km. Furthermore, given the length of the typical time series data relative to the frequencies of interest, the processing error bars on the data points are often much smaller than the apparent scatter in the data over frequencies especially toward the higher frequencies. This is pervasive with MT data and it has become standard to apply an error floor to the data points more typical of the scatter; in our case this is 5% of the impedance determinant magnitude. This floor still is much smaller than the overall or broad-scale variation of the soundings over the whole frequency range and is not a detriment to resolution of resistivity structure to the extent feasible with a diffusive EM wave technique like MT.

[15]However, the recording period was required to achieve the down-sampled soundings used in the inversion, because although there was a smaller number of frequencies used the total span was similar. Frequencies used in the inversion herein, were (1) 4 from 10 to 2, (2) 4 from 1 to .2, and (3) 4 from 0.1 to 0.02.

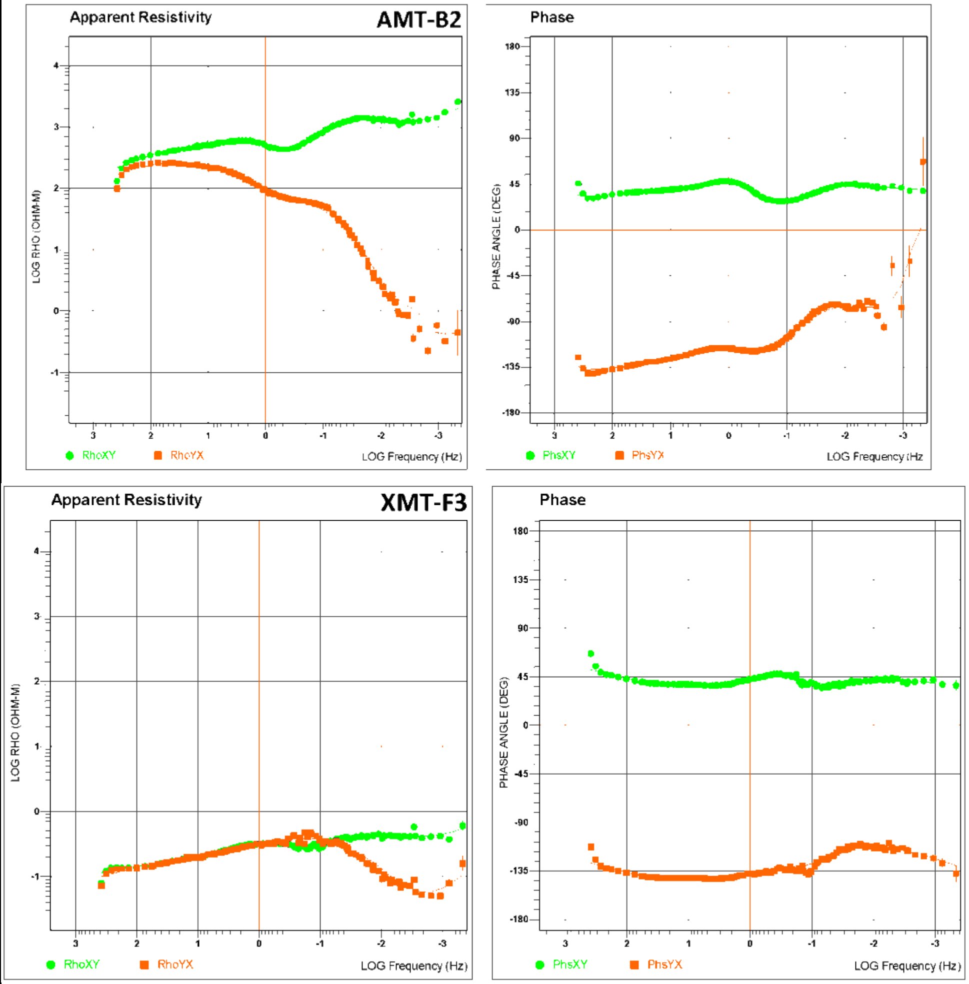

Figure 140. Two example soundings from the Dixie Valley MT survey (Figure 138) data set with apparent resistivity on the left and impedance phase on the right exemplifying data quality in the field.

The four complex elements of the multi-frequency impedance, described above, at each MT sounding were input to a non-linear (iterative), regularized inversion program to produce a 3D model of electrical resistivity under the Dixie Valley region with particular detail in the central Dixie Valley Geothermal Wellfield or calibration area (Figure 138). The algorithm used is based on that described by Sasaki (2004), which has been loaned to Dr. Wannamaker, MT Task Leader, for research for about 10 years. Dr. Wannamaker and his post-doctoral researcher, Dr. Maris, have significantly modified the program by replacing the parameter step solver after Tarantola (1987) and parallelizing the code on multi-core linux workstations to improve speed (Maris and Wannamaker, 2010). Such inversion algorithms function by representing the earth domain probed by the MT fields as a large series of prismatic parameters or 'bricks' (Figure 143). Our code uses finite difference (FD) approximations to Maxwell's equations to simulate the MT response of the 3D earth and the sensitivities of the response to incremental changes in the resistivity of each parameter (i.e., the jacobians); deGroot-Hedlin and Constable, 1990).

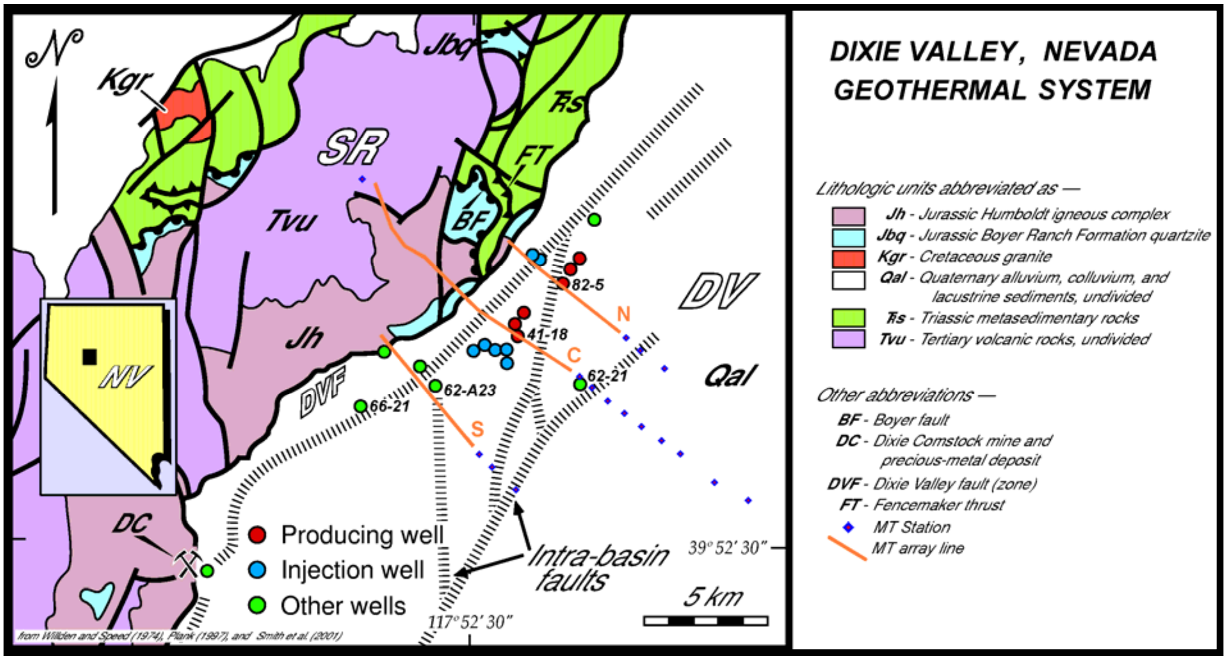

Figure 141. Simplified geology map of the central Stillwater-Dixie Valley area including major faults, MT profiling array lines (N, C, S), and geothermal wells (Wannamaker et al., 2007, after J. Hulen).

The bricks are made so small that the individual geometries are essentially immaterial but instead serve as mere sample points in 3D space. A parameter step equation is used that jointly minimizes, in a least-squares sense, the misfit between the computed MT response of the 3D earth model and the data as well as the roughness of the 3D model in the sense of the first spatial derivative or slope of the model in 3D space (deGroot-Hedlin and Constable, 1990; Sasaki, 2004). This is a widely accepted means of suppressing small-scale artifacts in the model not demanded by the data which can result from attempting to resolve subsurface structure with a diffusive wavefield that provides finite data with scatter or noise (e.g., deGroot-Hedlin and Constable, 1990). The model grid in Figure 141 is comprised of 79x65x28 = 143,780 parameters with the upper layer being 200m thick and deeper layers thickening but geometrically according to resolution of diffusive EM wavefield. This lies within a FD grid of 153x125x43 nodes in x, y, and z directions. In the calibration area, typical parameter (brick) widths are 400m, which is 1/4 to 1/5 typical station spacing there. The mesh extends to just over 20km in depth, well below levels of geothermal prospectively but still interesting from the standpoint of deep heat sources and the possible role of magmatism.

The program was run on a new workstation with 24 cores and 0.5 Tb RAM using the Lahey linux Fortran compiler parallelized under the OpenMP protocol (Maris and Wannamaker, 2010). A workstation of this size was acquired because our previous machine with 8 cores and 32 GB RAM only could handle ~80,000 parameters which was deemed insufficient to sample and span the resistivity domain affecting the data set. The Dixie Valley data set is unusually demanding of parameters for 94 sites because a portion of the sites are concentrated in the calibration area (with the remainder having a much larger station spacing over the greater project area. Model run times were on the order of one week. Misfit in a normalized root-mean-square (nRMS) started at ~36 for the initial 20 ohm-m half-space and converged to ~3.4, which is considered reasonable and typical for such inversion runs in the sense that an ideal nRMS value of unity is very rarely achieved, and is spread fairly evenly over the data set.

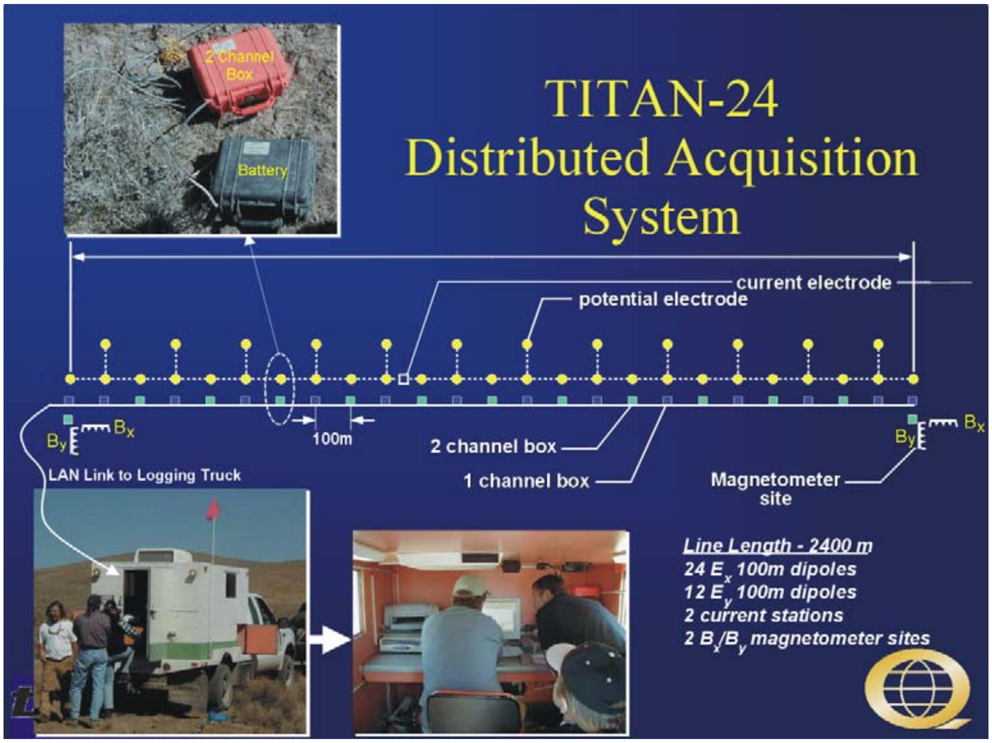

Figure 142. The Quantec Geoscience Inc. Titan MT distributed acquisition system used to collect the baseline MT data; see text for an explanation.

9.3.3 Model Presentation

Various section and plan views through the 3D model are depicted in Figures 144-150. MT plan view maps at a depth of approximately 1km to 12km in 1km increments and from 13/14km to 19/20km in 1km increments are presented in Part II-Appendix 11. The model brick distribution of values is sampled every 200m x-y-z and plotted using the Voxler graphics platform of Golden Software Inc. The following discussion of the 3D modeling is independent of any integration with other geoscience data sets.

The first view is at a depth of only 500m (Figure 144). Here is apparent the NE-SW trend of conductive sediments of the shallow Dixie Valley against the Stillwater Range to its NW. Stillwater Range rocks near surface are quite heterogeneous in resistivity at small scales. The geothermal significance of that is unclear and much could represent conductive shales and clastics in the late Paleozoic/early Mesozoic host rocks. Apparent though less clearly defined is Buena Vista Valley further northwest. The next view

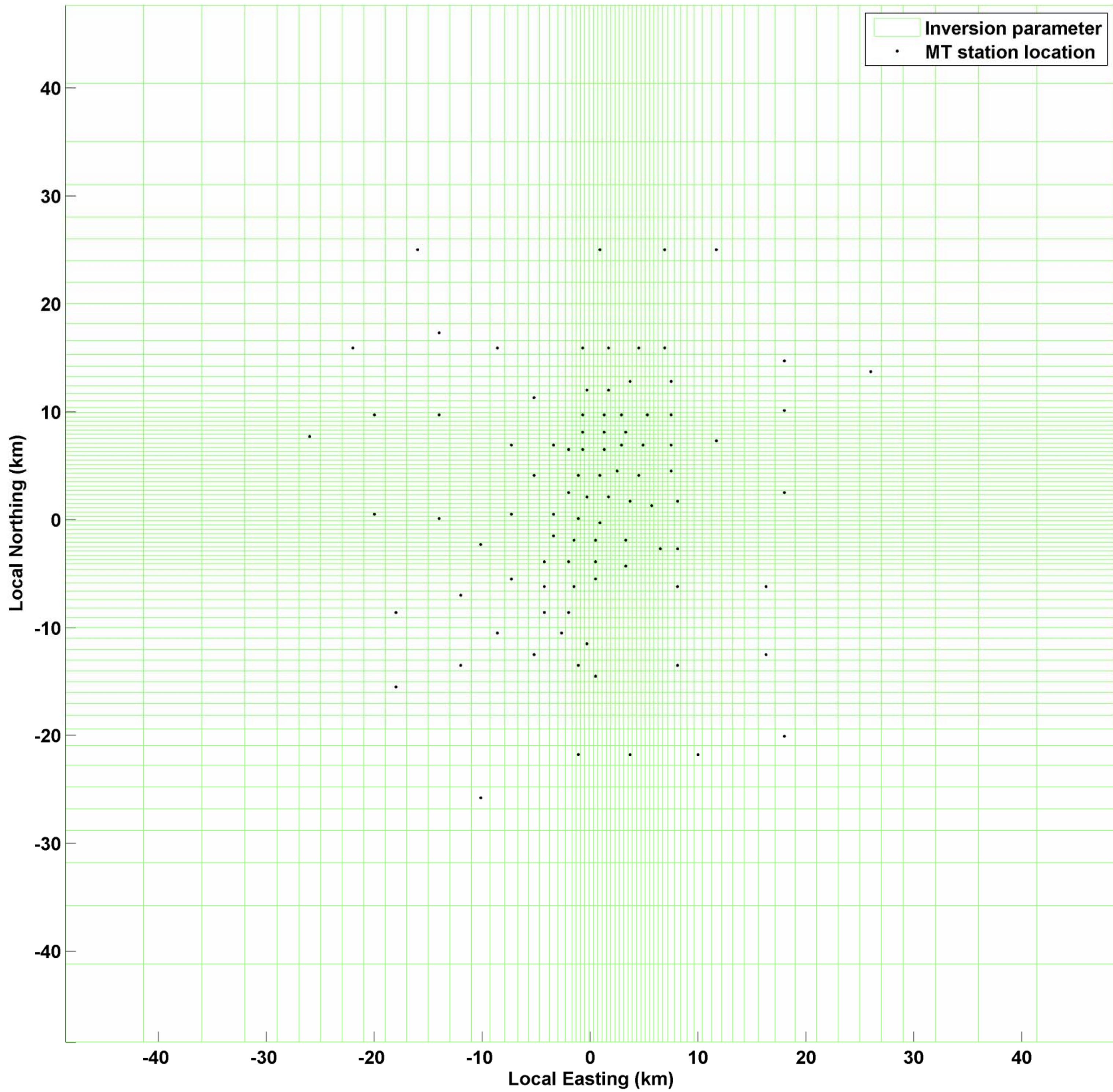

Figure 143. Central region of the parameter or 'brick' collection representing 3D resistivity variations in the earth that fit or simulate the observed MT response at Dixie Valley area. Each brick in plan view is made up of 2x2 Finite Difference (FD) cells while in section view only the top layer of bricks is two FD cells thick with the remainder below just one FD cell thick.

(Figure 145) is at the greater depth of 2000m which begins to reveal basement features. For one, resistive pediment rocks at shallow depths between the Stillwater topographic scarp (the Dixie Valley range-front fault segment of the DVFZ (Johnson and Hulen, 2002; Blackwell et al., 2005; Iovenitti et al. 2011; 2012) and the main graben bounding fault (the piedmont fault segment of the DVFZ) into which the production and injection wells are drilled are clear as the dark blue band hugging the wells on their NW side. Local resistive 'fingers' which we take to be protrusions of shallow bedrock further into the valley seem to appear SW of the power plant area wells and more weakly in the neighborhood of Senator fumaroles (e.g., wells 38-32, 45-33). Second, there is a suggestion of NW-aligned conductive bands toward the SE margins of the MT site coverage, although the MT station spacing is coarse there.

The plan view at 3500m depth (Figure 146) reaches depths which are below the unconsolidated Dixie Valley basin fill and yet pronounced low resistivity is still quite evident in the central valley areas, especially east and south of well 45-14. This is confirmed even by a plan view at 5000m below ground surface (Figure 145). In the latter view, one sees some coalescing and rotation of the conductive elements under Dixie Valley to start to suggest a somewhat northerly orientation. This becomes even more apparent in the perspective view of Figure 149 at a depth of 6500m below the surface. Interpretively, we have drawn three grey arrows which we suggest highlight conductive lineaments with a N-S component of orientation. Since renewed structural study following early observations of Waibel (1987), there has emerged the possibility that the intersection of older N-S fault zones with modern NE-SW extensional fault zones may be important in creation of dilatancy and deep geothermal conduits in the DVGS (Iovenitti et al., 2011; 2012). In any event, particular low resistivity zones in the upper middle crust appear to be associated with near surface geothermal manifestations around wells 45-14, 66-21 and the main power producing area. These likely could be more firmly established with MT station densification to the southeast in the valley and western Clan Alpine range. The fence section in Figure 150 roughly corresponds to the original transect of Wannamaker et al. (2007).

Finally, we present a series of fence diagrams in Figure 150 to provide a view of the relation between upper and deep crustal low resistivity structure in the project area. The fences correspond to Wannamaker et al. (2007) transect plus two others ~5km and ~13km further SW developed in this study. The main purpose is to illuminate the 3D equivalent of the crustal scale low-resistivity break in the earlier 2D that extended from base of Dixie Valley steeply westward under the Stillwater Range. This break joined a near sub-horizontal low resistivity zone under Buena Vista Valley and the East Humboldt Range which was suggested from earlier seismic studies to be a zone of active magmatic underplating (Catchings and Mooney, 1991). In Figure 148, one sees that a similar albeit strike-varying conductive zone projects from under Dixie Valley westward to the deep crust. Precisely under the fence of the original transect (central section in Figure 148), the deep conductive zone appears double lobed as it descends from the valley whereas only a single zone was seen in the original 2D model. The 3D structure here portrays the convergence of NE-SW and NS conductors shown in Figures 146 and 147. A short distance further NE in the vicinity of well 62-21, these structures essentially join. The original transect passed through at a fortunate position; if it had gone much further north, evidence for the large scale, steep conductor joining deep crustal magmatism to the west with the Dixie Valley thermal field might have been missed. Nevertheless this experience confirms early theoretical simulations (Wannamaker et al., 1984; Wannamaker, 1999) that fixed-axis, TM mode modeling of data in many 3D situations can yield fundamentally significant information about the earth section below an MT profile.

9.3.4 Discussion

The 3D data coverage and inversion reveal intersection of NE-SW, nearly N-S and perhaps NW-SE low resistivity trends in the DVGS. Concentrations of low resistivity appear to occur at the geothermal manifestations associated with wells 45-14, 66-21 and the main power production area. These concentrations may be promoted by intersection of NE-SW and N-S structural trends at upper middle crustal levels. Strong resistivity structures in the upper 5km such as these are not characteristic within the Stillwater Range, although very limited MT stations are present in the range. The 3D model appears to confirm the presence inferred from a previous MT transect through the producing area of a crustal-scale conductive break dipping steeply under the Stillwater Range and connecting with a previously suspected zone of deep crustal magmatic underplating to the west. However, this data set highlights the value of full 3D coverage to pinpoint geothermal concentrations associated with the intersection of varying trends.

For EGS prospectively, identification of suitable reservoir rocks which can support brittle fracturing and are at high temperatures is crucial. Candidate reservoir rocks include the Jurassic mafic/ultramafic Humboldt Formation (Fm) and the Cretaceous granodioritic New York Canyon intrusives. At this point it is considered unlikely that hot (up to ~300°C) dry rocks can be distinguished from cold dry rocks based on bulk electrical resistivity. At fixed salinity, pore fluid resistivity will reduce by a factor of ~5 from room temperature to 300°C (Nesbitt, 1991). Thus, for example, a tight granitic rock with a resistivity of 5000 ohm-m at room temperature would exhibit a resistivity of 1000 ohm-m at 300C. Using typical Archie's Law mixing relations (Grant and West, 1965), one also could cause such a resistivity reduction by increasing the porosity by a factor of 2-5 at fixed salinity and temperature depending upon whether conduction was predominantly through tortuous pores or straight fractures. Furthermore, values of 5000 and 1000 ohm-m would both be considered resistive and difficult to resolve from MT data that are imaged via smoothing-stabilized inversion such as we have employed in the face of burial and proximity to other lithologies. Perhaps it would be more fruitful to establish the location of general resistivity lithologies from the inversion, and then examine whether other structures may be responsible for bringing heat into the area and increasing the temperature of potential reservoir rocks. Candidates for that might include the conductive linear features in the 5-6.5km depth range discussed above.

The values of the lowest resistivities at depths of several km can be quite small, of order 1 ohm-m. Expected temperatures should be well over 200°C and probably more like 300°C based on encountered well temperatures (Blackwell et al., 2007). Thus we do not expect presence of high cation exchangeable clays such as smectite to exist and contribute to lowering resistivity. The root cause is expected to be presence of saline aqueous fluids interconnected over distances comparable to the size of the resolved structures. Highly saline (20+ wt%), deep crustal fluids such as are exsolved during magmatic crystallization are perhaps suitable as they have resistivity around 0.002 ohm-m at such temperatures (Nesbitt, 1993). In a medium of aligned fractures, the necessary porosity to achieve 1 ohm-m is only ~0.5 vol. % assuming ideal interconnection. However, such saline fluids are not characteristic of the wells and would imply disconnection of such deep fluids from the production domain. This remains an area of further study.

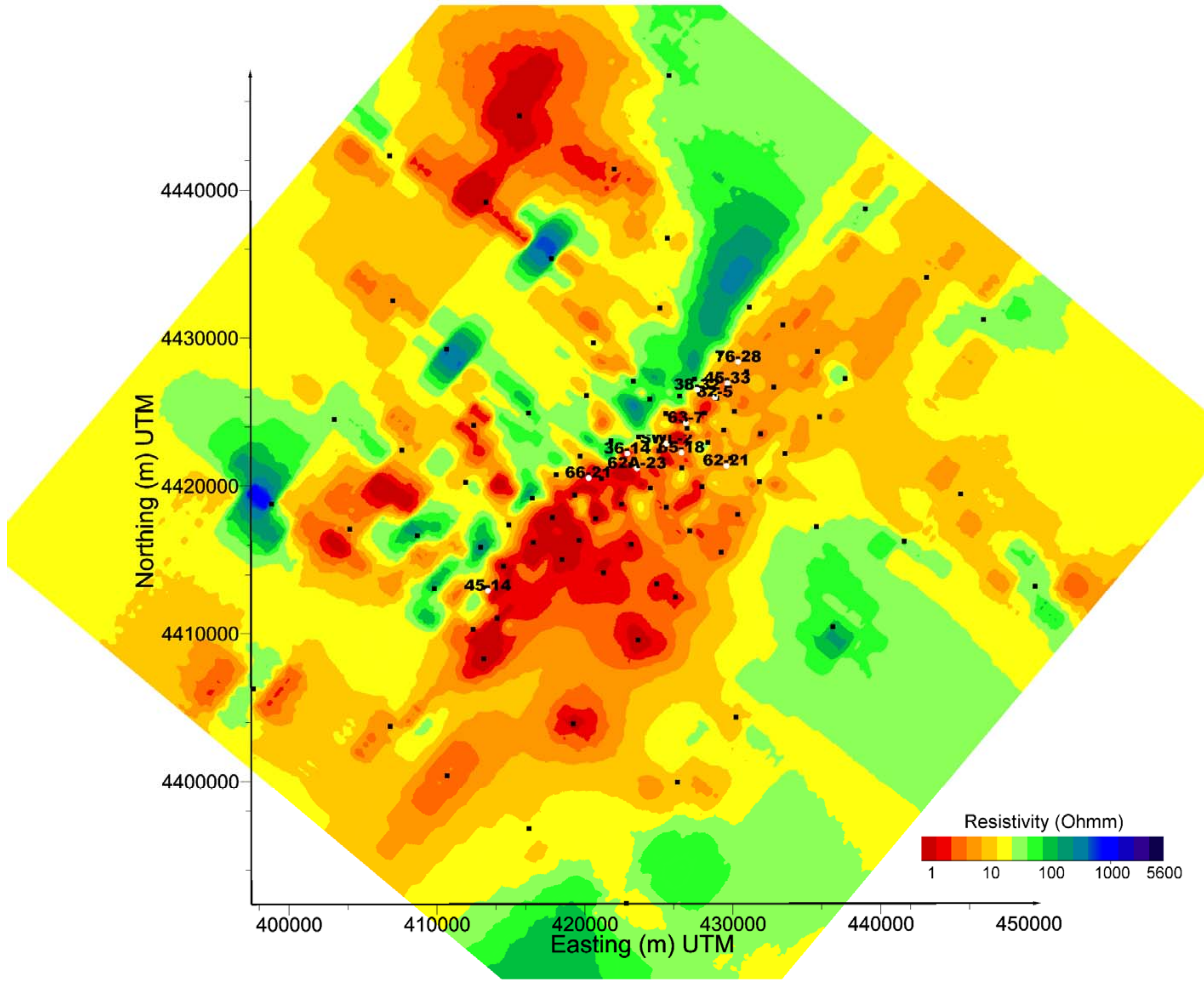

Figure 144. Vertical plan view of the 3D resistivity model from non-linear inversion for a depth slice at 500m below the surface. The inversion assumes a flat earth. Small black squares denote MT station locations while white circles are geothermal well locations.

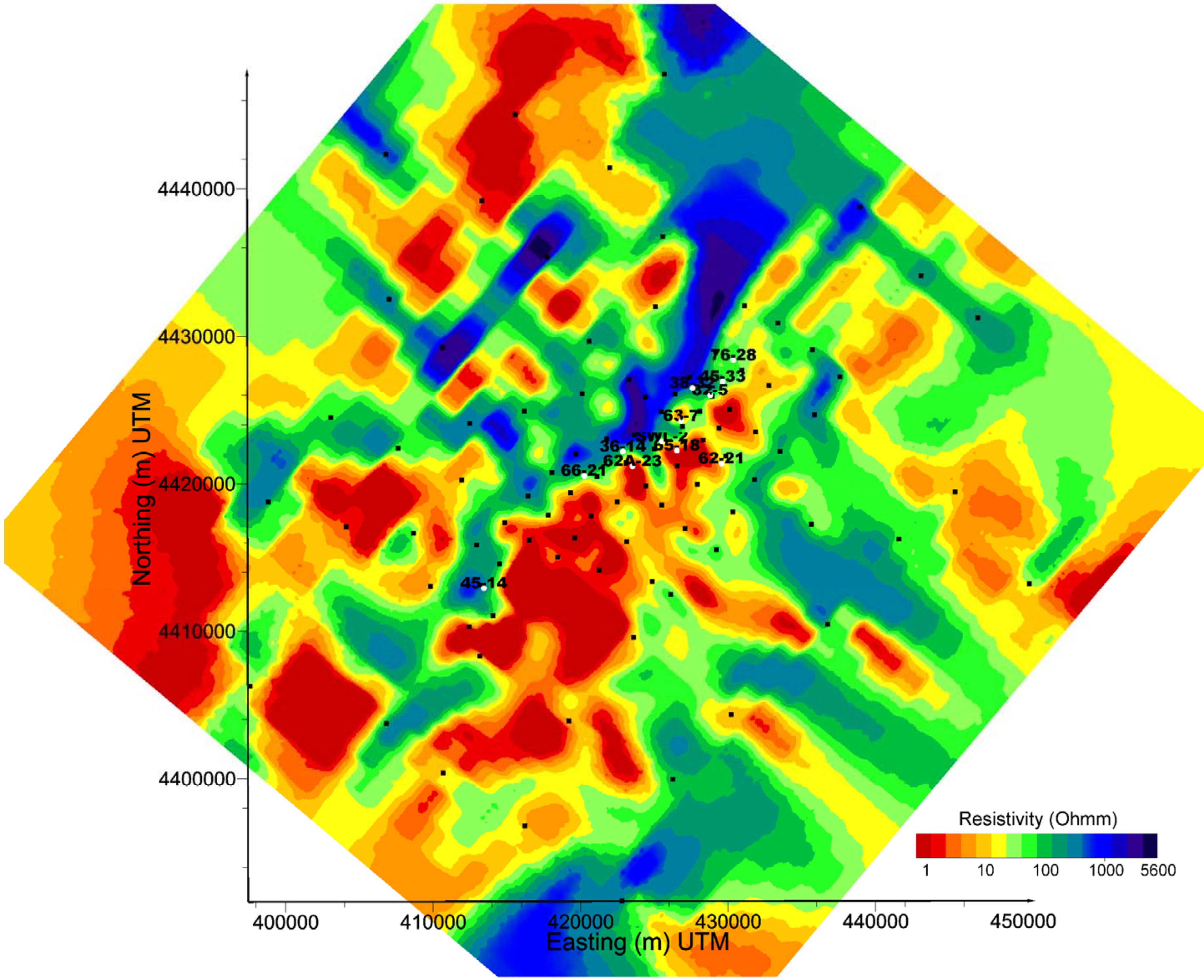

Figure 142. Vertical plan view of the 3D resistivity model from non-linear inversion for a depth slice at 2000m below the surface.

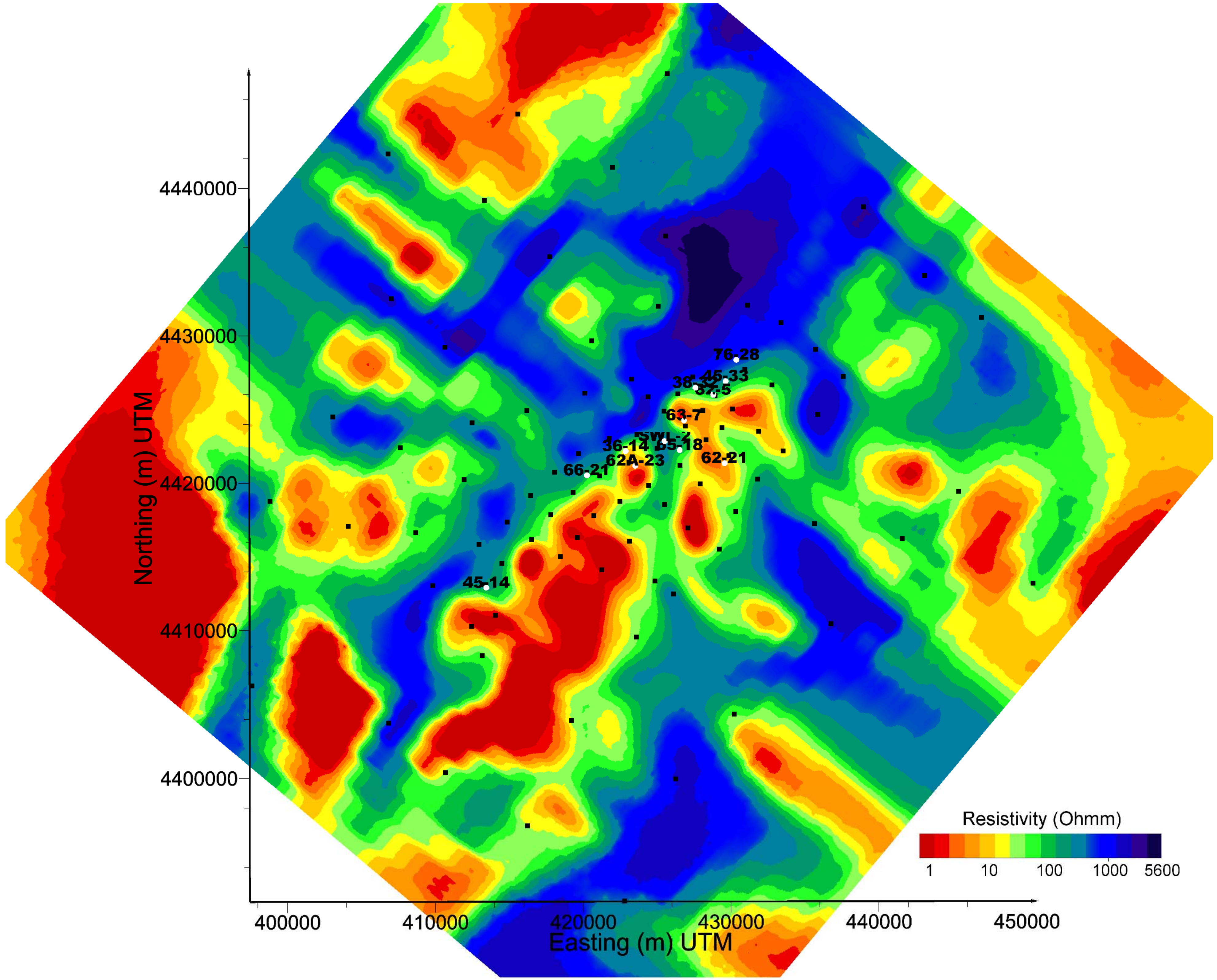

Figure 145. Vertical plan view of the 3D resistivity model from non-linear inversion for a depth slice at 3500m below the surface.

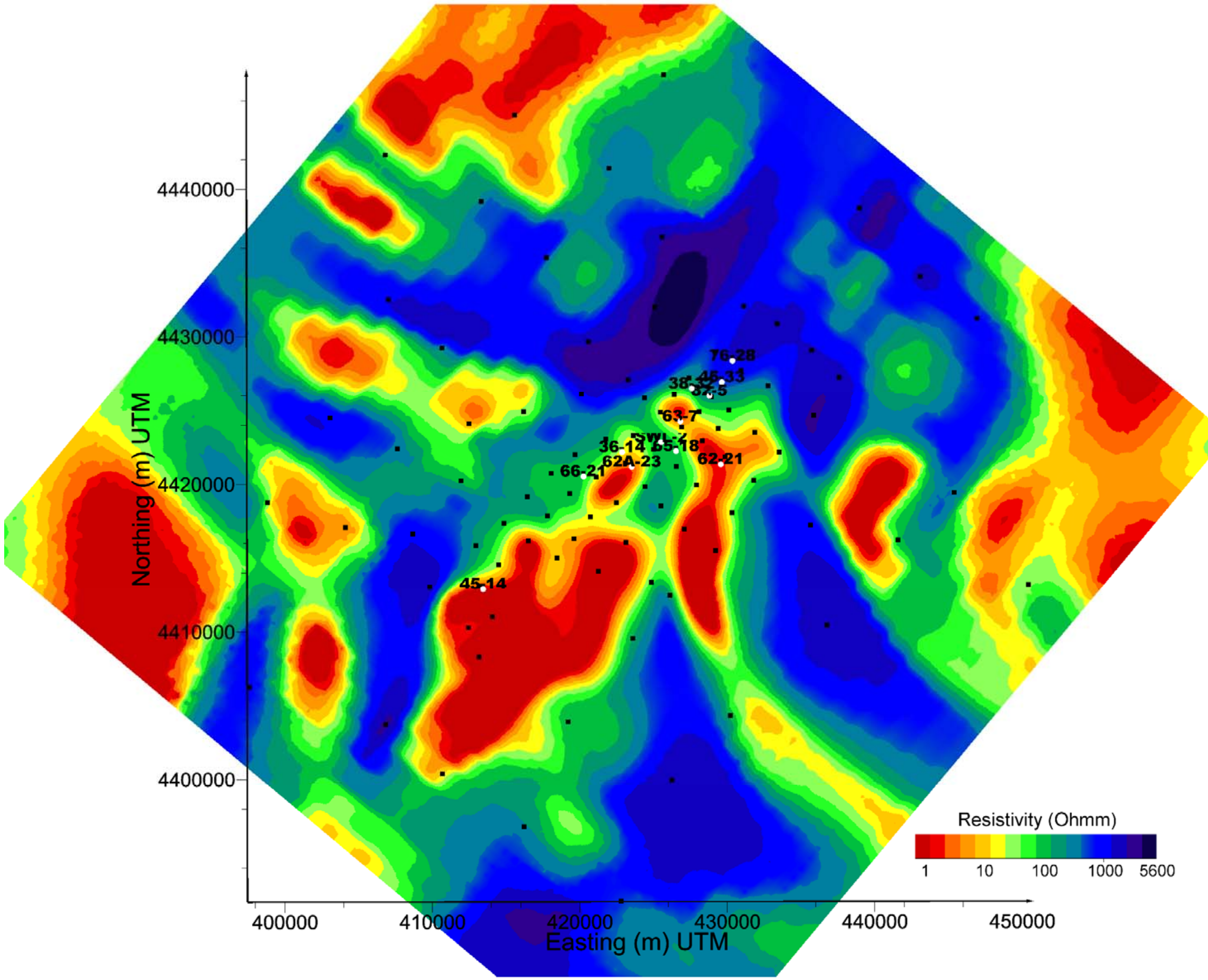

Figure 148. Vertical plan view of the 3D resistivity model from non-linear inversion for a depth slice at 5000m below the surface.

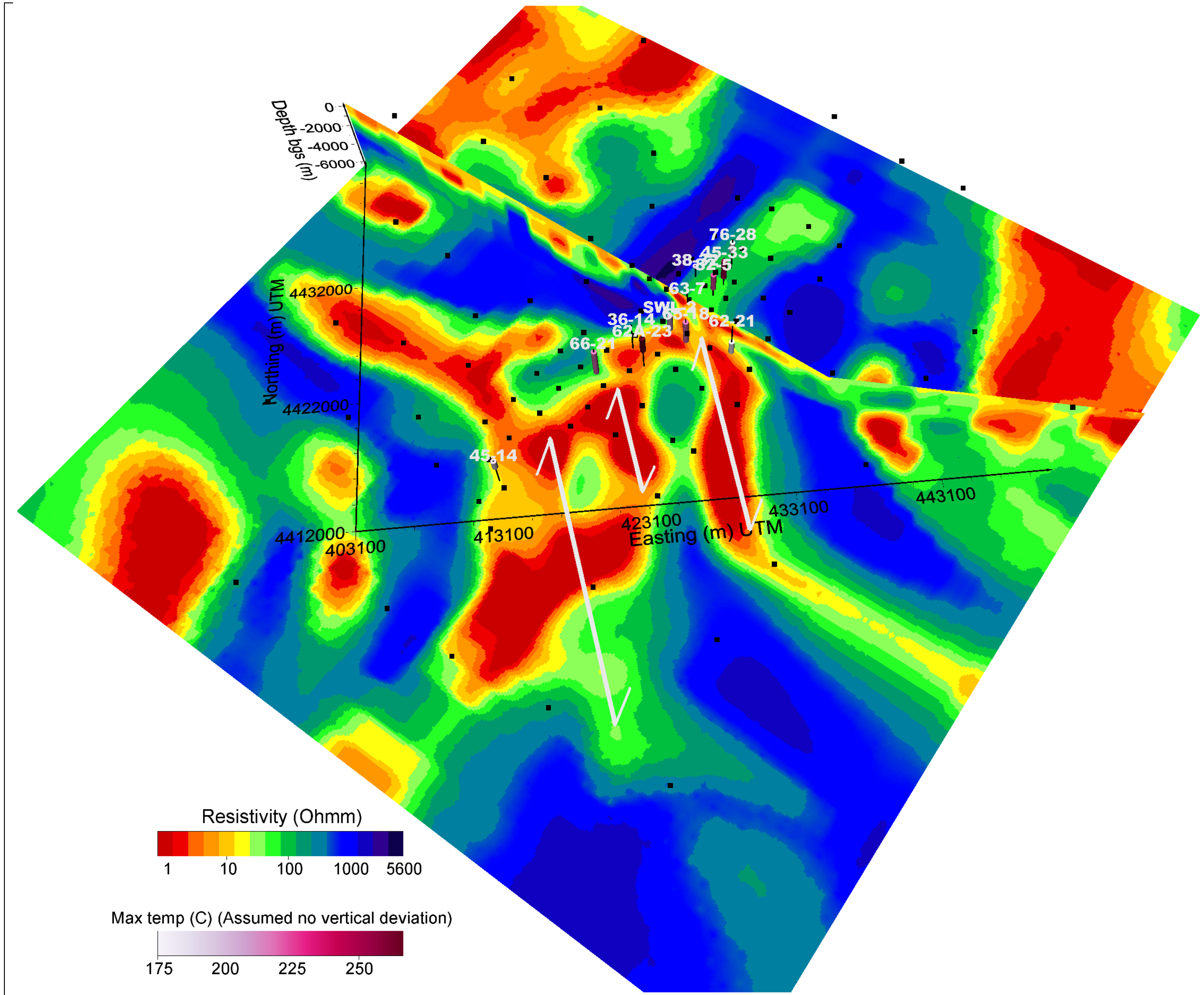

Figure 149. Perspective view from the south of 3D resistivity model for a depth slice at 6500m below surface. Grey arrows suggest approximately N-S conductive alignments together with NE-SW and possible NW-SE alignments. The wells are color coded and have diameter defined by maximum downhole temperature. The MT site symbols are at zero elevation.

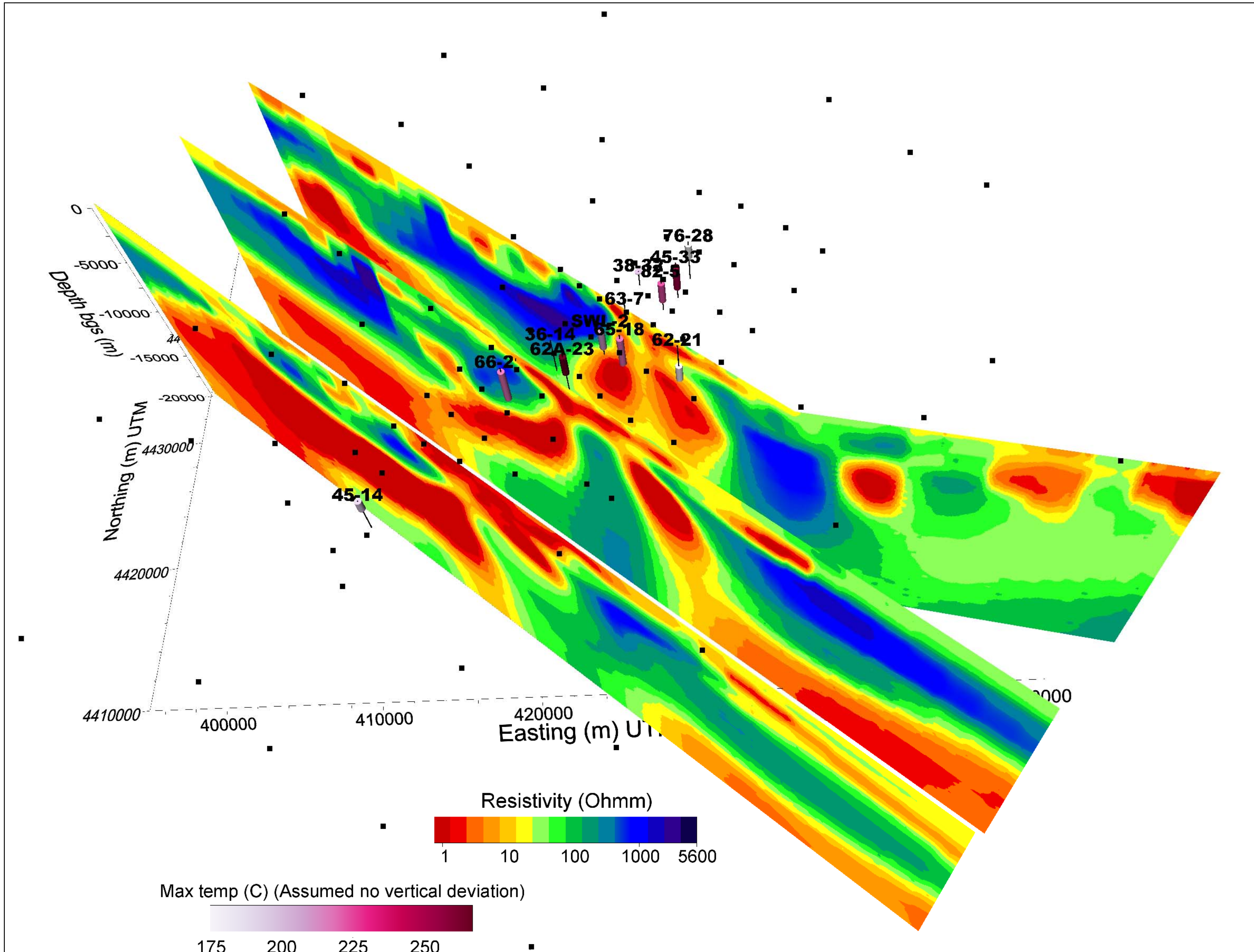

Figure 150. Perspective view from the south of 3D resistivity model in three fence diagrams extending to a depth of ~20km below the surface. The wells are not color coded by temperature here. The MT site symbols are at zero elevation.

9.4 THERMAL MODELING

9.4.1 Conductive Model

Summary

A 3D conductive thermal model for the Project Area (Figure 151) has been developed[16]. The model is based on a 3D basement map and the assumption of conductive heat transfer. Major variations in heat flow and temperature are due to (1) elevation differences of ~1400 m that cause topographic effects on the subsurface temperatures and (2) the geometry of the ~2km thick valley fill that causes the refraction of heat due to the thermal conductivity difference of approximately a factor of 100 % between valley fill sediments and basement/range rock types.

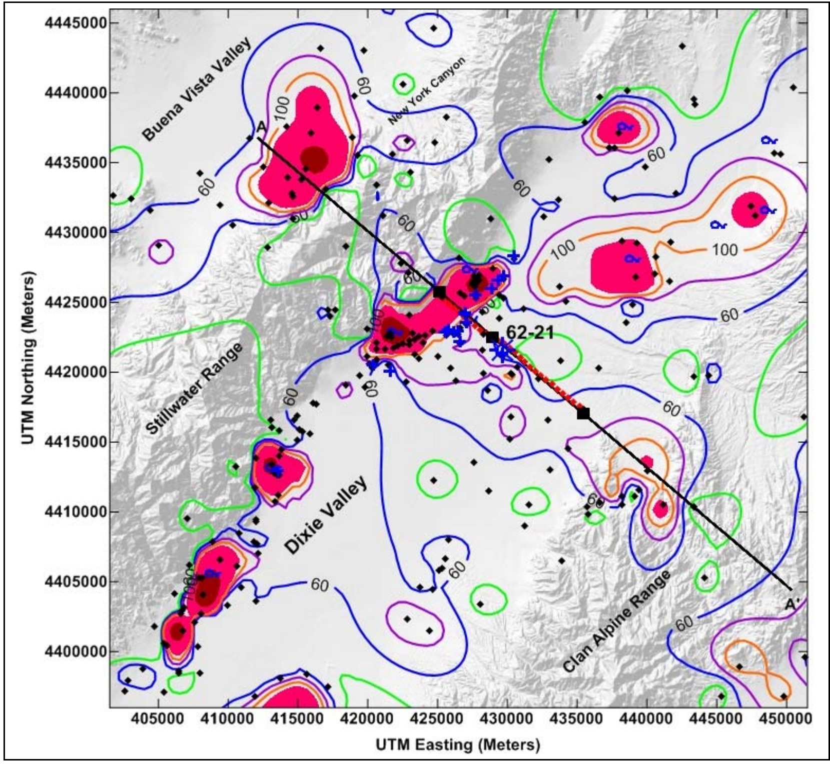

Figure 151. Thermal gradient and well locations of Dixie Valley project area. Contours intervals are 20°C /km. The contours in pink color represent thermal gradient from 150-300°C/Km. Red fill represents thermal gradients more than 300–500°C/km. Springs in Dixie Valley are shown in blue color. The black squares represent synthetic well locations TD1, TD2 and TD3 identified in Figure 12C.

A 3D inversion of gravity data is used to infer a depth map of valley fill sediments. A pseudogravity transformation of magnetic data is used to model the possible effects of the Humboldt mafic igneous complex in the central and northern part of the Dixie Valley. The temperature distribution due to the refraction of heat flow is quantified as a function of shape of valley fill geometry. Both refraction and topographic effects tend to enhance geothermal gradient in Dixie Valley. Refraction due to the thermal conductivity contrast and shape of the valley fill sediments causes heat flow variation about 30% of the 90 ± 30 mWm^{-2} average regional heat flow. Moderately high heat flow anomalies along the valley range contact can be due to refraction of heat flow and may not be associated with any geothermal system.

Introduction:

The Dixie Valley geothermal district (DVGD) is an active regional scale geothermal system with measured subsurface temperatures of up to 285°C at a relatively shallow depth of ~ 3km (Blackwell et al., 2007). The system is considered to be non-magmatic in origin based on helium isotope ratios in the geothermal fluids (Kennedy et al., 2000). However, "…as much as ~7.5% of the total reservoir helium is mantle-derived (Kennedy et al., 2000)." and reported by Kennedy and Soest (2006). Also Lutz et al (2002) have reported magmatic gases in fluid inclusions from select vein material in Dixie Valley.

[16]Section provided by Dr. David Blackwell, Thermal Task Leader, and his post-doctoral researcher, Dr. Mahesh Thakur and has been modified by Joe Iovenitti, the Principal Investigator to include additional information developed by the EGS exploration Methodology Team, as appropriate.

See Section 10.1 for a further discussion of this topic. Nevertheless, the geothermal system is principally related to deep fluid circulation in an area of high regional heat flow. The extensive exploration activity in the area has resulted in a large data set of geological and geophysical results (Blackwell et al., 2007) that allow a unique characterization of the regional thermal regime in a Basin and Range setting as a help to understand the origin and characteristics of the geothermal occurrences there. DVGD is defined as several systems associated with normal fault zones bounding both sides of the Stillwater Range, and Dixie Valley, and both sides of the Clan Alpine Range (Figure 152). Most Basin and Range geothermal systems are fault- controlled, but the detailed structure of the systems is still debated (Wright, 1991). The meteoric water which recharges in the ranges is heated during deep circulation in an area of high heat flow and highly fractured upper crust and ascends along the range bounding fault system (McKenna and Blackwell, 2004; Blackwell et al., 2000; 2007).

Faults that cut sediments in the valley floor adjacent to the main topographic displacement, including piedmont faults (Bell and Katzner, 1987), are resurfaced so quickly by alluvial and eolian processes that evidence of surface rupture along these faults is quickly buried. Large gravity gradients on the west side to the valley define a large structural offset between the basement and valley fill that is 1 to 2km basin ward of the range/valley contact (Blackwell et al., 1999) and shows that along much of the steep east side of the Stillwater Range, piedmont faults in the valley accommodate most of the displacement between the range and the valley bottom.

The section describes a 3D steady state subsurface temperature of the Dixie Valley EGS Exploration Project Area (Figure 151) due to conduction only. The Project Area is defined by a 50km x 50km square (Figure 151) 5km deep with respect to the valley floor. Its boundary coordinates in UTM WGS84 as easting and northings are (401500, 4446000), (451500, 4446000), (451500, 4396000), (401500, 4396000). Existing and new thermal data are assembled and analyzed from Dixie Valley to generate and develop a 3-D temperature model and improve the resolution of crustal thermal structure and rock type estimates in the Dixie Valley for development of exploration concepts for EGS resources using a wide range of geological and geophysical data (Iovenitti et al., 2011; 2012; 2013).

The regional geology of Dixie Valley and west central Nevada has been described by Willden and Speed (1974) and the local geology has been extensively studied by Speed (1976). The geology of the Dixie Valley geothermal reservoir rocks in the order encountered in the majority of the drill holes is shown in Figures 152. In majority of drill holes rocks are encountered in the following order (unpublished Oxbow report by A. Waibel), Quaternary basin fill sediments (Qal), Silicic tuff-rich sediments (Tts), Miocene Basalt (Tb), Miocene Sediments (Ts), Miocene Rhyolites, Oligocene silicic volcanics (Tsv), Cretaceous granodiorite (Kgd), Jurassic Oceanic crust (Js & Jpg), Jurassic marine sediments (Jms) and Triassic marine sediments (Trc). All Dixie Valley geothermal reservoir rocks are exposed on the Stillwater and Clan Alpine Range.

Data

Regional Heat Flow of Dixie Valley

The shallow temperature gradient map of the study area is based on 503 thermal gradient wells (less than 500 m deep, Figure 152). Shallow thermal gradient locations in the public domain are shown as black diamonds. Thermal gradient for Dixie Valley study area is contoured using contour interval of $20^{o}C\ Km^{-1}$, contours with geothermal gradient between 150-$300^{o}CKm^{-1}$ are filled with pink and high geothermal gradients between 300-$500^{o}CKm^{-1}$ are shown with the dark red fill (Figure 152). The high geothermal gradient anomalies are mainly located along range-valley contacts along the western edge of Dixie Valley (Stillwater Range), and along antithetic faults on the eastern side of Dixie Valley.

Heat flow values for ranges and valleys were averaged separately because of their difference in the topography and the geology. For calculating the background heat flow within the Dixie Valley, wells that were in the Dixie Valley as were separated from the wells outside of the valley. The task of calculating the background heat flow also required removing all the wells that had been affected by geothermal water circulation; as a result of this condition wells in the vicinity of anomalies shown were not included in the analysis. Most of the wells in the Senator Fumaroles and DVPP (Figures 151 and 17A) were excluded for example. Using the remaining data, 78 well sites, the background heat flow was calculated.

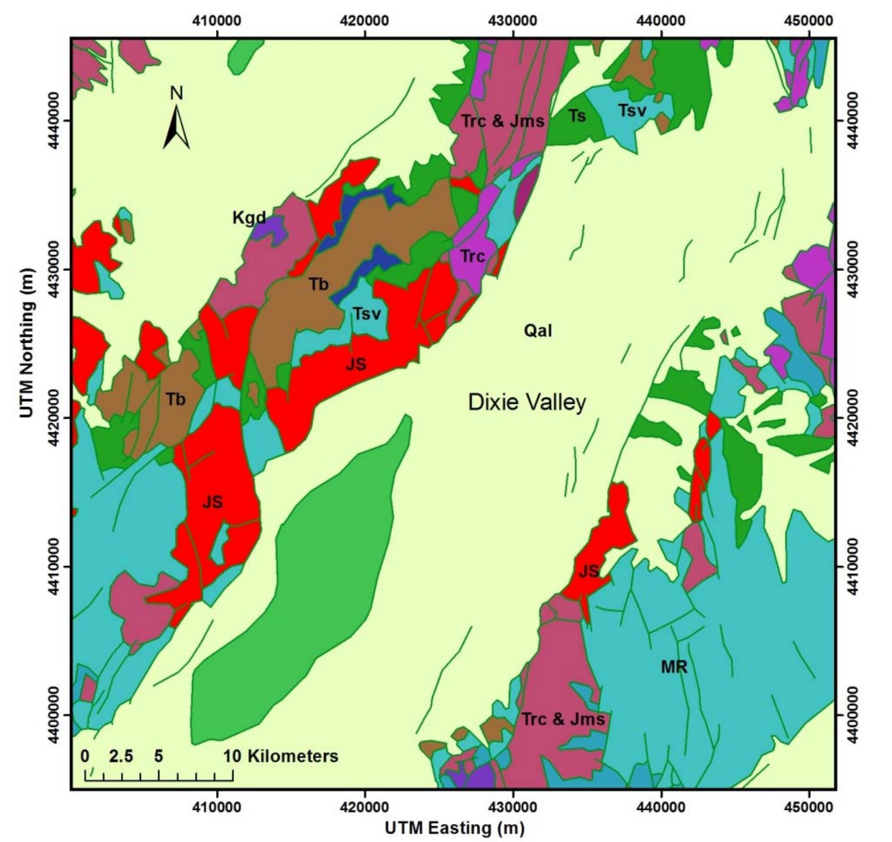

Figure 152. Geologic map of Dixie Valley (map source USGS). Quaternary basin fill sediments (Qal), Silicic tuff-rich sediments (Tts), Miocene Basalt (Tb), Miocene Sediments (Ts), Miocene Rhyolites, Oligocene silicic volcanics (Tsv), Cretaceous granodiorite (Kgd), Jurassic Oceanic crust (Js & Jpg), Jurassic marine sediments (Jms) and Triassic marine sediments (Trc).

A frequency distribution of the thermal gradient data is shown in (Figure 153). The most of the data lie between 48-60^{o}CKm^{-1}. A Gaussian curve fit to the distribution showed a peak at 63^{o}CKm^{-1}. Parts of the high gradients in the distribution are probably due to the convective transfer of heat and there is no straightforward way to differentiate the convective part from the conductive part. Allowing for some high bias, a gradient of 55^{o}CKm^{-1}was chosen to be the best value representing the purely conductive heat flow in the valley. Measurement of thermal conductivity of various alluvium samples at shallow depth (<200m) yields thermal conductivity values from 1.41 to 1.5 Wm^{-1}K^{-1} (Blackwell et al., 1994). The average thermal conductivity of 1.25Wm^{-1}K^{-1} assumed in the numerical modeling for the valley fill is lower because the sediments in the basin are probably much more clay rich on average than samples from the alluvial fans near the range front (on which thermal conductivity is measured. The average thermal conductivity for the shallow part of the valley fill does not vary much and is 1.41Wm^{-1}K^{-1} to 1.5 Wm^{-1}K^{-1}. Using these values, the background heat flow in the valley is determined to be 81 ± 3mWm^{-2}. As shown below (in Figure 12), the heat flow in the valley varies with depth due to heat refraction effects.

In analysis of ranges, the only 14 wells are available. Thus the range average is poorly determined. Wells that were close to range bounding faults were eliminated from consideration because, in these wells, heat flow might be affected from the circulation of geothermal water along the faults and secondly, wells that are close to the edges are more prone to the terrain effects. Since the geology is not the same in ranges and there were no well samples available, wells were located on a geological map and generic thermal conductivity values were assigned based on lithology. The average value for volcanic rocks was assumed to be 1.4 Wm^{-1}K^{-1}and the value for intrusive and meta-sedimentary rocks was assumed to be 2.5 Wm^{-1}K^{-1}.

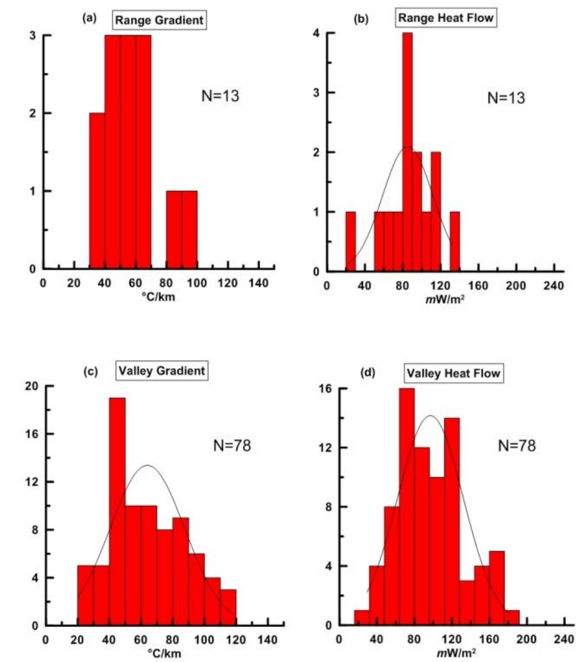

Figure 153. Thermal gradients and heat flow distribution in Dixie Valley

The distribution of heat flow in the ranges as a result of above analysis is shown in Figure 153. The heat flow values are quite dispersed and do not clearly define an average value. The most prominent factors in this data inconsistency are the distortion of regional heat flow due to terrain effects, the small number of available data points, and the lack of thermal conductivity data. Since most of the wells were drilled in small valleys within the ranges and the wells are shallow, the apparent heat flow might be higher than the background heat flow in these wells. Looking at distribution, highest frequency is observed around 91 mWm^{-2}, which can be considered as the average heat flow in ranges. The wells in the range will be further studied for topographic effects and a topographic correction will be applied to access the range heat flow. Two large-scale effects play role in the average value of the ranges: First, the terrain effects, which require detailed study of each well to make a viable correction. Second, the refraction effect due to the thermal conductivity contrast between valleys and ranges.

Refraction of heat affects both ranges and valleys. Since valleys are filled with low conductivity materials and ranges are filled with high conductivity material, higher than average heat flow is found in ranges and less than average heat flow is found in valleys (Blackwell, 1983). The regional heat flow in the vicinity of Dixie Valley is 82 mWm^{-2}, which is close to the average heat flow of the Basin and Range region of 85-90 mWm^{-2} (Lachenbruch and Sass, 1977; Blackwell et al., 1991).

Magnetics

The bedrock geology of the Dixie Valley/Stillwater Range area is very complex and the various units have large differences in physical properties that will need to be taken into account in preparing synthetic temperature models from non-thermal geophysical data. For example there are large masses of dense, high velocity magnetic mafic rock present in the area, a lithology not typically found in the upper crust. These bodies will affect the interpretation of all the geophysical data. The next sections of the report briefly address the quantification of this problem in a general way.

High resolution aeromagnetic surveys were flown over part of Dixie Valley (Grauch, 2002). The high resolution aeromagnetic data reveal subtle, northeast-trending linear to sinuous features superposed on large amplitude anomalies produced by magnetic bedrock (Grauch, 2002). Unfortunately this high resolution data do not cover the entire Project Area (Figure 1-Grauch, 2002). We downloaded regional magnetic data for all of Nevada from the USGS website (Kucks et al., 2006). USGS magnetic data are girded at a spacing of 1.5-3km and depict the magnetic field measured or calculated at 305 m above ground. Magnetic data for the Project Area varies from -400 to 750 nT (Figure 154). Magnetic data by Kucks et al. (2006) covers the area of interest (includes Stillwater Range, Dixie Valley, Clan-Alpine Range and Buena Vista Valley), and can be used for pseudo-gravity inversion in and around Dixie Valley. The magnetic data for Nevada by Kucks et al. (2006) was in Geosoft Oasis Montaj format and therefore we rescaled the data by 3875000m for northing and 500000m for easting.

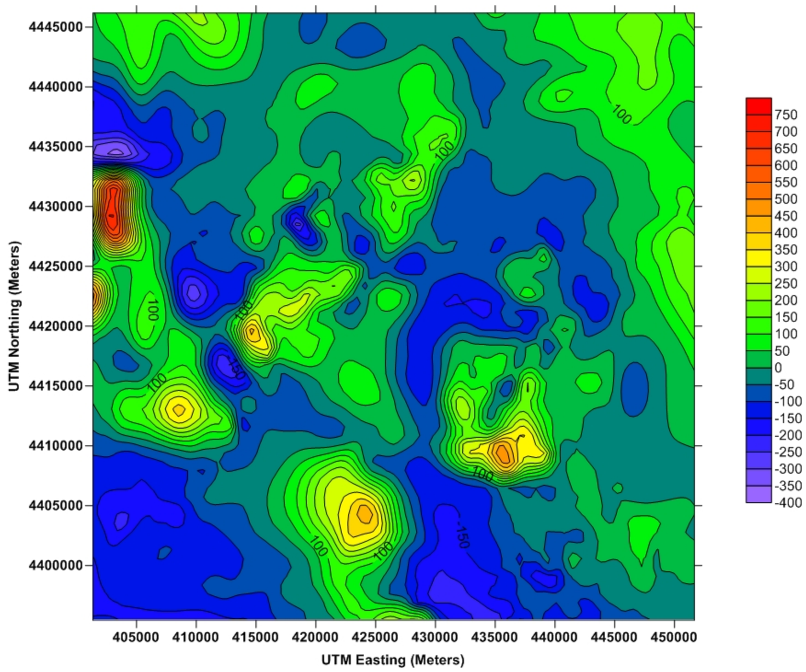

Figure 154. Magnetic field data units (nT) used to infer pseudo gravity for Dixie Valley

Gravity

Three gravity surveys cover the area around and in between Stillwater and Clan Alpine Range.

1. Regional gravity data are available on CD-ROM published by NOAA (Hittelman et al., 1994). These data consist of scattered lines across the valley and bench marks points; which were used to produce the Gravity Map of Nevada (Saltus, 1988). Blackwell et al. (1997) used this data set for control in producing the regional Bouguer gravity contour map. The absolute reference of this survey was an average of the gravity values available for bench marks in the area that were measured and for which gravity data are available from the US Coast and Geodetic Survey (Blackwell et al., 1997).

2. AMOCO completed a Bouguer gravity survey with relatively dense control in the Dixie Valley was available to Oxbow (SRC, 1979). There is no information on the details of the survey, the quality of the data, the correction made, etc. The point locations were digitized from a 1:62,500 scale map and the values of the points input with the location. A total of 464 gravity data points were extracted from AMOCO Bouguer gravity survey and merged with other gravity data. Additional gravity data (total 225 stations) collected by SMU Geothermal Laboratory in Dixie Valley in August 1996 were compared with AMOCO data and they agree within ± 1 mgal when a constant is subtracted from the AMOCO data (Blackwell et al., 1997).

3. Merging the different gravity data sets from AMOCO (464 gravity stations), SMU data (1996, 2000 480 gravity stations), regional data (1167 gravity stations, Hittelman et al., 1994), and Pirouette Mountains (321 gravity stations, Smith, 1979) yields a total of 2432 gravity data points with complete Bouguer gravity anomaly around the Dixie valley geothermal system. Figure 155 shows the complete Bouguer gravity anomaly map of the study area.

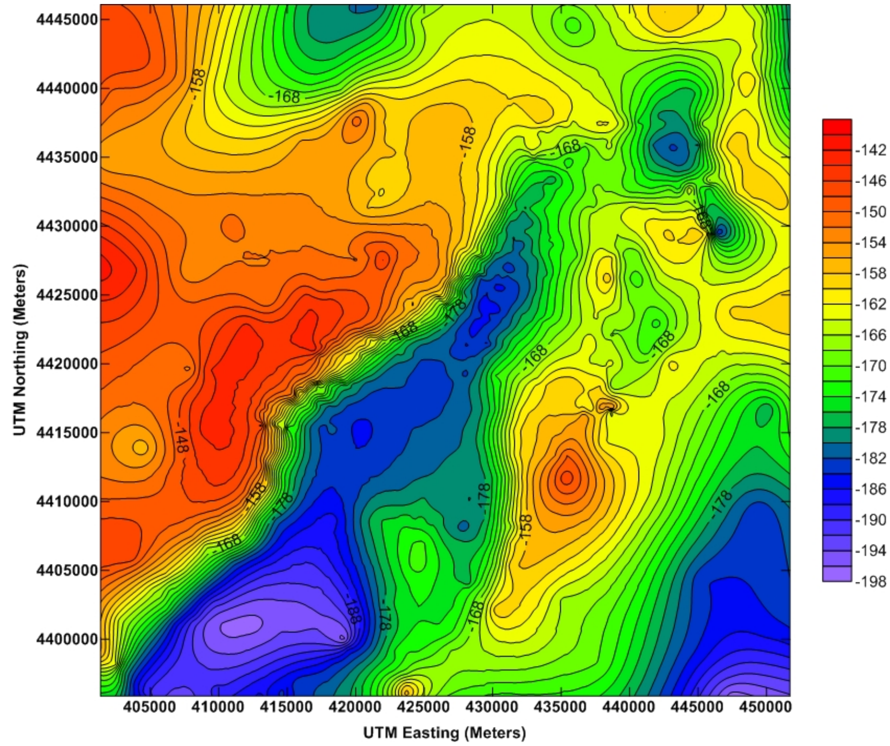

Figure 155. Complete Bouguer gravity (mgal) map of Dixie Valley

Methodology

Pseudogravity

Constant magnetization of material can be converted to gravity like acceleration using the Poisson relationship, called as pseudogravity (Baranov, 1957). The relationship between the gravitational and magnetic potential caused by a body of uniform distribution of density and magnetization can be used to achieve more information of the subsurface geological structures. Pseudogravity anomalies from magnetic surveys can be used to enhance the geologic interpretation of subsurface structures, such as their depth determination. In the Stillwater Range/Dixie Valley area, Triassic marine sediments (carbonaceous shales and siltstones, and silty limestones) of Star Peak Group are the oldest rocks (Speed, 1976). Jurassic mafic igneous complex are tectonically "interleaved" with the Triassic sections (Willden and Speed, 1974). The igneous rocks were originally interpreted to be an intrusive "lopolithic" body of gabbro intruded into the Jurassic and Triassic sediments (Willden and Speed, 1974; Speed, 1976). The origin of these rocks in an oceanic setting is still controversial (Dilek and Moore, 1995). This unit will be referred to in this paper as the Jurassic mafic igneous complex. Therefore, magnetic data from Dixie Valley is used to model the effect of Jurassic mafic igneous complex (Humboldt lopolith) in the central and northern part of the study area.

The empirical relationship between mass-density and magnetic susceptibility, as compiled from Telford et al. (1990) is logarithmically-scaled, therefore is not linear (Figure 151 in Jekeli et al., 2010). This implies that main field is quite uniform in local regions; the magnetization and the mass density, in fact are not linearly related. The mass density variation may be small in the material within a volume, the magnetic susceptibility may vary by an orders of magnitude. For pseudogravity transformation of magnetic field data we assumed a susceptibility value of S = 0.2 and density of 2.7 Kgm^{-3}, the result is shown in Figure 156. Susceptibility value of S = 0.2 used to produce pseudogravity map, produced a gravity anomaly of ~ 20 mgals for the Humboldt lopolith. The pseudogravity anomaly as shown in (Figure 156) is subtracted from complete Bouguer gravity anomaly (Figure 155) with the objective of removing the effect of the lopolith from central and northern part of the Project Area. The complete Bouguer gravity anomaly without the lopolith is shown in Figure 157. The basement depth inferred from gravity inversion was ~ 400m in the southern part of Dixie Valley. The basement depth in the southern part of Dixie Valley increased by 1200m due to lopolith removal, therefore a total basement depth in southern part is close 1600m. The pseudogravity anomaly removal is tentative and needs conformation from seismic studies of Dixie Valley which will provide more robust constrains on the location and thickness of the Humboldt lopolith.

It should be noted that the thermal results shown by the 3D steady state conductive model are independent of effects of Humboldt lopolith in the valley.

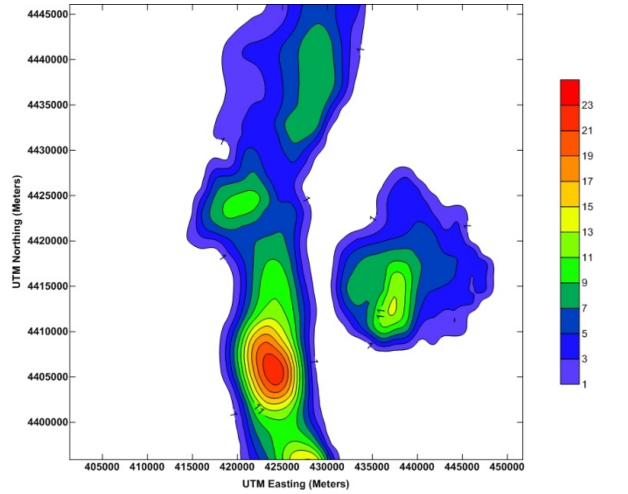

Figure 156. Pseudo gravity anomaly (mgal) used to extract the possible effect of lopolith

Residual Gravity

Dixie Valley is in Basin and Range Province (B&R) which is characterized by a series of north- to northeast-trending ranges and is extensional in origin (Gilbert, 1875, Dickinson, 1979; King et al., 1994; Stewart, 1998; Sonders and Jones, 1999). Continental rift basins have relatively have thin crust of (~25-30km), surface elevations are anomalously high (valleys generally >1-2km above sea level [asl]), suggesting underlying anomalously low mantle densities, compared with other parts of the North American continent. The B&R has been divided into two domains the northwestern Great Basin and southeastern Sonoran-Mexican domains (Stewart, 1998; Dickinson, 2002) separated by the Transition zone in the southern Colorado Plateau. The northern Great Basin Province is dominated by valleys above 1200m asl in elevation, with ranges above 2500m asl, whereas the southern Great Basin contains lower valleys >500m asl. Dixie Valley, itself, represents a low point with mean elevation of ~1100m asl in the western Great Basin.

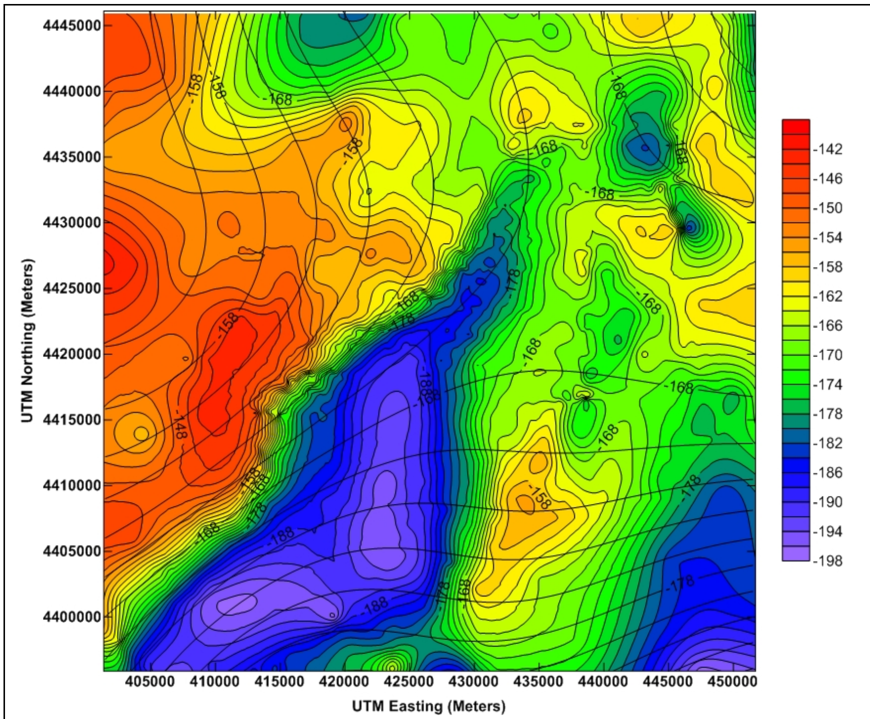

Figure 157. Bouguer gravity map of Dixie Valley area after removal of pseudo gravity anomaly and the effect of lopolith in the southern part of the valley. The regional gravity contours are also shown which are used to extract residual gravity.

The Complete Bouguer gravity map, which shows typical values of -190 mgal in the valley and -150 mgal in the ranges (Figure 155), regional gravity has been subtracted to obtain residual gravity map of Dixie Valley (Figure 158), with residual gravity variation from -26 to 20 mgal. Residual gravity in the valley is -26 mgal and in the ranges is 20 mgal. The residual gravity map of Dixie Valley (Figure 158) is used to obtain basement depth in the valley.

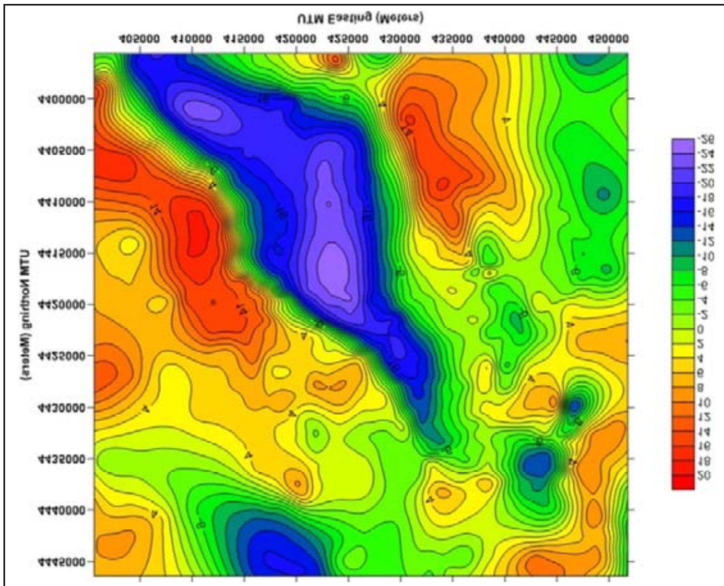

Figure 158. Residual gravity (mgal) of the Dixie Valley, Nevada

Inversion of Gravity Anomaly

Residual gravity data from and around Dixie Valley was iteratively inverted for basin depth using the prism method described by Cordell et al. (1968). In this method, the gravity body is digitized on a rectangular grid and it is assumed that the causative body can be approximated by means of vertical prisms, each having a cross- sectional area of one grid square and a uniform density. In this method once the density and reference plane depth are specified, the gravity effect due to the prism element vertically beneath the grid point is a function of only prism thickness and relative position. The largest error $\Phi_n = \sup \{|g_{obs,\,p} - g_{cal,\,n,p}|\}$: for all p, then the rate of decrease of Φ_n is a measure of the efficiency of the iterative process. The largest error Φ_n is less than 0.005 gals after second iteration and total of 10 iterations were performed. A MATLAB code for inversion of residual gravity data using Cordell et al. (1968) method was used. A grid spacing of 1km and density difference of 165 kgm^{-3} were assumed. The maximum depth inferred by the gravity inversion is 2400m. The 3D basement depth map was then combined with elevation data to obtain a 3D map of the top of the basement in the area (Figure 159).

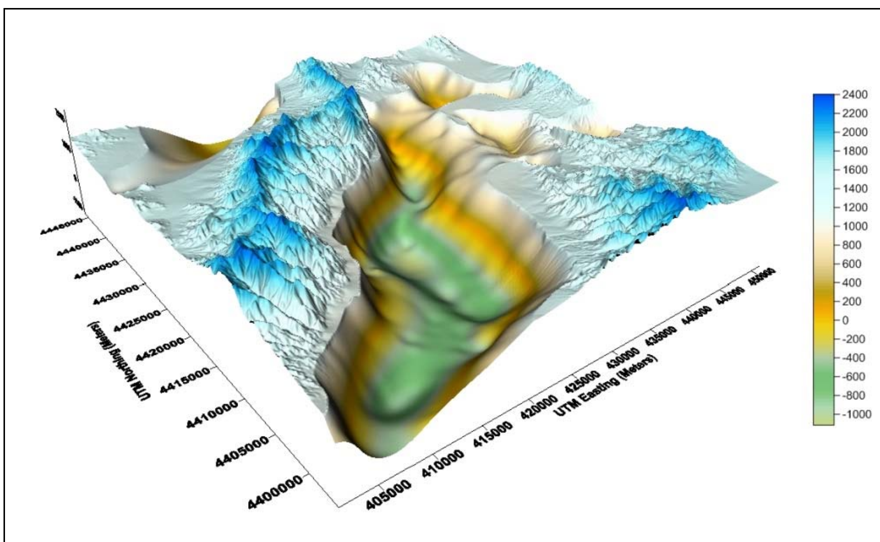

Figure 159. Three dimensional basement depth of Dixie Valley geothermal system as inferred by inversion of gravity data. Also shown in the elevation of the ranges. All heights and depths are in meters and relative to the sea level.

Heat Flow and Geothermal Gradient Maps of Dixie Valley

Forward modeling was used to calculate steady state subsurface temperatures of the Project Area using the model dimensions 50km x 50km x 12km (Figure 160). COMSOL multi physics was used to generate the 3D thermal model of Dixie Valley. A thermal conductivity of 2.5 $Wm^{-1}K^{-1}$ is used for pre-Cenozoic basement and 1.25 $Wm^{-1}K^{-1}$ for Cenozoic valley fill sediments. Boundary conditions used for the model are an inward heat flux of 90 mWm^{-2}, a surface temperature gradient of -4 ^{o}C/Km is applied to account for changes in surface temperature due to elevation with valley surface temperature of 20^{o}C, and the sides of the model are insulated for heat flow. Heat capacity at constant pressure of 1000 $JKg^{-1}K^{-1}$ and density of 2700kgm^{-3} are used. The model is run until steady state solution is reached. The solution generated 3D temperatures for the 3D conductive thermal model. Slices of 3D conductive thermal model provide temperatures at various depths. From these temperature slices, conductive temperatures for the calibrated area are extracted using the UTM coordinates.

Topographic effects due to the elevation difference of ~ 1400m between ranges and valleys control the subsurface temperatures at shallow depths. Refraction of heat flow due to thermal conductivity contrast, of a factor of 2, between valley fill sediments and basement rock also causes variation in subsurface temperatures in the model volume.

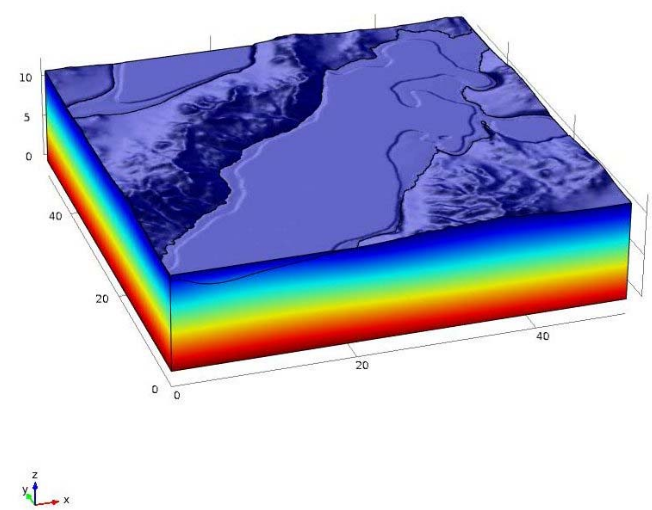

Figure 160. Three dimensional conductive model of Dixie Valley. Temperatures are shown in degree Celsius. The x-axis is 50km, y-axis is 50km and z axis is 12km in this model.

Well 62-21 (location shown in Figures 14, 16A, 17a, 40A, 48, 49A-D, and 67) was used to compare the subsurface temperatures of the 3D conductive model of Dixie Valley to observations. Well 62-21 represents the conductive regime of Dixie Valley, with temperature of 168^{o}C at 2.8km. This well is away from the thermal anomalies caused by hot fluids found along the range boundary fault zone (DVFZ). This well has been logged for temperature 3 times: in February 1987 and August 1991 by SMU Geothermal Laboratory and by Sandia National Laboratory in July 1995 (unpublished SMU data and Williams et al., 1997). The temperature depth curves of well 62-21 and the temperature depth curve from the 3D conductive model are in good agreement with temperature difference less than 10^{o}C between the two (Figure 161).

2D Refraction of Heat Flow in Dixie Valley

Heat flows preferentially through regions of higher thermal conductivity from the interior of the Earth to the surface. In Dixie Valley, high-conductivity basement rocks are buried beneath a blanket of low conductivity sediments; heat is refracted away from the regions of thick sediment cover and preferentially channeled through thinly covered areas. An analytical solution of 2D sinusoidal series of parallel ridges of amplitude and wavelength covered by sediments was provided by Bullard et al. (1956) and they found that more heat flows through the crests compared through the troughs. A semi-ellipsoid packet of sediments to a depth within a basement succession was examined by Von Herzen et al. (1963) and they found that surface heat flow above the packet of sediment $Q_{s,}$ will have a constant ratio to the mean heat flow Q.

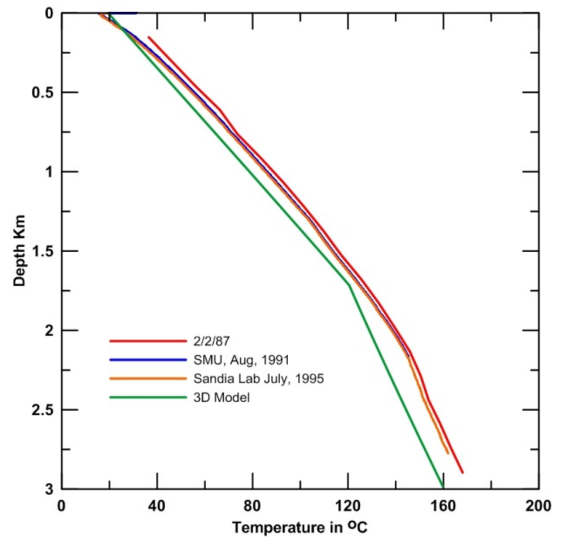

Figure 161. Comparison of temperature-depth curve of well 62-21 with the temperature-depth curve obtained from the three dimensional model.

In an ideal case, where the sediment with low thermal conductivity can be considered as semicircle inside a high thermal conductivity basement rock, the heat flow with depth should be constant within the sediment basin even though the base of the sediment is curved. To study the effect of vertical variation of heat flow due to refraction, the 2D seismic cross-section Line 6' is shown in Figure 151 as the red points, was modeled. A 50km profile A-A' (Figure 161) where depth of the basement is constrained by the seismic Line 6 (Figure 162b). The model dimensions are 50km x 14km, heat flow of 90 mWm^{-2} on the bottom boundary, side walls are thermally insulated, and the top boundary is a constant surface temperature of 20°C (Figure 162a). Basement rocks have a thermal conductivity of 2.5 $Wm^{-1}K^{-1}$, valley fill sediments are 1.25 $Wm^{-1}K^{-1}$ and basalt layer is 1.76 $Wm^{-1} K^{-1}$. The vertical heat flow variations due to heat refraction are shown in Figure 162c. Even though the basal heat flow is 90 mWm^{-2}, the calculated heat flow varies from 60-120 mWm^{-2} within and around the valley.

Vertical Variation of Heat Flow

To understand vertical variation of heat flow in sedimentary valley fill due to heat refraction, three vertical slices of heat flow with depth are taken at the three locations TD1 at 17km, TD2 at 22km, and TD3 at 27.5km shown in Figure 162c. The horizontal distances for these three hypothetical well locations shown as back squares on Figure 161 are measured from point A at 0km in the cross-section A-A'. The location of site TD1 is also shown in Figure 162c. The heat flow at site TD1 (Figure 163) decreases from 120 mWm^{-2} at the surface to 90 mWm^{-2} at a depth of 5km. This site is located in basement block but it is close to the edge of the sedimentary basin. Due to the proximity of site TD1 to a large thermal conductivity contrast (the steeply dipping contact between basement rock (2.5 $Wm^{-1}K^{-1}$), and the sedimentary fill (1.25 $Wm^{-1}K^{-1}$), the high flow (120 mWm^{-2}) is caused by focusing of heat along the contact between basement rock and sedimentary basin (Figure 163). Any well which is drilled in close proximity of the basin edge, will show a decrease in heat flow with depth which will be function of basin thermal conductivity contrast and shape of the contact with the basement rock accentuated by the topographic effect.

Site TD2 is located inside the sedimentary basin and intersects three layers; sediments of thickness 2-2.5km, a basaltic layer of thickness 300-500m, and basement rock as shown in Figures 162a and 162c. At site TD2 the heat flow at the surface is 72 mWm^{-2} and does not vary significantly in the sedimentary section in the depth range of 2.5km. In the basaltic layer the heat flow increases from 65 mWm^{-2} to 72 mWm^{-2}, but in the basement rock at 3km the heat flow increases with depth from 70 mWm^{-2} to 90 mWm^{-2} at 10km depth. In Figure 163, the heat flow for site TD2 show the same pattern; heat flow is constant in the sedimentary basin, but increases with depth in the basement rock. Therefore heat flow varies because of repeated thermal conductivity contrast and shape of the basin.

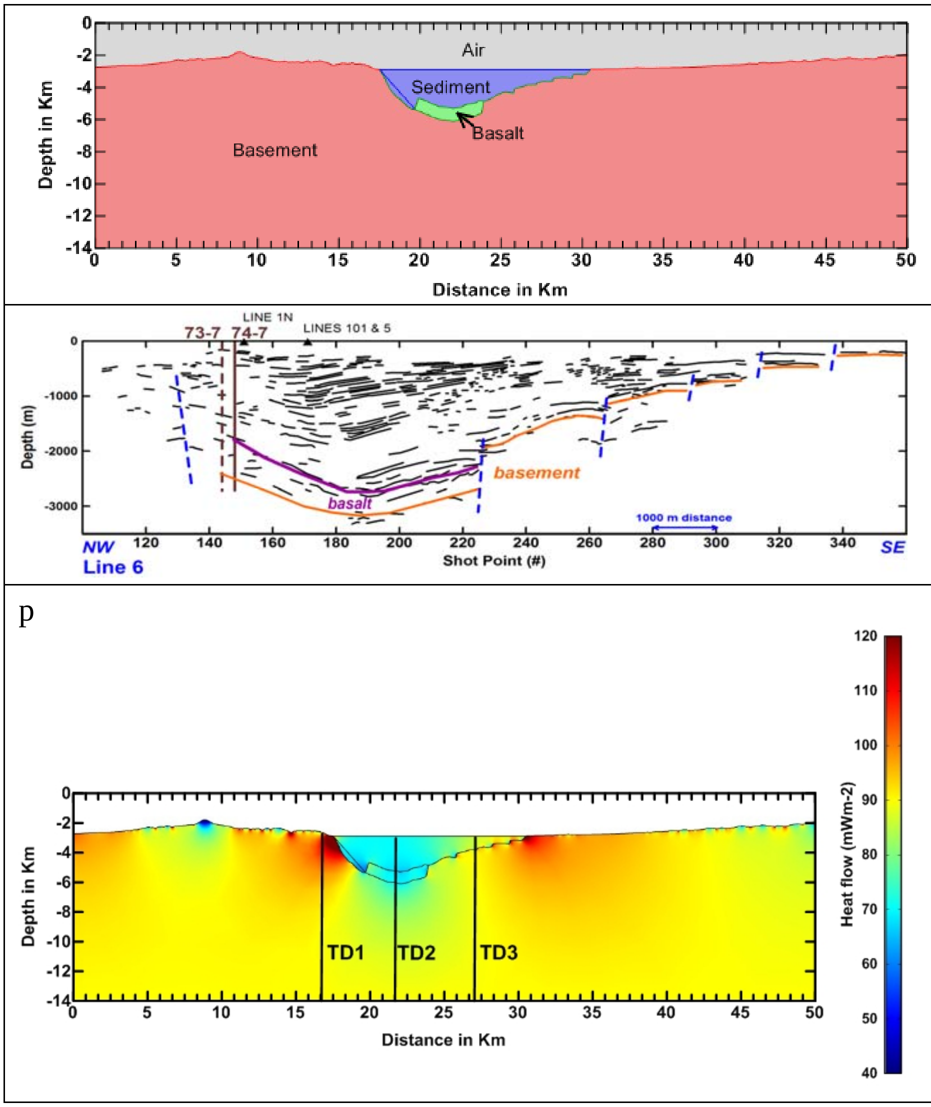

Figure 162. (a) Geometry of the cross-section with three rock types; (b) Interpreted line drawings of the reflection section dip line 6. The vertical brown lines are wells. The blue dashed lines represents approximate fault locations, solid purple and orange are top of basalt and basement; (c) Heat flow variation due to thermal conductivity contrast between sediments and basement rock.

Site TD 3 is located on the gently dipping slope on eastern edge of the Dixie Valley asymmetric basin, which has small antithetic faults (Figure 162b). Heat flow gradually increases near the surface (Figure 162c) from 60 mWm^{-2} to 90 mWm^{-2} to 120 mWm^{-2} on the western edge of the basin. Heat flow does not vary much with depth in this well, in the upper 1km heat flow increases from 87 mWm^{-2} to 93 mWm^{-2}, there is a spike in heat flow at ~ 1km and is due to small fault structures. Along the small faults, which are near vertical, there is a large thermal conductivity contrast of 1.25 $Wm^{-1}K^{-1}$ between sedimentary rocks and basement rocks. Due to this contrast small heat flow anomalies occur along the contact and heat flow values are discontinuous across the fault structure. These small heat flow anomalies are the spike in heat flow with depth as shown at site TD3. Below a depth of 1km heat flow is constant at 90 mWm^{-2}.

Heat Refraction in 3D

In the specific case of Dixie Valley, a numerical solution of heat refraction must be used. The 3D conductive model shows that due to shape of the basement and the thermal conductivity contrast of 100% between sediments and the basement, the surface heat flow varies from 60mWm^{-2} to 120mWm^{-2}. The 3D conductive models also show that heat flow will not be constant with depth in the valley. Figure 164 shows the slices of heat flow at depths of 500m below the valley floor (500m asl) and 1km below the valley floor (0m asl).The maximum difference in heat flow will be close to the surface and difference in the heat flow decreases as depth increases. The amount of extra heat in ranges can be as large as 11% of the background heat flow and 25% of the heat flow observed in valleys. The percentage of difference is a function of the (1) valley/range geometry and (2) magnitude of the valley/range thermal conductivity contrast. In Dixie Valley, heat flow in ranges appears to be 25% more than heat flow in the valley as shown in Figure 12a.

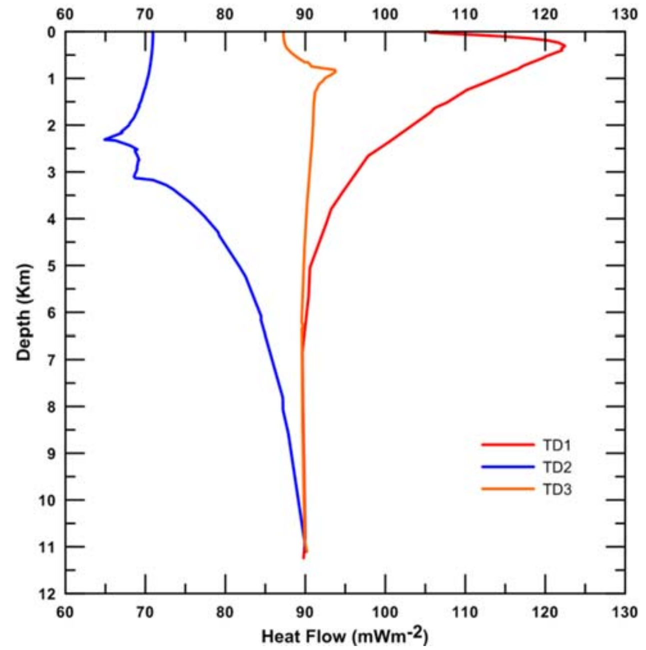

Figure 163. Vertical variation of heat flow with depth for sites TD1, TD2 and TD3. Locations shown in Figure 162c.

The analysis of heat flow with depth shows that in sedimentary basins such as Dixie Valley with depth of sedimentary fill ~ 3km and width ~15-20km, surrounded by basement rocks of high thermal conductivity, there are large heat refraction effects. Based on the three and two dimensional thermal models, the heat flow varies by 100% (~ 90 ± 30 mWm^{-2}) due to the shape of the basement and the thermal conductivity contrast. Wells drilled in the vicinity (~ 2-5km) of sedimentary basins edges, even in the absence of a geothermal anomaly will in general show variations in heat flow with depth. This behavior happens due to the fact that heat flow is focused along the edges of the basins; in other words more heat is flowing than the background in the basement rocks near the edge of the basin. Because of this, wells drilled in the basement rock near the edge of sedimentary basins will show a decrease in heat flow with depth; i.e. changes in gradient with depth will not be accounted by thermal conductivity variation in the well.

3D Conductive Subsurface Temperatures in Dixie Valley.

The thermal regime in the B&R is complicated because of the complex structure and geologic history. The complexity involves both conductive and convective thermal effects. In Dixie Valley major conductive complexities are due to:

1. the difference in thermal properties in the valleys and the ranges; and
2. the resulting refraction effects and to the effects of the topography on the thermal regime.

The convective effects are related to large scale deep circulation of meteoric fluids related to the generation of the B&R geothermal systems and to shallow hydrologic effects due to the topography and the geology. *Hence the thermal regime can be quantified only if extensive thermal data are available.* So development of an independent prediction of temperature would be a step forward in the regional and local geothermal resource delineation in the Great Basin. The basis of the analysis of the thermal regime for the B&R in general and Dixie Valley particularly is described.

A full 3D steady state temperature of the study area is shown in Figure 160. Slices of temperature at various depths relative to the sea level were produced at 1000m, 0m,-1000m, -2000m, -3000m and -4000 m (see Figures 165A and 165C). These temperature depth maps take into account (1) the elevation difference between ranges and valley and (2) the thermal conductivity difference between valley fill sediments and the country rocks. They are based on the assumption of a conductive heat transfer averaging 90 mWm^{-2} and an average thermal conductivity ratio of 1:2 between sediment fill and basement. These temperatures represent a base state for comparison of the thermal effects of convection and as a base case for the effects of temperature in other geophysical property models.

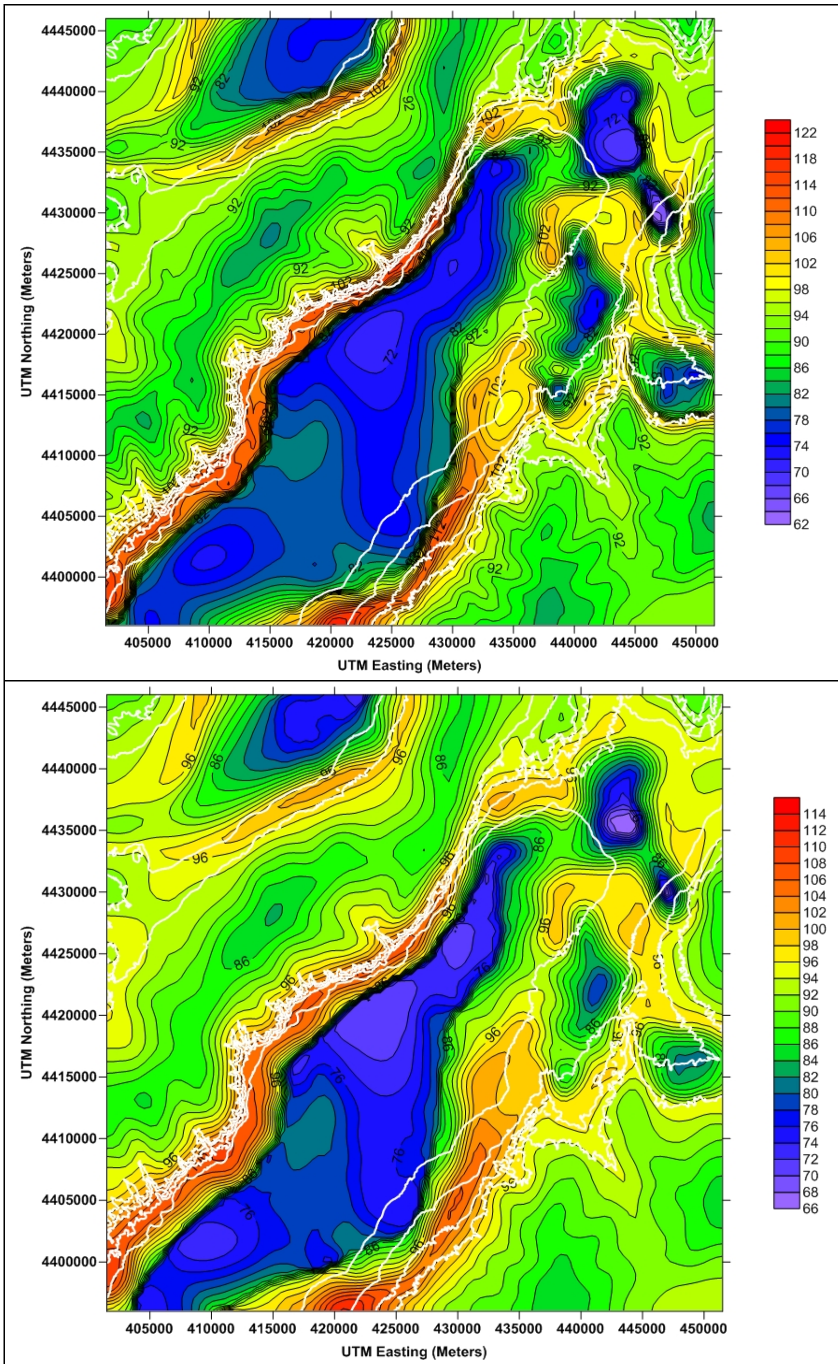

Figure 164. Heat flow slice at depth of 500m asl (a) and 0m asl (b) in the Project Area. Due to thermal refraction, heat flow varies from 60-120 mWm^{-2}.

At 1000m asl, close to the mean elevation of Dixie Valley (1100m), temperatures are higher beneath the ranges compared to the valley (Figure 165A). At a depth of -1km asl the conductive steady state temperatures are higher in the valley compared to the ranges (Figure 165A). Below -1km asl, the valley always has higher temperatures than the range. At a depth of -4000m asl, the maximum conductive steady state temperature reaches a predicted value of 248°C (Figure 165B). Therefore, the 3-D temperature model improves the resolution of crustal geothermal structure estimates in the Dixie Valley for EGS geothermal resources and can be used to compare the temperature estimate from other geophysical techniques in the Dixie Valley.

Due to lopolith removal, the sediment thickness increased from 400m to 1600m in the southern part of the Dixie Valley. Temperature increased from 88°C to 123°C at 1.6km after lopolith removal, temperature increases because sediment thickness of low thermally conductivity 1.25 $Wm^{-1}K^{-1}$ increased by 1200m.The lopolith temperature effect decreases with depth, e.g., at a depth of 5km temperatures are 230°C, which are 22°C hotter because of lopolith removal (Figure 166).

Conclusions

The Humboldt lopolith in the central and northern part of the Dixie Valley will cause high velocities in the seismic studies causing difficulty in the interpretation of the basement depth. Therefore lopolith removal using magnetic data increases sediment thickness in the central and northern part of Dixie Valley is open to various interpretations and needs to be confirmed after a seismic study of the central and northern part of the Dixie Valley. Temperature increases by 33°C at 1.6km and 22°C at 5km due to lopolith removal. A maximum of 248°C temperature is reached at a target depth of 5km in the Dixie Valley using a 3D conductive steady state model. Comparisons of temperature-depth curves from well 62-21 with 3D thermal models predict less than 10°C temperature difference at depth of ~3km. Heat flow variation with depth in a well will depend on well location in/around the sedimentary basin and the magnitude of thermal conductivity contrast between sediments and the basement rocks. Due to topographic effects and heat refraction isotherms will be compressed in the Dixie Valley. The heat flow in the ranges is higher compared to the valley for same elevation and the difference between heat flow decreases with depth.

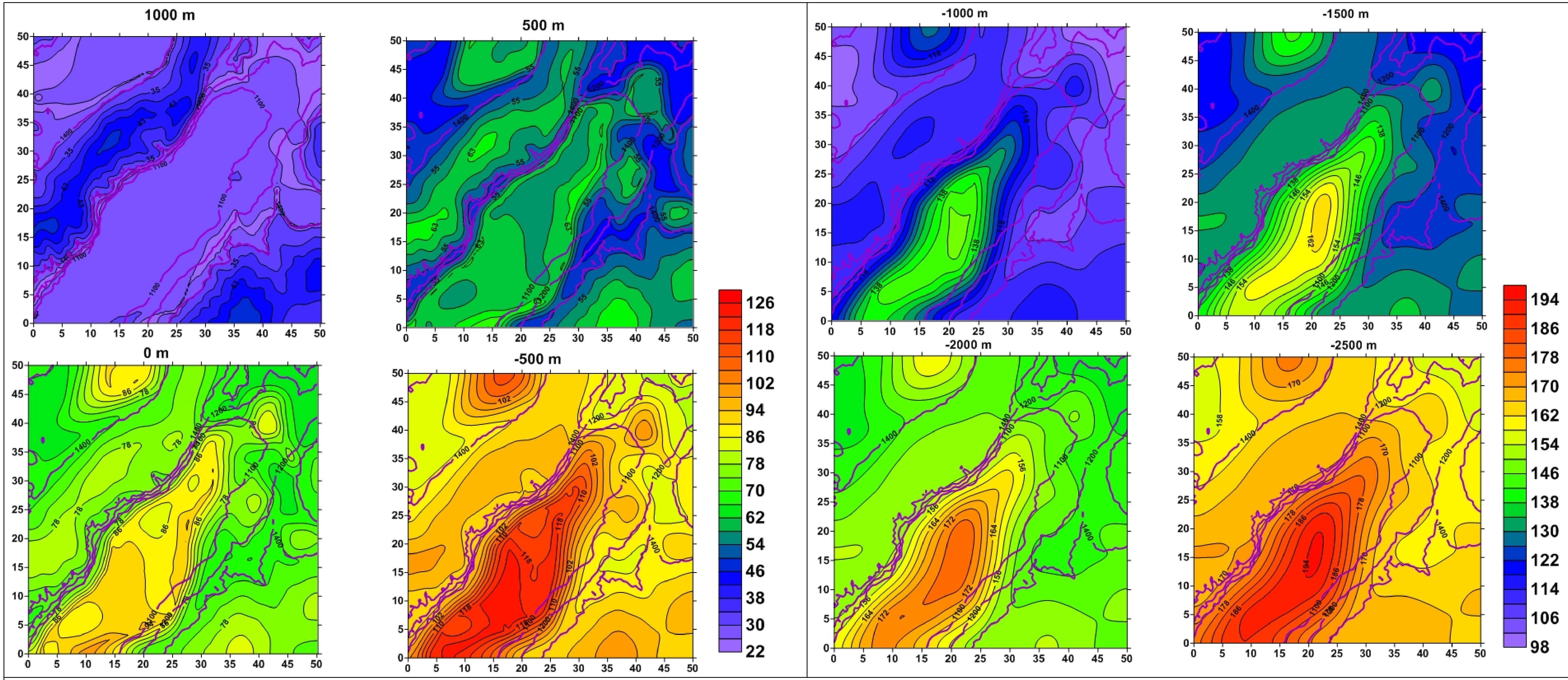

Figure 165A. Conductive temperature slices of the Project Area at 100m asl to -2500m asl in 500m increments. Temperatures are in degree Celsius.

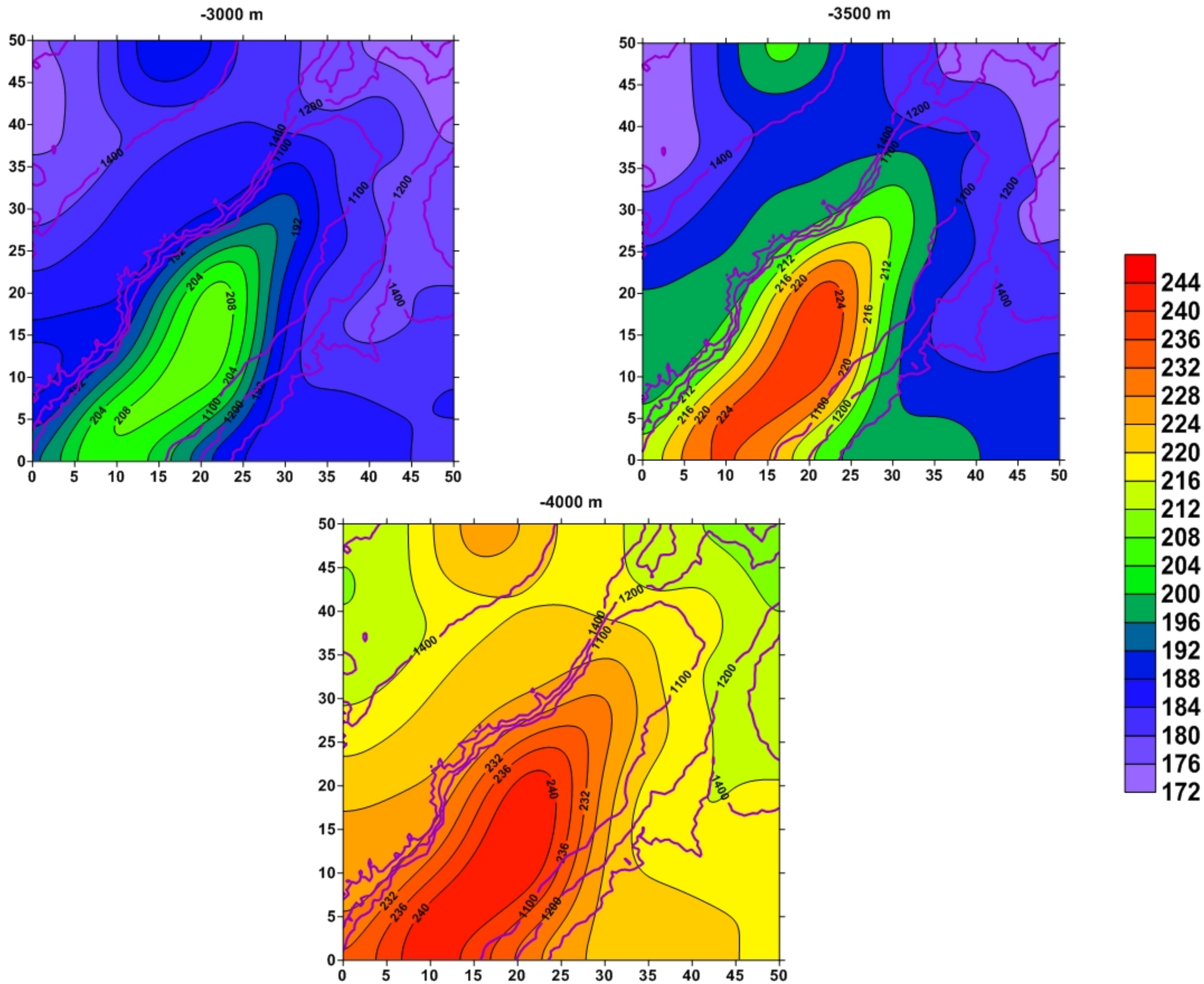

Figure 165B. Conductive temperature slices of the Project Area at -3000m asl to -4000 asl in 500m increments. Temperatures are in degree Celsius.

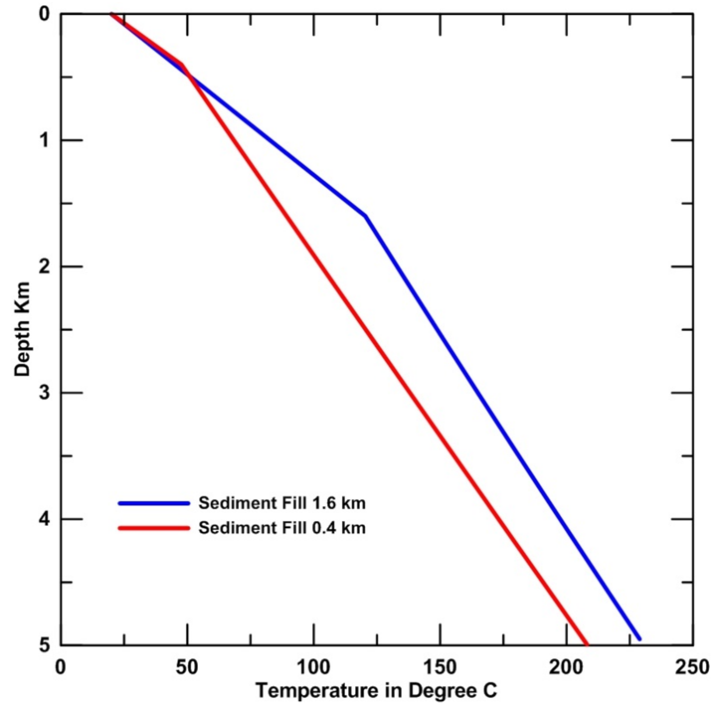

Figure 166. Temperature effect of lopolith, red geotherm represents temperature before lopolith removal and blue geotherm after lopolith removal.

9.5.2 Convective Model

Abstract

A 3D convective model for the local thermal regime of the Dixie Valley/Stillwater Range contact zone has been developed[8] as a part of the Dixie Valley EGS project. This section describes the model of the convective thermal regime based on temperature-depth data from deep wells used to constrain the fault zone temperatures. The model is based on the assumption of conductive heat transfer outside the fault zones (see Section 9.4.1). Thermal sections of the Dixie Valley Power Partners (DVPP) producing area and the Dixie Valley Producing Field (DVPF) area (Figure 1) were constrained by matching the observed temperature data using a two-fault finite difference numerical model (Blackwell et al., 2002). The 2D numerical models are virtually identical even though these two areas, DVPP and DVPF, are located at least 5km apart. Both have similar temperatures of 225°C to 245°C at depths of 2500m. The DVPP area reaches temperatures in excess of 265°C below 3000m. The fluid flow has operated over a long enough time that the thermal regime is near conductive equilibrium in the 3km scale. The 2D model was expanded to 3D based upon the temperature and geological constraints provided by area wells, i.e. the temperatures along this portion of the DVFZ fault zone were extracted and extruded to the NE and SW to form a 3D temperature model along the segment of the DVFZ fault zone that is included in the Calibration Area (Figures 1, 48, and 67) and more speculatively extended to the north and south toward the limits of the 50x50km Project Area (Figure 1) as far as justified by present thermal data.

The temperatures in the valley are relatively well constrained but the temperatures in the Stillwater Range have no empirical data to constrain them. They are therefore assumed to be conductive even though on the basis of 2D convection modeling they may not be. Major variations in conductive heat flow and temperature outside the effects of the fault zone flow are due to elevation differences of ~1400m that cause topographic effects in the subsurface temperatures as well as the geometry of the ~2km thick valley fill (see Section 9.4.1). The sediments comprising the valley fill have a significantly different thermal conductivity (~100%) than the basement/range rock types, causing the refraction of heat.

Finally the 3D convective model at thermal equilibrium is compared with the 3D conductive model (Section 9.4.1) and the measured temperatures in the deep wells.

Introduction

The Dixie Valley geothermal system is a large area along a fault zone bounding the Stillwater Range and Dixie Valley in Churchill and Pershing Counties, Nevada (Blackwell et al., 2007). It extends from the Dixie Valley Producing Field (DVPF) on the north side, to the Dixie Comstock thermal area on the south, or possibly as far south as the Dixie Meadows area (which is outside the area of the present study). The DVPF (Figure 1) operated since 1988 has been producing electrical power at a rated output of ~ 62 MW. This field represents the classic Basin and Range active fault hosted geothermal system. The thermal source (285°C maximum) measured temperature in the DVPP area (Blackwell et al., 2000) is deep fluid circulation along the normal fault zone that bounds the Stillwater Range and Dixie Valley. The heating is due to deep circulation in an area of highly fractured upper and middle crust with high heat flow, and without a significant magmatic thermal input. Helium-isotopic studies indicate that as much as ~7.5% of the total reservoir helium is mantle-derived (Kennedy et al., 2000) and Lutz et al (2002) have reported magmatic gases in fluid inclusions from select vein material in Dixie Valley. Numerical modeling of generic natural state Basin and Range 2-D flow systems and specific applications to the Dixie Valley geometry were used to develop constraints on the larger scale aspects of the flow system (Wisian and Blackwell, 2004, and McKenna and Blackwell, 2004). Example conductive and convective thermal cases displayed on a 2D generalized structure model are shown in Figure 167. While there are data in the valley to constrain the temperatures, the implication of cooling in the ranges cannot be tested with the existing thermal data.

These prior thermal modeling studies help in the evaluation of other Basin and Range systems by confirming that the Dixie Valley flow system is probably in a transient state to reach the high temperatures observed in the flow system. The geothermal system is probably in a transient condition related to events on a 10,000 to 100,000 year time frame (Blackwell et al., 2007).

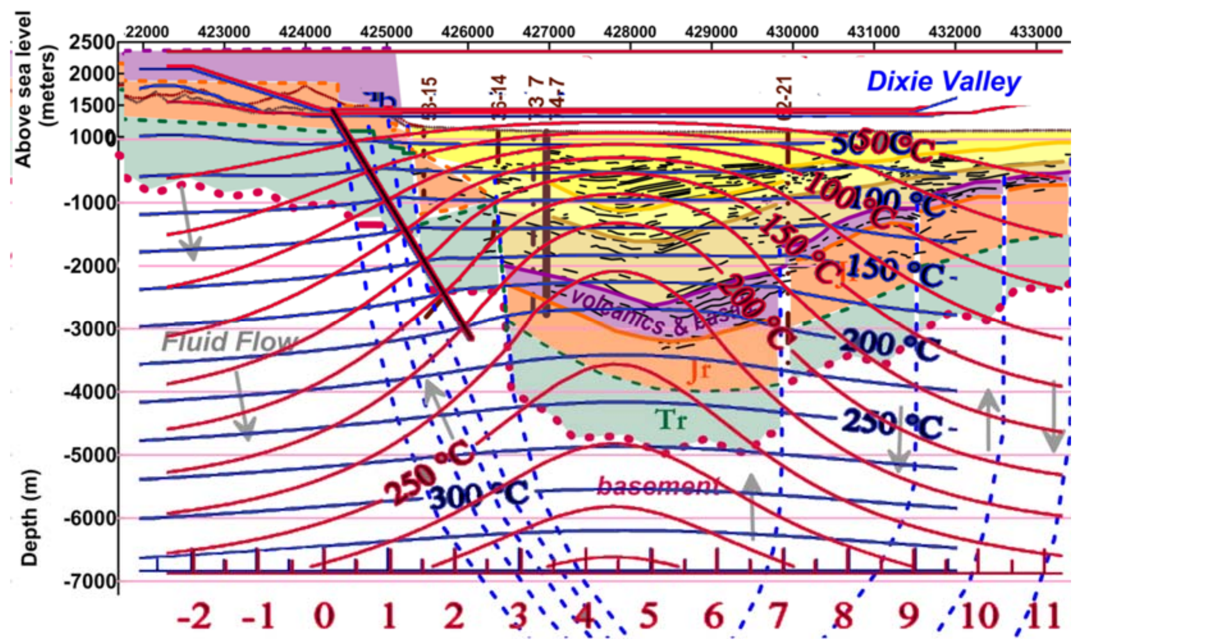

Figure 167. Preliminary conductive (blue contours), steady state 2D convective (red contours), and structural sections

The focus of the convective model temperatures presented below is on the Calibration Area (Figure 1) and the range/basin bounding zone and temperatures outside that area are assumed to be the same as the conductive model.

Fault Locations

There are numerous Quaternary/Holocene faults in the Dixie Valley whose surface evidence is quickly erased by erosion. The evidence for these faults at depth comes from seismic reflection profiles, the high-resolution aeromagnetic surveys, and detailed air photo interpretation (Smith et al., 2002), as well as gravity and magnetic modeling discussed in Section 9.1.1.

The horizontal gradient of the gravity field was used to identify subsurface contacts of greatest density contrast (Blackwell et al., 1999). Surface evidence of piedmont faults & intra-basin faults occurs at or near gravity gradient maxima (Figure 13), many of which have been supported by the current gravity and magnetic modeling results (Figure 98). The terrain slope is the slope of the contours in the direction of steepest descent so it locates the magnitude and direction of the steepest gradient in any area of the map. Two-dimensional modeling of the gravity data (Blackwell et al., 1999) and the gravity-magnetic modeling described in Section 9.1.1 shows that along much of the steep east side of the Stillwater Range, piedmont faults in the valley accommodate most of the displacement between the range front and the valley bottom.

The fault locations in the 3D thermal model are constrained by surface mapping, drilling, seismic reflection, and gravity data as described previously (Blackwell et al. 1999; Smith et al. 2002; Blackwell et al., 2007) and gravity-magnetic modeling presented in Section 9.1.1. The west side in Dixie Valley is relatively well-defined by rapid horizontal changes in the gravity anomaly value because of the piedmont fault system, whereas along the east side horizontal changes are more subdued (Figure 13). Therefore, steepest gravity gradient coincides with the main displacement of valley against bedrock and so defines the location of the "piedmont" fault. This line nearly parallels the Stillwater Range/Dixie Valley topographic boundary but is displaced about 2-3km into the valley as shown in Figure 13. This close parallelism is the justification for the simplification of the fault geometry used in the convective model below.

2D Thermal Modeling

Drilling of the 62-23/62-A23, and 36-14 wells (Figure 45A) demonstrated that the range bounding fault system dips steeply and consists of multiple strands (Blackwell et al., 2000, 2007). A two-fault finite difference numerical model (Blackwell et al., 2002) for the DVPP area based on the temperature and geological constraints from the wells has been described (McKenna and Blackwell, 2004; Blackwell et al., 2007). The two-fault finite difference numerical model position is shown in Figure 168 (cross section A and B, the light blue lines). The geometry of the 2D finite difference models is shown in Figure 45A. The boundary conditions of the 2D thermal model include:

1. a surface temperature of 15°C,
2. an assumed background heat flow of 80 mWm^{-2},
3. thermal conductivity values for the Cenozoic units (1.25 $Wm^{-1}K^{-1}$) and for the pre-Cenozoic rocks (2.5 $Wm^{-1}K^{-1}$),
4. a period of existence of the system of 70,000 years (Blackwell et al., 2007).
5. temperatures on the fault zones derived from drilling as approximated in Figure 169.

Additionally, heat transfer was assumed to be conductive except for convective flow along the fault zone.

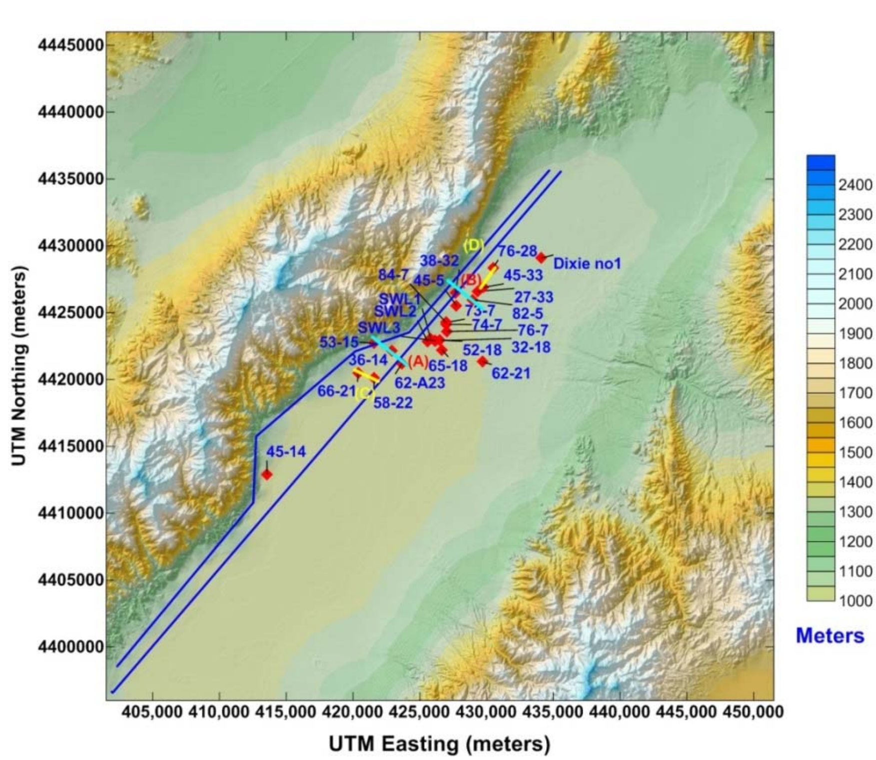

Figure 168. The generalized range bounding fault and piedmont fault (solid blue lines) used for the convective model. Deep well temperature locations are shown as diamond symbols. Thermal cross sections A and B are shown in the figure with light blue color. Sections C and D in Figures 172 and 173 are shown in yellow.

The structural and thermal cross section for the Section 32/33 area of the DVPF (Figures 1 and 40A) is shown in Figure 45B. The existing thermal model from the DVPP area required almost no modification to match the temperatures in well 38-32 in the DVPF area (Figure 45B).

The two areas depicted in the cross-sections (Figures 45A and 45) are about 5km apart and 2km wide, have similar temperatures of 225°C to 245°C at depths of 2500m, and temperatures over 265°C below 3000 m (Blackwell et al., 2007). In this region the fluid flow has operated over a long enough time that the thermal regime is locally near equilibrium in the 3km+ scale range (Blackwell et al., 2007). Therefore these two areas are thermally quite homogenous. The assumed fault temperatures of the range bounding fault and the piedmont fault were extracted from the solution of 2D finite difference model shown in (Figure 170a). The temperatures are constrained using deep temperature -depth data in the range bounding fault and piedmont fault area and are shown in (Figure 169). The fault convective boundary temperatures are based on well 53-15 which is located roughly on top of the range bounding fault and well 36-14 which is located on top of piedmont fault and crosses the block between the two faults (Figure 45A). The temperatures extracted from the 2D thermal model are higher than the conductive model because of fluid flow along the faults. These temperatures are applied to the fault planes in the 3D convective thermal model (Figure 169) assuming that fluid flow in the fault zone only and conduction of heat outside the fault zone.

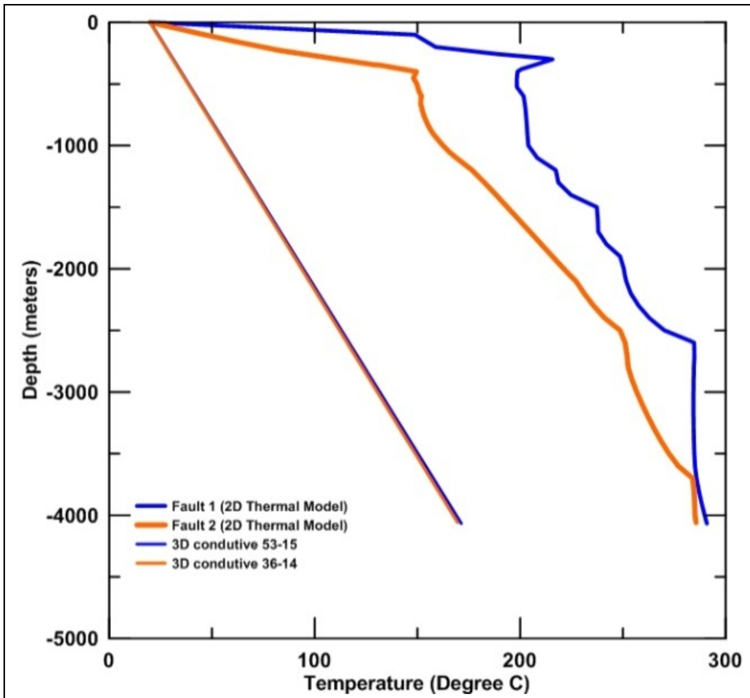

Figure 169. Temperature-depth curves extracted along the two faults in the Dixie Valley model. Also shown are the conductive temperature-depth curves along the range fault (fault 1, close to well 53-15), and the piedmont (fault 2, close to well 36-14, see Figure 45A).

3D Convective Model

The dimensions of the 3D convective model are the 50km x 50km x 5km region of the proposed Project Area (Figure 170). The material properties are the same as in the conductive model: basement thermal conductivity of 2.5Wm^{-1}K^{-1} and a valley fill thermal conductivity of 1.25Wm^{-1}K^{-1} (see Section 9.4.1). Basal heat flow is 80mWm^{-2}, surface temperature is 15^{o}C and other boundaries were insulated. The length of the piedmont fault is ~ 50km, dip is 70^{o} and the depth of fault thermal anomaly reaches to ~4km. The fault planes represent fixed boundary temperature conditions, the range bounding fault has higher temperature than the piedmont fault (Figure 168). The steady-state solution of the 3D convective model temperature maps at 500m depth intervals of the 3D convective model between the elevations of 1000m asl and -4000masl is shown in (Figure 171).

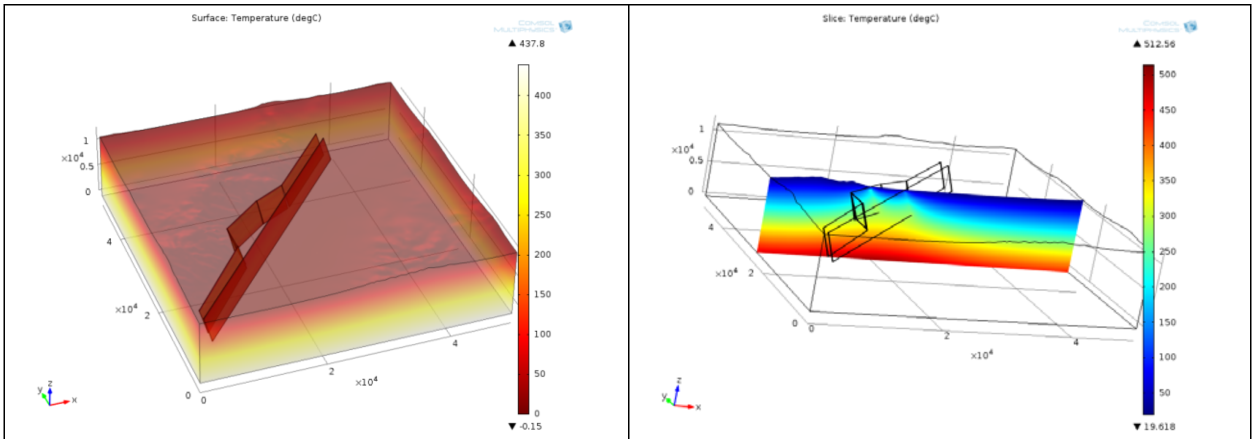

Figure 170. Structure model used for Dixie Valley 3-D convective model. (a) 3D thermal model (°C) of the Dixie Valley study area in with placement of two faults shown. (b) Slice of steady-state temperature solution (°C) within Dixie Valley in east-west direction through the center of the model where the two faults are furthest a part.

Deep Wells and 3D Convective Model

The 3D convective model predictions are compared with the measured temperature depth curves for deep wells in the Dixie Valley EGS Exploration Project Area, in the north to wells 27-33, 45-33, 76-28, in the center to well 66-21, and in the south to well 45-14 (Figures 172 and 173). The measured temperatures in wells 27-33 and 45-33 are close to the 3D convective model temperatures, but the measured temperatures in 76-28 are significantly below the 3D convective model predictions. This result implies that north-east along the range/valley contact from the section 33 producers (Figures 40A and 42), the thermal anomaly approaches background temperatures by 76-28, as shown in Figure 172, unless the well is actually further into the valley with respect to the fault position than projected. South of the DVPP and DVPF (Figure 1) in the southern portion of the study area the measured temperature of 66-21 at the bottom is 42°C lower than the 3D convective model (Figure 173). This implies either there is not as much fluid or cooler fluids flowing along the fault zone in the vicinity of 66-21. A third possibility is that 66-21 is further from the fault than modeled. There is a poor match between the measured temperature-depth data and the 3D convective model for 45-14 (Figure 173). The same three reasons could apply to explain the discrepancy as with the 66-21. The slightly anomalous temperatures and weak flow in both of the southern wells are evidence that the thermal anomaly extends at least between DVPF to the north and the Dixie Comstock site to the south (Figure 1) although conditions may vary along this length. No thermal data exist between the Dixie Comstock and Dixie Meadows areas so the thermal regime of the area immediately south of the area modeled is unknown.

Conclusions

Comparison of temperature-depth data derived from the 3D convective model, the measured temperature-depth data of 76-28, and geothermal thermal gradient map all show that 76-28 marks the northeast edge of the Dixie Valley thermal anomaly. Wells 66-21 and 45-14 indicate that the southern ends of the Dixie Valley thermal anomaly extends in some fashion at least to the Dixie Comstock area. This result is consistent with the 3D convective model and measured temperature-depth data. Currently, heat flow data in the Stillwater Range is limited and is of low quality. Therefore, it is not possible to resolve the issue of whether the ranges are consistent with the predicted temperatures in either the conductive or convective models or not.

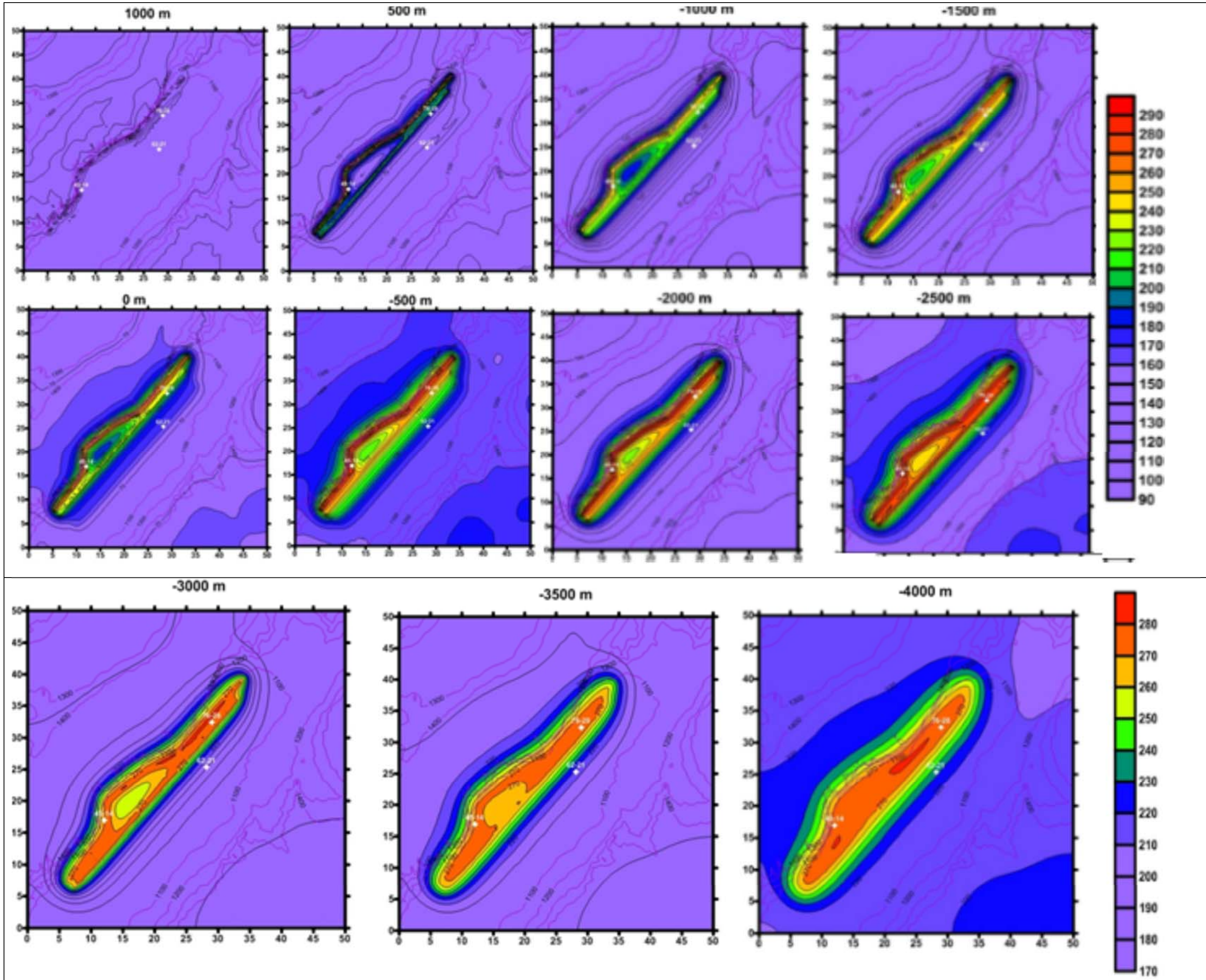

Figure 171. 3D convective thermal model of the Dixie Valley study area. Slices of temperatures are in °C at 500m increments from +1000m above sea level (asl) to -4000m asl. Also shown the location of wells 45-14, 62-21, 76-28 and elevation contours for reference.

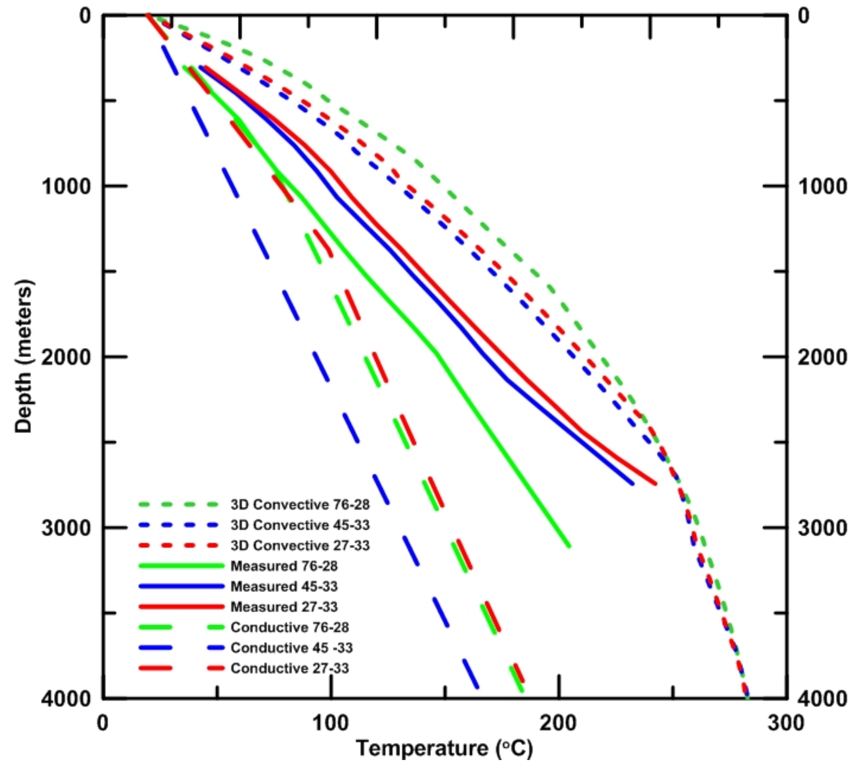

Figure 172. Comparison of measured temperature depth (solid lines) data for deep wells 27-33, 45-33, 76-28 in the Dixie Valley with temperature (dashed lines) extracted from the 3D convective model.

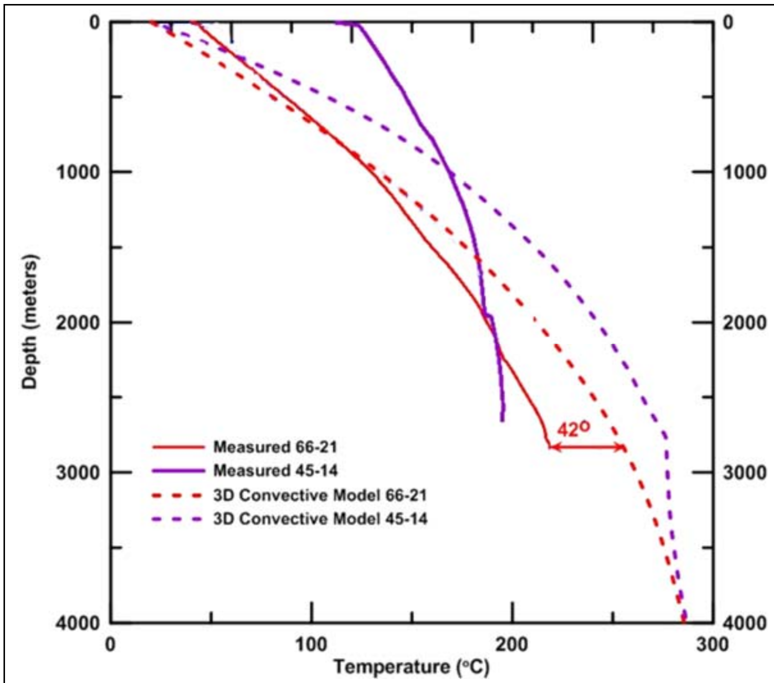

Figure 173. Comparison of measured temperature depth (solid lines) data for deep wells 66-21 and 45-14 in the central portion of Dixie Valley with temperature (dashed lines) extracted from the 3D convective model.

There is no indication of significant heat input from magmatism to the Dixie Valley system and to the high heat flow of the Basin and Range in general. While Lachenbruch and Sass (1978) proposed an "underplating" intrusion model for the origin of the high heat flow, the geological evidence and simple thermal models show that such a thermal model cannot satisfy the geological and geophysical observations (Blackwell, 1986). Kennedy and Van Soest (2007) have concluded on the basis of He-isotopes that there is little evidence of magmatic input into B&R systems in general except those associated with Quaternary silicic magmatism. To cite the conclusions of Kennedy and Van Soest (2007):

> "Our regional He isotope study of fluids across the northern B&R clearly demonstrates a strong correlation between an east-to-west increase in the magnitude of dextral shear strain and an east-to-west increase in baseline He isotope ratios. In the absence of active or recently active magmatism, the elevated He isotope ratios require amagmatic flow of mantle fluids through the ductile lower crust, suggesting that the increase in dextral shear strain rates creates and maintains permeable pathways through the ductile zone. Elevated He isotope ratios in surface fluids along amagmatic sections of the San Andreas fault (*1*) and a recently observed series of nonvolcanic tremors deep (20km to 40km) beneath the same section of the fault provide additional support for the existence of deep-mantle fluids, their potential importance in fault mechanisms (*27*), and nonmagmatic fluid flow through the ductile zone. "

However, MT investigations by Wannamaker (2006, 2007) and this report (Section 9.3.1) suggest the potential presence of underplated material at mid-crustal depths. Fluid inclusion geochemistry of vein minerals in the DVGS by Lutz et al. (2002) suggests the presence of magmatic gases in some of the material analyzed. These relationships are further discussed in Section 10.

9.5.3 Pseudo-Convective Model

Initial considerations of a 3D convective model suggested issues with the lack of thermal data within the Stillwater Range. As a result, an approximation of the convective field for the calibration area (Figures 1 and 48) was developed. We refer to this approximation of the convective field as the 3D pseudo-convective model.

Using all measured temperature data in wells available to the project, the temperature field was modeled along eight cross-sections within the wellfield considering the general hydrothermal model where there are two major thermal-bearing structures in the DVFZ and a fall-off in temperature toward the valley (Blackwell et al. 2005). Cross-sectional data was gridded within 500m by 500m cells and applied to the calibration area at various depths, by interpolating and extrapolating values in Microsoft EXCEL. This model consisted of three types of temperature data (1) measured values, (2) modeled values along the major cross-sections, and (3) interpolated and extrapolated values which filled in missing areas in the calibration area within 1km of the cross-sectional or well data. The temperature model is comprised both the convective and conductive components of the system and is referred to as the overall temperature model. The next step was to take the conductive temperature field determined by Thakur et al. (2012) and grid the conductive data in the same manner described above. \By subtracting the expected conductive temperature component from the overall temperature model, a first approximation of the convective component was derived using the following equation:

$$T_{convective} \approx T_{overall} - T_{conductive}$$

We refer to the Tconvective data as the pseudo-convective component of the system. Figures 174 and 175 present this pseudo-convective model at a depth of -1km asl and -2km asl, respectively, along with faults, shallow thermal anomalies, and the location of active fumaroles. Areas within the Stillwater Range and to the southwest of the producing field are not included in the model due to a lack of data. The model shows that (1) the area within the DVFZ has elevated temperatures as expected, (2) temperatures fall-off and approximates the conductive regime both valley ward towards 62-21 and southwestward towards 45-14, and (3) the location of shallow thermal anomalies and fumaroles correlate with areas that show an elevated convective component. This pseudo-convective model provides a first estimation of the accuracy of the conductive model described above. As such, areas of excess temperature potentially due to convection relative to the conductive model indicated in moderate to warm colors.

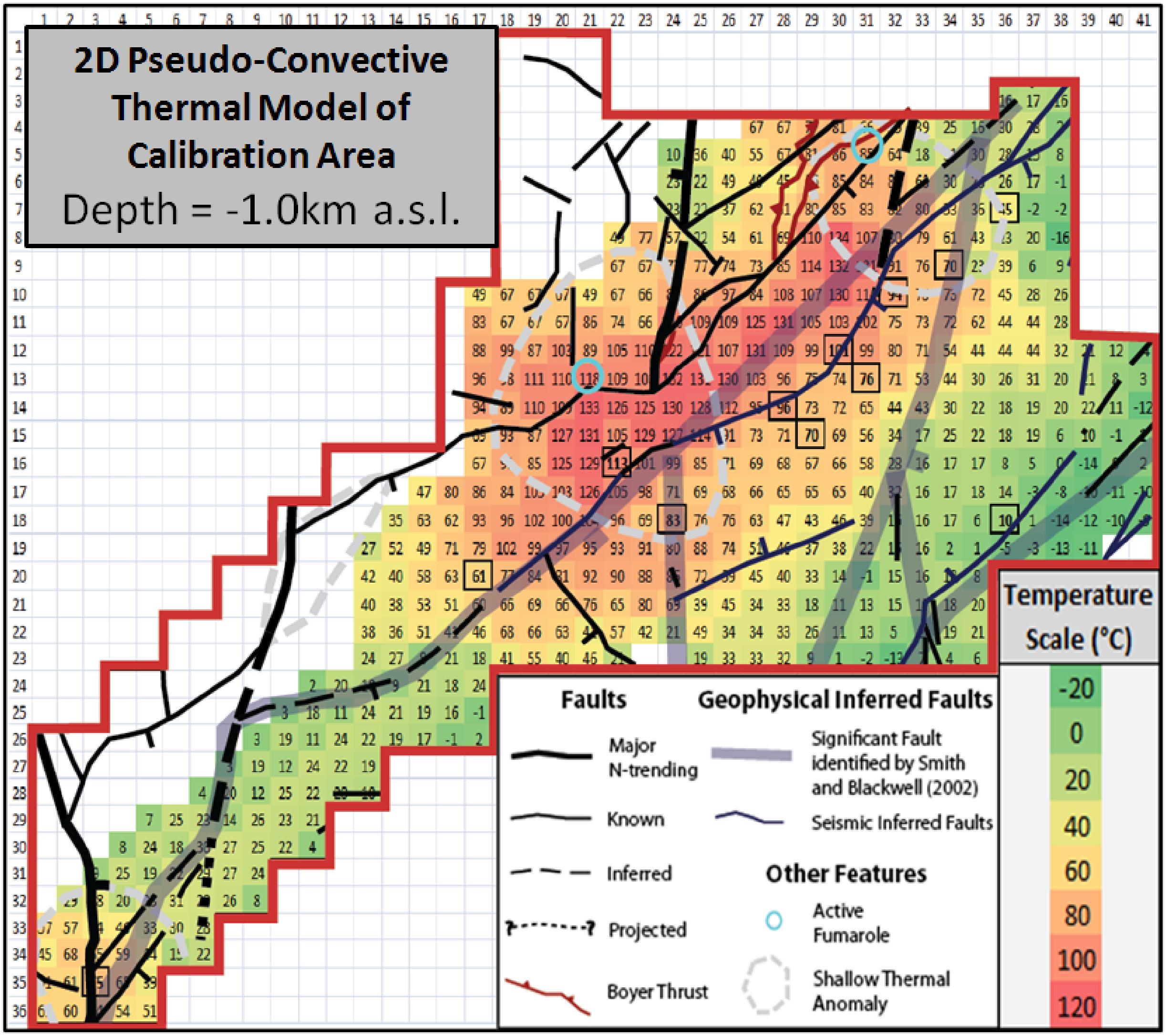

Figure 174. Pseudo-Convective Thermal Model of the Dixie Valley Calibration Area at a depth of 2km (-1km asl) Warm colors indicate a significant convective component, while cooler colors indicate a minimal convective component. Bolded and outlined temperature values represent hard data that was derived directly from a well measurement. The location of shallow thermal anomalies is derived from Blackwell et al. (2005).

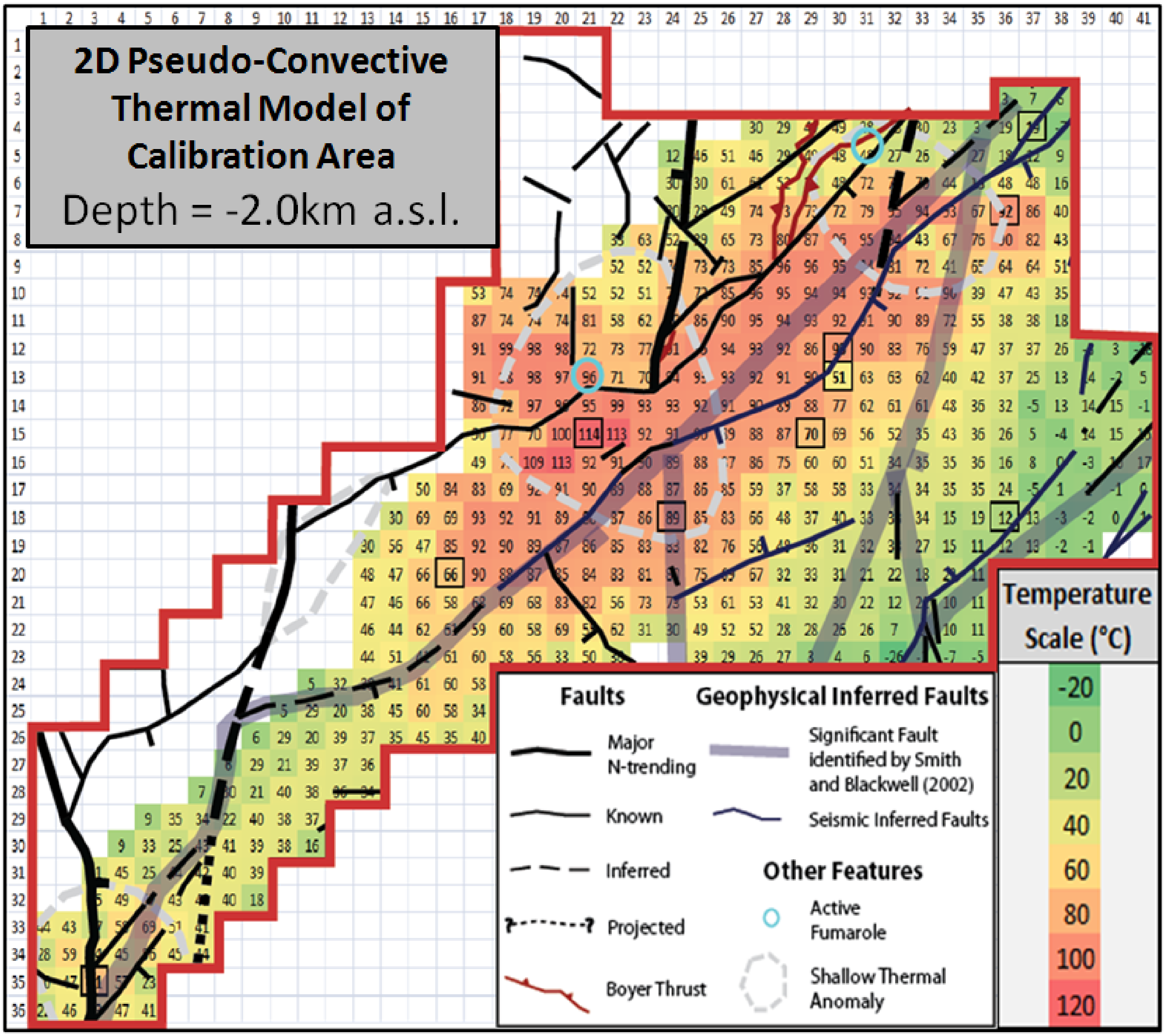

Figure 175. Pseudo-Convective Thermal Model of the Dixie Valley Calibration Area at a depth of 3km (-2km asl). Warm colors indicate a significant convective component, while cooler colors indicate a minimal convective component. Bolded and outlined temperature values represent hard data that was derived directly from a well measurement. The location of shallow thermal anomalies is derived from Blackwell et al. (2005).

10. ENHANCED DATA IMPLICATIONS AND QUALITATIVE CORRELATIONS

The enhanced data set consists of both baseline data (Sections 1-8) and new data (Section 9). Implications of and correlations within the enhanced data developed in this Project, are described below at three different scales (1) regional, (2) Project Area, and (3) Calibration Area.

10.1 REGIONAL SCALE

10.1.1 Pertinent Available Data

There are five geoscientific data sets of varying quality and quantity available at the regional scale as it pertains to this investigation. Each of these data sets is discussed below along with a summary section as to the potential significance relative to the PA and DVGS.

Geology

Figure 176 presents a regional geologic map highlighting the N-S trending structures in the region which formed the basis of a re-interpretation of the structural setting of the DVGS; see Section 7.2. These structures where they intersect the NE-SW trending normal faults have a marked influence in localizing the thermal anomalies along both side of the Stillwater Range and the geothermal reservoir (Section 7.2), and influence the enhanced magnetotelluric data at depths below 5km (Figures 148 and 149) and seismic anomalies (Figures 120, 212, and 122).

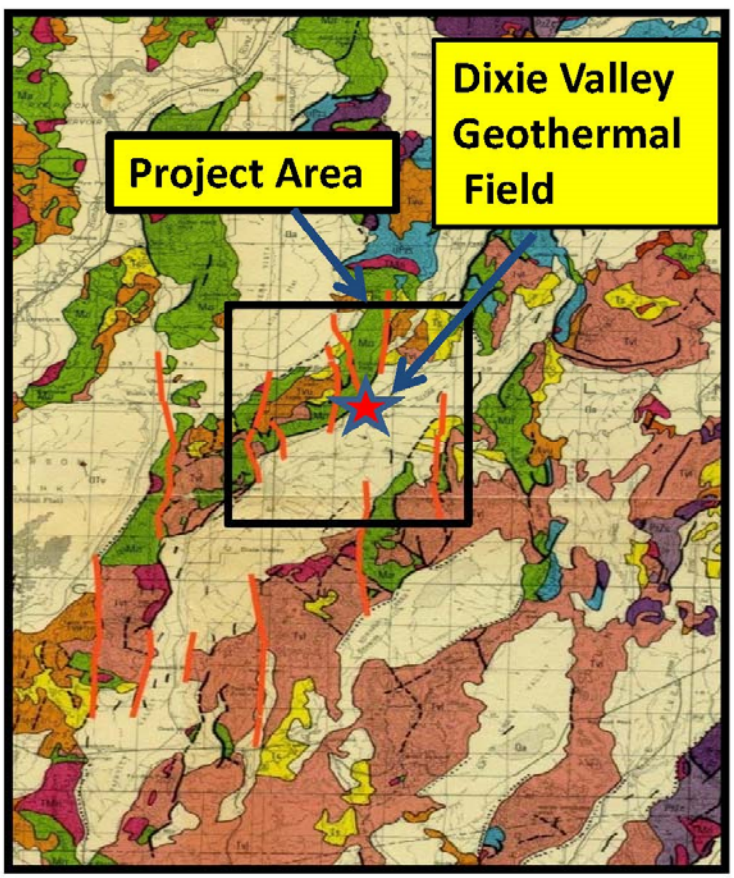

Figure 176. Regional geologic map for the Dixie Valley Geothermal Field (red/blue star). The Project Area is shown in black. Figure is from Stewart and Carlson (1977). North-South trending structures are observed in the Stillwater Range (due west of the geothermal field), in the Clan Alpine Range to the south, and at the north end of the Carson Sink (to the west of the Project Area.

Geochemistry (He data)

Hunt el al. (2011) reported high levels of excess He, He-isotopic data, after correction for atmospheric components, from two geothermal systems on the area of the Carson Sink which lies west-southwest of the DVGW, Brady's Hot Springs and Soda Lake. The excess He in these systems is 10% and 54-59%, respectively, indicating that a magmatic component interacting with the shallow geothermal system. Kennedy and van Soest (2006) reported that ~7.5% of the He in the Dixie Valley system is derived from mantle sources. Lutz (2002) reported a small component of magmatic gas in fluid inclusions in quartz-calcite veins and from production wells based on N2/Ar ratios up to 300.

Hydrology (intra-basin flow)

Dixie Valley lies at the lowest elevation in this part of central Nevada (Figure 4B). If intra-basin flow occurs the general area, there would most likely be a large watershed region feeding into the Dixie Valley geothermal area. Additionally, the N-trending structures may be a fluid pathway between valleys adjacent to Dixie Valley.

Magnetotellurics

Figure 16E presents the results of a 2D inversion of a regional Great Basin MT transect (Figure 177). Wannamaker (2006) has postulated that these results (Figure 16E) evidence multi-scale magmatic-hydrothermal residence zones and pathways to the upper crust and geothermal systems. Of particular interest to this invesigation is the area of suspected magmatic underplating at approximatley 15-20km depth. Note that the transect lines passes north-northeast of the Carson Sink.

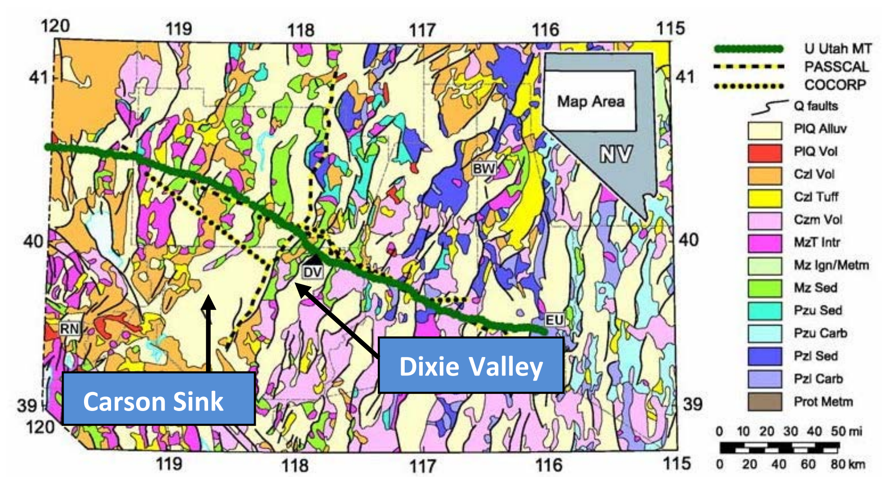

Figure 177. Great Basin magnetotelluric transect line superimposed on a generalized geologic map of northwestern Nevada. Figure is from Wannamaker (2006).

Seismic Data

An E-W trending and a NW-SE trending low Vs anomaly has been defined in the upper crust (<10km depth) and at depths of 10-20km, respectively (Figure 124B). Our Seismic Task Leader (Section 1.4) has interpreted the E-W low-velocity trend in the upper crust as corresponding to the ~ 180km E-W extension along the 40th parallel during the latter part of the Cenozoic (middle Miocene and Holocene) as reported by Bogen and Cshwieckert (1985). This extension was accompanied by volcanism manifested as younger (23-26Ma) calderas identified between Austin and Reno, NV (McKee and Moring, 1996). The NW-SE low-velocity trend corresponds to an earlier extension, in the late Eocene-Oligocene, accompanied by volcanism and calderas 30-36 Ma old (McKee and Moring, 1996). The intersection of the upper and lower crustal trends under the PA may explain the complex system of faults underlying the PA, which is interpreted as a region of elevated crustal temperature (as suggested by a pronounced low velocity in the

SW of the PA). At this intersection, low velocity anomalies start in the lower crust beneath Fairview Peak, "raising" from SW to NW towards the mid-crust, and breaking up in narrower "conduits" at the surface.

10.1.2 Regional Scale Correlations

It is speculated that the deep Vs anomaly in the DVESA may reflect magma underplating found in the regional scale MT data. The elevated excess He-isotopic data in the Dixie Valley, Soda Lake, and Brady's Hot Springs geothermal systems may result from the interaction of deeply circulating meteoric water with mid-crustal depth magma. This would be consistent with the report of magmatic gases in vein material fluid inclusions and production fluid from Dixie Valley by Lutz (2002). However, there is no evidence of magma contributing to the heat flow in the DVGS (see Section 9.4.1). To explain these limited observations, it is speculated that episodic release of mantle material to mid-crustal depths (as evidenced by the seismic and MT data) with accompanying fluid–rock interaction resulting in the elevated He and N/Ar ratios. This interaction however appears to add not significant heat to the overall systems. The presence of N-S structures present in the northern Carson Sink area may facilitate the transmission of fluids from depth to shallower portions of the geothermal system as possibly suggested by the MT data (Sections 9.3.3 and 9.3.4).

Additional the structural intersection of NW-SE and E-W seismic structures at Dixie Valley at mid-crustal depths and the shallower N-S/NE-SW structures intersection may play a significant role in channeling deeply circulating meteoric water + an apparently small amount of magmatic gas from depth into the shallow crust (~3km).

10.2 PROJECT AREA SCALE

10.2.1 Pertinent Available Data

There are four geoscientific data sets of varying quality and quantity available on the Project Area (Figure 1) generated in this investigation.

Geology, Structure, and Shallow Thermal Anomalies

Figure 49A and 49B present a geologic map of the Project Area. The correlation of shallow thermal areas of with identified compression and dilatation zones indicated in Figure 49C. Correlation of the areas of compression and dilatation with known well status are indicated in Figure 49D. Section 7.2.2 provides a detail discussion of these correlations. The fundamental assumption here is that the surface structure and be correlated with the well conditions at depth. This assumption is supported by the results of the enhanced gravity-magnetic modeling described below.

Magnetotellurics

A detailed review of the MT models at depths from 1-20km along with correlation of these data with the enhanced seismic data are presented in Table 19. Presented in Part II-Appendix 11 are the MT aforementioned depth superimposed on the Project Area DEM along with the surface faults identified. These figures compliment Figures 144-150. Basically, the resistivity model identifies the general structural setting of the Dixie Valley Geothermal System area. Note the marked resolution contrast between the MT survey results, on order of 250m in the shallow subsurface, and the ambient seismic noise results, on the order of 5km.

Gravity-Magnetics

Project Area gravity-magnetic modeling results are indicated along four longline cross-sections presented in Figures 82, 86, 92, and 95 and described in Sections 9.1.4, 9.1.5, and 9.1.7.

Seismic

Project Area seismic model results are presented in Figures 107,110, 120, 121A, 121B, 122A, 122B and described in Sections 9.2.3.

10.2.2 Project Area Scale Correlations

While the seismic velocity models for the DVESA scale are useful for identifying episodes of crustal extension and magmatic heat sources at depth (>6km), seismic velocities at the Project Area scale may be useful as a key identifier of fracturing in geothermal reservoirs for shallow formations (<6km). Because the thermal effects on seismic velocities can be seen from the low seismic velocity anomaly covering the Project Area on the DVESA scale, slight variations of seismic velocities from the mean values within the Project Area may be used to infer various degrees of fracturing and fluid saturation at that scale. O'Connell and Budiansky (1974) proposed theoretical constraints on the effective elastic properties of rocks based on the presence of fractures and fracture density. They also found that the degree of fluid saturation causes significant variation in the effective values of elastic moduli for fractured rocks. Figure 178 plots the ratio of fractured/un-fractured Vs, Vp, and Vp/Vs to give effective values of these seismic properties on the vertical axes against fracture density on the horizontal axes $\varepsilon = N\{a^3\}$, where N is the number of fractures per unit volume, and a is the mean fracture radius. The curves in the plots represent varied degrees of fluid saturation ξ from 0 (dry) to 1 (saturated). Both the effective Vp and Vs decrease with increasing fracture density but at different rates, which causes Vp/Vs to increase in saturated fractured rocks and decrease in dry fractured rocks.

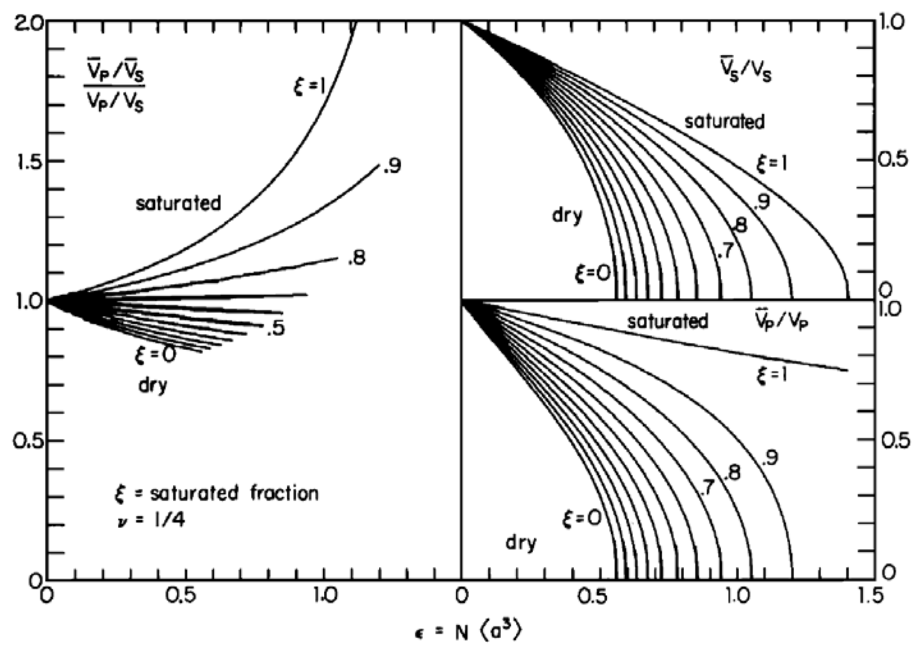

Figure 178. Effective shear wave velocity (upper right figure), compressional wave velocity (lower right figure) and velocity ratio (left-side figure) for a partially saturated cracked solid. The figure is from O'Connell and Budiansky (1974).

If the local mean values of Vp, Vs, and Vp/Vs are used to approximate the 'un-fractured' values, then variations from the mean values can not only be used to infer degrees of fracturing locally, but can also be used to distinguish conventional geothermal resources from potential EGS areas when compared to local temperature anomaly maps (Figure 179 a and b). Higher Vp/Vs anomalies with high conductive geothermal gradients, such as in the northeastern part of the Calibration Area correspond to conventional geothermal reservoirs, whereas areas with lower Vp/Vs values and high gradients such as near well 45-14 in the southwestern part of the calibration area represent potential EGS stimulation targets. Higher degrees of fractures can also be corroborated by the presence of large fault intersections that locally concentrate stress and increase fracture density as evidenced by surface mapping and at depth from horizontal gravity gradients (Figure 179c).

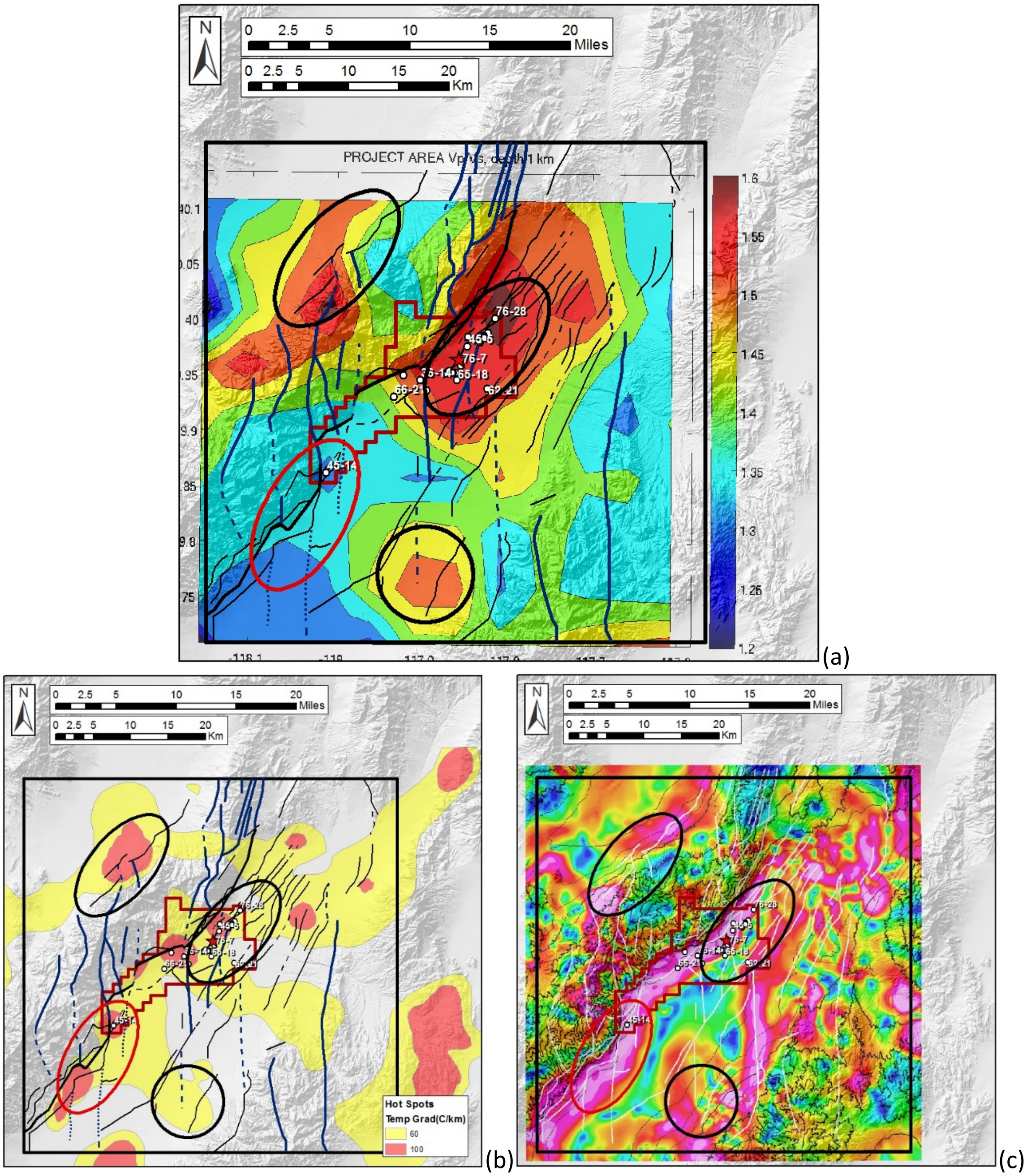

Figure 179. (a) Vp/Vs, (b) conductive geothermal gradient and (c) horizontal gravity gradient for the Project Area. Anomalies of higher Vp/Vs and conductive gradient are circled in black (hydrothermal favorable) and areas of lower Vp/Vs and higher conductive gradient are circled in red (EGS favorable).

10.3 CALIBRATION AREA SCALE

10.3.1 Data Available

There are six geoscientific data sets of varying quality and quantity available on the Project Area (Figure 1) generated in this investigation. These are geology and well data along with the modeling results for gravity-magnetics, MT, seismic, and three thermal conditions: conductive, convective, and pseudo-convective. These results are discussed in Section 9.

Detailed qualitative cross-section analysis is presented in Plates 3-6. The major implications of these correlations or lack thereof are presented below.

10.3.2 Major Qualitative Implications

Detailed qualitative enhanced data correlations are presented In Tables 20, 21, 22, and 23 relative to Plates 3-6, respectively.

Major qualitative correlations in the enhanced data are described below.

1. The Gravity-Magnetic inferred lithology/structure model does an excellent job in identifying the major basin-fill/basement geometry and significant faulting. It can in most cases accurately identify faults of significant offset, infer minor faults that are significant to structure, fault dips, and buried faults with no surface trace. Additionally, it has identified identify major north-trending structures in the valley that have previously only been identified by seismic reflection surveys and/or inferred on the basis of structural continuation from the range. Note that some of the fault dips shown the sections identified by dashed lines (Figures XXX) can be significantly modified and still be consistent with the sections shown. Other significant observations are:
    a. The area of production/injection are generally associated with the magnetic Jz unit where dilatational zones have been identified (Figure 49C and Plate 3 base map).
    b. The model shows that the area of the DVFZ specifically between the range-front fault and piedmont fault, evidences reduced thickness, minor or no magnetized Jz units. The magnetized Jz is apparently de-magnetized, not originally emplaced in this area, or non-magnetic Jz units may be present.

2. The Magnetotellurics (MT) resistivity model identifies:
    a. Generally model the basin-fill/basement geometry.
    b. Basin-filling sediments are very conductive (1-10 ohm-m).
    c. Generally, major structures occur along maximum horizontal resistivity gradients between 500-1000m.
    d. The older, inherited set of N-trending faults and fault intersections occur as relatively low resistivity structures or areas of extreme low resistivity both laterally and vertically.
    e. Active hydrothermal areas (both production and injection) generally correlate with moderate resistivity (~100 Ω-m) blocks along the hanging wall block of the piedmont fault but this correlation may not be unique.
    f. Low resistivity (<10 Ω-m) observed in the MT data appears directly correlated in large part to the presence of N-trending faults.
    g. Low resistivity (<10 Ω-m) zones generally extend to significant depths in the valley.

    MT provides a very general impression of structure and it is non-unique with respect to the well data.

3. The Seismic Velocity (SV) Model shows some correlations to structure as breaks in the velocity model coinciding with known faults, but this relationship is non-unique (i.e., it is not consistent throughout the sections). The resolution of the seismic model is generally much greater, ~5km, than the grid system employed in the Calibration Area (500m by 500m) and could be a principal factor to the lack of consistent correlations.
4. The Thermal Convective Numerical Model identifies the convective nature of the geothermal system. Since the locations of the thermal-bearing structures (range-front and piedmont fault) are fixed model parameters, the model used well data, there is no relevant correlations that can be made with the other enhanced data sets.
5. The Pseudo-Convective Thermal Model shows the difference between the Conductive Modeled Temperature and the Temperature expected from the Analog Thermal Model. The model shows that the elevated temperatures are restricted to the DVFZ and beneath portions of the Stillwater Range (along intra-range faults) due to the convective nature. The temperatures fall off dramatically outside of the DVFZ as expected, and reflect the conductive conditions. No relevant correlations can be made with the other enhanced data sets.

Table 19. Major magnetotelluric model correlations with surface structure and the Dixie Valley Geothermal Wellfield (DVGW) as well as the enhanced seismic model results (Section 10.2.1) in the Project Area (PA) and Calibration Area (CA). Note that for the purposes of this correlation analysis, the surface structure is assumed to extend to depth. Additionally, this analysis focused on the low resistivity zones, but the high resistivity zones are also a significant in identifying structure.

Depth (km)	Range Front Fault (RFF) of DVFZ	Piedmont Fault (PF) of DVFZ	Producing Region of the DVGW	Well	Other	Enhanced Seismic Data
1	High resistivity zone (HRZ) NE of Coyote Canyon (Cyn) NW of the power plant	---	The producing portion of the DVGW lies at the transition from high to low resistivity	----	---	---
2	HRZ throughout most of its length in the CA. However, most clearly at ~2 km depth (Fig A11-2), resistive "fingers" extend SE the range front and separate the main production area from Senator Fumaroles and from the Coyote Cyn high-T area.	Generally lies between a high and low resistivity zone (LRZ) with a general NE-SW trend but also several NW-Se trends lie nearby (see RFF description).		No clear relationship exists between the wells in the DVGW and the resistivity data. However, MT may be identifying resistive barriers between different producing or high-T zones.	• A significant NW-SE trending LRZ extends to S of the northern portion of the Calibration Area (CA). This LRZ bifurcates at the southern border of the northern portion of the CA. One LRZ trends to the NW and terminates around well 62A-23. The other trends to the NE, apparently along a NE-trending fault, spreading out in the area of well 65-18. • Two small LRZ NW-SE trending zones lie in the northern portion of the CA. Note that similar zones may occur in the southwestern portion of the CA but these may be obscured by a major LRZ trending NE-SW.	---
3			---		• The NW-SE trending LRZ reduces in size to the eastern portion of Dixie Valley. The LRZ extending into the well 62A-23 area has been pinched off and only a small resistivity anomaly exists in the area of 62A-23. The other NE-trending LRZ (see discussion above) is now oriented N-S. This N-S trending zone of low resistivity extends to the area slightly N of the power plant. • A moderate LRZ lies between wells 65-18 and 62A-23, and between 62A-23 and 66-21. • A major LRZ lies SSW of well 66-21. • A major LRZ lie SE of well 45-5.	1. The bifurcation of the low LRZ tin two LRZs in the area of well 62A-23 is approximately coincident with the low Vs anomaly in the northern CA bounded by a N-S fault on the west and NE-trending fault on the east (Figure 121B).
4		Generally separate high to moderate resistivity from low resistivity throughout its length in the CA except in its NE corner.	---		• There is a N-S trending LRZ south of well 65-18; a NW-SE trending LRZ from approximately the power plant area to well 62-21 and E of 45-5; and a LRZ in the area of well 62A-23. • A significant moderate LRZ lies between wells 65-18 and 62A-23. • A major LRZ lays SSW of well 66-21. • Conductors remain close to the known main production, Coyote Cyn and Senator fumaroles area, although the last has essentially petered out by 4 km depth. However, this determination is non-unique with respect to the productivity or lack thereof of wells.	1. The moderate LRZ in the area of well 62A-23 is approximately coincident with a moderate Vs anomaly (Figure 121B).
5			---	No clear relationship exists between the wells in the DVGW and the LRZ data. However, it may be argued that N-S trending LRZs feed from the south into the areas of well 45-14, 66-21/36-14, and the Main Production/Senator fumaroles. They may be channels for fluids and heat.	• There is a N-S trending LRZ south of well 65-18 which merges with a NW-SE trending zone that appears to be bounded on the east side in the valley by a N-S trending fault. This presumes said fault projects vertically to depth as stated in the figure caption. • A NW-SE trending LRZ from approximately the power plant area to well 62-21. This zone merges with a NE-SW trending zone and is coincident with a fault with the same trend in the area of well 62-21. • A small LRZ NE-SW trending zone in the hanging wall of the PF in the area of well 66-21. • A significant moderate LRZ lies between wells 65-18 and 62A-23. This zone is "L-shaped" with NW-SE and NE-SW components. • A major LRZ lays SSW of well 66-21.	1. The HRZ in the lower center of the Project Area appears to be approximately coincident with the high Vs zone shown in Figure 107.
6	Exhibits variable resistivity along its length in the CA.	----	-----		• A N-S trending LRZ south of well 65-18 which merges with a NW-SE trending zone that appears to be bounded on the east side in the valley by a N-S trending fault. • A NW-SE trending LRZ from approximately the power plant area to well 62-21. This zone merges with a NE-SW trending zone and is coincident with a fault with the same trend in the area of well 62-21. • A small LRZ NE-SW trending zone in the hanging wall of the PF of the DVFZ in the area of well 66-21. This zone seems to merge with a NW-SW trending LRZ SSE of well 66-21. • A significant moderate LRZ lies between wells 65-18 and 62A-23. This zone is "L-shaped" with NW-SE and NE-SW components described at 5km depth has been modified to an oval shape anomaly on the hanging wall side of the PF and a LRZ in the hanging wall side of the RFF. • A major LRZ lays SSW of well 66-21 but a moderate resistivity zone has developed east of well 45-14.	1. The LRZ in the valley bounded on the east side by N-S trending fault is not expressed in the Vs model (Figure 121B). The low Vs zone is further east, on the other side of the N-S fault. However, limited seismic resolution in the Calibration Area may be responsible. 2. The NW-SE trending LRZ in the area of 66-21 is coincident with a low Vs anomaly trending in the same direction. OK. 3. The relatively LRZ in the WhiteRock Cyn (Figure 1) area extending west into the Carson Sink is approximately coincident with a low Vs anomaly in the same area (Figure 121B). Slightly elevated Vp/Vs in SW CA and south of CA in valley. Otherwise, it does not appear that the Vp/Vs is useful, possibly due to the limited seismic resolution in the Calibration Area.

Table 19. Major magnetotelluric model correlations with surface structure and the Dixie Valley Geothermal Wellfield (DVGW) as well as the enhanced seismic model results (Section 10.2.1) in the Project Area (PA) and Calibration Area (CA). Note that for the purposes of this correlation analysis, the surface structure is assumed to extend to depth. Additionally, this analysis focused on the low resistivity zones, but the high resistivity zones are also a significant in identifying structure.

Depth (km)	Range Front Fault (RFF) of DVFZ	Piedmont Fault (PF) of DVFZ	Producing Region of the DVGW	Well	Other	Enhanced Seismic Data
					• A major LRZ trending NW-SE on the west side of the Stillwater Range which appears to transect the Stillwater Range and extend into the hanging wall of the PF in this area.	
7	---	---	---		• Four major LRZs are identified 1. A hook shaped anomaly that encompasses the (a) N-S trending LRZ south of well 65-18 which merges with a NW-SE trending zone that appears to be bounded on the east side in the valley by a N-S trending fault, (b) NW-SE trending LRZ from approximately the power plant area to well 62-21. This zone merges with a NE-SW trending zone and is coincident with a fault with the same trend in the area of well 62-21, (c) a LRZ trending NE-SW in the hanging wall and footwall of the RFF, (d) a N-S trending LRZ which is on trend with a N-S in the valley. Note that this latter N-S LRZ merges with an apparent NW-SE trending LRZ south of well 66-21. 2. A LRZ in the hanging wall of the RFF and the PF. 3. An apparent N-S trending LRZ transecting the Stillwater Range in the area of WhiteRock Cyn (Figure 1) which merges with a NW-SE trending LRZ west of the Stillwater Range. 4. A major LRZ south of 45-14. 5. The family of conductors at this level appears to lie along sides of rhombic fault sets including N-S faults just east of 66-21 and going south from 45-14, and NE-SW trending PF and the fault on the SE side of DV. The N-S fault just east of 66-21 is parallel to the N-S fault running S of 62-21 with a conductor also alongside. N-S trends clearest at this level.	1. The LRZ in the WhiteRock Cyn area (Figure 1) is coincident with a low Vs anomaly (Figure 121B).
8					• Same as at the depth of 7km.	1. As in item no. 1 at 7km depth.
9					• Same as at the depth of 7km, except for a weakening of the LRZ in the area of well 36-14. • A LRZ developed N of the CA on the west side of the CA.	1. The low N-S trending LRZ is approximately coincident with a low Vp anomaly (Figure 120). 2. The LRZ in the WhiteRock Cyn (Figure 1) area is coincident with a low Vs anomaly in Figure 121B). 3. The LRZ in the valley S of well 45-14 is approximately coincident with the low Vs anomaly in the same area (Figure 121B). 4. The NW-SE trending LRZ on the west side of the Stillwater Range are roughly coincident with the low Vs anomaly identified in Figure 121B in the same area.
10	---	---	---	---	• Same as at the depth of 7km, except the LRZ in the area of 36-14 has been replaced by a NW-SE trending moderate resistivity which merges with a N-S moderate to higher resistivity zone in the valley and extending into the Clan Alpine Range. • At these greater depths, the LRZs in the rhombic feature above appear to diverge northward and southward with depth. This continues to a depth beyond 15 km where they appear under and beyond the Stillwater and Clan Alpine Ranges.	1. The LRZs on the west side of the Stillwater Range approximately overlap the low Vs area identified in Figure 107. 2. The LRZ in the south-central Project Area is approximately coincident with a low Vs anomaly in the same area (Figure 121B). 3. The LRZ in the WhiteRock Cyn area (Figure 1) is coincident with the low Vs anomaly in the same area (Figure 121B). 4. The LRZ areas on the west side of the Stillwater Range appear to coincide with the low Vs areas in the same location shown in Figure 121B).
11					• Major LRZ in the White Rock Cyn (Figure 1) area persists. • The N-S trending LRZ zone SSE of well 65-18 persists. • The moderate HRZ in the area of well 36-14 persists. • NNW of the well 36-14 a NE-SW trending LRZ exists on the footwall and hanging wall side of the RFF. • The LRZ N of the CA on the west side of the Stillwater Range is better developed.	1. The low N-S trending LRZ is approximately coincident with a low Vp anomaly (Figure 120). 2. As item no. 2 at 10km depth. 3. As item no. 3 at 10km depth. 4. As item no. 4 at 10 km depth. 5. The NE-SW trending LRZ NE of well 36-14 is approximately coincident with a low Vs anomaly shown in Figure 121B. 6. The NW-SW component of the LRZ described in item no. 5 at a depth of 11lm is approximately coincident with a NW-Se trending Vs anomaly shown in Figure 121B.
12					• Major LRZ in the WhiteRock Cyn (Figure 1) area persists.	1. The low N-S trending LRZ is approximately coincident with a low Vp anomaly (Figure 120).

Table 19. Major magnetotelluric model correlations with surface structure and the Dixie Valley Geothermal Wellfield (DVGW) as well as the enhanced seismic model results (Section 10.2.1) in the Project Area (PA) and Calibration Area (CA). Note that for the purposes of this correlation analysis, the surface structure is assumed to extend to depth. Additionally, this analysis focused on the low resistivity zones, but the high resistivity zones are also a significant in identifying structure.

Depth (km)	Range Front Fault (RFF) of DVFZ	Piedmont Fault (PF) of DVFZ	Producing Region of the DVGW	Well	Other	Enhanced Seismic Data
					• A LRZ extends in the footwall of the RFF extending across the Stillwater Range and apparently merging into a NW-SW LRZ on the west side of the Stillwater Range parallel to the NW-SW LRZ related to the WhiteRock Cyn LRZ described above. • The N-S trending LRZ zone SSE of well 65-18 persists. • The moderate HRZ in the area of well 36-14 and across the Stillwater Range persists. • NNW of the well 36-14 a NE-SW trending LRZ exists on the footwall and hanging wall side of the RFF and extending somewhat into the hanging wall of the PF. • The LRZ N of the CA on the west side of the Stillwater Range persists.	2. . Items no. 2-6 as at 10km depth. 3. The low N-S trending LRZ is approximately coincident with a high Vs anomaly however (Figure 121B). Thus there is little expression in Vp/Vs. A N-S HRZ band parallels this LRZ just to the west, on the gradient between high and low Vs.
13					• As above but the LRZ on the N side of CA is merging with the LRZ NE of 36-14 and the LRZ to the SW on the west side of the Stillwater Range.	1. As item no. 5 at 11km depth. 2. As item no. 6 at 11km depth.
16					• The WhiteRock Cyn LRZ has decreased significantly along with the NW-SW LRZ on the west side of the Stillwater Range. • The N-S LRZ S of well 65-18 is disappearing significantly. • The LRZ N of well 36-14 persists along with the LRZ in the northern Stillwater Range and on the west of the range in this area. • The NE-SW trending LRZ in the area of well 45-14 is increasing in resistivity significantly. • The LRZs have approached lower crustal depths may represent high-T feeder zones from magmatic underplating.	• As item no. 5 at 11km depth. 2. As item no. 6 at 11km depth.
18	---	---	---	---	• The LRZ D of well 65-18 is redeveloping. • The LRZ N of well 36-14 persists along with the LRZ in the northern Stillwater Range and on the west of the range in this area. • The NE-SW trending LRZ in the area of well 45-14 is persisting.	1. The HRZ in the well 36-14 area is approximately coincident with the high Vs area identified in Figure 107. 2. The northern LRZ on the west side of the Stillwater Range appears to be approximately coincident with the NW-SE trending Vs zone in Figure 107.
20					• As above at a depth of 20km.	1. The large scale seismic images show pronounced Vp and Vs anomalies under and SW of the DVESA (Figs 123 and 124). These low velocities can be correlated with the family of low resistivity structures dipping under and SW of the DVESA and the Stillwater Range as well (Fig 150).

Table 20. Preliminary enhanced geoscience data correlations along serial cross-sections within the Northern Calibration Area (Plate 3). Detailed are the enhanced data correlations relative to the baseline geologic sections (Plate 1) and coincident sections of enhanced data sets. These correlations are made with respect to the major features of the Dixie Valley Geothermal System (DVGS). Note that references to grid columns can be correlated to grid columns indicated on the respective section lines on Plate 3. Correlations that (1) exist are noted in black font, (2) do not exist are in red font, (3) are not expected but observed are in blue font, (4) are expected but not observed are labeled with "No expression", (5) are not expected, not observed, and data sets that are self-generated (i.e., feature is a result of model input parameters) are labeled as NA (Not Applicable), and (6) suspected but not certain are labeled as "Unclear". Sections below are described from south to north relative to the plan view map in Plate 3.

Cross-Section	DVGS Major Features	Geologic Model	Gravity-Magnetics (G-M) Model	Magnetotellurics (MT) Resistivity Model	Vp Model	Vs Model	Thermal Numerical Model	Thermal Analog Model	Pseudo-Convective Model
C-C'	Structure	Dixie Valley Fault Zone (DVFZ) composed of a range-front fault and piedmont fault (grid column 5-6 and 9-10)	Good correlation for both faults Additional fault identified in the DVFZ (grid column 8) and intra-range faulting (west of section)	Good correlation with horizontal gradient changes.	Break (or offset) in the P-wave velocity model is within 500m of the piedmont fault Higher velocity associated with piedmont fault Range front fault is not detected.	Break (or offset) in the S-wave velocity model is within 500m of the location of piedmont fault Higher velocity associated with piedmont fault Range front fault is not detected.	Upwelling geothermal fluid between the two major faults in the DVFZ. This apparent discrepancy with the geologic section (with thermal contouring) can be explained by the way the faults were modeled as straight lines. Upwelling thermal zone around grid column 12 is a	Convective upwelling occurs along main faults in the DVFZ. Note that this analog model is based on the geologic section data and occurrence of the thermal-bearing faults.	Highest pseudo-convective component occurs at range-front and piedmont fault to a depth of 3km with coincides with the depth of the hard temperature data.

Table 20. Preliminary enhanced geoscience data correlations along serial cross-sections within the Northern Calibration Area (Plate 3). Detailed are the enhanced data correlations relative to the baseline geologic sections (Plate 1) and coincident sections of enhanced data sets. These correlations are made with respect to the major features of the Dixie Valley Geothermal System (DVGS). Note that references to grid columns can be correlated to grid columns indicated on the respective section lines on Plate 3. Correlations that (1) exist are noted in black font, (2) do not exist are in red font, (3) are not expected but observed are in blue font, (4) are expected but not observed are labeled with "No expression", (5) are not expected, not observed, and data sets that are self-generated (i.e., feature is a result of model input parameters) are labeled as NA (Not Applicable), and (6) suspected but not certain are labeled as "Unclear". Sections below are described from south to north relative to the plan view map in Plate 3.

Cross-Section	DVGS Major Features	Geologic Model	Gravity-Magnetics (G-M) Model	Magnetotellurics (MT) Resistivity Model	Vp Model	Vs Model	Thermal Numerical Model	Thermal Analog Model	Pseudo-Convective Model
							not supported by any hard data.		
		North-trending faults (grid columns 10, 13-14 and 17-18)	Magnetized Jz unit terminates within major N-trending fault in grid column 17	Vertically-trending low resistivity zone (grid columns 8-12) coincides with intersection of a North-trending fault with piedmont fault Major low resistivity interval extends to depth and coincides with pre-Miocene N-trending structure A relatively higher resistivity block is bounded by the N-trending faults in grid columns 13-14 and 17-18	No expression	No expression	No expression	No expression	NA
		Seismic-inferred fault (grid column 13-14)	Magnetized Jz unit thins in area of fault in grid column 13	No expression	No expression	No expression	No expression	No expression	NA
		West dipping antithetic fault occurs on eastern side of east of valley	Antithetic fault is not manifested	Low resistivity at depth in area of antithetic fault but the relationship between the fault structure and the low resistivity is not known	No expression	No expression	No expression	No expression	Conductive conditions on east side of the Calibration Area are consistent with the analog geologic-thermal model.
		Fumarolic zone along range-front fault (grid column 5-6)	No expression	Associated with shallow resistivity gradient Footwall block more conductive than hanging wall block – this is probably marginally resolved at best.	No expression	No expression	No expression	No expression	NA
	Lithology	Basement/Basin-fill geometry	Basement geometry shows an excellent correlation	Basin fill appears conductive Origin and significance of relatively higher resistivity block (grid columns 14-17) is unknown. High resistivity block separates NE-trending from N-trending low resistivity fault zones that intersect farther to the NE.	No expression	No expression	NA	NA	NA
		Occurrence of Jurassic unit	Good correlation Jz unit within the DVFZ appears to be missing. This could be due to demagnetization of that portion of the unit or the body was originally non-magnetic.	Gap in Jz within DVFZ (de-magnetized) coincides with higher resistivity block. Note however, that the resistivity structure in the DVFZ is complicated by the local N-trending fault intersection. But, at depth within the DVFZ, the moderate resistivity (~100 Ω-m) extends into the footwall of the range-front fault. This is also coincident with the location of the highest measured temperature in the Basin and Range (~285°C) and sub-commercial production in 36-14. – Perhaps the vertical deep conductor is a high T upflow zone.	No expression	No expression	NA	NA	NA

Table 20. Preliminary enhanced geoscience data correlations along serial cross-sections within the Northern Calibration Area (Plate 3). Detailed are the enhanced data correlations relative to the baseline geologic sections (Plate 1) and coincident sections of enhanced data sets. These correlations are made with respect to the major features of the Dixie Valley Geothermal System (DVGS). Note that references to grid columns can be correlated to grid columns indicated on the respective section lines on Plate 3. Correlations that (1) exist are noted in black font, (2) do not exist are in red font, (3) are not expected but observed are in blue font, (4) are expected but not observed are labeled with "No expression", (5) are not expected, not observed, and data sets that are self-generated (i.e., feature is a result of model input parameters) are labeled as NA (Not Applicable), and (6) suspected but not certain are labeled as "Unclear". Sections below are described from south to north relative to the plan view map in Plate 3.

Cross-Section	DVGS Major Features	Geologic Model	Gravity-Magnetics (G-M) Model	Magnetotellurics (MT) Resistivity Model	Vp Model	Vs Model	Thermal Numerical Model	Thermal Analog Model	Pseudo-Convective Model
	Temperature	Thermal upwelling within DVFZ along the two-principal faults (Area is hot/dry)	Jz rocks are non-continuous within DVFZ, see above	No correlation observed, except for the apparent correlation between the high temperature observed in the Basin and Range and moderate resistivity at depth in the footwall of the range front fault – in general this is not surprising. Low T-clays and high-T saline fluids both are low resistivity.	Vertical trending higher velocity zone coincides with upwelling along piedmont fault (within 500m)	Vertical trending higher velocity zone coincides with upwelling along piedmont fault (within 500m)	NA	NA	Highest pseudo-convective component within the DVFZ
	Wells	36-14: hot, sub-commercial well[17]	36-14 completed in basement (Kgr)	36-14 completed in moderate resistivity block beneath Stillwater Range (Kgr)	Bottomhole location is completed in a high velocity zone.	Bottomhole location is completed in a high velocity zone.	Well completed in hot convective portion with T >250C (agrees with its T-depth profile)	NA	Highest pseudo-convective component within the DVFZ
		62-23A: hot, dry well	62-23A completed in basement[18]	62-23A completed in low resistivity zone near fault intersection)	No expression	No expression	Well completed in hot convective portion with T >250C (agrees with its T-depth profile)	NA	NA
		36-14 encountered permeable fracture zone at TD	No expression	TD occurs at resistivity horizontal gradient	No expression	No expression	NA	NA	NA
D-D'	Structure	Intra-range faulting (grid columns 2-3 and 3-4)	Good correlation with N-trending intra-range fault (grid column 2-3) No expression for second fault	Unclear (complicated shallow resistivity)	No expression	No expression	No expression	No expression	NA
		DVFZ composed of a range-front fault (grid column 4) and piedmont fault (grid column 8)	Good correlation with piedmont fault Range-front fault not identified Intermediate fault within DVFZ identified.	Good correlation along both faults Moderately dipping fault in G-M model (grid column 10-12) correlates very well with similar resistivity gradient trend Moderate resistivity at depth in and around the DVFZ.	Weak correlation as observed horizontal velocity gradient along piedmont fault only occurs at 4-5 km depth A shallow horizontal gradient change (~1km) occurs but is uncorrelated with any known structure.	Same as the Vp model	NA	NA	Highest convective component within DVFZ
		North-trending faults (grid column 13-15)	No expression Missing Jz section within vicinity of N-trending faults around grid column 13.	Good correlation as horizontal gradient extends to depth along fault (grid column 14-15).	No expression	No expression	No expression	No expression	NA
		West dipping antithetic fault occurs on eastern side of east of valley (grid column 16-17)	Good correlation Bounds Jz in the footwall block of the fault	Moderate correlation with fault as horizontal gradient is apparent across fault, but not at intermediate depths	No expression	No expression	No expression	No expression	NA
	Lithology	Basement/Basin-fill Geometry	Very good correlation	Moderate correlation High resistivity block in footwall of range from fault correlates with granitic basement	No expression	No expression	NA	NA	NA

[17] Reportedly, the last 100ft of the well intersected fluid-filled fractures but the well-produced at a sub-commercial rate.
[18] Basement in this well is either Tr (Blackwell et al, 2005) or Kgr per anecdotal data from Terra-Gen Power Company.

Table 20. Preliminary enhanced geoscience data correlations along serial cross-sections within the Northern Calibration Area (Plate 3). Detailed are the enhanced data correlations relative to the baseline geologic sections (Plate 1) and coincident sections of enhanced data sets. These correlations are made with respect to the major features of the Dixie Valley Geothermal System (DVGS). Note that references to grid columns can be correlated to grid columns indicated on the respective section lines on Plate 3. Correlations that (1) exist are noted in black font, (2) do not exist are in red font, (3) are not expected but observed are in blue font, (4) are expected but not observed are labeled with "No expression", (5) are not expected, not observed, and data sets that are self-generated (i.e., feature is a result of model input parameters) are labeled as NA (Not Applicable), and (6) suspected but not certain are labeled as "Unclear". Sections below are described from south to north relative to the plan view map in Plate 3.

Cross-Section	DVGS Major Features	Geologic Model	Gravity-Magnetics (G-M) Model	Magnetotellurics (MT) Resistivity Model	Vp Model	Vs Model	Thermal Numerical Model	Thermal Analog Model	Pseudo-Convective Model
		Occurrence of magnetized Jurassic unit	Weak correlation Continuous 500m-thick Jz section in DVFZ is deeper than geologic interpretation (grid column 3-8) which is unconstrained Jz thicker (grid columns 9-11) than expected in region coinciding with location of injection wells. This suggests magnetization is related to geothermal conditions given accurate reporting of lithology in wells.	Magnetized Jz unit coincides with higher resistivity blocks (100-1000 Ω-m)	No expression	No expression	NA	NA	NA
	Temperature	Thermal upwelling within DVFZ	No expression	No expression	No expression	No expression	NA	MA	Highest convective component within DVFZ
	Wells	Injection wells in grid columns 9-11 (Section 18 wells in text)	Area of injection coincides with thick (>1.5km) magnetized body (Jz) as described above	Moderate resistivity block in hanging wall of piedmont fault coincides with area of injection	No expression	No expression	NA	NA	Elevated convective component limited to DVFZ
E-E'	Structure	DVFZ composed of a range-front fault (grid column 3-4) and piedmont fault (grid column 7-8)	Good correlation with piedmont fault Range-front fault not identified due to the lack of magnetic rocks at depth but in the shallow subsurface Intermediate fault within DVFZ identified	Major resistivity horizontal gradients occurs at both faults within DVFZ	No expression A relatively lower velocity zone occurs within 500m west of the geologic inferred fault at a depth of about 2.5km below ground surface The identified relatively lower velocity zone coincides with a relatively lower resistivity than expected zone at about the same depth in the footwall of the range-front fault	No expression but a relatively lower velocity zone occurs within 500m west of the geologic inferred fault at a depth of about 2.5km below ground surface. The identified relatively lower velocity zone coincides with a relatively lower resistivity that expected zone at about the same depth in the footwall of the range-front fault	Thermal upwelling along both faults	NA	Highest convective component within DVFZ
		North-trending faults (grid column 11)	Jz unit thins out and terminates near fault (within 500m)	N-trending fault lies in the approximate center of a very low resistivity which is also very wide (grid columns 10-13); low resistivity zone is about 3km deep and 1.5-2km wide)	No expression	No expression	NA	NA	NA
		West dipping antithetic fault occurs on eastern side of east of valley (grid column 16-17)	Good correlation Dip is steeper than the geologic model	Moderate correlation with fault (horizontal gradient)	No expression but a relatively higher velocity zone occurs about 1km west of the west dipping antithetic fault (geology inferred) at a depth of about -3km below ground surface (bgs). This zone is also coincident with a low resistivity zone at the same depth. Additionally a low velocity zone lies west about 0.75km east of the near-surface expression of	No expression but the lower and higher velocity zones observed in the Vp model do occur in the Vs model but further to the east than in the Vp model.	NA	NA	NA

Table 20. Preliminary enhanced geoscience data correlations along serial cross-sections within the Northern Calibration Area (Plate 3). Detailed are the enhanced data correlations relative to the baseline geologic sections (Plate 1) and coincident sections of enhanced data sets. These correlations are made with respect to the major features of the Dixie Valley Geothermal System (DVGS). Note that references to grid columns can be correlated to grid columns indicated on the respective section lines on Plate 3. Correlations that (1) exist are noted in black font, (2) do not exist are in red font, (3) are not expected but observed are in blue font, (4) are expected but not observed are labeled with "No expression", (5) are not expected, not observed, and data sets that are self-generated (i.e., feature is a result of model input parameters) are labeled as NA (Not Applicable), and (6) suspected but not certain are labeled as "Unclear". Sections below are described from south to north relative to the plan view map in Plate 3.

Cross-Section	DVGS Major Features	Geologic Model	Gravity-Magnetics (G-M) Model	Magnetotellurics (MT) Resistivity Model	Vp Model	Vs Model	Thermal Numerical Model	Thermal Analog Model	Pseudo-Convective Model
					the west dipping geologically inferred antithetic fault. This zone is also coincident with a low resistivity zone.				
	Lithology	Basement/Basin-fill Geometry	Excellent correlation	Moderate to good correlation Basin-fill correlates with very low resistivity High resistivity block beneath Stillwater Range correlates with granitic basement. Low resistivity feature in mid-valley (grid columns 9-13) extends below basin-fill contact	No expression	No expression	NA	NA	NA
		Occurrence of magnetized Jurassic unit	Moderate correlation Jz (magnetized portion) unit is thinner within DVFZ Thicker Jz in area of production (Section 7 wells [84-7, 76-7]) Thin to no Jz observed in a portion of the valley (grid columns 13-15)	Unclear Missing magnetized Jz in the valley from the G-M model (columns 13-15) coincides with complex low resistivity structure	No expression	No expression	NA	NA	NA
	Temperature	Thermal upwelling within DVFZ	No expression Jz is thinner than expected in the DVFZ	No expression	No expression	No expression	NA	NA	NA
	Wells	Section 7 production wells (grid column 7-8)	Encounters 1km thick magnetized rocks (Jz) within production zone not associated exclusively with the Jz rocks encountered in well logs	Production intervals in Section 7 encounter moderate resistivities in hanging wall of piedmont fault	No expression	No expression	NA	NA	Elevated pseudo-convective component within producing interval
		62-21, conductive/dry well (grid column 15-16)	Good correlation with known basement contact	Vertical resistivity change occurs at basement contact in well	No expression	No expression	NA	NA	Conductive regime agrees with drilling results
F-F'	Structure	DVFZ composed of a range-front fault (grid column 4), and main piedmont fault (grid column 6-7)	Good correlation with piedmont fault No significant range-front fault identified Major intra-range fault (grid columns 1-2) identified	Major resistivity horizontal gradients occur at both main faults within DVFZ	No expression but a relatively lower velocity zone occurs within 500m west of the geologic inferred fault at a depth of about 2.5km below ground surface. The identified relatively lower velocity zone coincides with a relatively lower resistivity that expected zone at about the same depth in the footwall of the range-front fault	No expression but a relatively lower velocity zone occurs within 500m west of the geologic inferred fault at a depth of about 2.5km below ground surface. This identified relatively lower velocity zone is more significant and complicated than the similar zone identified on section E-E' and it coincides with a relatively lower resistivity that expected zone at about the same depth in the footwall of the range-front fault	NAA	NA	Elevated convective component within DVFZ

Table 20. Preliminary enhanced geoscience data correlations along serial cross-sections within the Northern Calibration Area (Plate 3). Detailed are the enhanced data correlations relative to the baseline geologic sections (Plate 1) and coincident sections of enhanced data sets. These correlations are made with respect to the major features of the Dixie Valley Geothermal System (DVGS). Note that references to grid columns can be correlated to grid columns indicated on the respective section lines on Plate 3. Correlations that (1) exist are noted in black font, (2) do not exist are in red font, (3) are not expected but observed are in blue font, (4) are expected but not observed are labeled with "No expression", (5) are not expected, not observed, and data sets that are self-generated (i.e., feature is a result of model input parameters) are labeled as NA (Not Applicable), and (6) suspected but not certain are labeled as "Unclear". Sections below are described from south to north relative to the plan view map in Plate 3.

Cross-Section	DVGS Major Features	Geologic Model	Gravity-Magnetics (G-M) Model	Magnetotellurics (MT) Resistivity Model	Vp Model	Vs Model	Thermal Numerical Model	Thermal Analog Model	Pseudo-Convective Model
		DVFZ also consists of a transfer/relay fault (grid column 5-6),	Good correlation	Unclear	No expression	No expression	NA	NA	NA
		North-trending fault intersection (grid column 8-9)	No correlation and no offset observed in the Jz unit but a vertical fault was identified about 500m west in grid column 7	Good correlation as fault coincides with resistivity horizontal gradient	No expression	No expression	NA	NA	NA
		West dipping antithetic fault occurs on eastern side of east of valley (grid column 15 and 17)	Major west-dipping fault agrees with geologic model	Moderate correlation with west-dipping resistivity structure (horizontal gradient)	No expression but section shows the same velocity intervals as in E-E' on the eastern side of the valley (see plan view section location map)	No expression but section shows the same velocity intervals as in E-E' on the eastern side of the valley (see plan view section location map)	NA	NA	NA
		Senator fumaroles at range-front fault	No expression	Low resistivity anomaly in the hanging wall of the range-front fault in local of the fumarole	No expression	No expression	NA	NA	Elevated convective component
	Lithology	Basement/Basin-fill Geometry	General basement geometry very similar to geologic model Slightly deeper basin-fill section	Low resistivity feature in mid-valley (primarily grid columns 9- 13 to depth and extending to 18 following the basin shape) The low resistivity feature extends into the basement and is generally consistent with the G-M model	No expression	No expression	NA	NA	NA
		Occurrence of magnetized Jurassic unit	Excellent agreement with hanging wall of piedmont fault No correlation with Jz from geologic model, except in area of 82-5 completed in the hanging wall of the piedmont fault Thick section of magnetized Jz in Stillwater Range does not correlate with postulated Jurassic mafic section occurrence Jz unit beneath Stillwater Range does not correlate with geologic model Jz unit on east side of section correlates with the geologic model but thinner than expected	No expression	No expression	No expression	NA	NA	NA
	Temperature	Thermal upwelling within DVFZ	No expression	Unclear	No expression	No expression	NA	NA	Elevated convective component
	Wells	38-32 (injector) (grid column 6)	Good correlation; similar lithology as expected from well log	Resistivity change at fault encountered near total depth correlates with lithology break in well	No expression	No expression	NA	NA	NA

Table 20. Preliminary enhanced geoscience data correlations along serial cross-sections within the Northern Calibration Area (Plate 3). Detailed are the enhanced data correlations relative to the baseline geologic sections (Plate 1) and coincident sections of enhanced data sets. These correlations are made with respect to the major features of the Dixie Valley Geothermal System (DVGS). Note that references to grid columns can be correlated to grid columns indicated on the respective section lines on Plate 3. Correlations that (1) exist are noted in black font, (2) do not exist are in red font, (3) are not expected but observed are in blue font, (4) are expected but not observed are labeled with "No expression", (5) are not expected, not observed, and data sets that are self-generated (i.e., feature is a result of model input parameters) are labeled as NA (Not Applicable), and (6) suspected but not certain are labeled as "Unclear". Sections below are described from south to north relative to the plan view map in Plate 3.

Cross-Section	DVGS Major Features	Geologic Model	Gravity-Magnetics (G-M) Model	Magnetotellurics (MT) Resistivity Model	Vp Model	Vs Model	Thermal Numerical Model	Thermal Analog Model	Pseudo-Convective Model
		82-5 (hot/dry) (gird column 8)	Magnetized Jz correlates with Tmb and Tv, not the expected Jz at total depth	Bottom of well correlates with low resistivity as piedmont fault at total depth has abundant talc alteration in log	No expression	No expression	NA	NA	NA
G-G'	Structure	Intra-range structure (grid column 3)	Block of magnetized Jz could be bounded by intra-range fault	NA (out of section)	No expression	No expression	NA	NA	N
		DVFZ composed of a range-front fault (grid column 4, and main piedmont fault (grid column 7)	Good correlation with range-front fault Piedmont fault occurs 500m to the west compared to fault in geologic model	Good correlation as resistivity structures (horizontal gradients) occur along range-front and piedmont fault	No expression	No expression	NA	NA	Elevated convective component in the DVVZ No convection indicated in the eastern portion of the valley
		DVFZ contains an intermediate fault (grid column 5-6)	Good correlation	Unclear	No expression	No expression	NA	NA	NA
		West dipping antithetic fault occurs on eastern side of east of valley (grid column 17-18 and 19)	NA (factor outside dimensions of the section)	Unclear Possible correlation with horizontal gradient change	No expression	No expression	No expression	No expression	No convection indicated in the eastern portion of the valley
	Lithology	Basement/Basin-fill Geometry	Moderate to good correlation Deeper basin-fill than geologic model	Good correlation Low to moderate resistivity extend to depth -2.5 km asl (grid columns 10-11) occurs in area of seismic inferred west dipping fault	No expression	No expression	NA	NA	NA
		Occurrence of Jurassic magnetized unit Jz is nearly faulted out in this portion of the range and valley	Jz thins out as expected Jz occurs shallower than expected from well logs	No expression	No expression	No expression	NA	NA	NA
	Temperature	Thermal upwelling within DVFZ	Missing magnetized Jz unit in the DVFZ	No expression	No expression	No expression	NA	NA	NA
	Wells	Section 33 producing wells lie along this section (grid column 8)	Hanging wall of the piedmont fault shows a deeper basin-fill section than the geologic model which is based on well lithology data Jz identified shallower than expected from well logs	Production wells occur proximal to piedmont fault which is identified by a high horizontal gradient and an approximate 100 Ω-m resistivity block within the hanging wall of the piedmont fault	No expression	No expression	NA	NA	NA
H-H'	Structure	Intra-range structure (grid column 1-2)	No expression	Unclear	No expression	No expression	NA	NA	NA
		Range-front fault (grid column 2-3)	Good correlation	Good correlation with resistivity gradient	No expression	No expression	NA	NA	NA
		DVFZ composed of three piedmont faults; two minor faults (grid column 5-6), and main piedmont fault (grid column 7-8)	Good correlation as multiple faults are identified G-M model fault dips most likely steeper than shown on section	Good correlation with resistivity structures for range-front and piedmont fault	Multiple faulting in grid columns 8-12 (which are east of the piedmont fault) and there is higher than expected P-wave velocity observed in the shallow portion of the system and lower than expected P-wave velocity deeper in the system	Multiple faulting in grid columns 8-12 (which are east of the piedmont fault) and there is higher than expected S-wave velocity observed in the shallow portion of the system and lower than expected S-wave velocity deeper in the system	NA	NA	NA

Table 20. Preliminary enhanced geoscience data correlations along serial cross-sections within the Northern Calibration Area (Plate 3). Detailed are the enhanced data correlations relative to the baseline geologic sections (Plate 1) and coincident sections of enhanced data sets. These correlations are made with respect to the major features of the Dixie Valley Geothermal System (DVGS). Note that references to grid columns can be correlated to grid columns indicated on the respective section lines on Plate 3. Correlations that (1) exist are noted in black font, (2) do not exist are in red font, (3) are not expected but observed are in blue font, (4) are expected but not observed are labeled with "No expression", (5) are not expected, not observed, and data sets that are self-generated (i.e., feature is a result of model input parameters) are labeled as NA (Not Applicable), and (6) suspected but not certain are labeled as "Unclear". Sections below are described from south to north relative to the plan view map in Plate 3.

Cross-Section	DVGS Major Features	Geologic Model	Gravity-Magnetics (G-M) Model	Magnetotellurics (MT) Resistivity Model	Vp Model	Vs Model	Thermal Numerical Model	Thermal Analog Model	Pseudo-Convective Model
					No correlation with range-front fault	No correlation with range-front fault			
		3-4 west-dipping antithetic fault occurs on eastern side of east of valley within valley (grid columns 11, 14-15, 16, and 19)	No expression No faults identified although section subject to interpretation	Unclear Moderate to weak correlation with resistivity gradients	No expression	No expression	NA	NA	NA
	Lithology	Basement/Basin-fill Geometry	Excellent correlation	Good correlation	No expression	No expression	NA	NA	NA
		Occurrence of Jz is nearly faulted out in this portion of the Project Area	Jz unit beneath Stillwater Range (grid columns 1-2) and west of piedmont fault (grid columns 5-6) does not correlate with geologic model	No expression	No expression	No expression	NA	NA	NA
	Temperature	Limited Thermal upwelling within DVFZ and much lower temperatures than the area to the south-southwest	Missing magnetized unit (Jz) within DVFZ	Unclear	No expression	No expression	NA	NA	Conductive conditions as expected in area
	Wells	76-28 (warm/dry)	Jz section correlated with well log	No correlation	No expression	No expression	NA	NA	NA

Table 21. Preliminary enhanced geoscience data correlation along cross-sections within the Southern Calibration Area (see Plate 4). Detailed are the enhanced data correlations relative to the baseline geologic sections (Plate 1) and coincident sections of enhanced data sets. An applicable segment of the geologic section C-C' (Plate 2 and 3) is over-laid on A6 for comparison asl well as, an applicable segment of the geologic section line C-C' is over-laid on LL3 for comparison. These correlations are made with respect to the major features of the Dixie Valley Geothermal System (DVGS). Correlations that (1) exist are noted in black font, (2) do not exist are in red font, (3) are not expected but observed are in blue font, (4) are expected but not observed are labeled with "No expression", (5) are not expected, not observed, and data sets that are self-generated (i.e., feature is a result of model input parameters) are labeled as NA (Not Applicable), and (6) suspected but not certain are labeled as "Unclear". Note that references to grid column cells can be correlated to grid cells indicated on the respective section lines and in the plan view map on Plate 4. Sections go from south to north as indicated on Plate 5.

Cross-Section	DVGS Major Features	Geologic Model	Gravity-Magnetics Model	Magnetotellurics (MT) Resistivity Model	Vp Model	Vs Model	Thermal Numerical Model	Thermal Analog Model	Pseudo-Convective Model
LL1	Structure	N-trending range-front fault (grid column 2-3)	Minor offset along range-front	No expression Basement is very resistive (~1000 Ω-m)	No expression	No expression	NA	Insufficient data for analysis	Insufficient data for analysis
		Complex piedmont fault zone (grid column 3-4)	Major offset along piedmont fault Only one fault identified	Resistivity break at east end of section correlates with piedmont fault Correlations in LL1, A4 and LL2 difficult because MT site coverage was rather sparse.	Vp increases in depth from <3.5km/s to 6.5km from 1km above sea level (asl) to -3km asl where a lower velocity zone at 5.5km/s interval has been detected at depths of 3-4 km	Vs systematically increases with depth	Convective upflow along both major faults		
	Lithology	No geologic model for comparison but well data indicates 0.5km of basin-fill, 1km of Tertiary volcanics and Triassic meta-sediments exists in the subsurface	Correlates with well results	Basin-fill correlates with very low resistivity, except for the low resistivity identified under the Stillwater Range.	The change in Vp at -3km asl identified above correlates with the resistivity decrease at a comparable depth.	No expression	As above		
	Temperature	Thermal anomaly correlation	No expression	No expression	NA	No expression	NA		

Table 21. Preliminary enhanced geoscience data correlation along cross-sections within the Southern Calibration Area (see Plate 4). Detailed are the enhanced data correlations relative to the baseline geologic sections (Plate 1) and coincident sections of enhanced data sets. An applicable segment of the geologic section C-C' (Plate 2 and 3) is over-laid on A6 for comparison asl well as, an applicable segment of the geologic section line C-C' is over-laid on LL3 for comparison. These correlations are made with respect to the major features of the Dixie Valley Geothermal System (DVGS). Correlations that (1) exist are noted in black font, (2) do not exist are in red font, (3) are not expected but observed are in blue font, (4) are expected but not observed are labeled with "No expression", (5) are not expected, not observed, and data sets that are self-generated (i.e., feature is a result of model input parameters) are labeled as NA (Not Applicable), and (6) suspected but not certain are labeled as "Unclear". Note that references to grid column cells can be correlated to grid cells indicated on the respective section lines and in the plan view map on Plate 4. Sections go from south to north as indicated on Plate 5.

Cross-Section	DVGS Major Features	Geologic Model	Gravity-Magnetics Model	Magnetotellurics (MT) Resistivity Model	Vp Model	Vs Model	Thermal Numerical Model	Thermal Analog Model	Pseudo-Convective Model
	Wells	45-14 (sub-commercial well) (grid column 3-4)	Correlates with lithology from 45-14 and assumption that well lies in a stranded fault block	Fluid exit zone considered being near TD correlates with a resistive body, possibly identifying the Triassic metasediments	No expression	No expression	NA		
A4	Structure	N-trending range-front fault (grid column 1)	Good correlation No expression of range-front fault at surface	Unclear	Velocity does not consistently increase with depth; same structure as in section LLI Decrease in Vp with depth as described above	Velocity does not consistently increase with depth; dramatic velocity reversal at about -2km asl; this change is not observed in the section above or below this section line	As above	Insufficient data for analysis	Insufficient data for analysis
		Complex piedmont fault structure (grid column 3-4)	Major piedmont fault correlates with geologic model Two other minor piedmont faults identified	No expression	No expression	No expression	NA		
	Lithology	No geologic model for comparison (lack of well data	Jz unit (magnetized) occur broken by structure within DVFZ Jz identified within hanging wall of piedmont fault	No expression Low resistivity zone at depths below -3km asl	No expression	No expression	As above		
	Temperature	As above	No expression	No expression	No expression	No expression	As above		
	Other	Comstock Mine (ancestral hydrothermal cell)	Jz unit found in shallow subsurface below fault/mine location	No expression	No expression	No expression	No expression		
LL2	Structure	Intra-range N-trending fault (grid column 1)	Good correlation Shallow dip not in agreement with structural interpretation	Unclear Lower resistivity at depth associated with N-trending fault segment	No expression	No expression		Insufficient data for analysis	Insufficient data for analysis
		Range-front (grid column 3)	Good correlation with mapped range-front fault; shallow dip not in agreement with structural interpretation	No expression	No expression	No expression	Convective upflow along range-front fault	No expression	
		Piedmont fault (grid column 7-8)	Piedmont fault is steeply dipping and in agreement with overall geologic model Possible steeply dipping range-front fault in grid columns 2-3 not indicated on geologic section Possible shallow dipping range-front fault as shown in section	Unclear Possible near vertical faults at strong horizontal gradient Low resistivity at depth within the DVFZ	No expression Vp increases systematically with depth Shallow Vp higher than observed in A4 to the southwest No change in Vp at depth as observed in lines A4 and LLIs	No expression Upper 0.5 km depth higher Vs than in section lines to the southwest Vs increases with depth systematically No change in Vs at depth	NA		
	Lithology	No geologic model for comparison (lack of well data)	Jz unit is offset by piedmont fault and mostly continuous through DVFZ	No expression	No expression	No expression	NA		
	Temperature	No thermal data	Possible demagnetized rocks (Jznm) show vertical trend consistent with	Low resistivity detected under Stillwater Range	No expression	No expression	NA		

Table 21. Preliminary enhanced geoscience data correlation along cross-sections within the Southern Calibration Area (see Plate 4). Detailed are the enhanced data correlations relative to the baseline geologic sections (Plate 1) and coincident sections of enhanced data sets. An applicable segment of the geologic section C-C' (Plate 2 and 3) is over-laid on A6 for comparison asl well as, an applicable segment of the geologic section line C-C' is over-laid on LL3 for comparison. These correlations are made with respect to the major features of the Dixie Valley Geothermal System (DVGS). Correlations that (1) exist are noted in black font, (2) do not exist are in red font, (3) are not expected but observed are in blue font, (4) are expected but not observed are labeled with "No expression", (5) are not expected, not observed, and data sets that are self-generated (i.e., feature is a result of model input parameters) are labeled as NA (Not Applicable), and (6) suspected but not certain are labeled as "Unclear". Note that references to grid column cells can be correlated to grid cells indicated on the respective section lines and in the plan view map on Plate 4. Sections go from south to north as indicated on Plate 5.

Cross-Section	DVGS Major Features	Geologic Model	Gravity-Magnetics Model	Magnetotellurics (MT) Resistivity Model	Vp Model	Vs Model	Thermal Numerical Model	Thermal Analog Model	Pseudo-Convective Model
		Dilational zone identified at structural intersection of N-trending and NE trending faults	narrow focused dilatation zone (grid column 2)	In Wanamaker et al. (2013), a N or NNW fault comes into this region at depth, ~5km					
A5	Structure	N-trending segment of range-front fault (grid column 2)	Agrees with mapped range-front fault at surface	Good correlation with resistivity gradient across this structure	No expression	No expression	Modeled thermal upwelling	Insufficient data for analysis	Insufficient data for analysis
		Piedmont fault (grid column 6)	Major piedmont fault and offset agrees with location of fault at surface DVFZ is complex in area and consists of multiple faults (5-6)	Good correlation with horizontal resistivity gradient across structure identified in G-M model Horizontal gradients suggest multiple steeply dipping faults	No expression	No expression	NA Note that upwelling along piedmont fault is offset to east as a consequence of structure modeling parameter input)		
		Dilatational zone at structural intersection (grid column 3-4)	Gap in magnetized Jz unit at range-front fault	No expression	No expression	No expression	NA		
	Lithology	No geologic model for comparison due to lack of well data	Thick magnetized Jz units exist in the subsurface	Good correlation with basin shape Basin-fill is very conductive	No expression	No expression	No expression		
	Temperature	Thermal upwelling along major faults – unknown (no hard data)	Gap in magnetized Jz units within DVFZ	No expression	No expression	No expression	NA		
LL3	Structure	DVFZ comprised of range-front fault (grid column 1) and piedmont fault (grid column 6)	Poor correlation due to faults having a shallower dip than expected from structural interpretations	Good to very good correlation on range-front and piedmont fault Extensive low resistivity region on hanging wall of piedmont fault which persists to depth	Offset in velocity at depth correlates with location of piedmont fault	Offset in velocity at depth correlates with location of piedmont fault	NA	NA	Elevated convective component occurs within the DVFZ and in the hanging wall of the piedmont fault
	Lithology	Basement/Basin-fill geometry	Good correlation with geologic model	Moderate correlation	No expression	No expression	No expression	No expression	No expression
		Occurrence of Jz unit	Thick magnetized Jz sections agrees with geologic section	No expression	No expression	No expression	No expression	No expression	No expression
	Temperature	Thermal upwelling within the DVFZ	No missing non-magnetic units	No expression	No expression	No expression	No expression	No expression	No expression
	Wells	66-21 (hot/dry well)	Model correlates with well log results	Low permeability nature of well correlates with lower resistivity to TD	No expression	No expression	No expression	Well lies between upwelling zones along the range front and piedmont fault	Area around well shows moderate convective component
A6	Structure	DVFZ comprised of range-front fault (grid column 1) and piedmont fault (grid column 4-5)	Moderate correlation Piedmont fault is more steeply dipping than expected from geologic model	Very low resistivity bounded in hanging wall of piedmont fault Low resistivity associated with N-trending fault intersection with piedmont fault Range-front fault has moderate to low correlation with resistivity gradient A low resistivity zone underlies the bottomhole location of 36-14 and at	Higher velocity vertical structure (break) correlates with piedmont fault break (within 500m)	Higher velocity vertical structure (break) correlates with piedmont fault break (within 500m)	Thermal upwelling along range-front fault only	NA	Highest convective component within DVFZ

Table 21. Preliminary enhanced geoscience data correlation along cross-sections within the Southern Calibration Area (see Plate 4). Detailed are the enhanced data correlations relative to the baseline geologic sections (Plate 1) and coincident sections of enhanced data sets. An applicable segment of the geologic section C-C' (Plate 2 and 3) is over-laid on A6 for comparison asl well as, an applicable segment of the geologic section line C-C' is over-laid on LL3 for comparison. These correlations are made with respect to the major features of the Dixie Valley Geothermal System (DVGS). Correlations that (1) exist are noted in black font, (2) do not exist are in red font, (3) are not expected but observed are in blue font, (4) are expected but not observed are labeled with "No expression", (5) are not expected, not observed, and data sets that are self-generated (i.e., feature is a result of model input parameters) are labeled as NA (Not Applicable), and (6) suspected but not certain are labeled as "Unclear". Note that references to grid column cells can be correlated to grid cells indicated on the respective section lines and in the plan view map on Plate 4. Sections go from south to north as indicated on Plate 5.

Cross-Section	DVGS Major Features	Geologic Model	Gravity-Magnetics Model	Magnetotellurics (MT) Resistivity Model	Vp Model	Vs Model	Thermal Numerical Model	Thermal Analog Model	Pseudo-Convective Model
				depth in the footwall of the range front fault This well possibly overlies intersection of NE and N trending fault zones (low resistivity alignments)					
	Lithology	Basement/Basin-fill geometry	Moderate correlation Basin-fill deeper than expected from geologic model	A correlation is not apparent in this section	No expression	No expression	No expression	No expression	No expression
		Occurrence of Jz unit	Good correlation No magnetized rock (Jz) in DVFZ	Lower resistivity associated with magnetized Jz unit	No expression	No expression	No expression	No expression	No expression
	Temperature	Thermal upwelling within the DVFZ	Gap in magnetized JZ unit within DVFZ	No expression	No expression	No expression	No expression	NA	NA
	Wells	36-14 (hot/dry; sub-commercial fracture at TD)	Moderate correlation Basin-fill contact 500m shallower than expected from well results	TD occurs at a transition from high to lower resistivity gradient	No expression	No expression	No expression	Highest temperature well reported in Nevada	Very high convective input
		62-23A (hot/dry)	Good correlation with J known lithology	TD occurs within low resistivity zone at fault intersection	No expression	No expression	NA	NA	Elevated convective input
	Other	Section 10 fumaroles	Magnetized Jz within footwall of range-front fault below fumarolic area	Lower resistivity at fumarole area than surrounding rock	No expression	No expression	NA	NA	Elevated convective input

Table 22. Preliminary enhanced data correlation along short-line cross-sections developed in the joint gravity-magnetic modeling targeting key structural intersections (see Plate 5). Detailed are the enhanced data correlations relative to the major features of the Dixie Valley Geothermal System (DVGS) baseline geologic sections (Plate 2) for line A6, and relative to the gravity-magnetic model for the remaining sections shown (A1-A6). Note that references to grid column cells can be correlated to grid cells indicated on the respective section lines and the plan view map on Plate 5. Correlations that (1) exist are noted in black font, (2) do not exist are in red font, (3) are not expected but observed are in blue font, (4) are expected but not observed are labeled with "No expression", (5) are not expected, not observed, and data sets that are self-generated (i.e., feature is a result of model input parameters) are labeled as NA (Not Applicable), and (6) suspected but not certain are labeled as "Unclear". Sections go from south to north as indicated on Plate 5.

Cross-Section	Major DVGS Features	Geologic Model	Gravity-Magnetics Model	Magnetotellurics (MT) Resistivity Model	Vp Model	Vs Model	Thermal Numerical Model
A1	Structure geoscience	Range-front (grid column 1-2)	Good Correlation Two range-front faults shown with a moderate dip	No expression (no major gradients associated with faulting along the section)	No expression (layered velocity model with no abnormalities)	No expression (layered velocity model with no abnormalities)	NA (no section for comparison as line is mostly outside project area)
		Multiple Piedmont Faults "The Bend" (grid column 3-11)	Good correlation with steeply-dipping piedmont fault (grid column 11)	No expression	No expression	No expression	NA
	Lithology	Basement/Basin-fill shape; no geologic model for comparison (lack of well data)	Shallow valley-fill in "The Bend" area as expected (grid columns 3-11) Major offset along piedmont structure	No expression	No expression	No expression	NA
		Occurrence of magnetized rocks (Jz)	Occurs intermittently between the major faulting and within hanging wall block of piedmont fault	No expression	No expression	No expression	NA

Table 22. Preliminary enhanced data correlation along short-line cross-sections developed in the joint gravity-magnetic modeling targeting key structural intersections (see Plate 5). Detailed are the enhanced data correlations relative to the major features of the Dixie Valley Geothermal System (DVGS) baseline geologic sections (Plate 2) for line A6, and relative to the gravity-magnetic model for the remaining sections shown (A1-A6). Note that references to grid column cells can be correlated to grid cells indicated on the respective section lines and the plan view map on Plate 5. Correlations that (1) exist are noted in black font, (2) do not exist are in red font, (3) are not expected but observed are in blue font, (4) are expected but not observed are labeled with "No expression", (5) are not expected, not observed, and data sets that are self-generated (i.e., feature is a result of model input parameters) are labeled as NA (Not Applicable), and (6) suspected but not certain are labeled as "Unclear". Sections go from south to north as indicated on Plate 5.

Cross-Section	Major DVGS Features	Geologic Model	Gravity-Magnetics Model	Magnetotellurics (MT) Resistivity Model	Vp Model	Vs Model	Thermal Numerical Model
	Temperature	Thermal anomaly not present along section	Intermittent magnetized rocks in the DVFZ	No expression	No expression	No expression	NA
A2	Structure	Intra-range fault (grid column 1)	Good correlation	Good correlation Range-front projected at depth is conductive: moderate resistivity at depth (grid columns 4-7)	No expression (layered velocity model with no abnormalities)	No expression (layered velocity model with no abnormalities)	NA
		Range-front (grid-column 2)	Good correlation	No expression	No expression	No expression	NA
		Piedmont Fault (grid column 6)	Good correlation	No expression			
		N-trending fault projection (grid column 7)	Good correlation Major offset along indicated fault, steeply east dipping agrees with geologic interpretation	No expression	No expression	No expression	NA
	Lithology	No geologic model for comparison (lack of well data)	Shallow valley-fill out to piedmont fault with complex faulting	Unclear Shallow basin-fill is very conductive	No expression	No expression	NA
		Occurrence of magnetized rocks (Jz); Jurassic rocks exposed within the range	Magnetized rocks bounded by faults and within hanging wall block of main piedmont fault	No expression	No expression	No expression	NA
	Temperature	Section transects through SW edge of Dixie Meadows thermal anomaly	Intermittent magnetized rocks in the DVFZ	Projected range-front fault is conductive at depth (up to -2km asl) which could be related to thermal anomaly	No expression	No expression	NA
A3	Structure	Range-front (grid column 1)	Good correlation Fault has shallow dip (30-45°)	Correlates with resistivity gradient	No expression (layered velocity model with no abnormalities)	No expression (layered velocity model with no abnormalities)	NA
		Piedmont fault (grid column 2-3)	Good correlation Complicated structure (multi-fault) as expected Fault has shallow dip (45-50°)	No expression	No expression	No expression	NA
		N-trending fault projection (grid column 6)	Good correlation Magnetized zone along expressed fault	Very conductive regime to depth could be due to N-trending structure	No expression	No expression	NA
	Lithology	No geologic model for comparison (lack of well data)	Valley-fill thickens east of piedmont fault as expected	No expression Majority of section is very conductive except for footwall block of range-front fault to -1.5km asl depth	No expression	No expression	NA
		Magnetized unit (Jz) within subsurface	Limited occurrence; occur along range-front and piedmont fault only Infers fault-influenced magnetization	No expression	No expression	No expression	NA
	Temperature	Section transects through Dixie Meadows anomaly and warm surface springs	Lack of magnetized rocks in place (not related to faulting)	Unclear	No expression	No expression	NA

Table 22. Preliminary enhanced data correlation along short-line cross-sections developed in the joint gravity-magnetic modeling targeting key structural intersections (see Plate 5). Detailed are the enhanced data correlations relative to the major features of the Dixie Valley Geothermal System (DVGS) baseline geologic sections (Plate 2) for line A6, and relative to the gravity-magnetic model for the remaining sections shown (A1-A6). Note that references to grid column cells can be correlated to grid cells indicated on the respective section lines and the plan view map on Plate 5. Correlations that (1) exist are noted in black font, (2) do not exist are in red font, (3) are not expected but observed are in blue font, (4) are expected but not observed are labeled with "No expression", (5) are not expected, not observed, and data sets that are self-generated (i.e., feature is a result of model input parameters) are labeled as NA (Not Applicable), and (6) suspected but not certain are labeled as "Unclear". Sections go from south to north as indicated on Plate 5.

Cross-Section	Major DVGS Features	Geologic Model	Gravity-Magnetics Model	Magnetotellurics (MT) Resistivity Model	Vp Model	Vs Model	Thermal Numerical Model
				Very conductive regime to depth within majority of section			
A4	Structure	N-trending range-front fault (grid column 1)	Good correlation Range-front fault shows offset as expected Comprised of multiple step-faults	No expression	No expression	No expression	NA
		Two mapped piedmont faults (grid column 3-4)	Good correlation Two other minor piedmont faults identified	No expression	No expression	No expression	NA
	Lithology	No geologic model for comparison due to lack of well data	NA	No expression	No expression	No expression	NA
		Magnetized unit (Jz)	Occur within DVFZ and the hanging wall of main piedmont fault	No expression	No expression	No expression	NA
	Temperature	NA	No expression	No expression	No expression	No expression	NA
	Other	Comstock Mine (ancestral hydrothermal cell)	Magnetized Jz unit found in shallow subsurface coincident with fault/mine location	No expression	No expression	No expression	NA
A5	Structure	N-trending segment of range-front fault (grid column 2-3)	Good correlation	Good correlation with resistivity horizontal gradient across structure Inferred dips are steeper	No expression	No expression	NA
		Piedmont fault (grid column 6)	Good correlation DVFZ is complex consisting of multiple faults (5-6)	Good correlation with resistivity gradient across structure Suggest multiple steeply dipping faults	No expression	No expression	NA
		Dilatational zone at structural intersection	Gap in magnetized Jz unit at range-front fault	No expression	No expression	No expression	NA
		No expression	Multiple faults within the DVFZ and area to the east (grid column 7-9)	Horizontal gradients strongly correlate with gravity-magnetic modeled faults	No expression	No expression	NA
	Lithology	Basin shape and Jz exposed in Stillwater Range (No geologic model for comparison due to lack of well data)	Good correlation	Basin-fill is very conductive (grid column 4-13) Basin-fill conductive to total depth of section	No expression	No expression	NA
		Magnetized unit (Jz)	Thick magnetized Jz unit in subsurface	No expression	No expression	No expression	NA
	Temperature	No well data	Gap in magnetized Jz unit within DVFZ	No expression	No expression	No expression	NA
A6	Structure	Range-front fault (grid column 1-2)	Good correlation	Moderate correlation with resistivity gradient	No expression	No expression	NA
		Piedmont fault (grid column 4-5)	Good correlation; location and dip on piedmont fault lies within 500m	Major horizontal gradients in grid columns 4-5 correlated with piedmont fault Very low resistivity bounded on hanging wall side of piedmont fault which merges into the bottomhole location of the 36-14, the hottest well in the Basin and Range 36-14 lies near the intersection of NE and N conductive "fault zones"	Higher velocity vertical structure correlates with piedmont fault break (within 500m)	Higher velocity vertical structure (break) correlates with piedmont fault break (within 500m)	NA
		N-trending fault (grid column 5-6)	No expression	Good correlation with major horizontal gradient change	North-trending fault within 500m the aforementioned velocity anomaly	North-trending fault within 500m the aforementioned velocity anomaly	No expression

Table 22. Preliminary enhanced data correlation along short-line cross-sections developed in the joint gravity-magnetic modeling targeting key structural intersections (see Plate 5). Detailed are the enhanced data correlations relative to the major features of the Dixie Valley Geothermal System (DVGS) baseline geologic sections (Plate 2) for line A6, and relative to the gravity-magnetic model for the remaining sections shown (A1-A6). Note that references to grid column cells can be correlated to grid cells indicated on the respective section lines and the plan view map on Plate 5. Correlations that (1) exist are noted in black font, (2) do not exist are in red font, (3) are not expected but observed are in blue font, (4) are expected but not observed are labeled with "No expression", (5) are not expected, not observed, and data sets that are self-generated (i.e., feature is a result of model input parameters) are labeled as NA (Not Applicable), and (6) suspected but not certain are labeled as "Unclear". Sections go from south to north as indicated on Plate 5.

Cross-Section	Major DVGS Features	Geologic Model	Gravity-Magnetics Model	Magnetotellurics (MT) Resistivity Model	Vp Model	Vs Model	Thermal Numerical Model
				Low resistivity associated with N-trending fault intersection with piedmont fault			
	Lithology	Basement/Basin-fill geometry	Moderate correlation Basin-fill contact 500m shallower than expected from well results	No expression	No expression	No expression	NA
		Occurrence of magnetized Jz unit	Good correlation No magnetized Jz in DVFZ	Lower resistivity associated with magnetized Jz unit in shallow subsurface (grid column 1, 4-6)	No expression	No expression	NA
	Temperature	Thermal upwelling within the DVFZ	Gap in magnetized rock within DVFZ	Unclear; resistivity structure is complex Low resistivity area at depth	No expression	No expression	NA
	Wells	36-14 (hot/dry; sub-commercial fracture at TD)	No expression	TD occurs at resistivity horizontal gradient Area of low resistivity at depth	No expression	No expression	NA
		62-23A (hot/dry)	Good correlation with known lithology	TD occurs within low resistivity zone at fault intersection Lower resistivity identified below well	No expression	No expression	NA
	Other	Section 10 fumaroles (grid column 1)	Magnetized body within the footwall of range-front fault below fumarole area	Lower resistivity at fumarole area than surrounding rock	No expression	No expression	NA

Table 23. Preliminary enhanced geoscience data correlation along long-line cross-sections focused on the Project Area-scale structure. The 5km by 5km grid used in Plate 5 is for comparative purposes in line with the resolution of the seismic velocity model across the project area scale. Table shows correlations across data sets with respect to the defined principal implications. Correlations that exist are noted and in black font. Correlations that do not exist are in red font. Correlations that are not expected but observed are in blue font. Correlations that are expected but not observed are labeled with "No expression". Correlations that are not expected, not observed and data sets that are self-generated (input parameters designed to provide desired result) are labeled with a NA (Not Applicable). Sections are described from south to north.

Cross-Section	Major DVGS Features	Geologic Model	Gravity-Magnetics Model	Magnetotellurics (MT) Resistivity Model	Vp Model	Vs Model	Thermal Numerical Model
LL1	Structure	Carson Sink (west side of Stillwater Range) fault (grid column 1-2)	No expression	No expression	No expression	No expression	No expression
		North-trending fault (grid column 2)	Good correlation Dip of 30-45°	No expression	Vertical break in layered model in grid column 2 may reflect gravity-magnetic fault but dip is markedly steeper	Vertical break in layered model in grid column 2 may reflect gravity-magnetic fault but dip is markedly steeper	No expression
		N-trending Stillwater Range structure (east side of grid column 3)	No expression	Correlation with major horizontal gradient change which suggests a vertical structure	Correlation with vertical break in layered model in east side of grid column 3	Correlation with vertical break in layered model in east side of grid column 3	No expression
		No expression	Possible thrust fault at depth in grid columns 3-4	No expression	No expression Vertical breaks in layered model may reflect gravity magnetic faults n grid columns 3 and 4 but much steeper	No expression Vertical breaks in layered model may reflect gravity magnetic faults n grid columns 3 and 4 but much steeper	No expression

Table 23. Preliminary enhanced geoscience data correlation along long-line cross-sections focused on the Project Area-scale structure. The 5km by 5km grid used in Plate 5 is for comparative purposes in line with the resolution of the seismic velocity model across the project area scale. Table shows correlations across data sets with respect to the defined principal implications. Correlations that exist are noted and in black font. Correlations that do not exist are in red font. Correlations that are not expected but observed are in blue font. Correlations that are expected but not observed are labeled with "No expression". Correlations that are not expected, not observed and data sets that are self-generated (input parameters designed to provide desired result) are labeled with a NA (Not Applicable). Sections are described from south to north.

Cross-Section	Major DVGS Features	Geologic Model	Gravity-Magnetics Model	Magnetotellurics (MT) Resistivity Model	Vp Model	Vs Model	Thermal Numerical Model
		N-trending Dixie Valley (DV) range-front fault (west side of grid column 5)	Good correlation Minor offset along range-front	Good correlation with horizontal resistivity gradients	No expression	No expression	NA
		Multiple piedmont faults (grid column 5); piedmont fault breaks surface along two traces	major offset along piedmont fault Only one fault identified	Horizontal gradients suggest structure but position and dip not clear Horizontal gradients suggest presence of a listric fault but the interpretation is not unique			
		N-trending fault projection (mid-grid column 5)	Potential good correlation but at the scale of the section lines, the piedmont and N-trending fault cannot be differentiated	Unclear	No expression	No expression	NA
		No expression	Potential magnetized Jz offset which correlates with seismic velocity anomalies	Potential correlation	Vertical velocity anomaly	Vertical velocity anomaly	NA
		Buckbrush Fault Zone in geographic center of valley (grid columns 6-7)	No expression	Approximate vertical horizontal gradient	No expression	No expression	NA
		West side of Clan Alpine range bounding fault (grid column 8)	No expression	Unclear	Break in layered model approximately correlates with fault in grid column 8 but fault is vertical	Break in layered model approximately correlates with fault in grid column 8 but fault is vertical	NA
		West side of Clan Alpine N-trending fault (grid column 9)	Good correlation, range-bounding fault identified with moderate west dip	No expression	No expression	No expression	NA
	Lithology	Stillwater Range geology- Jurassic rocks and Tertiary volcanics exposed (grid columns 2-4)	Good correlation, Shallow dipping fault infers buried thrust sheet (grid columns 3 and 4)	Complex resistivity structures below range approximately correlate with gravity-magnetic model – There are some strong conductive lithologies in the Range that seem non-geothermal. Looks like some correlation with the Jur rhyolite, possibly ancestral alteration	Unclear	Unclear	NA
		General geologic model of Dixie Valley; no geologic model for comparison	Correlation with geology not possible Model evidences asymmetric basin shape (grid columns 5-9)	Approximate correlation between gravity-magnetic model basin features and the resistivity model for area Very low resistivity at depth	No expression	No expression	NA
		Clan Alpine (grid columns 8-9) geology Tertiary volcanics overlying Jurassic basement	Correlation with magnetized Jz unit in basement	Approximate correlation with resistive basement (grid columns 7-9)	No expression	No expression	NA
	Temperature	Thermal anomaly (west end of grid column 5)	No magnetized Jz in subsurface	No expression	No expression	No expression	NA
	Wells	45-14 (sub-commercial well) on west end of grid column 5	Gravity-magnetics lithology correlates with 45-14	Fluid entry zone near TD correlates with an 100 Ω-m area	No expression	No expression	NA
LL2	Structure	Stillwater Range N-trending faults (grid columns 2-3)	Westernmost N-trending fault not identified Correlation with N-trending fault (grid column 3) Shallow dip on N-trending fault in grid column 3 not in agreement with structural interpretation	Correlated with horizontal gradients	Near vertical velocity anomalies correlate with N-trending fault (grid column 2)	Near vertical velocity anomalies correlate with N-trending fault (grid column 2)	NA

Table 23. Preliminary enhanced geoscience data correlation along long-line cross-sections focused on the Project Area-scale structure. The 5km by 5km grid used in Plate 5 is for comparative purposes in line with the resolution of the seismic velocity model across the project area scale. Table shows correlations across data sets with respect to the defined principal implications. Correlations that exist are noted and in black font. Correlations that do not exist are in red font. Correlations that are not expected but observed are in blue font. Correlations that are expected but not observed are labeled with "No expression". Correlations that are not expected, not observed and data sets that are self-generated (input parameters designed to provide desired result) are labeled with a NA (Not Applicable). Sections are described from south to north.

Cross-Section	Major DVGS Features	Geologic Model	Gravity-Magnetics Model	Magnetotellurics (MT) Resistivity Model	Vp Model	Vs Model	Thermal Numerical Model
		DV Range-front fault (west side grid column 4)	Correlates with mapped range-front fault Shallow dip not in agreement with steeper dips in the geologic model	Fair correlation in shallow subsurface	No expression	No expression	NA
		Piedmont fault steeply dipping (grid column4)	Good correlation	Potential correlation at depth	Near-vertical velocity break	Near-vertical velocity break	NA
		Buckbush Fault Zone (grid column 6)	Potential correlation at depth, no surface expression of fault, possibly due to lack of contrast in shallow basin fill sediments	Good correlation Good correlation with gravity-magnetic model	Correlation with break in velocity layer model in grid column 6 Dip in velocity model inferred structure in opposite direction relative to geologic model in the shallow subsurface	No surface expression of fault, possibly due to lack of contrast in shallow basin fill sediments	NA
		Clan Alpine Range faulting (multiple NNE-trending faults in grid columns 8-10	No expression	No expression	No expression	No expression	NA
	Lithology	Stillwater Range (Tertiary volcanics and Jz unit at surface; grid columns 2-3))	Magnetized Jz unit is offset by piedmont fault and mostly continuous through DVFZ	Unclear	Good correlation with higher velocity at a shallower depth under the range	Good correlation with higher velocity at a shallower depth under the range	NA
		Dixie Valley (grid columns 4-8)	Agrees with general basement geometry interpretation	Good correlation as basin is conductive Conductive to total depth of cross-section	Unclear	Unclear	NA
		Clan Alpine Range (grid columns 8-10)	Good correlation to surface geology	No expression	Approximate correlation with break in velocity	Approximate correlation with break in velocity	NA
	Temperature	Correlation with zone of dilatation at structural intersection	No expression	Unclear	Unclear	Unclear	NA
LL3	Structure	Stillwater Fault Zone (west side of Stillwater Range, west side of grid column 3)	Good correlation	Unclear	Break in velocity structure Dip in velocity near vertical	Break in velocity structure Dip in velocity near vertical	NA
		N-trending fault within range (east side of grid column 3)	No expression	Unclear	No expression	No expression	NA
		Range-front fault (grid column 5)	Good correlation	Moderate correlation with resistivity gradient	No expression	No expression	NA
		DVFZ contains an intermediate fault and main piedmont (grid column 5)	Good correlation Shallower dip than expected from geologic interpretations	Good correlation with piedmont fault; Extensive Good correlation	Offset in velocity model correlates Very good correlation with piedmont fault	Very good correlation with Very good correlation with piedmont fault	NA
		N-trending valley fault (grid column 6)	No expression	Potential correlation	Potential correlation	Potential correlation	NA
		Buckbrush Fault Zone (grid column 7)	No expression	Unclear	No expression but anomalous velocity structure observed in western portion of grid column 8	No expression but anomalous velocity structure observed in western portion of grid column 8	NA
		N-trending inferred structure (grid column 8)	NA (fault defined by gravity horizontal gradients)	Unclear to moderate correlation	Elevated shallow velocity and depressed deep velocity in basin area	Elevated shallow velocity and depressed deep velocity in basin area	NA
	Lithology	Carson Sink Basin (grid columns 1-2)	Good correlation	Good correlation with shallow low resistivity	No expression	No expression	NA
		Stillwater Range geology (basement [Tr] on west side and Jz rocks on east side; grid columns 3-4)	Good correlation	Unclear	No expression	No expression	NA

Table 23. Preliminary enhanced geoscience data correlation along long-line cross-sections focused on the Project Area-scale structure. The 5km by 5km grid used in Plate 5 is for comparative purposes in line with the resolution of the seismic velocity model across the project area scale. Table shows correlations across data sets with respect to the defined principal implications. Correlations that exist are noted and in black font. Correlations that do not exist are in red font. Correlations that are not expected but observed are in blue font. Correlations that are expected but not observed are labeled with "No expression". Correlations that are not expected, not observed and data sets that are self-generated (input parameters designed to provide desired result) are labeled with a NA (Not Applicable). Sections are described from south to north.

Cross-Section	Major DVGS Features	Geologic Model	Gravity-Magnetics Model	Magnetotellurics (MT) Resistivity Model	Vp Model	Vs Model	Thermal Numerical Model
		Basement/Basin-fill geometry (grid columns	Moderate correlation with geologic model Symmetrical basin along section	Moderate correlation	No expression	No expression	NA
		Occurrence of Jz unit	Continuous magnetized Jz section agrees with geologic section and exposed geology in the range	No expression	No expression	No expression	NA
	Temperature	Thermal upwelling within the DVFZ	No missing (de-magnetized) rocks	No expression	No expression	No expression	NA
	Wells	66-21 (hot/dry well)	Gravity-magnetics lithology correlates with 66-21	Well intersects area of lower resistivity to total depth (low permeability well)	No expression	No expression	NA
LL4	Structure	Intra-range N-trending fault (grid column 1)	Good correlation; Faults have shallow to moderate easterly dips	Good correlation with resistivity gradient	Break in velocity layered model within range	Break in velocity layered model within range	NA
		Range-front fault (grid column 1)	No expression No major offset along range-front	Good correlation with resistivity gradient;	No expression	No expression	NA
		Piedmont fault (grid column 2)	Good correlation	Good correlation Piedmont fault associated with extensive (1.25km-wide) low resistivity zone	No expression	No expression	NA
		Valley structure: N-trending fault (grid column 2), west-dipping antithetic fault(grid column 3)	No faulting emphasized; correlation with breaks in basement contact; N-trending fault occurs within 1km of gap in magnetized rocks	N-trending structure tightly bounds lower resistivity to the east; antithetic fault show moderate correlation with resistivity break	No expression	No expression	NA
		Clan Alpine range-bounding fault (grid column 4-5)	Good correlation	No expression	Potential correlation Major break in velocity model and high velocity zone	Potential correlation Major break in velocity model and high velocity zone	NA
	Lithology	Stillwater Range (mixed Jz mafic rocks and quartzite)	Good correlation	Highly resistive body below Stillwater Range likely infers basement rocks	No expression	No expression	NA
		Basement shape/basin-fill geometry	Moderate to good correlation with geologic model; Basin-fill contact deeper (grid columns 2-3) than expected from geologic model	Good correlation Conductive regime continues to total depth of cross-sections (-4km asl)	No expression	No expression	NA
		Occurrence of magnetized Jz unit	Good correlation below Stillwater Range and beneath eastern part of valley Magnetized Jz unit in production area (grid column 2) shows a thicker exposure than expected from the Jurassic aged rocks from well logs	No expression Magnetized body in area of production wells occur within lower resistivity	No expression	No expression	NA
	Temperature	Thermal upwelling within the DVFZ	Gap in magnetized Jz unit within DVFZ	Low resistivity along piedmont fault to depth	No expression	No expression	NA
	Well	Bolivia well (grid column 1)	No expression	Coincides with area of lower resistivity	No expression	No expression	NA
		Section 7 producers (grid column 2)	Magnetized Jz section thicker than expected from well logs	Correlates with lower resistivity	No expression	No expression	NA
		62-21 (conductive well) (grid column 3)	No expression	Moderate to good correlation with lithology (Jz rocks are more resistive)	No expression	No expression	NA

11. ENHANCED EXPLORATORY DATA ANLAYSIS

The treatment of the enhanced data follows many of the same procedures identified and used for the baseline data (see Sections 7.4.1 and 7.4.2). The Calibration Area contains 658 data cells for each depth ranging from +1km asl to -4km asl in 0.5km increments. The enhanced data set is too large (i.e., >400 pages) to be included in this report. It has been provided as a Geostatistical data set to the National Geothermal Data Repository.

11.1 CORRELATION ANALYSIS, SCATTERPLOT MATRIX FOR SELECTED VARIABLES

As a first step in analyzing the enhanced data, we examined bivariate correlations between all the key geoscience variables (Table 24) identified in the baseline model (Section 7.4), except vertical stress which was included in the baseline model and determined to be a surrogate for Depth. Note that Vertical Stress was so highly correlated with Depth (Appendices 15 and 17; Section 7.4) that it serves little purpose in the analysis. Since objective one of the objectives of this study is to find locations that would be viable for EGS power generation, we are focused primarily on discovering relationships that are independent of depth.

Table 24. Enhanced data correlation coefficients for key geoscience parameters In the Calibration Area (as determined in the baseline geostatistical data analysis, Appendices 15 and 17; Section 7.4.)

Geoscience Variables	Depth	CSC[1]	Dilatation (Dil)	Temperature	Vp[2]	Vs[3]	MT[4]
Depth (asl[5])	1	0.122	-0.015	-0.808	-0.978	-0.879	-0.185
CSC	0.122	1	0.115	-0.147	-0.119	-0.11	-0.079
Dil	-0.015	0.115	1	-0.015	0.023	0.007	-0.232
Temp	-0.808	-0.147	-0.015	1	0.823	0.705	0.07
Vp	-0.978	-0.119	0.023	0.823	1	0.898	0.186
Vs	-0.879	-0.11	0.007	0.705	0.898	1	0.157
MT	-0.185	-0.079	-0.232	0.07	0.186	0.157	1

[1]Coulomb Stress Change
[2]P-wave velocity
[3]S-wave velocity
[4]Magnetotellurics
[5]Correlations are made relative to depth (asl) so a -0.978 so for example, the Depth-Vp correlation means that Vp increases as depth below sea level increases.

Table 24 shows that (1) Temperature is very weakly correlated with everything except for Vp, Vs, and Depth, and (2) Vp and Vs are strongly correlated. As discussed later in the Regression Analysis (Section 11.2.1), Vp and Vs are unable to predict Temperature when the effect of depth is removed.

Scatter plots for all these variables, as well as for the residuals from a linear fit of temperature based on depth (labeled TDRes and discussed in Section11.2.1), are shown in Figure 180.

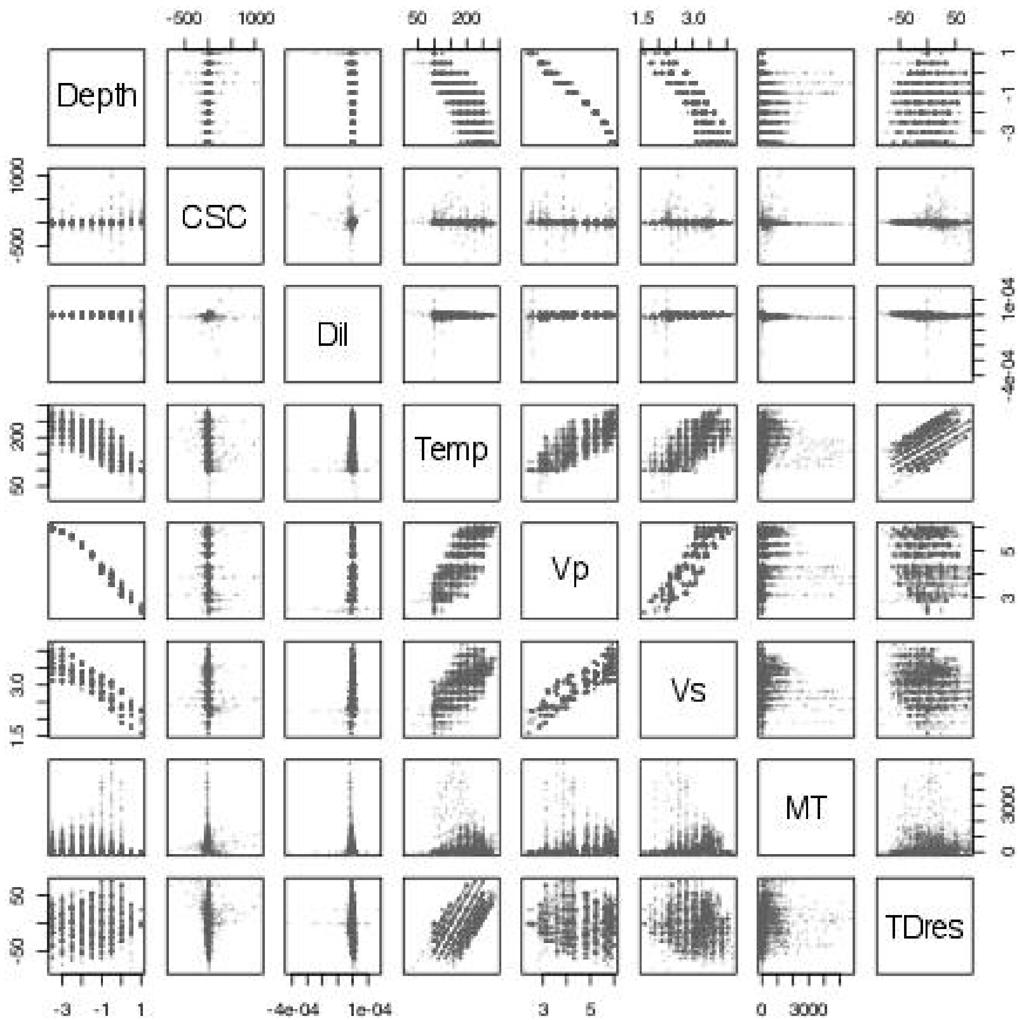

Figure 180. Scatter plot for all enhanced data key geoscience parameters; see text Section 11.1 for an explanation of TDres.

11.2 REGRESSION ANALYSIS

As a first step in doing regression analysis, all the above variables were included in predicting temperature (Table 25). All were significant at a 0.05 significance level[19], and the R^2 value is 0.678. However, leaving out all variables except for Vp results in a very minimal reduction in R^2, to 0.658. The best fit with two variables is Vp and CSC, giving an R^2 of 0.659. With all variables except for Vp, R^2 is 0.659. With Vp and Depth omitted (leaving CSC, Dil, Vs and MT) drops to 0.501. Dropping Depth and both Vp and Vs (since both are highly correlated with Depth) reduces R^2 to 0.046 (using only CSC, Dil, and MT). This drastic reduction in R^2 identifies Depth as a powerful confounding but a significant contributing factor. Consequently, the next phase of the analysis will focus on looking at the relationship between Vp and Temperature independent of Depth.

[19] Statistical significance at the 5% level is a condition used as evidence that the results cannot be reasonably explained by chance, instead they describe some real phenomenon or relationship.

Table 25. Enhanced data correlation coefficients between Temperature Residuals and key geoscience parameters in the Calibration Area as determined by the baseline geostatistical data analysis (Appendices 15 and 17; Section 7.4).

Parameter	Depth	CSC[1]	Dilatation	Temperature	Vp[2]	Vs[3]	MT[4]
Temperature Residual Correlation Coefficient	0	-0.063	-0.183	0.596	0.037	0	0.098

[1]Coulomb Stress Change
[2]P-wave velocity
[3]S-wave velocity
[4]Magnetotellurics

11.2.1 Temperature Residuals

Because of the strong relationship between depth and many of the variables, an approach used to control for the confounding effect of depth was to predict temperature based on depth and use the residuals as a dependent variable in multiple regression.

Figure 181 illustrates the relationship between Temperature and Depth and contrasts two methods used to remove the dependence of Temperature on Depth. The blue line is the simple regression line predicting Temperature and Depth. The red X's show the average Temperature at each depth. The Temperature Residuals are the vertical distances between each point and the blue line. In other words, the Temperature Residuals are the differences between the actual Temperatures and the predicted Temperatures based on the line. Our first approach to control for Depth was to use the Temperature Residuals as a dependent variable in multiple regression.

The logic of this method is that the Temperature Residuals represent how unusually hot (or cold) each cell is compared to what we would expect at that Depth (along the blue line). An alternative was explored using the difference between each Temperature and the average Temperature at that Depth (the red X's). These differences are referred to below as Temperature Differences. Essentially these two variables (Temperature Residuals and Temperature Differences) have the same logic of looking at how hot a cell is compared to cells at the same depth. However, the red X's give Temperature predictions that are not constrained to be on a line. Correlations between each of the seven main variables and the Temperature Residuals are shown above (Table 25). The correlation coefficient between the residuals and depth is constrained to be 0 because essentially the effect of depth has been removed. In general, the correlation coefficient between temperature itself and the residuals, 0.596 (Table 25) should tend be fairly large and positive since high temperatures in general tend to correspond to high temperatures at a given depth.

Using multiple regression with these variables, except for Temperature itself, the Temperature residuals cannot be predicted very well. The R^2 value for the Temperature residuals in the multiple regression analysis is only 0.091, in spite of the fact that the large number of observations results in highly statistically significant[1] predictors, notably Dilatation, Vp, and Vs. The regression analysis model used is:

$$Temperature\ Residuals = \beta_1 Depth + \beta_2 CSC + \cdots + \beta_6 MT + \mathcal{E}$$

where the β_i are coefficients (shown in Table 26) estimated using multiple regression and Ɛ is the error[20]. The standard errors in Table 26 reflect the precision in the estimates, or the typical absolute size of the errors. Also in Table 26, the t-values are the coefficient estimates divided by the standard errors and provide an estimate of how much the coefficients deviate from 0. If the relationship between each particular variable and the Temperature Residuals is due to chance (i.e., the variable represents random noise) then the coefficient estimate follows Student's t-distribution and the t-value should be close to 0 for complete randomness or up to 2. If the variable represents random noise, then we would expect the

[20] Each cell has an actual Temperature Residual as well as a predicted Temperature Residual based on the multiple regression fit. The difference between these two is the error term. Another way to conceptualize the error term is think of it as any amount, either random or based on variables not in the model, that the model is unable to explain

t-value to be random, and typically in the range of -2 to +2 or slightly larger. The last column in this table, shows the p-values (based on the t values) that are used to determine statistical significance[1]. Small p-values indicate that the relationship cannot reasonably be explained by chance. In this particular case, all the p-values are less than 0.05, indicating statistical significance at the 5% level, and all but the one corresponding to MT are less than 0.001. Figure 182 illustrates how the t- and p-values are related. Indicated is a p-value of 0.05, the cutoff for statistical significance. Thus any t-value bigger than that shown (i.e., farther from 0 either positive or negative) would yield a p-value smaller than illustrated and would be deemed statistically significant. The R^2 value[21] (0.091 based on the model used to generate Table 26) is fairly small, indicating that the model is not able to account for much of the variability in temperature (controlling for depth). The statistical significance indicates that we are not just fitting noise, the variables have do have some ability to predict Temperature Residuals, although the variables used are not highly correlated with the Temperature Residuals.

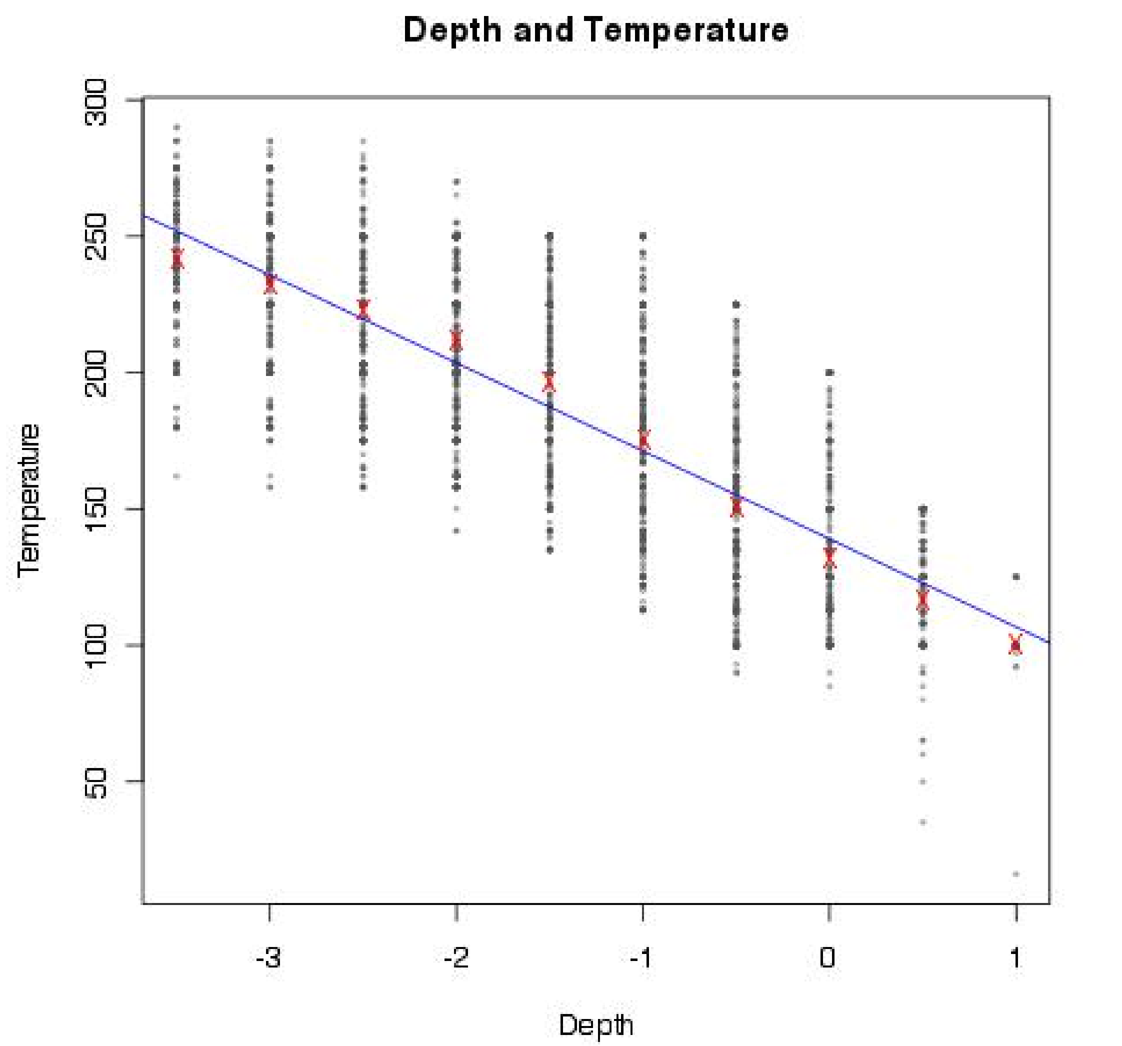

Figure 181. Temperature vs Depth with a linear fit

[21] R^2 measures the proportion of variance explained by the model. A value of 0 would indicate a model that does no better than using simply an intercept term with no other variables; a value of 1 would indicate that the variables used can predict the dependent variable (Temperature Residuals in this case) perfectly.

Table 26. Fit of Residuals from Linear Fit of Temperature based on Depth; see text for a discussion of t- and p-values.

Parameter	Regression Coefficient Estimate (β_i)	Standard Error (+/-)	t-value	Pr(>|t|) (=the p-value)
(Intercept)[22]	-1.154e+02	8.331e+00	-13.856	<2e-16***
Depth	2.701e+01	1.864e+00	14.492	<2e-16***
CSC	-3.122e-02	8.038e-03	-3.885	0.000104***
Dilatation (Dil)	-4.958e+05	3.616e+04	-13.711	<2e-16***
Vp	3.717e+01	2.371e+00	15.675	<2e-16***
Vs	-6.118e+00	1.774e+00	-3.448	0.000570***
MT	1.707e-03	8.421e-04	2.027	0.042708*

***Pr value is between 0 and 0.001 (i.e., probability of noise causing this effect is between 0-0.1%)
*Pr value is between 0.01 and 0.05 (i.e., probability ability of noise causing this effect is between 1-5%)

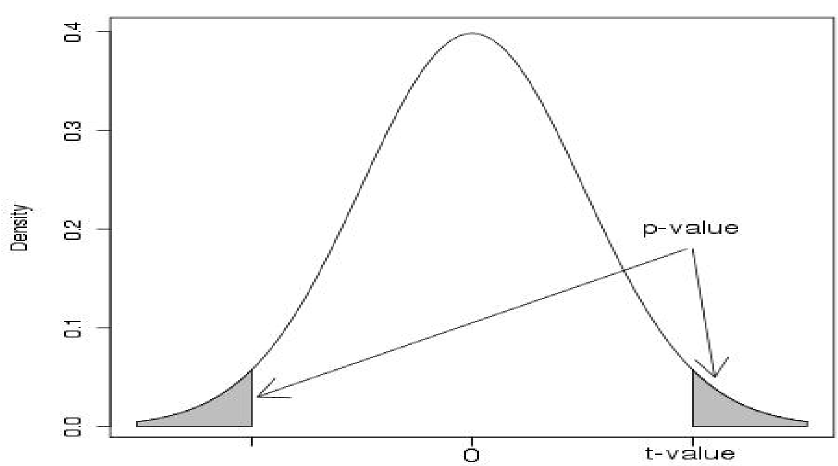

Figure 182. Illustration of the t-value and p-value relationships; see text for an explanation.

The results (correlations between Temperature Differences and other variables, and summary of fit) were very similar to the analogous results using Temperature Residuals. Using multiple regression with all seven variables (including depth) to predict the Temperature Differences gives an R^2 of 0.062 based on the model used to create Table 28. The Temperature Difference Correlations coefficients and summary of the multiple regression fit, Tables 27 and 28, respectively. Table 27 shows the correlation coefficients between the Temperature Differences and each of the seven parameters, analogous to Table 25, and Table 28 gives the detail of the multiple regression done with the Temperature Differences, analogous to Table 26.

Table 27. Enhanced data correlation coefficients for the Temperature Differences and other key geoscience variables

Parameter	Depth	CSC[1]	Dilatation (Dil)	Temp-erature	Vp[2]	Vs[3]	MT[4]
Temperature Differences Correlation Coefficient	0	-0.056	-0.206	0.58	0.003	-0.039	0.086

[1]Coulomb Stress Change; [2]P-wave velocity; [3]S-wave velocity; [4]Magnetotellurics

Yet another technique we could have used would be to use the residuals of Vp and Vs after fitting based on Depth, in the same way that we took the Temperature residuals. Since the difference between Vp

[22] The intercept term behaves much as the y-intercept term in the usual equation for a line, y=mx+b. The value is not of interest but it is necessary in the model to allow the line to fit the data better by not constraining that the line goes through the origin.

itself and the Vp Residuals would be independent of the Temperature Residuals, this would not change the strength of the prediction.

Table 28. Fit of Deviations from Average Temperature at Depth

Parameter	Regression Coefficient Estimate (β_i)	Standard Error (+/-)	t value	Pr(>|t|) (=the p-value)
(Intercept)[7]	-1.151e+01	8.270e+00	-1.392	0.16414
Depth	3.939e+00	1.851e+00	2.128	0.03336 *
CSC	-2.574e-02	7.980e-03	-3.225	0.00127 **
Dilatation (Dil)	-4.794e+05	3.590e+04	-13.353	< 2e-16 ***
Vp	1.003e+01	2.354e+00	4.263	2.06e-05 ***
Vs	-1.026e+01	1.761e+00	-5.827	6.04e-09 ***
MT	1.359e-03	8.360e-04	1.625	0.10422

***Pr value is between 0 and 0.001 (i.e., probability of noise causing this effect is between 0-0.1%)
*Pr value is between 0.01 and 0.05 (i.e., probability ability of noise causing this effect is between 1-5%)

11.2.2 Lithology

To determine if breaking down the data based on lithology (i.e., formation types for the purposes of this statistical analysis) would allow better prediction of temperature, the same multiple regression model was used for each lithology by itself, predicting temperature residuals based on the same geostatistical variables. The R^2 values are shown Table 29.

Table 29. Multiple regression model predicting temperature residuals based on the same geostatistical variables (see Tables24) by formation type (see Appendix 15.4 for description of formation types)

Formation Type	Jbr	Jz	Kgr	Tbf	Tmb	Tr	Tv
R^2	0.14	0.34	0.24	0.18	0.43	0.06	0.64

It is of some interest that the highest R^2 values do not seem to correspond to more favorable EGS and hydrothermal reservoir lithologies such as Kgr and Jbr. If those lithologies had high R^2 values then we might be encouraged to think that we could do a good job predicting temperature in the most favorable lithologies.

The high R^2 value for Tv seems to be a consequence of the rapid rise in temperature in Tv with depth, compared to other formation types. Because of this property in the Tv data, a correlation between the Temperature Residuals and both Vp and Vs remains. If the entire procedure of finding Temperature Residuals is replicated just for Tv, the R^2 value drops to 0.22. So although the original R^2 value of 0.64 tells us that the model can make reasonable predictions of how hot Tv is relative to all formation types at a particular depth, the value of 0.22 tells us that the model does not do a very good job of predicting how hot Tv is relative to only other Tv cells at the same depth.

11.3 CART (CLASSIFICATION AND REGRESSION TREES)

As in the baseline model analysis (Section 7.4), we used CART to model the ability of the geoscience parameters to predict several variables of interest. In addition to predicting Temperature and whether cells would be productive for hydrothermal or inferred EGS, we also predicted Temperature Residuals. The basic results for the enhanced data are summarized in Table 30. The ability to predict temperature (R^2 of 0.74) is fairly similar to the baseline analysis (R^2 from 0.62 to 0.78 for different models using well data, from 0.8 to 0.91 using section data).

CART performs somewhat better than multiple regression for predicting both temperature and temperature residuals. CART is not restricted to linear relationships and breaks the data into categories, so this is not particularly surprising: to the extent that some variables do not have a linear relationship with Temperature (perhaps for MT in Figure 180, most others are quite linear), CART should be able to capture any such irregularities. In particular, if there is an interval with respect to a variable where Temperature is high but surrounding values of that variable correspond to lower Temperatures, CART will capture these patterns.

Table 30. Summary of Enhanced CART Analyses conducted

Description of Analysis Conducted	**Selected Geoscience Parameters Considered(x) and Used (X) in the Data Splitting Process**						**R^2 - value**
	T	*Vp*	*Resistivity (MT)*	*CSC[1]*	*Dilatation*	*Grav-Mag[2] Lithology*	
Predicting Temperature	---	X	X	x	X	x	**0.74**
Predicting Temp Residuals after fitting Depth	---	X	x	X	X	X	**0.38**
Predicting Productive (hydrothermal) Wells cells	X	X	X	x	X	x	**0.19**
Predicting EGS cells	X	X	X	X	X	x	**0.15**

[1]Coulomb Stress Change
[2]Gravity-Magnetics

The low R^2 value for predicting productive hydrothermal and inferred EGS cells is not a particularly good indication of the success of this method because of the sparseness of favorable cells. However, only 18 cells out of 4297 cells (with no variables missing) were productive hydrothermal, and only 21 were inferred EGS favorable. Perhaps a more appropriate way of looking at this result is that we are looking for a needle in a haystack. CART cannot explain a very high proportion of the variability in the predicted variable (that's what R^2 measures), but it does do a reasonable job of reducing the size of the haystack we are searching in, as discussed in the following section.

Any analysis of the inferred EGS cells is limited by the fact that the criteria used to infer EGS viability in the baseline data were not then applied to the enhanced data to identify additional cells likely to be viable for EGS. Thus there may be some cells in the enhanced data that might in fact be viable for EGS but we are asking CART to treat these cells as though they are not viable (perhaps in spite of parameter values that would indicate that they are likely to be viable).

11.3.1 Full CART Results

Additional CART analyses were performed, considering all subsets of variables that could be used to predict Temperature, Lithology, Productive Hydrothermal, and Inferred EGS favorable cells. The results are summarized in Table 30. The R^2 values for Productive Hydrothermal and inferred EGS favorable cells are still quite low (0.250 and 0.144, respectively), illustrating as before that the sparseness of hydrothermal productive or EGS favorable cells makes high R^2 values difficult to attain.

Figures 183 and 184 show the trees corresponding to the fewest variables that still achieve the maximum observed R^2 value for hydrothermal and EGS favorable cells, respectively. Like the multiple regression results, the large number of data points makes p-values extremely close to 0. To establish statistical significance a chi-squared (χ^2) test was used[23] .For the hydrothermal tree this gives χ^2=1068 with 11

[23] The details of the test are somewhat technical. A reasonably succinct explanation of the chi-squared goodness of fit test can be found here: http://en.wikipedia.org/wiki/Pearson%27s_chi-squared_test

degrees of freedom. For EGS, χ^2=614 with 7 degrees of freedom. In both cases the p-value is astronomically small.

The tree for productive hydrothermal cells (Figure 183) has three terminal nodes worth examination. In the figure these nodes have the number of cells displayed in blue and in a slightly larger font.

1. For Dilatation >-1.49 x10^{-6}, CSC <-23.5, Vp <5.26, and MT >108.5, three out of six cells are productive hydrothermal.
2. For Dilatation between 3.58 x 10^{-6} and 3.75 x10^{-6}, and CSC >18.5, two out of five cells are productive hydrothermal.
3. For Dilatation between -1.49 x10^{-6} and 3.58 x 10^{-6}, CSC between 18.5 and 24.5, and Vp between 4.41 and 5.27, four out of eight cells are productive hydrothermal.

For these three nodes taken together, CART has identified 19 cells that seem to have characteristics that make them likely to be Productive Hydrothermal, and 9 of these cells actually are. Although the R^2 value is not very impressive, CART has managed to reduce the size of the haystack from over 4000 cells down to 19, of which nearly half are Productive Hydrothermal.

For the EGS tree (Figure 184), there are two nodes with a substantial proportion of inferred EGS cells. In the figure these nodes have the number of cells displayed in blue and in a slightly larger font.

1. For Vp <5.63, Temp >239.5, and Dilatation >1.39 x 10^{-6}, three out of eight cells are inferred EGS.
2. For Vp < 5.63, Temp between 197.5 and 239.5, MT between 37.5 and 40.5, and Dilatation more than -8.99 x 10^{-7}, three out of five cells are inferred EGS.

For these two nodes, we have a similar reduction in haystack size as in the Productive Hydrothermal analysis, down to 13 cells of which six are Inferred EGS favorable cells.

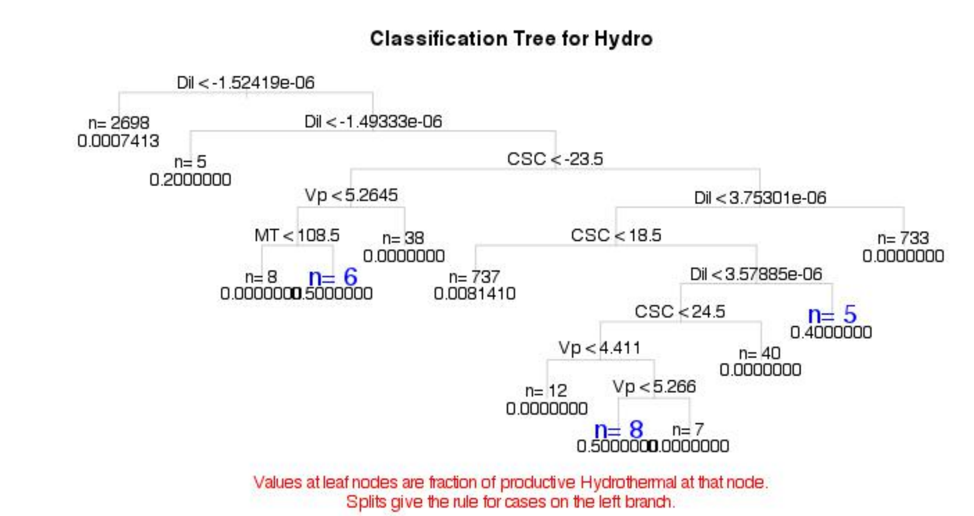

Figure 183. CART predicting productive Hydrothermal based on Dilatation, CSC, Vp, MT (Table 30)

Note that the assumptions of the test are not fulfilled with such sparse data (expected values of all nodes should be at least 5), but because the p-values are so astronomically small anyway, second order corrections are superfluous.

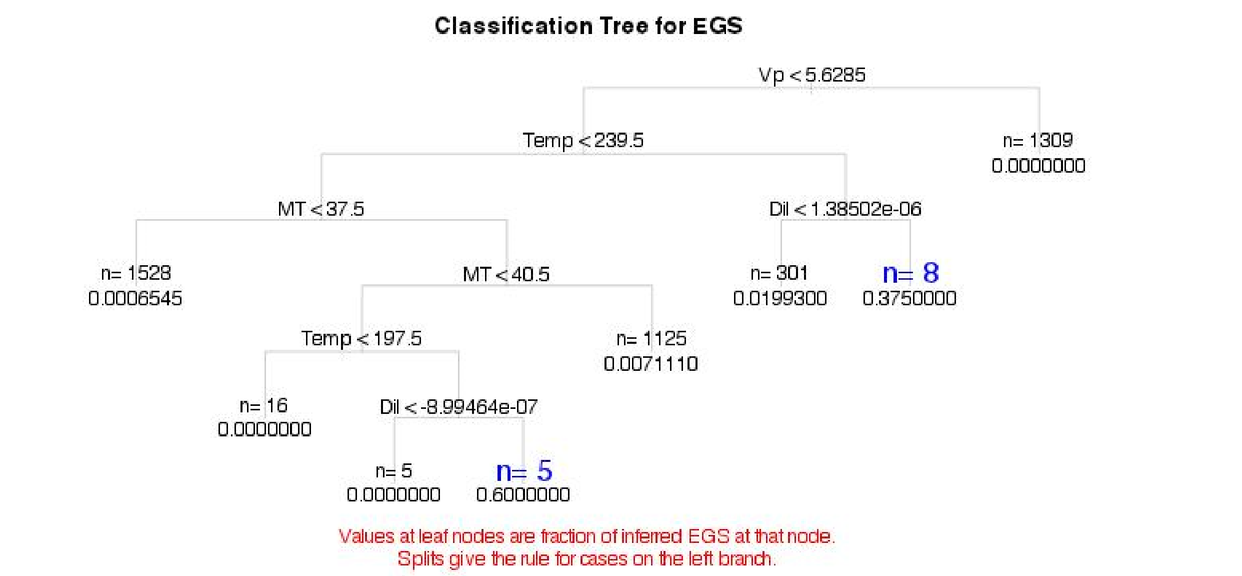

Figure 184. CART predicting inferred EGS based on Vp, Temp, MT, Dilatation (see Table 30)

11.3.2 CART Sensitivity Analysis

The CART analyses described above explored differing combinations of multiple explanatory variables to find the highest r^2-values in predicting one of the four key response variables: temperature, lithology type, productive hydrothermal cells, and inferred EGS favorable cells. This is presented to determine which combination of six key geoscience parameters (described above and excluding depth) may provide the R^2 values. Table 31 presents the result of this analysis. The details of this analysis are presented in Part II-Appendix 12. Predicting Temperature using variables correlated with Depth (notably Vp, used for the first split in every best tree) is somewhat problematic as discussed above with respect to the regression analysis. This was done for consistency with the baseline model analysis (Section 7.4). To address the confounding effect of Depth, Temperature Residuals were used in place of Temperature in the next CART results. Under this model, Dilatation was always used in the first split, and all the R^2 values are fairly low, though better than for multiple regression and better than for predicting productive Hydrothermal and inferred EGS. The lower R^2 value compared to predicting raw Temperature illustrates how important it is to control for the confounding of Depth.

Note that Lithology was used in different ways in predicting different variables. For Temperature and Temperature Residuals, both assigned lithology and lithology based on gravity-mag modeling were used as categorical variables. For productive Hydrothermal and inferred EGS, gravity-mag lithology was also used as a categorical variable. The logic behind using categorical variables here rather than numerical density is that the different formation types may have a relationship with the predicted variables that is not simply dependent on density. Using categorical variables allows the model to take advantage of any such relationships. For predicting lithology, we used numerical density (from gravity-mag modeling) as the predicted variable since the goal was to be able to predict density, not just formation type. Further, numerical density from assigned lithology was used to predict since this is more consistent with using numerical density as the predicted variable. Note that using lithology density to predict lithology density is somewhat circular, though the densities are from different sources, and the high R^2 values (with the first split always made using lithology density) partly reflect this.

Sometimes R^2 values go up slightly when fewer variables are considered. This is because CART always considers the best single split possible at each step, and sometimes the best single step will split the data in a way that makes subsequent steps less effective. Thus considering fewer variables will sometimes constrain the tree making procedure that will fortuitously lead to a more successful final tree.

Table 31. Enhanced CART analysis results in predicting parameters of interest: temperature, lithology, productive hydrothermal cells, and inferred EGS favorable cells

Predicted Response Variable	Best R^2 when Explanatory Variables are Removed						Geoscience Parameters used (in order of splits) and considered
	0	1	2	3	4	5	
Temperature	0.727						Vp, Dilatation, MT, CSC, Lithology, G-M Lithology
		0.727					Vp, Dilatation, MT, CSC Lithology
			0.727				Vp, Dilatation, MT, CSC
				0.727			Vp, Dilatation, MT
					0.717		Vp, Dilatation
						0.659	Vp
Temperature Residuals	0.348						Dilatation, CSC, Vp, MT, G-M Lithology, Lithology
		0.348					Dilatation, CSC, Vp, MT, G-M Lithology
			0.348				Dilatation, CSC, Vp, MT
				0.348			Dilatation, CSC, Vp
					0.318		Dilatation, CSC
						0.227	Dilatation
Lithology[24], (as defined by grav-mag density)	0.704						Lithology Density[25], CSC, Vp, Dilatation, Temperature, MT
		0.704					Lithology Density, CSC, Vp, Dilatation, Temperature
			0.704				Lithology Density, CSC, Vp, Dilatation
				0.690			Lithology Density, CSC, Vp
					0.634		Lithology Density, Vp
						0.604	Lithology Density
Productive Hydrothermal cells	0.189						Dilatation, Temperature, Vp, MT, G-M Lithology, CSC
		0.199					Dilatation, Temperature, CSC, G-M Lithology, MT
			0.250				Dilatation, CSC, Vp, MT (see Figure 183)
				0.207			Dilatation, Vp, MT
					0.209		Dilatation, Vp
						0.035	Dilatation

11.4 PARAMETER DIFFERENCES BASED ON PROXIMITY TO THE DIXIE VALLEY FAULT ZONE

Getting more data for the enhanced dataset has not particularly improved the ability to predict productive hydrothermal and EGS favorable cells. To look at how the enhanced data differs from the baseline data, we subdivided the data into regions based on proximity to the DVFZ. Presented in Table 32 are the six key geoscience parameters analyzed (not including Depth) and their summary statistics in four regions: in a well, in and within 500m of DVFZ, in and within 1000m of DVFZ, and all enhanced data. The dilatation values are multiplied by one million for easier readability. The column for mean is shown with a different color to facilitate comparison of the means.

Temperature, Vp, and Vs are all fairly similar for the four regions considered. MT has values a little more than half as large in the well data, but fairly consistent values outside of the wells. Dilatation has the

[24] Defined by the gravity-mag modeling identified density values for the different formations (i.e., Tr = 2.88, Jv = 2.47, Jzm 2.876, QTbf = 2.445; Appendix 15-Table 15-5)

[25] Assigned densities (i.e., QTbf = 1.3, Tmb = 2.5, Jz = 2.6, Jbr = 2.5, Tr = 2.4, Tv = 2.4, Kgr = 2.5; Appendix 15-Table 15-4)

somewhat odd pattern of having highest values in the wells, lowest in the two regions close to DVFZ, and medium values average over all the data. The reason for this may be related to the geologic occurrence of the dilatation zones in that they are limited to zones of structural intersection. CSC values don't seem to follow any particular pattern. The distributions for these last three variables, especially CSC, are complicated by the presence of large outliers, which affect the average greatly. For CSC, the region with the largest average is in and within 500m of DVFZ while the lowest average is in the region in and within 1000m of DVFZ. However, all the quartiles, as well as the minimum and maximum, are very similar if not identical. This is an indication that a few outliers between 500m and 1000m are lowering the average, but it must be only a few values since the quartiles are largely unchanged. These distributions are shown in more detail in Figures 184-187 and discussed further below.

Figures 185 – 187 present smoothed histograms of the relationship of the key geoscience parameters with respective to the 4 regions proximal in and near the DVFZ described above. The parameter values corresponding to Inferred EGS favorable and productive Hydrothermal cells are shown as black and orange cures on the same figures. The density refers to the density of data values; as in a standard histogram the curve is tallest where the data values are most concentrated and the total area under each curve is constrained to be 1.

Temperature in Figure 185(a) shows that both the inferred EGS favorable cells and productive Hydrothermal cells tend to have higher temperatures, no surprise there. For Vp, shown in Figure 184(b), both inferred EGS favorable and productive Hydrothermal cells tend to have lower values of Vp but not many very small values. This is also reflected in the CART analysis for productive Hydrothermal (Figure 183). Three splits are based on Vp: two that split nodes with a high concentration of productive Hydrothermal cells and Vp below about 5.3, and one split that divides off a group without any productive Hydrothermal cells and Vp below 4.4. In the inferred EGS CART tree (Figure 183), the first split is the only one using Vp, it separates out over 1300 cells with Vp over 5.63 without any inferred EGS favorable cells

Because the data for MT, Dilatation, and CSC is mostly so tightly clustered but has a few outliers, Figures 187 and 188 show expanded versions to show more detail where the bulk of the data points are. For the MT data, we see that in the enhanced data (all data), the additional points were mostly values quite close to 0, while the inferred EGS favorable and productive Hydrothermal values tended to be a bit larger. For Dilatation, an even more sharp contrast can be seen that the productive Hydrothermal points (in orange) have larger values of Dilatation. This serves as visual confirmation of what CART does in the tree (Figure 183), where four out of the eleven splits, including the first, are based on Dilatation. The EGS curve (black) is also a bit higher than (but not as tightly clustered as) the general data. Higher dilatation is used in both of the final splits for the nodes with highest concentration of inferred EGS. For CSC, all the curves are less regular, but productive Hydrothermal has somewhat higher values of CSC in general, though the relationship is not simple. The tree in Figure 183 shows three splits for CSC, one of which separates out a branch with a high concentration of productive Hydrothermal cells that has very low levels of CSC (below -23.5) while the other two splits separate productive Hydrothermal cells with a relatively high value of CSC: above 18.5, and between 18.5 and 24.5.

11.5 OMISSIONS FROM BASELINE CONCEPTUAL MODEL

Several techniques were used to investigate the reliability of methods being used in Section 7, the baseline conceptual model. Specifically, cross validation was used to assess the precision of the R^2 values, bootstrap was used to construct confidence intervals for those R^2 values, and several different weighting schemes were used based on the trust values for the data. All three of these methods made very little difference in the results and were omitted from the enhanced data analysis for this reason.

Table 32. Six geostatistical parameters (not including Depth) restricted to different regions relative to the Dixie Valley Fault Zone (DVFZ): in a well, within a distance of 500m, within 1000m, and all the data in the Calibration Area

Parameter	Region/ Distance	Min	1stQ[1]	Median (2ndQ)	Mean	3rdQ	Max
Temp	In Well	16	150	215	197.9	250	280
Temp	Within 500	90	158	203	198.1	250	290
Temp	Within 1000	60	158	203	197.8	250	290
Temp	All Data	16	150	200	192.8	235	290
Vp	In Well	3.342	4.676	5.654	5.233	5.848	6.001
Vp	Within 500	3.28	4.817	5.657	5.275	5.892	6.018
Vp	Within 1000	3.28	4.821	5.666	5.301	5.892	6.018
Vp	All Data	3.28	4.929	5.687	5.388	5.892	6.018
Vs	In Well	2.288	3.018	3.34	3.239	3.503	3.974
Vs	Within 500	1.899	3.095	3.327	3.252	3.484	4.042
Vs	Within 1000	1.899	3.095	3.327	3.274	3.484	4.042
Vs	All Data	1.899	3.125	3.386	3.351	3.614	4.386
MT	In Well	0	7	24.5	132.8	190.5	1071
MT	Within 500	0	20	93	230	300	2622
MT	Within 1000	0	16	83	242.4	290.5	4179
MT	All Data	0	8	36	236.5	202	5712
Dilatation	In Well	-63.38	-4.02	-1.433	-1.551	0.9747	25.33
Dilatation	Within 500	-422.9	-7.514	-4.945	-6.401	-3.292	164.3
Dilatation	Within 1000	-422.9	-7.333	-4.58	-6.019	-3.066	164.3
Dilatation	All Data	-422.9	-6.026	-3.458	-3.109	1.366	164.3
CSC	In Well	-290	-10.25	-1	-0.347	15.25	765
CSC	Within 500	-808	-13	-8	0.7585	-1	1093
CSC	Within 1000	-808	-14	-8	-1.628	-1	1093
CSC	All Data	-808	-12	-4	0.5909	11	1093

[1]Quantile

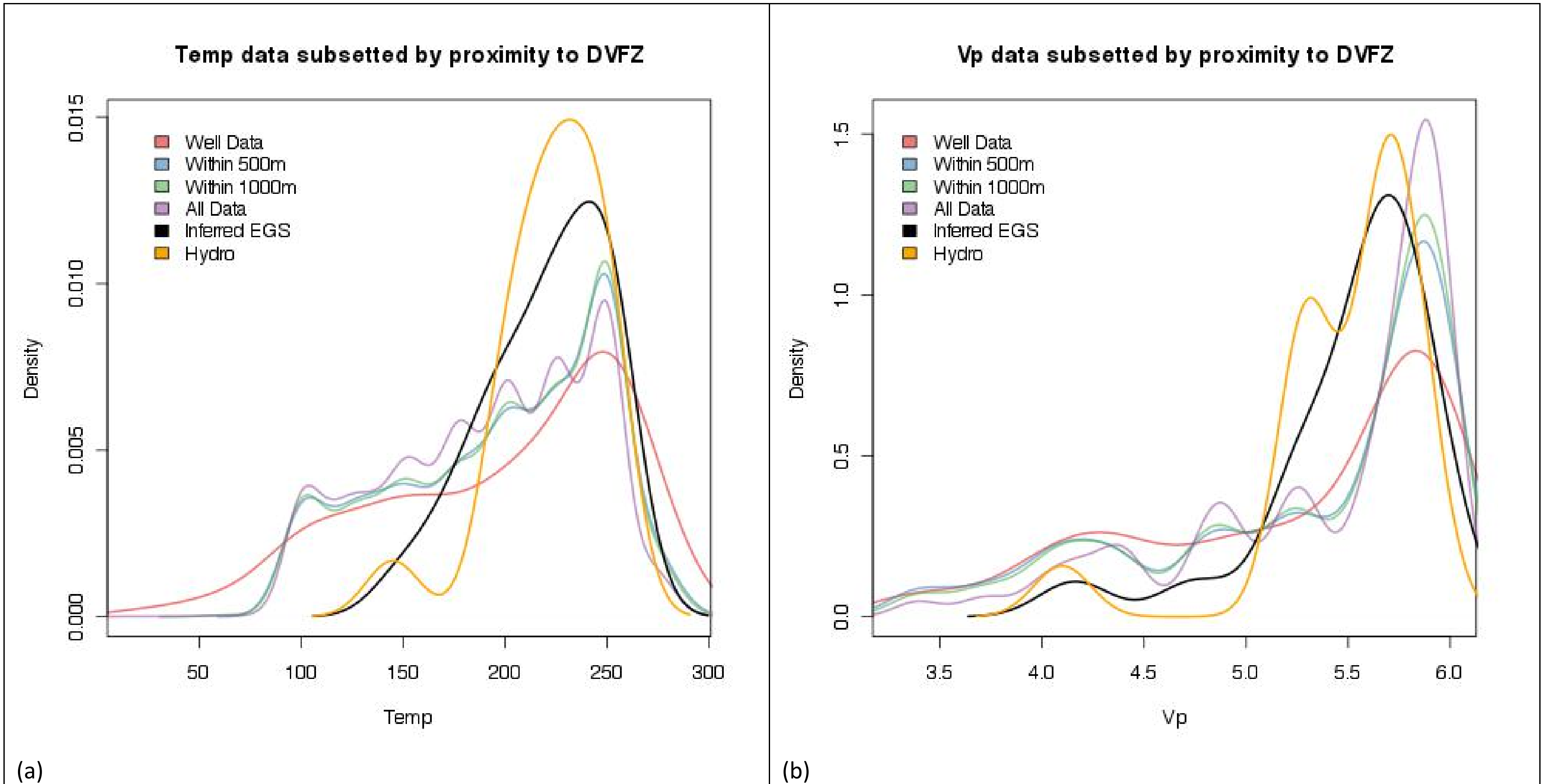

Figure 185. Enhanced data relative to the proximity to the Dixie Valley Fault Zone (DVFZ) for data density vs (a) Temperature data (°C) and (b) Vp (cm/s)

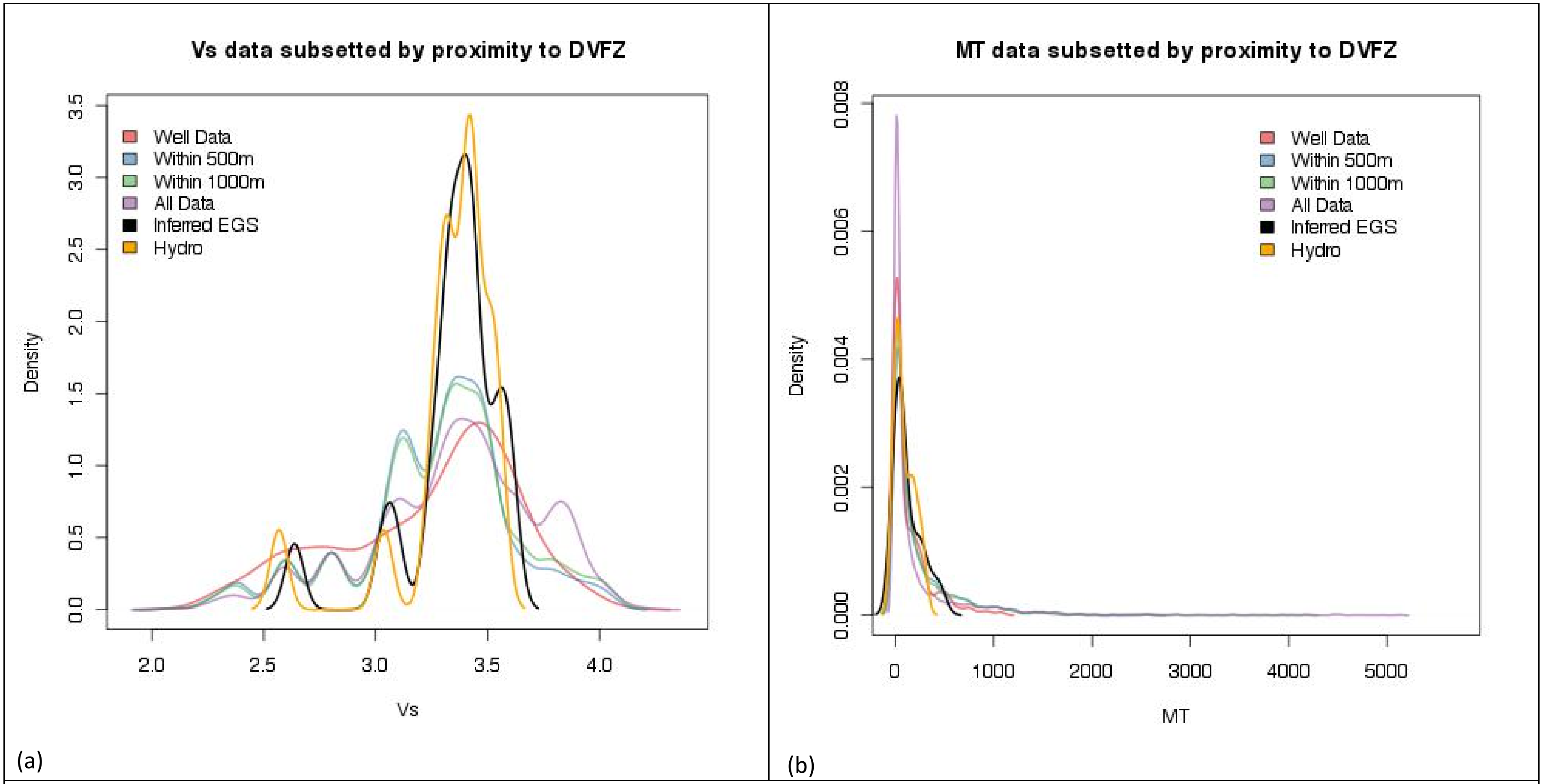

Figure 186. Enhanced data relative to the proximity to the Dixie Valley Fault Zone (DVFZ) for data density vs (a) Vs (cm/s) and (b) MT data (Ω-m)

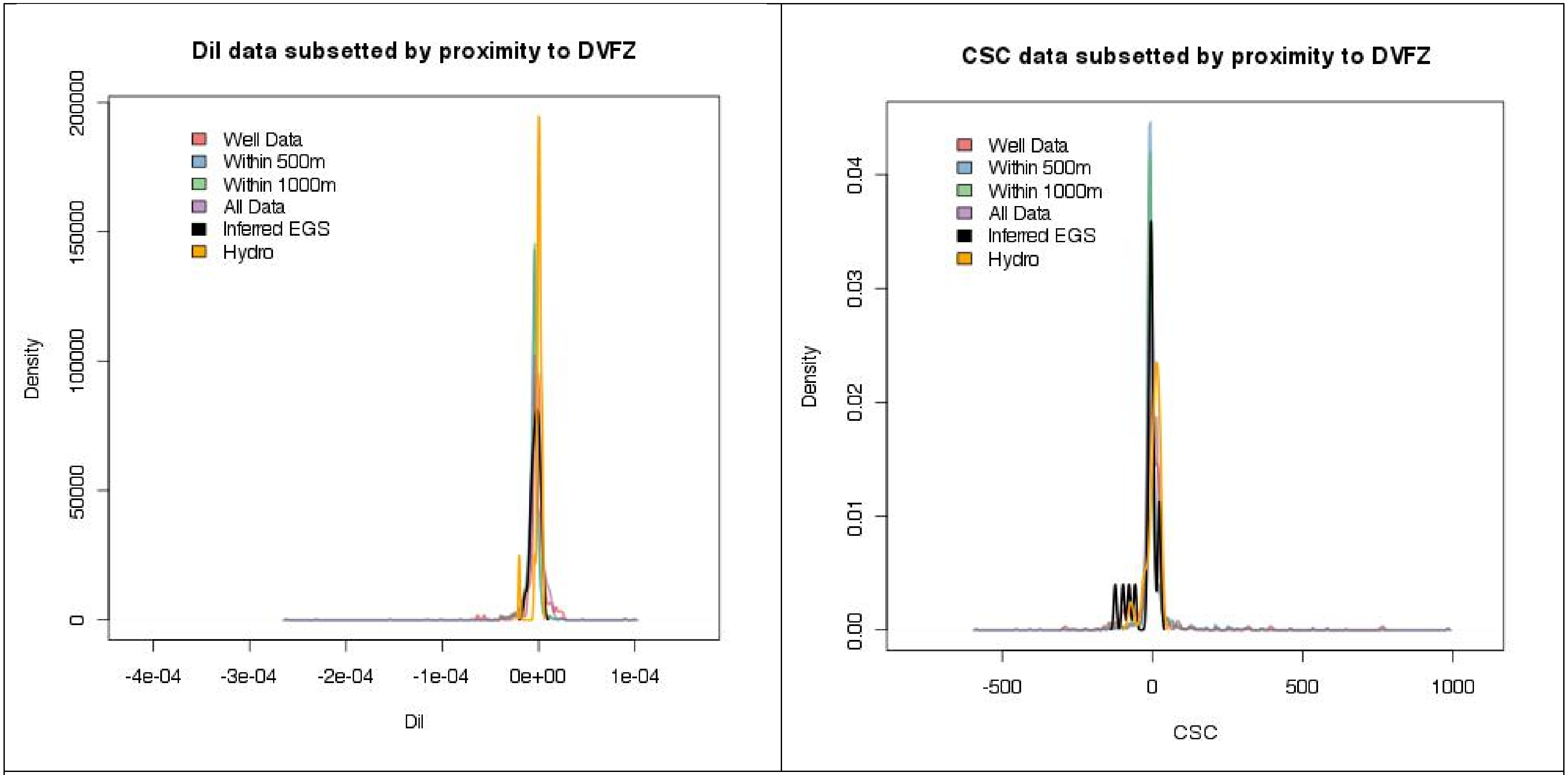

Figure 187. Enhanced data relative to the proximity to the Dixie Valley Fault Zone (DVFZ) for data density vs (a) Dilatation (DIL) and (b) Coulomb Stress Change (CSC in bars) data

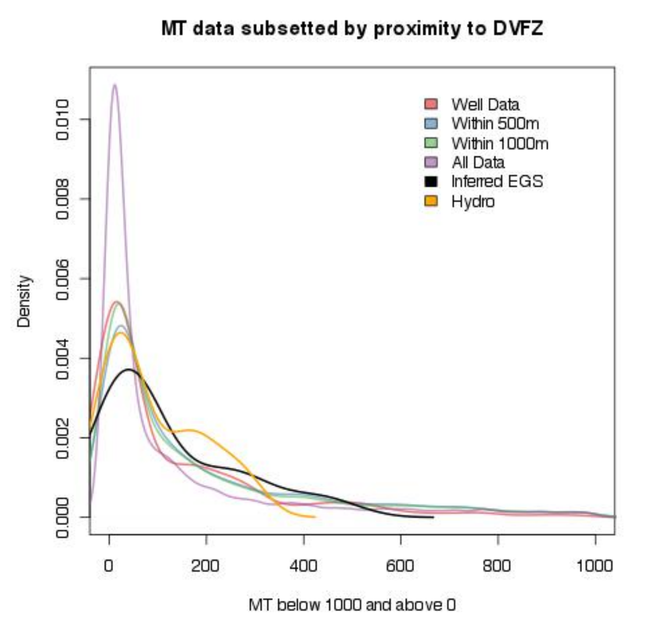

(a)

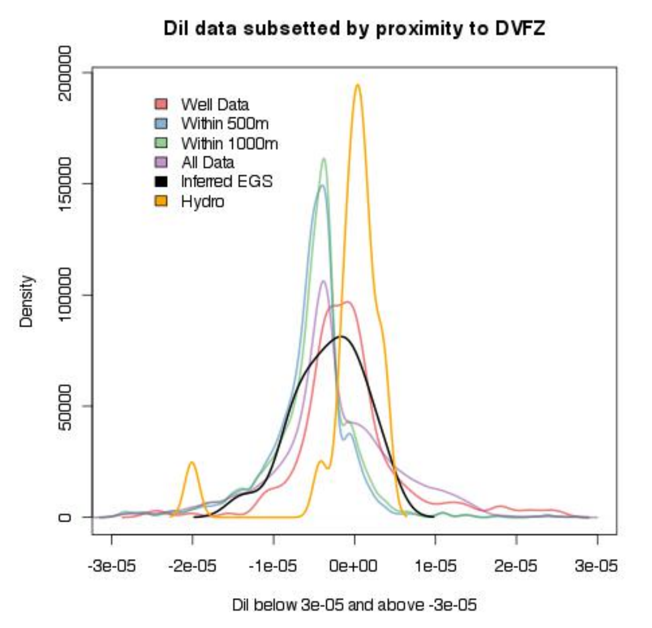

(b)

Figure 187. Expanded versions of the enhanced data relative to the proximity to the Dixie Valley Fault Zone (DVFZ) for data density vs (a) MT data (Ω-m) and (b) Dilatation (DIL); see Figures 186b and 187a.

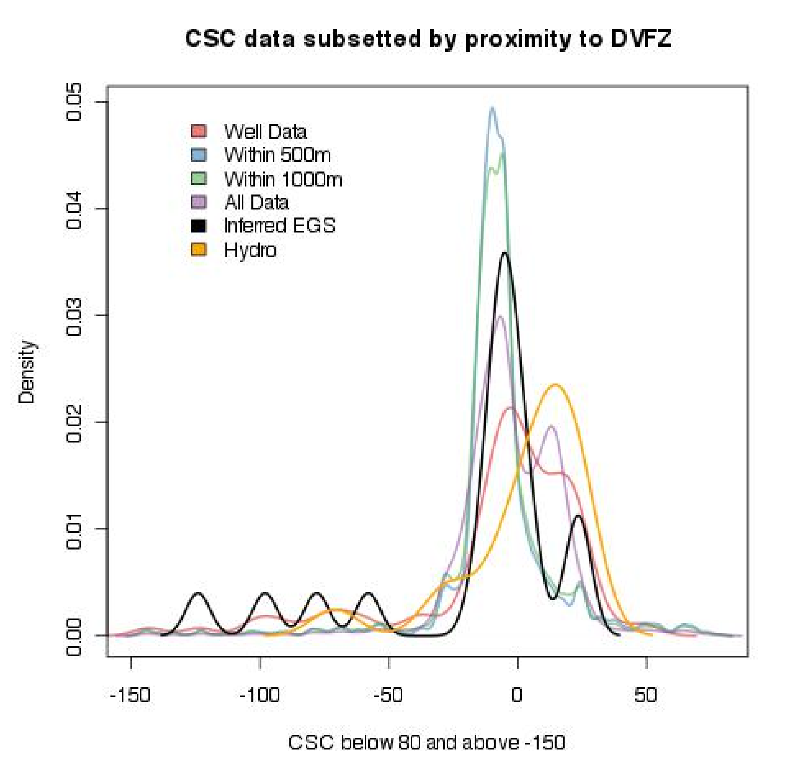

Figure 188. Expanded versions of the enhanced data relative to the proximity to the Dixie Valley Fault Zone (DVFZ) for data density vs CSC (bars); see Figure 187 (b).

11.6 SUMMARY AND RECOMMENDATIONS

The search for a clear road map for finding locations likely to be viable for either Hydrothermal or EGS, based on measurements made without drilling, remains elusive. However, the task of searching a haystack (4297 cells without missing data) for the scarce needles (18 productive Hydrothermal and 21 inferred EGS) is not simple, and the goal of identifying those cells is perhaps overly optimistic. What can be done reasonably successfully is to reduce the size of the haystack to a set of cells likely to be either productive for Hydrothermal or EGS. The tree in Figure 183 identifies 19 cells as likely to be productive Hydrothermal, and 9 actually are. Similarly the tree in Figure 184 identifies 13 cells as likely to be viable for EGS, and 6 of these correspond to the cells for which EGS is inferred. As a tool for facilitating the discovery of potential Hydrothermal or EGS sites, the methodology shows promise.

Some patterns in the data remain unexplained, especially for the regional differences in MT, CSC, and Dilatation. The complexities in these variables make it difficult to evaluate whether the methodology and results presented her would transfer to locations outside the calibration area. Data from other locations would be necessary to make such an evaluation. Much of the data outside of the wells is modeled, interpolated, and extrapolated, so the analysis has an additional layer of uncertainty. Because the criteria for inferring EGS favorable cells was not applied to the entire dataset, and productive Hydrothermal cells may exist outside of where Hydrothermal power is currently being generated, there may be additional needles in the haystack that we technically misclassify in our initial conditions. In other words, if we had perfect knowledge of which cells have conditions suitable for Hydrothermal or EGS, the modeling procedure would change. If those additional hypothetically suitable cells were similar to the cells currently identified, the model would be strengthened and look even more promising. If those additional cells were different from those already identified, the model would look less promising.

Depth is related to many of the variables of interest (most strongly with Temperature, Vp, Vs, and Lithology) and this was an issue with many parts of this analysis. Attempts to control for Depth (through using Temperature Residuals, for example) were made. However, a cell 10 degrees above the predicted value has the same Temperature Residual (10) whether this cell is near the surface or deep subsurface. The deep cell (10 degrees warmer than its Depth cohort) may be hot enough to be viable for energy production while the shallow cell will not be. In short, Depth complicates all analyses in this report and no perfect solution presents itself. Further research and site geostatistical evaluations are required to develop a better understanding of this confounding but significant parameter.

12. ENAHNCED FAVORABILITY AND TRUST MAPS

The generation of the favorability maps for the Calibration Area (Figure 1) are based on three critical EGS geoscience parameters: temperature, rock type, and stress. The Baseline (existing data, see Section 1) Conceptual Model submitted to the National Geothermal Data Repository provides the baseline favorability and trust mapping conducted in the referenced area.

The enhanced thermal data, conductive thermal modeling of the Project Area, convective modeling of the Dixie Valley Fault Zone (DVFZ), and pseudo-convective modeling (Section 9.4), provided a variety of new insights into the thermal setting of the Dixie Valley Geothermal System, but it did not provide new temperature data that would supercede the temperature data used in the baseline mapping discussed above. The enhanced seismic data analysis (the July – September 2013 Progress Report for this Project) did develop an interesting prediction of temperature at depth. However, the methodology is new and not validated at other sites. As such, it is not considered viable ti supercede the baseline data previously mentioned. Finally, while new earthquakes were detected in the Project Area during the deployment of ambient passive seismic survey and sufficient microseismic data was generated to allow inversion for stress, there was insufficient budget to analyze the data. As such, no new stress data was generated.

The enhanced data did provide a greater confidence in the integrated interpretation of the geothermal setting of the in the Calibration Area (Figure 1), the Principal Investigator made the decision that it was not feasible to generate new trust maps given the budget condition previously described. Thus, the Project did not generate enhanced trust maps.

13. DISCUSSION OF QUESTIONS POSED IN THE PROPOSAL FOR THIS INVESTIGATION[26]

The AltaRock Team identified nine questions in the proposal for this project that it sought to address through this investigation. These are:

1. What can be currently ascertained in terms of identifying EGS drilling targets by a panel of geothermal experts using a combination of available public-domain geoscience data?
2. To what extent can the non-uniqueness and uncertainty inherent in geophysical data be reduced by integrating data from two or more sources and analyzing the data collectively?
3. Can substantial improvements in seismic-velocity resolution, on the order of 5km x 5km at depths of 1-5km, be obtained using newly developed ambient seismic noise methods?
4. Can temperature and rock type be reliably inferred from seismic data?
5. Can temperature and rock type be more reliably inferred from seismic data when it is used in conjunction with other geoscience data?
6. Can statistical methods help to evaluate what combination of geoscience data are most useful for characterizing EGS prospects in terms of temperature, rock composition, and stress, and in identifying drilling targets?
7. Can exploration costs be reduced by eliminating survey methods that do not appreciably reduce exploration uncertainty?
8. Does the EGS drilling favorability map produced for Dixie Valley have sufficient accuracy to identify favorable drilling sites? and
9. Do geoscience experts judge the exploration methodology to be sufficiently non-site specific so as to have a high likelihood of identifying favorable drilling targets at other sites?

Each of these questions is addressed below.

1. What can be currently ascertained in terms of identifying EGS drilling targets by a panel of geothermal experts using a combination of available public-domain geoscience data?

The DVGS has a considerable amount of geoscientific data and information in the public domain (see Sections 1 through 8) that has been used to identify EGS drilling targets: see Sections 1-6 for an assessment of the geothermal setting, Section 7 for qualitative and quantitative geoscience correlations, and Section 8 for the baseline (existing data) favorability and trust maps based on the AltaRock identified critical parameters (temperature, rock type, and stress) for EGS drilling target selection. Given the large geoscience database, the AltaRock Team was able to make a creditable and defensible determination. The key factors here allowing the determination were the large and comprehensive data set available.

2. To what extent can the non-uniqueness and uncertainty inherent in geophysical data be reduced by integrating data from two or more sources and analyzing the data collectively?

Integrating multiple, relevant geoscience data sets is the only way to reduce the non-uniqueness and uncertainty inherent in any given geophysical data. Key elements in doing this is having (1) sufficient geographically dispersed wells, slim-holes and temperature gradient holes and number available to provide "hard" data to constrain and potentially calibrate the geophysical interpretations, and (2)

[26] Given budgetary issues, this section was prepared solely by the Principal Investigator, Joe Iovenitti.

sufficient resolution in the multiple data sets being integrated. However, in early stage exploration projects, well data is typically not available. In this Dixie Valley exploration project, non-uniqueness and uncertainty was significantly reduced:

a. enhanced gravity-magnetics modeling correlated well with interpreted seismic lines;
b. baseline and enhanced gravity-magnetics modeling showed good correlation with geological-well models; and
c. baseline and enhanced gravity-magnetics modeling corroborated the multiple faults within the DVFZ.

To a lesser extent, the Baseline and Enhanced MT data also supported the presence of the DVFZ but independently did not do so. Enhanced seismic ambient noise survey and enhanced MT data have a rough correlation at the regional scale (see Section 10.1). The correlation between the enhanced MT and seismic data was comprised by the signification resolution difference between the two data sets in the Calibration Area. However, some key insights were generated by the enhanced seismic data and a promising approach was developed by the Seismic Task Leader, Dr. Ileana Tibuleac, to predict temperature at depth. The methodology and approach (see Section *Rock Type, Temperature and Seismic Velocity in the DVSA*).

3. Can substantial improvements in seismic-velocity resolution, on the order of 5km x 5km at depths of 1-5km, be obtained using newly developed ambient seismic noise methods?

Based on the results presented in Section 9.2.3, the answer to this question is "Yes it can." The ambient seismic noise survey proved very valuable in improving model resolutions by a factor of 2 with a less than optimal station resolution in the Calibration Area. The seismic survey station density in the Calibration Area was not sufficient to change the Baseline Conceptual Model and the Favorability/Trust maps, even though very intriguing relationships between seismic data and temperature were defined based on the available enhanced data. It is highly recommended that the methodology developed by the Seismic Task Leader, Dr. Ileana Tibuleac, to predict rock type and temperature be tested at other geothermal sites in the B&R and at a higher resolution in the DVGW, i.e., the Calibration Area.

4. Can temperature and rock type be reliably inferred from seismic data?

Based on the seismic results described in the response to Question No. 3, it certainly appears so with the caveat mentioned noted. Wells with lower temperature were found to generally have the lowest Vp, Vs, and Vp/Vs at depths less than 4km. Seismic velocities for the formations in Dixie Valley are similar to values estimated by other researchers. The temperature-seismic relationship identified in Dixie Valley is still debated. Nevertheless, the techniques used in this study for determining rock type and temperature need to be validated in other areas.

5. Can temperature and rock type be more reliably inferred from seismic data when it is used in conjunction with other geoscience data?

The inference that seismic data can reliably infer rock type has been available for some time. Until sufficient data and information is developed to demonstrate the variability in density of the lithologies/formations in Dixie Valley as compared to the seismic determination of density of these lithologies/formations the issue remains an open question for that geothermal area as an exploration tool. The temperature inference the interpretation of the enhanced seismic data is very interesting. However, until higher resolution data is obtained the utility of the method remains open. As cited above, the Principal Investigator believes that the seismic methodology developed in this study warrants for research and testing.

6. Can statistical methods help to evaluate what combination of geoscience data are most useful for characterizing EGS prospects in terms of temperature, rock composition, and stress, and in identifying drilling targets?

The baseline and enhanced geostatistical results generated in this study are of great interest. Baseline CART analysis showed that temperature, lithology, productive hydrothermal cells (500m by 500m grid cell), and expected inferred EGS favorable cells can be predicted with a R^2 value ≥ 0.55. Enhanced CART analysis provided more complicated results for the productive hydrothermal cells, and expected inferred EGS favorable cells used for the analysis determinations but it was also recognized that the enhanced data created a “needle in the haystack” issue. Countering this was the finding that close examination of the trees developed in the CART analysis identified (1) 19 cells that seem to have characteristics that make them likely to be Productive Hydrothermal, and nine of these cells actually and (2) 13 cells appeared to have EGS favorable characteristics of which six are Inferred EGS favorable cells. More work is required to expand the analysis to more parameters identified in the enhanced data set. These findings are very intriguing and further research and testing of this methodology at other geothermal sites is recommended.

7. Can exploration costs be reduced by eliminating survey methods that do not appreciably reduce exploration uncertainty?

The results of this study indicate that all the surveys conducted are important for they provide insight into the geothermal system from different perspectives. Additionally, survey methods are a matter of technical objectives and cost-benefit analysis for any given project. Each survey method investigated in this study has its own specific objectives and possible range of outcomes. For this Dixie Valley investigation:

1. the geologic mapping and gravity-magnetic modeling proved most useful;
2. The ambient seismic noise modeling results did not have sufficient resolution (station density) in the Calibration Area to be as useful as other data sets but it did provide intriguing insights that should be further researched and applied to other sites, as described above;
3. The enhanced MT data could (a) resolve cold dry rocks from hot dry rocks; both could be fairly resistive and (c) the apparent hydrothermal upflow areas;
4. The enhanced MT data did provide a general sense of structure in the area which was corroborated when integrated with other geoscience data.
5. The thermal conductive modeling and the pseudo-convective modeling provided some interesting results useful in understanding the geothermal resource in the area.
6. The CO_2 soil gas survey deployed in the Calibration Area.

8. Does the EGS drilling favorability map produced for Dixie Valley have sufficient accuracy to identify favorable drilling sites?

The cumulative data set suggests it does. The complimentary trust maps d were also useful in identifying areas and parameters of for further definition.

9. Do geoscience experts judge the exploration methodology to be sufficiently non-site specific so as to have a high likelihood of identifying favorable drilling targets at other sites?

The answer to this question can only be ascertain after the approach, method, and techniques utilized in this study are applied at other sites.

14. REFERENCES

Abbott, R. E., Louie, J. N., Caskey, S. J., and Pullammanappallil, S., 2001, Geophysical confirmation of low-angle slip on the historically active Dixie Valley fault, Nevada, Journal of Geophysical Research, v. 106, no. B3, p. 4169-4181.

Abers, G. A., Mutter, C. Z., and Fang, J., 1997, Shallow dips of normal faults during rapid extension: Earthquakes in the Wooklark-D'Entrecasteaux rift system, Papua New Guinea, Journal of Geophysical Research, v. 102, no. B7, p. 15,301-15,317.

Anderson, D. L., 1967, A seismic equation of state, Geophys. J. R. Astron. Soc., v. 13, p. 9-30.

Anderson, E. M., 1942, The Dynamics of Faulting, Oliver and Boyd, White Plains, N.Y., 183p.

Anonymous, 1998, Report on Application of advanced seismic reflection imaging techniques to mapping permeable zones at Dixie Valley, Nevada, DOE ID 13465-TI.

Allis, R. G., Johnson, S., Nash, G. D., and Benoit, R., 1999, A model for shallow thermal regime at Dixie Valley geothermal field, Geothermal Resources Council (GRC) Transactions, v. 23, p.493-498.

Barruol, G., and Kern, H., 1996, Seismic anisotropy and shear-wave splitting in lower-crustal and upper-mantle rocks from the Ivrea Zone experimental and calculated data, Physics of the Earth and Planetary Interiorism, v. 95, p. 175-194.

Barton, C. A., Hickman S., Morin, R. M., Zoback M. D., Finkbeiner T., Sass J., and Benoit D., 1997, In-situ stress and fracture permeability along the Stillwater Fault Zone, Dixie Valley, Nevada, Proceedings 22nd Geomechanical Wellbore Imaging: A Key to Managing the Asset Life Cycle, Proceedings, 46th Workshop on Geothermal Reservoir Engineering, SGP-TR-156, Stanford University, Stanford, California, p. 147–152.

Barton, C. A., Hickman S., Morin R., Zoback M. D., and Benoit, D., 1998, Reservoir-scale fracture permeability in the Dixie Valley, Nevada, Geothermal Field, Proceedings SPE/ISRM 47371, Eurock 98', Trondheim, Norway, July 8-10.

Baranov, V., 1957, A new method for interpretation of aeromagnetic maps-pseudogravity anomalies, Geophysics, v. 22, p. 359-383.

Bassin, C., Laske, G., and Masters, G., 2000, The Current Limits of Resolution for Surface Wave Tomography in North America. EOS Trans AGU, F897, p.81.

Batini, F., Fiordelisi, A., Graziano, F., and Toksoz, M. N., 1995, Earthquake tomography in the Larderello geothermal area, Transactions, World Geothermal Congress, Florence, 18–31 May, v. 2, p. 817–820.

Batini, F, Console, R., Luongo, G., 1985, Seismological study of Larderello — Travale geothermal area, Geothermics, 14, p. 255–272.

Batzle, M. L., De-Hua, H., and Hofmann, R., 2006, Fluid mobility and frequency-dependent seismic velocity —Direct measurements. Geophysics, v. 71, no. 1 (January-February); p. n1–n9, 15 figs.

Becker, D. J., and Blackwell, D. D., 1993, Gravity and hydrothermal modeling of the Roosevelt hot springs area, southwestern Utah, Journal of Geophysical Research, v. 98, no. 17, p. 787-97,800.

Bell, J. W., and Katzner, T., 1990, Timing of late Quaternary faulting in the 1954 Dixie Valley earthquake area, central Nevada, Geology, v. 18, p. 622-25.

Bell, J. W., and Katzner, T., 1987, Surficial geology, hydrology and late Quaternary tectonics of the IXL Canyon area, Nevada, Nevada Bureau of Mines and Geology Bulletins, v. 102, 52 p.

Benoit, D., 1999, Conceptual models of the Dixie Valley, Nevada Geothermal Field, GRC Transactions, v. 23, p. 505-511.

Bensen, G.D., Ritzwoller, M. H., Barmin, M. P., Levshin, A. L., Lin, F., Moschetti, M.P., Shapiro, N.M., and Yang. Y.,2007, Processing seismic ambient noise data to obtain reliable broad-band surface wave dispersion measurements, Geophys. J. Int. 169, 1239-1260.

Bevington, P. R., 1969, Data reduction and error analysis for the physical sciences: McGraw-Hill, New York, 336 pp.

Biasi, G., Preston, L., and Tibuleac, I. M, 2009, Body Wave Tomography for Regional Scale Assessment of Geothermal Indicators in the Western Great Basin, Geothermal Resources Council Transactions, v. 33, p. 437-440.

Biasi, G., Tibuleac, I., and Preston, L., 2008, Regional resource area mapping in Nevada using the USArray Seismic Network, Geothermal Energy 2008 Conference and Expo, Reno, NV, Oct 5-8.

Birch, F., 1961, The velocity of compressional waves in rocks to 10 kilobars, Journal of Geophysical Research, v. 66, p. 2199-2224.

Blackwell, D. D., Smith, R. P., Waibel, A. F., Richards, M. C., Stepp, P., 2009, Why Basin and Range Systems are Hard to Find II: Structural Model of the Producing Geothermal System in Dixie Valley, Nevada, GRC Transactions, v. 33, p. 441-446.

Blackwell, D. D., Smith, R. P., and Richards, M. C., 2007, Exploration and Development at Dixie Valley, Nevada: Summary of DOE Studies, Proceedings 32nd Workshop on Geothermal Reservoir Engineering, Stanford University, California, Jan. 22-24, 16 pp.

Blackwell, D.D., Smith, R.P., Bergman, S., Goff, F., Kennedy, M., McKenna, J., Richards, M., Smith, R., Waibel, A. F., and Wannamaker, P. E., 2007, Description, Synthesis, and Interpretation of the Thermal Regime, Geology, Geochemistry and Geophysics of the Dixie Valley, Nevada Geothermal System, Nevada Bureau of Mines Open File Report, in review.

Blackwell, D. D., Bergman, S., Goff, F. Kennedy, B. M., McKenna, J. R., Richards, M. C., Smith, R. P., Waibel, A. F., and Wannamaker, P.E., 2005, Description, Synthesis, and Interpretation of the Thermal Regime, Geology, Geochemistry and Geophysics of the Dixie Valley, Nevada Geothermal System, in D.D. Blackwell and R.P. Smith, ed., unpublished DRAFT DOE Technical Report, 195 p.

Blackwell, D. D., Leidig, M., Smith, R. P., Johnson, S., and Wisian, K. W., 2002, Exploration and Development Techniques for Basin and Range Geothermal Systems: Examples From Dixie Valley, Nevada, GRC Transactions, v. 26, p. 513-518.

Blackwell, D. D., Leidig, M., and Smith, R. P., 2002, Regional Geophysics of the Dixie Valley Area: Example of a Large Basin and Range Geothermal Resource, GRC Transactions, v. 26, p. 519-522.

Blackwell, D. D., Iglesias, E., Hunt, T., Lund, J., Tamanyu, S., and Kimbara, K., 2000, Thermal Regime in the Dixie Valley, Nevada geothermal system, Blackwell, D. D., Gollan, B., and Benoit, D., ed. Transactions, World Geothermal Congress, p. 991-996.

Blackwell, D. D., Gollan, B., and Benoit, D., 2000, Temperatures in the Dixie Valley, Nevada geothermal system, GRC Transactions, v. 24, p. 223-228.

Blackwell, D. D., Wisian, K.W., Benoit, D., and Gollan, B., 1999, Structure of the Dixie Valley geothermal system: A typical Basin and Range geothermal system, from thermal and gravity data, GRC Transactions, v. 23, p. 525-531.

Blackwell, D. D., and Wisian, K., 1997, Gravity analysis of Dixie Valley, Nevada Geothermal System. unpublished report submitted to Oxbow Geothermal Corporation, Reno, Nevada.

Blackwell, D. D., Waibel, A. W., and Kelly, S. A., 1994, Results of Dixie Valley Power Partners/Oxbow 1994 thermal gradient drilling program, unpublished report submitted to Oxbow Geothermal Corporation, Reno, Nevada.

Blackwell, D. D., Steele, J. L. and Carter, L. S., 1991, Heat-flow patterns of the North American continent: a discussion of the Geothermal Map of North America, in Slemmons, D. B., Engdahl, E. R., Zoback, M. D., and Blackwell, D. D., ed., Neotectonics of North America, Decade Map, v. 1, Geologic Society of America Bulletin, Boulder, CO, v. 103, p. 423–436.

Blackwell, D. D., 1983, Heat flow in the Northern Basin and Range Province, GRC Trans., Special Report No. 13, p. 81-92.

Blakely, R. J. and Jachens, R. C., 1991, Regional study of mineral resources in Nevada: Insights from three-dimensional analysis of gravity and magnetic anomalies, GSA Bulletin, vo. 103, p. 795-803.

Blewitt, G., Coolbaugh, M., Holt, W., Kreemer, C., Davis, J., Bennett, R., 2002, Targeting of potential geothermal resources in the Great Basin from regional relationships between geodetic strain and geological structures, GRC Transactions, v. 26, p. 523-526.

Bogen N. L. and Cshwieckert, R. A, 1985, Magnitude of crustal extension across the Basin and Range Province: constraints from paleomagnetism, Earth and Planetary Science Letters, v. 75, p. 93-100.

Boitnott, G. N. and Kirkpatrick, A., 1997, Interpretation of Field Seismic Tomography at The Geysers Geothermal Field, California, Proceedings 22nd Workshop on Geothermal Reservoir Engineering Stanford University, Stanford, California, January 27-29, SGP-TR-155.

Brocher, T., 2008, Compressional and Shear-Wave Velocity versus Depth Relations for Common Rock Types in Northern California, Bulletin of the Seismological Society of America, v. 98, no. 2, April, p. 950–968. doi: 10.1785/0120060403.

Brocher, T. M., and Christensen, N. I., 2001, Density and velocity relationships for digital sonic and density logs from coastal Washington and laboratory measurements of Olympic Peninsula mafic rocks and greywackes, USGS Open-File Report 01-264, 39.

Bruton, C. J., Nimz, G., Counce, D., Bergfeld, D., Goff, F., Johnson, S. D., and Moore, J. N., 2002, Preliminary investigation of scale formation and fluid chemistry at the Dixie Valley Geothermal field, Nevada, Presentation to Dixie Valley Geothermal Workshop, June 12-13, Reno, Nevada: http://www.unr.edu/geothermal/oldermeetings.htm.

Bullard, E. C., Maxwell, A. E., and Revelle, R., 1956, Heat flow through the deep sea floor, Advanced Geophysics, v. 3, p. 153-81.

Buntebarth, G., 1982, Density and seismic velocity in relation to mineralogical constitution based on an ionic model for minerals, Earth Planet. Sci. Lett. doi:10.1016/0012-821x(82)90156.

Burke, M. M. and Fountain, D. M., 1990, Seismic properties of rocks from an exposure of extended continental crust-new laboratory measurements from the Ivrea Zone, Tectonophysics, v. 182, p. 119-146.

Calkins, J. A., Abers, G. A., Ekström, G., Creager, K. C., and Rondenay, S., 2011, Shallow structure of the Cascadia subduction zone, beneath western Washington from spectral ambient-noise correlation, Journal of Geophysical Research, v. 116, B07302, doi:10.1029/2010JB007657.

Campillo, M. and Paul, A., 2003. Long-Range correlations in the diffuse seismic coda, Science, 229, 547-549.

Caskey, S. J., and Wesnousky, S. G., 2000, Active Faulting and Stress Redistributions in the Dixie Valley, Beowawe, and Bradys Geothermal Fields: Implications for Geothermal Exploration in the Basin and Range, Proceedings 25th Workshop on Geothermal Reservoir Engineering, Stanford University, California, Jan. 24-26, 16 p.

Caskey, S. J., and Wesnousky, S. G., 1997, Static stress changes and earthquake triggering during the 1954 Fairview Peak and Dixie Valley earthquakes, Central Nevada, Bulletin of the Seismological Society of America, v. 87, p. 521-527.

Caskey, S. J., Wesnousky, S. G., Zhang, P., and Slemmons, D. B., 1996, Surface Faulting of the 1954 Fairview Peak (Ms 7.2) and Dixie Valley (Ms 6.8) Earthquakes, Central Nevada, Bulletin of the Seismological Society of America, v. 86, no. 3, p. 761-787.

Catchings, R. D., 1992, A relation among geology, tectonics and velocity structure, western to central Nevada Basin and Range, GSA Bulletin, September, v. 104; no. 9; p. 1178-1192.

Catchings, R. D. and Mooney, W. D., 1991, Basin and Range crustal and upper mantle structure, northwest to central Nevada, Journal of Geophysical Research, v. 96 (B4), p. 6247-6267.

Chave, A. D., and A. G. Jones, eds., 2012, The magnetotelluric method: Theory and practice, Cambridge Univ. Press, Cambridge, 530 pp.

Christensen, N. I., Mooney, W. D., 1995, Seismic velocity structure and composition of the continental crust: A global view, J. Geophys. Res., 100, 9761–9788.

Christensen, N. I., and Wepfer, W. W., 1989, Laboratory techniques for determining seismic velocities and attenuations, with applications to the continental lithosphere, In Pakiser, L.C., and Mooney, W.D. (Eds.), Geophysical Framework of the Continental United States, Mem. Geol. Soc. Am., 172:91-102.

Christensen, N. I., 1979, Compressional wave velocities in rocks at high temperature and pressures, critical thermal gradients, and crustal low velocity zones, Journal of Geophysical Research, v. 84, p. 6849-6857.

Christensen, N. I., 1978, Ophiolites, seismic velocities and ocean crustal structure, Tectonophysics, 47, 131-157.

Christensen, N. I.,1968, Compressional wave velocities in basic rocks, Pacific Science, V. XXII, January.

Chung, D. J., 1977, Pn velocity and partial melting—Discussion, Tectonophysics, v. 42: T35-T42.

Coolbaugh, M. F., Taranik, J. V., Raines, G. L., Shevenell, L. A., Sawatzky, D. L., Bedell, R., and Minor, T. B., 2002, A geothermal GIS for Nevada: defining regional controls and favorable exploration terrains for extensional geothermal systems, GRC Transactions, v. 26, p. 485–490.

Cordell, L. and Henderson, R.G., 1968, IIterative three-dimensional solution of gravity anomaly data using a digital computer, Geophysics, v.33, p.596-601.

Crafford, A. E. J., 2007, Geologic Map of Nevada: U.S. Geological Survey Data Series 249, 1 CD-ROM, 46 p., 1 plate.

deGroot-Hedlin, C. and Constable, S. C., 1990, Occam's inversion to generate smooth, two-dimensional models from magnetotelluric data, Geophysics, v. 55, p. 1613-1624.

Denton, J. M., Bell, E. J., and Jodry, R. L., 1980, Geothermal Reservoir Assessment Case Study: Northern Dixie Valley, Nevada, DOE/ET/27006-1, 517 p.

DePolo, D. M., and DePolo, C. M., 1999, Earthquakes in Nevada, 1850-1998, Nevada Bureau of Mines and Geology, Map 119.

Dickinson, W.R., 1979, Cenozoic plate tectonic setting of the Cordilleran region in the United States in Cenozoic paleogeography of the western United States, in Armentrout, J. M., Cole, M. R., and TerBest, H., ed., Pacific Coast Paleogeography Symposium, Pacific Section, Society of Economic Paleontologists and Mineralogists, v. 3, p. 1-13.

Dickinson, W. R., 2006, Geotectonic evolution of the Great Basin, Geosphere, v. 2, no. 7, p. 353-368.

Dilek, Y., and Eldridge, M. M., 1995, Geology of the Humboldt igneous complex, Nevada, and Tectonic implications for the Jurassic magmatism in the Cordilleran Orogen, GSA Special Bulletin, v. 290, p. 229-248.

Drakos, P., Spielman, P., and Bjournsson, G., 2011, Jersey Valley Exploration and Development, GRC Trans., v. 35, p. 751-759.

Dixon, E. T., Murrell, M., Goff, F., and Goldstein, S., 2003, Uranium-Series Geochronology of Hydrothermal Deposits, Dixie Valley, Nevada, EOS, Transactions American Geophysical Union, Fall Meeting, San Francisco (Dec. 8-12), v.84, no. 46, p. F1613-1614.

EarthScope Automated Receiver Survey (EARS): http://ears.iris.washington.edu/Data/Summary/

ESRI/ArcGIS World Imagery Service for satellite imagery: http://www.arcgis.com/home/item.html?id=a5fef63517cd4a099b437e55713d3d4

Evans, J. R., and Zucca, J. J., 1993, Active source, high-resolution (NeHT) tomography; velocity and Q. in Iyer, J.R., and Hirahara, K., editors, Seismic Tomography: Theory and Practice, Chapman and Hall, London.

Evans, J. R. and Zucca, J. J., 1988, Active high resolution seismic tomography of compressional wave velocity and attenuation structure at Medicine Lake volcano, northern California Cascade range, Journal of Geophysical Research, v. 93, p. 15,016-15,036.

Faulds, J. E., Hinz, N. H., Coolbaugh, M. F., Cashman, P. H., Kratt, C., Dering, G., Edwards, J., Mayhew, B., and McLachlan, H., 2011, Assessment of Favorable Structural Settings of Geothermal Systems in the Great Basin, Western USA, GRC Trans., v. 35, p. 777-783.

Faulds, J. E., Garside, L., Johnson, G., and Anooshehpoor, R., 2003, Geologic and Geophysical Analysis of the Desert Peak-Brady Geothermal Fields: Structural Controls on Geothermal Reservoirs in the Humboldt Structural Zone, IRIS report.

Feng, C. C. and Teng, T. L., 1983. Three-dimensional crust and upper mantle structure of the Eurasian continent, J. Geophys. Res., 88, 2261-2272.

Fielitz K. , 1971. Elastic wave velocities in different rocks at high pressure and temperature up to 750°C, Z. Geophys., 37, 943–956.

Foulger, G. R., Grant, C. C., Ross, A. and Julian, B. R., 1997, Industrially induced changes in Earth structure at the Geysers Geothermal Area, California, Geophysical Research Letters 24: doi: 10.1029/96GL03152. issn: 0094-8276.

Forster, C. B., Caine, J. S., Schulz, S., Nielson, D. L., 1997, Fault Zone Architecture and Fluid Flow: An Example from Dixie Valley, Nevada, Proceedings 22nd Workshop on Geothermal Reservoir Engineering, Stanford University, California, Jan. 27-29, 8p.

Foxall, B., Vasco, D., 2003, Inversion of Synthetic Aperture Radar Interferograms for Sources of Production-Related Subsidence at the Dixie Valley Geothermal Field, Proceedings 28th Workshop on Geothermal Reservoir Engineering, Stanford University, California, Jan. 27-29, 7p.

Frankel, A., Clayton, R. W., 1986, Finite difference simulations of seismic scattering: Implications for the propagation of short-period seismic waves in the crust and models of crustal heterogeneity, Journal of Geophysical Research: Solid Earth (1978–2012), Volume 91, Issue B6, pages 6465–6489, DOI: 10.1029/JB091iB06p06465.

Garside, L. J., and Schilling, J. H., 1979, Thermal waters of Nevada, Nevada Bureau of Mines and Geology Bulletin, v. 91, 163p.

Georgsson, L. S., Fridleifsson, G. O., Ólafsson, M., and Flóvenz, O. G., 2000, The geothermal exploration of the Öxarfjördur High-Temperature Area, NE-Iceland, Proceedings World Geothermal Congress, Kyushu - Tohoku, Japan, May 28 - June 10, p. 1157-1162.

Gibson, B. S. and Levander, A. R., 1988, Lower crustal reflectivity patterns in wide-angle seismic recordings, Geophysical Research Letters, 15, 617-620.

Gilbert, G. K., 1875, Report on the geology of portions of Nevada, California, and Arizona, examined in the years 1871 and 1872, U.S. Geographic and Geological Survey, W. 100th Meridian Rep., 3.

Gm-Sys manual, http://www.geosoft.com; http://www.geo.wvu.edu/~wilson/gmsys_49.pdfhttp://www.geo.wvu.edu/~wilson/gmsys_49.pdf

Goff, F., Bergfeld, D., Janik, C. J., Counce, D., and Murrell, M., 2002, Geochemical data on waters, gases, scales, and rocks from the Dixie Valley region, Nevada (1996-1999), Los Alamos National Laboratory Report LA-13972-MS, 71 p.

Goff, F., Janik, C. J., Bergfeld, D., Counce, D., Bruton, C., and Nimz, G., 1998, Geothermal chemistry/exploration investigations at Dixie Valley, Nevada. US/DOE Geothermal Program Review, Berkeley, California, April 1-2, 8p.

Goff, F., Shevenell, L., Gardner, J., Vuataz, F., and Grigsby, C., 1988, The hydrothermal outflow plume of Valles caldera, New Mexico and a comparison with other outflow plumes, Journal of Geophysical Research, v. 93(B6), p. 6041-6058.

Gourmelen, N., and Amelung, F., 2005, Postseismic mantle relaxation in the Central Nevada Seismic Belt, Science, v. 310, p. 1473-1476.

Grant, F. S., and West, G. F., 1965, Interpretation theory in applied geophysics, McGraw-Hill, New York, 584 pp.

Grauch, V. J. S., 2002, High-resolution aeromagnetic survey to image shallow faults, Dixie Valley geothermal field, Nevada, U.S. Geological Survey Open-File Report 02-0384, available on-line at http://pubs.usgs.gov/of/2002/ofr-02-0384/

Grauch, V. J. S., 2002, Detailed aeromagnetic studies: Fault interpretations from High-Resolution aeromagnetic data, Great Basin Center for Geothermal Energy and U.S. Department of Energy, Dixie Valley Workshop, June 12-13, Reno, Nevada: http://www.unr.edu/geothermal/oldermeetings.htm

Hammond, W. C., 2005, The ghost of an earthquake. Science, v. 310, p. 1440-1442.

Huang.Y. C., Huajian Yao, Bor-Shouh Huang, Robert D. van der Hilst Kuo-Liang Wen, Win-Gee Huang, and Chi-Hsuan Chen, 2010, Phase Velocity Variation at Periods of 0.5- 3 Seconds in the Taipei Basin in Taiwan from Correlation of Ambient Seismic Noise, Bulletin of the Seismological Society of America, Vol. 100, No. 5A, pp. 2250–2263, doi: 10.1785/01200.

Hauge, T. A., Allmendinger, R. W., Caruso, C., Hauser, E. C., Klemperer, S. L., Opdyke, S., Potter, C. J., Sanford, W., Brown, L., Kaufman, S., and Oliver, J., 1987, Crustal structure of western Nevada from COCORP deep seismic reflection data, GSA Bulletin., v. 98, p. 320-329.

Hauksson, E., and Haase, J. S., 1997, Three-dimensional Vp and Vp-Vs velocity models of the Los Angeles basin and central Transverse Ranges, California. Journal of Geophysical Research, v. 102, p. 5423–5453.

Herrmann, R. B., and Ammon. C. J., 2002, Computer Programs in Seismology – 3.30: Source inversion, available at URL: http://www.eas.slu.edu/People/RBHerrmann/CPS330.html, 99pp.

Heimgartner, M., Scott, J. B., Thelen, W., Lopez, C. T., and Louie, J. N., 2005, Variable crustal thickness in the western Great Basin: a compilation of old and new refraction data, GRC Transactions, v. 29, p. 239-242.

Hickman, S. H., Zoback, M. D., Barton, C. A., Benoit, R., Svitek, J., and Summers, R., 2000, Stress and Permeability Heterogeneity within the Dixie Valley Geothermal Reservoir: Recent Results from Well 82-5, Proceedings 25th Workshop on Geothermal Reservoir Engineering, Stanford University, California, Jan. 24-26, 10p.

Hickman, S., Zoback, M., and Benoit, R., 1998, Subsurface Electrical Measurements at Dixie Valley, Nevada, Using Single-Well and Surface-to-Well Induction Logging, Proceedings 23rd Workshop on Geothermal Reservoir Engineering, Stanford University, California, Jan. 26-28, 8p.

Hickman, S., Zoback, M., and Benoit, R., 1998, Tectonic Controls on Reservoir Permeability in the Dixie Valley, Nevada Geothermal Field, Proceedings 23rd Workshop on Geothermal Reservoir Engineering, Stanford University, California, Jan. 26-28, 8 p.

Hickman, S., and Zoback, M., 1997, In-Situ Stress in a Fault Hosted Geothermal Reservoir at Dixie Valley, Nevada, Proceedings, 22nd Workshop on Geothermal Reservoir Engineering, Stanford University, California, Jan. 27-29, 6p.

Hittelman, A. M., Dater, D. T., Buhmann, R. W., and Racey, S. D., 1994, Gravity-edition CD-ROM user's manual, NOAA Natl. Geophys. Data Center, Boulder, Colo.

Holbrook, W. S., Gajewski, D., Krammer, A., and Prodehl, C., 1988, An interpretation of wide-angle compressional and shear wave data in southwest Germany: Poisson's Ratio and petrological implications, Journal of Geophysical Research, v. 93, p. 12,081–12,106.

Holliger, K., Levander, A., Carbonell, R. and Hobbs, R., 1994, Some attributesof wavefields scattered from Ivrea-type lower crust, Tectonophysics, 232, 267–279.

Hulen, J. B., Hollister, J. W., Johnson, S. D., and Allis, R., 1999, Oils in the Dixie Valley and Kyle hot springs geothermal systems, Nevada — Potentially sensitive indicators of natural and induced reservoir processes, Proceedings 24th Workshop on Geothermal Reservoir Engineering, Stanford University, Stanford, California, Jan. 25-27, 15p.

Hunt, A.G., Breit, G., Bergfeld, D., Rytuba, J.J., Landis, G.P. Wolf, R.E., 2011, Clarification of the roles of magmatic versus amagmatic sources for modern geothermal systems associated with epithermal mineralization using noble gas geochemistry, in The Proceedings of Geological Society of Nevada Symposium, Great Basin Evolution and Metallogeny: Reno, NV, p. 513-522.

Iovenitti, J. L., Blackwell, D. D., Sainsbury, J. S., Tibuleac, I. M., Waibel, A. F., Cladouhos, T. T., Karlin, R., Kennedy, B. M., Isaaks, E., Wannamaker, P.E., Clyne, M. T., Ibser, F.H., Callahan, O. C., 2012, Towards Developing a Calibrated EGS Exploration Methodology Using the Dixie Valley Geothermal System, Nevada, Proceedings, 37th Workshop on Geothermal Reservoir Engineering Stanford University, Stanford, California, January 30 - February 1, 15p.

Iovenitti, J. L., Blackwell, D. D., Sainsbury, J. S., Tibuleac, I. M., Waibel, A. F., Cladouhos, T. T., Karlin, R., Kennedy, B. M., Isaaks, E., Wannamaker, P.E., Clyne, M. T., and Callahan, O. C., 2011a, EGS Exploration Methodology Development Using the Dixie Valley Geothermal District as a Calibration Site, A Progress Report, GRC Transactions, v. 35, 12p.

Iovenitti, J. L., Blackwell, D. D., Sainsbury, J. S., Tibuleac, I. M., Waibel, A. F., Cladouhos, T. T., Karlin, R., Kennedy, B. M., Isaaks, E., Wannamaker, P.E., Clyne, M. T., and Callahan, O. C., 2011b, EGS Exploration Methodology Development Using the Dixie Valley Geothermal District as a Calibration Site, A Progress Report, Poster Presentation, Annual GRC Meeting in San Diego.

Iovenitti, J. L., Blackwell, D. D., Sainsbury, J. S., Tibuleac, I. M., Cladouhos, T. T., Karlin, R., Kennedy, B. M., Isaaks, E., Wannamaker. P. E., Clyne, M. T., and Callahan, O. C., 2011c, EGS Exploration Methodology Development Using the Dixie Valley Geothermal District as a Calibration Site, A Progress Report, Abstract and Poster Presentation, American Geophysical Union (AGU), San Francisco, Paper Number H21E-1173.

Iovenitti, J. L., Blackwell, D. D., Tibuleac, I. M., Cladouhos, T. T., Karlin, R., Kennedy, B. M., Isaaks, E., Wannamaker, P. E., Clyne, M. T., and Callahan, O. C., 2010a, EGS Exploration Methodology Development Using the Dixie Valley Geothermal District as a Calibration Site, A Progress Report. Paper and Poster Presentation, Annual GRC Meeting in San Diego.

Iovenitti, J. L., Tibuleac, I. M., Hopkins, D., Cladouhos, T. T., Karlin, R., Wannamaker P. E., Kennedy, B. M., Blackwell, D. D., Clyne, M. T., and Issaks, E., 2010b, Development of Exploration Methods for Engineered Geothermal Systems through Integrated Geophysical, Geologic and Geochemical Interpretation, Abstract and Poster Presentation, American Geophysical Union (AGU), San Francisco.

Ito, H., De Vilbiss, J. and Nur, A., 1979, Compressional and shear waves in saturated rock during water¿stream transition, Journal of Geophysical Research 84: doi: 10.1029/0JGREA0000840000B9004731000001. issn: 0148-0227.

ITSI, 2005, Kinematic and Dynamic Studies: Genetic Occurrence Models for Geothermal Prospecting. Geothermal Program Office, Naval Air Weapons Station, 86p.

Iverson, W. P., Fahmy, B. A., a nd Smithson, S. B., 1989, Vp/Vs from mode-converted P-SV reflections: Geophysics, 54, 843-852.

Iyer, H. M., and Dawson, P.B., 1993, Imaging Volcanoes using Teleseismic Tomography, in Iyer, H.M., Hirahara, K., editors, Seismic Tomography: Theory and Practice. Chapman and Hall, London.

Janik, C., Nimz, G., and Goff, F., 2002, Origin, Age, and Geochemical Evolution of Dixie Valley Geothermal Fluid, Presentation to Dixie Valley Geothermal Workshop, June 12-13, Reno, Nevada. http://www.unr.edu/geothermal/oldermeetings.htm

Jaya, M. S., Shapiro, S. A., Kristinsdóttir, L. H., Bruhn, D., Milsch, H., and Spangenberg, E., 2010, Temperature dependence of seismic properties in geothermal rocks at reservoir conditions, Geothermics, v. 39, p. 115–123.

Jekeli, C., Erkan, K., Huang, O., 2010, Gravity vs pseudogravity: A comparison based on magnetic and gravity gradient measurements, Earth and Environmental Science, v. 135, Part 1, p. 123-127, DOI: 10.1007/978-3-642-10634-7_17.

John, D. A., 1995, Tilted middle Tertiary ash flow calderas and subjacent granitic plutons, southern Stillwater Range, Nevada: Cross sections of an Oligocene igneous center, Geological Society of America Bulletin, v. 107, p. 180-200.

Johnson, R. A., and Loy, K. L., 1992, Seismic reflection evidence for seismogenic low-angle faulting in southeastern Arizona, Geology, v. 20, p. 597-600.

Johnson, S. D. and Hulen, J. B., 2002, Subsurface stratigraphy, structure, and alteration in the Senator thermal area, Northern Dixie Valley geothermal field, NV – Initial results from injection well 38-32, and a new structural scenario for the Stillwater escarpment, GRC Transactions, v. 26, p. 533-542.

Julian, B. R., Ross, A., Foulger, G. R., Evans, J. R., 1996, Three-Dimensional seismic image of a geothermal reservoir: The Geysers, California, Geophysical Research Letters, 23, pp. 685–688.

Kampfmann W. and Berckhemer H., 1985, High temperature experiments on the elastic and anelastic behavior of magmatic rocks, Phys. Earth planet. Int., 40, 223–247.

Kennedy, B. M., van Soest, M. C., 2007, Flow of Mantle Fluids through the Ductile Lower Crust: Helium Isotope Trends, Science 30 November, 318, pp. 1433-1436, DOI: 10.1126/science.1147537.

Kennedy, B. M., Fischer, T. P., and Shuster, D. L., 2000, Heat and helium in geothermal systems, Proceedings 25thWorkshop on Geothermal Reservoir Engineering, Stanford Geothermal Program Report SGP-TR-165, 167–173.

Kennedy, B. M., van Soest, M. C., 2006, A Helium Isotope Perspective on the Dixie Valley, Nevada, Hydrothermal System, Geothermics, v. 35, p. 26-43.

Kennedy, B. M., Fischer, T. P., and Shuster, D. L., 2000, Heat and helium in geothermal systems, Proceedings 25th Workshop on Geothermal Reservoir Engineering, Stanford University, California, p. 167–173.

Kennedy, B.M., Janik, C., Benoit, D., and Shuster, D. L., 1999, Natural geochemical tracers for injectate fluids at Dixie Valley, Proceedings 24th Workshop on Geothermal Reservoir Engineering, Stanford University, California, p. 108 – 115.

Kennedy-Bowdoin, T., Silver, E. A., Martini, B. A., and Pickles, W. L., 2004, Geothermal Prospecting using Hyperspectral Imaging and Field Observations, Dixie Meadows, NV, GRC Transactions, v. 28, Aug. 29-Sept. 1, 4p.

Kennett, B. L. N., Engdahl, E. R., and Buland, R., 1995, Constraints on seismic velocities in the Earth from traveltimes, Geophysical Journal International, v. 122, p. 108 -124.

Kern, H., Popp, T., Gorbatsevich, F., Zharikov, A., Lobanov, K. V., and Smirnov, Y. P., 2001, Pressure and temperature dependence of Vp and Vs in rocks from the superdeep well and from surface analogues at Kola and the nature of velocity anisotropy, Tectonophysics, v. 338, p. 113-134.

Kern, H., 1982, Elastic-wave velocity in crustal and mantle rocks at high pressure and temperature: the role of the high—low quartz transition and of dehydration reactions, Physics of the Earth and Planetary Interiors, v. 29, p. 12-23.

Kern, H., Richter, A., 1981, Temperature derivatives of compressional and shear wave velocities in crustal and mantle rocks at 6 kbar confining pressure, J. Geophys., 49, 47–56.

King, G., Oppenheimer, D., Amelung, F., 1994, Block versus continuum deformation in the Western United States, Earth and Planetary Science Letters, v. 128, 55-64.

Klemperer, S. L., Hauge, T. A., Hauser, E. C., Oliver, J. E., and Potter, C. J., 1986, The Moho in the northern Basin and Range Province, Nevada, along the COCORP 40°N seismic reflection transect, Geological Society of America Bulletin, v. 97 (no. 5), p. 603–618.

Koch, M., 1992, Bootstrap inversion for vertical and lateral variations of the S wave structure and the Vp/Vs-ratio from shallow earthquakes in the Rhinegraben seismic zone, Germany, Tectonophysics, v. 210, p. 91–115.

Koulakov I., 2009, LOTOS code for local earthquake tomographic inversion. Benchmarks for testing tomographic algorithms, Bulletin of the Seismological Society of America, v99, No. 1, pp. 194-214, doi: 10.1785/0120080013.

Knopoff, L., 1967, Density-velocity relations for rocks. Journal of Geophysical Research Astron. Soc., v. 13, p. 1-8.

Kreemer, C., and Hammond, W. C., 2008, Geodetic Constraints on the Slip Rate of the Mohawk Valley Fault Zone, California, USGS Final Technical Report, award no. 08HQGR0027, http://earthquake.usgs.gov/research/external/reports/08HQGR0027.pdf

Krishna, A., 1988, Crustal velocity models in the western united states from travel times and amplitudes of seismic refraction data, Bulletin of the Seismological Society of America, v. 78, no. 2, p. 816-837.

Kucks, R. P., P.L. Hill, D. A. Ponce, D. A., 2006, Nevada magnetic and gravity maps and data: A website for distribution of data by USGS. URL:http://pubs.usgs.gov/ds/2006/234/data/.

Kulenkampff, J., Spangenberg, E., Flovenz, O.,Raab, S., and Huenges, E., 2005, Petrophysical parameters of rocks saturated with liquid water at high temperature geothermal reservoir conditions: Proc. World Geothermal Congress, 1-9.

Lachenbruch, A. H., and Sass, J. H., 1977, Heat flow in the United States and the thermal regime of the crust. Heacock, J.G., editor, The Nature and Physical Properties of the Earth's Crust, American Geophysical Union Monograph, v. 20, p.626–675.

Larosse, E., Derode, A., Clorennec, D., Margerin, L., and Campillo, M., 2005, Passive retrieval of Rayleigh waves in disordered elastic media, Phys. Rev. E 72, DOI:10.1103/PhysRevE.72.046607.

Lawrence, J. F. and Prieto, G. A., 2010, Attenuation tomography of the western United States from ambient seismic noise, Journal of Geophysical Research, v. 116, B06302, doi:10.1029/2010JB007836, 2011.

Lawrence, R. L., and Wright, L., 2001, Rule-Based Classification Systems using Classification and Regression (CART) Analysis, Photogrammetric Engineering & Remote Sensing, v. 67, no. 10, October, p. 1137-1142.

Lees, J.M., 2007, Seismic tomography of magmatic systems, Journal of Volcanology and Geothermal Research, v. 167, p. 37–56.

Lees, V., and Wu, H., 2000, Poisson’s ratio and porosity at Coso geothermal area, California, Journal of Volcanology and Geothermal Research, v. 95, p. 157–173.

Levander, A. R., Hobbs, R. W., Smith, S. K., England, R. W., Snyder, D. B., and Hollinger, K., 1994, The crust as a heterogeneous ‘optical’ medium, or ‘crocodiles in the mist’: Tectonophysics, 232, 281–297.

Lin, F. C., Moschetti, M. P., and Ritzwoller, M. H., 2008, Surface wave tomography of the western United States from ambient seismic noise: Rayleigh and Love wave phase velocity maps, Geophysical Journal International, 173, 281-298.

Lin, J., and Stein, R. S., 2004, Stress triggering in thrust and subduction earthquakes, and stress interaction between the southern San Andreas and nearby thrust and strike-slip faults, Journal of Geophysical Research, v. 109, B02303.

Lindquist, K. G., Tibuleac, I. M. and Hansen, R. A., 2005, A Semi-Automatic Calibration Method Applied to a Small-aperture Alaskan Seismic Array, Bull. Seism. Soc. Am. 97, 100pp.

Line, C. E. R., Hobbs, R. W., and Snyder, D. B., 1998, Estimates of upper-crustal heterogeneity in the Baltic Shield from seismic scattering and borehole logs, Tectonophysics, v. 286, p. 171 - 183.

Lobkis, O. I. and Weaver, R. L., 2001. On the emergence of the Green’s function in the correlations of a diffusive field, J. Acoust. Soc. Am., 110, 3011-3017.

Louie, J. N., Thelen, W., Smith, S. B., Scott, J. B., Clark, M., and Pullammanappallil, S., 2004, The Northern Walker Lane refraction experiment: Pn arrivals and the northern Sierra Nevada root, Tectonophysics, v. 388, no. 1-4, p. 253-269.

Lowell, R. P., and Stephen, R. A., 1991, Heat - flow and lateral seismic velocity heterogeneities near Deep Sea Drilling Project - Ocean Drilling program Site 504, Geology, v. 19, p. 1141-1144.

Lutz, S. J., Caskey, S. J., and Johnson S. D., 2003, Geyserite, faulted sinter terraces, and other fossil hot spring deposits, northern Dixie Valley fault system, Nevada, Nevada Petroleum Society Field Trip Guide-book, Aug. 22-24, p. 75-89.

Lutz, S. J., Moore, J. N., Blamey, N. J. F., and Norman, D. I., 2002, Fluid-Inclusion Chemistry of the Dixie Valley (NV) Geothermal System, Proceedings 27th Workshop on Geothermal Reservoir Engineering, Stanford University, California, Jan. 28-30, 11p.

Lutz, S. J., Caskey, S. J., Mildenhall, D. D., Browne, P. R. L., and Johnson, S. D., 2002, Dating sinter deposits in northern Dixie Valley, Nevada- thepaleoseismic record and implications for the Dixie Valley geothermal system, Proceedings, 27th Workshop on Geothermal Reservoir Engineering, Stanford University, California, Jan. 28-30. 10p.

Lutz, S. J., Moore, J. N., and Benoit, D., 1998, Integrated alteration mineralogy and fluid-inclusion study at the Dixie Valley geothermal field, Nevada, Proceedings, 23rd Workshop on Geothermal Reservoir Engineering, Stanford University, Stanford, California, January 26-28, p. 315-321.

Lutz, S. J., Moore, J. N., Benoit, D., 1997, Geologic Framework of Jurassic Reservoir Rocks in the Dixie Valley Geothermal Field, Nevada: Implications from Hydrothermal Alteration and Stratigraphy, Proceedings 22nd Workshop on Geothermal Reservoir Engineering, Stanford University, California, Jan. 27-29, 9pp.

Majer, E. L. and McEvilly, T.V., 1979, Seismological Investigations at The Geysers Geothermal Field, Geophysics, Vol. 44, No. 2, p. 246-269.

Malin, P. E., and Shalev, E., 1999, Shear-wave splitting crack density maps for the Geysers and Mammoth. Proceedings, 24th Workshop on Geothermal Reservoir Engineering Stanford University, Stanford, California, January 25-27.

Mallan, R., and Wilt, M., 2001, Subsurface Electrical Measurements at Dixie Valley, Nevada, Using Single-Well and Surface-Well Induction Logging, Proceedings, 26th Workshop on Geothermal Reservoir Engineering, Stanford University, California, Jan. 29-31, 6p.

Mankhemthong, Niti, 2008, Structure of the Inter-Basin Transition Zone between Dixie Valley and Fairview Valley, Nevada, USA, University of Nevada, Master of Science thesis, 132pp.

Mankhemthong, N., Oppliger, G.L., Aslett, Z., 2008, Structural Localization of Two Temperature Geothermal Systems within the Gravity Defined Linkage between Dixie Valley and Fairview Valley, Nevada, USA, GRC Transactions, v. 32, 5p.

Maris, V., and Wannamaker, P. E., 2010, Parallelizing a 3D finite difference MT inversion algorithm on a multicore PC using OpenMP: Computers & Geosciences, doi: 10.1016/j.cageo.2010. 03.001, 5pp.

Marqardt, D.W., 1963, An algorithm for least-squares estimation of non-linear parameters. Journal SIAM, v. 11, p. 431-441.

Mavko, G., 2008, Parameters that influence Seismic Velocity. Stanford Rock Physics Laboratory, Presentation, Stanford University, California.

Mavko, G.M., 1980, Velocity and attenuation in partially molten rocks. J. Geophys. Res., v. 85 (B10), p. 5173-5189.

McKee, E.H., and Moring, B.C., 1996, Cenozoic mineral deposits and related rocks: Nevada Bureau of Mines and Geology Open-File Report 96–2, p. 6–1 to 6–8.

McKenna, J. R., Blackwell, D. D., Richards, M. C., 2005, Natural State Modeling, Structure, Preliminary Temperature and Chemical Synthesis of the Dixie Valley, Nevada Geothermal Field, Proceedings, 32nd Workshop on Geothermal Reservoir Engineering, Stanford University, California, Jan. 31-Feb. 2, 8p.

McKenna, J. R., and Blackwell, D. D., 2004, Numerical modeling of transient Basin and Range extensional geothermal systems, Geothermics, v. 33, p. 457-476.

McLachlan, G. J., 2004, Discriminant Analysis and Statistical Pattern Recognition, Wiley Interscience, MR1190469, ISBN 0471691151.

McLin, K. S., Moore, J. N., Park, J., Norman, D. I., 2008, Mineralogy and Fluid Inclusion Gas Chemistry of Production Well Mineral Scale Deposits at the Dixie Valley Geothermal Field, USA. Proceedings, 23rd Workshop on Geothermal Reservoir Engineering, Stanford University, California, Jan. 28-30, 4 p.

Mickey, W. V., 1964, Microearthquake monitoring at the Shoal site, U.S. Coast and Geodetic Survey Report, AFTAC Project No. VELA T/4052/CGS/B31, p. 1-82.

Mickey, W. V., 1966, Seismic clusters, U.S. Dept. of Comm., ESSA Symposium on Earthquake Prediction, p. 63-68.

Mooney, W. D., Laske, G., and Masters, T. G., 1998, Crust 5.1: a global crustal model at 5x5 degrees, Journal of Geophysical Research, v. 103, p. 727-747.

Nakajima, J., and Hasegawa, A., 2003, Tomographic imaging of seismic velocity structure in and around the Onikobe volcanic area, northeastern Japan: implications for fluid distribution, Journal of Volcanology and Geothermal Research, v. 127, p. 1-18.

Nakajima, J., Matsuzawa, T., and Hasegawa, A., 2001, Three-dimensional structure of and beneath northeastern Japan' Implications for arc magmatism and fluids, Jour. Geophys. Res., v. 106, no. B10, p. 21843 -21 857.

Nesbitt, B. E., 1993, Electrical resistivities of crustal fluids: J. Geophys. Res., 98, 4301-4310.

Nicholson, C., and Simpson, D. W., 1985, Changes in Vp/Vs with depth. Bull. Seis. Soc. Am., v. 75, p. 1105-1123.

Nimz, G., Janik, C., Goff, F., Dunlap, C., Huebner, M., Counce, D., and Johnson, S., 1999, Regional hydrology of the Dixie Valley geothermal field, Nevada: Preliminary interpretations of chemical and isotopic data, Lawrence Livermore National Laboratory Publication, UCRL-JC-135417, 9 p.

O'Connel, R. J., Sumner, E. E., and Budiansky, B., 1983, Bulk thermoelastic attenuationof composite materials, J. Geophys. Res., v. 88, p. 10,343-10,348.

O'Connel, R. J., and Budiansky, B., 1974, Seismic Velocities in dry and saturated cracked solids, J. Geophys. Res., v. 79, p. 5412-5429.

Okaya, D. A., and Thompson, G. A., 1985, Geometry of Cenozoic extensional faulting: Dixie Valley, Nevada, Tectonics, v. 4, no. 1, p. 107-125.

Oliver, J., Ryall, A., Brune, J. N., and Slemmons, D.B., 1966, Microearthquake activity recorded by portable seismographs of high sensitivity, Bulletin Seismological Society of America, v. 56, p. 899-924.

Page, B. M., 1965, Preliminary Geologic Map of a part of the Stillwater Range, Churchill County, Nevada, Nevada Bureau of Mines, Map 28.

Palacky, G. J., 1988, Resistivity characteristics of geologic targets: in, Electromagnetic methods in applied geophysics, M. N. Nabighian, ed., Soc. Explor. Geophys., Tulsa, OK, v. 1, 53-130.

Peacock, S., Westbrook, G. K., and Graham, D. P., 1997, Seismic velocities in the Northern Barbados Ridge, accretionary complex, site 9491, Proceedings of the Ocean Drilling Program, Scientific Results, v. 156.

Peiffer, L. Wanner, C., Spycher, N., Sonnenthal, E., and Kennedy, B. M., 2012, Revisited multicomponent chemical geothermometry: Application to the Dixie Valley Geothermal Area, abs. and poster presentation at the Annual American Geophysical Union meeting San Francisco, California.

Peiffer, L. Wanner, C., Spycher, N., Sonnenthal, E., Iovenitti, J., and Kennedy, B. M., 2013, Mulitcoponent vs classical geothermometry: An evaluation using reactive transport modeling, Water-Rock Interaction Conference presentation, Avignon cedex 1, France.

Phillips, W. S., and Stead, R. J., 2008, Attenuation of Lg in the western US using the US Array, Geophysical Research Letters, v. 35, L07307.

Pickett, G. R., 1963, Acoustic character logs and their applications in formation evaluation: J. Petr.Tech., June, 659-66.

Plank, G .R., 1998, Structure, stratigraphy, and tectonics of a part of the Stillwater escarpment and implications for the Dixie Valley geothermal system, unpublished report for Oxbow Geothermal and Master's Thesis for University of Nevada Reno, 153 pp.

Ponce, D. A., 1997, Gravity data of Nevada. U.S. Geological Survey Digital Data Series DDS-41, 1-27.

Preston, L. A., 2010, P- and S-body wave tomography of the state of Nevada, SANDIA Report, SAND2010-2205.

Preston, L., and von Seggern, D., 2008, Joint Seismic Tomography/Location Inversion in the Reno/Carson City Area, Final Report to the National Earthquake Hazard Reduction Program, U. S. Geological Survey Award Number 07HQGR0022.

Priestley, K and Brune, J., 1978, Surface waves and the structure of the Great Basin of Nevada and western Utah, JGR, v. 83, 2265-2272.

Rasmussen, R., and Pedersen, L. B., 1979, End corrections in potential field modeling: Geophysical Prospecting, v. 27, p. 749-760.

Reed, M. J., 2007, An Investigation of the Dixie Valley Geothermal Field, Nevada, Using Temporal Moment Analysis of Tracer Tests, Proceedings, 32nd Workshop on Geothermal Reservoir Engineering, Stanford University, California, Jan. 22-24, 8 p.

Reheis, M., 1999, Extent of Pleistocene lakes in the western Great Basin, U.S. Geological Survey Miscellaneous Field Investigation Map, MF-2323, 1 sheet.

Reheis, M. C., and Morrison, R. B. Link, P. K., and Kowallis, B. J., 1997, High, old pluvial lakes of western Nevada Proterozoic to recent stratigraphy, tectonics, and volcanology, Utah, Nevada, southern Idaho, and central Mexico, Brigham Young University Geology Studies, v. 1, p. 459-492.

Reiter, M., 2008, Geothermal anomalies in the crust and upper mantle along Southern Rocky Mountain transitions. GSA Bulletin, March/April, v. 120, no. 3/4; p. 431-441.

Rial, J. A., Elkibbi, M., Yang, M., 2005, Shear-wave splitting as a tool for the characterization of geothermal fractured reservoirs: lessons learned, Geothermics, v. 34, p. 365-385.

Ritzwoller, M. H., Shapiro, N. M., Barmin, M. P., and Levshin, A. L., 2002, Global surface wave diffraction tomography, Journal of Geophysical Research, v. 107(B12), p. 23-35. Geothermics, v. 34, p. 365–385.

Rose, P.E., Johnson, S.D., Kilbourn, P., and Kasteler, C., 2002, Tracer testing at Dixie Valley, Nevada, using 1-naphthalene sulfonate and 2,6-naphthalene disulfonate, Proceedings 27nd Workshop on Geothermal Reservoir Engineering, Stanford University.

RStudio IDE, User Interface for R. http://www.rstudio.com

Rybach, L. G., and Bunterbath, M. ,1982, Relationships between the petrophysical properties density, seismic velocity, heat generation and mineralogical constitution, Earth Planet. Seis. Lett., v. 57, p. 367–376, 1982.

Sabra, K. G., Gerstoft, P., Roux, P., Kuperman, W. A., and Fehler, M. C., 2005, Surface wave tomography from microseisms in southern California, Geophys. Res. Lett., 32, L14311, doi:10.1029/2005GL023155.

Sasaki, Y., 2004, Three-dimensional inversion of static-shifted magnetotelluric data: Earth, Planets and Space, 56, 239-248.

Saltus, R. W., 1988, Regional, residual, and derivative gravity maps of Nevada, Nev. Bur. Mines and Geol. Map 94B, 1:1,000,000.

Schmeling, H., 1985, Partial melt below Iceland: A combined interpretation of seismic and conductivity data, J. Geophys. Res., v. 90 (B12), p. 10105-10116.

Shankland, T. J. and Waff, H. S., 1977, Partial melting and electrical conductivity anomalies in the upper mantle, Journal of Geophysical Research Volume 82, Issue 33, p. 5409–5417.

Shapiro, N. M., Campillo, M., Stehly, L., and Ritzwoller, M. H., 2005, High-resolution surface wave tomography from ambient seismic noise, Science, 307, 1615-1618.

Shapiro, N. M., and Ritzwoller, M. H., 2004, Thermodynamic constraints on seismic inversions, Geophysical Journal International, v. 157, p. 1175-1188.

Sharma, S. R., Sundar, A., Rao, V. K., and Ramana, D. V., 1991, Surface heat flow and pn velocity distribution in peninsular India, Journal of Geodynamics, v. 13, no. 1, p. 67-76.

Sherburn S., Bannister, S., and Bibby, H., 2003, Seismic velocity structure of the central Taupo Volcanic Zone, New Zealand, from local earthquake tomography, Journal of Volcanology and Geothermal Research, v. 122, p. 69-88.

Shevenell, L. and Garside, L. J., 2003, Nevada geothermal resources, Nevada Bureau of Mines and Geology, Map 141, 1 sheet, 1:750;000.

Shevenell, L., Kasameyer, P., Bruton, C., Renner, J. L., and Kennedy, B. M., 2002, The Department of Energy's Workshop: Dixie Valley Geothermal Research, Executive Summary, Group Conclusions and recommendations. PDF available online at: http://www.unr.edu/geothermal/pdffiles/intro_summarydv.pdf, and presentations at: http://www.unr.edu/geothermal/oldermeetings.htm#Dixie_Valley_Geo_2002

Shevenell, L., Garside, L. J., and Hess, R. W., 2000, Nevada Geothermal Resources: Nevada Bureau of Mines and Geology Map 126, scale 1:1,000,000 and Map 141, scale at 1:750,000.

Simiyu, S.M., 1999, Seismic Velocity Analysis in the Olkaria Geothermal Field, Proceedings, 24th Workshop on Geothermal Reservoir Engineering Stanford University, Stanford, California, January 25-27.

Smith, R. P., Grauch, V. J. S., and Blackwell, D. D., 2002, Preliminary Results of a High-Resolution Aeromagnetic Survey to Identify Buried Faults at Dixie Valley, Nevada, GRC Transactions, v. 26, p. 543-546.

Smith, R. P. and Grauch, V. J. S., 2002, High-resolution aeromagnetic survey reveals distribution of faults in Dixie Valley, Nevada, Geological Society of America, Annual Meeting, Denver, October 27, - Theme session on New Views of Extensional Basins and Related Volcanic Fields Using Geophysics and Remote Sensing.

Smith, R. P., Wisian, K. W., Blackwell, D. D., 2001, Geologic and Geophysical Evidence for Intra-basin and Footwall Faulting at Dixie Valley, Nevada, GRC Transactions, v. 25, Aug. 26-69. 8 p.

Smith, R.D., 1979. Geophysical Report: Magnetotellurics, gravity, magnetics in Dixie Valley Nevada, unpublished Geotronics Corp., Austin, TX, 53 p., plus 7 Plates.

Sonders, L.J., and Jones, C. H., 1999,The western United States: how the west was widened; Annual Reviews of Earth and Planetary Sciences, v. 27, 417-462.

Southland Royalty Corp., 1979, Bouguer gravity map. Plate 2.1A of Gravity and Magnetic Survey Dixie Valley, Nevada performed by Austin Exploration. Inc, for AMOCO Production Co, unpublished report.

Speed, R. C., 1976, Geologic Map of the Humboldt Lopolith and surrounding terrane, The Geologic Society of America, Map and Chart Series MC-14, 1:81050, 4 p.

Stauder, W., and Ryall, A., 1967, Spatial distribution and source mechanism of microearthquakes in Central Nevada, Bulletin of the Seismological Society of America, December 1, v. 57, no.6, p. 1317 -1345.

Stewart, J. H., 1998,Regional characteristics tilt domains, and extensional history of the late Cenozoic Basin and Range Province, western North America. in Faulds, J. E., and Stewart, J. H., editors, Accommodation zones and transfer zones: The regional segmentation of the Basin and Range Province, Geological Society of America Special Paper 323, Boulder, CO, 47-74.

Stewart, J. H. ,1980, Regional tilt patterns of late Cenozoic basin-range fault blocks, western United States, Bull. Geol. Soc. Am., 91,460-465.

Stewart, J. H., and Carlson, J. E., 1978, Geologic map of Nevada, U.S. Geological Survey, 1:500,000 scale.

Talwani, M., and Heirtzler, J. R., 1964, Computation of magnetic anomalies caused by two-dimensional bodies of arbitrary shape, in Parks, G. A., Editor, Computers in the mineral industries, Part 1: Stanford University Publications, Geological Sciences, v. 9, p. 464-480.

Talwani, M., Worzel, J. L., and Landisman, M., 1959, Rapid gravity computations for two-dimensional bodies with application to the Mendocino submarine fracture zone, Journal of Geophysical Research, v. 64, p. 49-59.

Tarantola, A., 1987, Inverse Problem Theory: Elsevier, New York, 613pp.

Tatham, R. H., 1982, Vp/Vs and lithology, Geophysics, 47, p. 336-344.

Taylor, R., 1990, Relationships between cognitive test-performance and everyday cognitive difficulties in multiple-sclerosis, British Journal of Clinical Psychology, v. 29, p. 251–252.

Telford, W.M., Geldart, L. P. and Sheriff, R. E., 1990, Applied Geophysics, 2nd ed. Cambridge U. Press, Cambridge,U.K.

Thompson, G. A., Catchings, R., Goodwin, E., Holbrook, S. Jarchow, C., Mann, C., McCarthy, J, and Okaya, D., 1989, Geophysics of the western Basin and Range Province. in Pakiser, L. C., and Mooney, W. D. editors, Geophysical Framework of the continental United States, Geol. Soc. of Amer. Memoir 172, p. 117-204.

Tibuleac, I. M. and von Seggern, D. H., in prep, An inexpensive, non-invasive method to estimate P/S seismic velocity models in the highly populated Reno Basin area, using ambient - seismic noise and signal, Seismological Research Letters.

Tibuleac, I. M., Iovenitti, J. L., von Seggern, D., Sainsbury, J., Biasi, G., and Anderson, J. A., 2013, Development of exploration of exploration methods for Engineered Geothermal Systems through integrated geophysical, geologic, and geochemical interpretation, The Seismic Analysis component, Proceedings38th Workshop on Geothermal Reservoir Engineering, Stanford University, Stanford, California, p. 1277-1285.

Tibuleac, I., von Seggern, D., Iovenitti, J. L., Sainsbury, J. Biasi, G. Anderson, J., 2012, EGS Exploration Methodology Development Using the Dixie Valley Geothermal District as a Calibration Site. The Seismic Analysis Component, abstract submitted to Annual American Geophysical Union Meeting in San Francisco.

Tibuleac, I. M, Herrin, E. T., and Negraru, P., 2001, Calibration Studies at NVAR, Seis. Res. Lett. 72, 754.

Tibuleac, I. M. and von Seggern, D. H., 2012, Crust-mantle boundary reflectors in Nevada from noise auto-correlations, Geophys. J. Int., Vol. 189, Issue 1, 493-500.

Tibuleac, I. M., von Seggern, D. H., Anderson, J. G., and Louie, J. N., 2011, Computing Green's Functions from Ambient Noise Recorded by Narrow-Band Seismometers, Accelerometers, and Analog Seismometers, doi: 10.1785/gssrl.82.5.661 Seismological Research Letters September/October 2011 v. 82 no. 5, 661-675.

Tivey, M. A., Sager, W. W., Lee, S., Tominaga, M., 2006, Origin of the Pacific Jurassic quiet zone, Geology, 34, p. 789-792.

Toda, S., Stein, R. S., Richards-Dinger, K., and Bozkurt, S., 2005, Forecasting the evolution of seismicity in southern California: Animations built on earthquake stress transfer, Journal of Geophysical Research, v. 110, 17 p.

Tosdal, R. M., Wooden, J. L., and Kistler, R. W., 2000, Geometry of the neopro- terozoic continental break-up, and implications for location of Nevadan mineral belts, in Cluer, J. K., Price, J. G., Struhsacker, E. M., Hardyman, R. F., and Morris, C. L., editors, Geology and Ore Deposits 2000: The Great Basin and Beyond, Geological Society of Nevada Symposium Proceedings, p. 451-466.

Unruh, J., Pullammanappallil, S., Honjas, W., and Monastero, F., 2001, New seismic imaging of the Coso geothermal Field, Eastern California, Proceedings 26th Workshop on Geothermal Reservoir Engineering, Stanford University, California, 7pp.

Ussher, G., Harvey, C., Johnstone, R., and Anderson, E., 2000, Understanding the resistivities observed in geothermal systems: Proc. World Geothermal Congress, 1915-1920.

UTEP PACES GEONET, Gravity and magnetic data set repository -Gravity and magnetic data base of the United States, http://irpsrvgis00.utep.edu/repositorywebsite

Vanorio, T., Virieux, J., Zollo, A., Capuano, P., and Russo, G., 2006, A rock physics and seismic tomography study to characterize the structure of the Campi Flegrei caldera, http://hdl.handle.net/2122/2171, p. 25–33.

Vikre, P. C., 1994, Gold mineralization and fault evolution at the Dixie Comstock Mine, Churchill County, Nevada, Economic Geology, v. 89, no. 4, p. 707-719.

Vlahovic, G., Elkibbi, M., and Rial, J. A., 2002, Shear-wave splitting and reservoir crack characterization: the Coso geothermal Field, Journal of Volcanology and Geothermal Research, v. 120, p. 123-140.

Von Herzen, R. P. and Uyeda, S., 1963, Heat flow through the eastern Pacific Ocean floor; Journal of Geophysical Research, v. 68, p. 4219-4250.

Von Seggern, D. H., Tibuleac, I. M. and Louie, J. N., 2009, Computing Green's Functions from ambient noise recorded by narrow-band seismometers, accelerometers, and analog seismometers, Abstract presented at the 2009 Annual Meeting Announcement Seismological Society of America, 8–10 April, Monterey, California.

Yoshikawa, M., and Sudo, Y., 2004, Three Dimensional Seismic Velocity Structure beneath the Otake-Hatchobaru Geothermal Area at Kuju Volcano in Central Kyushu, Japan, Annuals of Disaster Prevention Research Institute, Kyoto Univ., No. 47 B.

Vozoff, K., 1991, The magnetotelluric method: in Electromagnetic methods in applied geophysics, ed. by M. N. Nabighian, Soc. of Explor. Geophys., Tulsa, Okla., 2B, 641-711.

Waibel, A. F., 2011, Structural controls on the location of geothermal cells in and adjacent to Dixie Valley, Nevada, GRC Transactions, v. 35, 8 p.

Waibel, A. F., 1999, Dixie Valley Geology, unpublished report from Dave Blackwell.

Waibel, A. F., 1987, An Overview of the Geology and Secondary Mineralogy of the High Temperature Geothermal Systems in Dixie Valley, Nevada, GRC Transactions, v. 11, p. 479-486, and GRC Bulletin, v. 16, no. 9, p. 5-13.

Waldhauser, F., and Ellsworth, W. L., 2000, A double-difference earthquake location algorithm: Method and application to the northern Hayward fault, Bulletin Seismological Society of America, v. 90, p. 1353-1368.

Wallace, R. E., 1984, Fault scarps formed during the earthquake of Oct. 2, 1915, Pleasant Valley, Nevada, and some tectonic implications, U.S. Geological Survey Professional Paper 1274-A, p. 1-33.

Wallace, R. E., and Whitney, R. A., 1984, Late Quaternary history of the Stillwater seismic gap, Nevada. Bulletin of the Seismological Society of America, v. 74, no. 1, p. 301-314.

Wang, Z., Batze, M. L. and Nur, A. M., XXX, Effects of different fluids on seismic velocities in rocks, Canadian Journal of Exploration Geophysics, 26, pp. 104-112.

Wannamaker, P. E., 1999, Affordable magnetotellurics: interpretation in natural environments: in Three-dimensional electromagnetics, ed. by M. Oristaglio and B. Spies, Geophys. Devel. Ser., no. 7, Soc. Explor. Geophys., Tulsa, 349-374.

Wannamaker, P., Maris, V., Sainsbury, J., Iovenitti, J. L., 2013, Intersecting fault trends and crustal-scale fluid pathways below the Dixie Valley Geothermal Area, Nevada, inferred from 3D magnetotelluric surveying, Proceedings 38th Workshop on Geothermal Reservoir Engineering. Stanford University, Stanford, California, p. 1303-1311.

Wannamaker, P. E., Doerner, W. M., and Hasterok, D. P., 2007, Integrated Dense Array and Transect MT Surveying at Dixie Valley Geothermal Area, Nevada; Structural Controls, Hydrothermal Alteration and Deep Fluid Sources, Proceedings, 32nd Workshop on Geothermal Reservoir Engineering, Stanford University, California, Jan. 22-24, 6 p.

Wannamaker, P.E., Doerner, W. M., and Hasterok, D. P., 2006, Cryptic Faulting and Multi-Scale Geothermal Fluid Connections in the Dixie Valley-Central Nevada Seismic Belt Area: Implications from MT Resistivity Surveying, Proceedings, 31st Workshop on Geothermal Reservoir Engineering, Stanford University, California, Jan. 30-Feb. 1, 8pp.

Wannamaker, P. E., Hohmann, G. W., and Ward, S. H., 1983, Magnetotelluric responses of three-dimensional bodies in layered earths: Geophysics, 49, 1517-1533.

Wanner, C., Peiffer, L., Sonnenthal, E., Spycher, N., Iovenitti, J., Kennedy, B. M., 2012, On the use of chemical geothermometry: Reactive transport modeling of the Dixie Valley geothermal area, extended abs. submitted to Procedia Earth and Planetary Science, 5pp. available at www.sciencedirect.com.

Wanner, C., Peiffer, L., Sonnenthal, E., Spycher, N., Iovenitti, J., Kennedy, B. M., 2013, Assessing thermo-hydrodynamic-chemical processes at the the Dixie Valley Geothermal Area: A reactive transport modeling approach, Proceedings, 38th Workshop on Geothermal Reservoir Engineering, Stanford University, California, Jan. 30-Feb. 1, 9pp.

Weaver, R. L. and Lobkis, O. I., 2004, Diffuse fields in open systems and the emergence of the Green's function. J. Acoust. Soc. Am., 116, 2731-2734.

Wesnousky, S. G., Barron, A. D., Briggs, R. W., Caskey, S .J., Kumar, S., and Owen, L., 2005, Paleoseismic transect across the northern Great Basin, Journal of Geophysical Research, v. 110, 26 p.

Wesnousky, S., Caskey, S. J., and Bell, J. W, 2003, Recency of Faulting and Neotectonic Framework in the Dixie Valley Geothermal Field and Other Geothermal Fields of the Basin and Range, Final Technical Report, University of Nevada, Reno, 26 p.

Westphal, W. H. and Lange, A. L., 1967, Local seismic monitoring-Fairview Peak Area, Nevada, Bulletin Seismological Society of America, p. 1279-1298.

Willden, R. and Speed, R. C., 1974. Geology and mineral deposit of Churchill County, Nevada, Nevada Bureau of Mines and Geology Bulletin, v. 83, 95 p., 1:250,000.

Williams, C. F., Sass, J. H., and Grubb, F. V., 1997, Thermal signature of subsurface fluid flow near the Dixie Valley geothermal Filed Nevada, Proceedings 22thWorkshop on Geothermal Reservoir Engineering, Stanford Geothermal Program Report SGP-TR-155, 161–168.

Wright, P. M., 1991, Exploration for new hydrothermal resources for electrical power generation in the 48 contiguous U.S. states, GRC Transactions ,v.15,p. 217-228.

Wisian, K. W., and Blackwell, D. D., 2004, Numerical modeling of Basin and range geothermal systems. Geothermics, v. 33, p. 713-741.

Won, I .J., and Bevis, M., 1987, Computing the gravitational and magnetic anomalies due to a polygon: Algorithms and Fortran subroutines, Geophysics, v. 52, p. 232-238.

Wright, P. M., 1991, Exploration for new hydrothermal resources for electrical power generation in the 48 contiguous U.S. states, GRC Transactions ,v.15, p. 217-228.

Wu, R. S. and Flatté, S. M., 1990, Transmission fluctuations of seismic waves across seismic arrays, in "Seismic Wave Scattering and Attenuation" ed. by Wu and Aki, Applied Geophys., 132, p. 175-196.

Wu, R. S. and Aki, R., 1988, Seismic wave scattering in the three-dimensionally heterogeneous earth, in the special issue "Seismic Wave Scattering and Attenuation" ed. by Wu and Aki, P., Applied Geophys., 128, p. 1-6.

Yang, Y., 2007, Processing seismic ambient noise data to obtain reliable broad-band surface wave dispersion measurements, Geophys. J. Int. 169, 1239-1260.

Yang, Y., and Ritzwoller, M.H, 2008, 2008, Teleseismic surface wave tomography in the western U.S. using the Transportable Array component of USArray, Geophys. Res. Lett. 35, L04308, doi:10.1029/2007GL032278.

Yoshikawa, M., and Sudo, Y., 2004, Three Dimensional Seismic Velocity Structure beneath the Otake-Hatchobaru Geothermal Area at Kuju Volcano in Central Kyushu, Japan, Annuals of Disaster Prevention Research Institute, Kyoto Univ., No. 47 B.

Zoback, M.L., McKee, E. H., Blakely, R. J., and Thompson, G. A., 1994, The northern Nevada rift: Regional tectono-magmatic relations and middle Miocene stress direction, Geological Society of America Bulletin, March, v. 106, p. 371-382.

Zucca, J., and Evans, J. R., 1989, Seismic imaging for velocity and attenuation structure in geothermal fields, U.S. Geological Survey, Report UCRL--LOO 84 1, DE90 010742.

PART II-APPENDIX 1

COMPLETE BOUGER GRAVITY ANOMALY JOINTLY INVERTED GRAVITY-MAGNETIC MODELS

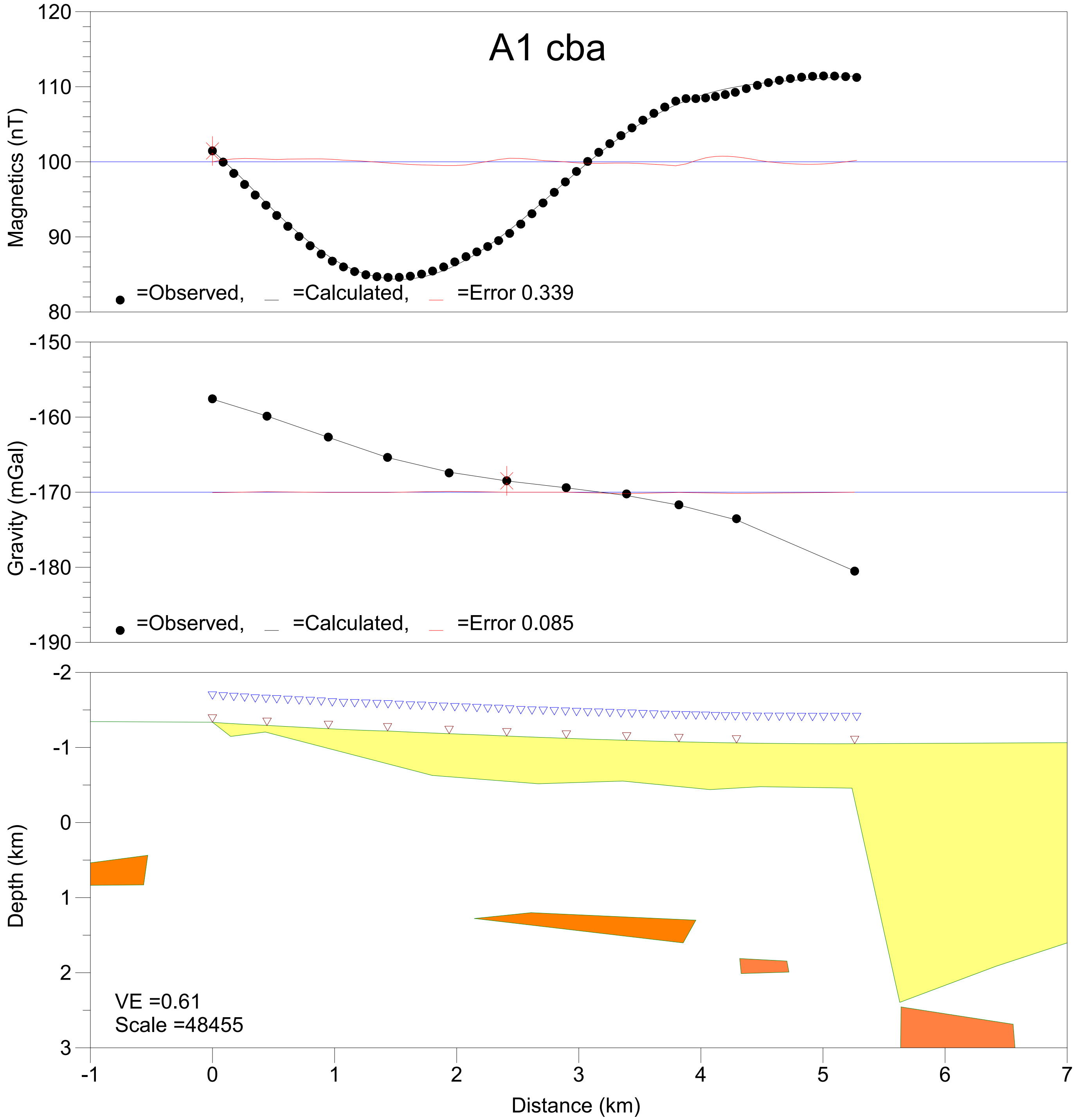

A1 cba
Magnetics (nT)
120
110
100
90
80
=Observed, =Calculated, =Error 0.339
Gravity (mGal)
-150
-160
-170
-180
-190
=Observed, =Calculated, =Error 0.085
Depth (km)
-2
-1
0
1
2
3
VE =0.61
Scale =48455
-1 0 1 2 3 4 5 6 7
Distance (km)

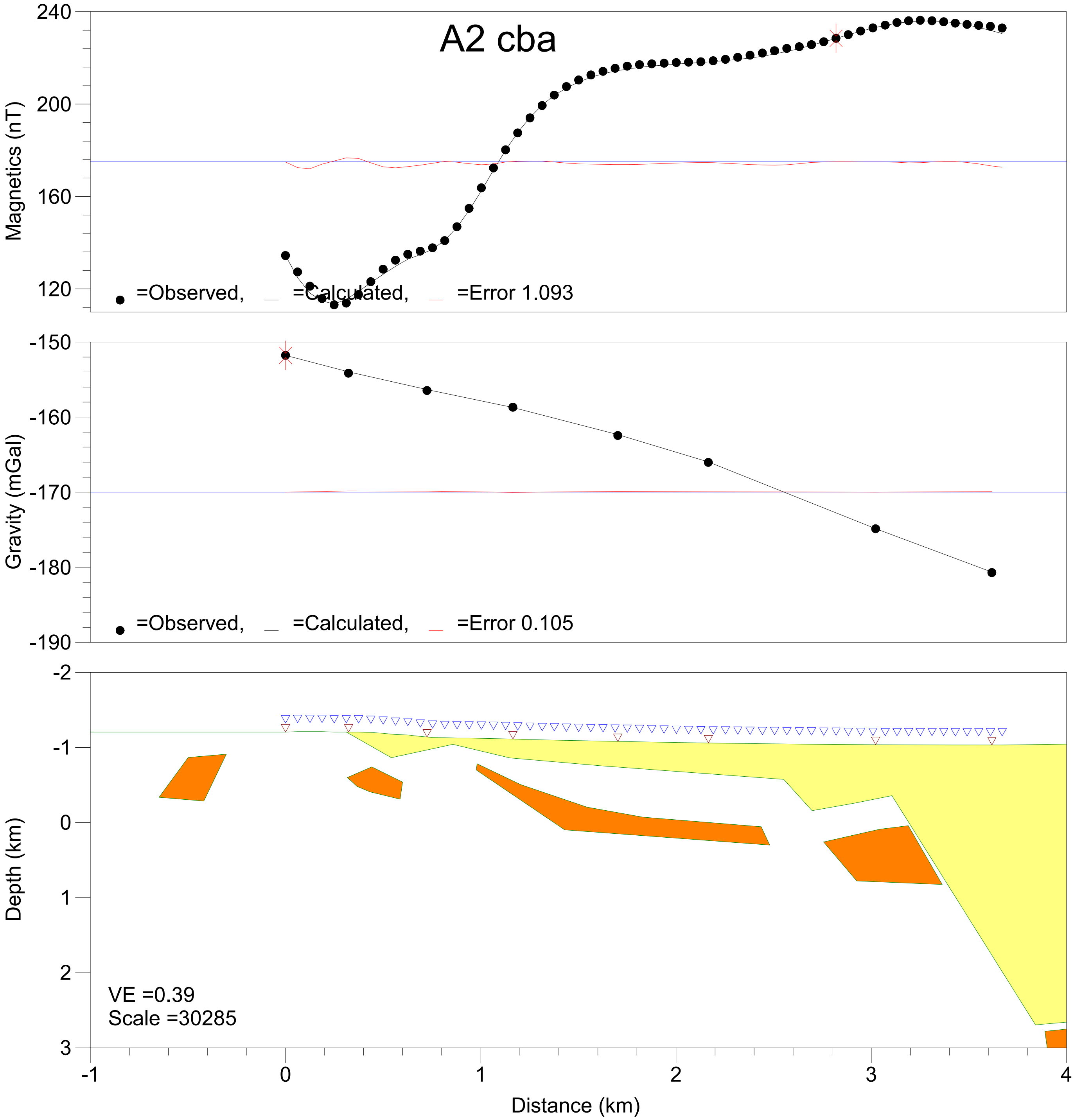

A2 cba
Magnetics (nT)
240
200
160
120
=Observed,
=Calculated,
=Error 1.093
Gravity (mGal)
-150
-160
-170
-180
-190
=Observed,
=Calculated,
=Error 0.105
Depth (km)
-2
-1
0
1
2
3
VE =0.39
Scale =30285
-1
0
1
2
3
4
Distance (km)

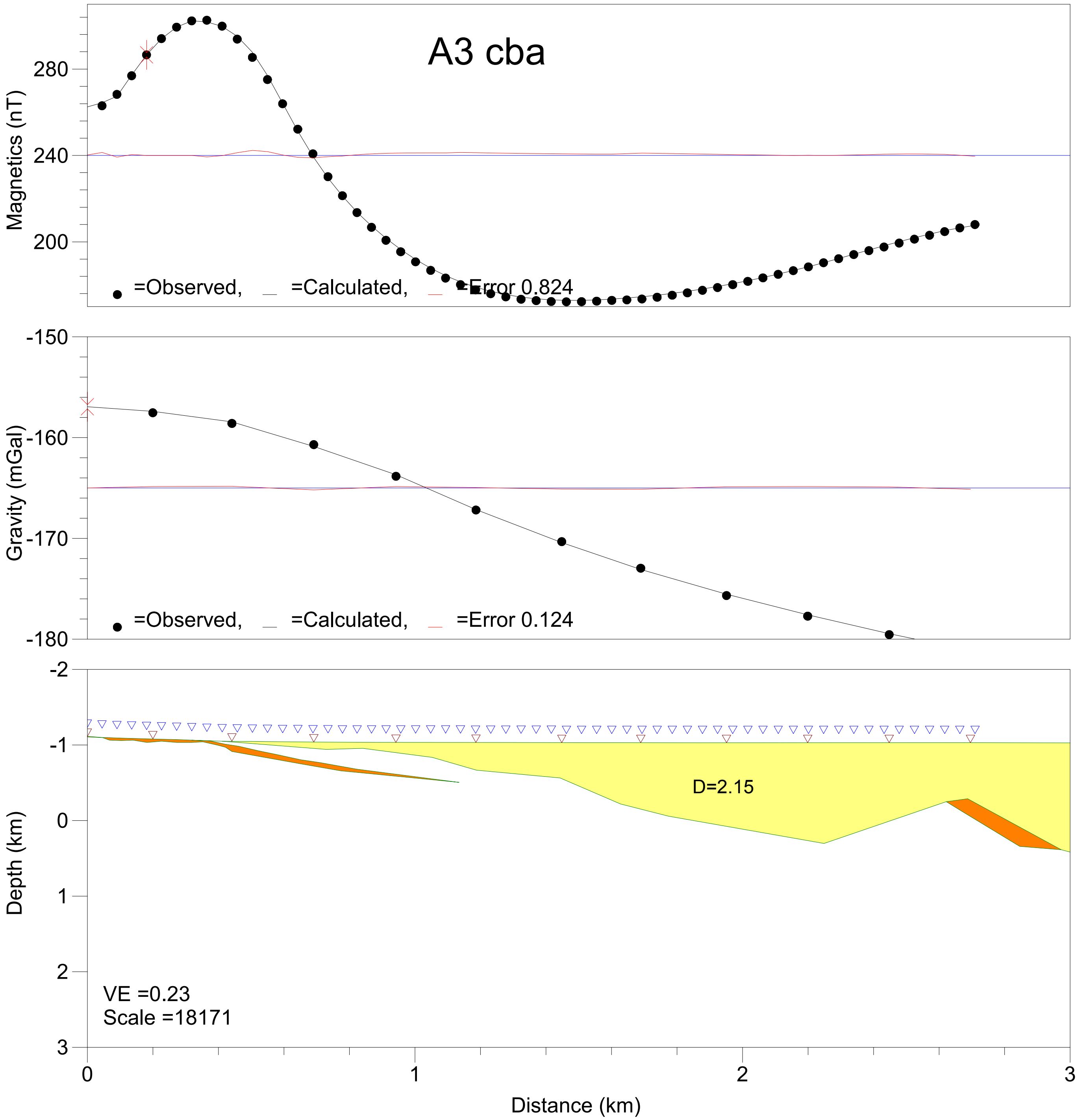
A3 cba
Magnetics (nT)
280
240
200
=Observed,
=Calculated,
=Error 0.824
-150
-160
-170
-180
Gravity (mGal)
=Observed,
=Calculated,
=Error 0.124
-2
-1
0
1
2
3
Depth (km)
D=2.15
VE =0.23
Scale =18171
0
1
2
3
Distance (km)

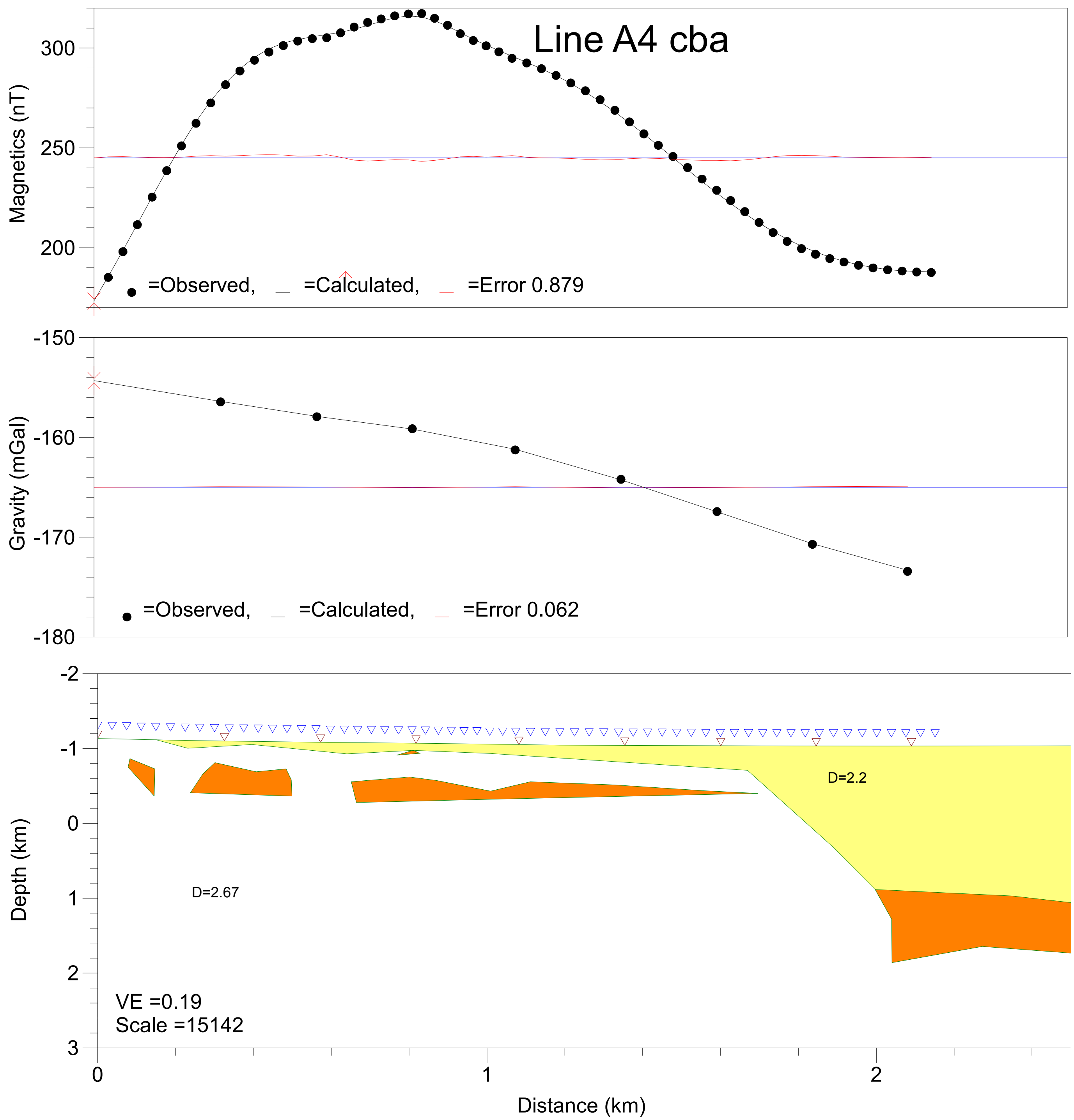

Line A4 cba
Magnetics (nT)
300
250
200
=Observed, =Calculated, =Error 0.879
Gravity (mGal)
-150
-160
-170
-180
=Observed, =Calculated, =Error 0.062
Depth (km)
-2
-1
0
1
2
3
D=2.2
D=2.67
VE =0.19
Scale =15142
0
1
2
Distance (km)

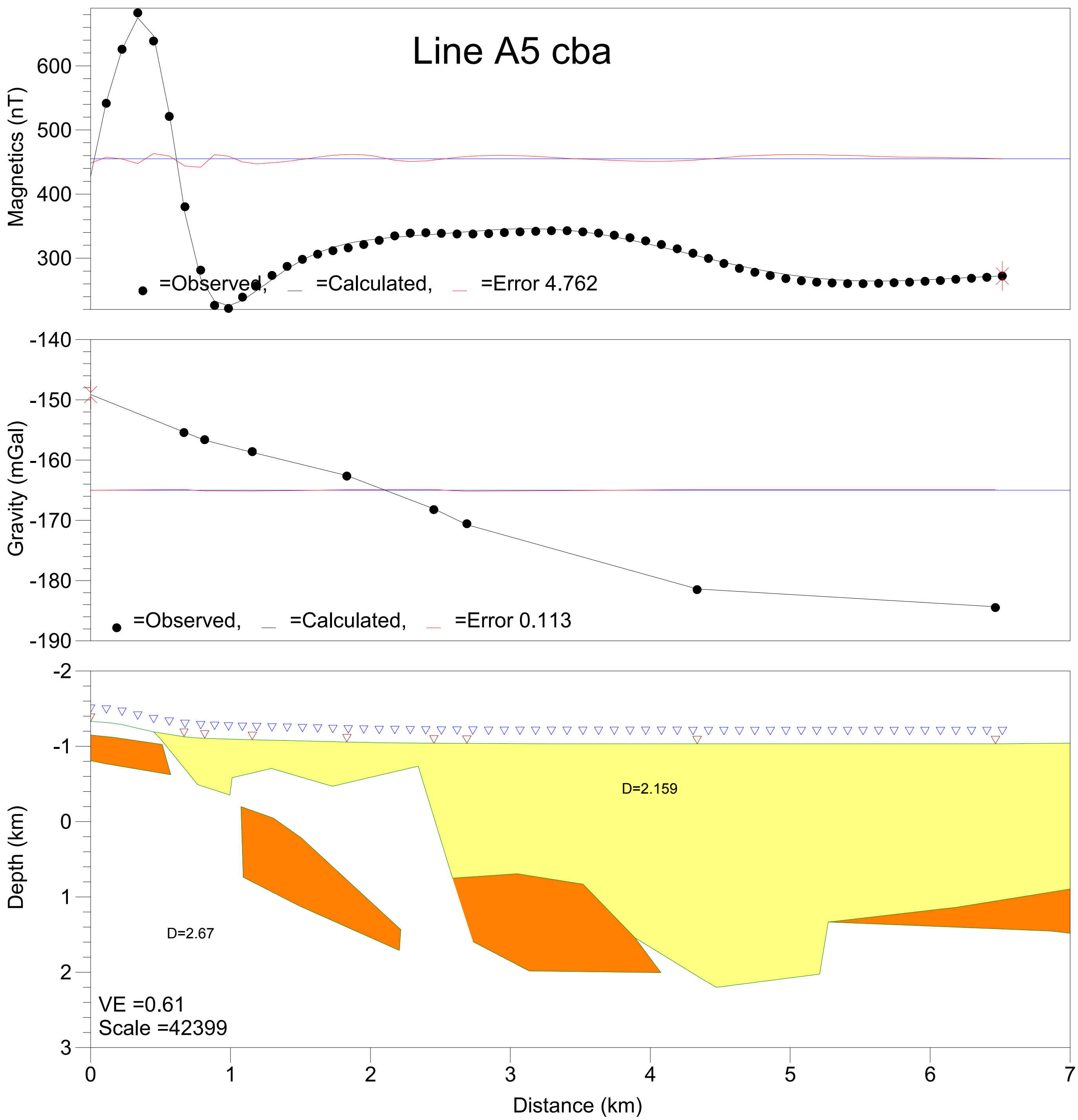

Line A5 cba
Magnetics (nT)
600
500
400
300
=Observed, =Calculated, =Error 4.762
Gravity (mGal)
-140
-150
-160
-170
-180
-190
=Observed, =Calculated, =Error 0.113
Depth (km)
-2
-1
0
1
2
3
D=2.159
D=2.67
VE =0.61
Scale =42399
0
1
2
3
4
5
6
7
Distance (km)

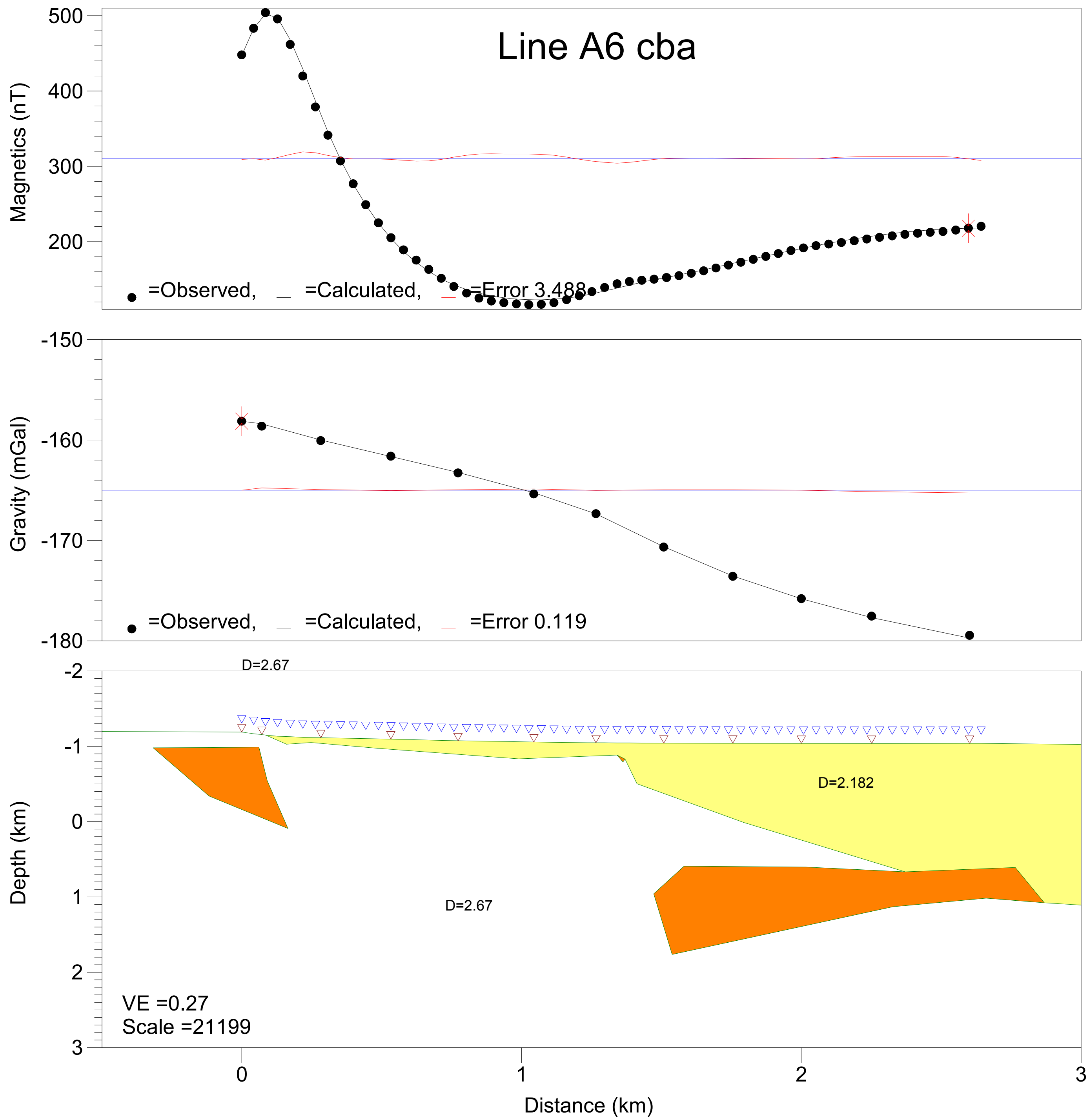

Line A6 cba
Magnetics (nT)
500
400
300
200
=Observed, =Calculated, =Error 3.488
Gravity (mGal)
-150
-160
-170
-180
=Observed, =Calculated, =Error 0.119
D=2.67
D=2.182
D=2.67
Depth (km)
-2
-1
0
1
2
3
VE =0.27
Scale =21199
0
1
2
3
Distance (km)

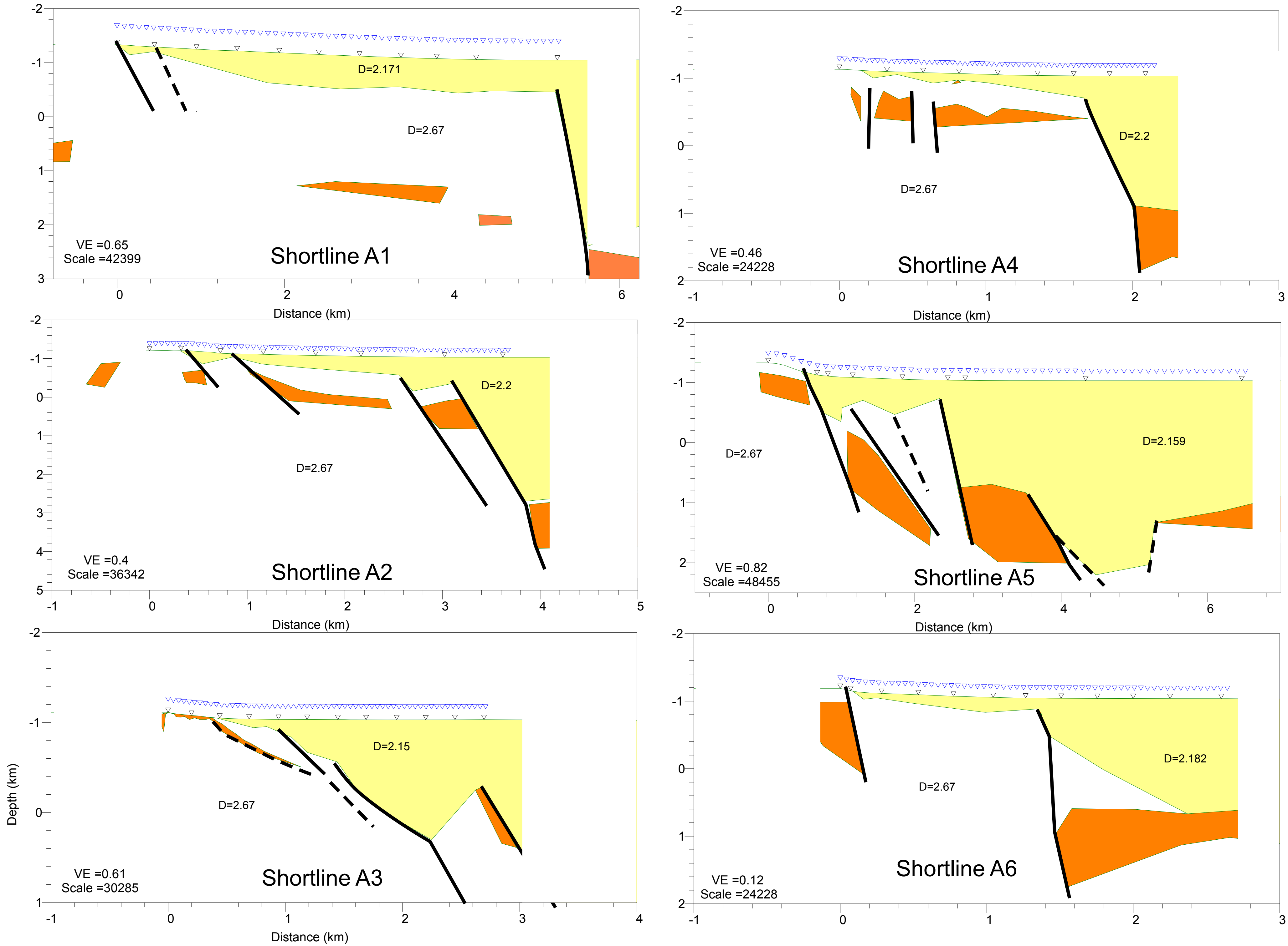

D=2.171
D=2.67
VE =0.65
Scale =42399
Shortline A1
Distance (km)
D=2.2
D=2.67
VE =0.46
Scale =24228
Shortline A4
Distance (km)
D=2.2
D=2.67
VE =0.4
Scale =36342
Shortline A2
Distance (km)
D=2.67
D=2.159
VE =0.82
Scale =48455
Shortline A5
Distance (km)
Depth (km)
D=2.15
D=2.67
VE =0.61
Scale =30285
Shortline A3
Distance (km)
D=2.67
D=2.182
VE =0.12
Scale =24228
Shortline A6

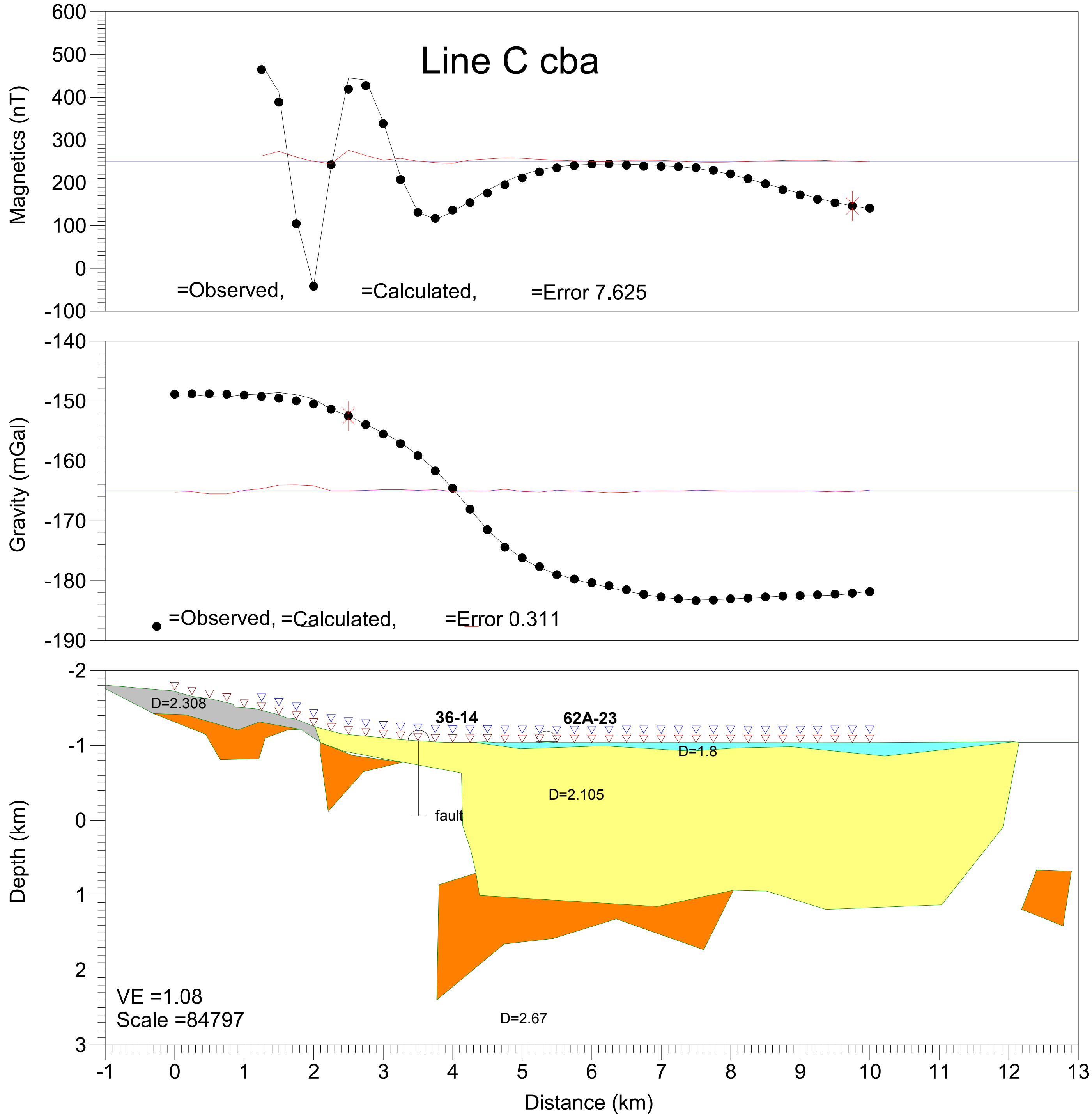

Line C cba
Magnetics (nT)
=Observed,
=Calculated,
=Error 7.625
Gravity (mGal)
=Observed, =Calculated,
=Error 0.311
Depth (km)
D=2.308
36-14
62A-23
D=1.8
D=2.105
fault
D=2.67
VE =1.08
Scale =84797
Distance (km)

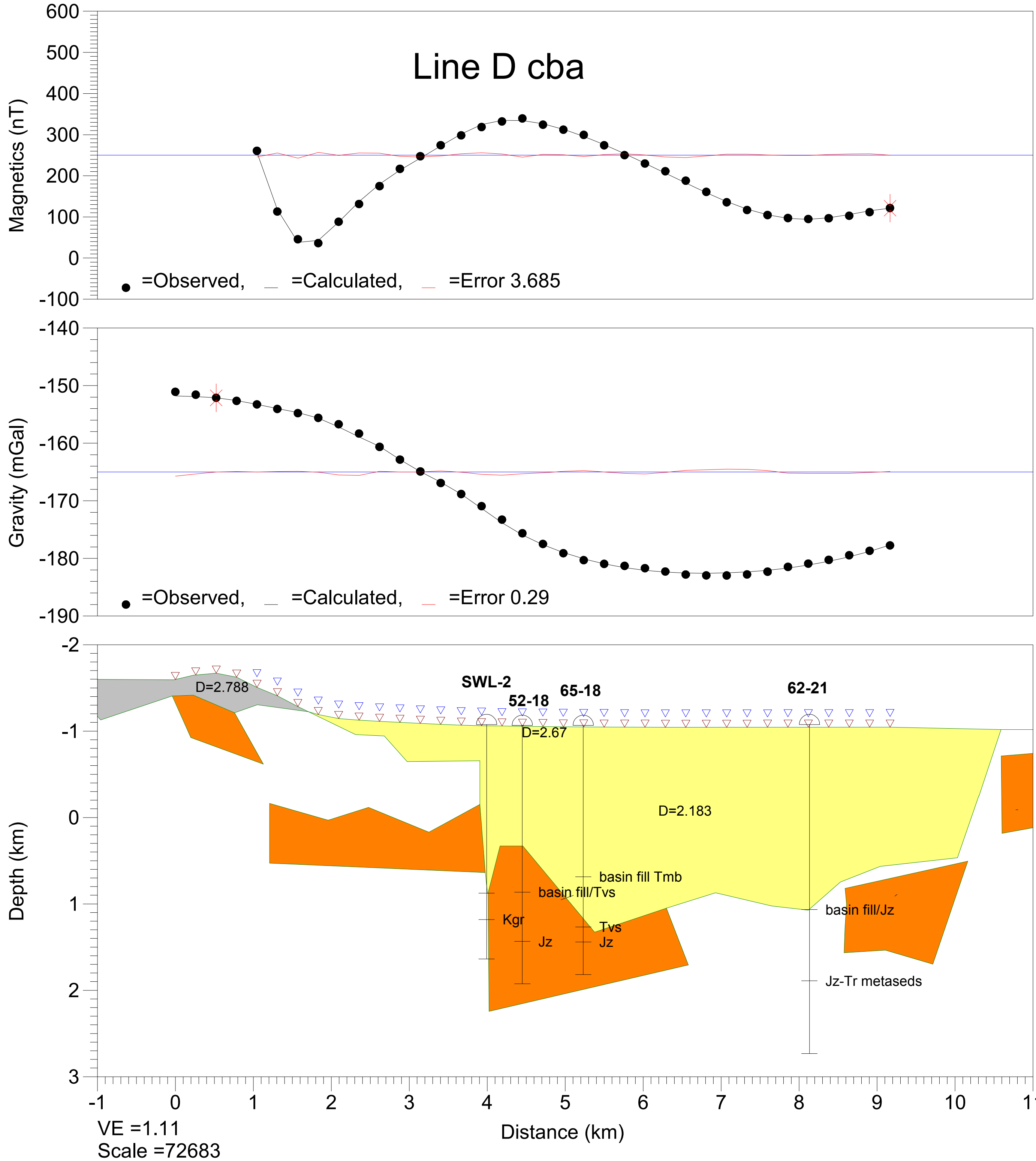

Line D cba
Magnetics (nT)
600
500
400
300
200
100
0
-100
=Observed,
=Calculated,
=Error 3.685
Gravity (mGal)
-140
-150
-160
-170
-180
-190
=Observed,
=Calculated,
=Error 0.29
Depth (km)
-2
-1
0
1
2
3
D=2.788
SWL-2
52-18
65-18
62-21
D=2.67
D=2.183
basin fill Tmb
basin fill/Tvs
Kgr
Jz
Tvs
Jz
basin fill/Jz
Jz-Tr metaseds
-1
0
1
2
3
4
5
6
7
8
9
10
11
Distance (km)
VE =1.11
Scale =72683

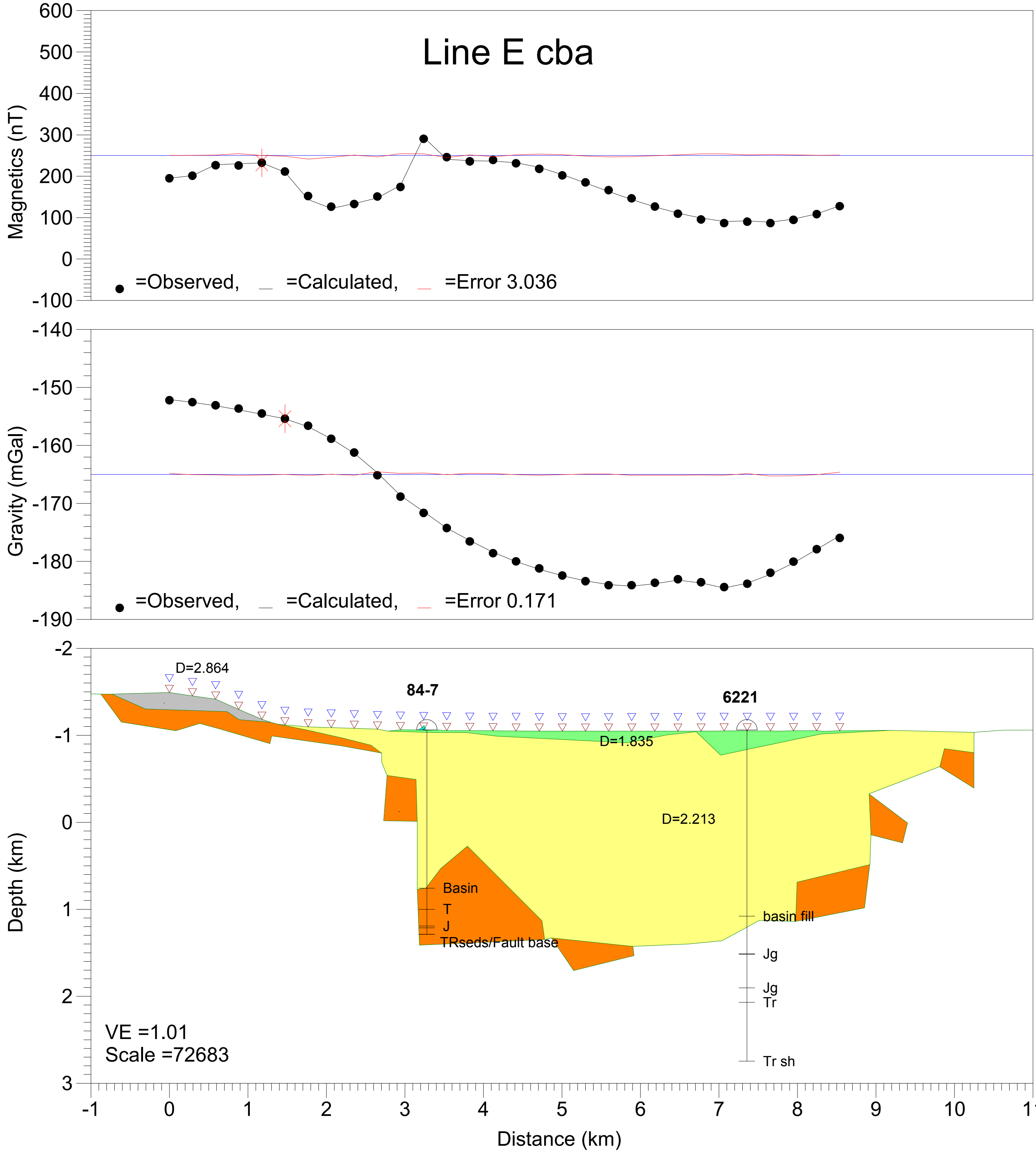
Line E cba
Magnetics (nT)
600
500
400
300
200
100
0
-100
=Observed, =Calculated, =Error 3.036
Gravity (mGal)
-140
-150
-160
-170
-180
-190
=Observed, =Calculated, =Error 0.171
Depth (km)
D=2.864
84-7
6221
D=1.835
D=2.213
Basin
T
J
TRseds/Fault base
basin fill
Jg
Jg
Tr
Tr sh
VE =1.01
Scale =72683
Distance (km)
-1
0
1
2
3
4
5
6
7
8
9
10
11

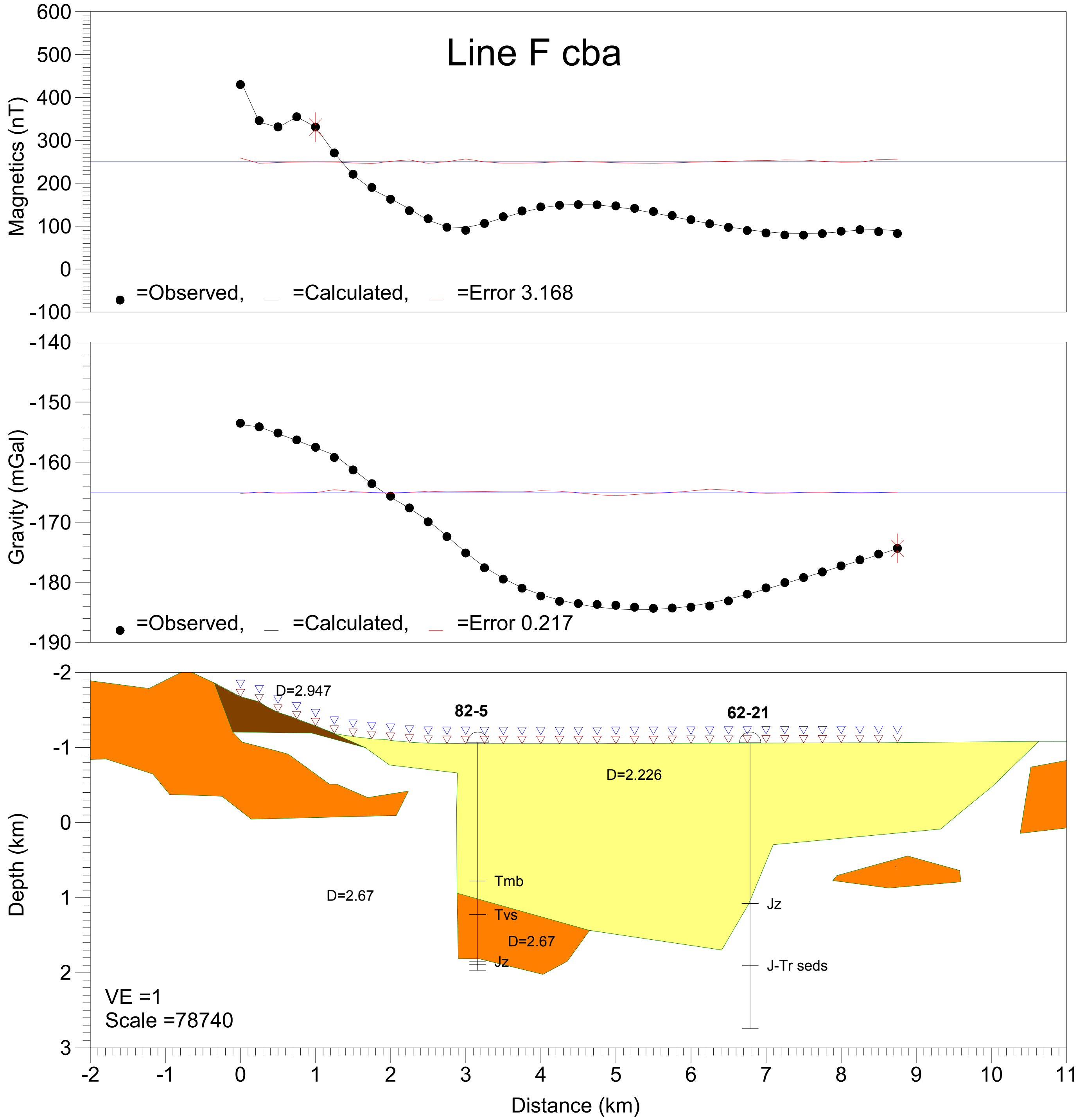

Line F cba
Magnetics (nT)
=Observed, =Calculated, =Error 3.168
Gravity (mGal)
=Observed, =Calculated, =Error 0.217
Depth (km)
D=2.947
82-5
62-21
D=2.226
D=2.67
Tmb
Tvs
D=2.67
Jz
Jz
J-Tr seds
VE =1
Scale =78740
Distance (km)

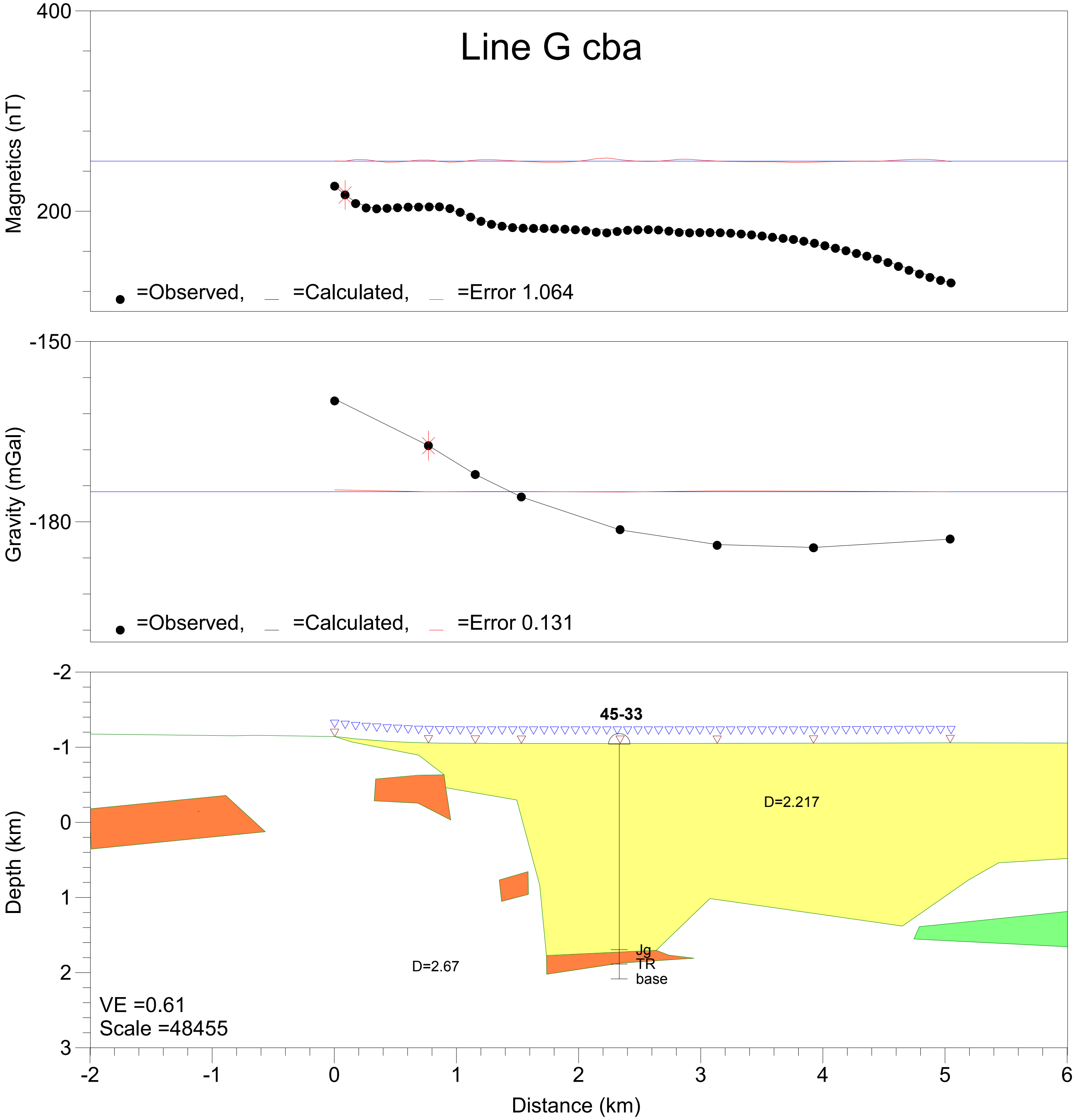

Line G cba
Magnetics (nT)
400
200
=Observed, =Calculated, =Error 1.064
Gravity (mGal)
-150
-180
=Observed, =Calculated, =Error 0.131
Depth (km)
-2
-1
0
1
2
3
45-33
D=2.217
D=2.67
Jg
TR
base
VE =0.61
Scale =48455
-2 -1 0 1 2 3 4 5 6
Distance (km)

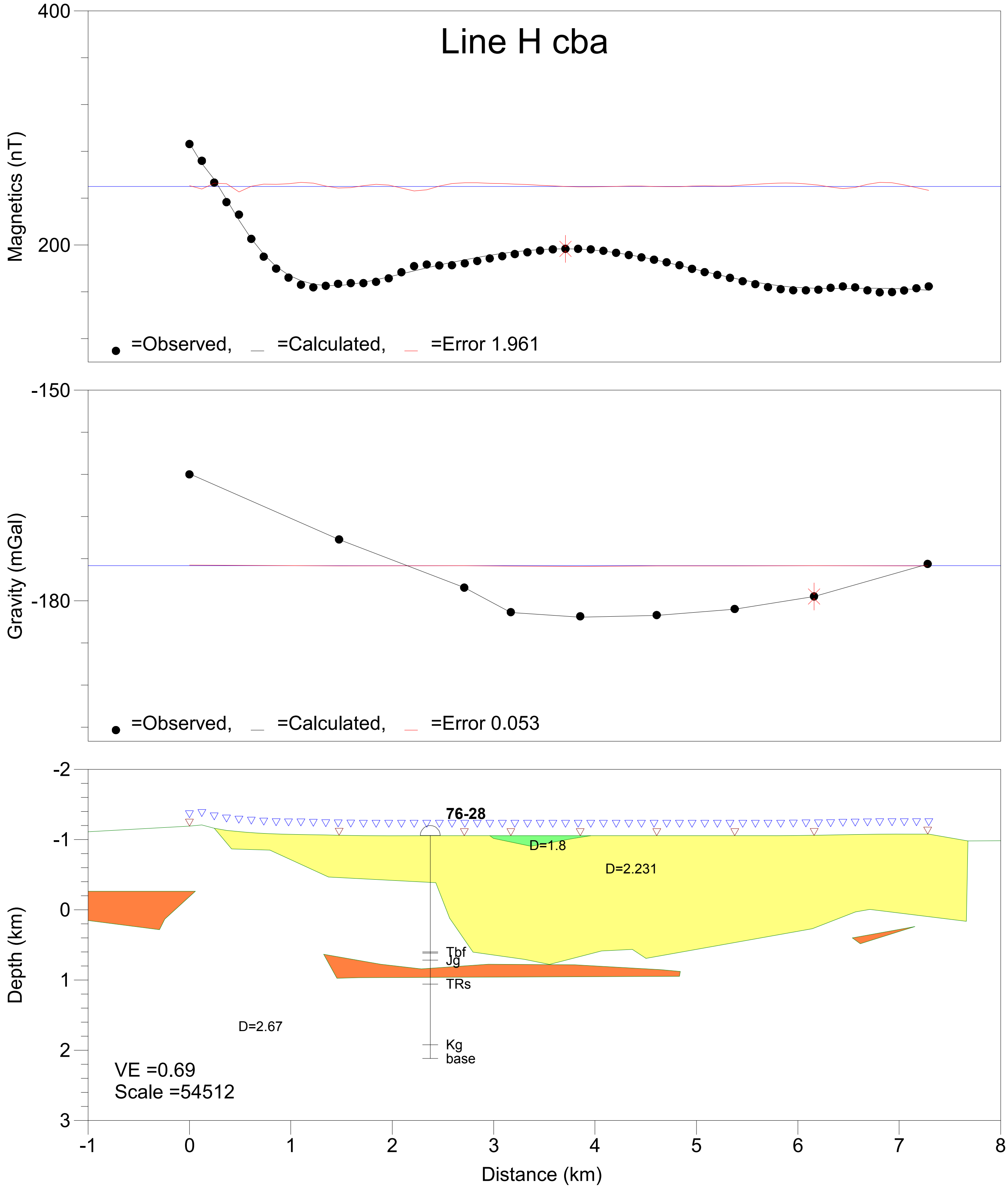

Line H cba
Magnetics (nT)
400
200
=Observed,
=Calculated,
=Error 1.961
Gravity (mGal)
-150
-180
=Observed,
=Calculated,
=Error 0.053
Depth (km)
-2
-1
0
1
2
3
76-28
D=1.8
D=2.231
Tbf
Jg
TRs
D=2.67
Kg
base
VE =0.69
Scale =54512
-1
0
1
2
3
4
5
6
7
8
Distance (km)

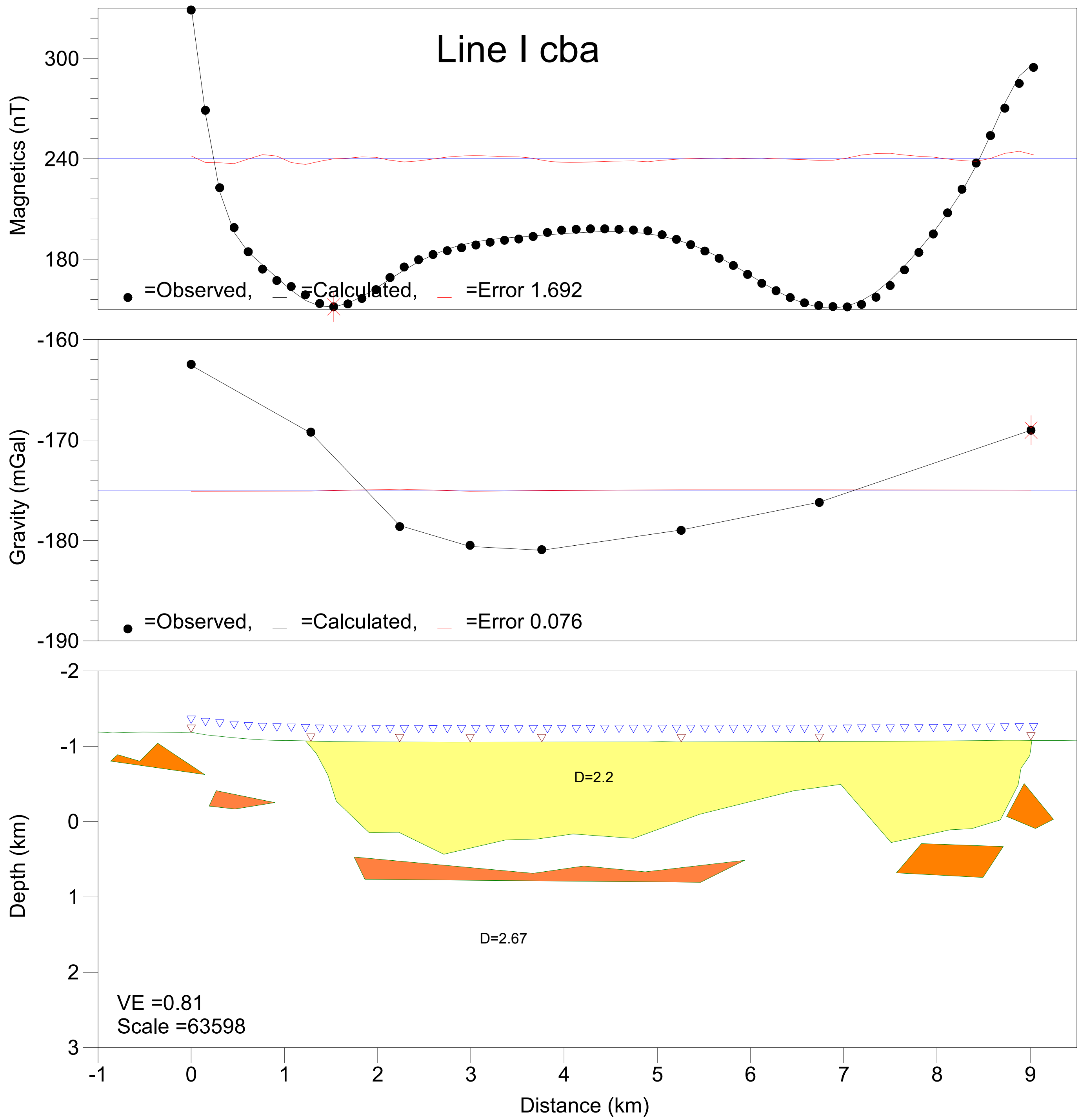

Line I cba
Magnetics (nT)
300
240
180
=Observed, =Calculated, =Error 1.692
Gravity (mGal)
-160
-170
-180
-190
=Observed, =Calculated, =Error 0.076
Depth (km)
-2
-1
0
1
2
3
D=2.2
D=2.67
VE =0.81
Scale =63598
-1
0
1
2
3
4
5
6
7
8
9
Distance (km)

Line J cba

Wed Oct 31 11:36:57 2012

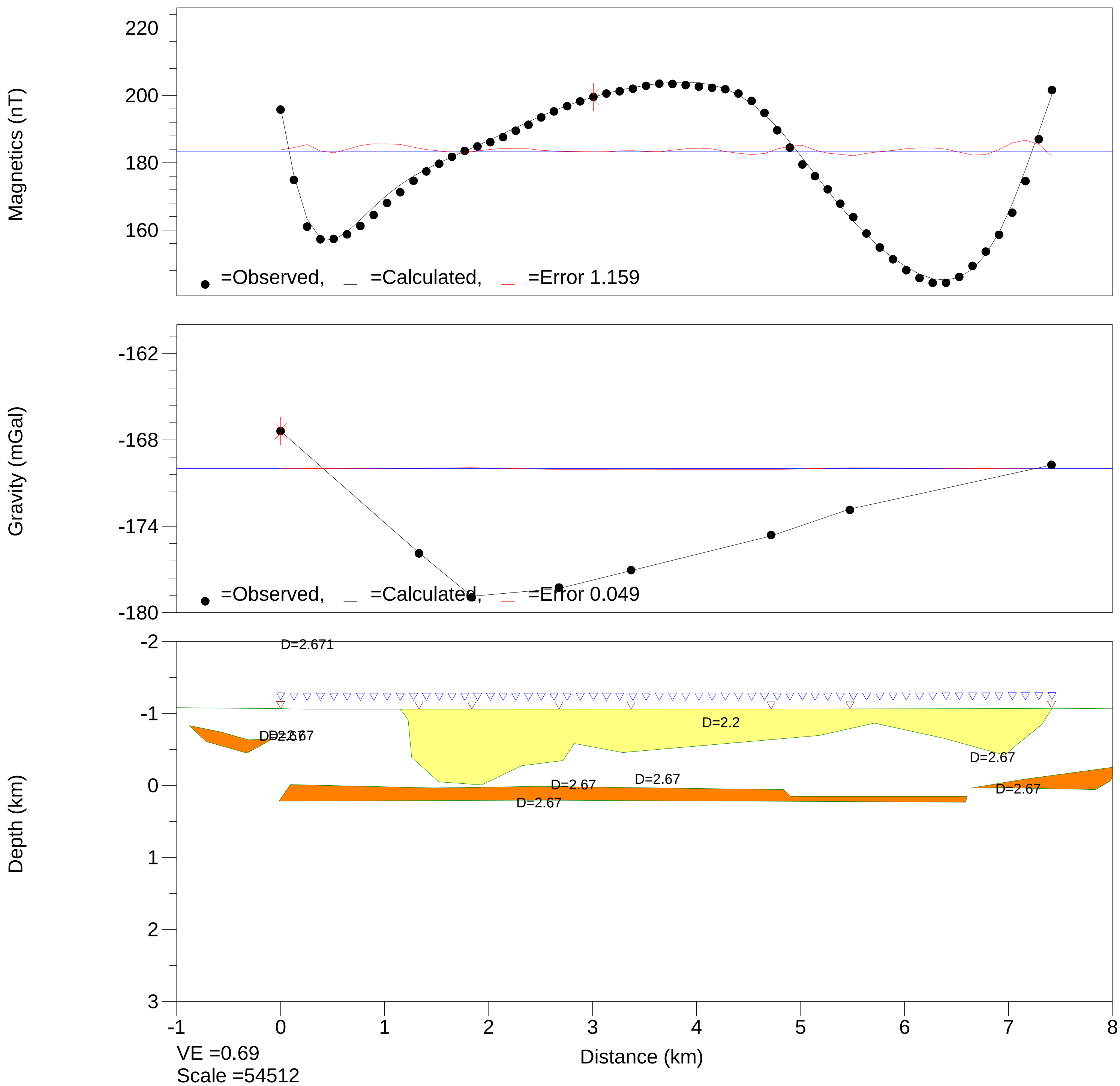

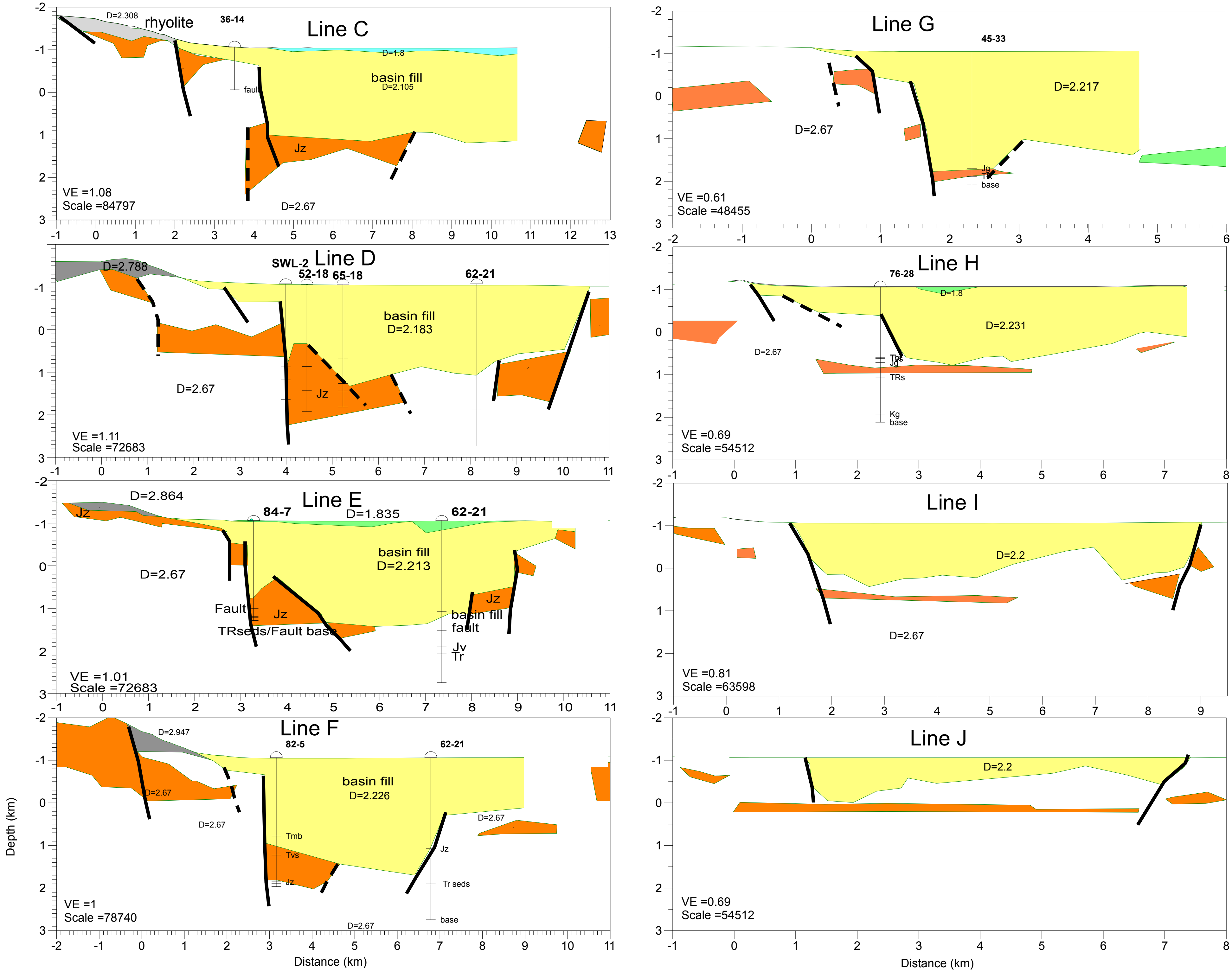

Line C
rhyolite
D=2.308
36-14
D=1.8
basin fill
D=2.105
fault
Jz
D=2.67
VE =1.08
Scale =84797
Line D
SWL-2
52-18
65-18
62-21
D=2.788
basin fill
D=2.183
D=2.67
Jz
VE =1.11
Scale =72683
Line E
D=2.864
84-7
D=1.835
62-21
Jz
basin fill
D=2.213
D=2.67
Fault
TRseds/Fault base
basin fill
fault
Jv
Tr
VE =1.01
Scale =72683
Line F
D=2.947
82-5
62-21
basin fill
D=2.226
D=2.67
Tmb
Tvs
Jz
Tr seds
base
VE =1
Scale =78740
Line G
45-33
D=2.217
D=2.67
Jg
Tr
base
VE =0.61
Scale =48455
Line H
76-28
D=1.8
D=2.231
D=2.67
Jg
TRs
Kg
base
VE =0.69
Scale =54512
Line I
D=2.2
D=2.67
VE =0.81
Scale =63598
Line J
D=2.2
VE =0.69
Scale =54512
Depth (km)
Distance (km)

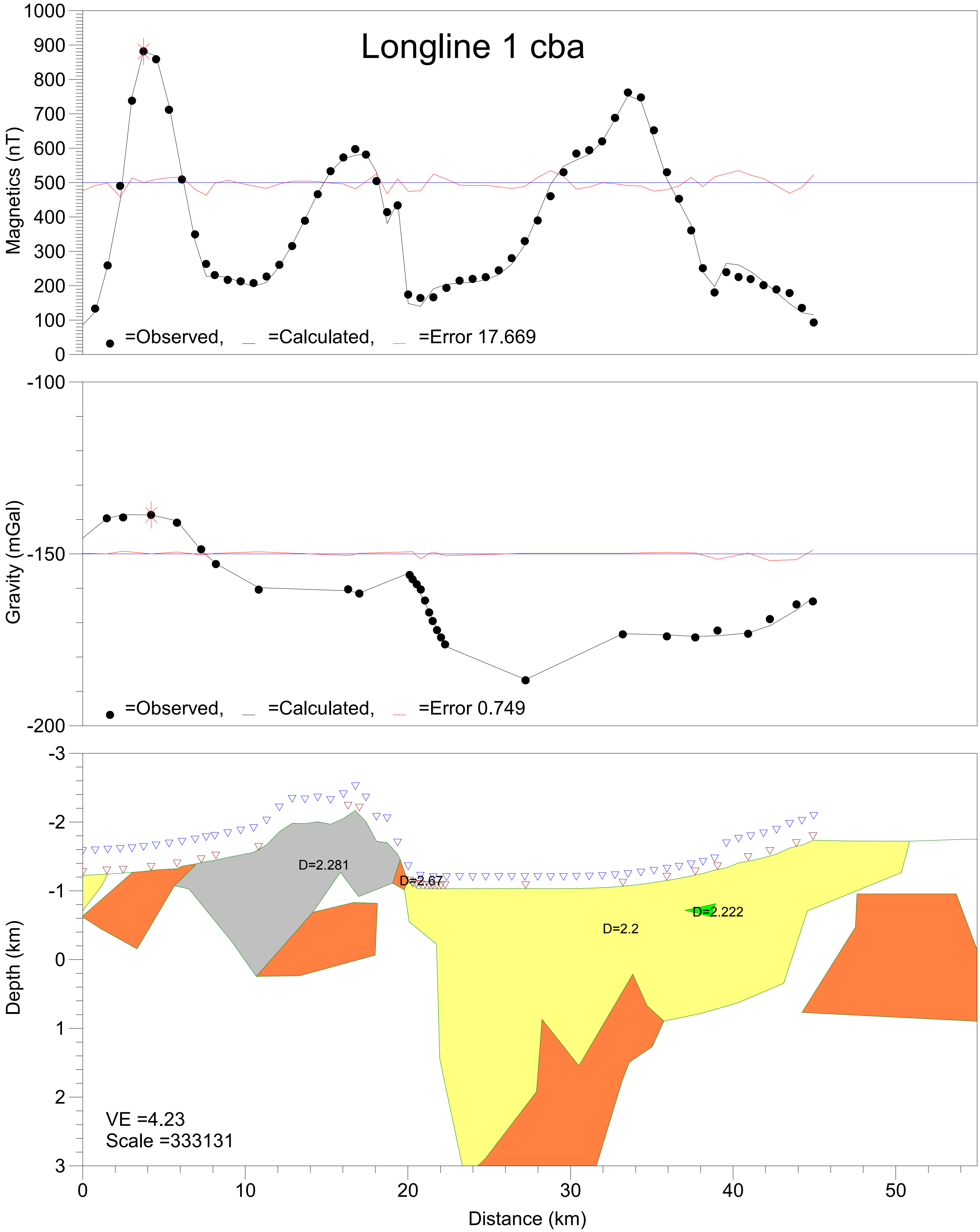

Longline 1 cba
Magnetics (nT)
1000
900
800
700
600
500
400
300
200
100
0
=Observed, =Calculated, =Error 17.669
Gravity (mGal)
-100
-150
-200
=Observed, =Calculated, =Error 0.749
Depth (km)
-3
-2
-1
0
1
2
3
D=2.281
D=2.67
D=2.222
D=2.2
VE =4.23
Scale =333131
0
10
20
30
40
50
Distance (km)

Longline 2 v3

Mon Nov 14 17:22:27 2011

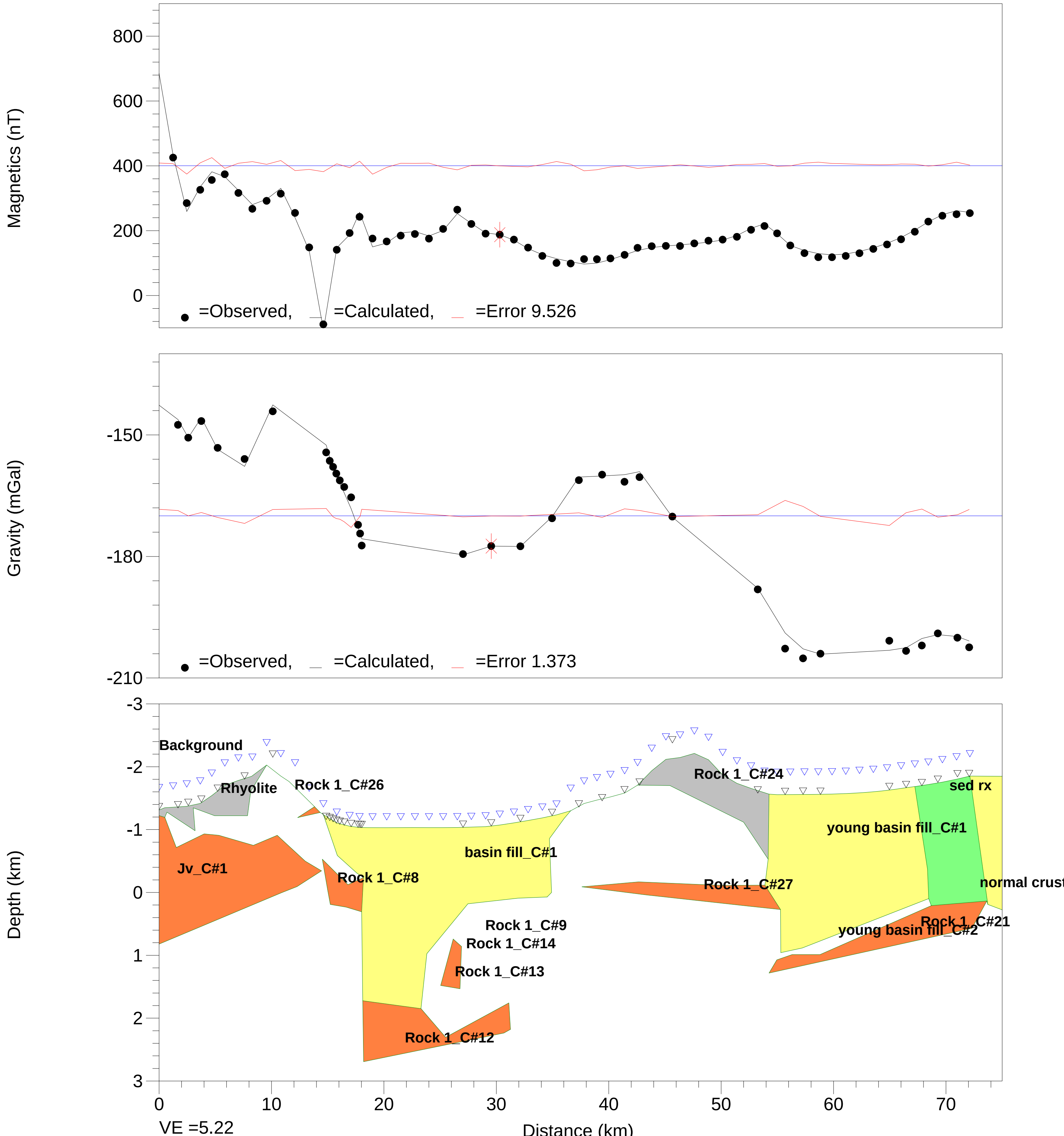

VE =5.22
Scale =454270

Longline 3 v4

Fri Oct 26 16:15:52 2012

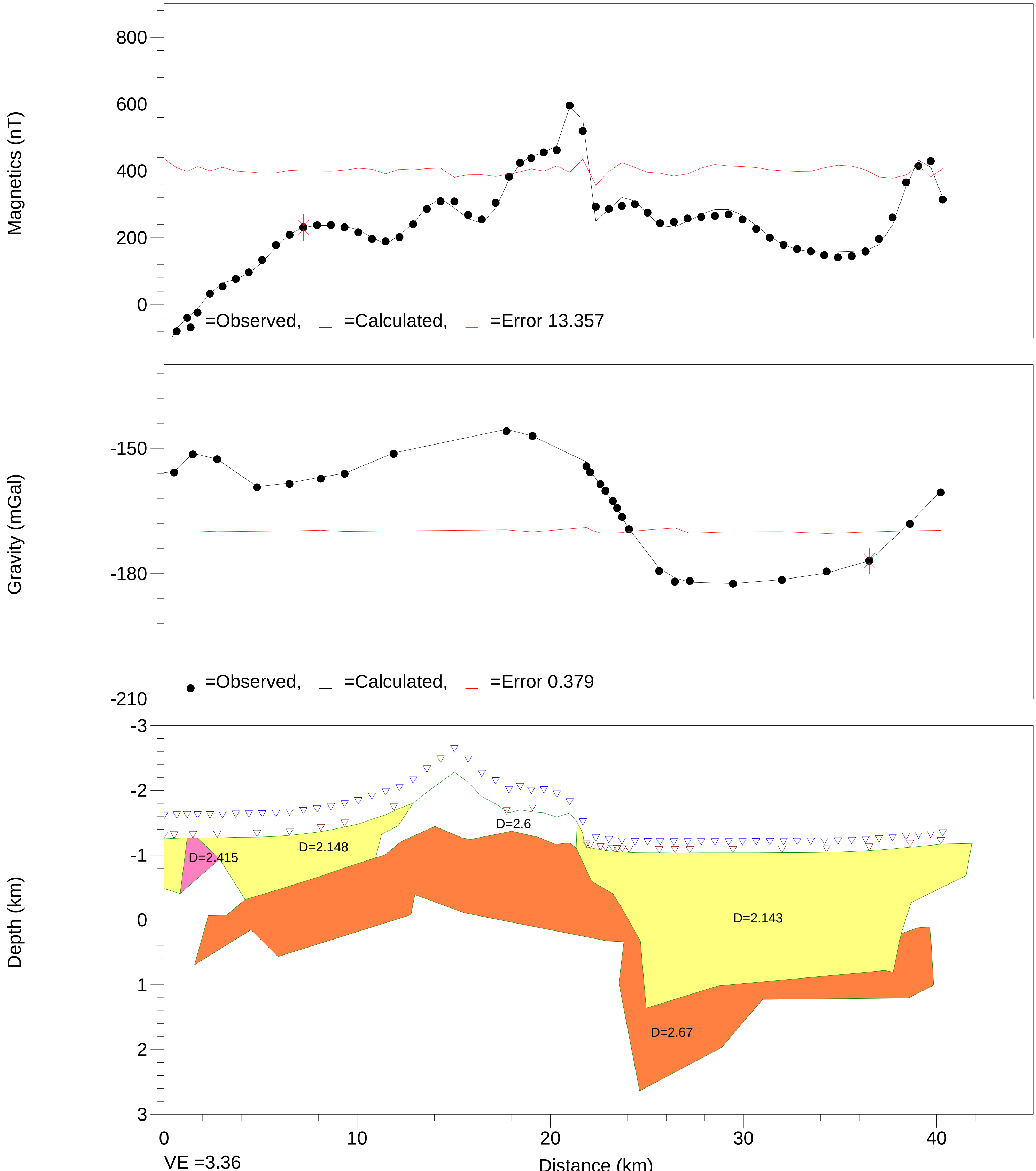

VE =3.36
Scale =272562

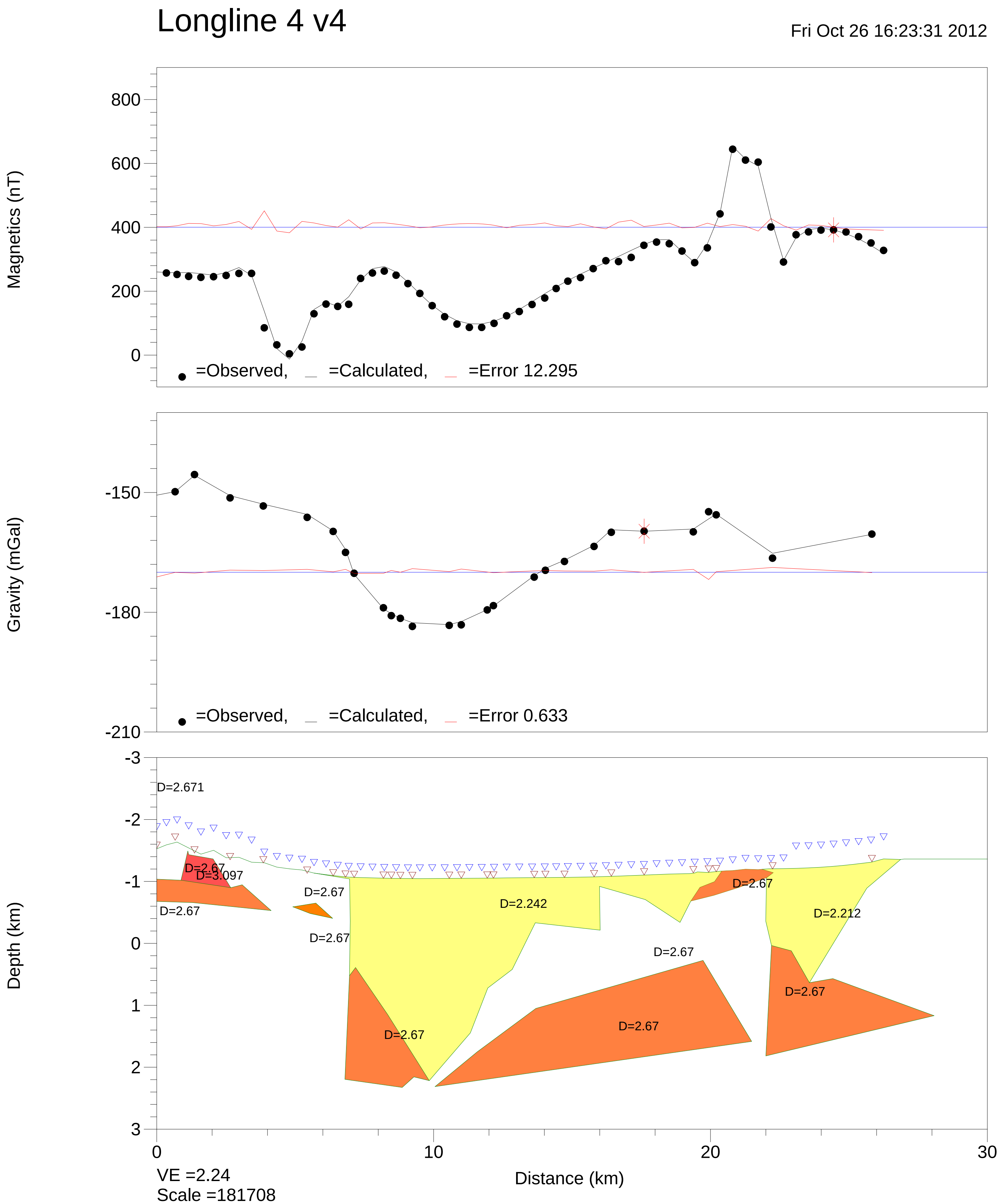
Longline 4 v4
Fri Oct 26 16:23:31 2012
Magnetics (nT)
800
600
400
200
0
=Observed, =Calculated, =Error 12.295
Gravity (mGal)
-150
-180
-210
=Observed, =Calculated, =Error 0.633
Depth (km)
-3
-2
-1
0
1
2
3
D=2.671
D=2.67
D=3.097
D=2.67
D=2.67
D=2.67
D=2.242
D=2.67
D=2.212
D=2.67
D=2.67
D=2.67
D=2.67
0
10
20
30
Distance (km)
VE =2.24
Scale =181708

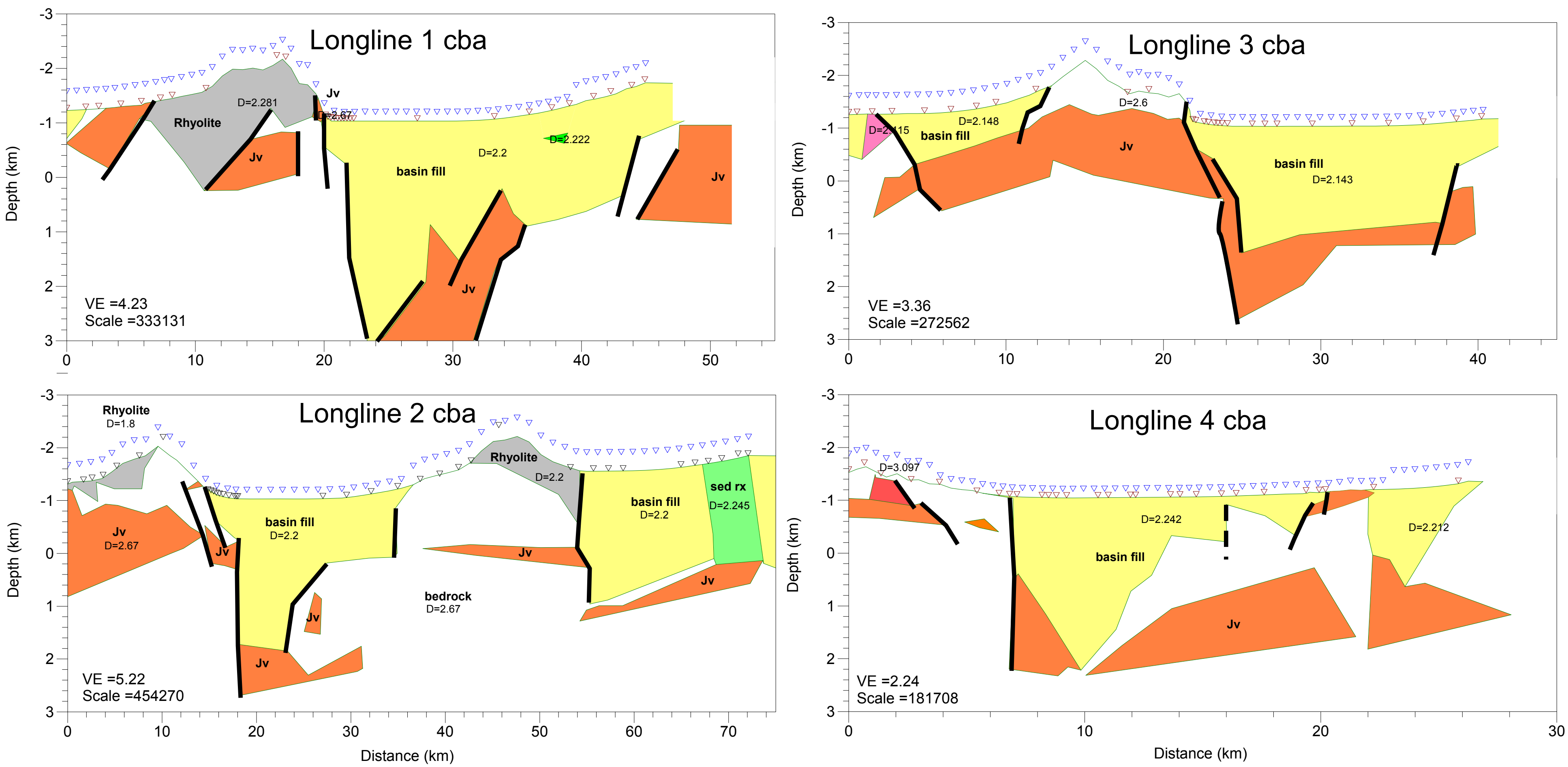

Longline 1 cba
Rhyolite
D=2.281
Jv
D=2.67
D=2.2
D=2.222
basin fill
Jv
Jv
Jv
VE =4.23
Scale =333131
Depth (km)
Longline 3 cba
D=2.115
D=2.148
basin fill
D=2.6
Jv
basin fill
D=2.143
VE =3.36
Scale =272562
Longline 2 cba
Rhyolite
D=1.8
Jv
D=2.67
Jv
basin fill
D=2.2
Jv
Jv
Jv
bedrock
D=2.67
Rhyolite
D=2.2
basin fill
D=2.2
sed rx
D=2.245
Jv
VE =5.22
Scale =454270
Distance (km)
Longline 4 cba
D=3.097
D=2.242
basin fill
D=2.212
Jv
VE =2.24
Scale =181708
Distance (km)

PART II-APPENDIX 2

RESIDUAL GRAVITY ANOMALY JOINTLY INVERTED GRAVITYMAGNETIC MODELS

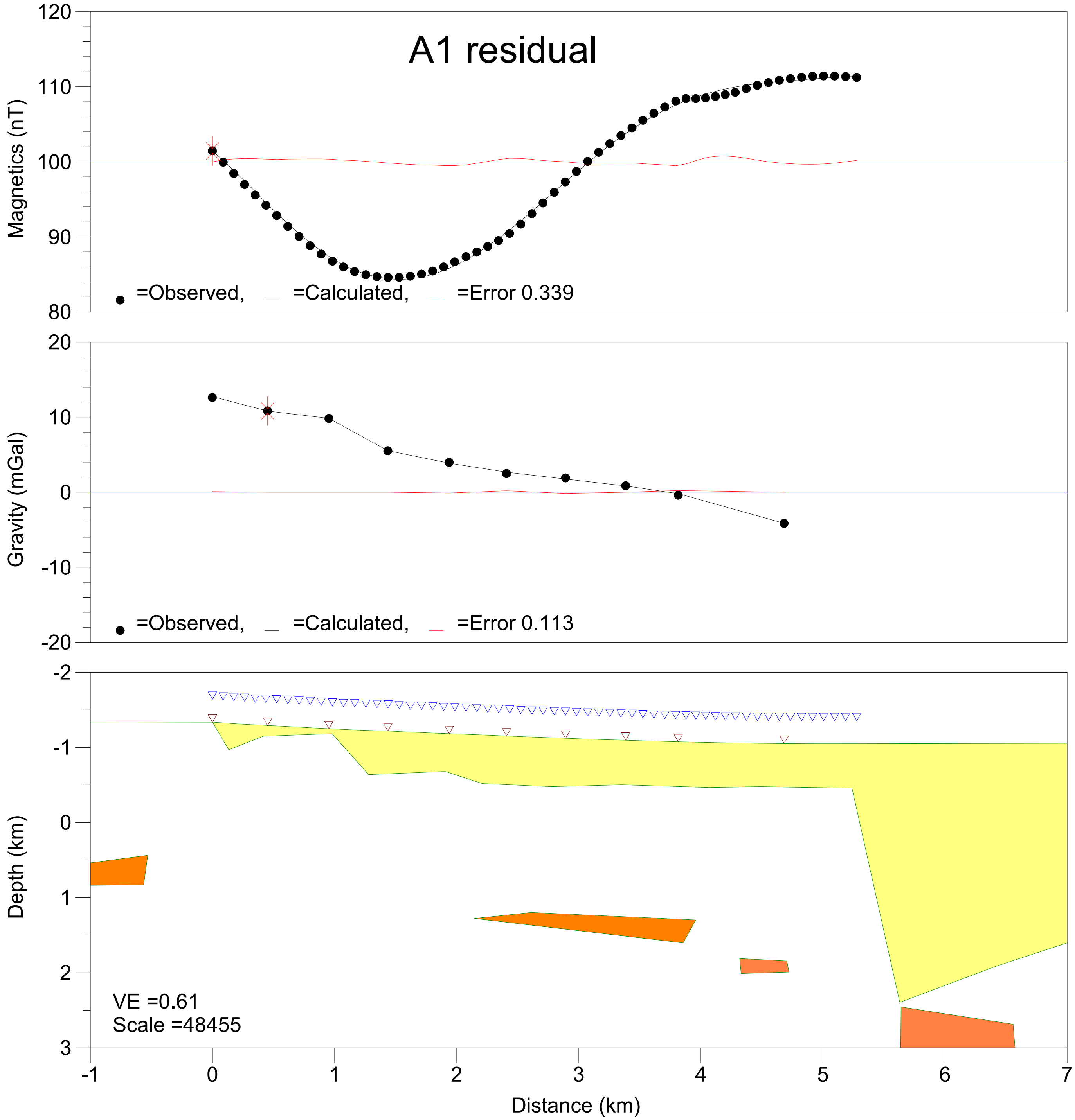
A1 residual
Magnetics (nT)
120
110
100
90
80
=Observed,
=Calculated,
=Error 0.339
Gravity (mGal)
20
10
0
-10
-20
=Observed,
=Calculated,
=Error 0.113
Depth (km)
-2
-1
0
1
2
3
VE =0.61
Scale =48455
-1
0
1
2
3
4
5
6
7
Distance (km)

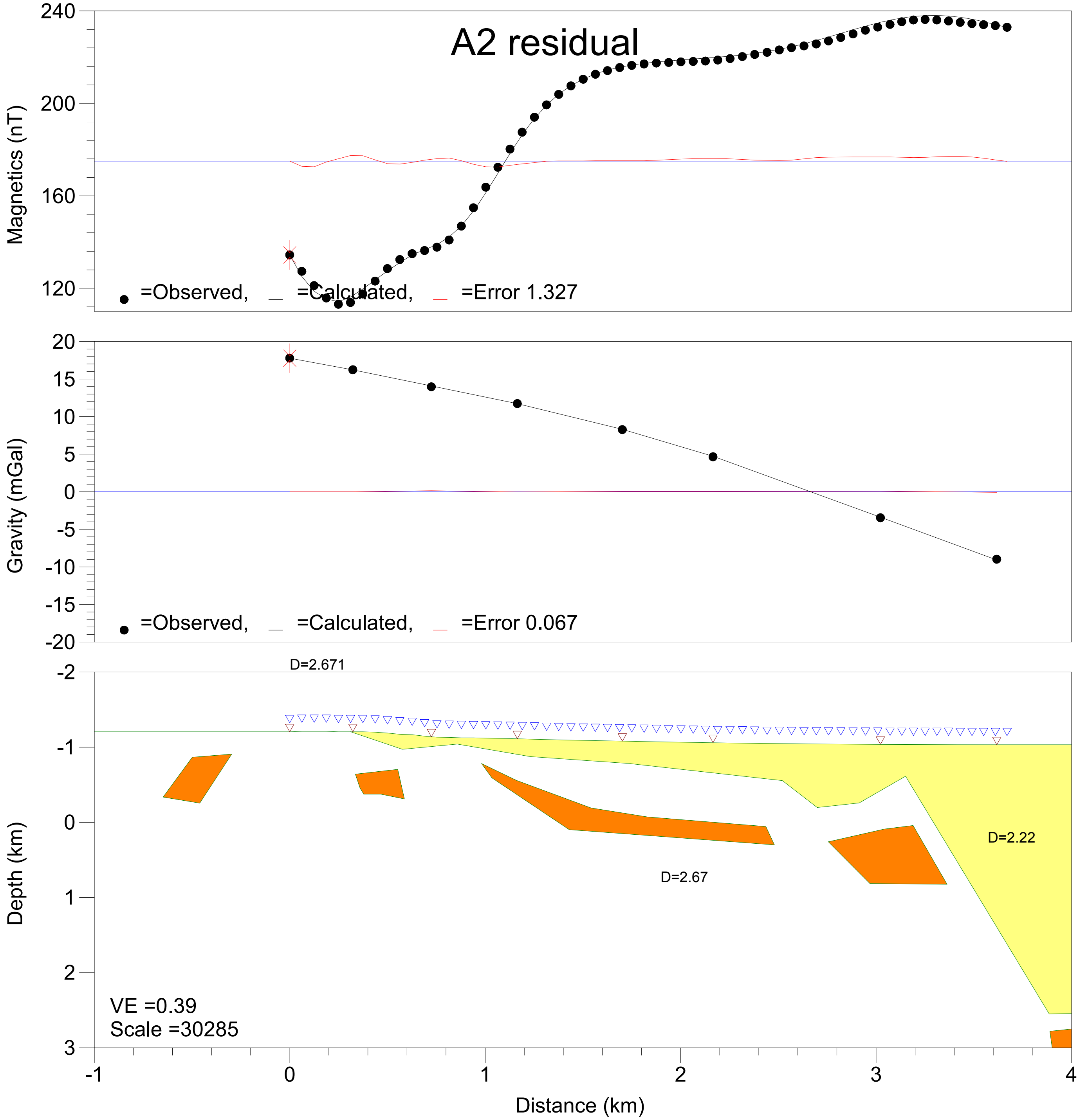

A2 residual
Magnetics (nT)
240
200
160
120
=Observed,
=Calculated,
=Error 1.327
Gravity (mGal)
20
15
10
5
0
-5
-10
-15
-20
=Observed,
=Calculated,
=Error 0.067
D=2.671
Depth (km)
-2
-1
0
1
2
3
D=2.22
D=2.67
VE =0.39
Scale =30285
-1
0
1
2
3
4
Distance (km)

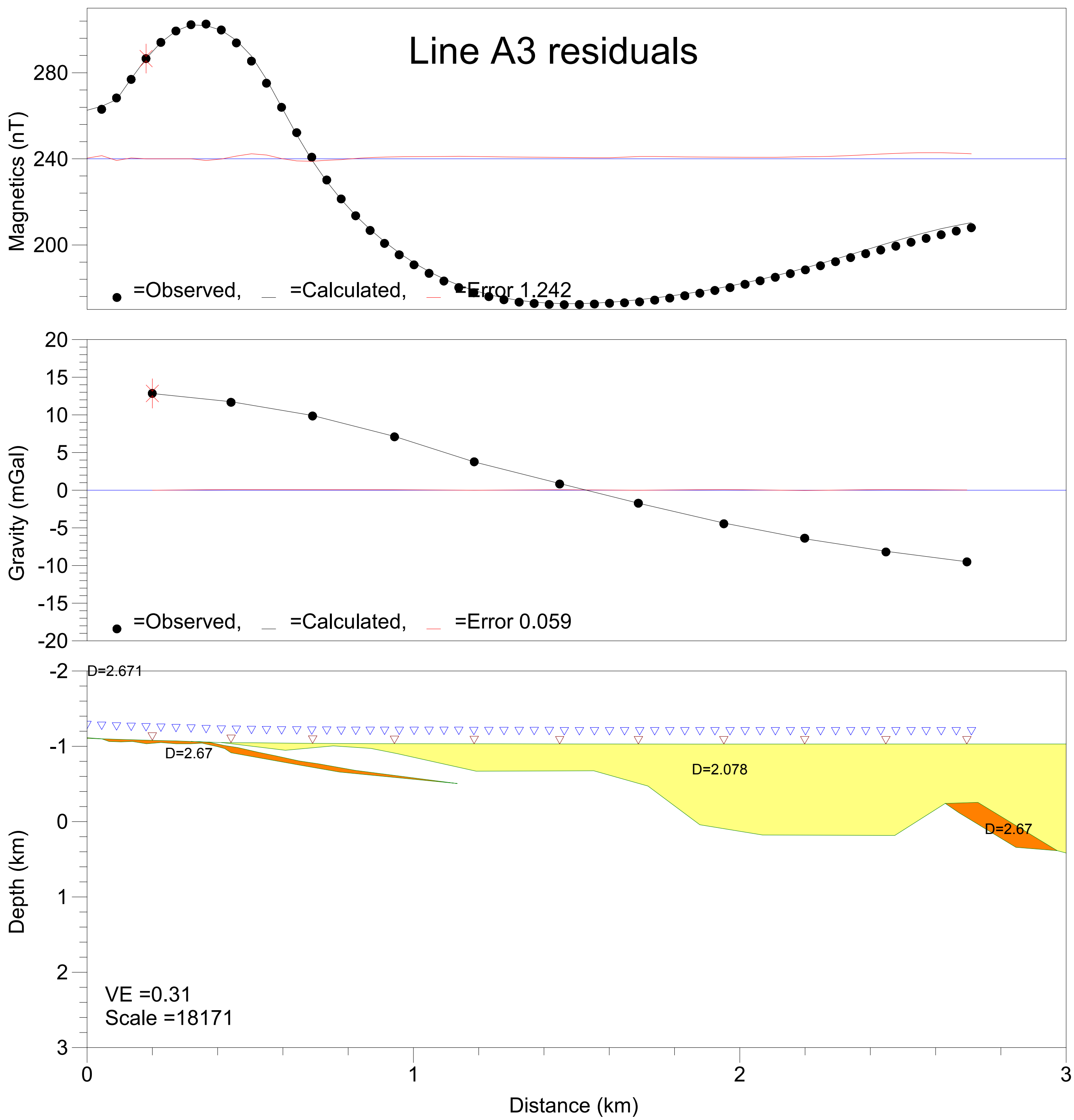
Line A3 residuals
Magnetics (nT)
280
240
200
=Observed,
=Calculated,
=Error 1.242
Gravity (mGal)
20
15
10
5
0
-5
-10
-15
-20
=Observed,
=Calculated,
=Error 0.059
-2
D=2.671
-1
D=2.67
D=2.078
0
D=2.67
1
2
3
Depth (km)
VE =0.31
Scale =18171
0
1
2
3
Distance (km)

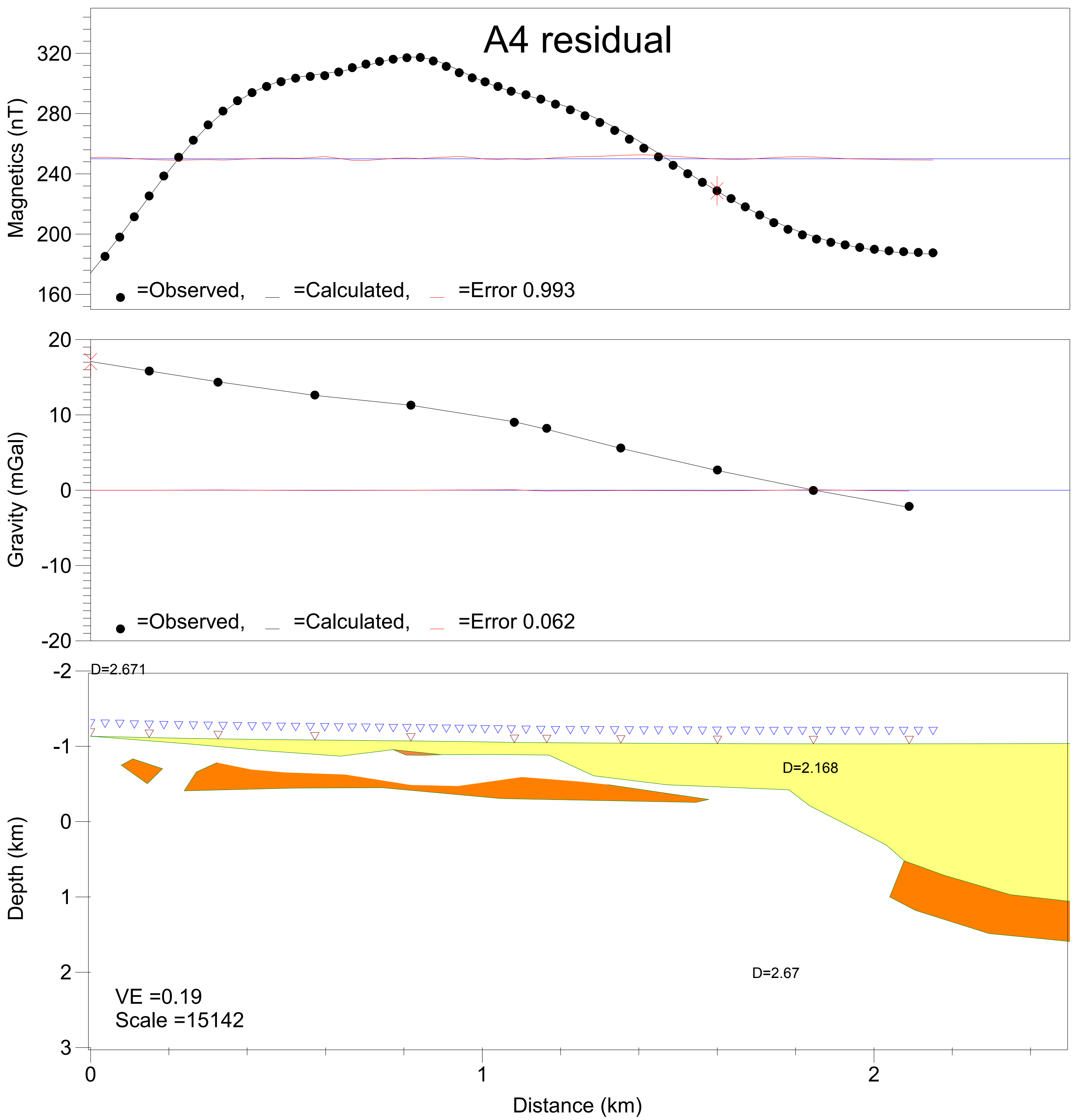

A4 residual
Magnetics (nT)
320
280
240
200
160
=Observed, =Calculated, =Error 0.993
Gravity (mGal)
20
10
0
-10
-20
=Observed, =Calculated, =Error 0.062
D=2.671
D=2.168
D=2.67
Depth (km)
-2
-1
0
1
2
3
VE =0.19
Scale =15142
0
1
2
Distance (km)

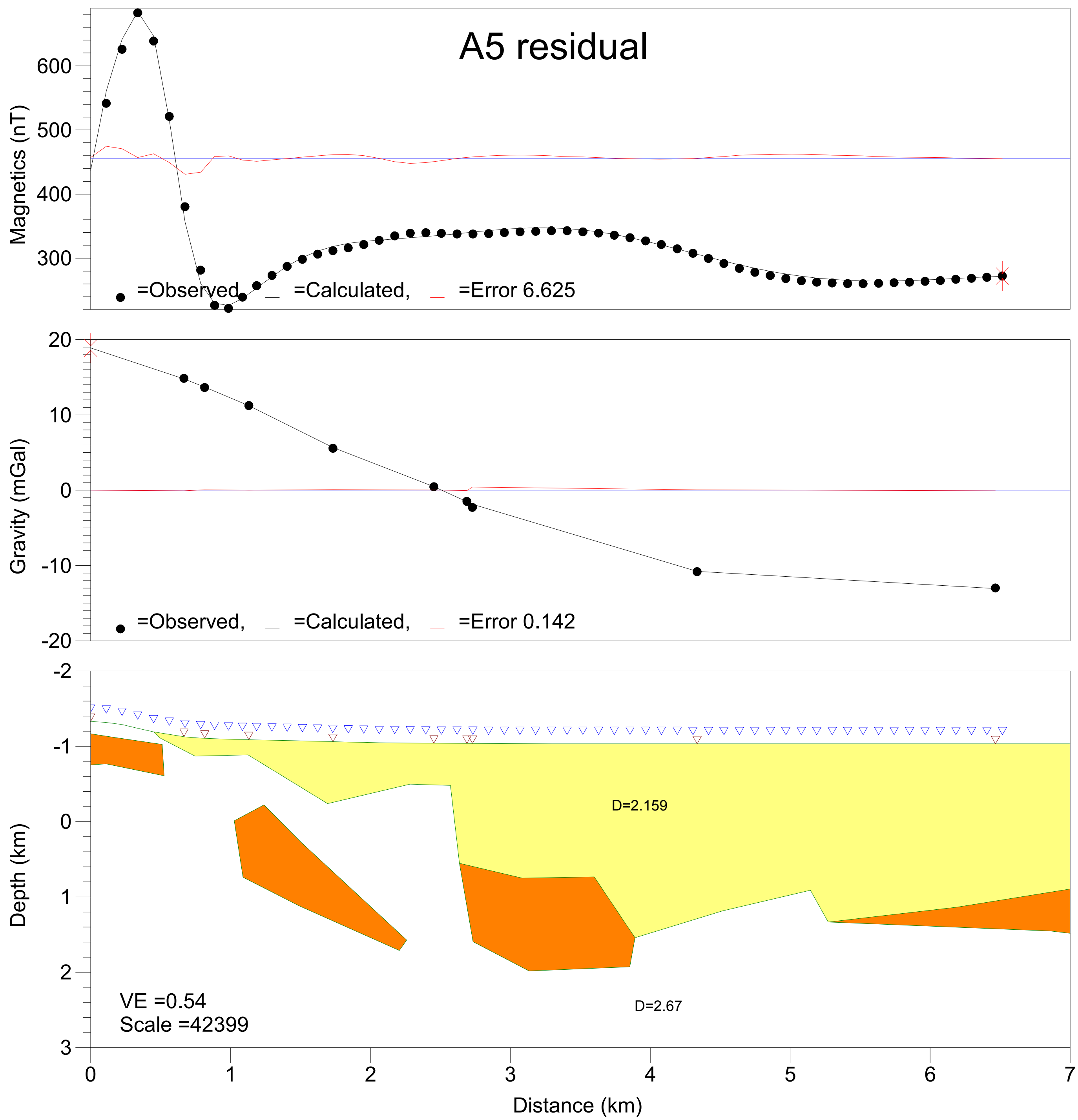

A5 residual
Magnetics (nT)
600
500
400
300
=Observed,
=Calculated,
=Error 6.625
Gravity (mGal)
20
10
0
-10
-20
=Observed,
=Calculated,
=Error 0.142
Depth (km)
-2
-1
0
1
2
3
D=2.159
D=2.67
VE =0.54
Scale =42399
0
1
2
3
4
5
6
7
Distance (km)

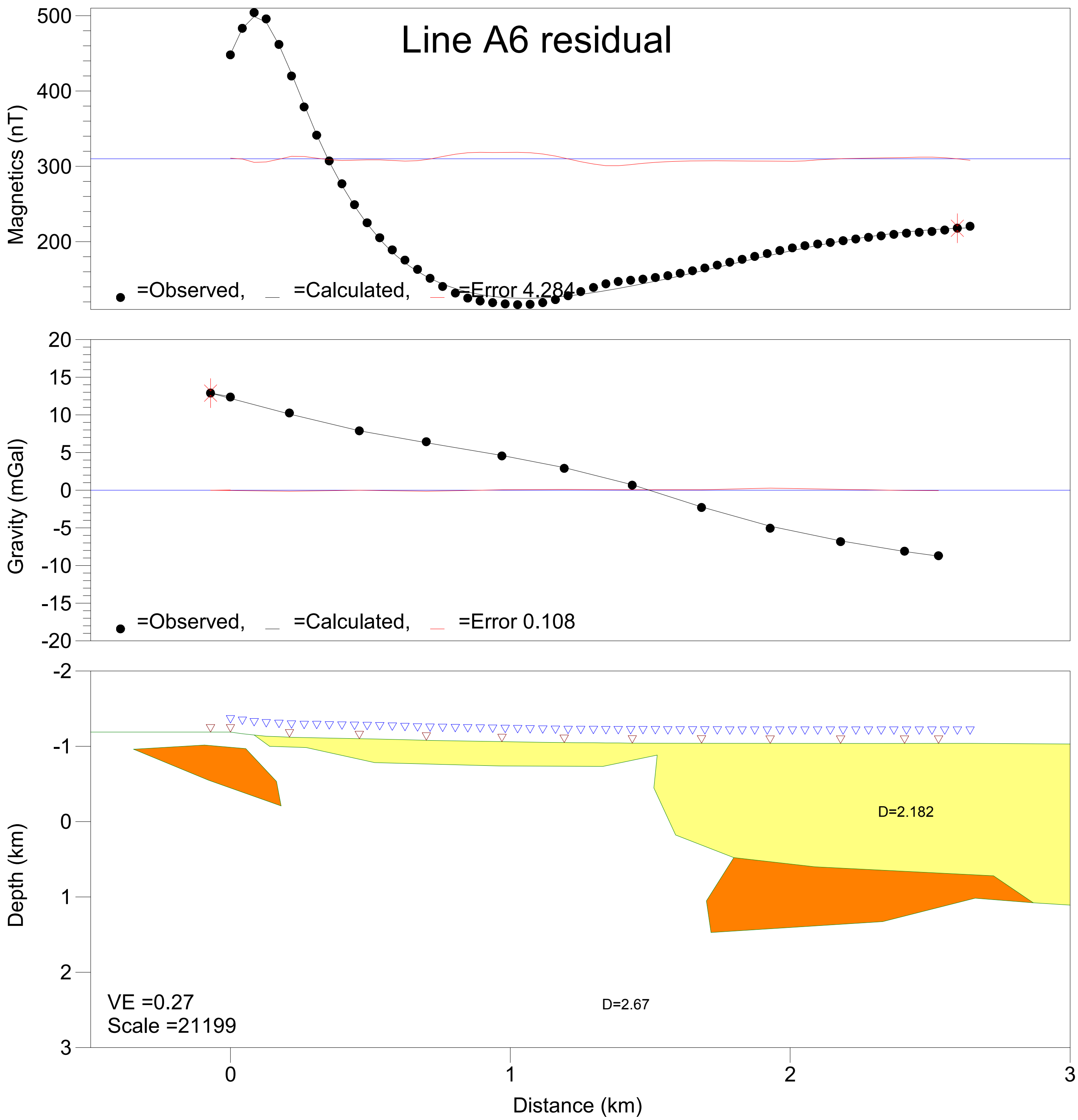

Line A6 residual
Magnetics (nT)
500
400
300
200
=Observed,
=Calculated,
=Error 4.284
Gravity (mGal)
20
15
10
5
0
-5
-10
-15
-20
=Observed,
=Calculated,
=Error 0.108
Depth (km)
-2
-1
0
1
2
3
D=2.182
D=2.67
VE =0.27
Scale =21199
0
1
2
3
Distance (km)

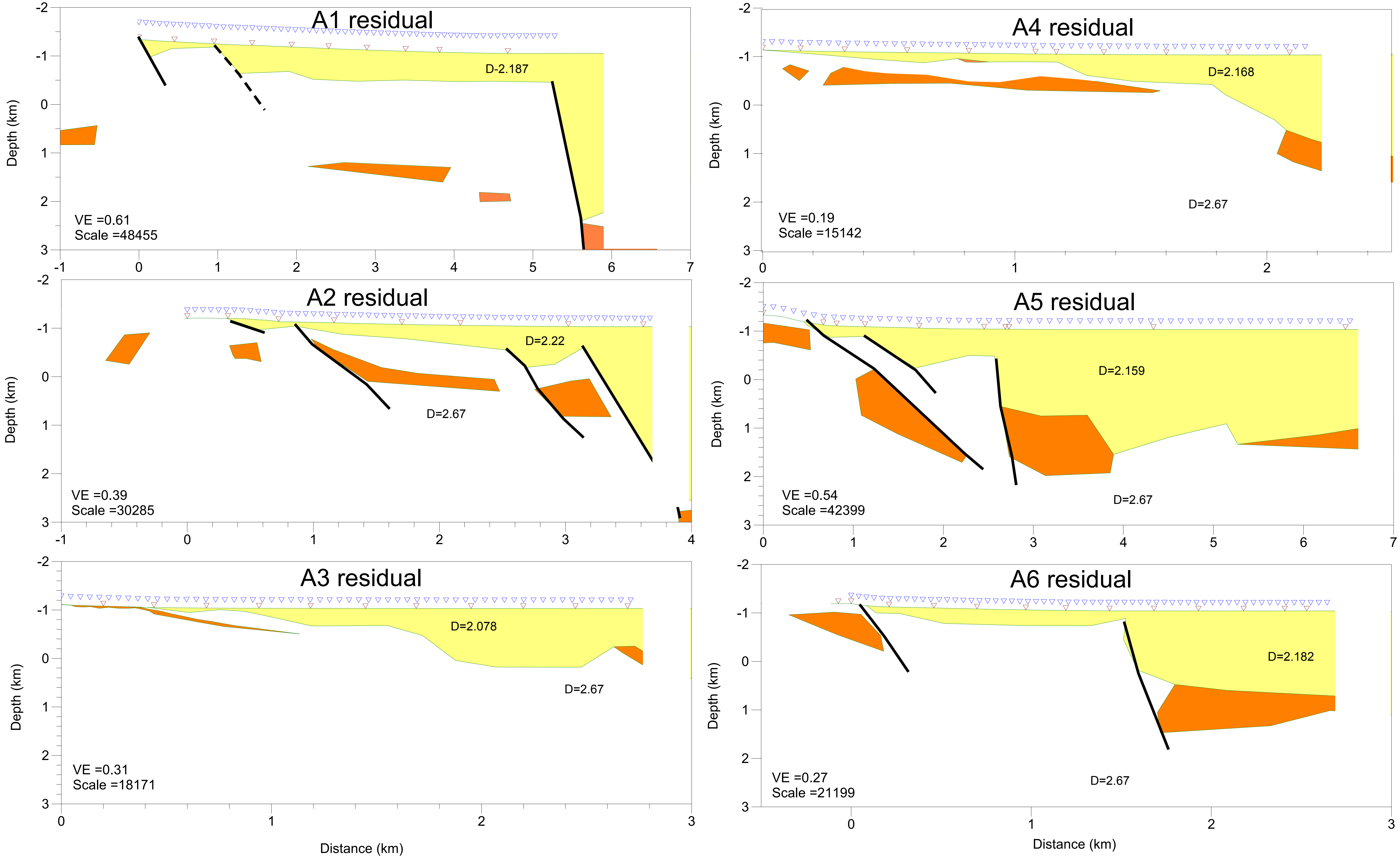

A1 residual
D-2.187
VE =0.61
Scale =48455
A2 residual
D=2.22
D=2.67
VE =0.39
Scale =30285
A3 residual
D=2.078
D=2.67
VE =0.31
Scale =18171
A4 residual
D=2.168
D=2.67
VE =0.19
Scale =15142
A5 residual
D=2.159
D=2.67
VE =0.54
Scale =42399
A6 residual
D=2.182
D=2.67
VE =0.27
Scale =21199
Depth (km)
Distance (km)

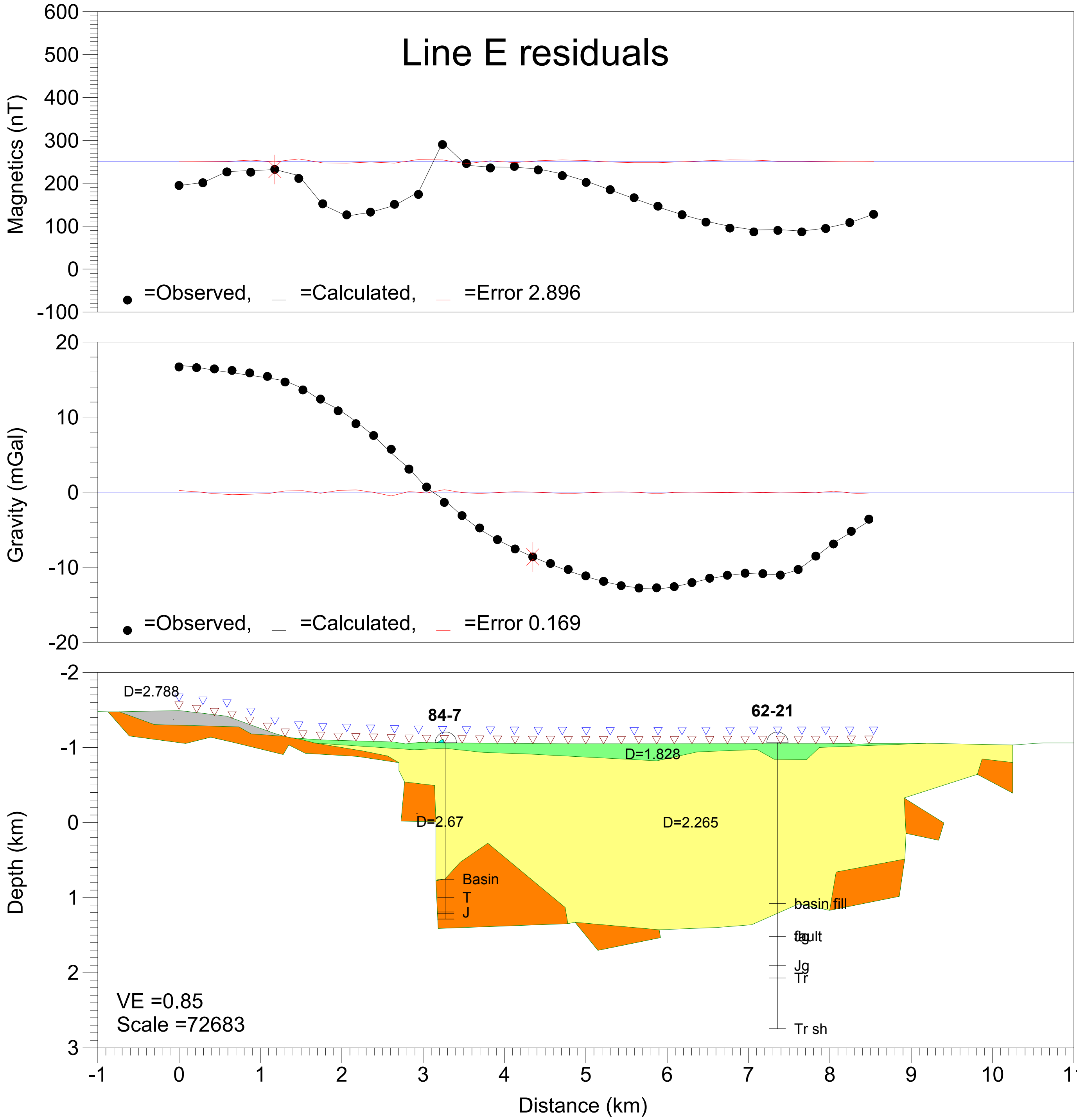

Line E residuals
Magnetics (nT)
=Observed, =Calculated, =Error 2.896
Gravity (mGal)
=Observed, =Calculated, =Error 0.169
D=2.788
84-7
62-21
D=1.828
D=2.67
D=2.265
Basin
T
J
basin fill
fault
Jg
Tr
Tr sh
VE =0.85
Scale =72683
Depth (km)
Distance (km)

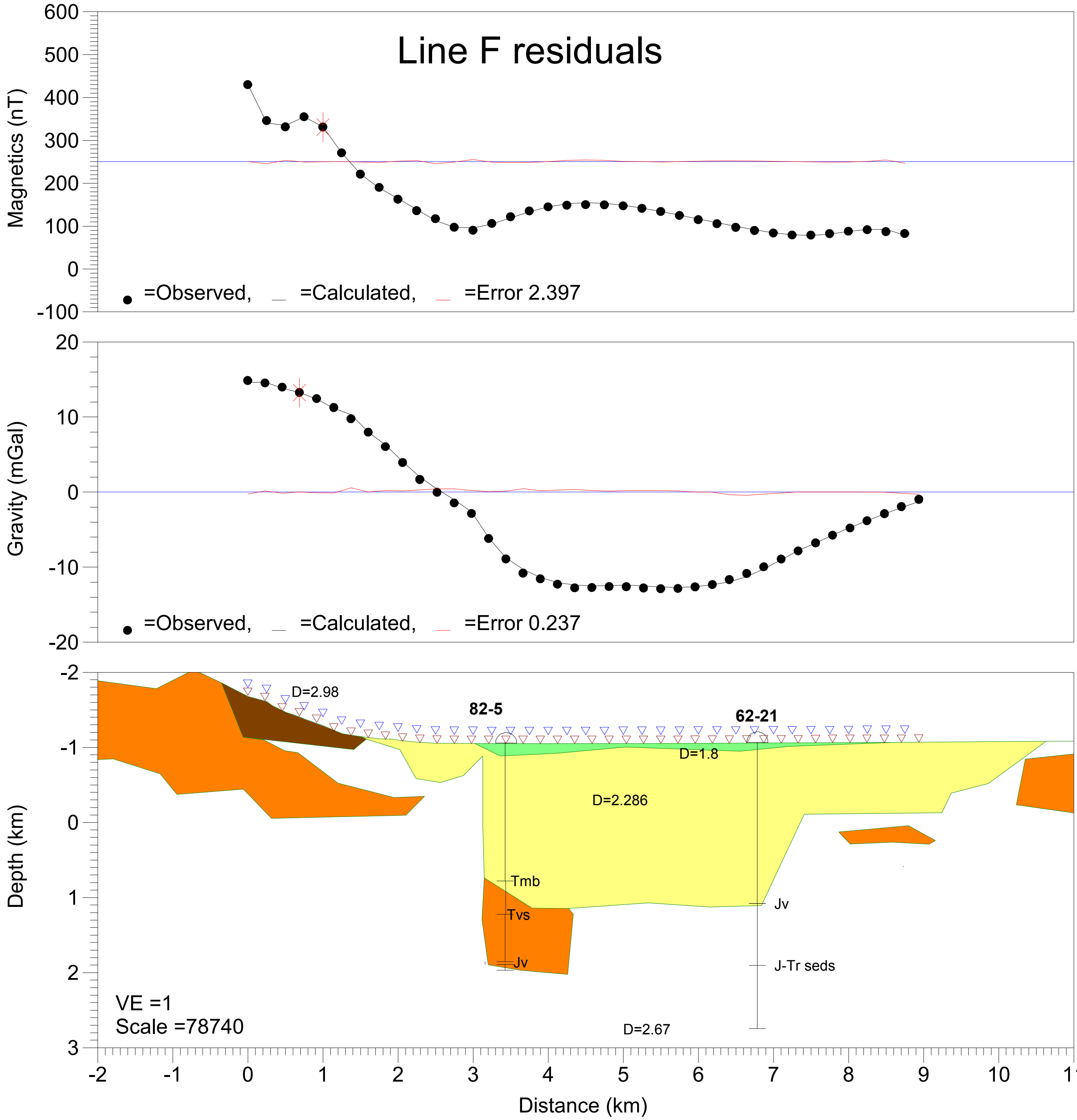

Line F residuals
Magnetics (nT)
600
500
400
300
200
100
0
-100
=Observed,
=Calculated,
=Error 2.397
Gravity (mGal)
20
10
0
-10
-20
=Observed,
=Calculated,
=Error 0.237
Depth (km)
-2
-1
0
1
2
3
D=2.98
82-5
62-21
D=1.8
D=2.286
Tmb
Tvs
Jv
Jv
J-Tr seds
D=2.67
VE =1
Scale =78740
-2
-1
0
1
2
3
4
5
6
7
8
9
10
11
Distance (km)

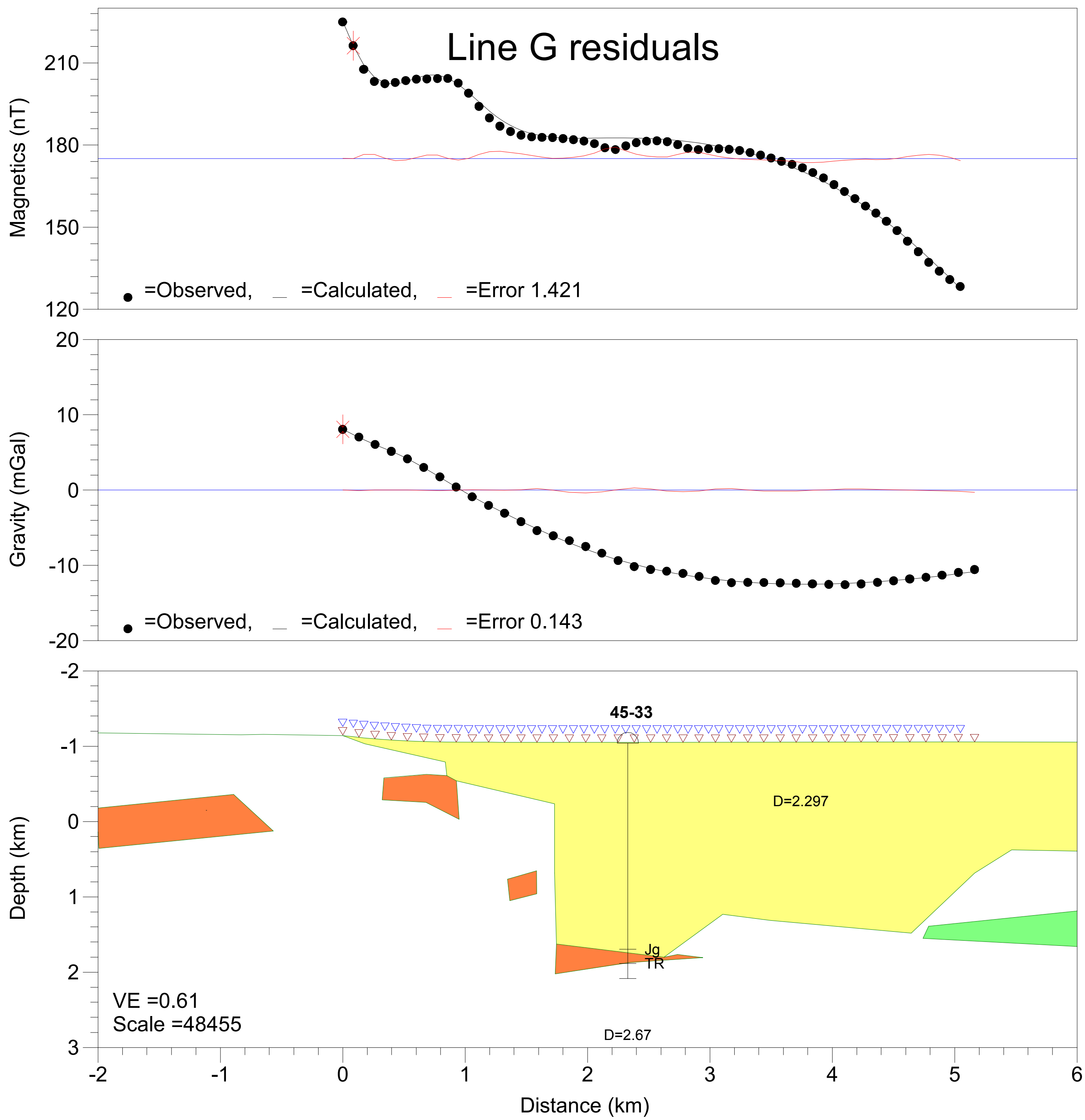

Line G residuals
Magnetics (nT)
210
180
150
120
=Observed,
=Calculated,
=Error 1.421
Gravity (mGal)
20
10
0
-10
-20
=Observed,
=Calculated,
=Error 0.143
Depth (km)
-2
-1
0
1
2
3
45-33
D=2.297
Jg
TR
D=2.67
VE =0.61
Scale =48455
-2
-1
0
1
2
3
4
5
6
Distance (km)

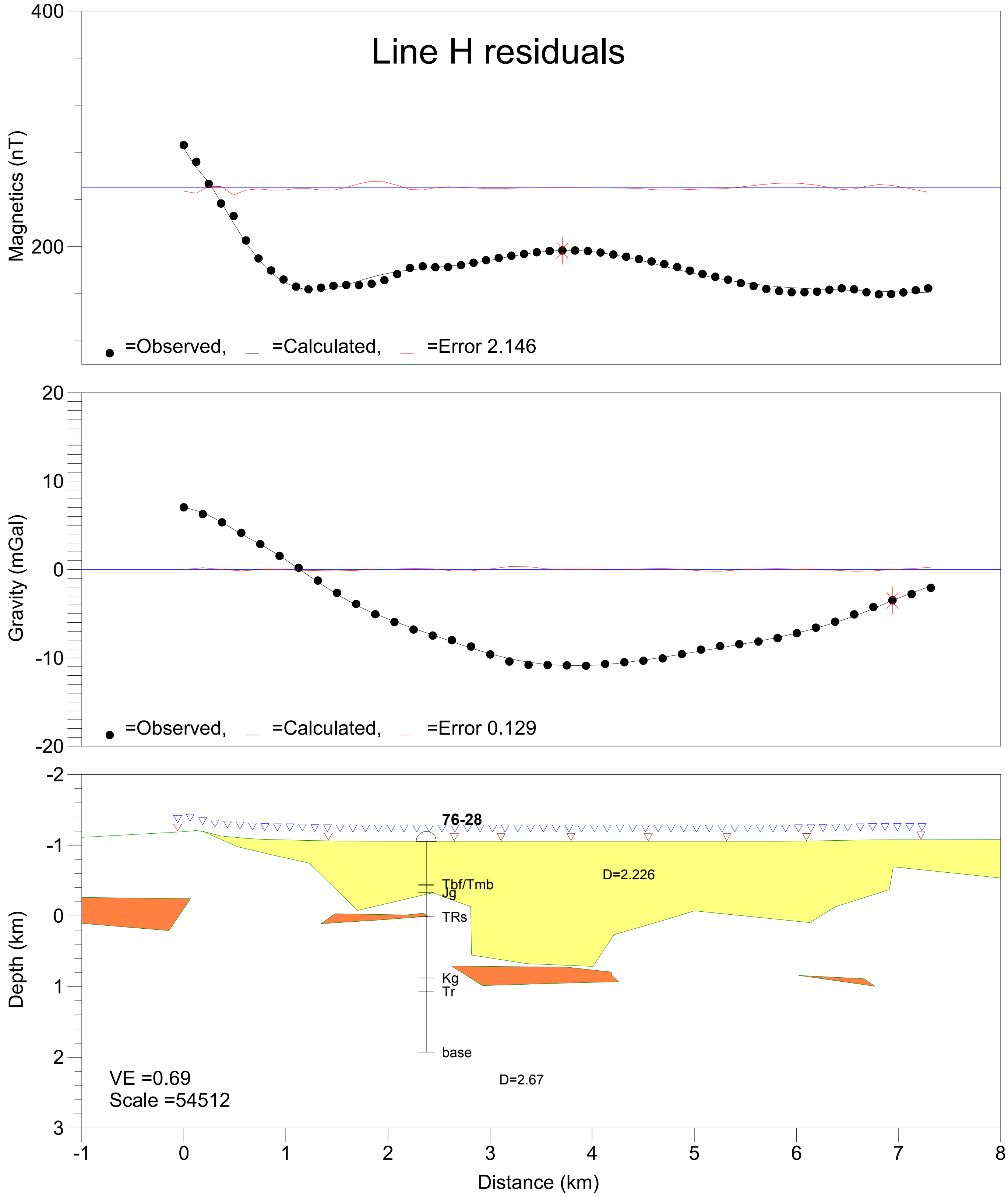

Line H residuals
400
200
Magnetics (nT)
=Observed,
=Calculated,
=Error 2.146
20
10
0
-10
-20
Gravity (mGal)
=Observed,
=Calculated,
=Error 0.129
-2
-1
0
1
2
3
Depth (km)
76-28
D=2.226
Tbf/Tmb
Jg
TRs
Kg
Tr
base
D=2.67
VE =0.69
Scale =54512
-1
0
1
2
3
4
5
6
7
8
Distance (km)

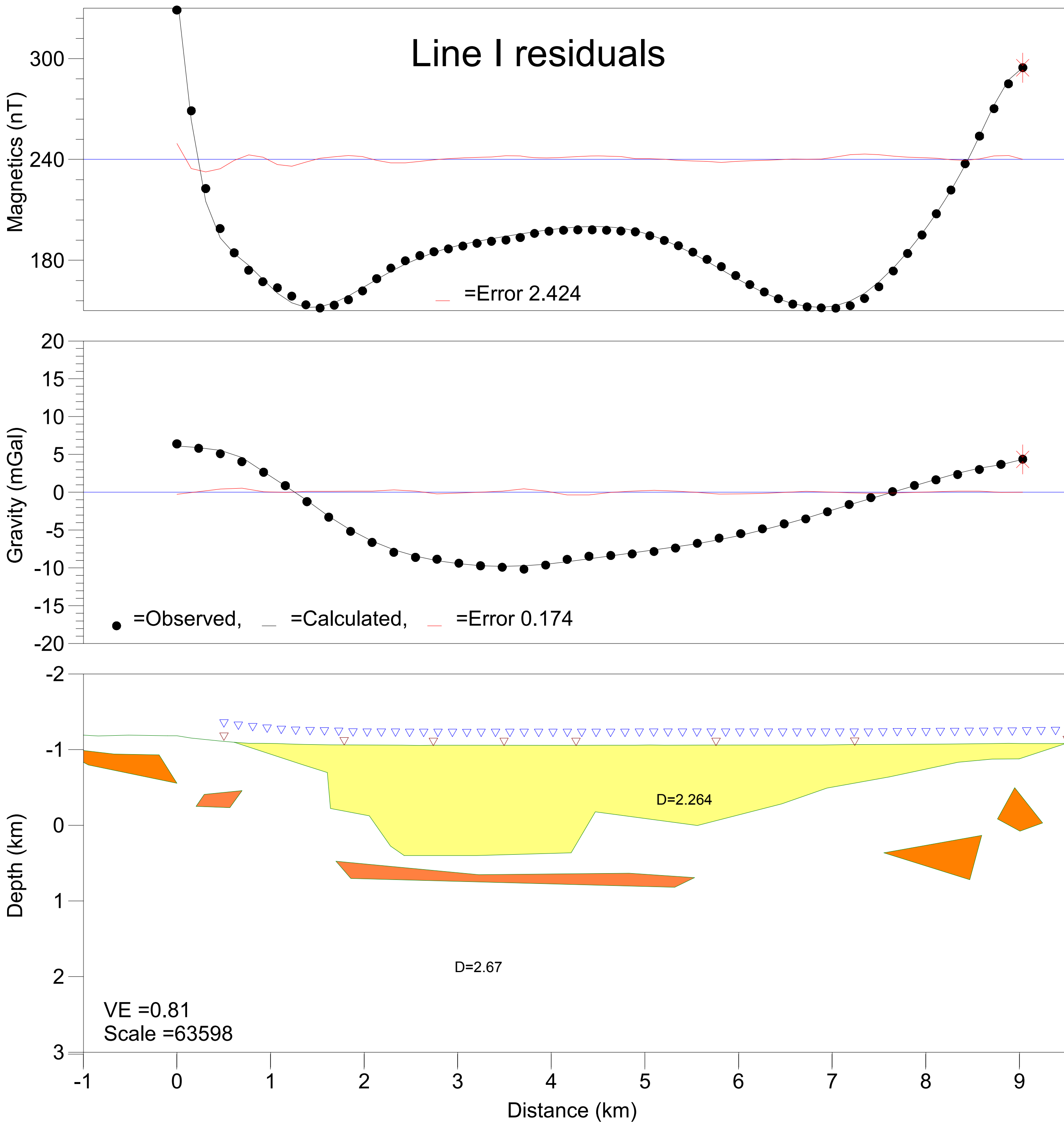

Line I residuals
Magnetics (nT)
300
240
180
=Error 2.424
Gravity (mGal)
20
15
10
5
0
-5
-10
-15
-20
=Observed,
=Calculated,
=Error 0.174
Depth (km)
-2
-1
0
1
2
3
D=2.264
D=2.67
VE =0.81
Scale =63598
-1
0
1
2
3
4
5
6
7
8
9
Distance (km)

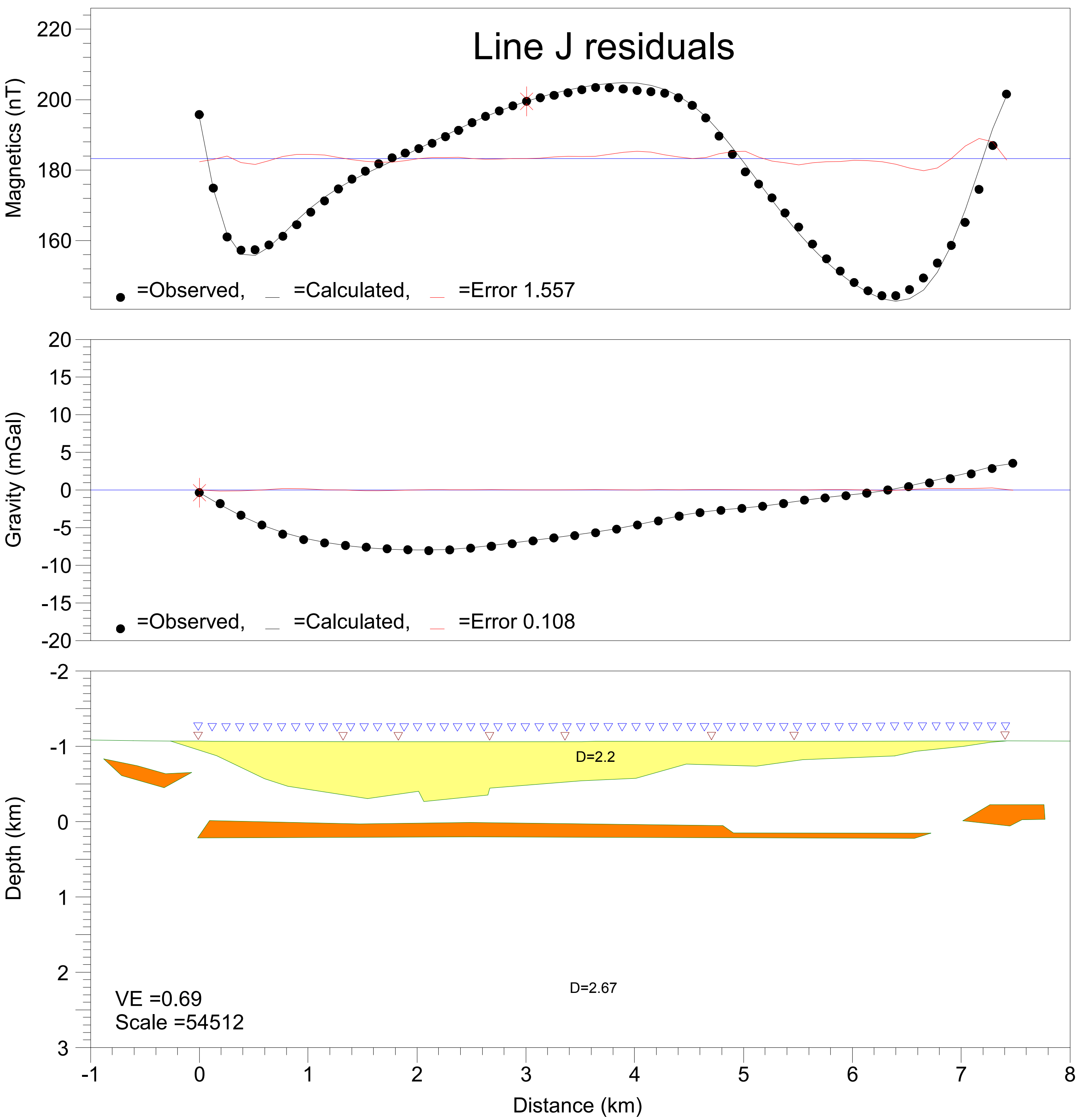

Line J residuals
Magnetics (nT)
220
200
180
160
=Observed,
=Calculated,
=Error 1.557
Gravity (mGal)
20
15
10
5
0
-5
-10
-15
-20
=Observed,
=Calculated,
=Error 0.108
Depth (km)
-2
-1
0
1
2
3
D=2.2
D=2.67
VE =0.69
Scale =54512
-1
0
1
2
3
4
5
6
7
8
Distance (km)

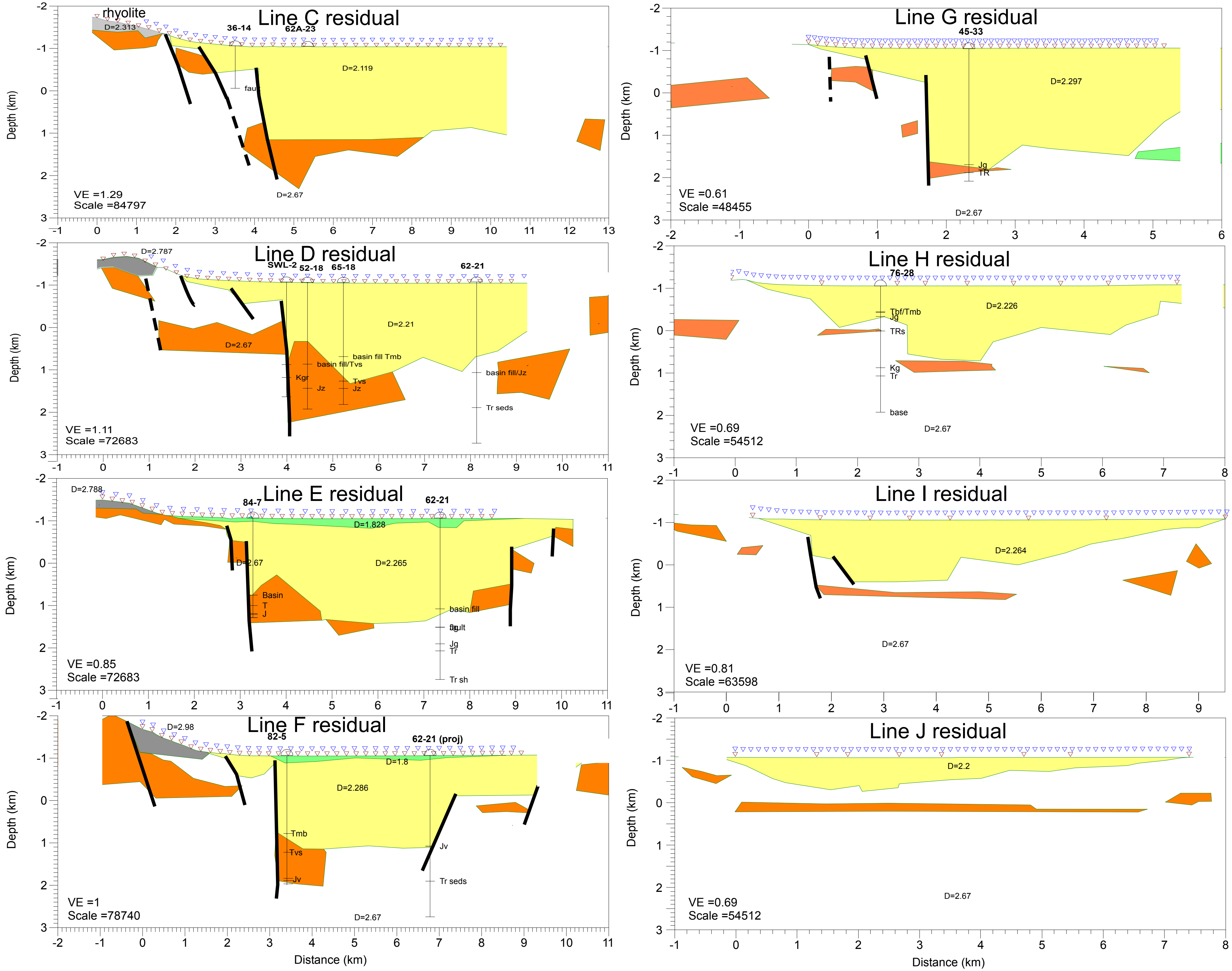

Line C residual
rhyolite
D=2.313
36-14
62A-23
D=2.119
D=2.67
VE =1.29
Scale =84797
Line D residual
D=2.787
SWL-2
52-18
65-18
62-21
D=2.21
D=2.67
basin fill Tmb
basin fill/Tvs
Kgr
Jz
Tvs
basin fill/Jz
Tr seds
VE =1.11
Scale =72683
Line E residual
D=2.788
84-7
62-21
D=1.828
D=2.67
D=2.265
Basin
T
J
basin fill
fault
Jg
Tr
Tr sh
VE =0.85
Scale =72683
Line F residual
D=2.98
82-5
62-21 (proj)
D=1.8
D=2.286
Tmb
Tvs
Jv
Tr seds
D=2.67
VE =1
Scale =78740
Line G residual
45-33
D=2.297
Jg
TR
D=2.67
VE =0.61
Scale =48455
Line H residual
76-28
D=2.226
Tbf/Tmb
Jg
TRs
Kg
Tr
base
D=2.67
VE =0.69
Scale =54512
Line I residual
D=2.264
D=2.67
VE =0.81
Scale =63598
Line J residual
D=2.2
D=2.67
VE =0.69
Scale =54512
Depth (km)
Distance (km)

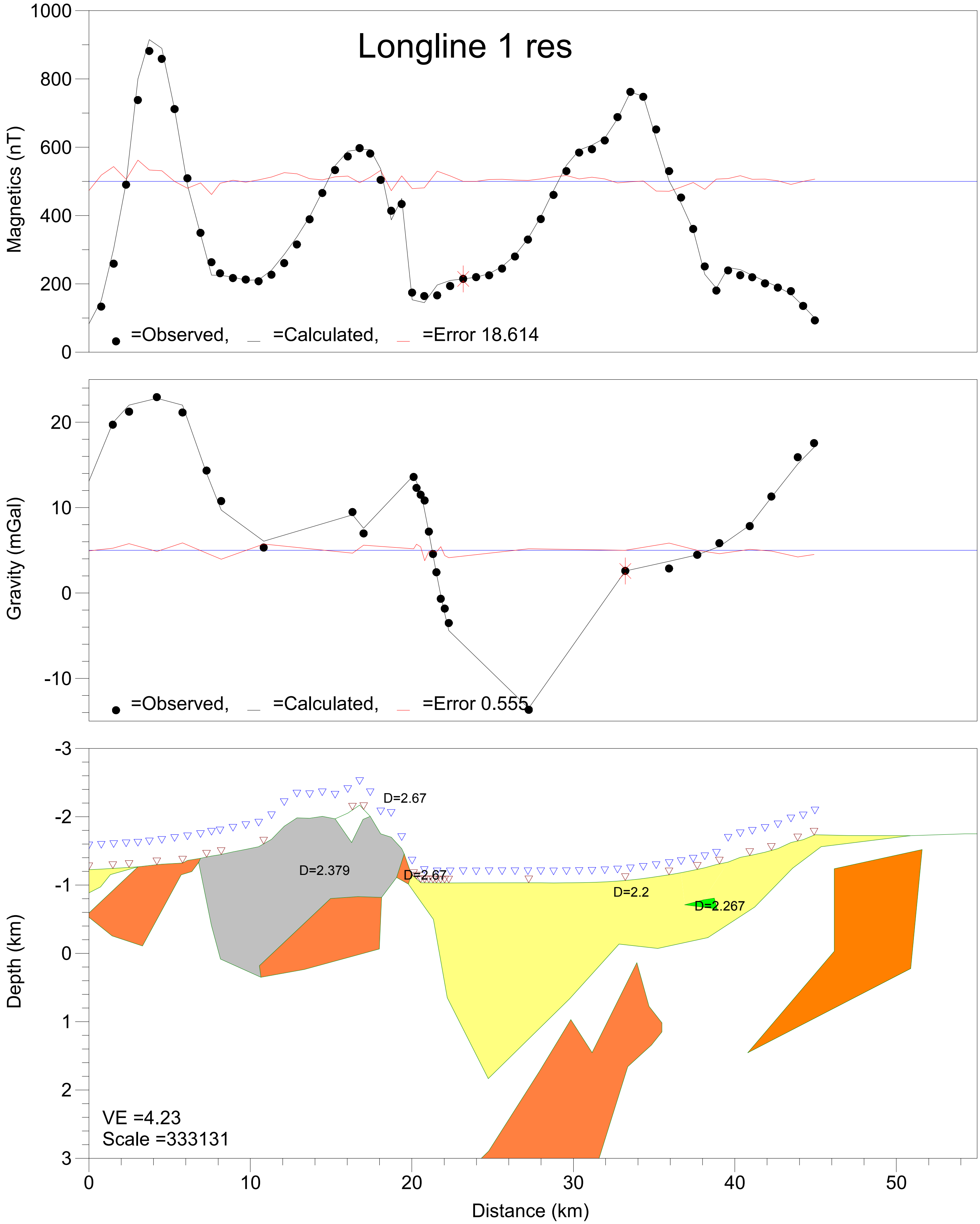

Longline 1 res
Magnetics (nT)
1000
800
600
400
200
0
=Observed, =Calculated, =Error 18.614
Gravity (mGal)
20
10
0
-10
=Observed, =Calculated, =Error 0.555
Depth (km)
-3
-2
-1
0
1
2
3
D=2.67
D=2.379
D=2.67
D=2.2
D=2.267
VE =4.23
Scale =333131
0
10
20
30
40
50
Distance (km)

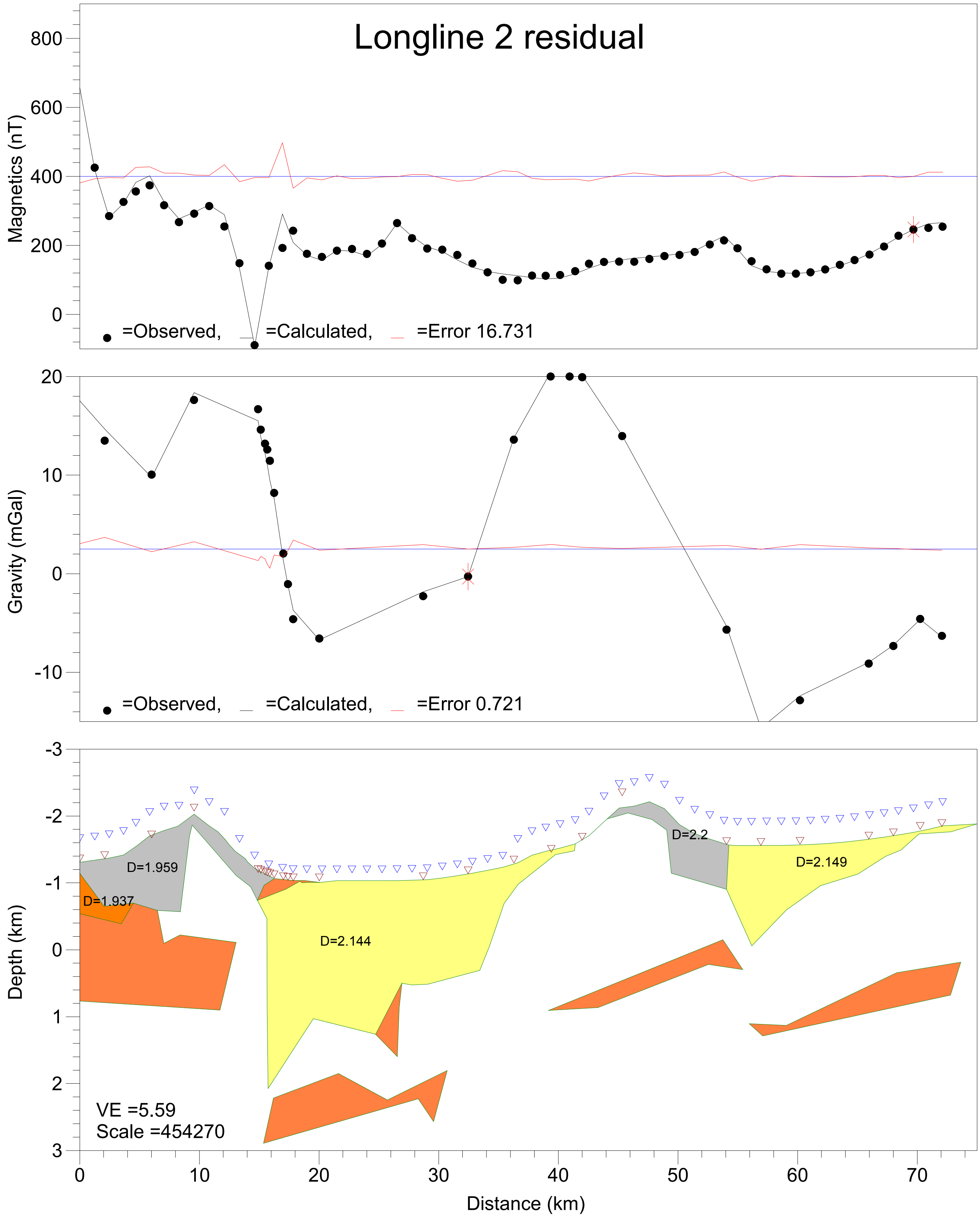

Longline 2 residual
Magnetics (nT)
800
600
400
200
0
=Observed, =Calculated, =Error 16.731
Gravity (mGal)
20
10
0
-10
=Observed, =Calculated, =Error 0.721
Depth (km)
-3
-2
-1
0
1
2
3
D=1.959
D=1.937
D=2.144
D=2.2
D=2.149
VE =5.59
Scale =454270
0
10
20
30
40
50
60
70
Distance (km)

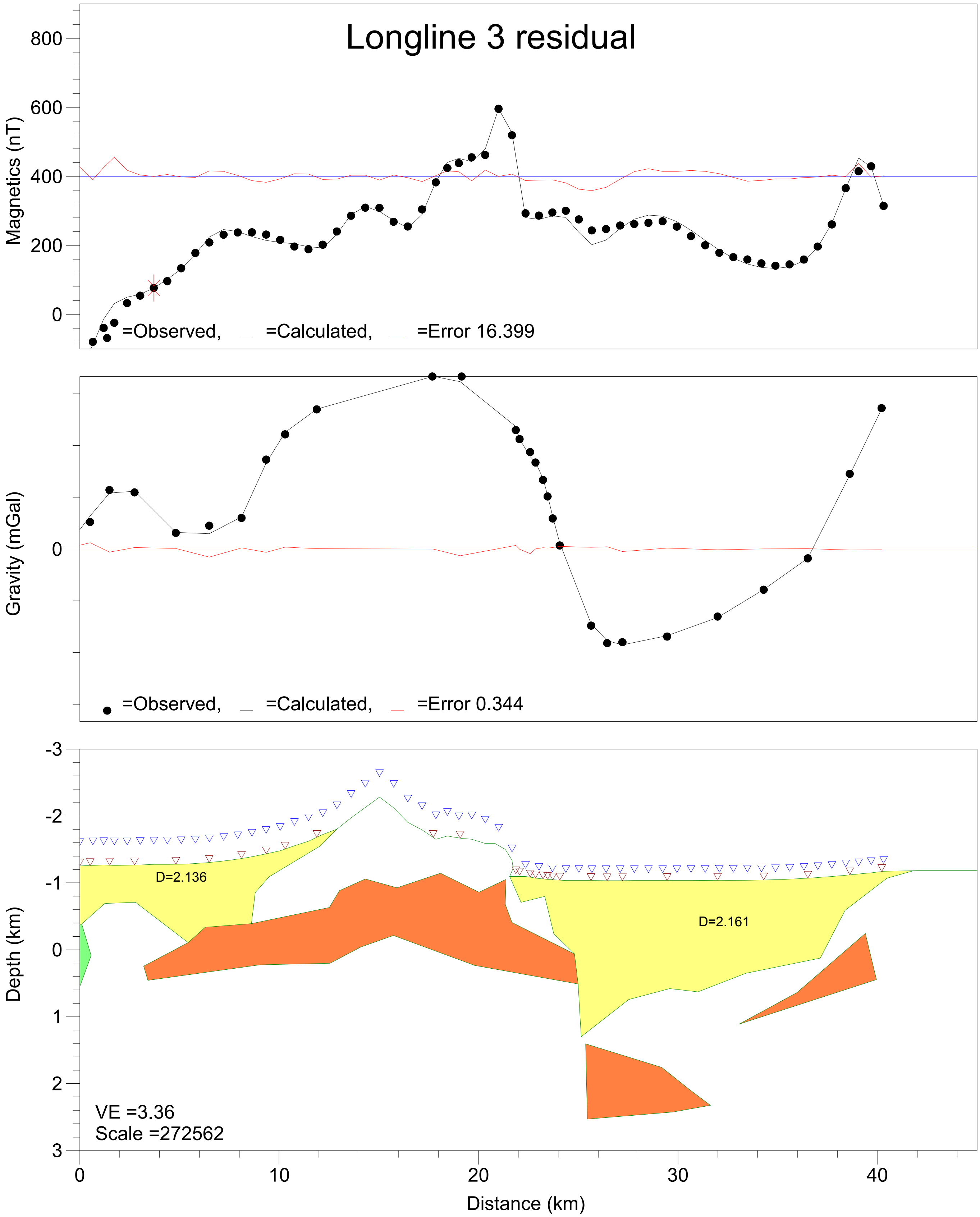

Longline 3 residual
Magnetics (nT)
800
600
400
200
0
=Observed,
=Calculated,
=Error 16.399
Gravity (mGal)
0
=Observed,
=Calculated,
=Error 0.344
Depth (km)
-3
-2
-1
0
1
2
3
D=2.136
D=2.161
VE =3.36
Scale =272562
0
10
20
30
40
Distance (km)

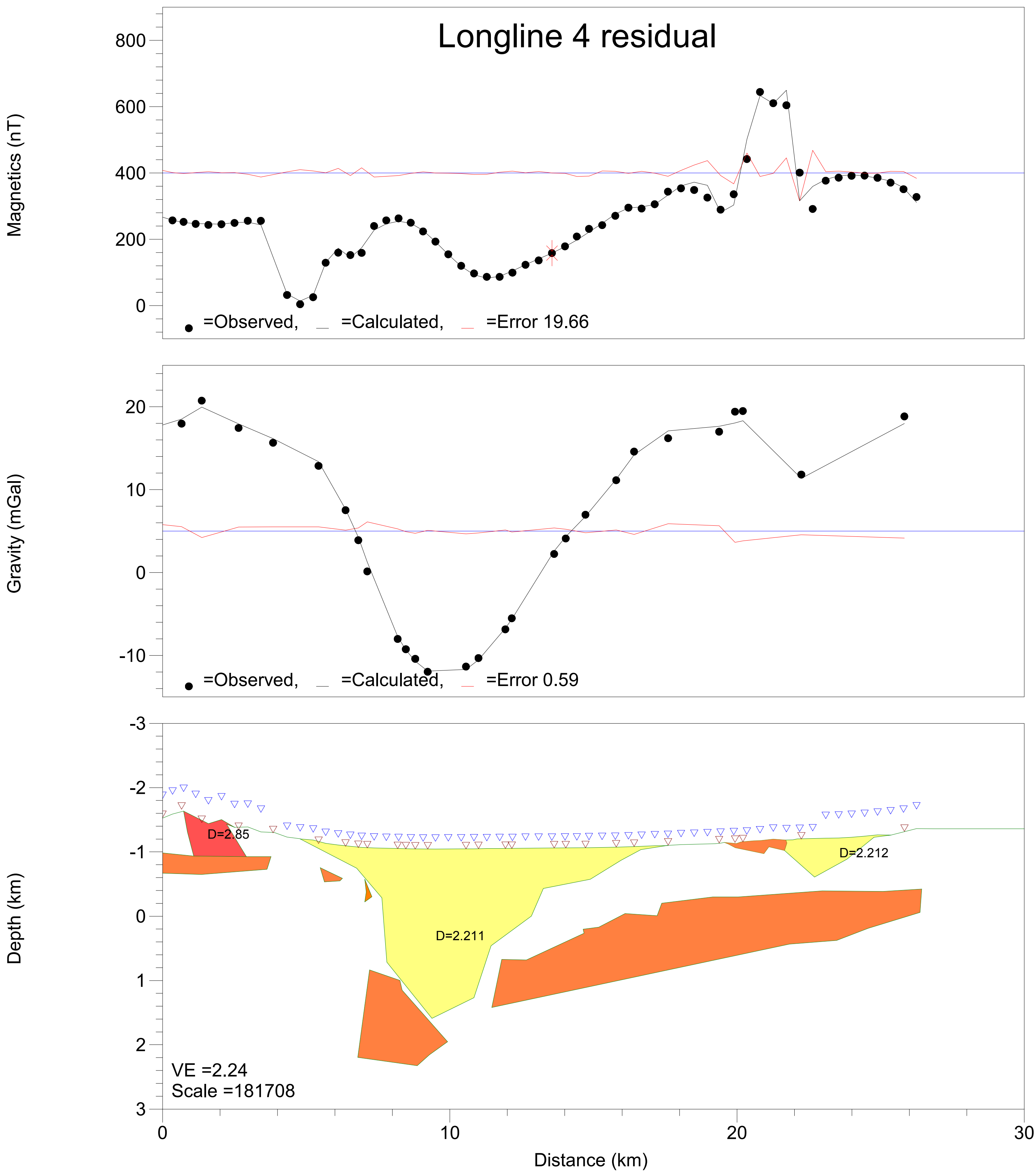
Longline 4 residual
Magnetics (nT)
800
600
400
200
0
=Observed, =Calculated, =Error 19.66
Gravity (mGal)
20
10
0
-10
=Observed, =Calculated, =Error 0.59
Depth (km)
-3
-2
-1
0
1
2
3
D=2.85
D=2.211
D=2.212
VE =2.24
Scale =181708
0
10
20
30
Distance (km)

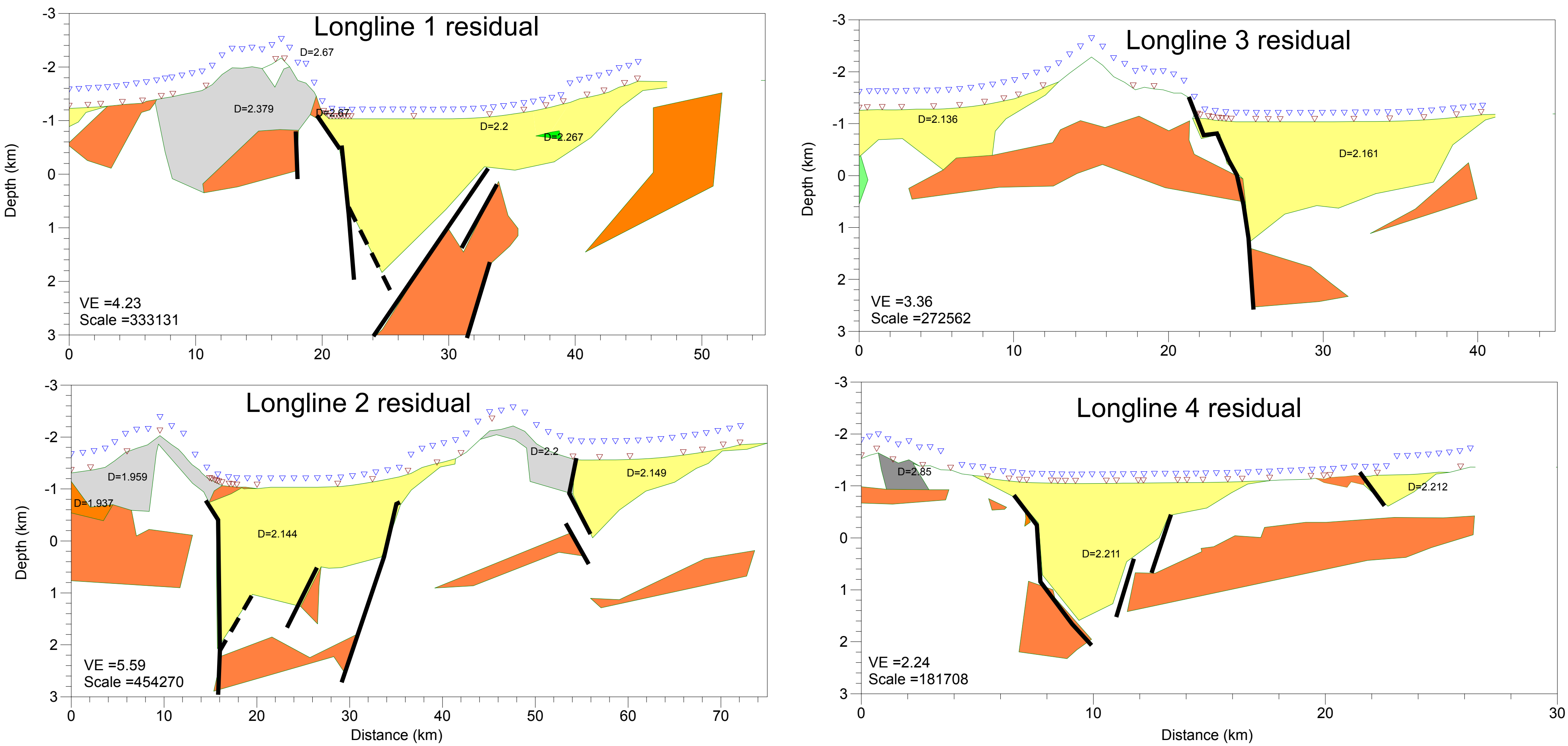

Longline 1 residual
D=2.67
D=2.379
D=2.67
D=2.2
D=2.267
VE =4.23
Scale =333131
Depth (km)
Longline 3 residual
D=2.136
D=2.161
VE =3.36
Scale =272562
Depth (km)
Longline 2 residual
D=1.959
D=1.937
D=2.144
D=2.2
D=2.149
VE =5.59
Scale =454270
Depth (km)
Distance (km)
Longline 4 residual
D=2.85
D=2.211
D=2.212
VE =2.24
Scale =181708
Distance (km)

PART II-APPENDIX 3

COMPLETE BOUGER GRAVITY AND RESIDUAL GRAVITY ANOMALY JOINTLY INVERTED GRAVITY-MAGNETIC MODELS COMPARISON

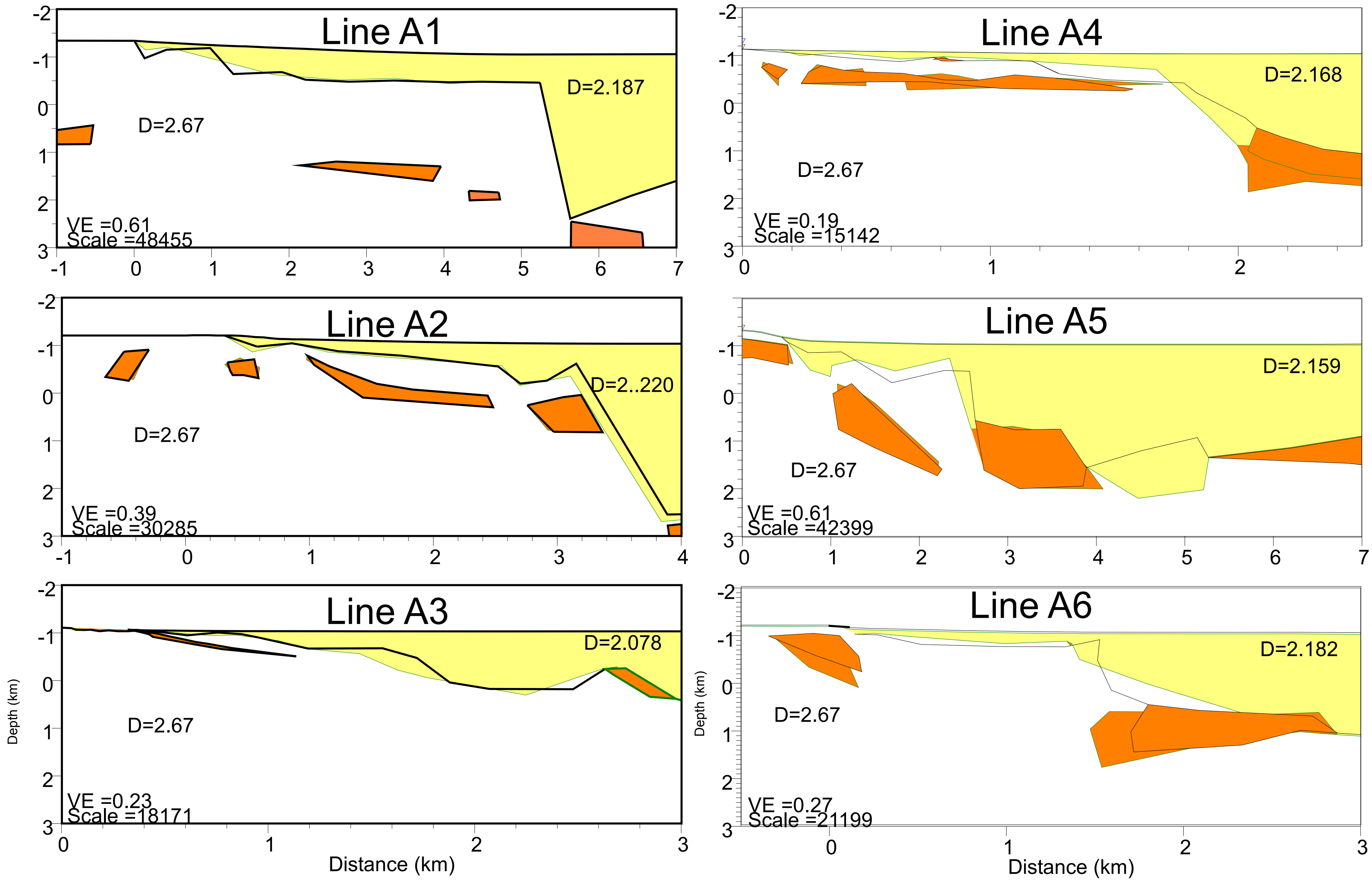

Line A1
D=2.187
D=2.67
VE =0.61
Scale =48455
Line A4
D=2.168
D=2.67
VE =0.19
Scale =15142
Line A2
D=2..220
D=2.67
VE =0.39
Scale =30285
Line A5
D=2.159
D=2.67
VE =0.61
Scale =42399
Line A3
D=2.078
D=2.67
VE =0.23
Scale =18171
Line A6
D=2.182
D=2.67
VE =0.27
Scale =21199
Depth (km)
Distance (km)

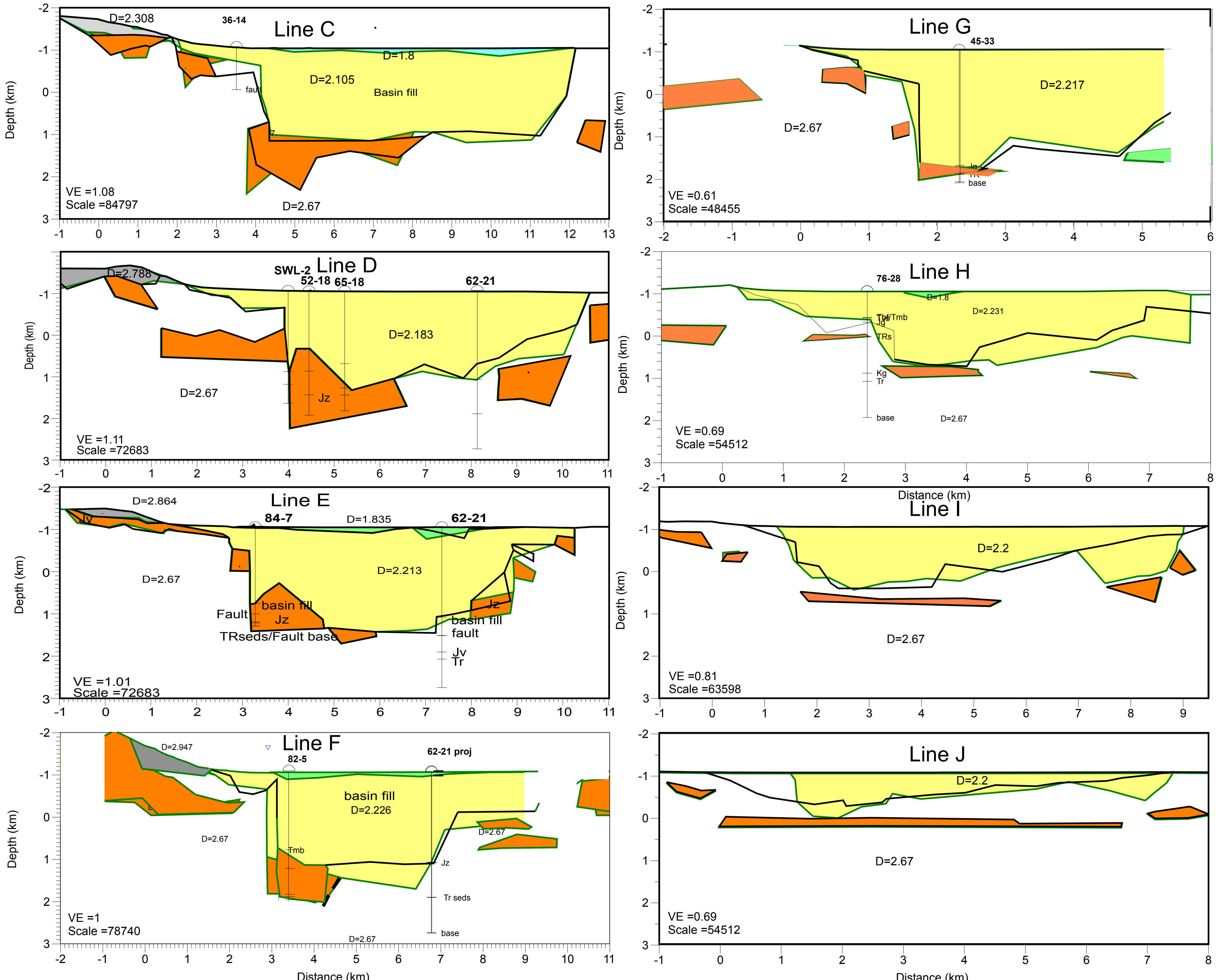

Line C
D=2.308
36-14
D=1.8
D=2.105
Basin fill
D=2.67
VE =1.08
Scale =84797
Depth (km)
Line G
45-33
D=2.217
D=2.67
base
VE =0.61
Scale =48455
Depth (km)
Line D
SWL-2
52-18
65-18
62-21
D=2.788
D=2.183
D=2.67
Jz
VE =1.11
Scale =72683
Depth (km)
Line H
76-28
D=1.8
D=2.231
Tg
TRs
Kg
Tr
base
D=2.67
VE =0.69
Scale =54512
Depth (km)
Distance (km)
Line E
D=2.864
84-7
D=1.835
62-21
D=2.213
D=2.67
basin fill
Jz
Fault
TRseds/Fault base
basin fill
fault
Jv
Tr
VE =1.01
Scale =72683
Depth (km)
Line I
D=2.2
D=2.67
VE =0.81
Scale =63598
Depth (km)
Line F
D=2.947
82-5
62-21 proj
basin fill
D=2.226
D=2.67
Tmb
Jz
Tr seds
base
D=2.67
VE =1
Scale =78740
Depth (km)
Distance (km)
Line J
D=2.2
D=2.67
VE =0.69
Scale =54512
Depth (km)
Distance (km)

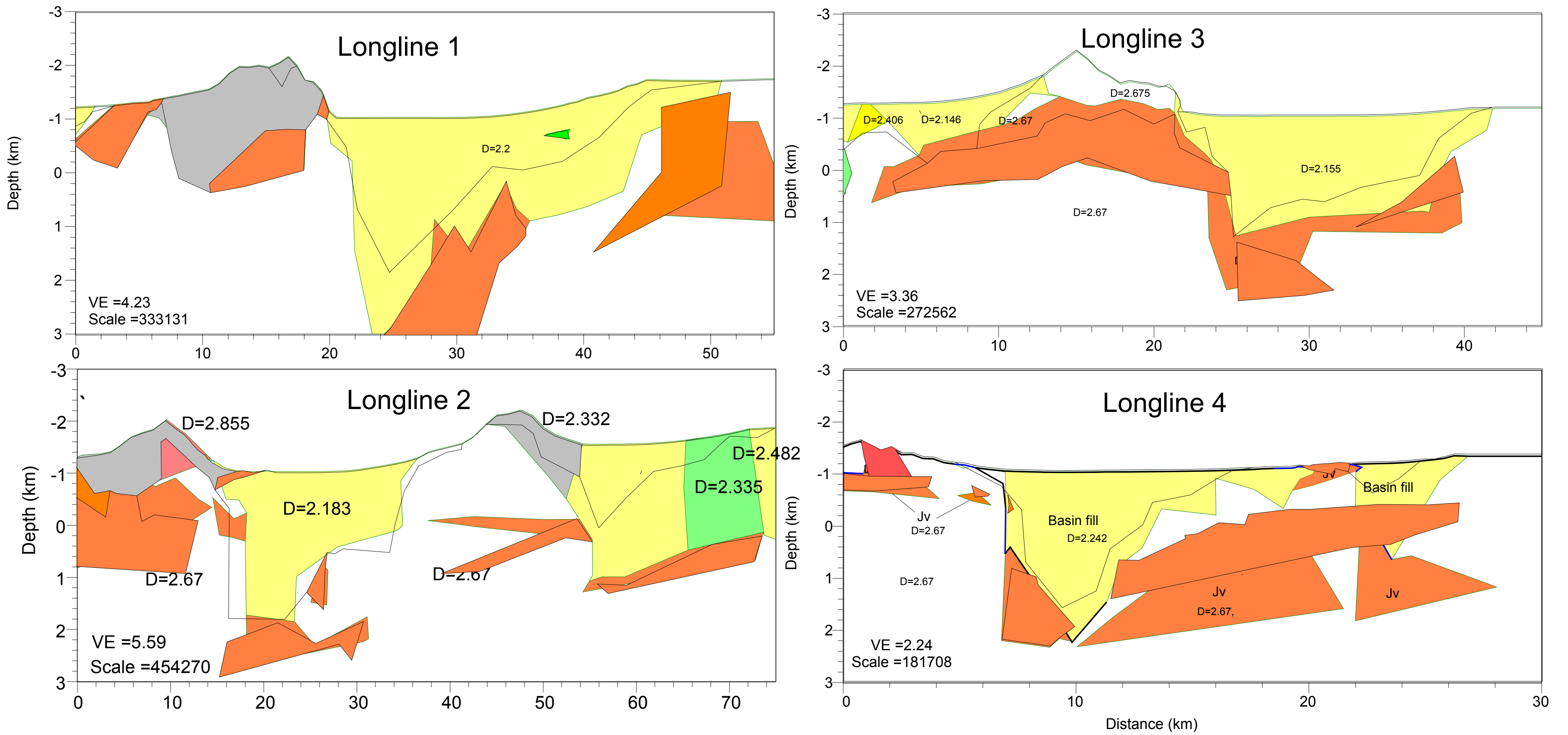

Longline 1
D=2.2
VE =4.23
Scale =333131
Longline 3
D=2.675
D=2.406
D=2.146
D=2.67
D=2.155
D=2.67
VE =3.36
Scale =272562
Longline 2
D=2.855
D=2.332
D=2.482
D=2.335
D=2.183
D=2.67
D=2.67
VE =5.59
Scale =454270
Longline 4
Jv
Basin fill
Basin fill
D=2.242
Jv
D=2.67
D=2.67
Jv
D=2.67,
Jv
VE =2.24
Scale =181708
Depth (km)
Distance (km)

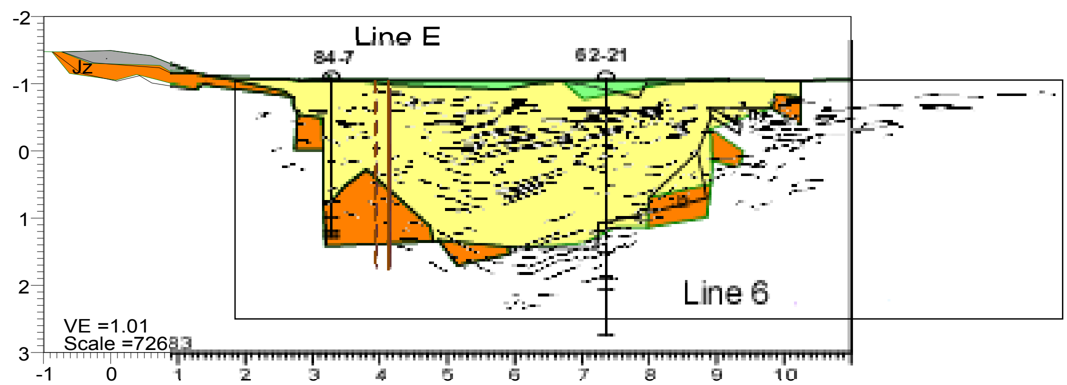

Line E
84-7
62-21
Jz
Line 6
VE =1.01
Scale =72683

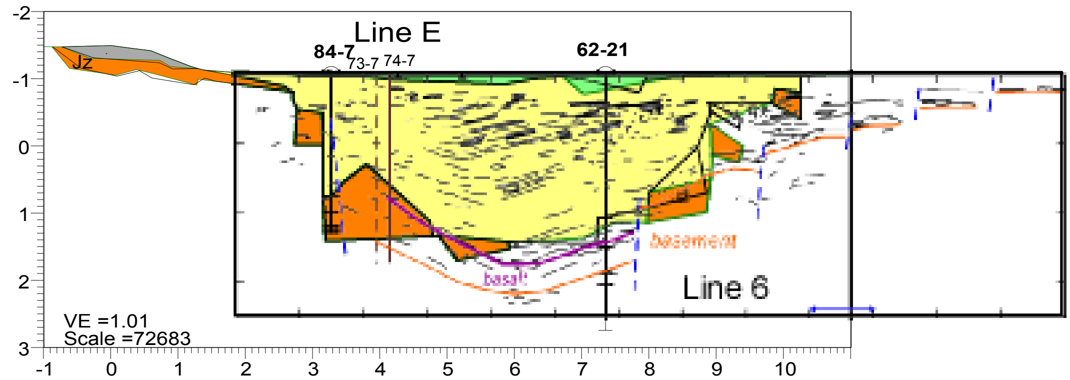
Line E
84-7
73-7
74-7
62-21
Jz
basement
basalt
Line 6
VE =1.01
Scale =72683
-2
-1
0
1
2
3
-1
0
1
2
3
4
5
6
7
8
9
10

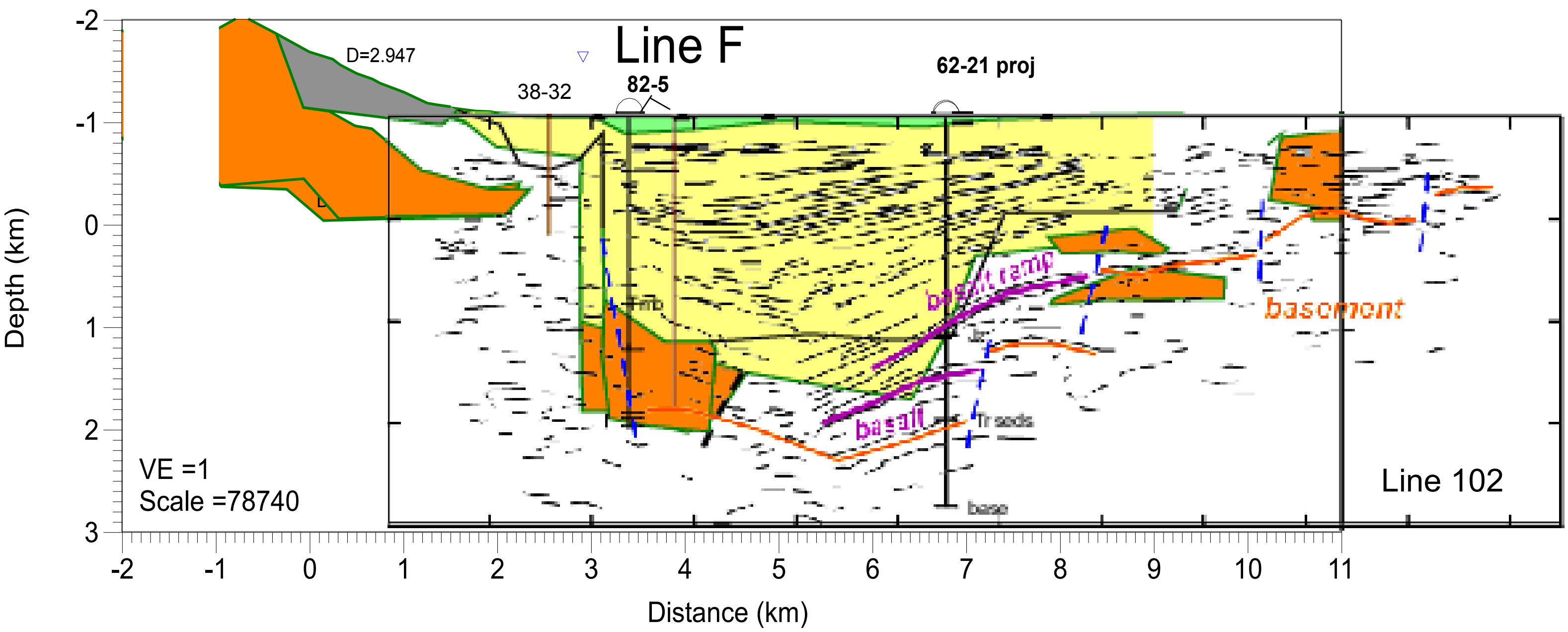

Line F
D=2.947
38-32
82-5
62-21 proj
basalt ramp
basalt
basement
Tr seds
Line 102
VE =1
Scale =78740
Depth (km)
Distance (km)

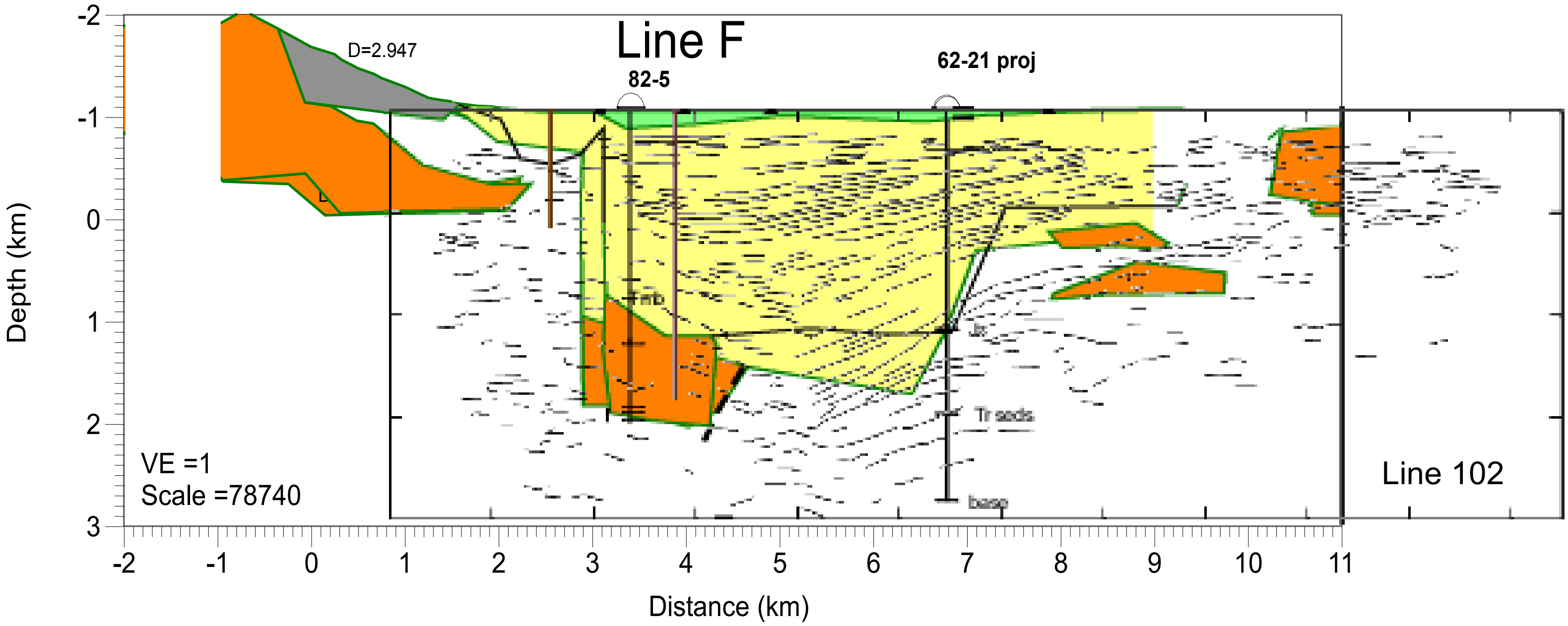

Line F
D=2.947
82-5
62-21 proj
Tr seds
base
VE =1
Scale =78740
Line 102
Depth (km)
Distance (km)
-2
-1
0
1
2
3
-2
-1
0
1
2
3
4
5
6
7
8
9
10
11

PART II-APPENDIX 4

MAGNETIC SUSCEPTIBILITY SENSITIVITY ANALYSIS FOR SECTIONS CC', DD', EE' AND FF'

The results of a magnetic susceptibility sensitivity analysis are presented in Figure A4-1.

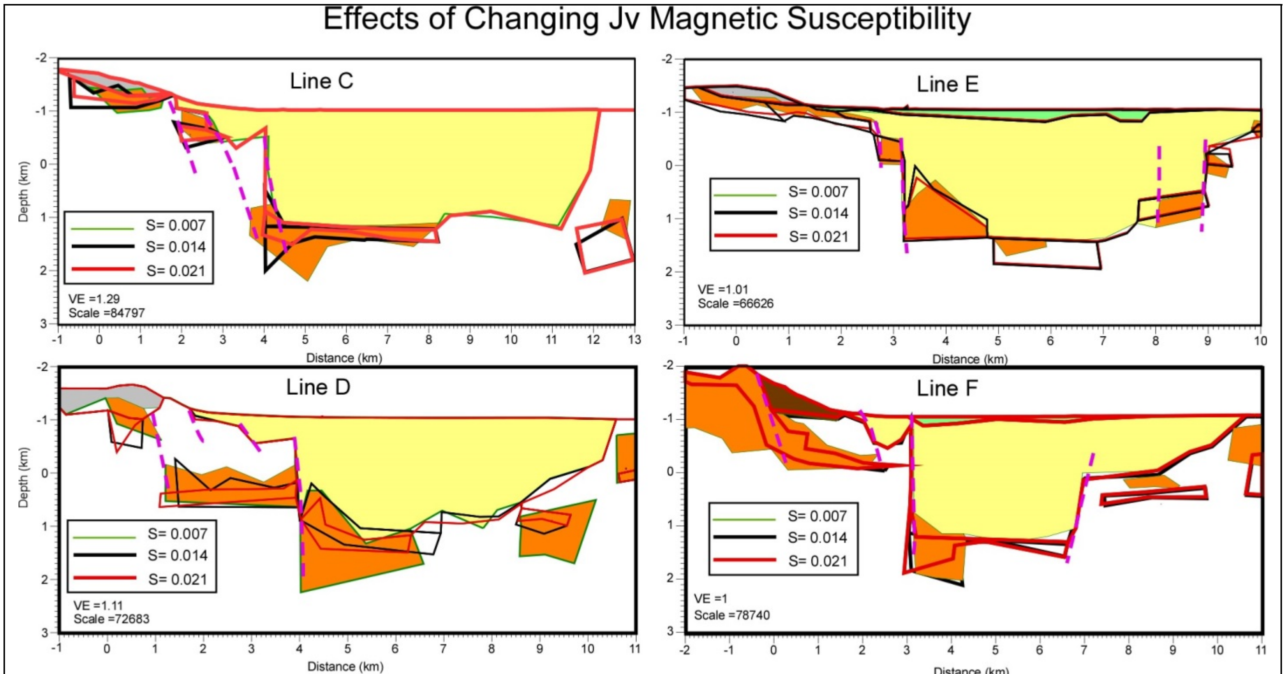

Figure A4-1. Effects of changing magnetic susceptibilities (S cgs) of magnetized Jurassic volcanics (Jv) on joint gravity and magnetic profiles for lines C, D, E, and F. Residual gravity values and helicopter magnetics were used in the modeling and the precision of fit was better than 2% in each case. The model with S= 0.007 is shown as filled orange polygons with green edges, while the models for S= 0.014 and S=0.21 are shown with black and red outlines. Faults inferred from the S=0.007 model (reported earlier) are shown as dashed lines in magenta.

PART II-APPENDIX 5

NEW AMBIENT SESIMIC SURVEY DATA AVAIABILITY, LOCATION OF POTENTIAL SOURCES OF SEISMIC EVENTS DURING THE SURVEYAND LOCATION OF SESIMIC STATIONS IN THE DIXIE VALLEY EXTENDED STUDY AREA (DVESA)

Table 5-1. Data availability for the two DVSA seismic surveys

Station	Start date	End date	Data gaps:
A01	06/15/2011	10/08/2011	
A02	06/17/2011	10/09/2011	07/01/2011 to 07/26/2011
A03	06/16/2011	10/01/2011	
A04	06/20/2011	10/07/2011	07/15/2011 to 07/17/2011 and 08/24/2011 to 09/23/2011
A05	06/20/2011	10/04/2011	
A06	06/20/2011	10/07/2011	06/21/2011 to 06/25/2011; 07/27/2011 to 07/29/2011;
A07	06/21/2011	10/06/2011	
A08	07/01/2011	10/03/2011	
A09	06/23/2011	10/05/2011	07/12/2011 to 07/23/2011
A10	06/20/2011	10/08/2011	
A11	06/30/2011	10/04/2011	
A12	06/17/2011	10/04/2011	
A13	06/16/2011	10/06/2011	
A14	06/24/2011	10/11/2011	
A15	06/22/2011	10/05/2011	
A16	06/22/2011	10/05/2011	
A17	06/20/2011	10/04/2011	07/01/2011 to 07/04/2011
A18	06/14/2011	10/02/2011	
A19	06/29/2011	10/13/2011	07/24/2011 to 08/23/2011
A20	06/22/2011	10/12/2011	
A21	06/23/2011	10/11/2011	
B01	10/12/2011	02/11/2012	
B02	10/12/2011	02/11/2012	
B03	10/11/2011	02/11/2012	
B04	10/06/2011	02/10/2012	
B05	10/09/2011	02/10/2012	
B06	10/10/2011	02/08/2012	
B07	10/10/2011	02/08/2012	
B08	10/09/2011	02/08/2012	
B09	10/07/2011	02/09/2012	
B10	10/07/2011	02/09/2012	
B11	10/06/2011	02/09/2012	
B12	10/10/2011	02/09/2012	
B13	10/12/2011	02/11/2012	10/15/2011 to 11/18/2011
B14	10/13/2011	02/11/2012	
B15	10/08/2011	02/08/2012	
B16	10/13/2011	02/08/2012	
B17	10/11/2011	02/11/2012	
B18	10/08/2011	02/11/2012	
B19	10/05/2011	02/10/2012	
B20	10/04/2011	02/09/2012	
B21	10/07/2011	02/09/2012	

Table 5-2. Presents the location of known mines in the DVESA area, the Dixie Valley geothermal power plant, and of the publicly available Navy bombing range locations near Fallon, NV. The Navy bombing range information is available at http://clui.org/ludb/site/bravo-20-bombing-range. The mine information is available on the Nevada Bureau of Mines website. This information was used to identify explosions and explosion locations and use them as an input to in the LOTOS P/S tomography calculations.

Possible explosion source	**Latitude (deg)**	**Longitude(deg)**
Bravo 20 Bombing Range	39.867588	-118.370476
Bravo 19 Bombing Range	39.151497	-118.704102
Bravo 17 Bombing Range	39.237156	-118.262032
Bravo 16 Bombing Range	39.332954	-118.873337
Black Rock Desert	40.820564	-119.144325
Lone Tree Mine,Newmont Mining Corp.	40.831789	-117.2109
Marigold Mine, Operator: Goldcorp, Inc.P.O. Box 160, Valmy, NV 89438	40.792206	-117.128145
MIN-AD Mine and Mill, *Operator:* MIN-AD, Inc.**,** P.O. Box 22**,** Winnemucca, NV 89446	40.970940	-117.757915
Colado Mine and Plant (10), Mill *Operator:*EP Minerals, LLC 150 Coal Canyon Road, Lovelock, NV 89419	40.240811	-118.359624
Empire Mine (11), Mill (11*)-in Washoe County *Operator:* United States Gypsum Co.*,* P.O. Box 130 Empire, NV 89405	40.577177	-119.341218
Florida Canyon Mine, *Operator:* Florida Canyon Mining, Inc.**,** P.O. Box 330**,** Imlay, NV 89418	40.577942	-118.242277
Argenta Mine and Mill, *Operator:* Baker Hughes Drilling Fluids**,** P.O. Box 277**,** Battle Mountain, NV 89820; **Battle Mountain Grinding Plant (Greystone Mine), Mill**	40.586655	-116.688473
Mule Canyon Mine; *Operator:* Newmont Mining Corp.**,** P.O. Box 388**,** Valmy, NV 89438	40.737700	-117.200900
Phoenix Project, *Operator:* Newmont Mining Corp.**,** P.O. Box 388**,** Valmy, NV 89438		
Ruby Hill Mine, *Operator:* Barrick Gold Corporation*,* P.O. Box 676**,**Eureka, NV 89316	39.553624	-115.989924
Moltan Company (2) *Operator:* Moltan Company P.O. Box 860 Fernley, NV 89408	39.789727	-119.016500
Other mines	40.2855	-118.149
	40.6335	-117.1336
	40.8740	-118.6852
	40.1251	-118.4296
	40.3162	-118.6104
	39.4273	-118.5209
Iron Mine west of Stillwater Range	40.0880	-118.1900
Geothermal plant	39.9664	-117.8557

Table 5-3. Station locations and elevations in the DVSA and DVESA (see text for an explanation). The bold letter stations were used for the DVSA_PHVEL_MOD; see text for an explanation.

Station	**Latitude (deg)**	**Longitude (deg)**	**Elevation (km)**
A01	39.9390	-117.7821	1.0677
A02	39.9331	-117.7880	1.0453
A03	39.9329	-117.7737	1.0757
A04	40.0134	-117.8121	1.0589
A05	39.9917	-117.7204	1.0651
A06	39.8799	-117.7297	1.2050
A07	39.8352	-117.8421	1.0516
A08	39.6749	-118.1448	1.0762
A09	40.0596	-117.9129	1.6678
A10	40.0588	-117.7561	1.0600
A11	39.9269	-117.6595	1.1781
A12	39.7376	-117.8376	1.4332
A13	39.7223	-117.9695	1.0650
A14	39.9943	-118.1851	1.2454
A15	40.1632	-117.9181	1.2485
A16	40.2143	-117.7827	1.6502
A17	40.0338	-117.6235	1.1372
A18	39.6635	-117.6927	1.5753
A19	39.5892	-117.8604	2.0357
A20	39.8096	-118.2340	1.2661
A21	40.1168	-118.1050	1.2637
B01	39.8848	-118.2397	1.1804
B02	39.9723	-118.2041	1.1942
B03	40.0746	-118.0648	1.2280
B04	39.9870	-117.8450	1.0325
B05	39.9433	-117.9408	1.0707
B06	39.8630	-118.0100	1.0200
B07	39.8704	-118.0161	1.0660
B08	39.8750	-118.0040	1.0220
B09	39.8350	-117.8420	1.0490
B10	39.8411	-117.7027	1.2990
B11	39.8030	-117.8720	1.0740
B12	39.7371	-117.9422	1.0710
B13	39.7541	-118.2750	1.1880
B14	39.6898	-118.2823	1.3530
B15	39.6720	-118.0780	1.0280
B16	39.5843	-118.0789	1.1110
B17	40.0975	-117.9939	1.2330
B18	40.0590	-117.7560	1.0550
B19	39.9910	-117.7200	1.0610
B20	39.6890	-117.9700	1.0990
B21	39.9077	-117.7625	1.0800
ADH	37.9682	-118.7163	2.0430
AMD	36.4526	-116.2818	0.7754
ANT	37.9177	-118.5650	2.0400
BAB	39.6024	-120.1059	2.6590
BFC	38.8938	-119.6094	1.7440
BMR	40.1086	-120.2920	2.1460

Table 5-3. Station locations and elevations in the DVSA and DVESA (see text for an explanation). The bold letter stations were used for the DVSA_PHVEL_MOD; see text for an explanation.

Station	**Latitude (deg)**	**Longitude (deg)**	**Elevation (km)**
BTW	36.9978	-116.5674	1.3910
CMB	38.0345	-120.3865	0.6970
DIX	39.8021	-118.0830	1.1430
DOM	37.0021	-116.4095	1.7110
EBP	38.5827	-119.8073	2.4320
ELK	40.7448	-115.2388	2.2100
EMB	38.9747	-120.1029	2.1342
EUR	39.7541	-120.7119	1.9510
FPK	39.2250	-118.1516	2.4940
GNO	38.9291	-119.8538	1.6460
GZY	39.9619	-120.6513	1.9350
HCK	38.0754	-118.5932	1.8900
IND	39.4342	-120.2927	2.1460
LHV	38.2513	-118.5049	2.3530
LOY	39.6586	-120.2368	1.5820
LUL	38.0522	-119.1813	2.2430
MPK	39.2928	-120.0364	2.5990
MPT	38.0633	-118.7804	2.1780
SAT	39.6024	-120.4480	1.9720
SBT	39.6267	-120.6669	2.1520
STRY	39.3151	-119.6386	1.8397
TAH	39.1515	-120.1630	2.0790
TIM	37.0667	-116.4703	1.8710
VPK	39.4722	-120.0398	2.5620
WENL	37.6221	-121.7569	0.0138
WHR	40.0362	-118.3621	1.4940
WVOR	42.4339	-118.6367	1.3440
PAH	39.7106	-119.3854	1.5200
YER	38.9852	-119.2406	1.8570
WVA	39.9444	-119.8250	1.6700
WAK	38.5043	-119.4382	1.8900
PNT	39.0891	-119.5997	2.0760
KVN	39.0484	-118.1012	1.8290
PEA	39.6075	-119.9613	2.1424
DON	39.3517	-120.3205	2.2680
RYN	38.6281	-118.5223	1.6510
BEK	39.8666	-120.3596	1.7430
SJC	38.349	-119.4400	2.2460
SMI	39.8672	-120.5306	2.3440

PART II-APPENDIX 6

LOTOS DVSA P/S TOMOGRAPHY RESULTS AND DVESA_LOTOS_MOD

INTRODUCTION

The tomographic algorithm, *LOTOS-10*[1] (Local Tomography Software) is designed for simultaneous inversion for P and S velocity structures and source coordinates. The main steps of the calculations are shown in Figures 6-1 and 6-2. The LOTOS-10 algorithm is available at ivan.science@gmail.com.

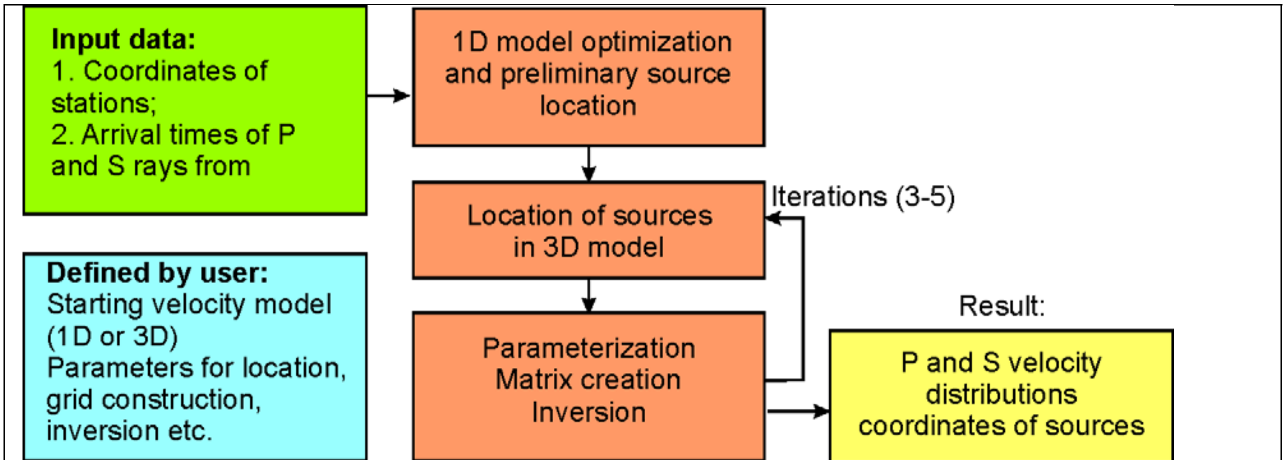

Figure 6-1. General structure of the LOTOS code. Red blocks indicate the main program steps. The green block describes the main input data; the blue block shows input parameters defined by user; the yellow block shows the output data. This figure is from the LOTOS documentation materials (Koulakov,2009).

The algorithm contains the following general steps:

1. Simultaneous optimization for the best 1D velocity model and preliminary location of sources;
2. Location of sources in the 3D velocity model; and
3. Simultaneous inversion for the source parameters and velocity model using several parameterization grids.

Steps 2 and 3 are repeated in several iterations.

METHOD

A parameter file (Table 6-1) containing all the input data is created before running LOTOS. Parameter files with horizontal and vertical (Table 6-2) sections are also created. The steps involved in using the LOTOS method are described below.

1D-velocity optimization and preliminary source locations

The starting 1D velocity model (Table 6-3), a model optimization (Table 6-4) and initial locations of sources (Table 6-5) are obtained by selecting the events with the maximum number of phase arrival time picks, from every available depth. The source location is based on calculating a "goal function" that reflects the probability of a source location in a current point. Searching for the GF extreme is performed using a grid search method, starting with a coarse grid and finishing with a fine grid.

[1] LOTOS information is provided by Dr Ivan Koulakov in the program description files. The following material is an extract from the files made available by Dr Koulakov (personal communication with Dr. Ileana Tibuleac).

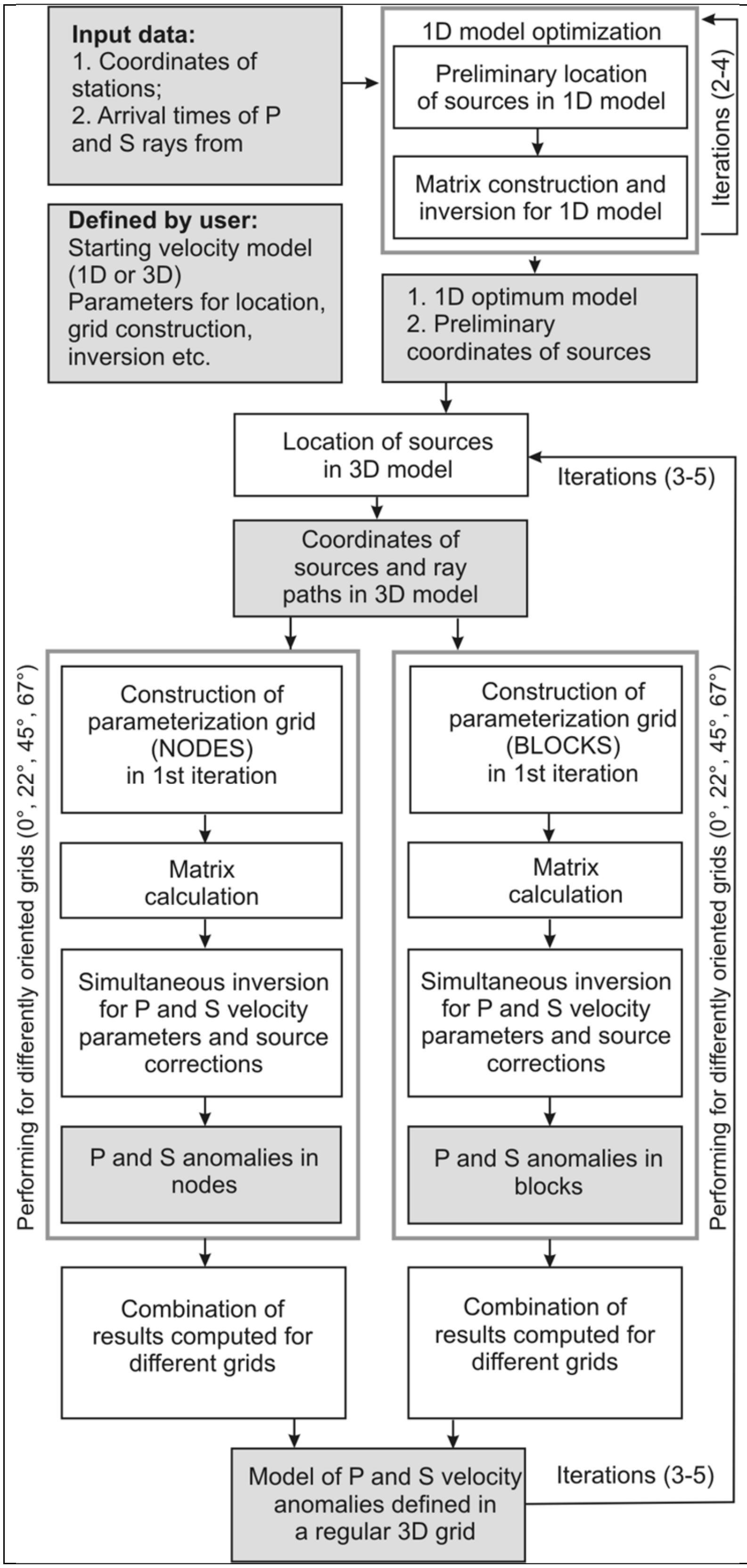

Figure 6-2. The main program steps and data blocks in the LOTOS code for the case of Vp-Vs inversion scheme, used in this study. This figure is from theLOTOS documentation materials (Koulakov,2009). The 1D model optimization results in new source locations and in a new, optimum model (Table 6-4). The relocated sources (red) and the DVSA seismic stations are shown in Figure 6-5.

The Sources Are Relocated Using a Code Based on 3D Ray Tracing (bending)

Because the grid search method, which is very efficient for 1D models, is time consuming when 3D ray tracing is applied, a gradient method is thus used (Koulakov et al., 2009) to locate sources in 3D models, which is not as robust as the grid search method, but is much faster.

Grid parameterization with nodes

IThe velocity perturbations are parametrized with nodes. The nodes are installed in the study volume using the algorithm described in Koulakov et al. (2006). The nodes are based on vertical lines distributed regularly in map view (e.g., with steps of 1km x1km). In each vertical line, the nodes are installed according to the ray distribution. A ray is the trajectory of the seismic wave through the Earth. In the absence of rays, no nodes are installed. The spacing between the nodes is chosen to be smaller in areas of higher ray density. However, to avoid excessive concentration of nodes, a minimum spacing is defined (e.g., 1km). Between the nodes, the velocity distribution is approximated linearly.

To reduce the effect of node/cell distributions on the results, the inversion is performed using several grids with different basic orientations (e.g., 0°, 22°, 45°, and 67°). After computing the results for grids with different orientations, they are stacked into one summary model, reducing model artifacts related to grid orientation. If the parameterization spacing is significantly smaller than the sizes of the expected anomalies, results of the inversion are almost independent of the distribution of nodes/cells. The construction of the parameterization grids is performed only in the first iteration. In the next iterations, the algorithm uses the same node/cell configurations.

The steps of grid construction, matrix calculation and inversion are performed for several grids with different basic orientations. The resulting velocity anomalies derived for all grids are combined. This model is added to the absolute velocity distributions used in a previous iteration. New iterations repeat the steps of source location, matrix calculation, and inversion.

Matrix Calculation and Inversion for the Case of Vp-Vs Scheme

The first derivative matrix is calculated using the ray paths computed after the source locations in the 3D model. Each element of the matrix, $A_{ij} = \partial t_i / \partial v_j$, is equal to the time (t) deviation along the *i*-th ray due to a unit velocity (v) perturbation in the *j*-th node/block. Inversion of the entire sparse matrix A is performed using an iterative *LSQR* code (see Koulakov, 2009 and references herein). In addition to *P* and *S* velocity parameters, the matrix contains the elements responsible for the source (*dx, dy, dz,* and *dt*), and station corrections. Amplitude and smoothness of the solution is controlled by two additional blocks. The first block is a diagonal matrix with only one element in each line and zero in the data vector. Increasing the weight of this block reduces the amplitude of the derived P or S velocity anomalies. The second block controls the smoothing of the solution. Each line of this block contains two equal nonzero elements of opposite sign that correspond to all combinations of neighboring node/cells in the parameterization grid. The data vector in this block is also zero. Increasing the weight of this block reduces the difference between solutions in neighboring nodes, resulting in smoothing of the computed velocity fields.

Results

The LOTOS resulting models were stored in MAT_MOD files and structures (Appendix 10) and were used to estimate the DVSA_INPUT_MODEL. Examples of horizontal slices through the resulting Vp and Vs models are shown in Figure 6-3. An example of Vp/Vs maps at selected depths are shown in Figure 6-4. The re-located sources used to estimate the models are shown in Figure 108 (main text). To illustrate the model resolution (lower below 3 km), examples of vertical and horizontal section nodes were shown in Figures 6-5 to 6-6. The resolution of the tomographic model estimated using LOTOS is best from 5 to 12km deep. Higher node density is equivalent to better resolution. Examples of vertical sections through the model were shown in Figures 6-7 to 6-12. In each figure, the plot shows P or S- velocity model anomalies (%) relative to the reference model. The red dots are earthquakes re-located within 2km of the vertical section.

Table 6-1. The model parameter file used in this study. The parameters are described by Dr Koulakov in the LOTOS instruction manual available from the LOTOS website.

```
********************************************************
GENERAL INFORMATION :
1          KEY 1: REAL; KEY 2: SYNTHETIC
2          KEY 1: Vp and Vs; KEY 2: Vp and Vp/Vs
0          KEY 0: all data, KEY 1: odd events, KEY 2: even events
1          Ref. model optimization (0-no; 1-yes)
********************************************************
AREA_CENTER :
-117.85 39.97     Center of conversion to XY
********************************************************
ORIENTATIONS OF GRIDS :
4                                    number of grids
0 22 45 67                 orientations
********************************************************
1D MODEL PARAMETERS :
5                    Iterations for 1D inversions
-2.5 3. 5                 zmin, dzstep depth step for finding the best event
0.25 0.25 300              dsmin, dzlay,zgrmax : parameters for 1D tracing
1                    dz_par, step for parameterization
0.2
6. 9.         sm_p,sm_s
0.0 0.0       rg_p,rg_s
5 5 1       w_hor,w_ver,w_time
300                  LSQR iterations
0            nsharp
30               z_sharp
********************************************************
INVERSION PARAMETERS :
40 1                         LSQR iterations, iter_max
1 0.8 Weights for P and S models in the upper part
1.3 1.6 level of smoothing (P, S and crust)
0.0 0.0 regularization level (P, S and crust)
0.0001   0.0001 weight of the station corrections (P and S)
2.0        wzt_hor
2.0        wzt_ver
1.0        wzt_time
```

****

Parameters for location in 1D model using reference table and data selection:

****

LIN_LOC_PARAM :

5 krat min Minimal number of records

80 km, maximum distance to nearest station

1.3 S max resid with respect to P max resid

60 dist_limit=100 : within this distance the weight is equal

1.5 n_pwr_dist=1 : power for decreasing of W with distance

10 ncyc_av=10

! For output:

30 bad_max=30 : maximal number of outliers

0.05 maximal dt/distance

30 distance limit

10 Frequency for output printing

1 Number of different grids

0.05 0.05 0.05 dx,dy,dz

0. res_loc1=0.2 : lower limit for location (for LT residuals, W=1)

1 res_loc2=1.5 : upper limit for location (for GT residuals, W=0)

2. w_P_S_diff=2 (+ causes better coherency of P and S)

****

Parameters for 3D model with regular grid

****

3D_MODEL PARAMETERS:

-80. 80. 1. xx1, xx2, dxx,

-80. 80. 1. yy1, yy2, dyy,

-2.5 20. 1. zz1, zz2, dzz

2 distance from nearest node

0 Smoothing factor1

****

Parameters for grid construction

****

GRID_PARAMETERS:

-80. 80. 1. grid for ray density calculation (X) km

-80. 80. 1. grid for ray density calculation (Y) km

-2.5 20. 1. min and max levels for grid km

1 ! Grid type: 1: nodes, 2: blocks

1 !min distance between nodes in vert. direction

0.05 100.0 !plotmin, plotmax= maximal ray density, relative to average

-2.5 !zupper: Uppermost level for the nodes

2 !dx= step of movement along x

2 !dz= step of movement along z

****

Parameters for location in 3D model using bending tracing
****
LOC_PARAMETERS:
! Parameters for BENDING:
1 ds_ini: basic step along the rays
5 min step for bending
0.01 min value of bending
5 max value for bending in 1 step

! Parameters for location
20 dist_limit=100 : within this distance the weight isequal
1 n_pwr_dist=1 : power for decreasing of W with distance
10 ncyc_av=10

0.0 res_loc1=0.2 : lower limit for location (for LT residuals, W=1)
1. res_loc2=1.5 : upper limit for location (for GT residuals, W=0)
2. w_P_S_diff=2 (+ causes better coherency of P and S)
5. stepmax
0.5 stepmin
5 Frequency for output printing
****
Parameters for calculation of the reference table:
****
REF_PARAM:

0.04 epi_step min step
40. zraymax max depth
110. distmax max distance
4 number of depth steps
0 1 depth, step
10 1 depth, step
16 2
40 5 depth, step
40 maximal depth

Table 6-2. Vertical section end points and denominations

Lon (deg)	Lat (deg)	Lon (deg)	Lat (deg)	End point 1	End point 2
-118.033473	39.849262	-117.794682	40.002172	A	A’
-117.943078	39.92406	-117.800561	40.01031	B	B’
-117.930928	39.973896	-117.849989	39.905748	C	C’
-117.899931	39.981321	-117.829468	39.920775	D	D’
-117.880476	39.988162	-117.814568	39.930797	E	E’
-117.864925	40.002445	-117.790978	39.946307	F	F’
-117.842959	40.003068	-117.801960	39.970401	G	G'
-117.831963	40.018905	-117.774954	39.970107	H	H'
-117.825960	40.030237	-117.755954	39.969503	I	I'
-117.807952	40.037698	-117.755952	39.984207	J	J'

Table 6-2. Vertical section end points and denominations

-118.181965	39.732535	-118.136960	39.708613	A1	A1'
-118.050956	39.826391	-118.022959	39.801972	A2	A2'
-118.025272	39.845262	-117.998450	39.832513	A3	A3'
-118.017669	39.874187	-117.994988	39.867176	A4	A4'
-117.986964	39.922402	-117.928957	39.885005	A5	A5'
-117.906453	39.957612	-117.893545	39.936377	A6	A6'
-118.196972	39.982895	-117.798867	39.719137	LL1	LL1'
-118.142998	39.988819	-117.679894	39.711876	LL2	LL2'*
-118.152963	40.061093	-117.796452	39.824507	LL3	LL3'
-117.927960	40.001733	-117.681424	39.867073	LL4	LL4'
-118.65	39.15	-117.15	40.65	X	X'

Table 6-3. Starting 1D velocity model (Vp/Vs ratio = 1.7)

Depth (km)	**Vp (km/s)**	**Vs (km/s)**
-1	2.7	1.6
3	3.8	2.22
4.0	5.5	3.2
5.0	6.0	3.5
7.0	6.3	3.67
15.0	6.8	3.96
35.0	8.0	4.42
74.0	8.3	4.54
Velocity model estimated from autocorrelations (shown here only for comparison)		
Depth (km)	**V_P (km/s)**	**V_S (km/s)**
-1.0	2.1	1.0
0.0	3.	1.98
2.0000	5.2	3.14
6.0000	5.63	3.38
10.0000	5.50	3.30
22.0000	7.43	4.01
30.00	8	4.5

Table 6.4. The reference model estimated after model optimization in LOTOS.

Depth (km)	Vp (km/s)	Vs (km/s)
0	2.662	1.846
1.0	2.939	1.998
2.0	3.223	2.144
3.0	3.509	2.285
4.0	5.224	3.248
5.0	5.746	3.529
6.0	5.906	3.581
7.0	6.007	3.598
8.0	6.016	3.566
9.0	6.042	3.551
10.0	6.057	3.554
11.0	6.059	3.545
12.0	6.085	3.541
13.0	6.185	3.652
14.0	6.464	3.737
15.0	6.603	3.770
16.0	6.680	3.824
17.0	6.82765	3.940
18.0	6.904	3.993
74.0	8.300	4.540

Table 6-5. Earthquake and explosion location - input values

Longitude (deg)	Latitude (deg)	Depth (km)
-118.4749	39.3412	5.1768
-118.3705	39.8675	0.0631
-118.3705	39.8675	0
-118.3677	39.867	4.6639
-117.845	39.9809	3.8477
-117.8542	39.9676	3.476
-117.8463	39.9765	4.9528
-117.8288	39.9751	6.9765
-118.489	39.3327	14.2688
-118.149	40.2855	0
-117.5645	39.3389	16.2053
-117.8721	39.967	0
-117.8571	39.9589	1.1741
-117.8689	39.9638	0
-117.8623	39.9681	4.4144
-117.8588	39.9622	2.1837
-117.9285	39.7129	7.0215
-117.9394	39.7191	4.8574
-117.9312	39.703	6.989
-118.3596	40.2408	0

Table 6-5. Earthquake and explosion location - input values

Longitude (deg)	Latitude (deg)	Depth (km)
-118.4296	40.1251	0
-118.149	40.2855	0
-117.1336	40.6335	7.6136
-118.3704	39.8675	0
-118.3095	40.4933	20.2938
-118.6104	40.3162	0
-118.5367	39.9182	0
-118.4789	39.5775	7.0434
-118.3704	39.8675	0
-118.4337	39.9148	0
-118.1578	40.2855	0
-118.3704	39.8675	0
-117.1336	40.6335	0
-117.1818	40.5375	14.2719
-118.056	39.6847	10.9425
-118.3704	39.8675	0
-118.5209	39.4273	0
-118.19	40.088	0
-118.0565	39.6983	9.8919
-117.8677	40.1074	7.5475
-117.8581	39.9809	3.1371
-117.7329	40.2665	9.7402
-118.149	40.2855	0
-117.8553	39.9837	0
-117.7808	40.2555	11.6424
-117.8149	40.2738	9.8909
-117.8006	40.1244	14.4489
-117.8635	39.954	0
-117.8474	40.111	4.8807
-117.8812	40.0139	0
-117.8557	39.968	2.4764
-117.7702	40.202	8.6834
-117.7315	40.262	13.9326
-117.8355	39.8	2.3361

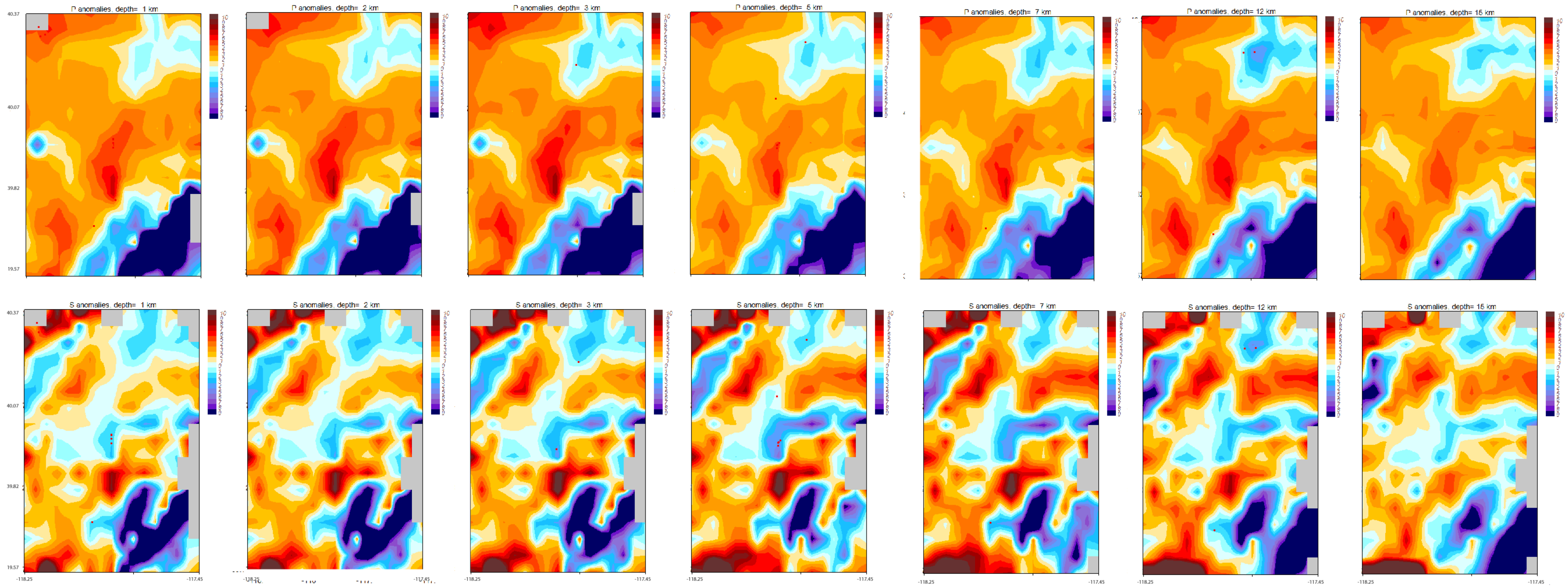

Figure 6-3. Tomographic images of P-wave velocity anomalies (% from the mean model) (upper plots) at 1km, 2km, 3km, 5km, 7km, 12km and 15km depth, from left to right. S-velocity anomalies are shown in the lower plots, at the same depths. Red dots are relocated earthquakes within 2 km of the horizontal section. The section boundaries are from 39.57N to 40.37 N and from 177.45 W to 118.25 W.

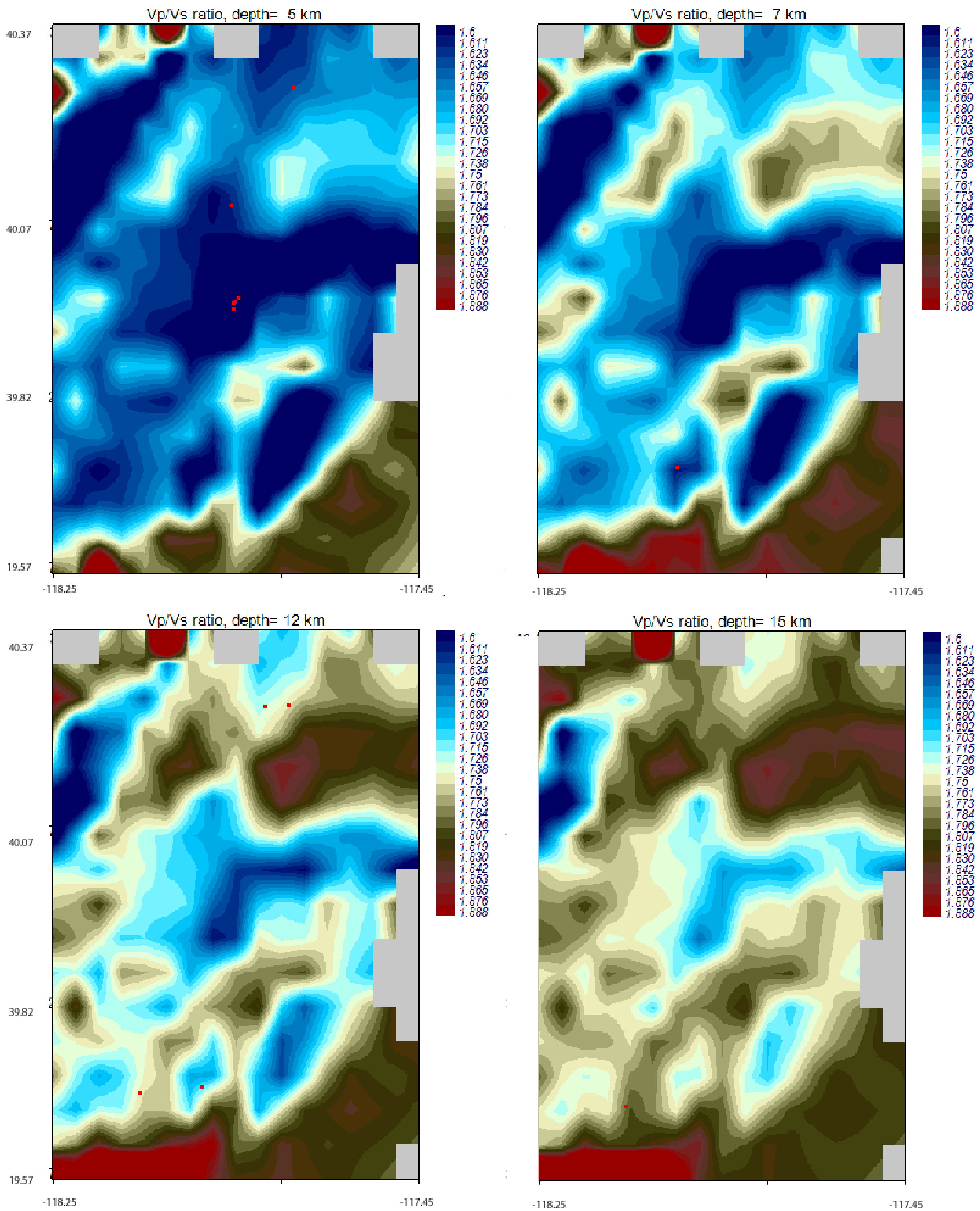

Figure 6-4. Tomographic images of Vp/Vs-wave velocity anomalies (%) 5km, 7km, 12km and 15km depth, from left to right. Red dots are relocated earthquakes within 2km of the horizontal section. The section boundaries are from 39.57N to 40.37 N and from 177.45 W to 118.25 W.

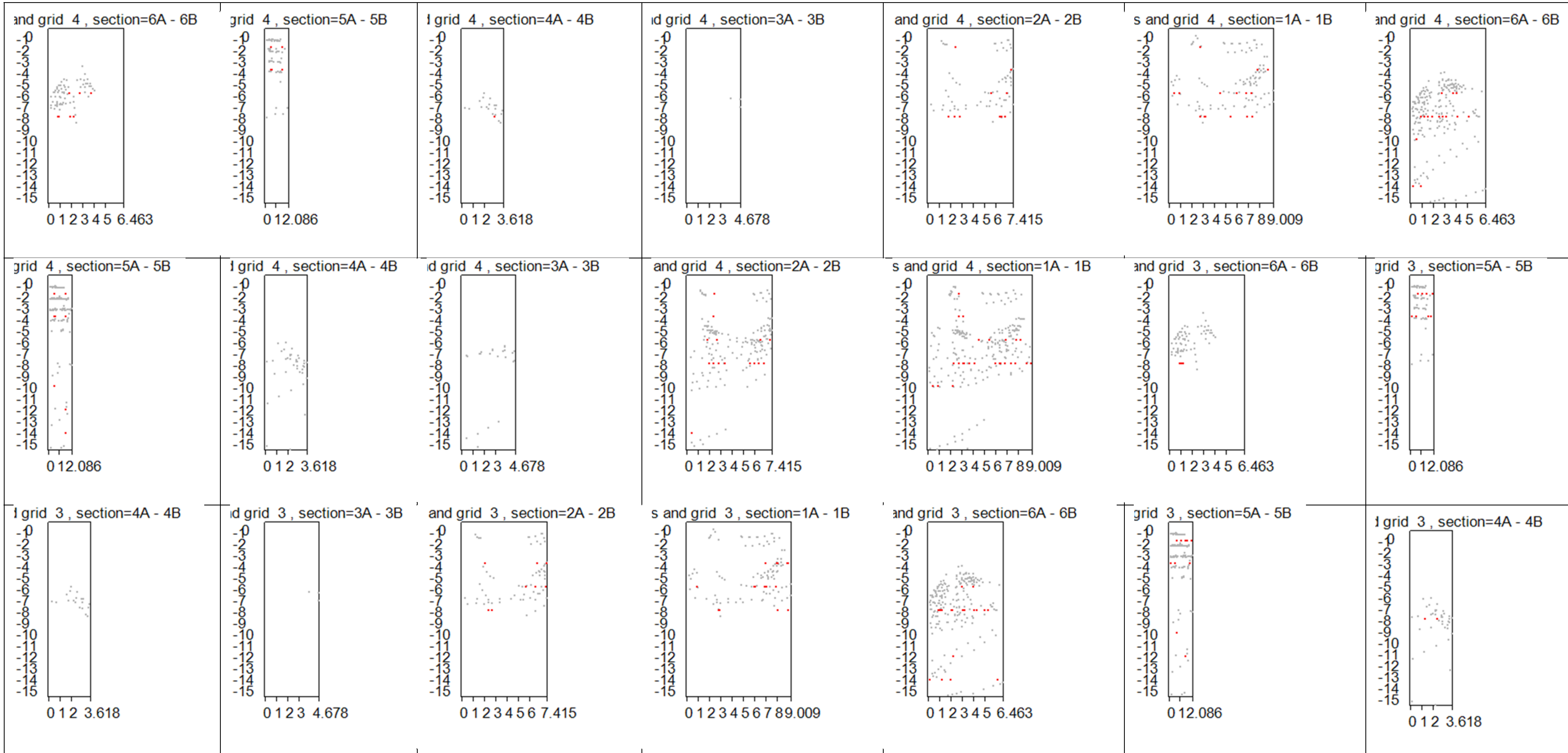

Figure 6-5A. The number of nodes (gray) used for each of the vertical sections for 4 separate grid orientations (Table 6-1), at 0, 22, 45 and 67 degrees from north.

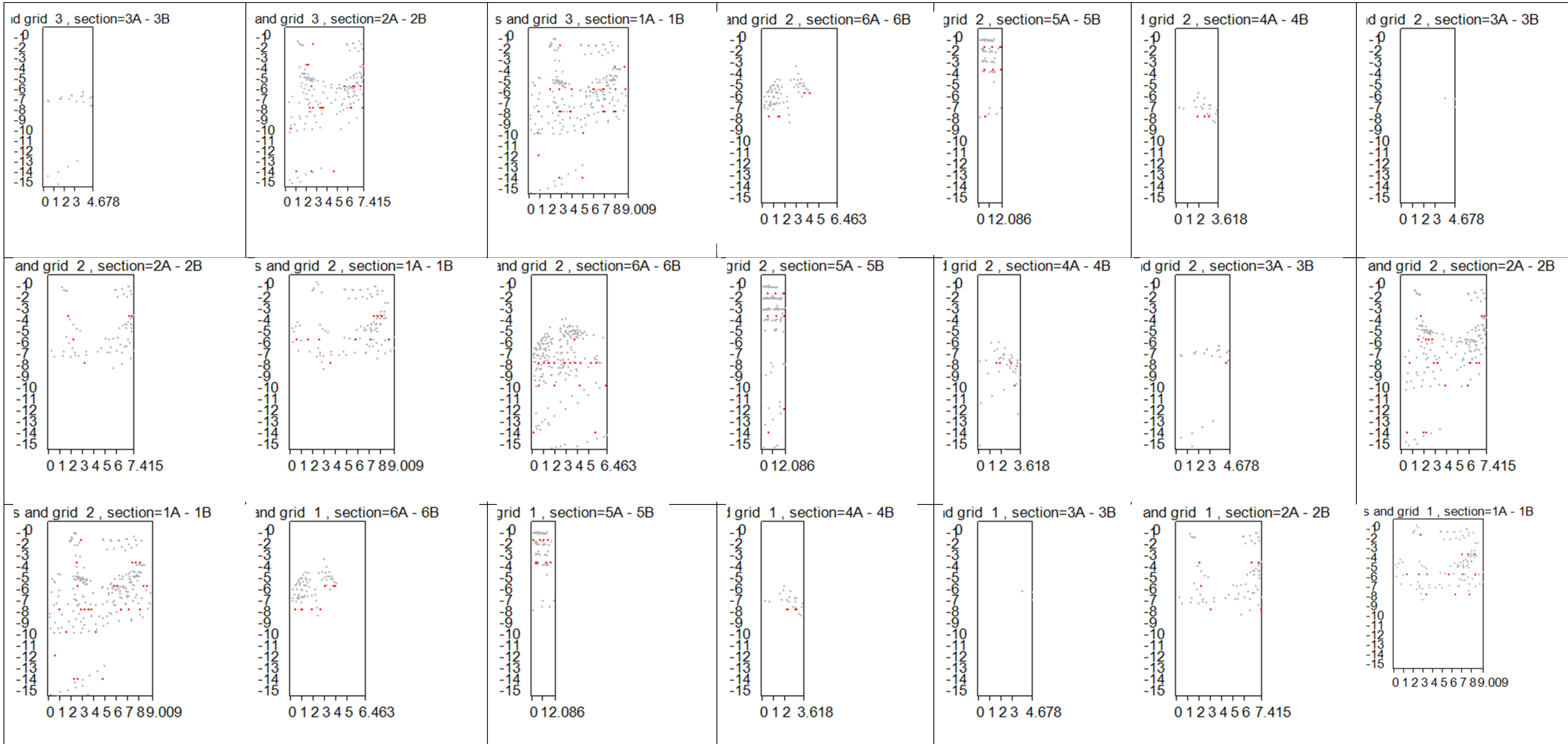

Figure 6-5B. The number of nodes (gray) used for each of the vertical sections for 4 separate grid orientations (Table 6-1), at 0, 22, 45 and 67 degrees from north.

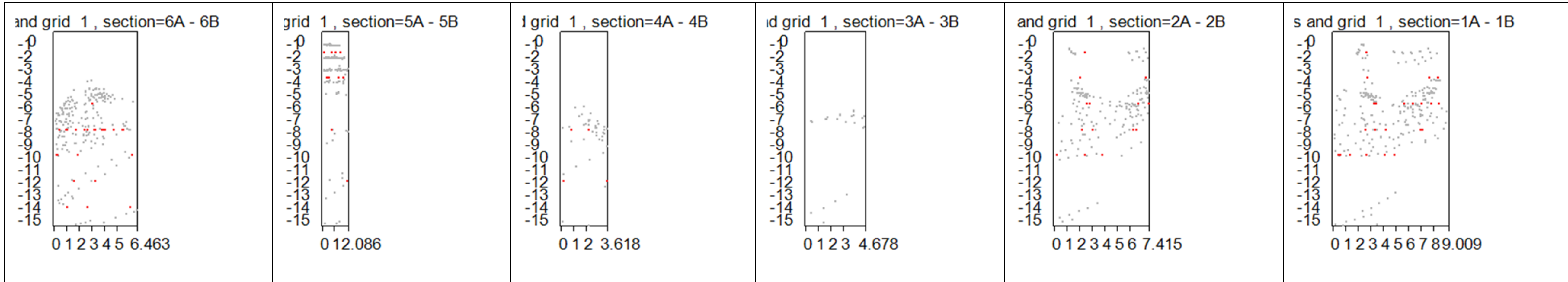

Figure 6-5C. The number of nodes (gray) used for each of the vertical sections for 4 separate grid orientations (Table 6-1), at 0, 22, 45 and 67 degrees from north.

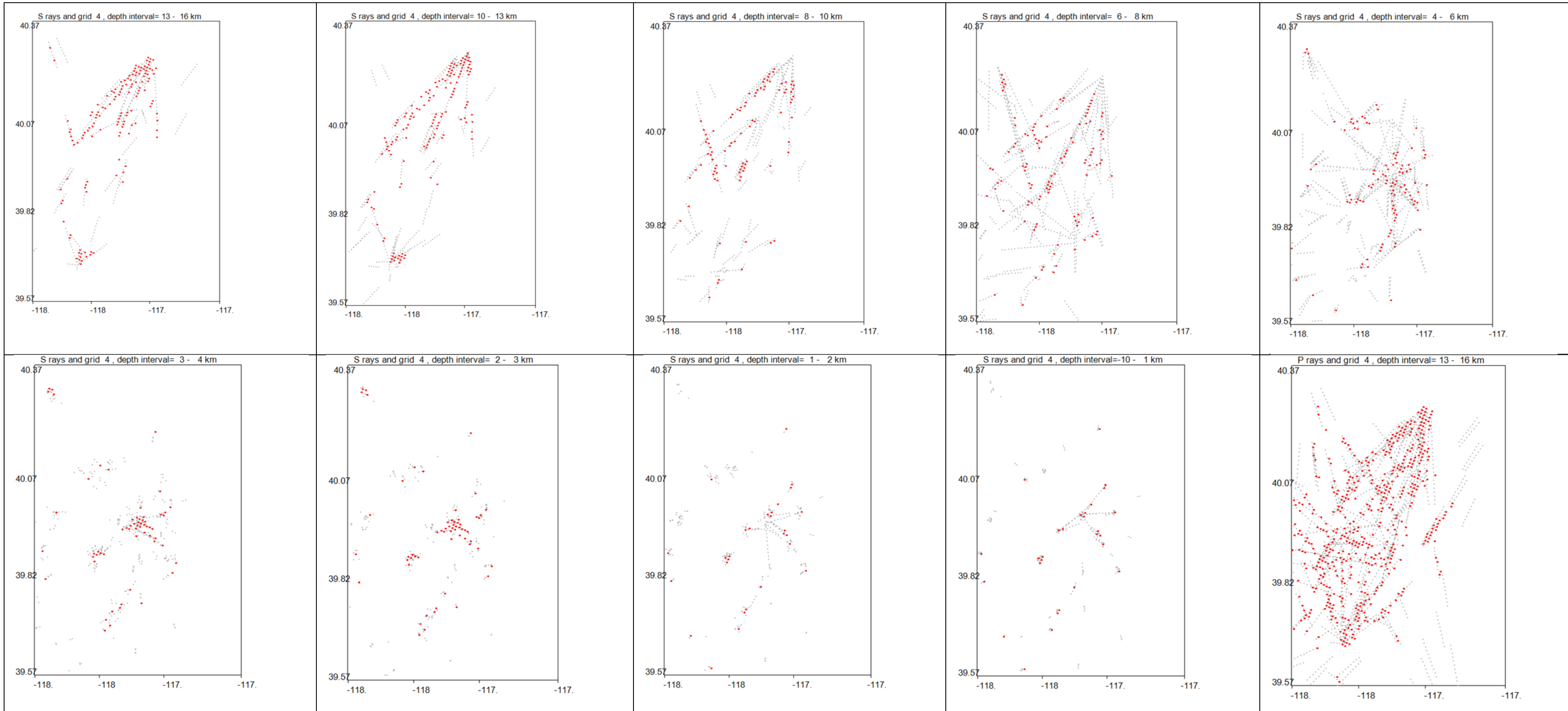

Figure 6-6A. Location of the grid points used to derive the tomographic models, in horizontal sections at various depths. Only grid No. 4 is shown here, the other grids are similar. Note low resolution at less than 5km depth.

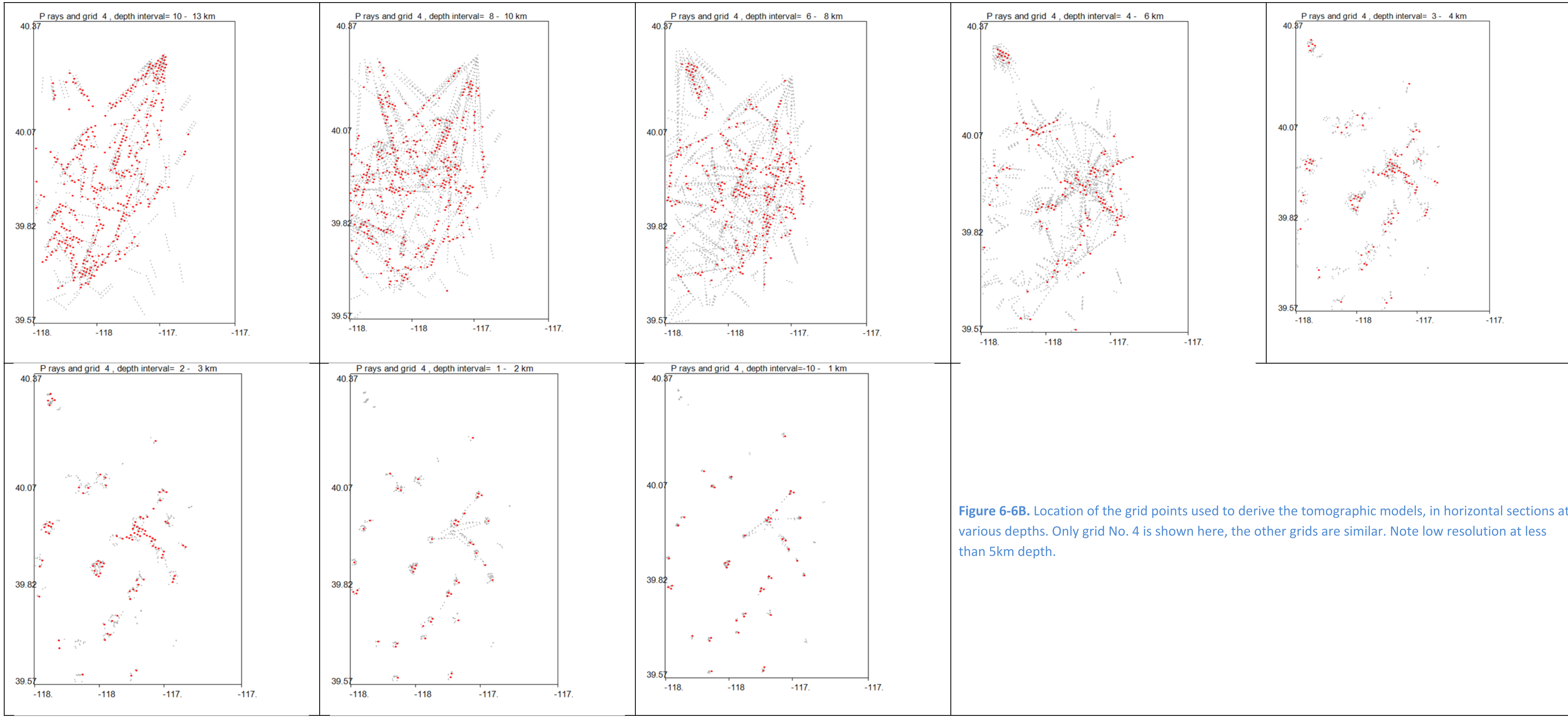

Figure 6-6B. Location of the grid points used to derive the tomographic models, in horizontal sections at various depths. Only grid No. 4 is shown here, the other grids are similar. Note low resolution at less than 5km depth.

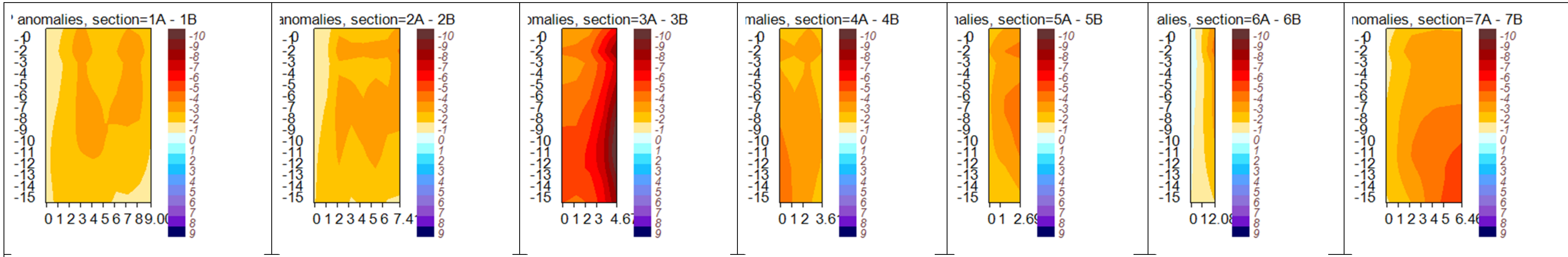

Figure 6-7. Vp anomalies (% from the mean model in Figure 109) in the vertical sections II' (1A-1B), JJ' (2A-2B), A1 (3A-3B), A2 (4A-4B), A3 (5A-5B), A4 (6A-6B) and A5 (7A-7B) in Table 6-2. If an empirical scale of 1 to 10 were associated with how much the models above 3 km are to be trusted, the number provided by the Seismic Task Leader is 3.

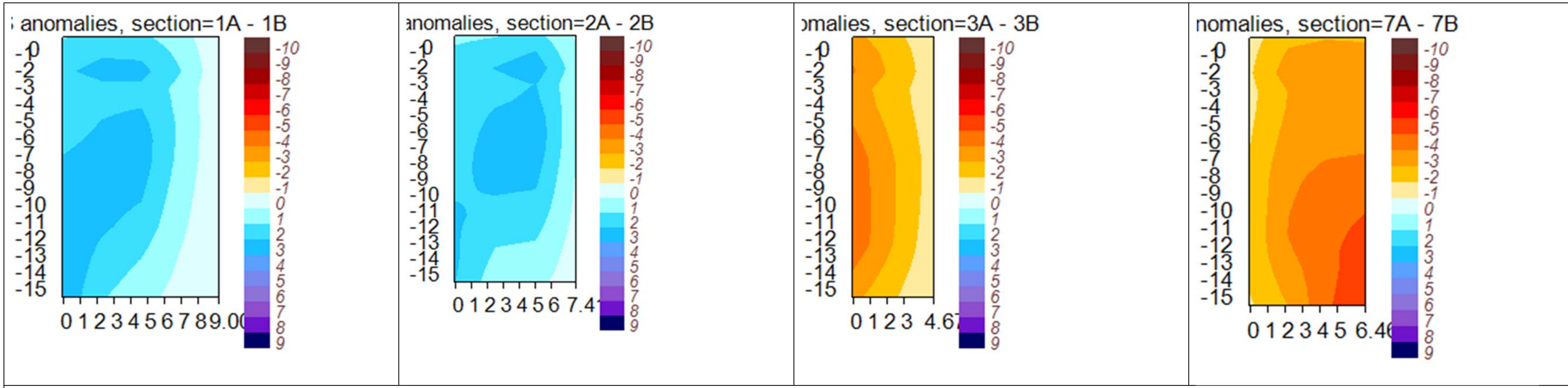

Figure 6-8. Vs anomalies (% from the mean model in Figure 109) in the vertical sections II' (1A-1B), JJ' (2A-2B), A1 (3A-3B) and A5 (7A-7B) in Table 6-2. Note that (a) some of the sections did not have enough S-data for S-velocity models to be estimated. If an empirical scale of 1 to 10 were associated with how much the models above 3 km are to be trusted, the number provided by the Seismic Task Leader is 3.

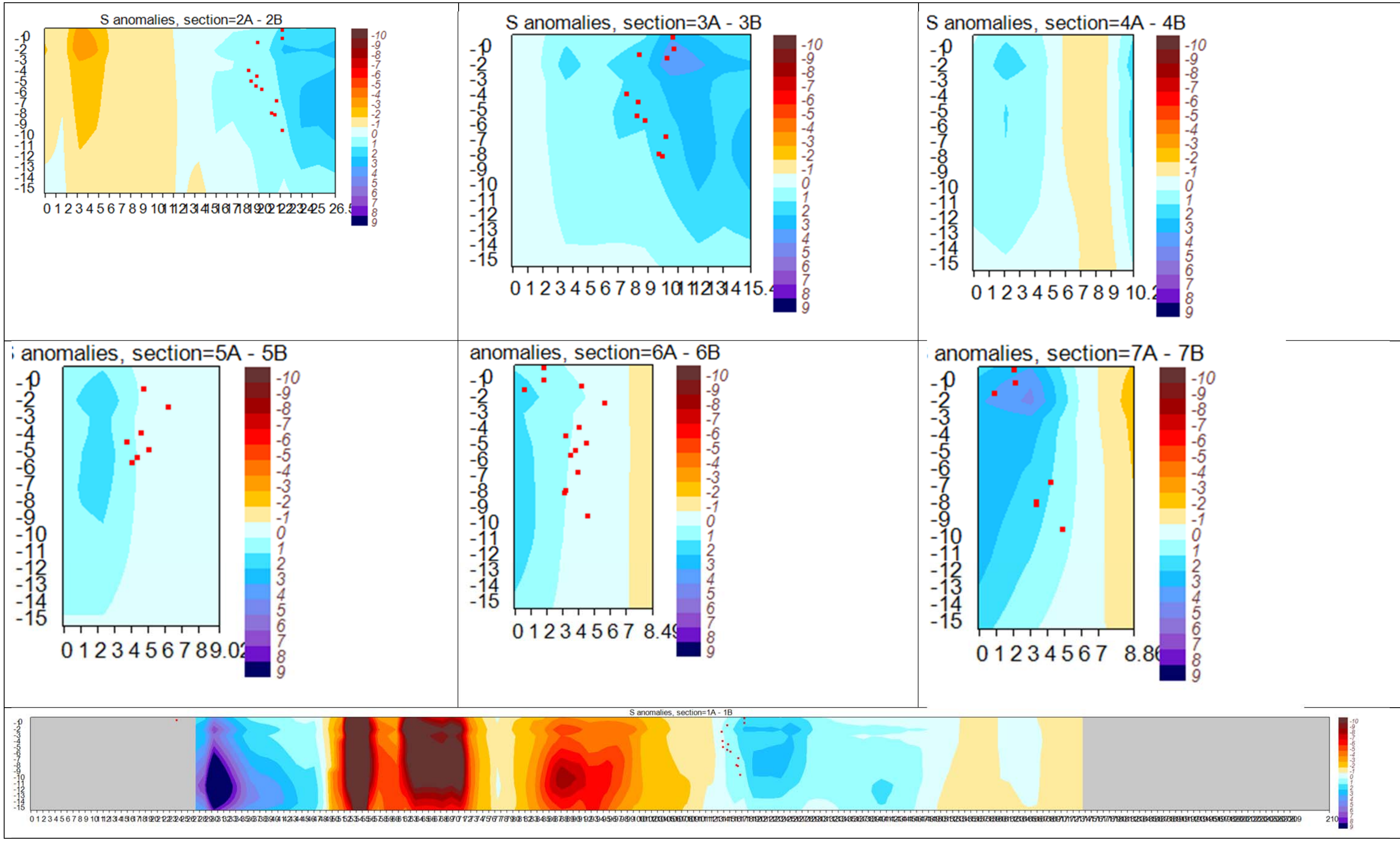

Figure 6-9. Vs anomalies (% from the mean model in Figure 109) in the vertical sections AA' (2A-2B), BB' (3A-3B), CC' (4A-4B), DD' (5A-5B), EE' (6A-6B), FF' (7A-7B), and XX' (-118.65 39.15 -117.15 40.65) in Table 6-2. Note that (a) the earthquakes (red dots) occur in regions of slower P-velocity. If an empirical scale of 1 to 10 were associated with how much the models above 3 km are to be trusted, the number provided by the Seismic Task Leader is 3.

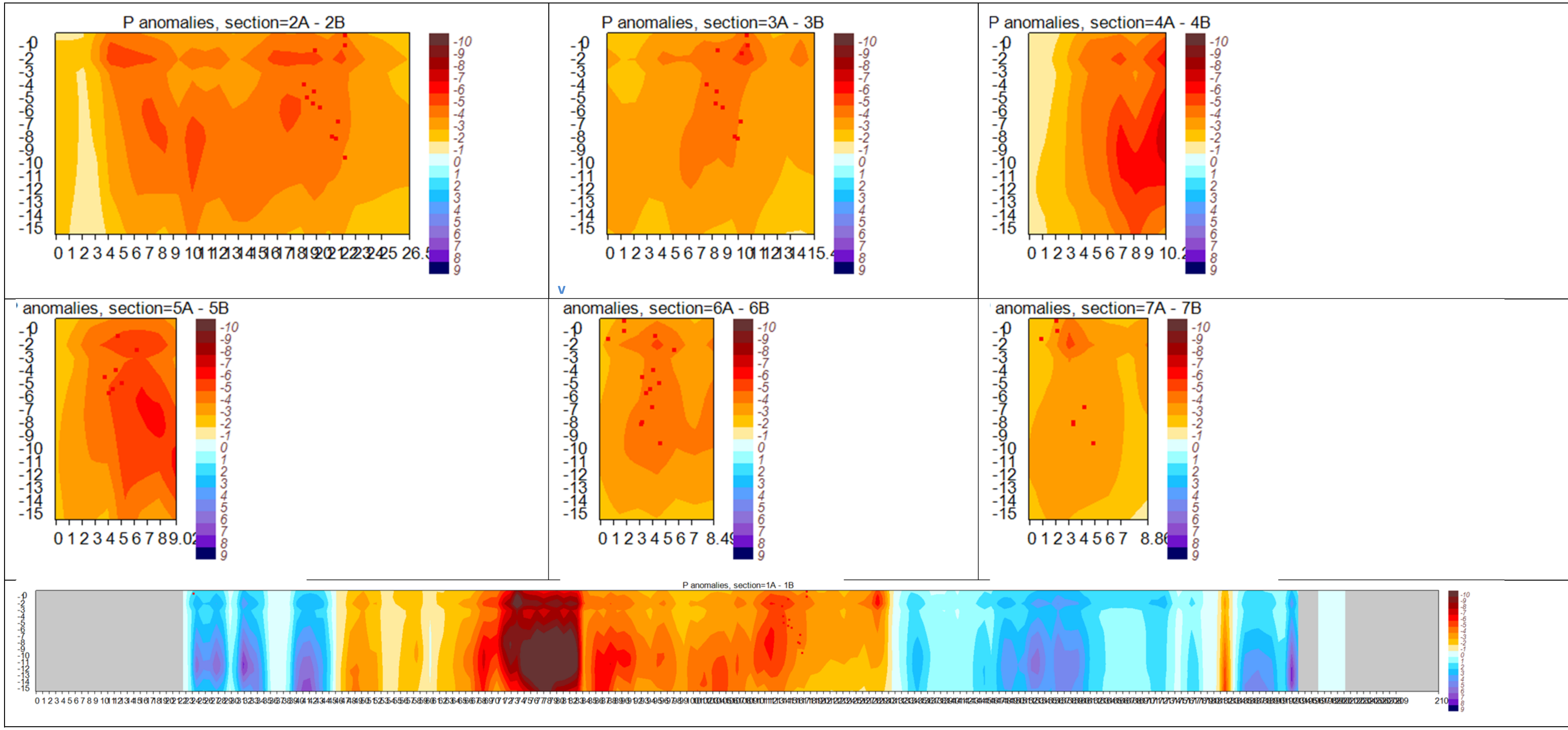

Figure 6-11. Vp anomalies from the mean model in the vertical sections AA' (2A-2B), BB' (3A-3B), CC' (4A-4B), DD' (5A-5B), EE' (6A-6B), and FF' (7A-7B), and XX' (-118.65 39.15 -117.15 40.65) in Table 6-2. Note that (a) the occurrence of the earthquakes (red dots) in the high gradient regions of the S-velocity anomalies. If an empirical scale of 1 to 10 would be associated with how much the models above 3 km are to be trusted, the number provided by the Seismic Task Leader was 3.

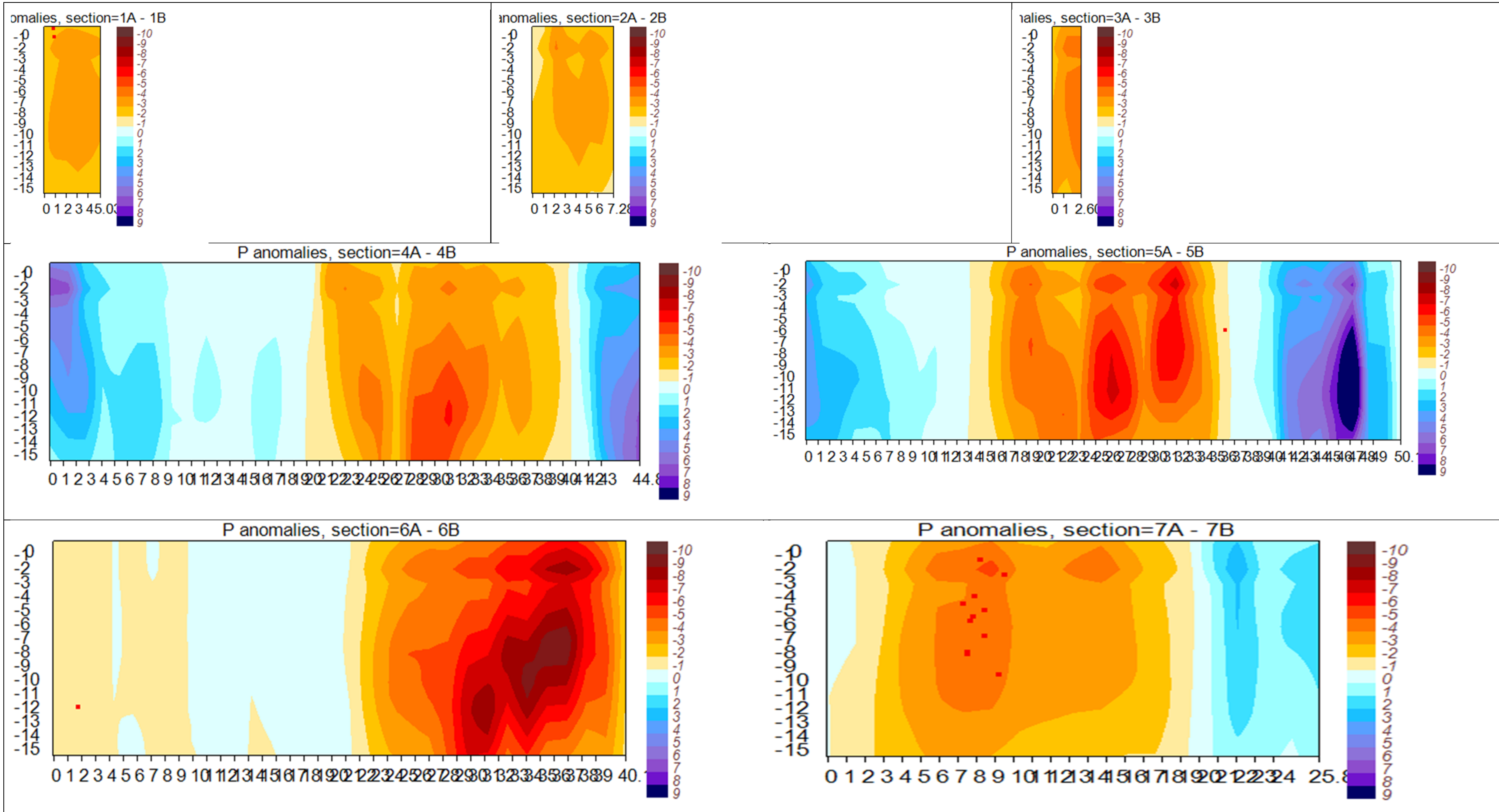

Figure 6-11. Vp anomalies from the mean model in the vertical sections GG' (1A-1B), HH' (2A-2B), A6 (3A-3B), L1 (4A-4B), L2 (5A-5B), L3 (6A-6B) and L4 (7A-7B) in Table 6-2. Note that (a) the earthquakes (red dots) occur in regions of slower P-velocity. If an empirical scale of 1 to 10 were to be associated with how much the models above 3 km are to be trusted, the number provided by the Seismic Task Leader is 3.

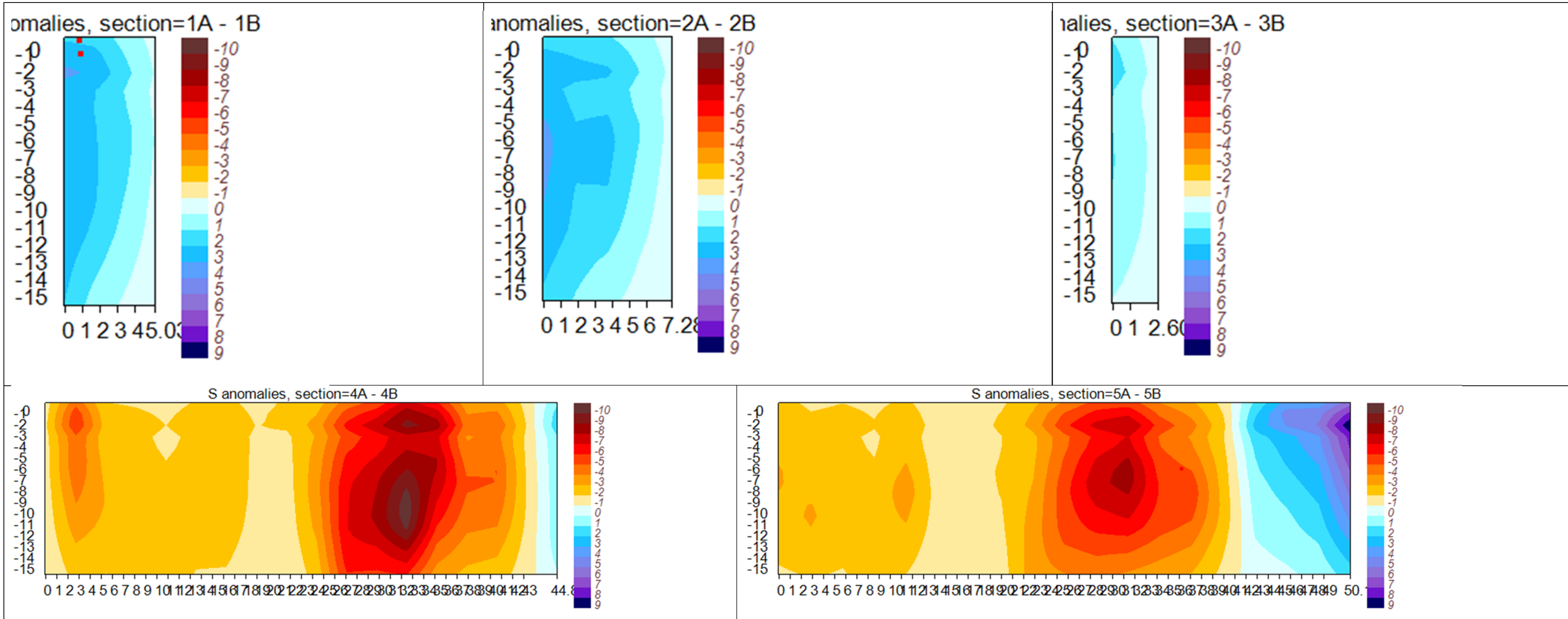

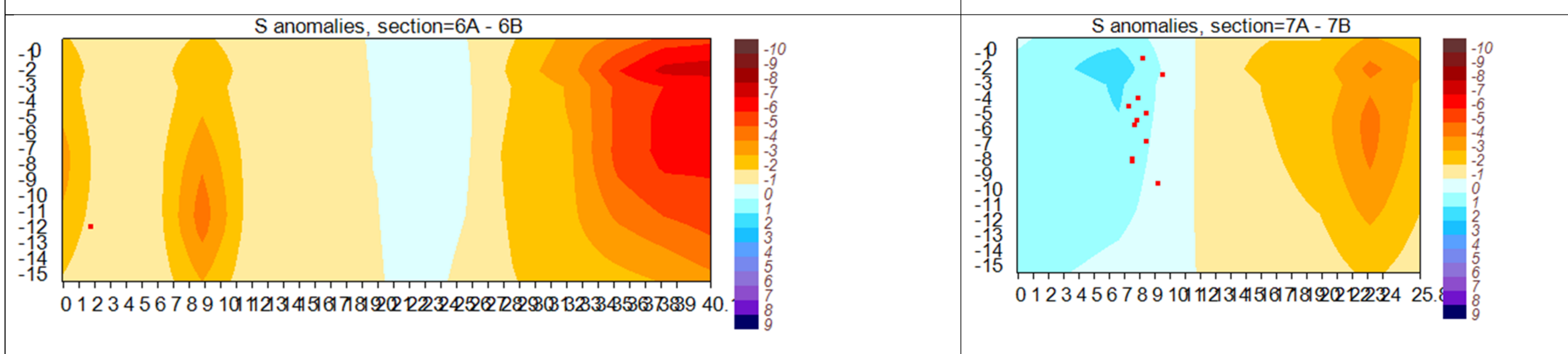

Figure 6-12. Vs anomalies from the mean model in the vertical sections GG'' (1A-1B), HH' (2A-2B), A6 (3A-3B), L1 (4A-4B), L2 (5A-5B), L3 (6A-6B) and L4 (7A-7B) in Table 6-2. Note that (a) the earthquakes (red dots) occur in regions of slower P-velocity, (b) the presence of a low S-velocity body on line L1 which continues at lower values on the other lines, (c) the location of the fault on the line L4. If an empirical scale of 1 to 10 were be associated with how much the models above 3 km are to be trusted, the number provided by the Seismic Task Leader is 3.

PART II-APPENDIX 7

AUTOCORRELATION RESULTS AND THE DVSA_ACOR_MOD

Autocorrelations have been estimated at all the stations (Figure 99a, main text). They represent the vertical reflection component of the Green's Functions. Groups of stations have been selected for analysis and Automatic Gain Control (AGC) has been applied in windows three times the length of the period corresponding to the center of the frequency band. We considered 11 cases of groups of stations, listed in Table 7-1. Because of the project scope and of time limitations, however, considered only the "all station" Case 1 in Table 7-1 for a first-order estimation of the model DVSA_ACOR_MOD. Interpretation of the results for the other cases in Table 7-1 will be the subject of further investigations.

Table 7-1. Groups of stations (some of these groups were approximately linear) used for vertical reflection component of the Green's Functions investigations.

CASE 1 (All stations**)**
STATIONS A01:A21 and B01:B21;
CASE 2
STATIONS A8 B6 B7 B8 B5 B4 A4 A10 A7 B18
CASE 3
STATIONS B14 B13 A20 B1 B2 A14 B3 A21 B17 A15
CASE 4
STATIONS B16 B20 B12 A13 A12 B11 B9 A7 A6 B21 B19 A5 A17
CASE 5
STATIONS A19 A12 B10 6 11
CASE 6
STATIONS A16 A10 B18 A5 B19 A11
CASE 7 (Line through the power plant location)
STATIONS B17 A9 B4 A4 A1 A2 A3 B21 A6 B10
CASE 8
% line transversal s of the power plant
STATIONS 21 B3 B5 7 B9 B11 12 18
CASE 9 (Line through 45-15)
LINE=[14 B2 B7 B8 B6 B12 13 B20 19
CASE 10
STATIONS B1 A20 B13 B14 A8 B15 B16
CASE 11 (Calibration Area)
STATIONS A4 B4 B5 B6 B7 B8 B11 A7 B9 A1 A2 A3 B21

A synthetic waveform was created using CPSS3.0 and the model in Table 7-2. The figures shown below are examples of autocorrelations for selected cases. We show results for Case 4 (Figures 7.1 and 7.2), Case 11 (Figure 7.3), Case 8 (Figure 7.4), for a line west of the Clan Alpine Range (Figures 7-5 and 7-6) and for lines east (Figure 7-7) and west of the Stillwater Range (Figure 7-8).

Table 7-2. The seismic velocity model used to create the synthetic reflection waveform. The synthetic waveform (Figure 112 in the main report) has been created using CPSS3.0 and the model in this table. H is the layer thickness (km), Vp is P-velocity, Vs is S-velocity, RH0 is density, and Qp and Qs are attenuation factors for P and S respectively.

H (km)	V_P (km/s)	V_S (km/s)	RHO (gm/cc)	Q_P	Q_S
1.0	2.1	1.0	2	50	25
1.0000	3.	1.98	2.53	300	150
4.0000	5.2	3.14	2.64	500	250
4.0000	5.63	3.38	2.62	500	250
12.0000	5.50	3.30	2.6	500	250
8.0000	7.43	4.01	3.11	500	250
10.00	8	4.5	3.3	1000	500

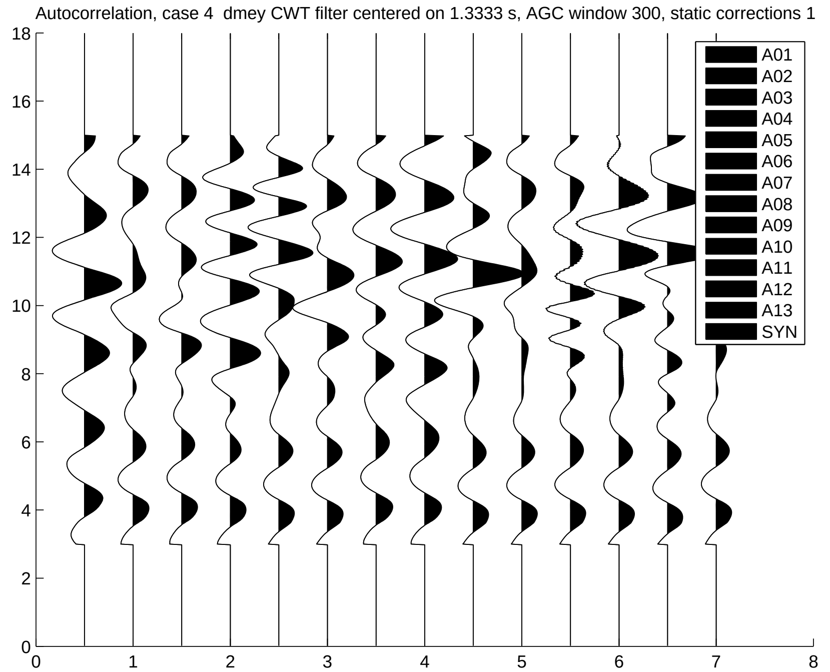

Figure 7-1. Autocorrelations at stations A01-13 for center period 1.3s, for station in Case 4. The autocorrelation beam at each station was shown in the order of the legend, starting with A01 at the left and ending with a synthetic waveform (SYN) at the right. The horizontal axis showing N/2 where N is the total number of stations. The vertical axis shows time(s) from the origin. Station A04 is in the production area, and it shows a stronger reflection at 8s than any other station. A strong lower crustal reflection is observed at 8s for stations A01-3, A04, A07, A08 and A13.

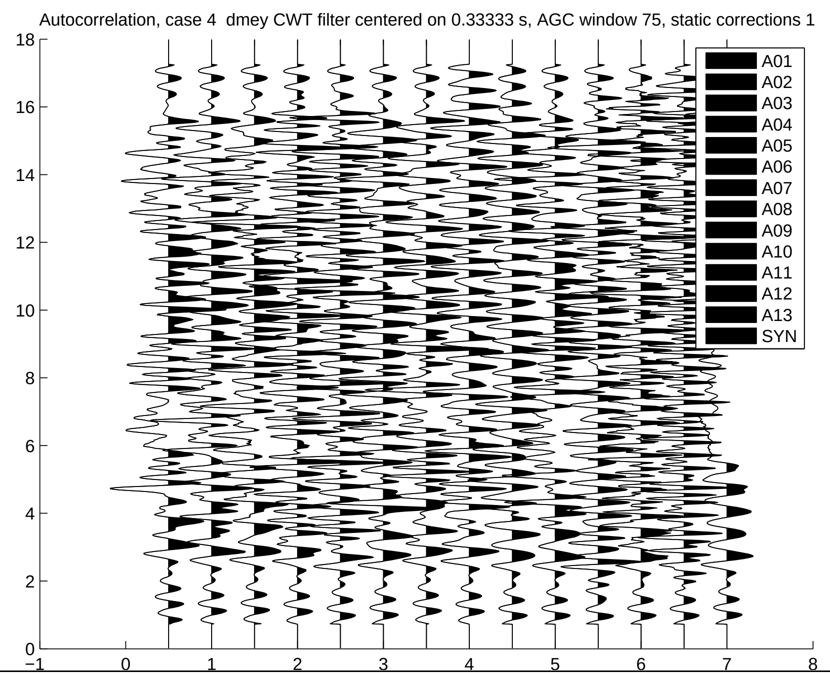

Figure 7-2. Same as in Figure 7-1, showing autocorrelations at stations A01-13 for CWT centered on a period of 0.33s, for Case 4. We interpret the arrival at ~3s as the two-way travel time of a P-reflection from an upper crustal layer (named the "3s reflector"). The stations are in the order of the legend, starting with A01 at the left and ending with a synthetic waveform at the right. Stations A04 is in the production area, however, these reflections have only slighly faster P-velocity at A04 when compared to other stations. Note the consistency of the ~3s reflector beneath all the array stations.

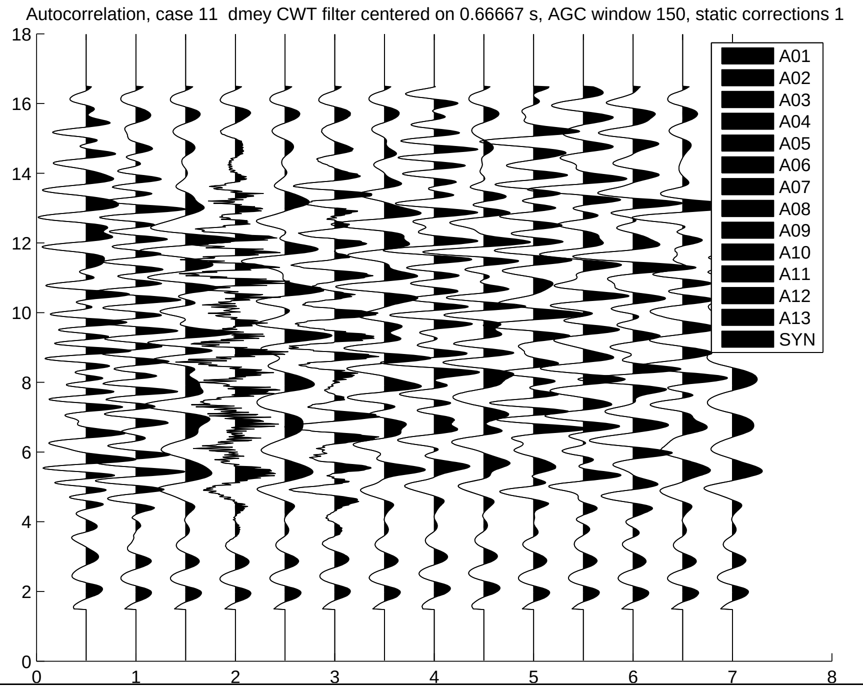

Figure 7-3. Same as in Figure 7-1, showing autocorrelations at stations A01-13 at center period 0.7s for Case 11 (stations in and adyacent to the Calibration Area). The arrival at 6s is interpreted as the P-reflection from a mid-crustal layer. The stations are in the order of the legend, starting with A01 at the left and ending with a synthetic waveform at the right. Note slightly higher P-velocity and higher amplitude mid-crustal reflections at stations A04 and A05. Note a deepening mid-crustal layer (later first arrivals) at stations A06, A07, A08 and A09 when compared to stations A04 and A05.

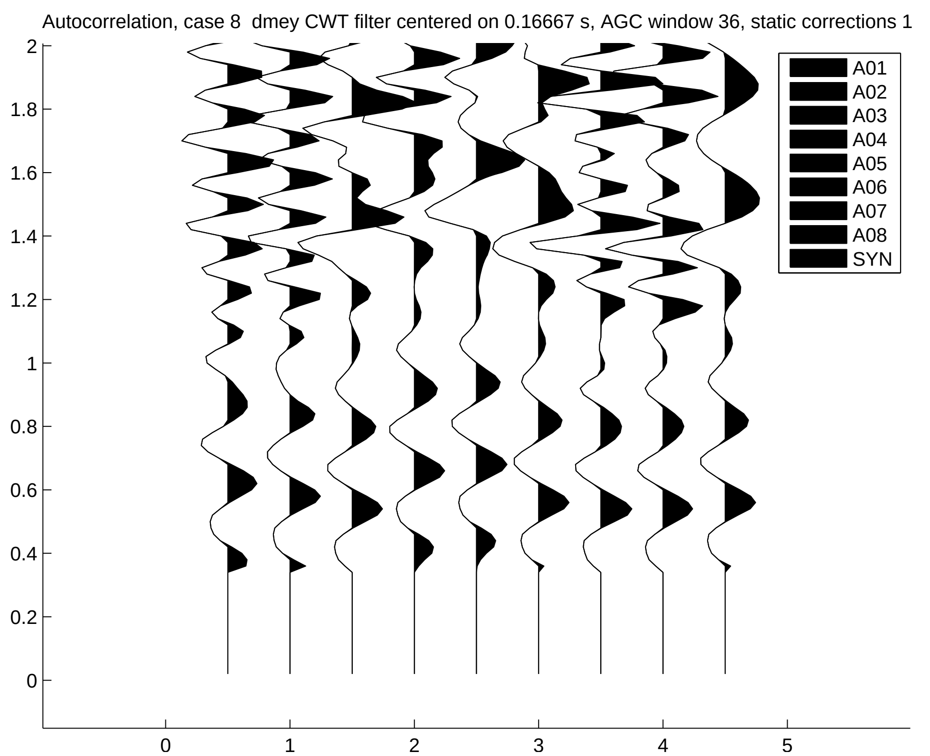

Figure 7-4. Same as in Figure 7-1, showing autocorrelations at stations A01-8 for CWT centered on a period of 0.17s, in Case 8. The stations are in the order of the legend, starting with A01 at the left and ending with a synthetic waveform at the right. Stations A04 and A05 are in the production area, and in this frequency band they are significantly different from other stations.

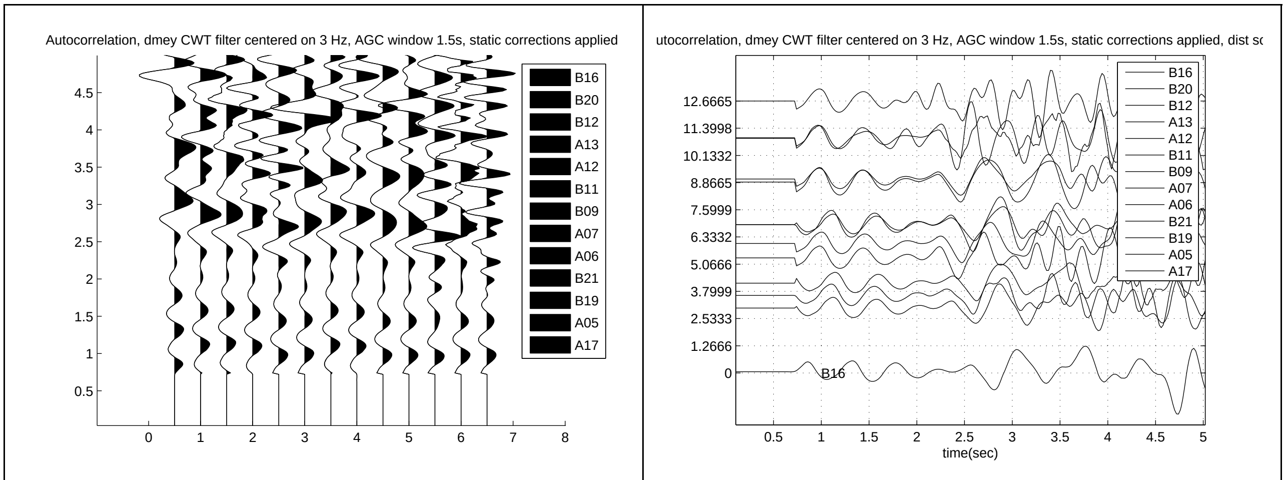

Figure 7-5. *Left plot:* Same as in Figure 7-1, showing autocorrelations at each station in the legend, west of the Clan-Alpine Range. When filtered at center frequency 3Hz the waveforms show a upper crustal arrival at ~ 2.5s (4-5km depth). The P-crustal velocity appears to be 0.5s slower at the southernmost stations (B16, B20, B12, A13). Of the entire set of stations, only B11, A12 and B10 show higher P-velocity for this reflection. The stations are shown in the order in the legend, starting with B16 far left. *Right plot:* A record section starting at B16 and ending at A17 shows first slower, then faster crustal arrivals. Note that a Continuous Wavelet Transform (CWT) filter centered on 3Hz has been applied before AGC (Automatic Gain Control). Static corrections were applied.

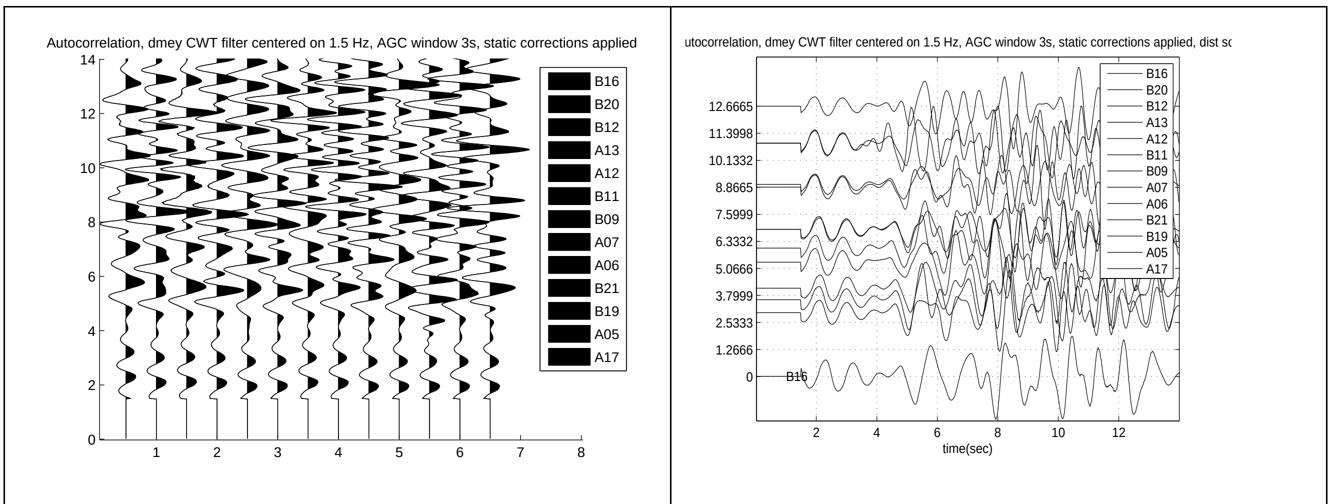

Figure 7-6. Same as in Figure 7-9, however, the CWT filter was centered at 1.5Hz. Note two arrivals, which we interpret as P-arrivals, one at ~5s (mid-crustal reflection) and another at ~8s (probably the start of the Moho transition).

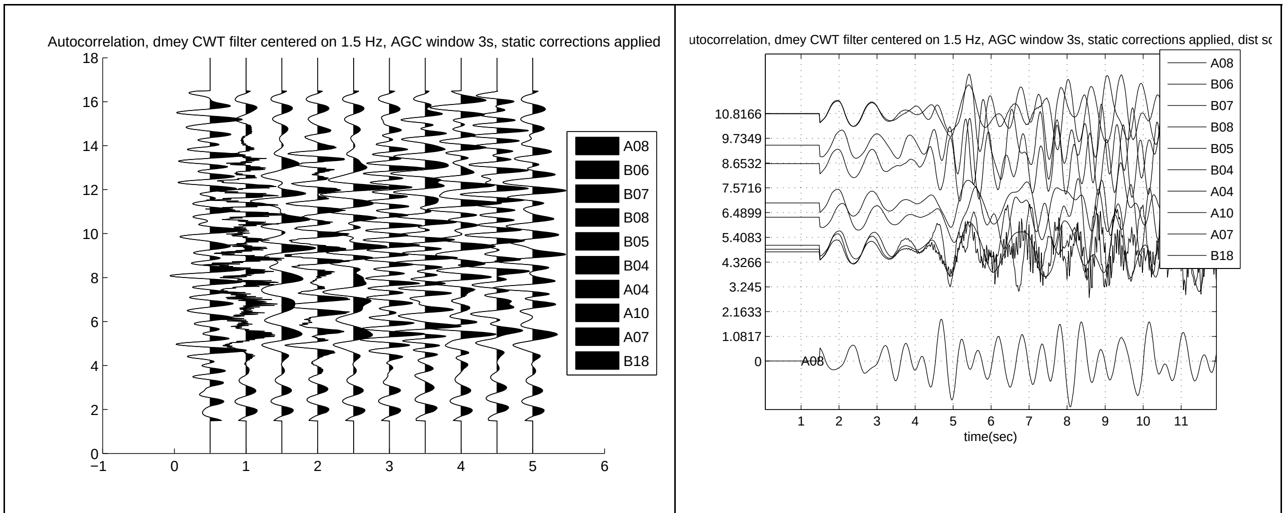

Figure 7-7. *Left Plot:* Same as in Figure 7-1 showing autocorrelations at each station in the legend, east of the Stillwater Range, with a mid-crustal arrival at ~ 5.5s. The P-crustal velocity seems to be slower at the stations near the power plant. The stations are shown in the order in the legend, starting with A08 far left. *Right plot:* A record section starting at A08 and ending at B18 shows progressively later mid-crustal arrivals at the northern stations. This could be due to lower P-velocity in the mid -crust. Note that a Continuous Wavelet Transform (CWT) filter centered on 1.5Hz has been applied before AGC (Automatic Gain Control). Static corrections were applied.

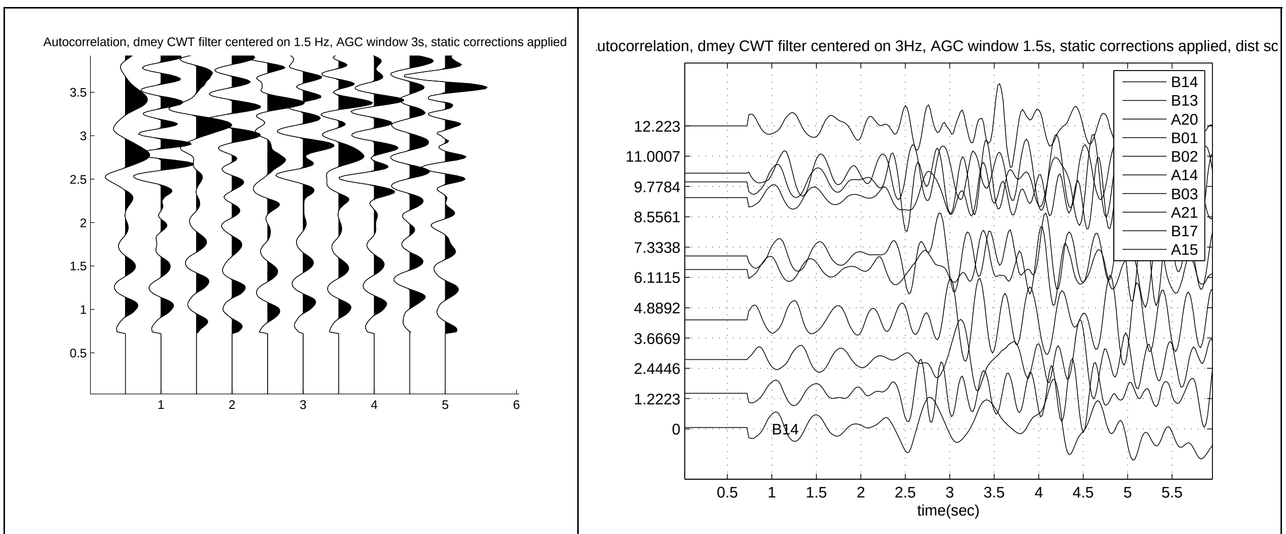

Figure 7-8. *Left Plot:* Same as in Figure 7-1 showing autocorrelations at each station in the legend, west of the Stillwater Range, with a crustal arrival at ~2.5s (Stations start from the left with B14, ending with A16, like in the legend in the right plot). *Right plot:* A record section west of the Stillwater Range starting at B14 and ending at A16 shows progressively later crustal reflection arrivals at some of the stations in the Carson Sink: A20, B01 and B02. The reflections are interpreted as from a layer 4-5km deep. Note that a Continuous Wavelet Transform (CWT) filter has been applied before AGC (Automatic Gain Control), centered on 3Hz. Static corrections were applied.

PART II-APPENDIX 8

STATIC CORRECTIONS FOR P-WAVE ARRIVALS

For a small array (100km aperture or less), one can neglect the wavefront curvature for body waves from teleseismic events and assume P-arrivals are plane waves with a vector slowness "s", which can be easily reduced to back azimuth and velocity.

We will determine the station delays from many events. For the arrival at the i^{th} station for the j^{th} event, its arrival time t_{ij} can be written simply as

$$t_{ij} = t_j + r_i \cdot s_j + \tau_i + e_{ij} \qquad (1)$$

where

t_j = a reference event arrival time (to be defined);

r_i = distance vector of the ith station from a reference station (constant for all events);

s_j = slowness vector of the jth event;

τ_i = the delay term for the ith station; and

e_{ij} = an error term.

Now instead of the absolute times t_{ij}, we will work with relative times between stations determined by cross-correlation of their P waves. This correlation has often been reported in the literature for finding delays, but practice seems to be limited to cross-correlation of all the signals for a given event with only the signal of a single reference station. Given N stations, this gives N-1 observations per event. A matrix of crosscorrelations between stations would have N(N-1) elements, and would be symmetrical relative to the diagonal. No particular station is picked as a reference. N(N-1)/2 independent observations (on the lower triangular part of the correlation matrix) are obtained from crosscorrelation of waveforms recorded at all stations. This should reduce the errors in the solution by the factor sqrt(N/2) with the assumption that errors diminish as the square root of the number of observations. For the Dixie Valley A and B deployments (see main text for an explanation), the number of elements was N = 21. Taking k and l as subscripts for the two stations in the correlation, we compute observations $t_{kj} - t_{lj}$. These observations are equivalent of the difference of equation (1) for two stations thus:

$$t_{kj} - t_{lj} = r_k \cdot s_j - r_l \cdot s_j + \tau_k - \tau_l + 2e_{klj} \qquad (2)$$

For convenience, the factor 2 is simply dropped from the error term. Note that the event term drops out of the equation.

We have culled the t_{ij} data used in equation 2. Each cross-correlation time difference has an associated cross-correlation coefficient which lies between 0 and +1. We also required that the coefficient be ≥ 0.7. Moreover, we discarded entirely any event for which an insufficient number of cross-correlation coefficients ≥ 0.7 were obtained. Given that, for the Dixie Valley arrays, the number of cross-correlations is 21(21-1)/2 = 210 per event, we set this number at 100. This ensured that only events with good quality signals were used to determine the station delays.

For N stations and M events, we have P = N + 2M unknowns. The 2M comes from the fact that slowness is a vector. We have Q = N(N-1)/2 observations. Let A be a column vector of length Q of observations, B be the Q×P matrix of coefficients (mostly sparse), and z be the P-length vector of unknowns; then

$$A = B \cdot z \qquad (3)$$

and the least squares solution is represented by

$$z = (B^T B)^{-1} B^T A \qquad (4)$$

Equation (4) can be solved with some routine in any numerical computing package. In order for the solution to be stable, an extra equation which states that the sum of the station terms equals zero needs to be added to the A vector and B matrix.

Note that equation (2) contains the slowness as unknowns. To greatly simplify the solution, one can use the slowness that is appropriate to each event, as determined by the earth model and the teleseismic distance. This reduces the solution space to N station delay terms and reduces the size of the B matrix.

Solutions with and without slowness included as unknowns were computed and compared, as in the Figures 8-1a and b where "Estimated delay1" is the solution with unknown slowness and "Estimated delay2" is the solution with known slowness. When slowness is considered known, the degrees of freedom are reduced and the variance of the error term goes up slightly. It is not clear which is the more correct solution, but a cross-plot of station terms from the two solution sets shows the differences to be negligible except in a few cases for deployment A (here named "array A"), which has the most background noise. The scatter in the cross-plot for array A (Figure 8-1a) is significantly greater than for deployment B (named here "array B") (Figure 8-1b). This scatter is probably due to noisier waveforms, as opposed to being explained entirely by the difference in the number of events used (12 for array A and 27 for array B). The solution which did not include solving for the slowness was chosen.

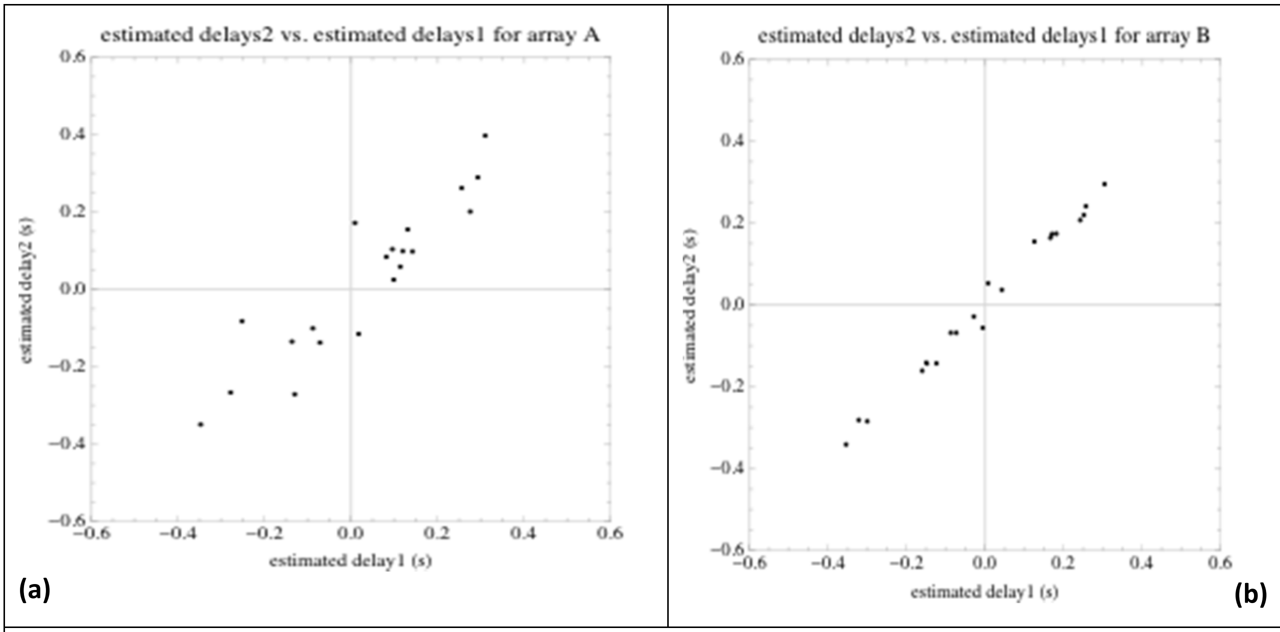

Figure 8-1. (a) Deployment A results: static corrections obtained using USGS slowness as a function of static corrections obtained with slowness as an unknown variable ; (b) Same as in the left plot for deployment B.

The sign of the delays is interpreted as follows: positive means that the signal arrives at that station later than expected and negative means that it arrives earlier than expected. Elevation does not positively correlate with static corrections (Figure 3-2). Thus, the exact nature of the material traversed by rays to each station needs to be taken into account. The static correction is a relative term and is an integrated effect along the exact raypath. Let Δd be the incremental raypath length, and v be the variable velocity along the raypath; then the total time from source to receiver is

$$t = \int (1/v)\, \Delta d \qquad (5)$$

The delays determined here are constrained to have zero mean, and so they are relative to some mean time of arrival; this can be expressed as done in equation (1) with t_j.

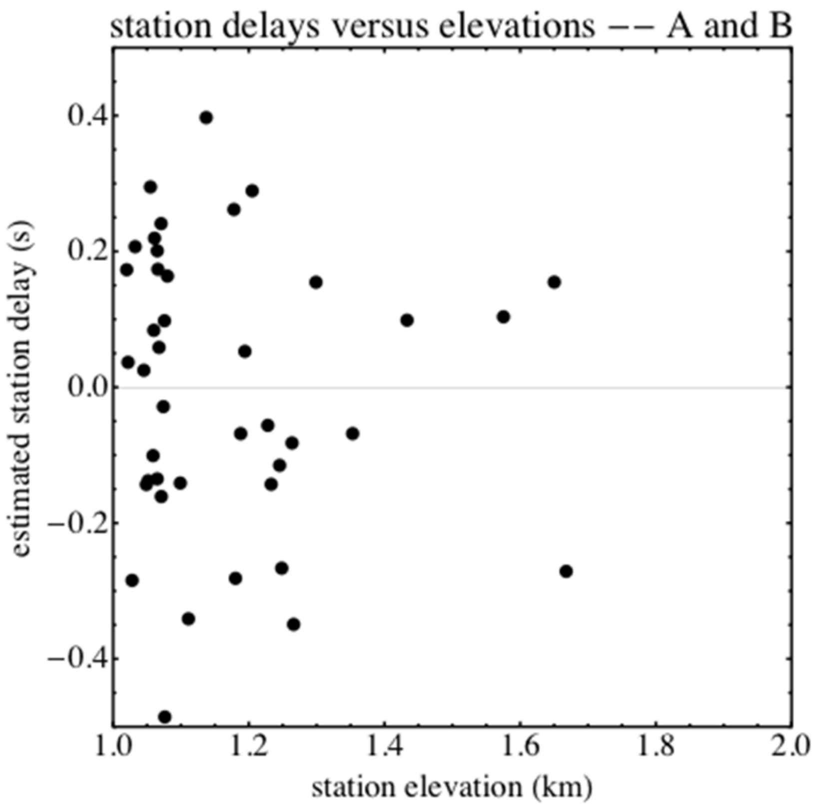

Figure 8.2. Estimated static correction (here named station delays) as a function of station elevation.

If all the stations would be on the same geological formations, the delays would be a linear function of elevation. Since there is no linear dependence between the relative station delays and the elevation, no replacement velocity can be used (Tibuleac et al, 2001) and the delays are used as static corrections.

PART II-APPENDIX 9

PHASE VELOCITY INVERSION AT AD-HOC ARRAYS ANALYSIS AND OF THE DVSA_PHVEL_MOD

This appendix shows supplementary information related to the estimation of the DVSA_PHVEL_MOD (Figure 100, main text). This model was derived by inversion of first Rayleigh mode phase velocity dispersion estimated at ad-hoc arrays of stations shown in Table 9-1 and Figure 9-1. An example of waveform complexity from two different back azimuths was shown in Figure 9-2. Figures 9-3 show examples of Green's Functions (GFs) record sections.

Table 9-1. The following areas have been considered when forming ad-hoc sub-arrays (Figure 9-1 and Lines and ad-hoc sub-arrays of stations in the main report.

Case Number	**Stations**
1	All the available stations were considered
2	ESR - east Stillwater Range
3	WSR west Stillwater Range
4	WCA west Clan Alpine Range
5	ECA east Clan Alpine Range
6	LL1 - transverse lines cases 6,7,8,9 and 10
7	
8	
9	
10	
11	A21 B6 B7 B8 A4 A10 A1 A2 A3 B21
12	A9 B4 A4
13	B4 A4 A10 B18 A5 B19 A1 A2 A3 B21
14	B4 A1 A2 A3 B21 B6 B7 B8
15	B5 A1 A2 A3 B6 B7 B8
16	B5 B4 B6 B7 B8
17	B5 B4 A9
18	Clan Alpine south [B16 A19 A18 A12 A13 B12 B20]
19	Clan alpine north [B11 A7 B9 6 B10 A18 A12]
20	DVSA south [A8 B15 B16 B14]
21	Stillwater south [A8 A20 B13 B14]
22	Stillwater south [A20 B6 B7 B8 A8 B15]
23	Stillwater west [A20 A22 A23 A14 A21 B17 B3]
24	Stillwater middle case [A20 B6 B7 B8 B5 9 B17 B3]
25	Stillwater north 1 [A15 A16 A9 A4 A10]
26	Stillwater N 2 [A21 A15 B17 B3 A9]
27	DVSA north [A10 A17 A5 A11 A6]
28	DVSA middle [B21 A1 A2 A3 B6 B7 B8 B20 B12 A13 B11 A7 B9]
29	DVSA middle S [B6 B7 B8 B12 A13 B20 B15 A8]

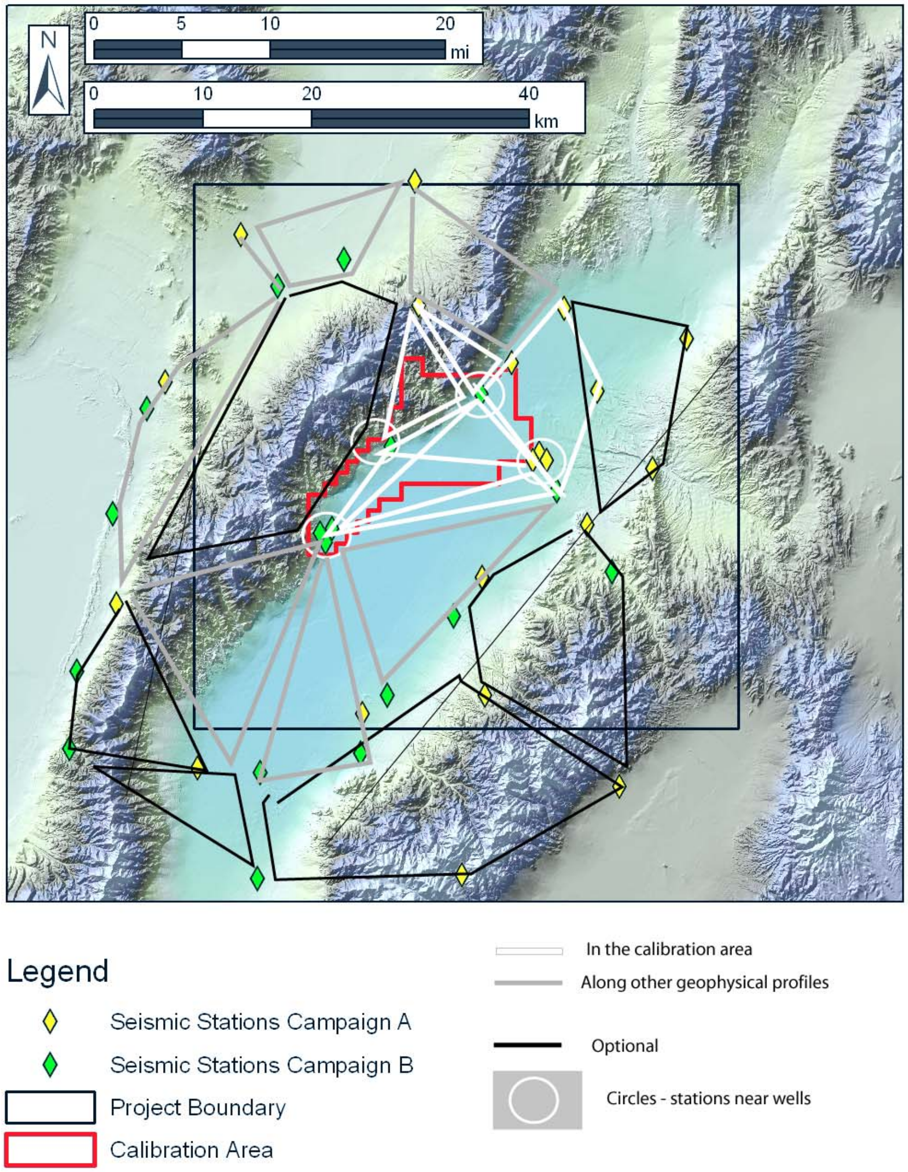

Figure 9-1. Seismic ad-hoc arrays (Table 9-1) used to analyze GFs extracted between DVSA stations and stations outside the DVSA.

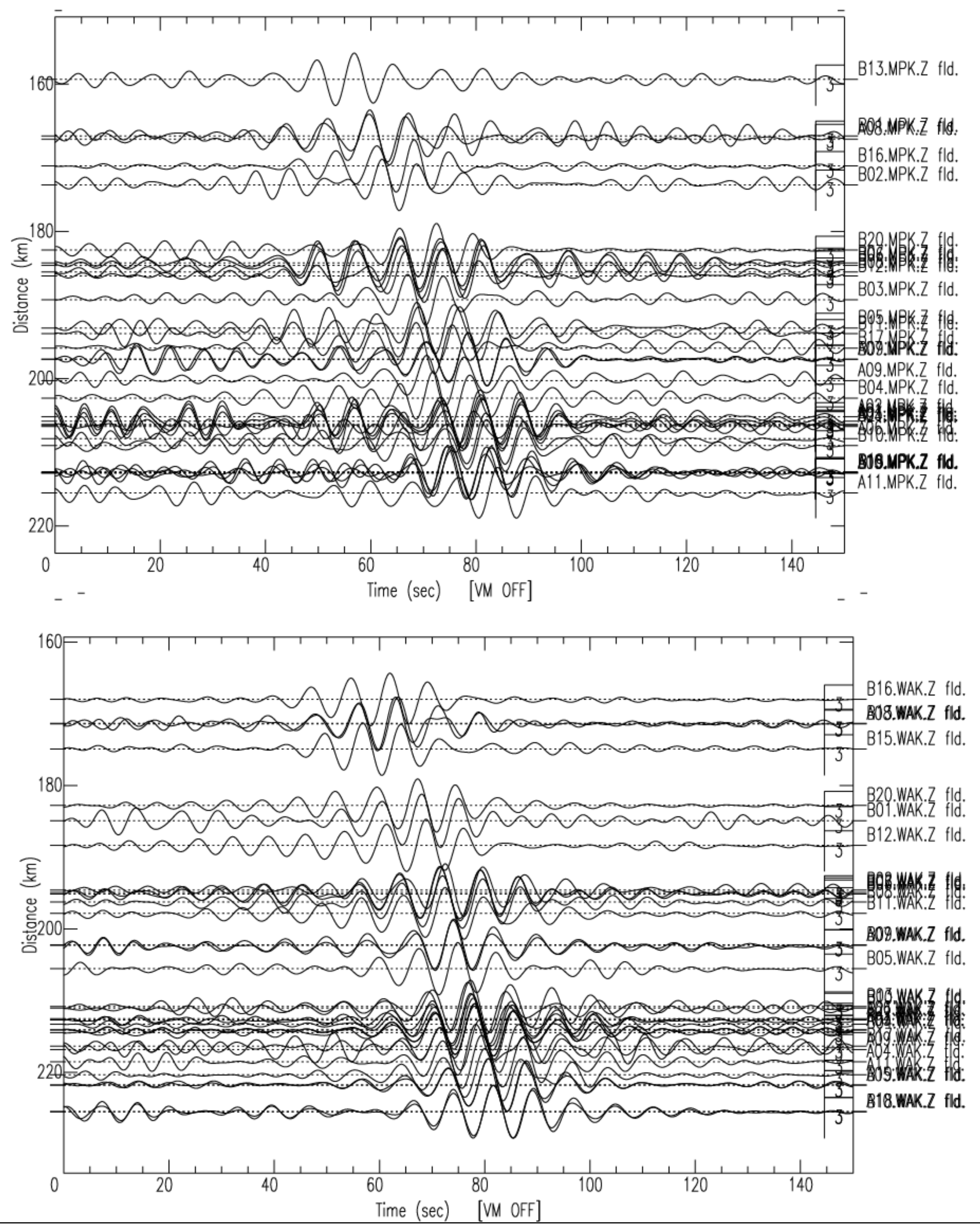

Figure 9-2. Complex (upper plot) versus simple (lower plot) fundamental mode Rayleigh GFs were observed in Dixie Valley from similar distance to stations WAK and MPK, which however, are located at different back azimuths. Note the arrival before 3km/s lag on the upper plot, which is interpreted as the first higher mode Rayleigh wave.

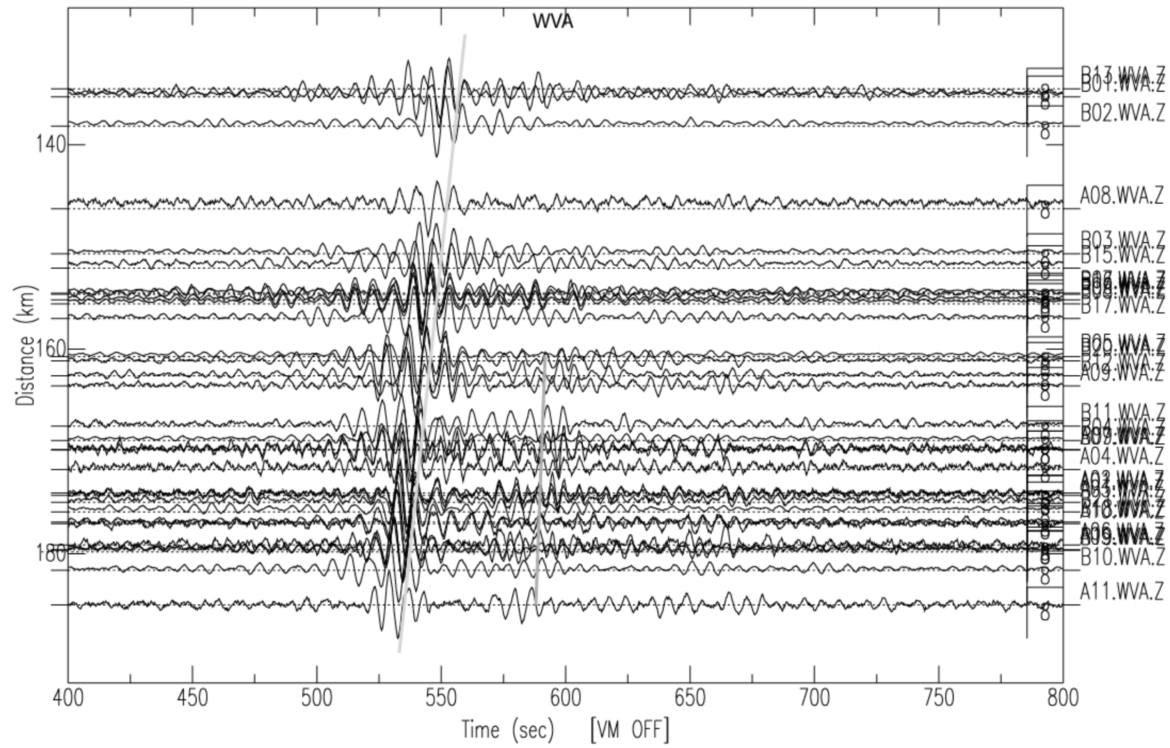

Figure 9-3A. Green Functions extracted between the Dixie Valley stations and station WVA. The left gray line shows the 3km/s time marks. The right gray line shows the 8km/s time marks.

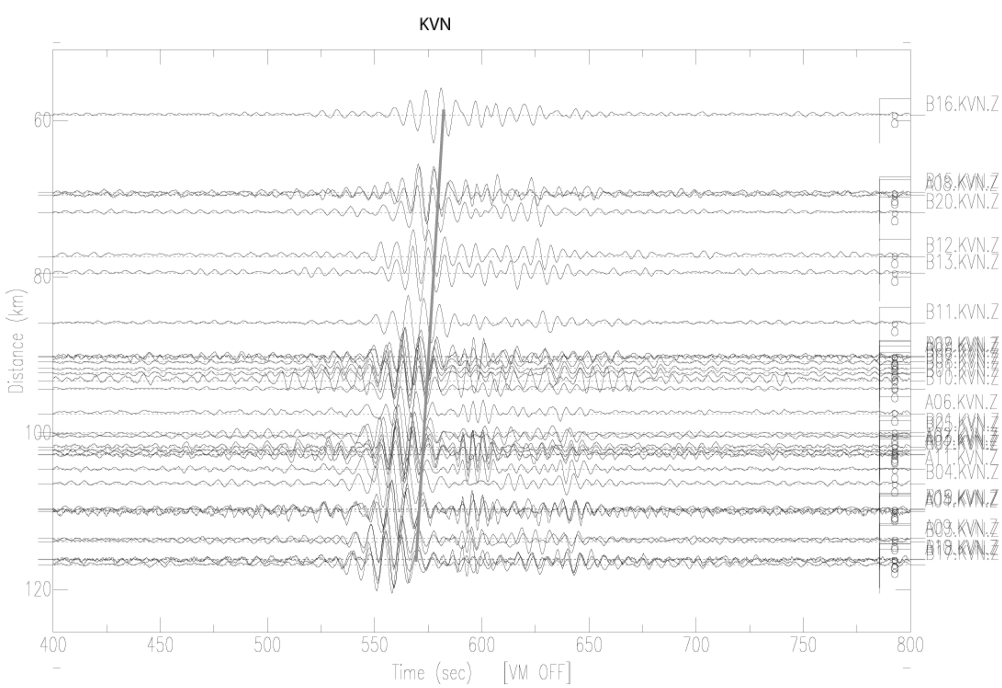

Figure 9-3B. Green's Functions extracted between DV stations and NN station KVN. The left gray line shows the 3km/s time marks

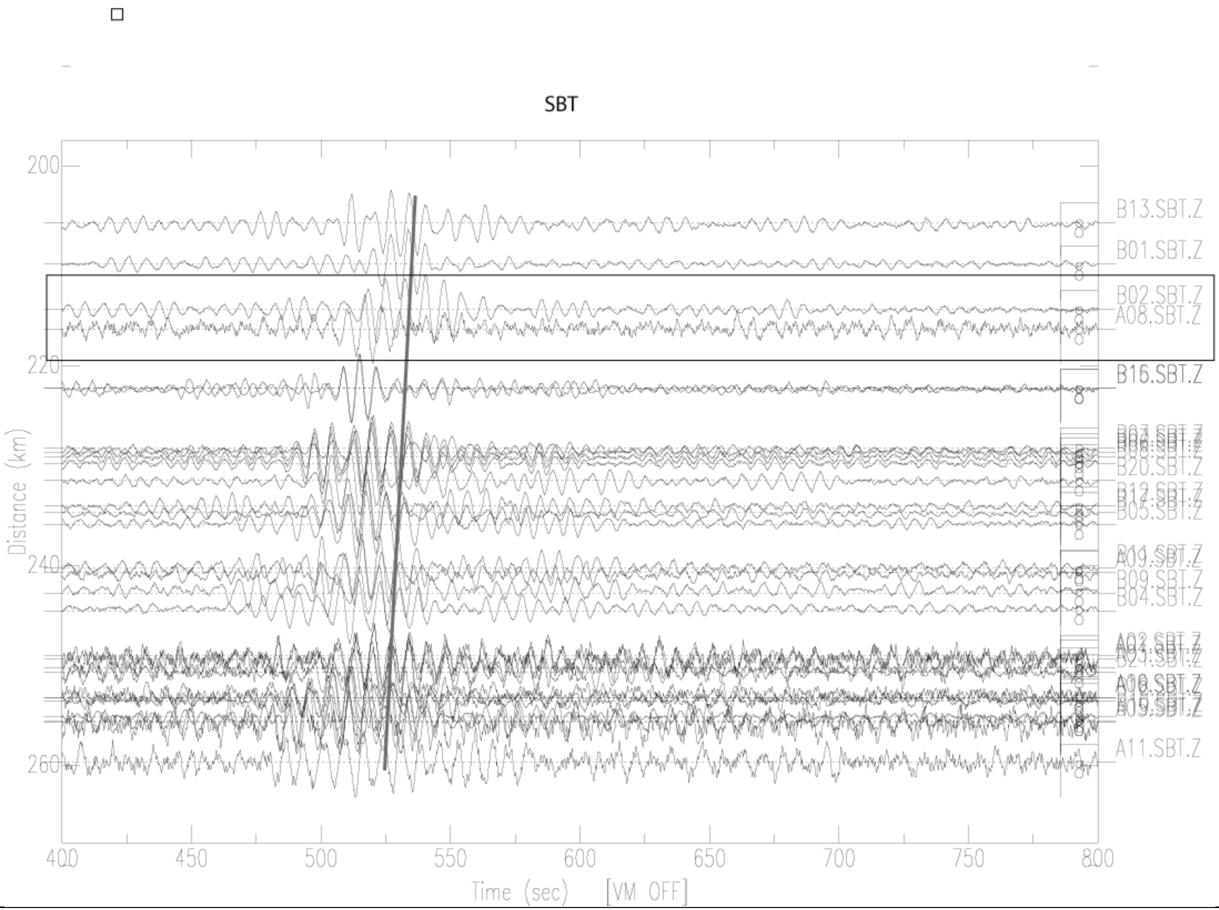

Figure 9-3C. Green's Functions (GFs) extracted between DV stations and station SBT. The left black line shows the 3km/s time marks. Similar distance GFs extracted using deployment A and B stations are shown in the black rectangle. Note that the deployment A GFs are noisier when compared to the deployment B GFs.

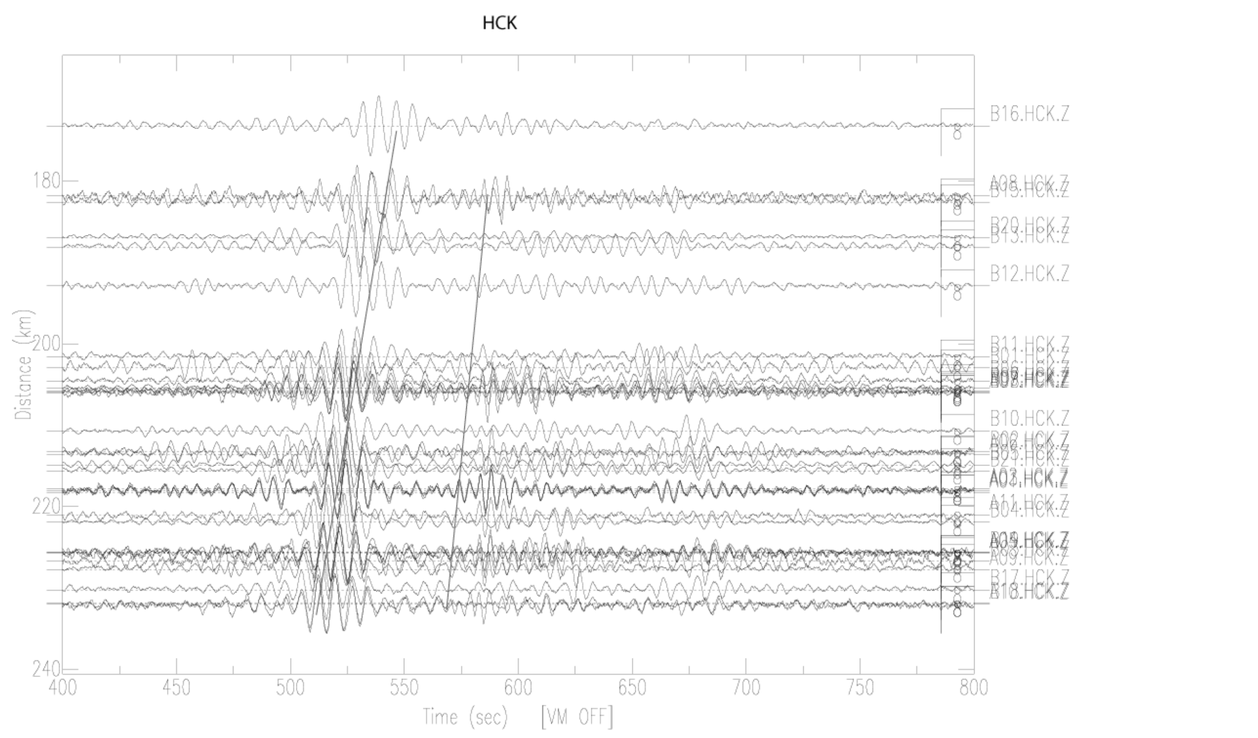

Figure 9-3D. Green's Functions (GFs) extracted between DV stations and NN station HCK. The left gray line shows the 3km/s time lags. The right gray line shows the 8km/s time marks, however, the observed first arrival is not Pn and is faster than 8km/s. This arrival needs investigation, which was outside the scope of our project.

PART II – APPENDIX 10

SUPPORTING MATERIALS

We have provided semnificative figures, data files and source code generated in this project in a directory structure organized as follows:

Appendix 10 directory
DVESA contains the following directories :
BASELINE_DVESA_INPUT contains all the files related to the
DVESA_INPUT_MOD
FINAL_VELMODELS contains the inverted velocity models
GROUPVEL contains all the group velocity models which were estimated from dispersion curves
DVESA_AREA_FINAL_MODELS
DVESA_AREA contains the Vp, Vs, density (RHO) and Qs and Qs and their trust factors at each grid point in the DVESA area. The depth at which these models have been calculated is shown in the table header.
COLOR (same as BW) contains *eps files with models at each depth. The files start with TP when trust factors are represented, and with VP or Vs when velocity maps are shown. The depth of the slice through the model is shown in the file name.
DVSA contains the following directories :
CALIB_AREA with COLOR (same as BW) contains
CALIB_AREA which has the Vp, Vs, density (RHO) and Qs and Qs and their trust factors at each grid point in the Calibration Area. The depth at which these models have been calculated is shown in the table header.
COLOR (same as BW) contains *eps files with models at each depth. The files start with TP when trust factors are represented, and with VP or Vs when velocity maps are shown. The depth of the horizontal slice through the model is shown in the file name.
linear_sections with
COLOR (same as BW)
all files were created by the Matlab script create_model_lines_06_17_2013.m
1) files with names AA_var1, … L4_var1 have Vp, Vs, density (RHO) and Qs and Qs and their trust factors models at each depth in
DEPTH1 DEPTH1=[-1 -0.5 0 0.5 1 1.5 2 2.5 3 3.5 4 4.5 5]; (km)
along every line.
2) files with names AA_var2, … L4_var2 have Vp, Vs, density (RHO) and Qs and Qs and their trust factors models at each depth in
DEPTH1=[-1 0 1 2 3 4 5 6 7 8 9 10 11 12 13 14 15 16 17 18 19 20]; (km)
along every line.
3) *eps files with models at each depth. The files start with TP when trust factors are represented, and with VP or Vs when velocity maps are shown. The name of the vertical slice through the model is shown in the file name.
figures_acors
contains all the autocorrelation figures
MODELS_FINAL contains
figgdc*eps files show observed (dots0 and interpolated (line) dispersion curves in each grid point
kernel*eps show resolution kernels in each grid point
lotos

DIXIEVAL contains the figures resulted from the tomographic inversion, one directory for each iteration

FIG_FILES contains the files to make the figures in DIXIEVAL

matlab_scripts

DVESA - scripts to create models and cut vertical and horizontal model slices in the DVESA

DVSA scripts to create models and cut vertical and horizontal model slices in the DVSA

INTEGRATED_MODEL: Codes including MAT_MOD, array analysis and crosscorrelation analysis

PROJECT_AREA

references

contains available references which were not added to the references for the baseline model

WELLS contains the velocity-temperature and rock-type analysis data

PART II-APPENDIX 10 DIRECTORY FILES

All files associated with Appendix 10 are presented are presented in a Part II-Appendix 10 folder submitted to the national Geothermal Data Repository.

APPENDIX 11

MAGNETOTELLURIC PLAN VIEW MAPS AT A DEPTH FROM 1KM TO 20KM

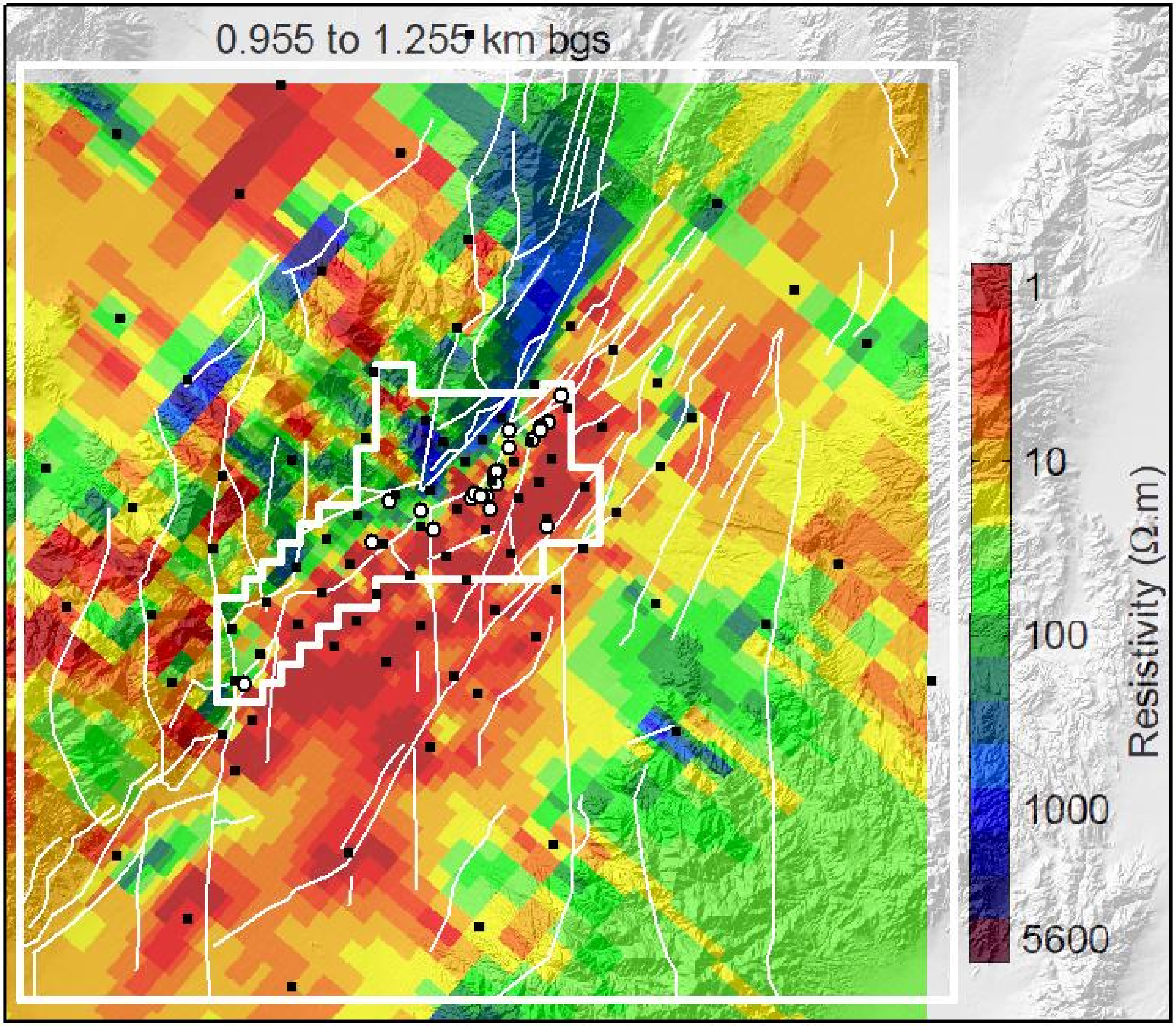

Figure A11-1. MT plan view map at approximately 1km depth below the surface. Note that Dixie Valley is nominally at +1km above sea level. The MT data is superimposed on a DEM for the Project Area (indicated by the large white square). Surface faulting (thin white lines), the Calibration Area (see Figure 1), MT stations (black squares), and wells (white circles) are also shown.

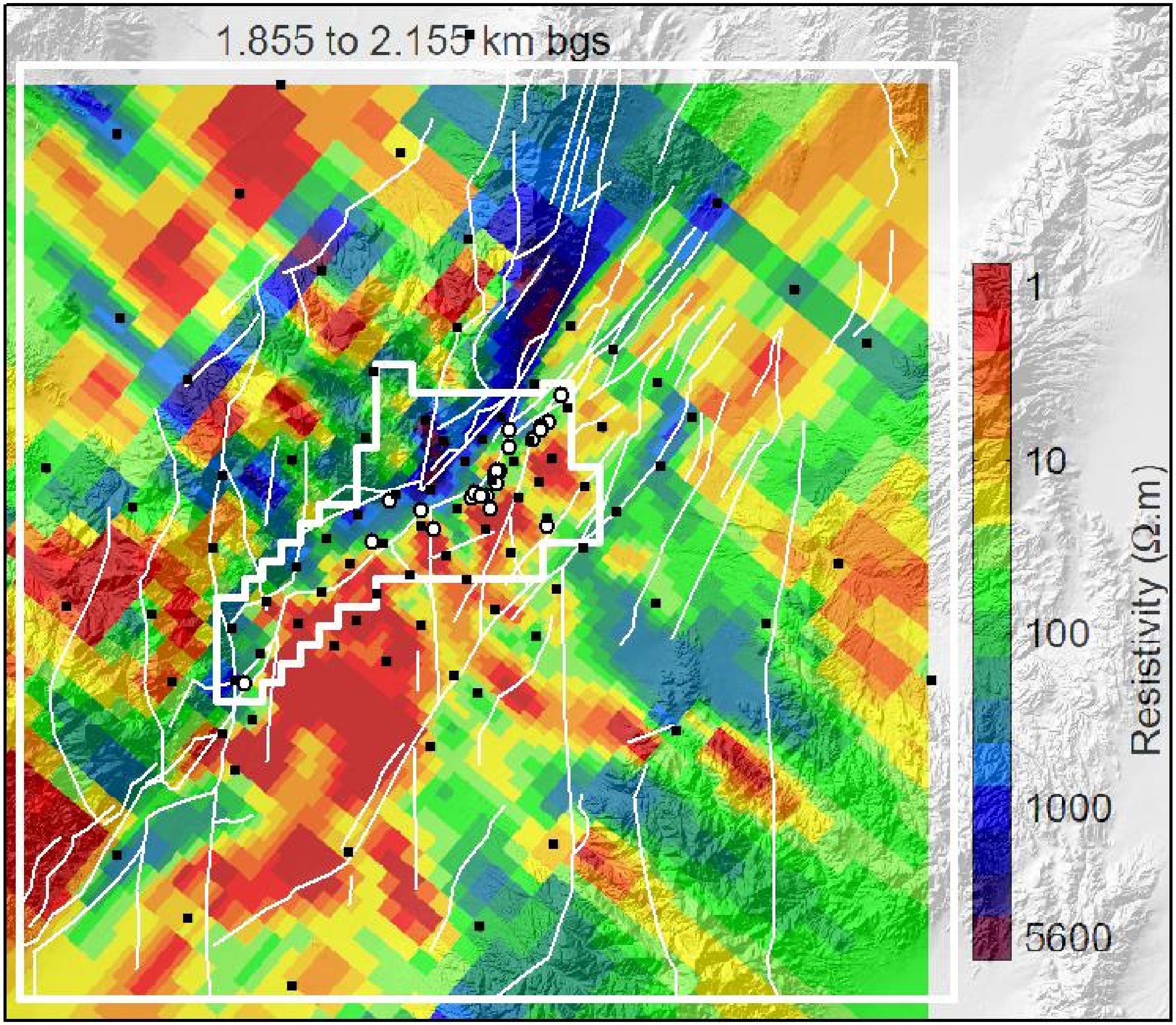

Figure A11-2. MT plan view map at approximately 2km depth below the surface. Note that Dixie Valley is nominally at +1km above sea level. The MT data is superimposed on a DEM for the Project Area (indicated by the large white square). Surface faulting (thin white lines), the Calibration Area (see Figure 1), MT stations (black squares), and wells (white circles) are also shown.

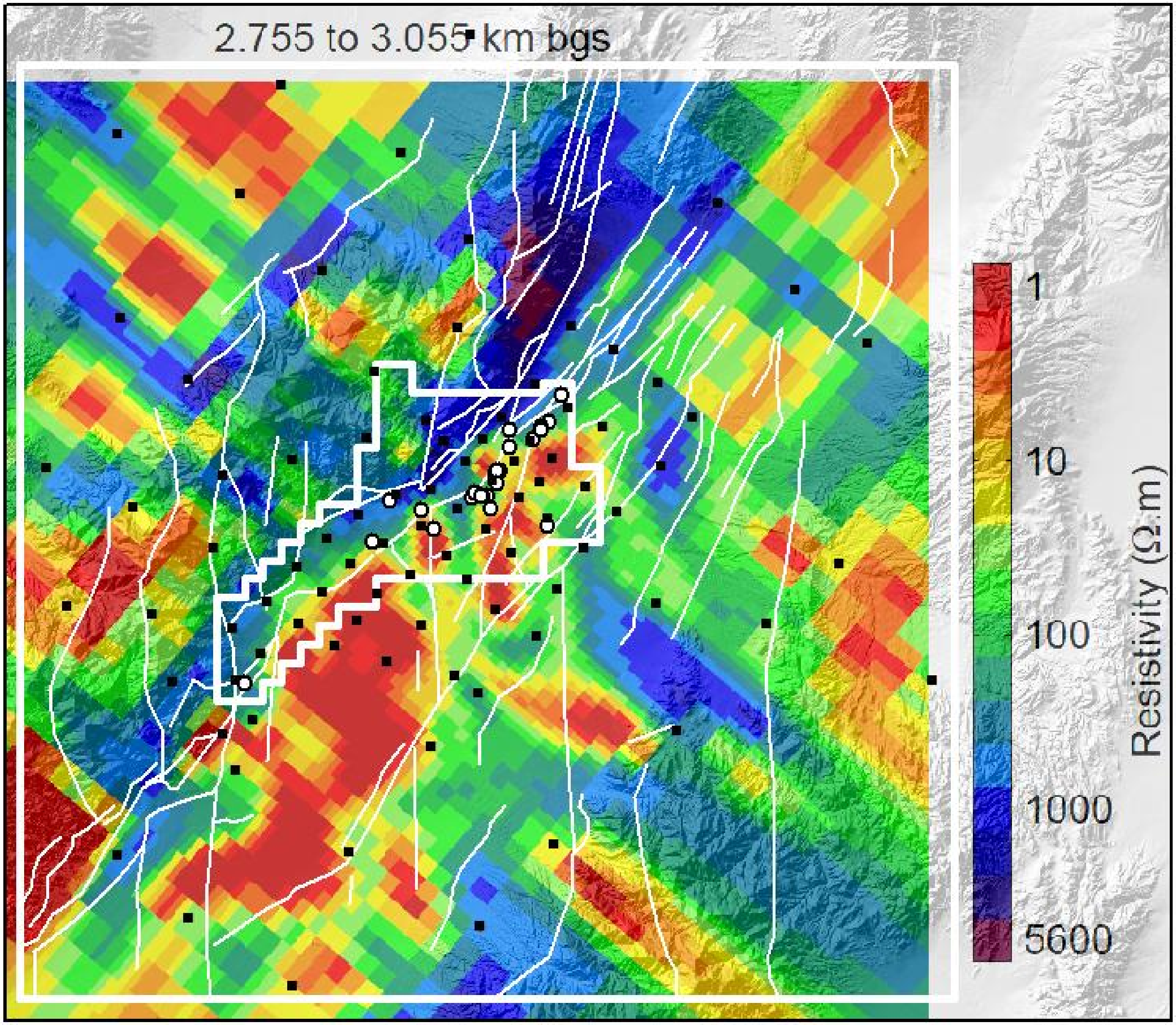

Figure A11-3. MT plan view map at approximately 3km depth below the surface. Note that Dixie Valley is nominally at +1km above sea level. The MT data is superimposed on a DEM for the Project Area (indicated by the large white square). Surface faulting (thin white lines), the Calibration Area (see Figure 1), MT stations (black squares), and wells (white circles) are also shown.

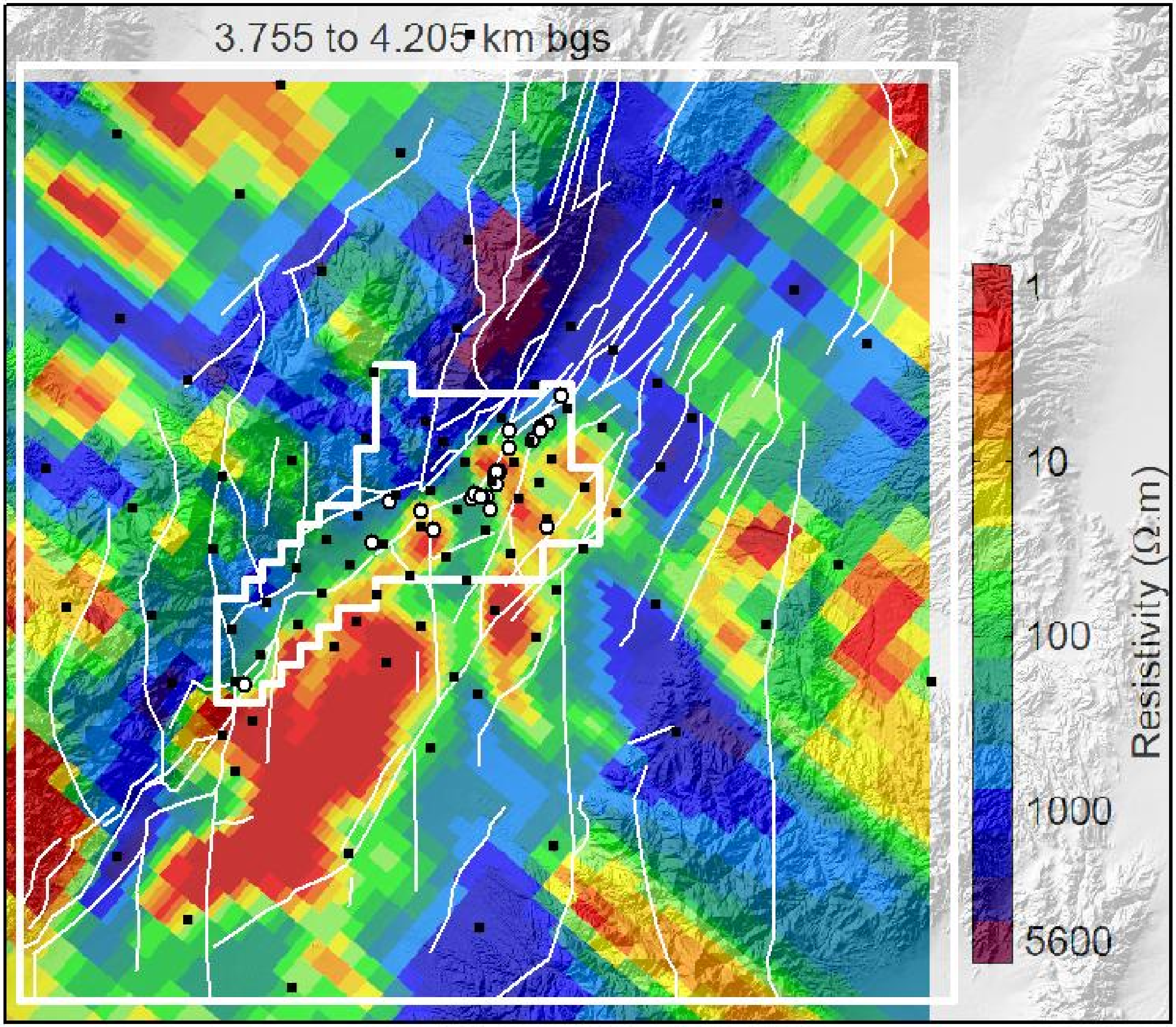

Figure A11-4. MT plan view map at approximately 4km depth below the surface. Note that Dixie Valley is nominally at +1km above sea level. The MT data is superimposed on a DEM for the Project Area (indicated by the large white square). Surface faulting (thin white lines), the Calibration Area (see Figure 1), MT stations (black squares), and wells (white circles) are also shown.

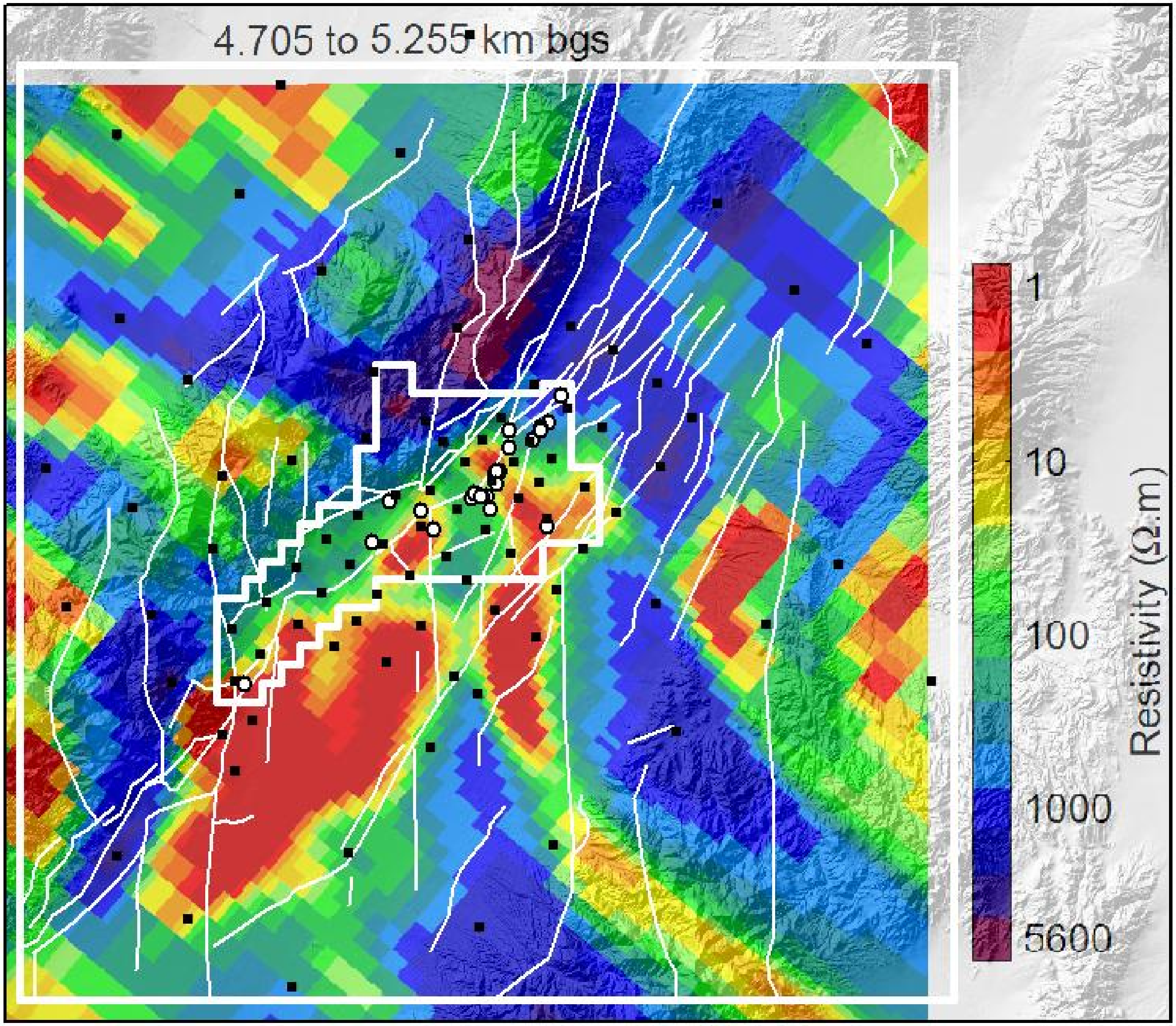

Figure A11-5. MT plan view map at approximately 5km depth below the surface. Note that Dixie Valley is nominally at +1km above sea level. The MT data is superimposed on a DEM for the Project Area (indicated by the large white square). Surface faulting (thin white lines), the Calibration Area (see Figure 1), MT stations (black squares), and wells (white circles) are also shown.

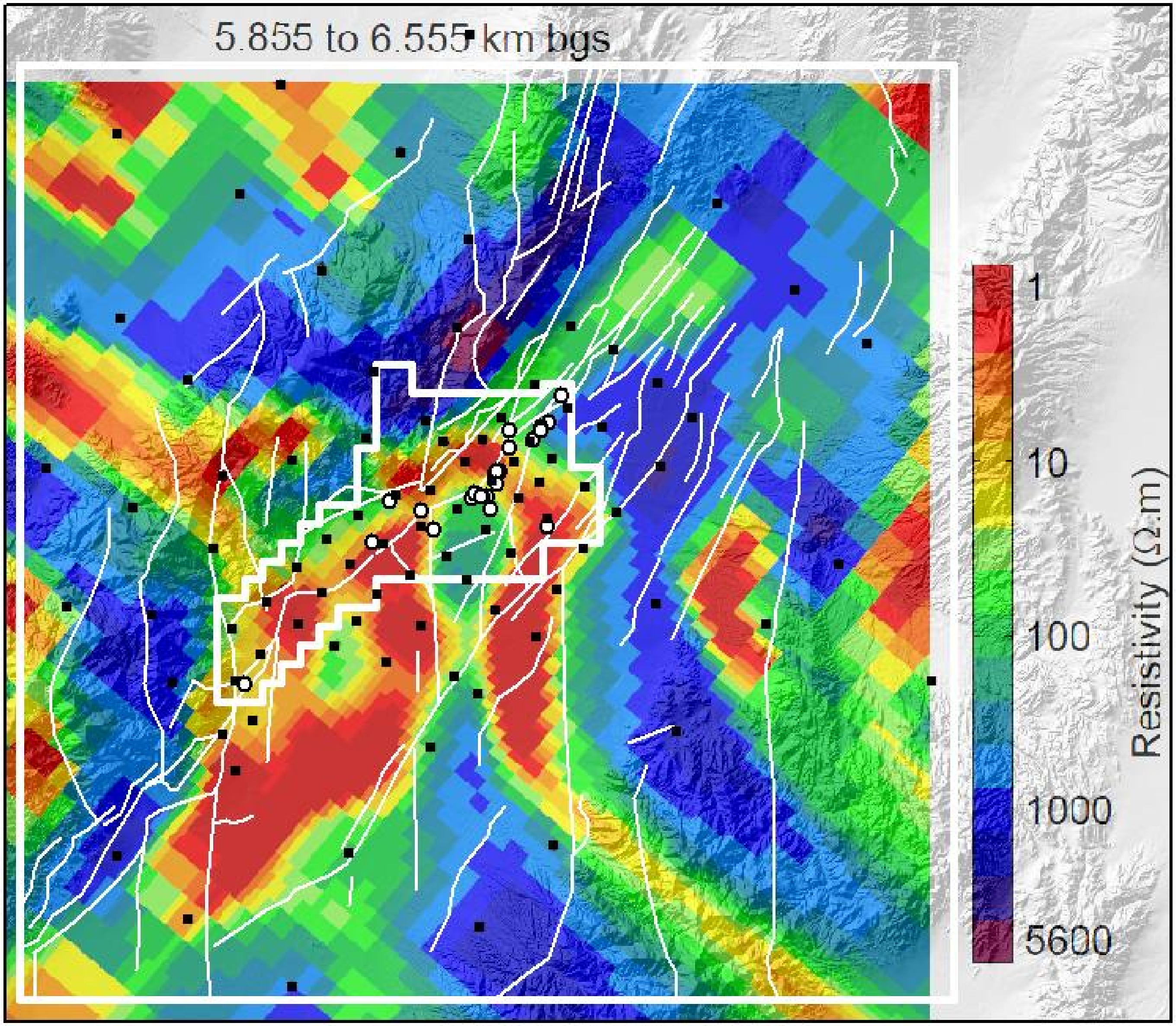

Figure A11-6. MT plan view map at approximately 6km depth below the surface. Note that Dixie Valley is nominally at +1km above sea level. The MT data is superimposed on a DEM for the Project Area (indicated by the large white square). Surface faulting (thin white lines), the Calibration Area (see Figure 1), MT stations (black squares), and wells (white circles) are also shown.

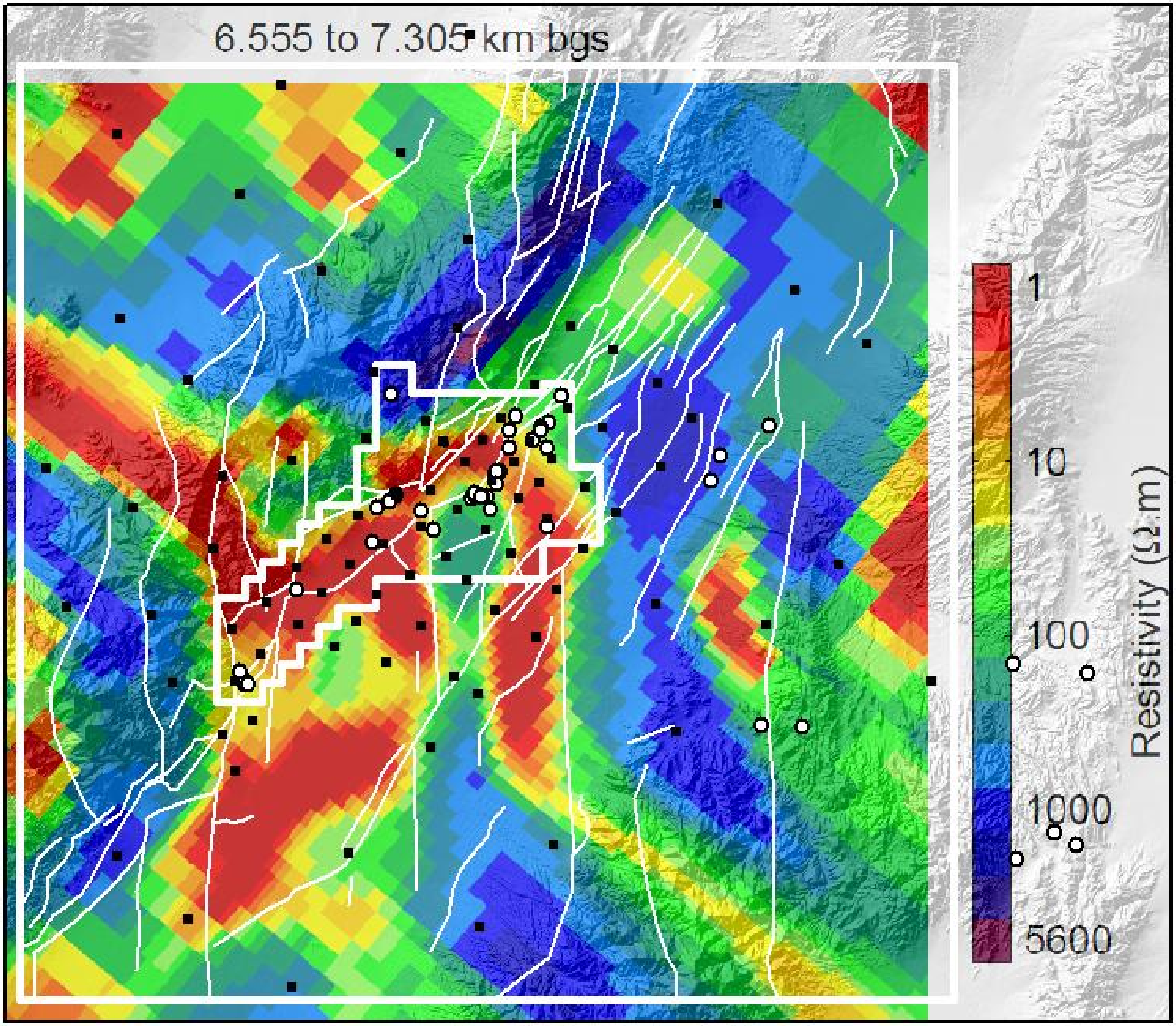

Figure A11-7. MT plan view map at approximately 7km depth below the surface. Note that Dixie Valley is nominally at +1km above sea level. The MT data is superimposed on a DEM for the Project Area (indicated by the large white square). Surface faulting (thin white lines), the Calibration Area (see Figure 1), MT stations (black squares), and wells (white circles) are also shown.

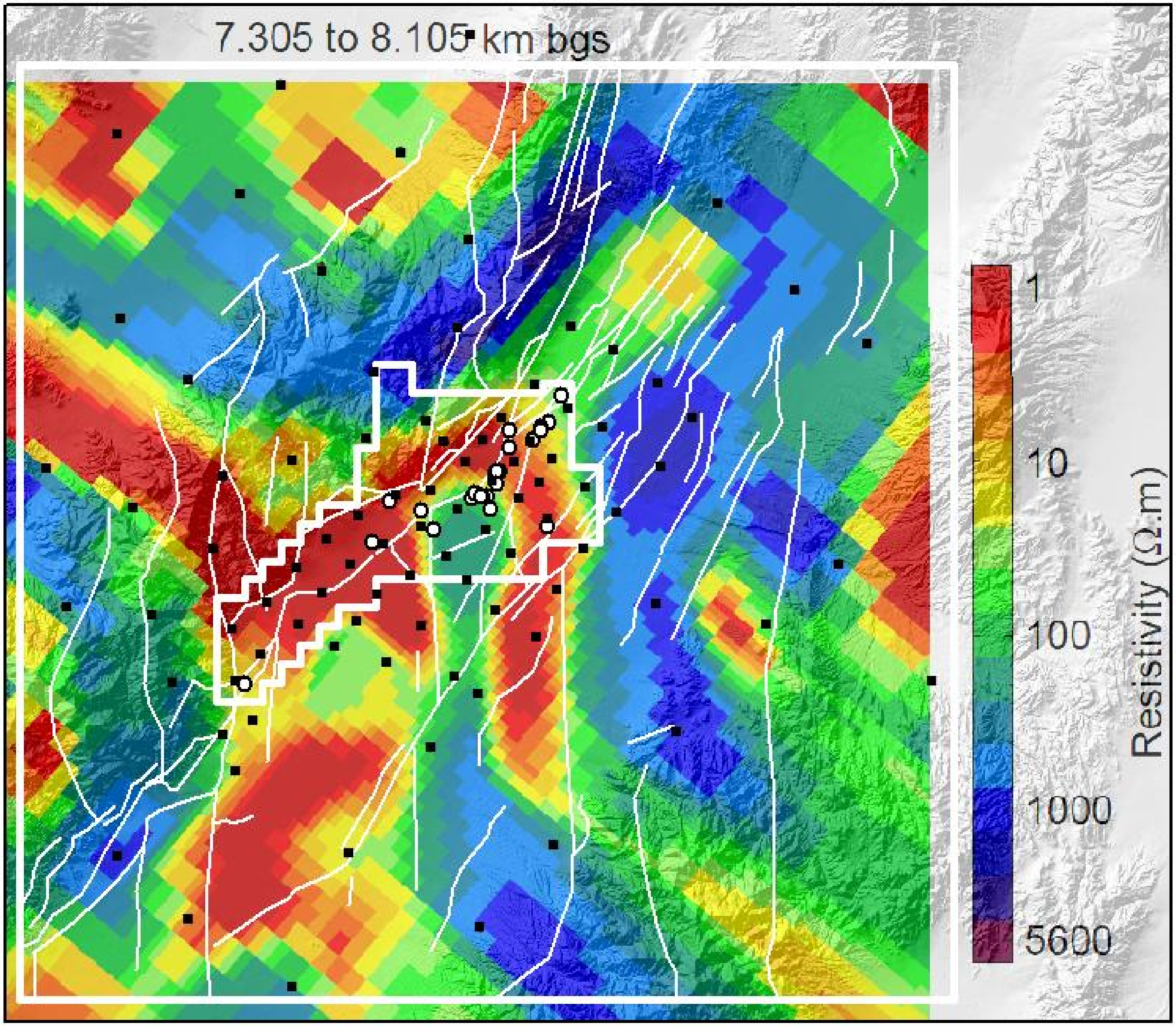

Figure A11-8. MT plan view map at approximately 8km depth below the surface. Note that Dixie Valley is nominally at +1km above sea level. The MT data is superimposed on a DEM for the Project Area (indicated by the large white square). Surface faulting (thin white lines), the Calibration Area (see Figure 1), MT stations (black squares), and wells (white circles) are also shown.

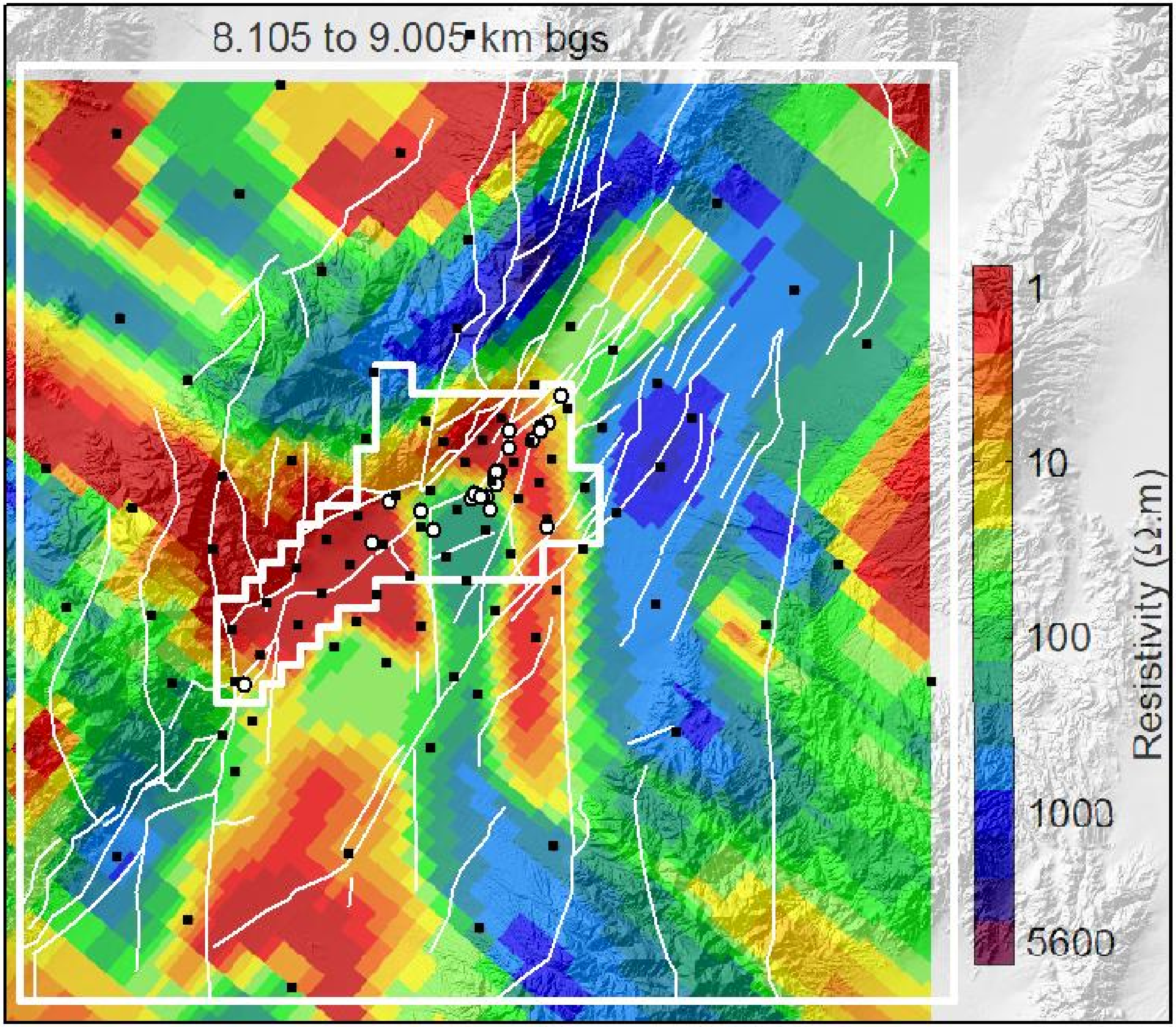

Figure A11-9. MT plan view map at approximately 9km depth below the surface. Note that Dixie Valley is nominally at +1km above sea level. The MT data is superimposed on a DEM for the Project Area (indicated by the large white square). Surface faulting (thin white lines), the Calibration Area (see Figure 1), MT stations (black squares), and wells (white circles) are also shown.

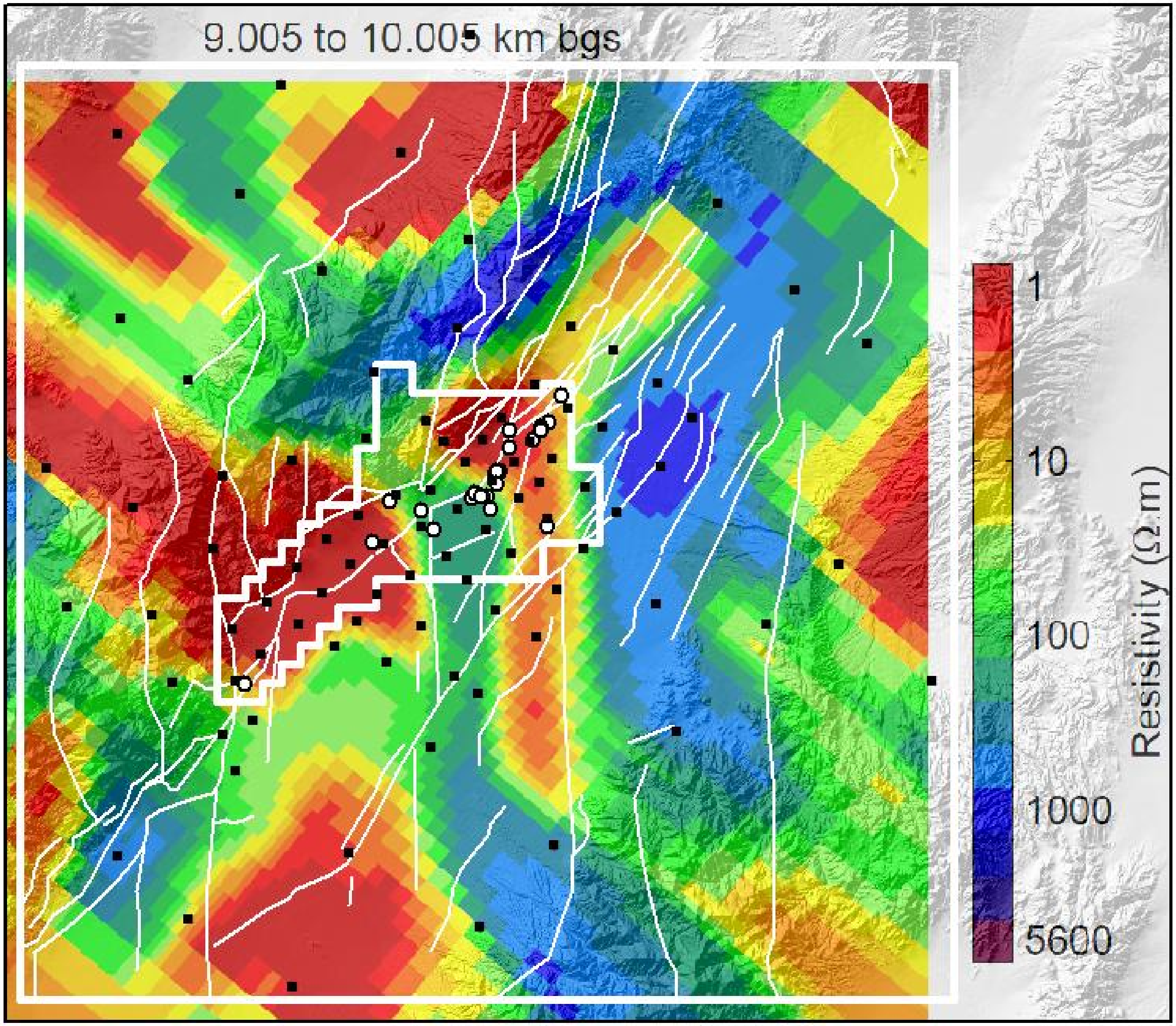

Figure A11-10. MT plan view map at approximately 10km depth below the surface. Note that Dixie Valley is nominally at +1km above sea level. The MT data is superimposed on a DEM for the Project Area (indicated by the large white square). Surface faulting (thin white lines), the Calibration Area (see Figure 1), MT stations (black squares), and wells (white circles) are also shown.

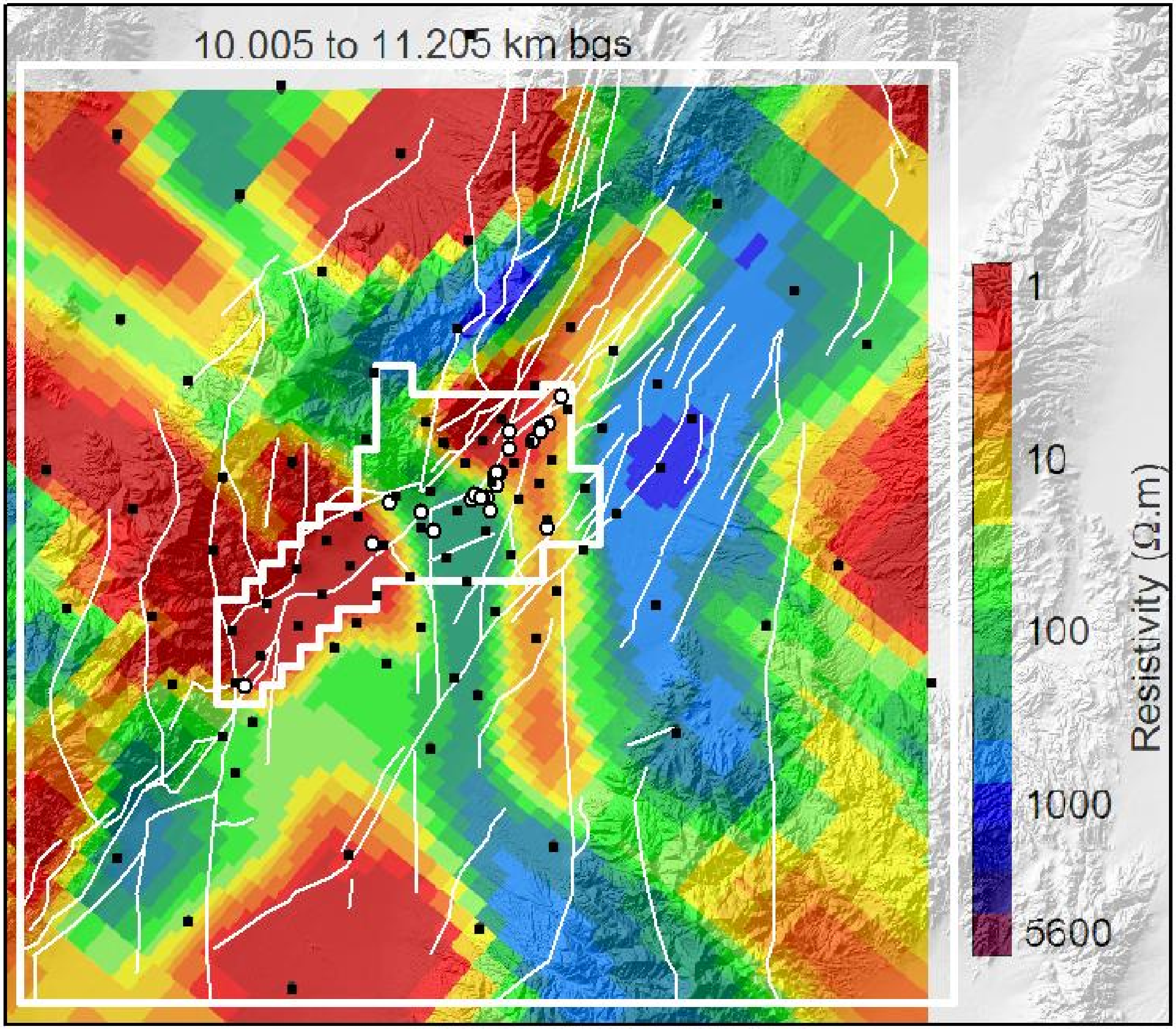

Figure A11-11. MT plan view map at approximately 11km depth below the surface. Note that Dixie Valley is nominally at +1km above sea level. The MT data is superimposed on a DEM for the Project Area (indicated by the large white square). Surface faulting (thin white lines), the Calibration Area (see Figure 1), MT stations (black squares), and wells (white circles) are also shown.

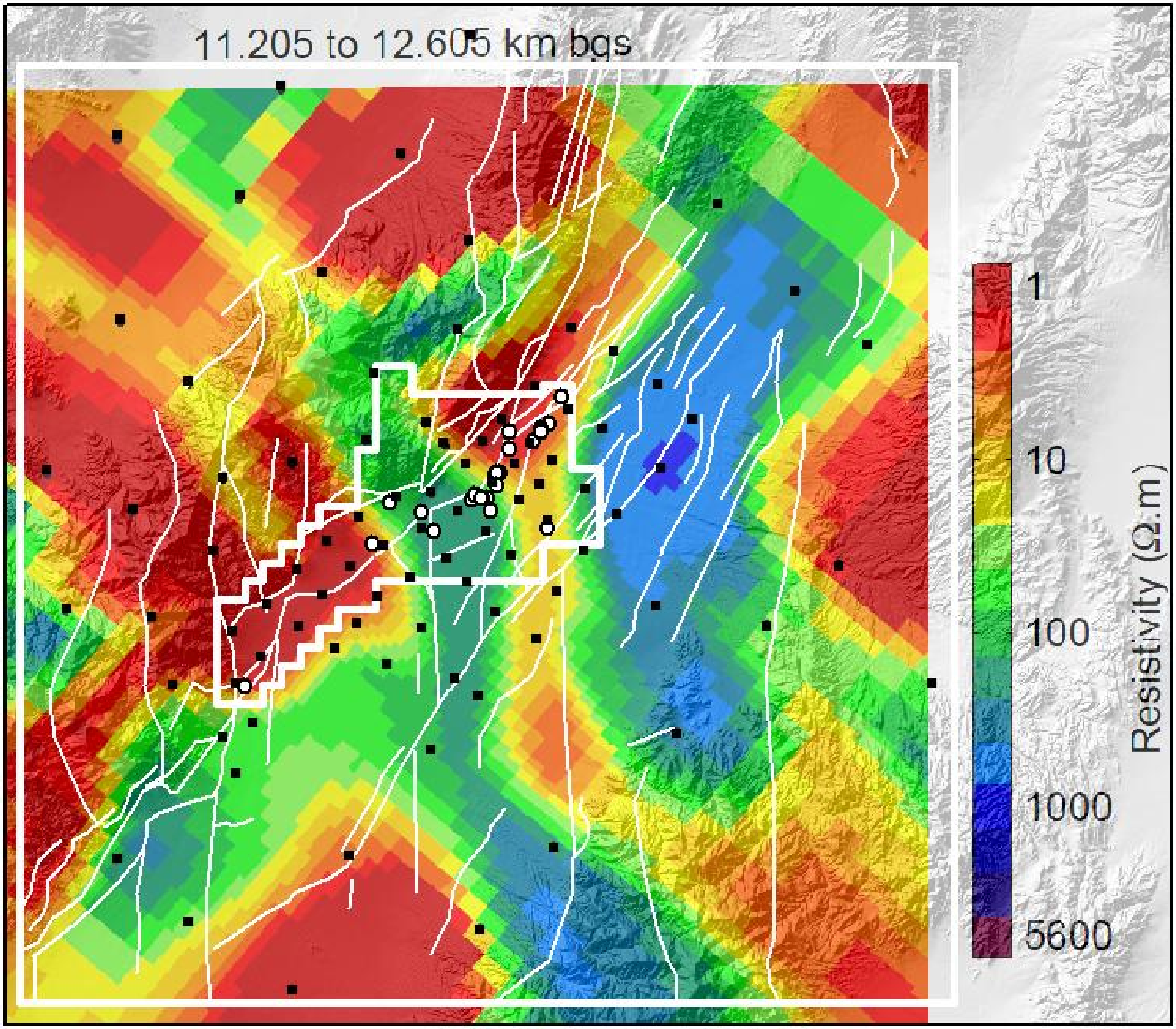

Figure A11-12. MT plan view map at approximately 12km depth below the surface. Note that Dixie Valley is nominally at +1km above sea level. The MT data is superimposed on a DEM for the Project Area (indicated by the large white square). Surface faulting (thin white lines), the Calibration Area (see Figure 1), MT stations (black squares), and wells (white circles) are also shown.

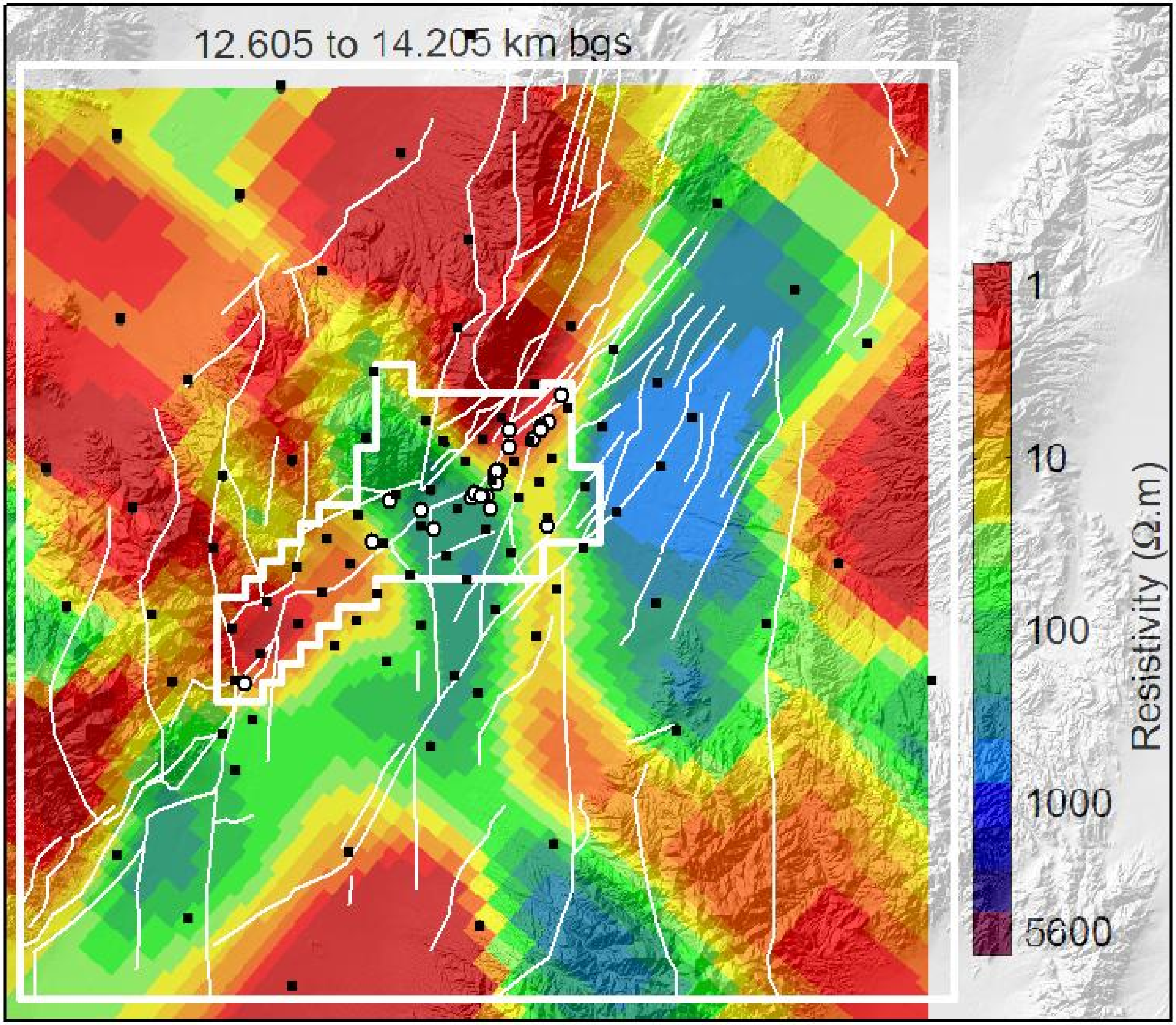

Figure A11-13. MT plan view map at approximately 13km depth below the surface. Note that Dixie Valley is nominally at +1km above sea level. The MT data is superimposed on a DEM for the Project Area (indicated by the large white square). Surface faulting (thin white lines), the Calibration Area (see Figure 1), MT stations (black squares), and wells (white circles) are also shown.

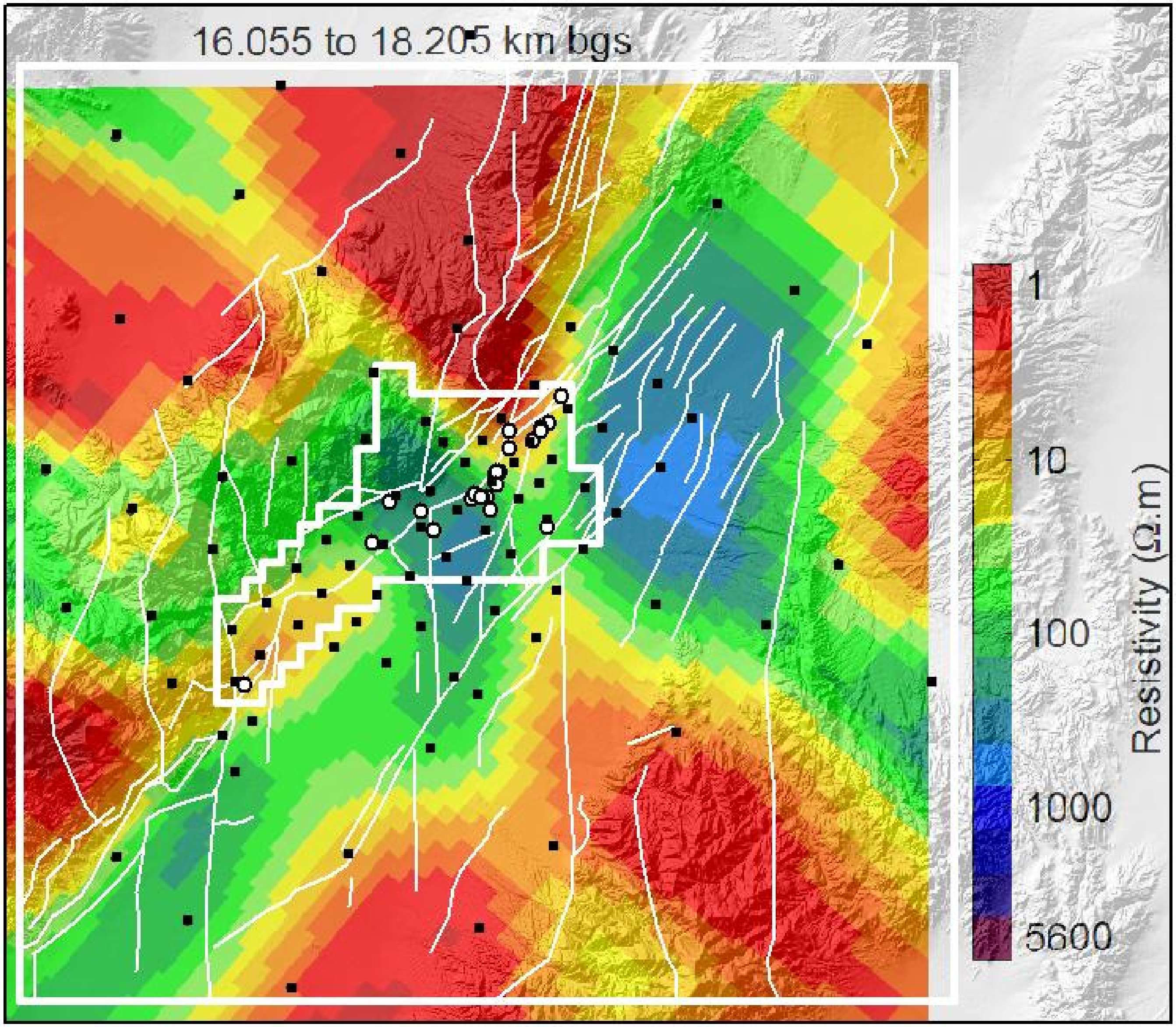

Figure A11-14. MT plan view map at approximately 18km depth below the surface. Note that Dixie Valley is nominally at +1km above sea level. The MT data is superimposed on a DEM for the Project Area (indicated by the large white square). Surface faulting (thin white lines), the Calibration Area (see Figure 1), MT stations (black squares), and wells (white circles) are also shown.

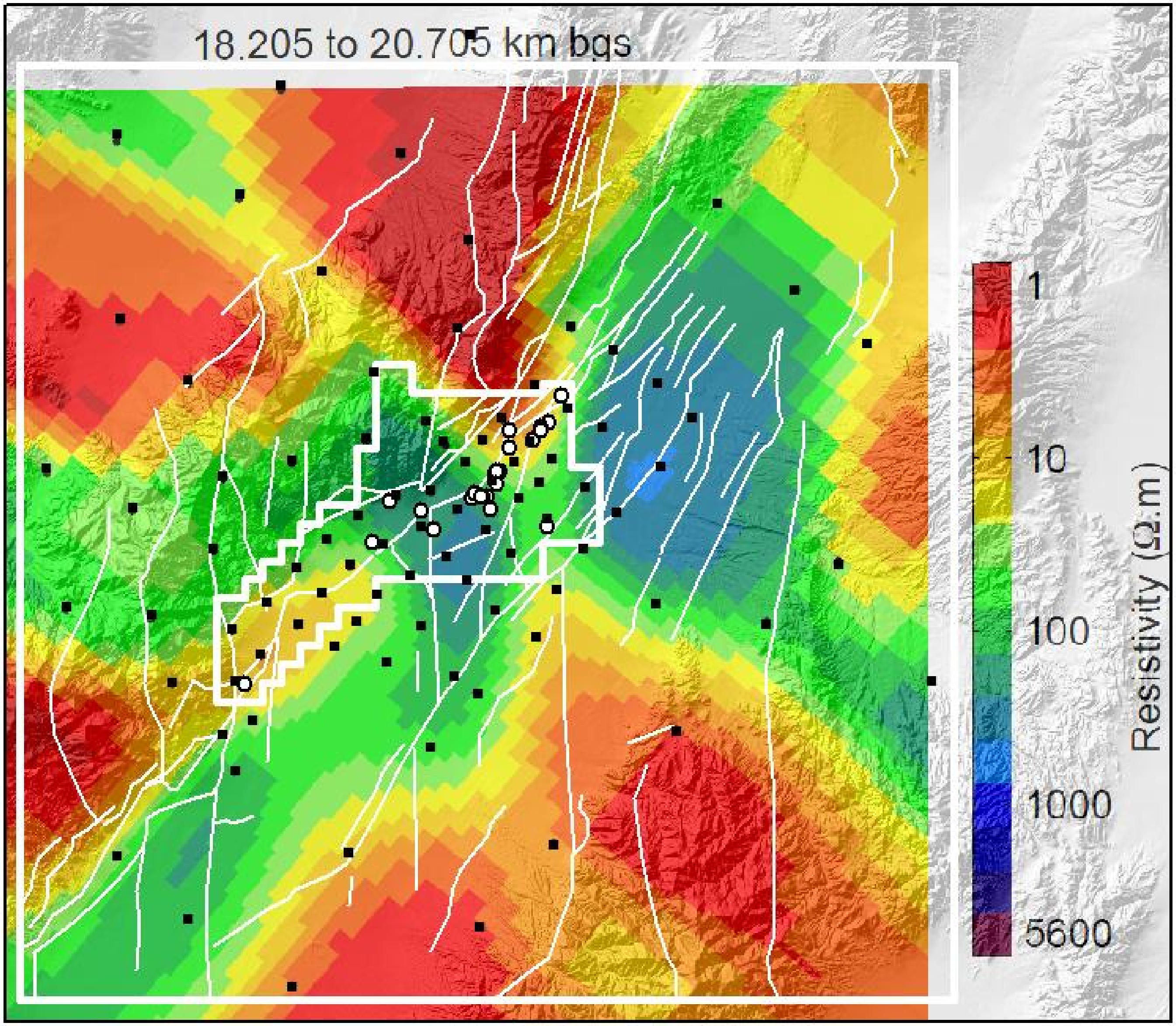

Figure A11-15. MT plan view map at approximately 20km depth below the surface. Note that Dixie Valley is nominally at +1km above sea level. The MT data is superimposed on a DEM for the Project Area (indicated by the large white square). Surface faulting (thin white lines), the Calibration Area (see Figure 1), MT stations (black squares), and wells (white circles) are also shown.

PART II - APPENDIX 12

ENHANCED DATA CART SENSITIVITY ANALYSIS DATA

This analysis was performed to understand the predictive powers and relationships between seven key geoscience parameters using Classification and Regression Tree Analysis (CART). The following table documents the CART sensitivity analysis exploring all possibilities of the indicated parameters for predicting inferred EGS viability using enhanced data. Each row of the table represents a subset of the parameters that were used to make these predictions. The cells are shaded grey to reflect parameters that were considered but not used by CART to make any splits, shaded yellow for parameters that were considered and used, and red for the parameter used to make the first split. The last column shows the R^2 value corresponding to this tree. In cases where no variables were used, the R^2 value will be 0. This happens because the EGS favorable cells are so sparse that no splits were found that would reduce the impurity beyond a certain threshold. In other words, no splits would separate the data into categories that were sufficiently different in the concentrations of EGS cells. The tables following this one show all trees for predicting productive Hydrothermal, Temperature, Temperature Residuals, and Lithology.

Number of Variables Considered	**Potential Variables Used in Predicting Inferred EGS Viability**						**R^2**
	Temp	***Vp***	***CSC***	***MT***	***Dil***	***GM_Lith***	
1	C						0
		C					0
			F				0.027
				C			0
					C		0
						C	0
2	C	C					0
	U		F				0.045
	C			C			0
	C				C		0
	C					C	0
		U	F				0.037
		C		C			0
		C			C		0
		C				C	0
			F	U			0.083
			F		U		0.068
			F			U	0.05
				C	C		0
				C		C	0
					C	C	0
3	U	U	F				0.045
	C	C		C			0
	C	C			C		0
	C	C				C	0
	C		F	U			0.083

Number of Variables Considered	Potential Variables Used in Predicting Inferred EGS Viability						R^2
	Temp	***Vp***	***CSC***	***MT***	***Dil***	***GM_Lith***	
3	U		F		U		0.092
	U		F			U	0.05
	C			C	C		0
	C			C		C	0
	C				C	C	0
		C	F	U			0.083
		U	F		U		0.092
		U	F			U	0.064
		C		C	C		0
		C		C		C	0
		C			C	C	0
			F	U	C		0.083
			F	U		C	0.083
			F		U	C	0.068
				C	C	C	0
4	C	C	F	U			0.083
	U	C	F		U		0.092
	U	U	F			U	0.064
	C	C		C	C		0
	C	C		C		C	0
	C	C			C	C	0
	C		F	U	C		0.083
	C		F	U		C	0.083
	U		F		U	C	0.092
	C			C	C	C	0
		C	F	U	C		0.083
		C	F	U		C	0.083
		U	F		U	C	0.092
		C		C	C	C	0
			F	U	C	C	0.083
5	C	C	F	U	C		0.083
	C	C	F	U		C	0.083
	U	C	F		U	C	0.092
	C	C		C	C	C	0
	C		F	U	C	C	0.083
		C	F	U	C	C	0.083
6	C	C	F	U	C	C	0.083

Number of Variables Considered	Potential Variables Used in Predicting Productive Hydrothermal						R^2
	Temp	*Vp*	*CSC*	*MT*	*Dil*	*GM.Lith*	
1	C						0
		C					0
			C				0
				C			0
					F		0.035
						C	0
2	C	C					0
	C		C				0
	C			C			0
	U				F		0.037
	C					C	0
		C	C				0
		C		C			0
		U			F		0.12
		C				C	0
			C	C			0
			U		F		0.153
			C			C	0
				C	F		0.035
				C		C	0
					F	U	0.074
3	C	C	C				0
	C	C		C			0
	U	U			F		0.231
	C	C				C	0
	C		C	C			0
	U		U		F		0.177
	C		C			C	0
	U			U	F		0.126
	C			C		C	0
	U				F	U	0.069
		C	C	C			0
		U	U		F		0.204
3		C	C			C	0
		U		U	F		0.267
		C		C		C	0
		U			F	U	0.085
			U	U	F		0.19
			C	C		C	0

Number of Variables Considered	Potential Variables Used in Predicting Productive Hydrothermal						R^2
	Temp	Vp	CSC	MT	Dil	GM.Lith	
			U		F	U	0.123
				U	F	U	0.117
4	C	C	C	C			0
	U	U	C		F		0.141
	C	C	C			C	0
	U	U		C	F		0.141
	C	C		C		C	0
	U	U			F	C	0.141
	U		U	C	F		0.177
	C		C	C		C	0
	U		U		F	C	0.177
	U			U	F	U	0.102
		U	U	C	F		0.204
		C	C	C		C	0
		U	U		F	U	0.09
		C		U	F	U	0.117
			U	U	F	U	0.16
5	U	U	C	C	F		0.141
	C	C	C	C		C	0
	U	U	C		F	C	0.141
	U	U		C	F	C	0.141
	U		U	C	F	C	0.177
		C	U	U	F	U	0.16
6	U	U	C	C	F	C	0.141

Number of Variables Considered	Potential Variables Used in Predicting Temperature						R^2
	Vp	CSC	MT	Dil	GM.Lith	Lithology	
1	F						0.659
		F					0.13
			F				0.157
				F			0.326
					F		0.278
						F	0.446
2	F	U					0.679
	F		U				0.69
	F			U			0.717
	F				C		0.659
	F						0.663

Number of Variables Considered	Potential Variables Used in Predicting Temperature						R^2
	Vp	***CSC***	***MT***	***Dil***	***GM.Lith***	***Lithology***	
		U	F				0.237
		C		F			0.326
		U			F		0.343
		U					0.521
			U	F			0.404
			U		F		0.341
			U				0.478
				U	F		0.456
				U			0.57
					C		0.446
	F	U	U				0.697
	F	C		U			0.717
	F	U			C		0.679
	F	U					0.684
	F		U	U			0.727
	F		U		C		0.69
	F		U				0.69
	F			U	C		0.717
3	F			U			0.717
	F				C		0.663
		C	U	F			0.404
		U	U		F		0.363
		U	U				0.528
		U		U	F		0.467
		C		U			0.57
		U			C		0.521
			U	U	F		0.493
			U	U			0.577
3			U		C		0.478
				U	C		0.57
	F	C	U	U			0.727
	F	U	U		C		0.697
	F	U	U				0.697
	F	C		U	C		0.717
4	F	C		U			0.717
	F	U			C		0.684
	F		U	U	C		0.727
	F		U	U			0.727
	F		U		C		0.69

Number of Variables Considered	Potential Variables Used in Predicting Temperature						R^2
	Vp	*CSC*	*MT*	*Dil*	*GM.Lith*	*Lithology*	
	F			U	C		0.717
		C	U	U	F		0.493
		C	U	U			0.577
		U	U		C		0.528
		C		U	C		0.57
			U	U	C		0.577
5	F	C	U	U	C		0.727
	F	C	U	U			0.727
	F	U	U		C		0.697
	F	C		U	C		0.717
	F		U	U	C		0.727
		C	U	U	C		0.577
6	F	C	U	U	C		0.727

Number of Variables Considered	Potential Variables Used in Predicting Temperature Residuals						*R^2*
	Vp	*CSC*	*MT*	*Dil*	*GM.Lith*	*Lithology*	
1	F						0.09
		F					0.143
			F				0.133
				F			0.227
					F		0.045
						F	0.051
2	U	F					0.163
	U		F				0.217
	U			F			0.264
	U				F		0.086
	U					F	0.071
		U	F				0.207
		U		F			0.318
		F			U		0.162
		F				U	0.164
			U	F			0.283
			F		U		0.15
			F			U	0.159
				F	C		0.227
				F		U	0.254
					U	F	0.066

Number of Variables Considered	Potential Variables Used in Predicting Temperature Residuals						R^2
	Vp	***CSC***	***MT***	***Dil***	***GM.Lith***	***Lithology***	
3	U	U	F				0.234
	U	U		F			0.348
	U	F			C		0.163
	U	F				U	0.167
	U		U	F			0.296
	U		F		C		0.217
	U		F			U	0.196
	U			F	C		0.264
	U			F		C	0.264
	U				C	F	0.071
		U	C	F			0.318
		U	F		U		0.216
		U	F			C	0.207
		U		F	C		0.318
		U		F		C	0.318
		F			C	U	0.164
			U	F	C		0.283
			U	F		U	0.271
3			F		U	U	0.175
				F	C	U	0.254
4	U	U	C	F			0.348
	U	U	F		C		0.234
	U	U	F			C	0.234
	U	U		F	C		0.348
	U	U		F		C	0.348
	U	F			C	U	0.167
	U		U	F	C		0.296
	U		U	F		C	0.296
	U		F		C	U	0.196
	U			F	C	C	0.264
		U	C	F	C		0.318
		U	C	F		C	0.318
		U	F		U	C	0.216
		U		F	C	C	0.318
			U	F	C	U	0.271
5	U	U	C	F	C		0.348
	U	U	C	F		C	0.348
	U	U	F		C	C	0.234

Number of Variables Considered	Potential Variables Used in Predicting Temperature Residuals						R^2
	Vp	***CSC***	***MT***	***Dil***	***GM.Lith***	***Lithology***	
	U	U		F	C	C	0.348
	U		U	F	C	C	0.296
		U	C	F	C	C	0.318
6	U	U	C	F	C	C	0.348

Number of Variables Considered	Potential Variables Used in Predicting Grav-Mag Lithology Density						R^2
	Vp	***CSC***	***MT***	***Dil***	***GM_Lith***	***Lithology***	
1	F						0.287
		F					0.318
			F				0.157
				F			0.136
					F		0.203
						F	0.604
2	U	F					0.437
	F		U				0.449
	F			U			0.376
	F				U		0.407
	C					F	0.604
		F	U				0.529
		F		U			0.514
		F			U		0.612
		U				F	0.634
			F	U			0.269
			U		F		0.241
			U			F	0.619
				U	F		0.272
				C		F	0.604
					U	F	0.614
3	U	F	U				0.578
	C	F		U			0.514
	U	F			U		0.615
	C	U				F	0.634
	F		U	U			0.478
	F		U		C		0.449
	C		U			F	0.619
	F			U	U		0.431
	C			C		F	0.604

Number of Variables Considered	Potential Variables Used in Predicting Grav-Mag Lithology Density						R^2
	Vp	*CSC*	*MT*	*Dil*	*GM_Lith*	*Lithology*	
	C				U	F	0.614
		F	U	U			0.598
		F	U		U		0.616
		U	U			F	0.69
		F		U	U		0.617
		U		U		F	0.646
		U			U	F	0.683
			U	U	F		0.295
3			U	C		F	0.619
			U		C	F	0.619
				C	U	F	0.614
4	C	F	U	U			0.598
	C	F	U		U		0.616
	C	U	U			F	0.69
	C	F		U	U		0.617
	C	U		U		F	0.646
	C	U			U	F	0.683
	F		U	U	C		0.478
	C		U	C		F	0.619
	C		U		C	F	0.619
	C			C	U	F	0.614
		F	U	U	U		0.65
		U	U	U		F	0.676
		U	U		U	F	0.704
		U		C	U	F	0.683
			U	C	C	F	0.619
5	C	F	U	U	U		0.65
	C	U	U	U		F	0.676
	C	U	U		U	F	0.704
	C	U		C	U	F	0.683
	C		U	C	C	F	0.619
		U	U	C	U	F	0.704
6	C	U	U	C	U	F	0.704

Legend

- Tbf: basin-filling sediments
- Tmb: Miocene basalt
- Tv: Oligocene silicic volcanics
- Kgr: Cretaceous granodiorite
- Jbr: Jurassic Boyer Ranch quartzite
- Jz: Jurassic mafic volcanics
- Tr: Triassic meta-sediments

Syncline axis

Temperature contour (° C) 100

Intersection with section tie-line A

Deep Well 53-15

Fumaroles

Contacts
- known/approximate
- inferred

Range-front (DVF)/Piedmont fault
- known/approximate
- inferred

Other Faults
- known/approximate
- inferred
- geophysical-inferred

*Mapped faults and geophysical faults projected to the surface are accurate to within 500m (1 cell)

Enhanced Data Legend
Gravity/Magnetic Inferred Lithologic Units

- Tls: Lake Sediments (D= 1.8-1.835)
- Tbf: Basin-filling sediments (D=2.105 - 2.226)
- Jv: Jurassic rhyolite (D= 2.308 - 2.947)
- Jg: Jz igneous group (D=2.67, M=0.007)
- Jg: Jz Igneous group (Off-Axis)
- Bedrock: Tr meta-seds, K granodiorite, Jz non-magnetic rocks (D=2.67)

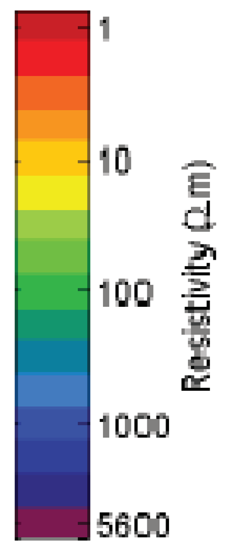

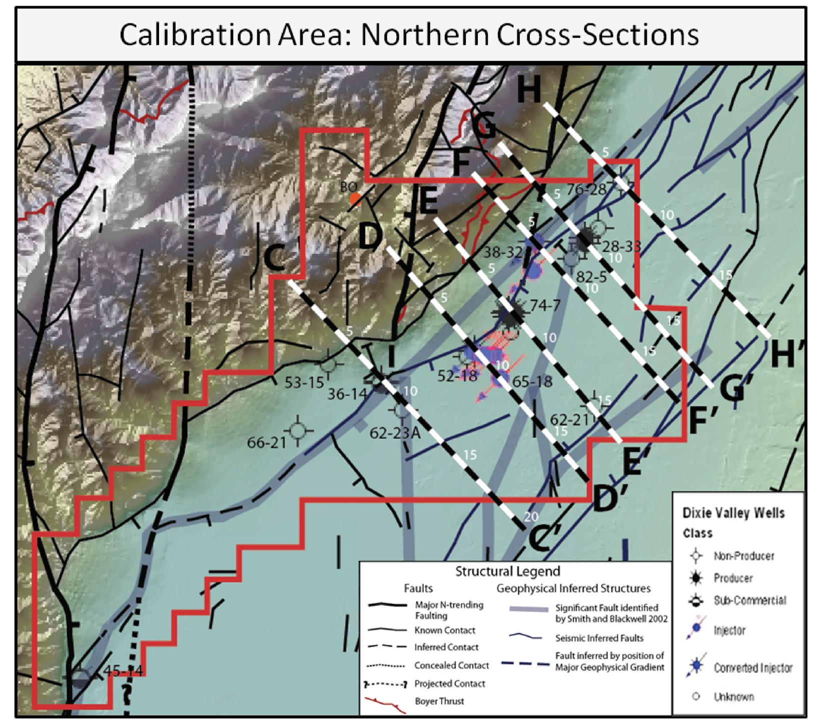

Convective Thermal Model Legend (°C)

- < 100 °C
- 100-150 °C
- 150-200 °C
- 200 °C
- 200-250 °C
- > 250 °C

* Temperature contours reflect 10 °C increments

Legend
Thermal Iso-Contours

- 100-150ºC
- 150-200ºC
- 200-250ºC
- 250+ºC

Psuedo-Convective Model Legend

Tconvective = Toverall - Tconductive

- -50° C
- -25° C
- 0° C
- 25° C
- 50 ° C
- 75° C
- 100° C
- 125° C
- No Data

Plate 3. Enhanced Data along NW-SE Oriented Cross-Sections within the Northern Calibration Area

Legend

- Tbf: basin-filling sediments
- Tmb: Miocene basalt
- Tv: Oligocene silicic volcanics
- Kgr: Cretaceous granodiorite
- Jbr: Jurassic Boyer Ranch quartzite
- Jz: Jurassic mafic volcanics
- Tr: Triassic meta-sediments

Syncline axis

Temperature contour (° C) 100

Intersection with section tie-line A

Deep Well 53-15

Fumaroles

Contacts
- known/approximate
- inferred

Range-front (DVF)/Piedmont fault
- known/approximate
- inferred

Other Faults
- known/approximate
- inferred
- geophysical-inferred

* Mapped faults and geophysical faults projected to the surface are accurate to within 500m (1 cell)
* A segment of the geologic cross-section C-C' (See Plate 3) has been overlayed on A6

Enhanced Data Legend
Gravity/Magnetic Inferred Lithologic Units

- Tls: Lake Sediments (D= 1.8-1.835)
- Tbf: Basin-filling sediments (D=2.105 - 2.226)
- Jv: Jurassic rhyolite (D= 2.308 - 2.947)
- Jg: Jz igneous group (D=2.67, M=0.007)
- Jg: Jz Igneous group (Off-Axis)
- Bedrock: Tr meta-seds, K granodiorite, Jz non-magnetic rocks (D=2.67)

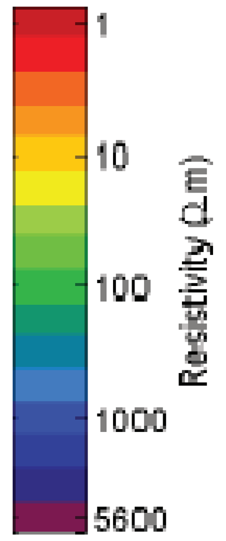

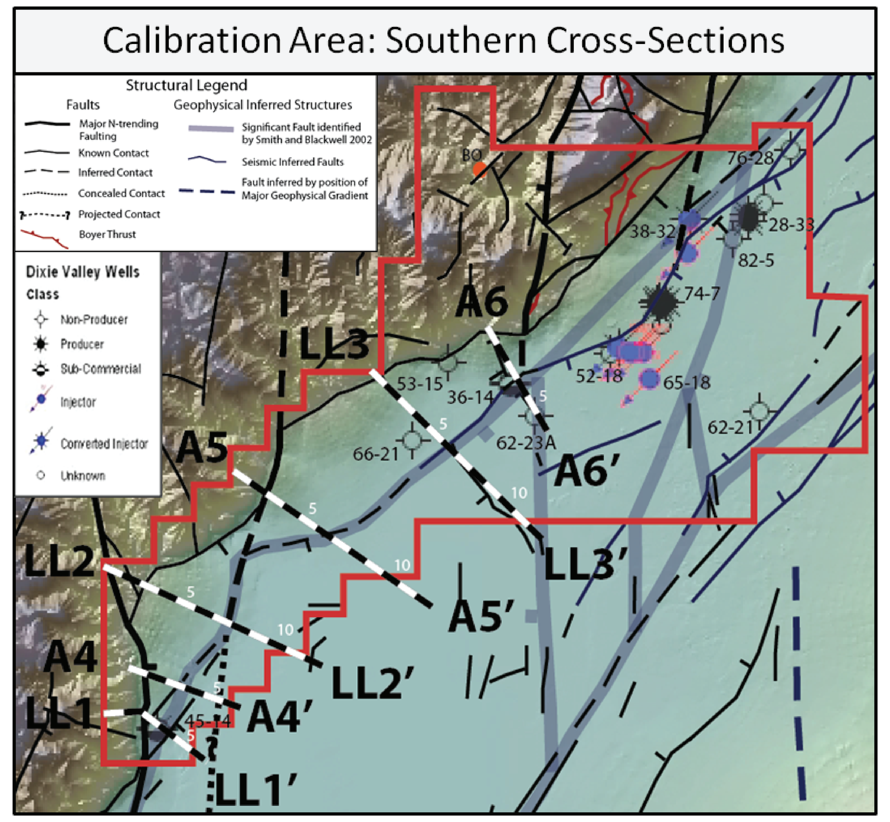

Convective Thermal Model Legend (°C)

- < 100 °C
- 100-150 °C
- 150-200 °C
- 200 °C
- 200-250 °C
- > 250 °C

300, 280, 260, 240, 220, 200, 180, 160, 140, 120, 100, 80, 60, 40, 20

* Temperature contours reflect 10 °C increments

Legend
Thermal Iso-Contours

- 100-150ºC
- 150-200ºC
- 200-250ºC
- 250+ºC

Psuedo-Convective Model Legend

Tconvective = Toverall - Tconductive

- -50° C
- -25° C
- 0° C
- 25° C
- 50 ° C
- 75° C
- 100° C
- 125° C
- No Data

Plate 4. Enhanced Data along NW-SE Oriented Cross-Sections within the Southern Calibration Area

Section | Gravity-Magnetics inferred Lithology | Magnetotellurics: Resistivity Model | Seismic Model: P-wave velocity | Seismic Model: S-wave velocity | Numerical Thermal Model

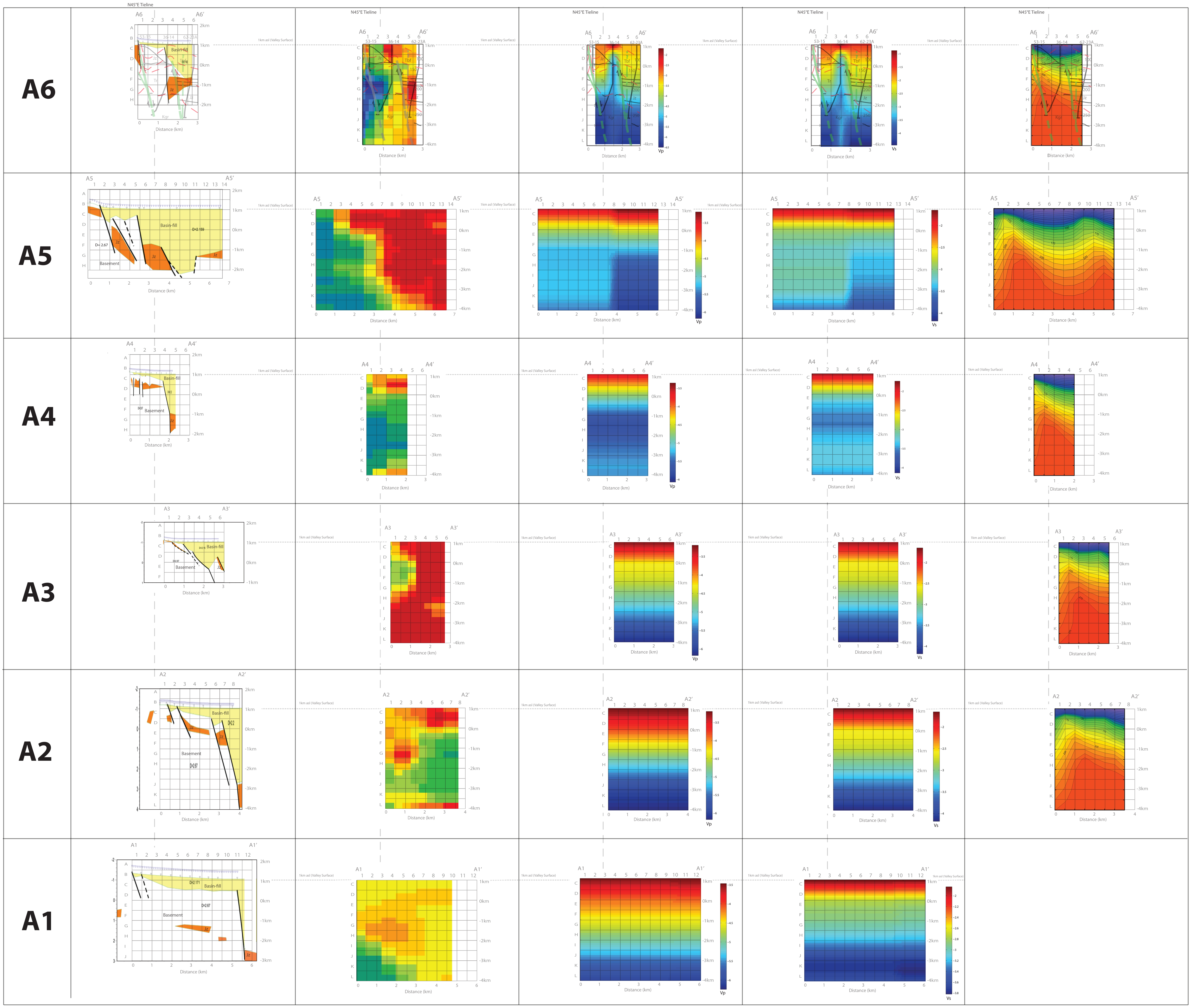

Enhanced Data Legend
Gravity/Magnetic Inferred Lithologic Units

- Tls: Lake Sediments (D= 1.8-1.835)
- Tbf: Basin-filling sediments (D=2.105 - 2.226)
- Jv: Jurassic rhyolite (D= 2.308 - 2.947)
- Jg: Jz igneous group (D=2.67, M=0.007)
- Jg: Jz Igneous group (Off-Axis)
- Bedrock: Tr meta-seds, K granodiorite, Jz non-magnetic rocks (D=2.67)

***Note**
A segment of geologic cross-section C-C' has been overlayed on A6.
See Plate 4 for full line and legend.
The remaining short-lines do not have corresponding geologic cross-sections.

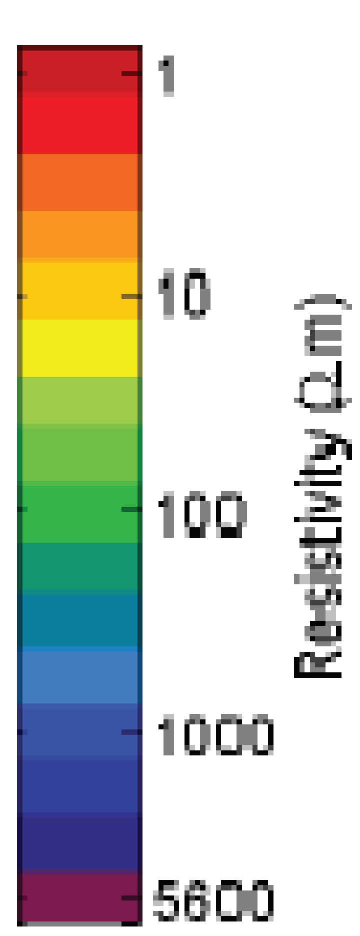

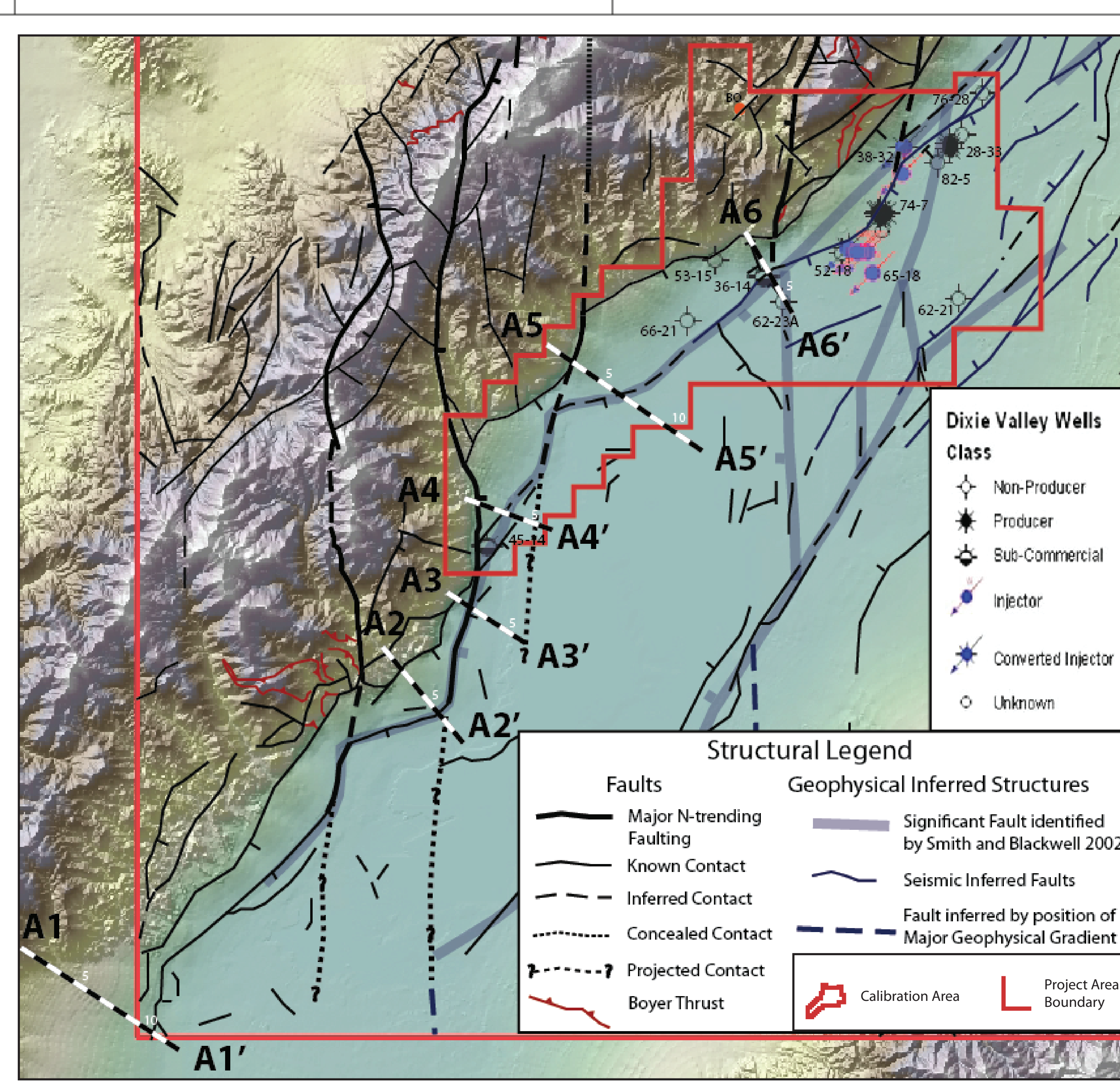

Convective Thermal Model Legend (°C)

- < 100 °C
- 100-150 °C
- 150-200 °C
- 200 °C
- 200-250 °C
- > 250 °C

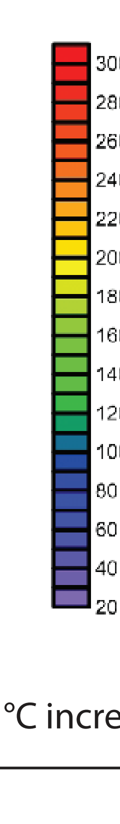

*Temperature contours reflect 10 °C increments

Plate 5. Enhanced Data along NW-SE Oriented "Short-line" Cross-Sections

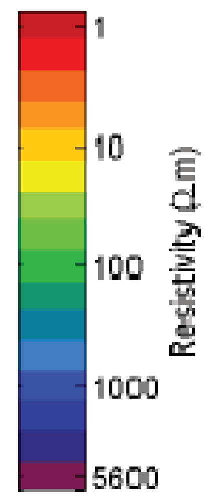

Enhanced Data Legend
Gravity/Magnetic Inferred Lithologic Units

- Tls: Lake Sediments (D= 1.8-1.835)
- Tbf: Basin-filling sediments (D=2.105 - 2.226)
- Jv: Jurassic rhyolite (D= 2.308 - 2.947)
- Jg: Jz igneous group (D=2.67, M=0.007)
- Jg: Jz Igneous group (Off-Axis)
- Bedrock: Tr meta-seds, K granodiorite, Jz non-magnetic rocks (D=2.67)

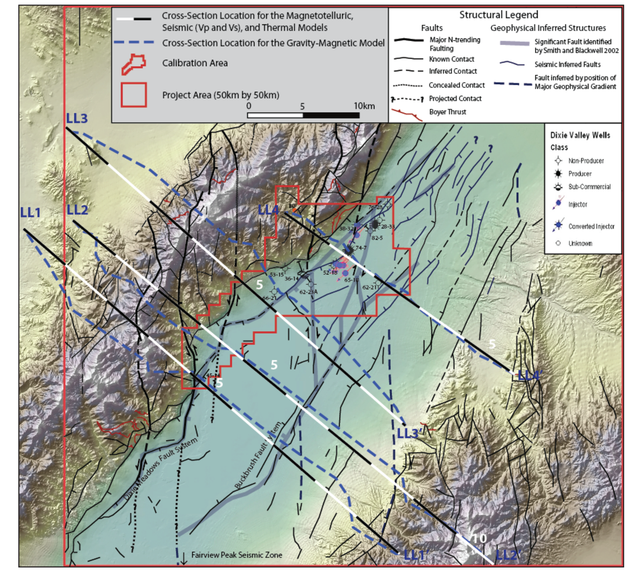

Convective Thermal Model
Legend (°C)

- < 100 °C
- 100-150 °C
- 150-200 °C
- 200 °C
- 200-250 °C
- > 250 °C

300 280 260 240 220 200 180 160 140 120 100 80 60 40 20

* Temperature contours reflect 10 °C increments

Plate 6. Enhanced Data along NW-SE Oriented "Long-line" Cross-Sections